

# **Generating Hydrogen Using Aromatic Systems and Metal Catalytic Centres.**



**This Thesis is Presented for the Degree of  
Doctor of Philosophy**

by

Jennifer Manton B. Sc.

Under the Supervision of:

Dr. Mary Pryce and Prof. Johannes G. Vos

at

School of Chemical Sciences,

Dublin City University,

Glasnevin,

Dublin 9.

**2013**

## Authors Declaration

I hereby certify that this material, which I now submit for assessment on the programme of study leading to the award of Doctor of Philosophy by research and thesis, is entirely my own work, and that I have exercised reasonable care to ensure that the work is original, and does not to the best of my knowledge breach any law of copyright, and has not been taken from the work of others save and to the extent that such work has been cited and acknowledged within the text of my work.

Signed: \_\_\_\_\_

## Jennifer Manton

Candidate I.D. No.: 53486063

Date: 5<sup>th</sup> April 2013

*Dedicated to my parents, for all their love and support.*

*And to Ross, my rock and my best friend.*

## Acknowledgements

First and foremost I would like to thank Dr. Mary Pryce for giving me this huge opportunity. Thank you for all your support and guidance over the past 4 years. You have always been there for direction and encouragement when I needed it the most. Your patience and reassurance has made me feel very lucky to have had this chance to work with you. I would also like to thank Prof. Han Vos for his invaluable advice and expertise. Likewise, thanks to Prof. Conor Long, all your advice was extremely helpful and I promise I will never bring you to a pub with no beer in it again! And to Dr. Danilo Dini for all his help in calculations and catalysis mechanisms.

Many thanks to all the support staff in DCU, without whom I would have gotten nothing done at all; Damien, Veronica, Ambrose, John, Vinnie, Brendan, Catherine, Maurice, Mary and Niamh. None of this work could have happened without your endless support.

To all the amazing people I have had the pleasure of working with over the years; firstly Nikki and Emma, you made me so welcome at the beginning of this process and weren't phased by my "stupid questions" and glassware breaking. We've had so many good times together (sound tracked by Spin 103.8- thanks Emma), great nights out and trips away. I'm so happy you are both off enjoying yourselves elsewhere but I secretly wish you guys were still here! Thanks to Suraj who can always brighten a room with his big smile and who is so kind. And Avi and Nive who have such interesting stories from India and are always ready and willing to help. Thanks to Yvonne for all your advice, I definitely used it all! I would also like to thank Finn, Liam and Suzanne who, although have only started, have made the last few months fun, the lab was getting awfully quiet! I want to say a very special thank you to Jane. We have had loads of fun on trips and conferences but your help over the last year has been so invaluable. I could not have gotten through this without all your advice and our endless chats over tea and toast! Your support in the run up to my viva was incredible. I really don't know how to thank you enough (but I am sorry about the Daily Mail addiction!). A big thanks to Aaron (see I put you first!), Kellie, Susan,



Kieran, Ciarán, Elaine, Shane and Zoe. We definitely killed a few brain cells off in McGowans!

Thank you to my parents, Shane and Barbara. Words can't express my appreciation for everything you have done for me, especially in the last few years. I can't imagine that there are parents who could have supported and encouraged me more in the hard times or been more excited and enthusiastic during the good times. I am the luckiest daughter in the world to have you two as my parents.

To my brother Dave and sister Triona, thanks for the encouraging pep talks and listening to me go on most Thursdays. Now back to big sister chats (I'm looking at you Triona!) and non-science waffle!

And lastly, I would like to thank Ross. You have been my rock, my shoulder to cry on and my biggest support. I am completely lost for words when it comes to thanking you..... You are one in 7 billion! You listened to all of my problems (and there were lots!) and comforted me in the hard times. You lifted me up at every stumbling point. You have been the main reason I have kept going and have gotten to this point. I am eternally grateful for all the millions of things, big and small, that you have done for me, especially over the past 4 years. You have had to put up with grumpy me for a long time now and I can't believe you stuck around (although you had little choice!). Well I'm back now so....eh, I'll do the washing up for the next year. Will that make up for it?!! x

# Table of Contents:

Publications	vii
Poster Presentations	viii
Oral Presentations	viii
Abbreviations	ix
Abstract	xi

## Chapter 1 Introduction

1.1. Hydrogen Production	2
1.1.1. Photosynthesis	4
1.1.2. Artificial Photosynthesis	6
1.1.3. Photocatalytic Hydrogen Production	7
1.1.4. Electrocatalytic Hydrogen Production	11
1.2. Cross Coupling Reactions	17
1.2.1. Early Methods of Sonogashira Coupling	20
1.2.2. New Methods of Sonogashira Coupling	21
1.3. Principals of Photophysics	22
1.4. Electrochemistry	25
1.4.1. The Electrode-Solution Interface	28
1.4.2. Double Layer Capacitance and Current Charging	30
1.4.3. Mass Transfer	31
1.4.4. Cyclic Voltammetry	32
1.4.5. Bulk Electrolysis	35
1.5. Gas Chromatography	36
1.5.1. TCD Detector	39
1.5.2. FID Detector/ Methaniser	40
1.6. Laser Flash Photolysis/Time Resolved Infra-red Spectroscopy	42
1.7. Time Correlated Single Photon Counting	43
Bibliography	46

Aim	53
2.1. Introduction	54
2.1.1. Metal Carbonyls	54
2.1.2. Cobalt Carbonyl	58
2.1.3. Alkyne Bonding with Cobalt Carbonyl	59
2.1.4. Photochemistry of $\mu_2$ -Alkyne-Cobalt Carbonyl Complexes	62
2.1.5. Cobalt Systems Used in Photocatalytic Hydrogen Generation	70
2.1.6. Carbonyl Systems Used in Photocatalytic Hydrogen Generation	73
2.1.7. Electrochemistry of $\mu_2$ -Alkyne-Cobalt Carbonyl Complexes	77
2.1.8. Cobalt Systems Used in the Electrocatalytic Generation of Hydrogen	82
2.1.9. Carbonyl Systems Used in the Electrocatalytic Generation of Hydrogen	87
2.2. Experimental	90
2.2.1. Materials	90
2.2.2. Equipment	90
2.2.3. Photocatalytic Hydrogen Generation Experiments	91
2.2.4. Cyclic Voltammetry	92
2.2.5. Electrocatalytic Hydrogen Generation Experiments	92
2.2.6. Synthesis	93
2.2.6.1. Synthesis of 1-trimethylsilylethynylpyrene (PyrTMS)	93
2.2.6.2. Synthesis of 1-ethynylpyrene (PyrH)	94
2.2.6.3. Synthesis of Pyrene-ethynylferrocene (PyrFc)	95
2.2.6.4. Synthesis of $\mu_2$ -3-ethynylthiophene $\text{Co}_2(\text{CO})_6$ ( $(\mu_2\text{-ThioH})\text{Co}_2(\text{CO})_6$ )	96
2.2.6.5. Synthesis of $\mu_2$ -1-ethynylpyrene $\text{Co}_2(\text{CO})_6$ ( $(\mu_2\text{-PyrH})\text{Co}_2(\text{CO})_6$ )	97
2.2.6.6. Synthesis of $\mu_2$ -Pyrene-ethynylferrocene $\text{Co}_2(\text{CO})_6$ ( $(\mu_2\text{-PyrFc})\text{Co}_2(\text{CO})_6$ )	98
2.2.6.7. Synthesis of $\mu_2$ -1-ethynylferrocene $\text{Co}_2(\text{CO})_6$ ( $(\mu_2\text{-FcH})\text{Co}_2(\text{CO})_6$ )	99
2.2.6.8. Synthesis of $\mu_2$ -3-ethynylthiophene $\text{Co}_2(\text{CO})_4$ DPPM ( $(\mu_2\text{-ThioH})\text{Co}_2(\text{CO})_4\text{DPPM}$ )	100
2.2.6.9. Synthesis of $\mu_2$ -1-ethynylpyrene $\text{Co}_2(\text{CO})_4$ DPPM ( $(\mu_2\text{-PyrH})\text{Co}_2(\text{CO})_4\text{DPPM}$ )	101

2.2.6.10. Synthesis of $\mu_2$ -Pyrene-ethynylferrocene $\text{Co}_2(\text{CO})_4$ DPPM (( $\mu_2$ -PyrFc) $\text{Co}_2(\text{CO})_4$ DPPM )	102
2.2.6.11. Synthesis of $\mu_2$ -1-ethynylferrocene $\text{Co}_2(\text{CO})_4$ DPPM (( $\mu_2$ -FcH) $\text{Co}_2(\text{CO})_4$ DPPM)	103
2.3. Results	104
2.3.1. UV-Vis Spectroscopy	104
2.3.2. IR Spectroscopy	105
2.3.3. Quantum Yields of CO Loss	107
2.3.4. Picosecond Time-Resolved Infra-Red (TRIR) Spectroscopy	110
2.3.5. Photocatalytic Hydrogen Generation Experiments	115
2.3.6. Cyclic Voltammetry	116
2.3.6.1. Reductive Electrochemistry	116
2.3.6.2. Oxidative Electrochemistry	117
2.3.7. Electrocatalytic Hydrogen Generation Experiments	118
2.3.7.1. Onset of Catalytic Current	119
2.3.7.2. $\text{H}_2$ Generation TONs	120
2.4. Discussion	122
2.5. Conclusion	146
Bibliography	148

## Chapter 3 Boron Dipyrromethene-Cobaloxime Complexes

Aim	156
3.1. Introduction	156
3.1.1. Photochemistry of Boron Dipyrromethene Complexes (BODIPYs)	156
3.1.1.2. Electrochemistry of BODIPY Complexes	162
3.1.2. bis(dimethylglyoximate)cobalt <sup>III</sup> Complexes (Cobaloximes)	166
3.1.2.1. Cobaloxime Complexes Used in the Photocatalytic Generation of Hydrogen	167
3.1.2.2. Electrochemistry of Cobaloxime Complexes	172
3.1.2.3. Cobaloxime Complexes Used in the Electrocatalytic Generation of Hydrogen	175

3.2. Experimental	179
3.2.1. Synthesis	179
3.2.1.1. Synthesis of bis(dimethylglyoximate)cobalt(III) (cobaloxime)	179
3.2.1.2. Synthesis of Pyridine-Cobaloxime	180
3.2.1.3. Synthesis of 4-[Bis-(4-ethyl-3,5-dimethyl-1H-pyrrol-2-yl)-methyl]-pyridine-borondifluoride (4-pyridine-BODIPY)	181
3.2.1.4. Synthesis of 3-[Bis-(4-ethyl-3,5-dimethyl-1H-pyrrol-2-yl)-methyl]-pyridine-borondifluoride (3-pyridine-BODIPY)	182
3.2.1.5. Synthesis of 4-BODIPY-Cobaloxime	183
3.2.1.6. Synthesis of 3-BODIPY-Cobaloxime	184
3.3. Results	185
3.3.1. UV-Vis Spectroscopy	185
3.3.2. Fluorescence Spectroscopy	186
3.3.3. Photocatalytic Hydrogen Generation Experiments	187
3.3.4. Cyclic Voltammetry	188
3.3.4.1. Reductive Electrochemistry	188
3.3.4.2. Oxidative Electrochemistry	189
3.3.5. Electrocatalytic Hydrogen Generation Experiments	189
3.3.5.1. Onset of Catalytic Current	190
3.3.5.2. Varying Potentiostatic Electrolysis Potential	191
3.3.5.3. H <sub>2</sub> Generation TONs	193
3.4. Discussion	195
3.5. Conclusion	215
Bibliography	217

## Chapter 4 Porphyrin-Cobaloxime Complexes

Aim	223
4.1. Introduction	223
4.1.1. Porphyrins	223
4.1.1.1. Synthesis of <i>meso</i> -Substituted Porphyrins	224
4.1.1.2. Photochemistry of Porphyrins	227



5.1.1. Pyrene and Ethynylpyrene systems	290
5.1.2. Platinum and Palladium Photocatalysts in Hydrogen Production	296
5.1.2.1. Pt/Pd systems Used in Intramolecular H <sub>2</sub> Production	296
5.1.2.2. Pt/Pd systems Used in Intermolecular H <sub>2</sub> Production	301
5.2. Experimental	306
5.2.1. Synthesis	306
5.2.1.1. Synthesis of 1-trimethylsilylethynylpyrene (Pyrene-TMS)	306
5.2.1.2. Synthesis of 1-ethynylpyrene (Pyrene-H)	307
5.2.1.3. Synthesis of 2-bromo-5-pyren-1-ylethynyl-thiophene (Pyrene-Thio-Br)	308
5.2.1.4. Synthesis of PtCl <sub>2</sub> (DMSO) <sub>2</sub>	309
5.2.1.5. Synthesis of PdCl <sub>2</sub> (DMSO) <sub>2</sub>	310
5.2.2. Attempted Synthesis of Covalently Bound Photosensitisers and Catalytic Centres	311
5.3 Results	325
5.3.1. Synthesis	325
5.3.2. UV-Vis Spectroscopy	325
5.3.3. Fluorescence Spectroscopy	326
5.3.4. Photocatalytic H <sub>2</sub> generation	327
5.4. Discussion	329
5.5. Conclusion	338
Bibliography	339

## **Chapter 6 Concluding Remarks and Future Work** 341

## **Appendix**

A1: Quantum Yield Method	i
A2: Quantum Yield Calculations	iv
B1: Photocatalytic Hydrogen Turnover Number Experiment	x
B2: Photocatalytic Hydrogen Turnover Number Calculations	xii
C1: Electrocatalytic Hydrogen Turnover Number (TON) Experiment	xiv
C2: Electrocatalytic Hydrogen Turnover Number Calculations	xv
D1: <sup>1</sup> H NMR Spectra	xx

## Publications:

- I. P. Clark, M. W. George, G. M. Greetham, E. C. Harvey, C. Long, **J. C. Manton**, H. McArdle and M. T. Pryce, “Photochemistry of ( $\eta^6$ -Anisole)Cr(CO)<sub>3</sub> and ( $\eta^6$ -Thioanisole)Cr(CO)<sub>3</sub>: Evidence for a Photoinduced Haptotropic Shift of the Thioanisole Ligand, a Picosecond Time-Resolved Infrared Spectroscopy and Density Functional Theory Investigation”, *J. Phys. Chem. A*, **2012**, 116, 3, 962-969
- I. P. Clark, M. W. George, G. M. Greetham, E. C. Harvey, C. Long, **J. C. Manton**, and M. T. Pryce, “Photochemistry of ( $\eta^6$ -Arene)Cr(CO)<sub>3</sub> (Arene = Methylbenzoate, Naphthalene, or Phenanthrene) in *n*-Heptane Solution: Population of Two Excited States Following 400 nm Excitation As Detected by Picosecond Time-Resolved Infrared Spectroscopy”, *J. Phys. Chem. A*, **2011**, 115, 14, 2985–2993.
- I. P. Clark, M. W. George, G. M. Greetham, E. C. Harvey, C. Long, **J. C. Manton**, and M. T. Pryce, “Excited State Dynamics and Activation Parameters of Remarkably Slow Photoinduced CO Loss from ( $\eta^6$ -Benzene)Cr(CO)<sub>3</sub> in *n*-Heptane Solution: A DFT and Picosecond-Time-Resolved Infrared Study”, *J. Phys. Chem. A*, **2010**, 114, 43, 11425–11431.
- S. Soman, G. Singh Bindra, A. Paul, R. Groarke, **J. C. Manton**, F. M. Connaughton, M. Schulz, D. Dini, C. Long, M. T. Pryce and J. G. Vos, “Wavelength Dependent Photocatalytic H<sub>2</sub> Generation Using Iridium–Pt/Pd Complexes”, *Dalton Trans.*, **2012**, 41, 12678.
- A. G. Harry, J. Murphy, W. E. Butler, R. Tiedt, A. Mooney, **J. C. Manton**, M. T. Pryce, N. O'Donovan, N. Walsh, J. Crown, D. K. Rai, P. T. M. Kenny, “The synthesis, structural characterization and *in vitro* anti-cancer activity of novel *N*-{6-(ferrocenyl) ethynyl-2-naphthoyl} amino acid and dipeptide ethyl esters”, *J. Organomet. Chem.*, Article in Press.



## Poster Presentations

- **J. C. Manton**, H. G. Vos, M. T. Pryce, “Novel Organometallic-Pt Photocatalysts for Intermolecular Catalytic Hydrogen Generation from Water.” Presented at The International Symposia on Advancing the Chemical Sciences -Challenges in Renewable Energy (ISACS4) in MIT, Cambridge, Massachusetts, 4-7<sup>th</sup> July 2011.

## Oral Presentations

- “Photocatalytic Generation of Hydrogen”. Presented at the annual EPA Postgraduate Conference in The Gresham Hotel, Dublin, 17<sup>th</sup> November 2011.

## Abbreviations

**<sup>1</sup>H NMR:** Proton nuclear magnetic resonance

**<sup>13</sup>C NMR:** Carbon nuclear magnetic resonance

**ACN/ MeCN:** Acetonitrile

**Ag/AgCl:** Silver/silver chloride reference electrode

**BODIPY:** Boron dipyrromethene

**Bpy:** Bipyridine

**CDCl<sub>3</sub>:** Deuterated chloroform

**Cobaloxime:** bis(dimethylglyoximate)cobalt<sup>III</sup>

**CoPc:** Cobalt phthalocyanine

**Co<sub>2</sub>(CO)<sub>4</sub>DPPM:** Dicobalt pentacarbonyl bis(diphenylphosphino)methane

**Co<sub>2</sub>(CO)<sub>6</sub>:** Dicobalt hexacarbonyl

**Co<sub>2</sub>(CO)<sub>8</sub>:** Dicobalt octacarbonyl

**CuI:** Cuprous iodide/ Copper(I) iodide

**DCM/ CH<sub>2</sub>Cl<sub>2</sub>:** Dichloromethane

**DFT:** Density functional theory

**DMF:** Dimethylformamide

**DPPM:** bis(Diphenylphosphino)methane

**DSSC:** Dye sensitised solar cell

**fs:** femtosecond

**gc:** Glassy carbon electrode

**GC:** Gas chromatograph

**IL:** Intraligand

**IR:** Infra-red spectroscopy

**LMCT:** Ligand-metal charge transfer

**MLCT:** Metal-ligand charge transfer

**N<sub>2</sub>:** Nitrogen gas

**NiO:** Nickel oxide

**ns:** Nanosecond

**OEC:** Oxygen evolving catalyst

**ps:** Picosecond

**PS:** Photosensitiser

**PS<sub>I</sub>**: Photosystem 1  
**PS<sub>II</sub>**: Photosystem 2  
**Pet Ether**: Petroleum ether  
**SA**: Sacrificial agent  
**SCE**: Saturated calomel reference electrode  
**SHE**: Standard hydrogen electrode  
**TEA/Et<sub>3</sub>N**: Triethylamine  
**TEOA**: Triethanolamine  
**TFA**: Trifluoroacetic acid  
**THF**: Tetrahydrofuran  
**TiO<sub>2</sub>**: Titanium oxide  
**TR-IR**: Time resolved infra-red spectroscopy  
**UV-Vis**: Ultra violet- visible spectroscopy.

## Abstract

Chapter one presents a detailed literature survey which is relevant to the complexes which were developed for the generation of hydrogen, both photocatalytically and electrocatalytically in this thesis. Also discussed are the methods used throughout the research together with the principals of photophysics and electrochemistry.

Chapter two begins with a short literature survey covering cobalt carbonyl complexes. The bonding, preparation and photochemistry of these complexes are discussed. Also included are cobalt complexes that have been reported in hydrogen generation. The synthetic procedures employed to prepare a number of alkynyl ligands and their cobalt hexacarbonyl and cobalt tetracarbonyl-diphenylphosphinomethane derivatives are discussed.  $^1\text{H}$  NMR,  $^{13}\text{C}$  NMR, elemental analysis, UV-vis spectroscopy, IR spectroscopy, and fluorescence spectroscopy were used, where applicable. Time resolved infra-red spectroscopy experiments were also performed. This is the first time that time resolved studies have led to the detection of a CO loss species for an  $\mu^2$ -alkynyl cobalt carbonyl complex. The results of cyclic voltammetry studies are presented along with the results of both photocatalytic and electrocatalytic approaches for hydrogen generation.

Chapter three begins with a concise literature survey focusing on the synthetic procedures which have been employed in the synthesis of boron-dipyrromethene (BODIPY) dyes and bis(dimethylglyoximate)cobalt<sup>III</sup> (cobaloxime) complexes. Briefly discussed are the photochemical and electrochemical properties of some relevant BODIPY-cobaloxime systems. A number of BODIPYs photosensitisers and cobaloxime catalytic centres which have been used for the photogeneration and electrogeneration of hydrogen previously are included. The synthetic procedures employed to prepare two BODIPY dyes and the addition of cobaloxime to the ligands are discussed.  $^1\text{H}$  NMR,  $^{13}\text{C}$  NMR, elemental analysis, UV-vis spectroscopy, IR spectroscopy, and fluorescence spectroscopy were used. The results of cyclic voltammetry studies are presented along with the results of both photocatalytic and electrocatalytic hydrogen generation studies.

Chapter 4 begins with a short literature survey on the synthetic procedures which have been employed in the synthesis of porphyrin dyes and their attachment to bis(dimethylglyoximate)cobalt(III) (cobaloxime) which have been previously reported. Briefly discussed are the photochemical and electrochemical properties of some similar porphyrin-cobaloxime systems which have been reported by other groups. The synthetic procedures employed to prepare three porphyrin dyes and the additions of cobaloxime to the ligands are discussed. Again,  $^1\text{H}$  NMR,  $^{13}\text{C}$  NMR, elemental analysis, UV-vis spectroscopy and fluorescence spectroscopy were used, where applicable, to characterise the final pure products. The results of cyclic voltammetry studies are presented along with the results of both photocatalytic and electrocatalytic approaches for the generation of hydrogen.

Chapter 5 begins with a short introduction to pyrene, showing some of its uses. The literature survey concludes with a look at platinum and palladium catalysts used in experiments for the photocatalytic generation of hydrogen. The synthetic procedures employed to prepare porphyrin photosensitisers and the platinum and palladium catalytic centres are discussed. Also included are synthetic procedures for intramolecular complexes which were endeavoured but proved unsuccessful throughout the study.

# **Chapter 1**

## **Introduction**

Chapter 1 serves as a general introduction. It introduces the main principles and methods used throughout this investigation. An overview of the compounds which were used in both the photochemical and electrochemical generation of hydrogen is discussed. Cross-coupling reactions are discussed along with a brief introduction to photophysics, laser flash photolysis, time resolved infra-red spectroscopy and gas chromatography.

The main aim of this thesis is to synthesise and analyse novel compounds with the aspiration that they could be utilised in the photocatalytic and electrocatalytic production of hydrogen from water. Complexes were designed utilising the combination of an organic photosensitiser and an earth abundant metal for use as a catalytic centre which could be readily synthesised in large amounts for commercial use. Ideally these complexes should be cheaper to produce than those presently used in hydrogen generation. Traditionally catalytic systems for hydrogen generation have been based on precious transition metals such as ruthenium, iridium, platinum and palladium. These systems have been shown to generate large amounts of hydrogen and the development of a system with non-noble metals must achieve similar results to be feasible for commercial development.

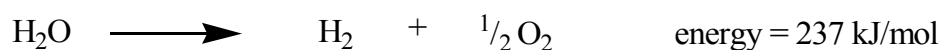
## **1.1 Hydrogen Production**

One of the greatest challenges of our time is finding a renewable and sustainable energy source. Most pressing is that this energy source must be clean and reliable to both produce and use. With the rapid population increase and technological advances in the last century our energy demands have put an ever increasing strain on important natural resources. Energy has been traditionally produced by the combustion of fossil fuels which leads to the emission of destructive “greenhouse gasses” such as carbon dioxide and methane into the atmosphere. In 2005, 86% of the energy produced in the world was produced through the combustion of petroleum, coal or natural gas<sup>1</sup>. These fuels are unsustainable, environmentally unfriendly and, at current times, in increasingly short supply due to depletion of natural reserves and political pressures within the countries in which they are located. Further industrial growth worldwide and larger populations will only lead to a higher demand for energy which is supplied by these fossil fuels; however, the detrimental nature of the by-products to the environment dictates that this energy source must be supplemented or even replaced by renewable and sustainable resources<sup>2</sup>.

Energy can, and has been, created through sustainable routes including; hydroelectricity, tide/ocean power, geothermal energy, biomass and wind power however the energy generated in these ways has by no means been sufficient to

supply the world's demand and compete with the energy provided through the combustion of fossil fuels. Sunlight is one of the few potential energy sources which could be utilised to replace traditional energy sources as it is the most abundant energy source at the world's disposal at this time. In fact the energy received by the earth from the sun is a four orders of magnitude greater than our current energy consumption. A system which would utilise this great natural and sustainable resource and convert it to usable energy would be the ideal answer to the current energy problem.

Hydrogen is an ideal energy carrier as it produces minimal emissions when combusted and little or no emissions when electrochemically converted to electricity in a fuel cell.<sup>3</sup> About three million joules of energy can be generated from splitting one litre of water.



**Reaction 1.1- Energy produced from water splitting.**

Utilising sunlight to generate hydrogen as useable energy, presents itself as an ideal resource to resolve the problems detailed above. Hydrogen can potentially replace fossil fuels as the energy carrier for transportation uses and in fuel cells for electrical energy generation when non-renewable energy becomes unavailable. Hydrogen is also potentially transportable by gas pipelines or can be generated on site and the only product of combustion of  $\text{H}_2$  is water.<sup>4</sup> Although hydrogen itself is the most abundant energy source in the universe it is not found readily in its elemental form. It is mainly found, on earth, bonded to oxygen to form water or locked in hydrocarbons. The use of the latter is less desirable as the extraction of hydrogen from hydrocarbons results in the release of carbon monoxide<sup>5</sup>; a highly poisonous gas, or carbon dioxide, one of the main causes of global warming. Utilising solar energy to induce the splitting of water to produce hydrogen is presently of great interest, especially with the further advancements in fuel cell technology of the last decade. Utilising hydrogen in a fuel cell has shown great potential, with low environmental impact.

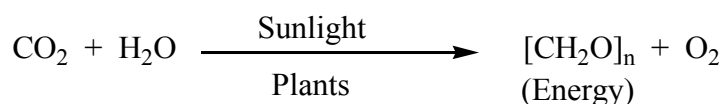
One of the major limiting factors in using hydrogen as a fuel is that it occupies a large amount of space in its gaseous form. A gram of hydrogen gas occupies about



11 litres (2.9 gallons) of space at atmospheric pressure, so for convenience the gas must be intensely pressurised to several hundred atmospheres and stored in a pressurised vessel.<sup>6</sup> This means that much of the energy produced will be utilised in maintaining high pressures to contain the hydrogen fuel which leads to inefficiencies when accounting for energy produced. Hydrogen must be stored under cryogenic temperatures to keep it in the liquid form. This is not practical for use in everyday items such as cars and for use in the home. The technology to safely and efficiently store hydrogen is key to the realisation of a hydrogen economy.

### 1.1.1 Photosynthesis

Photosynthesis and respiration provide the blueprints for artificial photosynthetic infrastructures based upon the conversion of solar energy to usable energy. The major chemical pathway in photosynthesis is the conversion of carbon dioxide and water to carbohydrates and oxygen (Rxn 1.2).



**Reaction 1.2 - Photosynthetic reaction pathway.**

The oxygen produced is released into the atmosphere where we use it to breathe, burn fuels etc. During photosynthesis the hydrogen produced is combined with carbon dioxide to make sugars and other organic molecules for use as energy in the plant. Applying the first steps used in photosynthesis forms the basis of much research aimed at hydrogen generation through the splitting of water.

Photosynthesis utilises a green coloured dye known as chlorophyll as its light harvesting moiety. Solar energy is absorbed by a series of dyes consisting of chlorophylls, carotenoid polyenes and other tetrapyrrole pigments, these make up the antenna like light harvesting complex II (LHC II). The resulting excitation energy is transferred efficiently to the chlorophyll-based primary electron donor and an excited-state electron transfer initiates a cascade of dark electron transfers that result in a movement of an electron and “hole” to opposite sides of a membrane. Two

photons of light are required to transfer just one electron from PS<sub>II</sub> (photosystem II) through a cytochrome complex to PS<sub>I</sub>. PS<sub>II</sub> is involved in the hydrogen generation within the plant, where hydrogen is stored as NADPH for use as energy within the plant. The “hole” is passed from the donor side of PS<sub>II</sub> to the oxygen evolving complex (OEC). Here four oxidising equivalents are collected and the elemental oxygen and four protons ( $4\text{H}^+$ ) are formed through the dissociation of two water molecules. Water is split when the excited  $\text{P680}^{\cdot+}$  species in PS<sub>II</sub> attracts electrons from the catalytic centre which is comprised of four manganese ( $\text{Mn}^{2+}$ ) ions and one calcium ( $\text{Ca}^{2+}$ ) ion. This  $\text{Mn}_4\text{Ca}$  cluster acts as a store of positive charge.

On the opposite side of the membrane at PS<sub>I</sub> the four electrons which have been liberated during the dissociation of water are eventually used to produce energy stores for the organism in the form of NADPH (the protonated form of nicotinamide adenine dinucleotide phosphate).

The components of PS<sub>II</sub> consist of chlorophyll-a (P680) and pheophytin-a (Pheo) which is a chlorophyll molecule which does not contain a magnesium ion coordinated to the tetrapyrrole ring.

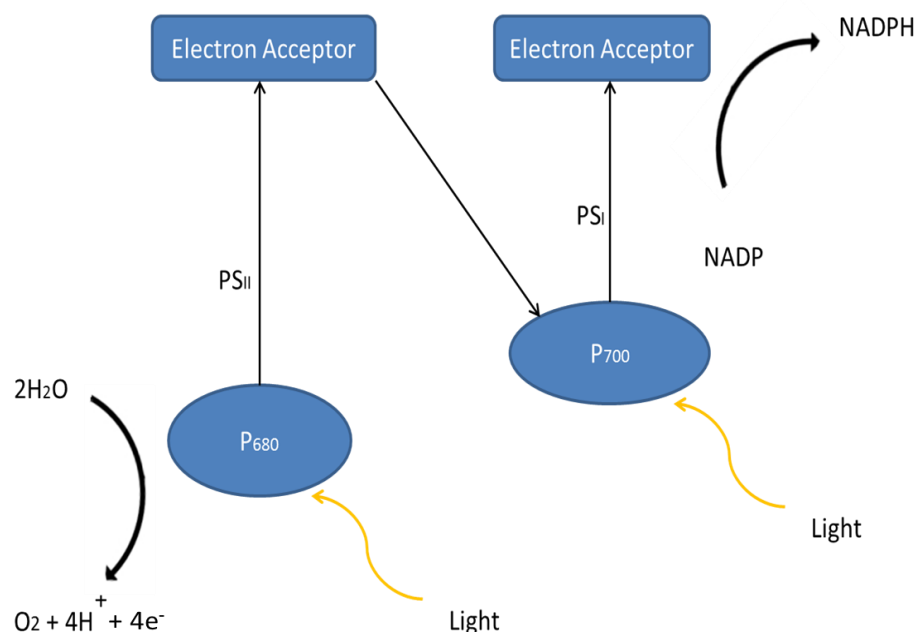


**Figure 1.1 - Simple Z-scheme diagram of light reactions in photosynthesis.**

As shown in the z-scheme shown in Fig. 1.1 the initial conversion of light occurs in PS<sub>II</sub>. Here the light induces an electrochemical potential which generates a radical pair between P680<sup>•+</sup> and Pheo<sup>•-</sup>. This reducing equivalent is passed along a series of molecules comprising an electron transport chain and eventually delivered to P700, a component of PS<sub>I</sub>. Here the reducing equivalent is excited yet again by another photon of light and it is used to oxidise NADP to form NADPH.

### 1.1.2 Artificial Photosynthesis

Natural photosynthesis provides an ideal model to design a system which can cleanly and efficiently generate hydrogen for use as energy through harnessing sunlight. Such a system should mimic the molecular organisation of the natural photosynthetic process. With this in mind there would need to be two components to the system; an elemental oxygen evolving component (like PS<sub>II</sub>) and a component capable of generating elemental hydrogen (similar to PS<sub>I</sub>). For this system to be successful charge separation between both components must occur. A model system is presented in Fig. 1.2.

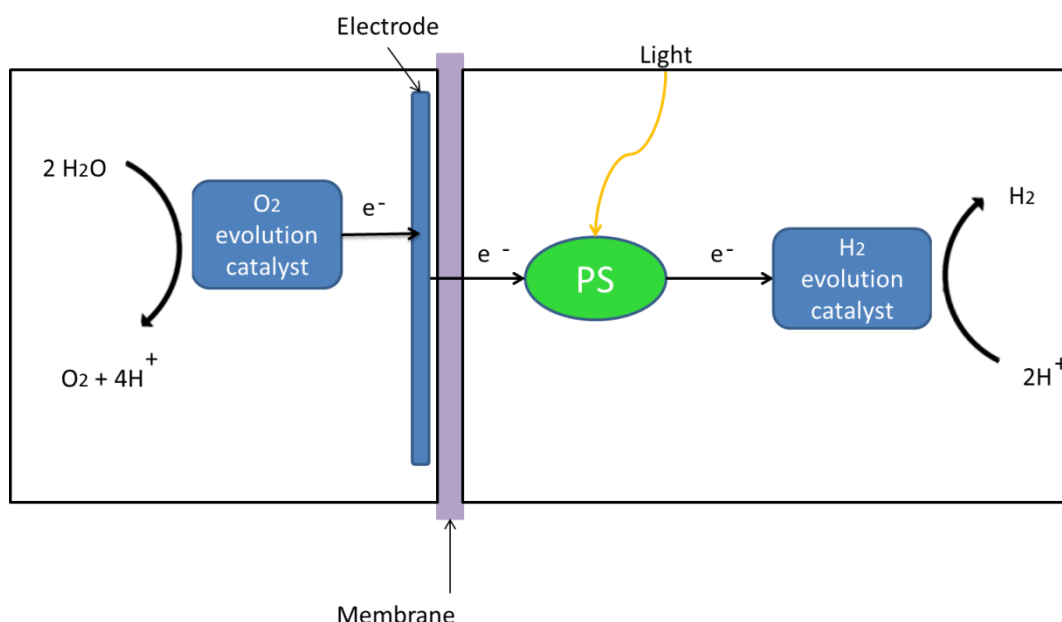


**Figure 1.2 - Schematic representation of artificial photosynthesis. PS = photosensitiser**

Within this model efficient hydrogen production depends on the utilisation of supramolecular structures with precisely designed excited states and redox potentials. Also important are rates of electron transfer (due to competing processes) and the orientation of the complexes in space. Once the  $4\text{H}^+$  ions are formed in the oxygen evolving process, these protons would then move through the membrane to the hydrogen evolving catalytic centre to produce  $\text{H}_2$ .

### 1.1.3 Photocatalytic Hydrogen Production

This study is focused on the hydrogen evolving catalytic process, however a great deal of studies have been based on the oxygen evolving catalyst in recent times.<sup>7,8,9,10</sup> Molecules designed and synthesised for the intramolecular studies carried out in this study are based on the proposed model below (Fig. 1.3)

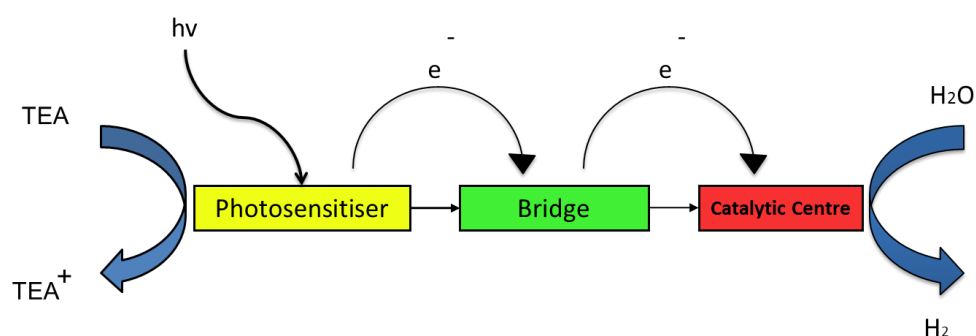


**Figure 1.3 - Proposed model of molecules designed for the generation on hydrogen from water.**

As with natural photosynthesis, there is a light absorbing photosensitiser and a catalytic centre. The photosensitiser consists of a highly conjugated system, which will absorb light and consequentially an electron will become excited. This newly excited electron will then be transferred to a bridging ligand and then on to the catalytic centre where it will be used to split water to produce hydrogen. The electron utilised from the photosensitiser is replenished using a sacrificial donor, in this case triethylamine (TEA). This process will occur twice to yield one molecule of  $\text{H}_2$ . An example of a system based on this model is shown below (Fig. 1.4)

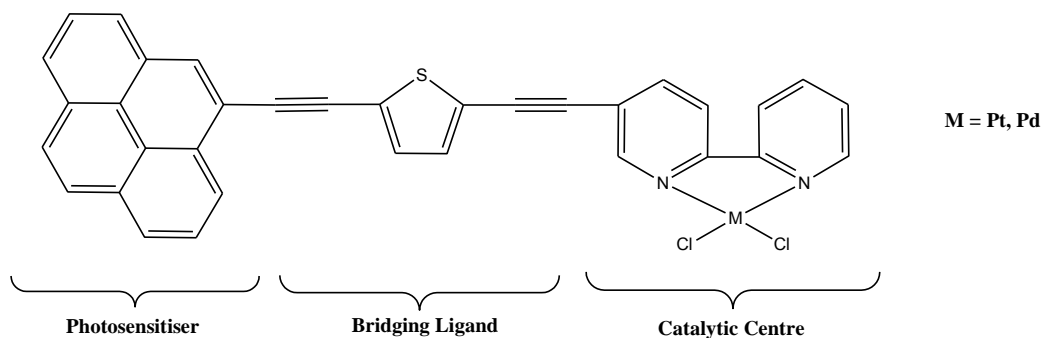


**Figure 1.4 - Model system for the generation of hydrogen**

The design of the photosensitiser and bridging ligand is very important. The bridging ligand must be carefully designed so that the HOMO-LUMO energy difference is lower than that of the photosensitiser to aid the flow of electrons through the system without the need for external factors such as heat. This is also necessary with regard to the catalytic centre; the HOMO-LUMO energy difference of the catalytic centre must be lower in energy again than the bridging ligand.

In this study organic photosensitisers were mainly used. These molecules should be cheaper to produce than their transition metal counterparts and generally can also have a higher absorption coefficient. Due to the ease of addition of various substituents to organic photosensitisers, their absorbances can be tailored towards the near infra-red region.

#### ***1.1.3.1. Dye Sensitised Solar Cells***

The central processes in natural photosynthesis are light-driven electron transfer from a special pair chromophore (porphyrin structures) to the primary acceptor, and the subsequent charge separation to enable the reduction of substrates e.g. water<sup>11</sup>. Utilising light as a source of energy is promising as the energy received by the earth in one hour is more than that which is consumed by the entire population in one year<sup>12</sup>. Using this as a basis many artificial systems have been developed which are involved in the photocatalytic reduction of carbon dioxide and the production of hydrogen.

The photocatalytic splitting of water employs light and a semiconductor surface to produce hydrogen. Semiconductor surfaces such as  $\text{TiO}_2$  can produce  $\text{H}_2$  photocatalytically using the Honda-Fujishima effect as the semiconductor is capable

of hydrolysing water itself. Coordination of a dye to the semiconductor surface allows a wider range of wavelengths be utilised. Organometallic catalytic systems will play a large role in the discovery of novel methods of hydrogen generation over the next century, specifically low cost molecules using non-precious metals. In the Grätzel cell, metal containing dye molecules which are bound to a surface consisting of a nanocrystalline metal-oxide (e.g. NiO, TiO<sub>2</sub>). The dyes absorb visible light and when excited pass an electron from the valence band of the dye to the conduction band of the metal-oxide inducing a current of electrons. As a result of these cells being produced from abundant metal oxides, especially TiO<sub>2</sub>, and the use of more cost effective dyes, rather than expensive and rare metals, the scaling up and commercialisation of these types of cells is a lot more feasible. Also many DSSCs are known to work in diffuse light. This means that they can avail of dawn and dusk hours and also be more competitive in replacing fossil fuels in the non-equatorial regions of the world.

Ruthenium based dyes have been the most popular photosensitiser for generating H<sub>2</sub>. Some of the earliest uses were reported in the late 1970's by Lehn and his co-workers.<sup>13</sup> They used a ruthenium polypyridyl photosensitiser, a rhodium bipyridine bridging molecule, colloidal platinum as the photocatalytic centre and triethanolamine (TEOA) as the sacrificial agent. Another group lead by Ling Zan<sup>14</sup> have reported on three different ruthenium dyes, one bimetallic and two monometallic, which have been shown to produce H<sub>2</sub> using methanol electron donors and platinum (Pt) catalytic centres. The dyes were attached to TiO<sub>2</sub> with three different linkage modes; (1) a traditional carboxylic acid linkage through two peripheral ligands, (2) a linkage of the TiO<sub>2</sub> to two nitrogen groups on two peripheral ligands, and (3) a direct metal Ru-TiO<sub>2</sub> linkage coupled with a C-TiO<sub>2</sub> linkage on a peripheral ligand. Their experimentation lead them to report that each dye showed different photosensitisation effects due to the different coordination of the dyes with the TiO<sub>2</sub> surface. Although no turnover numbers (TONs, number of moles of H<sub>2</sub> produced/ number of moles of catalyst) were quoted the dye tightly linked with TiO<sub>2</sub>, directly through the Ru centre, had the best durability against photodegradation but the lowest H<sub>2</sub> evolution efficiency, however the two more loosely attached dyes lead to higher H<sub>2</sub> evolution efficiencies and a reasonable durability. The binuclear Ru<sup>II</sup> dye shows better photosensitisation in comparison with mononuclear Ru<sup>II</sup> dyes due

to its greater conjugation which improves the visible light harvesting and electron transfer between the dye molecules and TiO<sub>2</sub>.

#### ***1.1.3.2. Supramolecular Photocatalytic Systems***

Another approach to solar cells has been to more closely mimic the natural processes and organisation of photosynthesis i.e. utilising a light harvesting chromophore leading to charge separation with the movement of energy to catalytic centres where the hydrogen, and oxygen, can occur. This study is concerned with the hydrogen production centre and so this aspect of the solar cell is further discussed.

A large amount of research has been based around the use of transition metals in catalytic centres with multi-ringed ligands as photosensitisers (the dyes). Most of the research has been centered on the use of ruthenium which shows a solar energy to electricity conversion rate of up to 11%.<sup>15</sup> Other systems have been based on iridium,<sup>16</sup> rhenium,<sup>17</sup> platinum,<sup>18</sup> osmium,<sup>19,20</sup> copper<sup>21</sup> and iron.<sup>22</sup>

Toshima *et al.*<sup>23</sup> have used a chromophore based on ruthenium coupled with a platinum catalytic centre to generate hydrogen from water in visible light. The electron transfer system consisted of a ruthenium tris-bipyridine dichloride light harvesting centre with a methyl viologen dichloride bridging molecule and a metal cluster of platinum as the catalytic centre. They measured high electron transfer rates leading to a high turnover of hydrogen produced. Especially in intramolecular H<sub>2</sub> generation between the Ru dye and the Pt catalytic centre which demonstrate a  $k_{H_2}$  (hydrogen generation constant) of 0.8 when compared to the intermolecular H<sub>2</sub> generation between unbound Ru chromophore and a Pt catalyst with  $k_{H_2}$  of 0.58.

Recently Bernhard<sup>24</sup> reported very large TONs of between 800 and 8300 when using an iridium dye containing a pendant pyridyl moiety with a platinum catalytic centre (Fig. 1.5). By varying the ligand complexed with the Ir photosensitiser it was found that 4,4':2',2'':4'',4'''-quaterpyridyl (qpy) gave the highest TON of 8300 in THF when irradiated with blue light in the presence of 20% H<sub>2</sub>O, and 13% TEA.

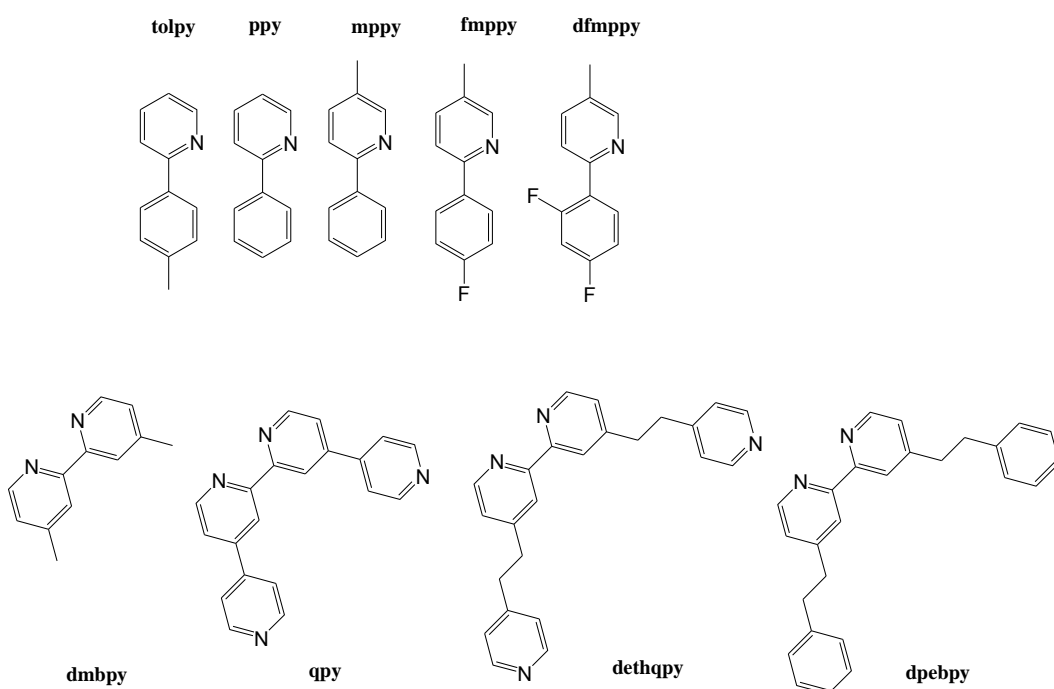


**Figure 1.5 – Pyridyl ligands complexed to an iridium metal centre by Bernhard et al<sup>24</sup> 2-p-tolylpyridine (tolpy), 2-phenylpyridine (ppy), 5-methyl-2-phenylpyridine (mppy), 2-(4-fluorophenyl)-5-methylpyridine**

**(fmppy), 2-(3,4-difluorophenyl)-5-methylpyridine (dfmppy), 4,4'-dimethyl-2,2'-bipyridyl (dmbpy), 4,4':2',2'':4'',4'''-quaterpyridyl (qpy), 4,4'-bis(2-(pyridin-4-yl)ethyl)-2,2'-bipyridine (dethqpy) and 4,4'-bis(phenylethynyl)-2,2'-bipyridine (dpebpy).**

Further examples of these systems are discussed in chapters 2, 3, 4, and 5. Many different dyes have been used including those from natural sources such as mulberry, blueberry, and jaboticaba's skin.<sup>25</sup> These types of cells would be even more environmentally friendly than those mentioned above but commercial synthesis of these dyes may be problematic due to their complex structures and extraction from their natural source is expensive.

#### 1.1.4. Electrocatalytic Hydrogen Production

As mentioned previously molecules which have been synthesised in this study have been modelled using a photosensitiser, to absorb light, a bridging group, to facilitate efficient electron transfer, and a catalytic centre based on an earth abundant metal. Despite the amount of energy provided by the sun and the harnessing of it efficiently



is promising, sunlight is an intermittent source of energy. This means that energy produced would have to be stored for use at night or in diffuse sunlight situations. Water electrolysis is a well-established method to produce hydrogen, and oxygen, from water. First utilised in the late 1700's this method involves the use of expensive electrodes such as platinum and carried out at high temperatures up to 100 °C. Developing an electrocatalytic system which produces net energy gains is the next step to sustainable energy which can be produced *in situ* and so avoids storage and transportation costs.

When discussing electrocatalytic generation of hydrogen the compounds are immobilised on to electrode surfaces. The efficiency of these now modified electrodes is often discussed with respect to the nature of the complex, the electrodes used and also the electrolytes used. Two techniques are commonly used to immobilise the compounds onto the electrode surface. One such method is drop-casting of catalyst solutions, while the other is the use of chemical/ electrochemical reactions to generate covalent bonds between the catalyst and the electrode surface itself. Electrocatalysis with surface modified electrodes will be discussed in more detail. A comprehensive review has been recently published with regard to electrocatalytic hydrogen generation using modified surfaces.<sup>26</sup>

#### ***1.1.4.1. Transition metal catalysts***

Surfaces modified with various transition metals has been widely investigated. Much of the research has been focused on the expensive and rare ruthenium compounds, however some groups have focused on research using more earth abundant metals or dimetallic systems incorporating ruthenium and a cheaper metal. The use of ruthenium purple ( $\text{Fe}_4[\text{Ru}(\text{CN})_6]_3$ ) as an electrocatalyst for  $\text{H}^+$  reduction has also been reported.<sup>27</sup> Ru purple was electrodeposited onto a basal-plane pyrolytic graphite (BPG) plate as working electrode and the cell was equipped with a spiral platinum wire and an Ag/AgCl reference electrode. A TON of  $51 \times 10^3$  was reported after one hour when potentiostatic electrolysis was carried out at -0.8 V in a  $\text{H}_3\text{PO}_4 + \text{NaH}_2\text{PO}_4$  ( $\text{Na}^+ = 0.1 \text{ mol L}^{-1}$ ) buffer solution at pH 1.5, where TON refers to the number of moles of  $\text{H}_2$  that a single mole of catalyst can produce during a given experiment. The authors suggested that the cyanide ions from the Ru purple work as

the active sites for proton reduction by coordinating the protons allowing them to be reduced to H<sub>2</sub>.

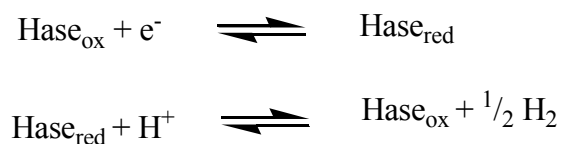
In 1997, Abe *et al.*<sup>28</sup> utilised Prussian white, K<sub>4</sub>Fe<sub>2</sub>[Fe(CN)<sub>6</sub>]<sub>3</sub>, as the catalyst in electrocatalytic proton (H<sup>+</sup>) reduction. The Prussian white was coated on a platinum (Pt) electrode and reportedly produced 12 times the amounts of H<sub>2</sub> than the bare electrode alone. Potentiostatic electrolysis was carried out at -0.274 V using the coated platinum electrode, a spiral platinum wire and an Ag/AgCl reference electrode in a pH 1.35 aqueous buffer containing 0.05M KCl. 6.35 μL and 0.23 μL of hydrogen were produced in one hour with the coated and bare electrodes respectively. An experiment using the same set up with potentiostatic electrolysis at -0.8 V vs. Ag/AgCl produced a TOF of 67 h<sup>-1</sup>, where TOF refers to TON per unit time.

Cu/Pt nanoparticles have been used to modify glassy carbon electrodes with the aim to produce hydrogen.<sup>29</sup> A Cu/Pt composite was fabricated on the surface of the electrode by electropolymerisation of poly(8-hydroxyquinoline) on the surface followed by incorporation of Cu<sup>2+</sup> ions through immersing the electrode in a solution of Cu<sup>II</sup> ions for 1 hour followed by an electrochemical reduction to -0.9 V vs. SCE. The copper loaded electrode was dipped in a 0.02 M PtCl<sub>4</sub> solution for 30 min in order to replace the metallic copper with Pt. No TONs were quoted however it was observed that the onset of the catalytic current was at a more positive potential than that of a bare glassy carbon electrode or the electrode modified with just the Cu.

#### **1.1.4.2. Macrocyclic Complexes:**

Zhao *et al.*<sup>30</sup> have reported electrocatalytic proton reduction by phthalocyanine cobalt derivatives incorporated in poly-4-vinylpyridine-co-styrene (P(VP-St)) films which films were coated onto a graphite electrode. The non-substituted cobalt phthalocyanine (CoPc), oct-cyanophthalocyanine cobalt(II) (CoPc(CN)<sub>8</sub>) and tetrasulfonatophthalocyanine cobalt(II) (CoPc(SO<sub>3</sub>H)<sub>4</sub>) were all investigated for their hydrogen generation efficiency. The researchers reported hydrogen generation in terms of TON for the series CoPc < CoPc(CN)<sub>8</sub> < CoPc(SO<sub>3</sub>H)<sub>4</sub>, with CoPc(SO<sub>3</sub>H)<sub>4</sub> yielding a TON of 2 x 10<sup>5</sup> h<sup>-1</sup>. Electron propagation through the polymer matrix was studied and it was found that the electron transfer process occurs through diffusion

mechanism and the diffusion coefficient decreased in the same order;  $\text{CoPc} < \text{CoPc}(\text{CN})_8 < \text{CoPc}(\text{SO}_3\text{H})_4$ . Phthalocyanines bearing thiophene moieties have been used for the electrocatalytic generation of hydrogen using water.<sup>31</sup> 2,9,16,23-tetrakis-6-(thiophene-2-carboxylate)-hexylthio-phthalocyaninato-zinc(II), copper(II) and cobalt(II) complexes were synthesised and glassy carbon working electrodes were modified with these CoPc, ZnPc and CuPc complexes. Electrocatalytic studies were carried out in  $0.1 \text{ mol dm}^{-3}$  NaCl in an aqueous phosphate buffer at different pHs with a platinum wire counter electrode and an SCE (saturated calomel electrode) reference electrode. The CoPc derivative showed the greatest electrocatalytic potential, with ZnPc having a much reduced potential while CuPc shows almost no activity. The author attributed the differences in activity to the redox differences of the complexes. CoPc has a metal-based reduction process, while ZnPc and CuPc have only ligand-based processes in the potential window of 0V to -1.5 V vs. SCE. Catalytic proton reduction occurred -1.02 V when using the CoPc modified electrode, representing a 0.04 V reduction in potential applied when compared to the bare electrode at pH 2.4 while also showing a significantly higher catalytic current. Lojou *et al.*<sup>32</sup> developed a system which was modelled on nature but incorporated naturally occurring enzymes also. They have extracted two [NiFe] hydrogenases from the hyperthermophilic bacterium *Aquifex aeolicus*. Pyrolytic graphite electrodes have been modified with these hydrogenases, in a system utilising a gold wire counter electrode and an Ag/AgCl reference electrode. This set-up efficiently reduced protons in a 10 mM sodium phosphate/ 10 mM tris chloride buffer solution. The primary action of hydrogenases is to oxidise  $\text{H}_2$  when pH is lowered in acidic conditions, however the authors propose that they can effectively reduce protons to yield  $\text{H}_2$  according to the reaction scheme 1.3.



**Reaction 1.3- Reduction of protons in acidic conditions by hydrogenases.**<sup>32</sup>

The catalytic current generated by the hydrogenases was monitored by cyclic voltammetry over a range of pH 5 to 8. No catalytic current was observed at pH 8

however lowering the pH induced a catalytic current owing to the increased levels of  $\text{H}^+$  substrate. Also the  $E^{1/2}$  of the reduction wave was shifted to less negative values when the pH was decreased. The pH dependence of  $E_{1/2}$  is linear with a slope of about 0.55 V vs. SHE per pH unit.

#### 1.1.4.3. Catalysts incorporated into Polymers:

Polymers have been renowned for use in electrocatalysis because of their electron transport improving properties which greatly enhance the regeneration of the electrocatalysts during redox processes. Electronic interactions between the metal-based  $d\pi$  orbitals and the polymer  $\pi$  or  $\pi^*$  orbital can provide additional mechanisms for electron transport between metal centers and facilitate the movement of electrons necessary for high electrocatalytic performances.<sup>33</sup> Nafion (Fig. 1.6) is a commercially available polymer which has been utilised by Abe *et al.* to incorporate ruthenium red ( $[(\text{NH}_3)_5\text{Ru}-\text{O}-\text{Ru}(\text{NH}_3)_4-\text{O}-\text{Ru}(\text{NH}_3)_5]\text{Cl}_6$ ).<sup>34</sup> The ruthenium red was dispersed into a Nafion membrane and coated onto a basal-plane pyrolytic graphite (BPG) plate as a working electrode. A spiral platinum counter electrode and an Ag/AgCl reference electrode were employed in the experiment.

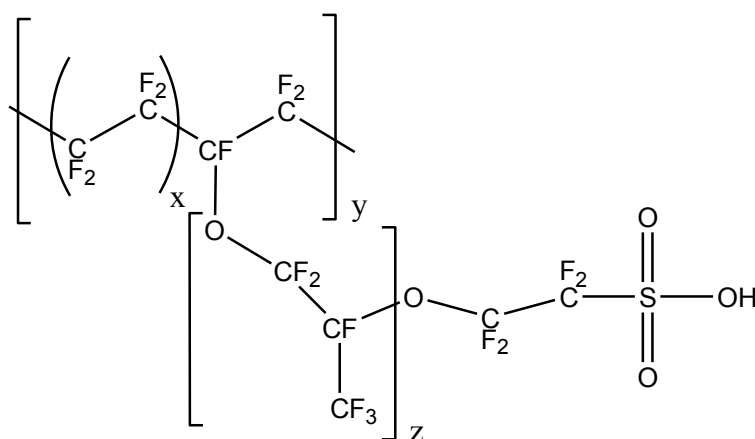


**Figure 1.6- Nafion: a sulfonated tetrafluoroethylene based fluoropolymer.**

A TON of  $1.8 \times 10^2$  was reported after one hour electrolysis at -0.6 V in a pH 1 phosphate buffer solution.  $H^+$  reduction occurred after formation of an electrochemically active species with was proposed as a  $Ru^0$  complex, which is

formed after the decomposition of the Ru red into two monomeric Ru complexes,  $[\text{Ru}^{\text{III}}(\text{NH}_3)_5(\text{H}_2\text{O})]^{3+}$  and  $[\text{Ru}^{\text{III}}(\text{NH}_3)_4(\text{H}_2\text{O})_2]^{3+}$  noted by the slight shift in reduction potential from -0.2 V to -0.18 V (vs. Ag/AgCl) during the course of the repeated CV scanning. Abe proposed that either both or one of these mononuclear species was further irreversibly reduced to yield the electrocatalytically active  $\text{Ru}^0$  species. Zhao *et al.*<sup>35</sup> have incorporated zinc phthalocyanine (ZnPc) into both a Nafion and a poly(4-vinylpyridine-co-styrene) polymer and coated these mixtures onto basal plane pyrolytic graphite electrodes.

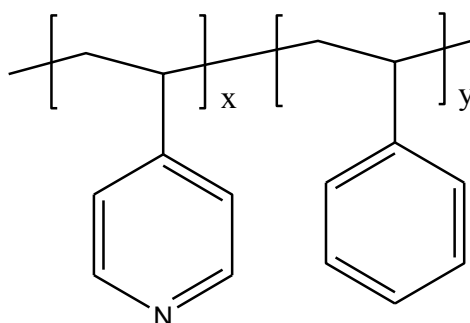
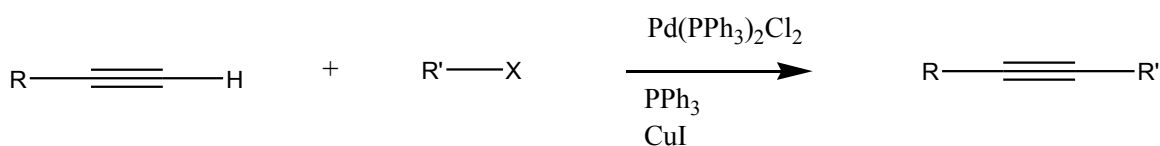


**Figure 1.7- Poly(4-vinylpyridine-co-styrene), P(VP-St)**

An Ag/AgCl reference electrode and a spiral platinum wire counter electrode were used together with a 0.1M  $\text{NaH}_2\text{PO}_4/\text{H}_3\text{PO}_4$  aqueous buffer at pH 1.0. When the ZnPc was incorporated into a polymer it exhibited a far greater electrocatalytic activity compared to the bare electrode of the electrode modified with the polymer alone, demonstrating that ZnPc is the catalyst for the  $\text{H}_2$  generation reaction. The potentiostatic electrolysis was carried out at -0.9 V vs. Ag/AgCl and it was noted that the amount of  $\text{H}_2$  evolved after 1 h increased with the ZnPc concentration incorporated within the Nafion or P(VP-St) matrix but this increase levelled off when a concentration of 0.02 M was used. The TON values for Nafion-ZnPc,  $4.33 \times 10^4$ , was almost greater than that of the reported value for P(VP-St) ZnPc,  $2.92 \times 10^4$ , indicating the influence of the polymer backbone in the electron transfer process and indicating that the electron propagation through the polymer matrix is most probably the rate determining step in the reaction.

## 1.2 Cross Coupling Reactions

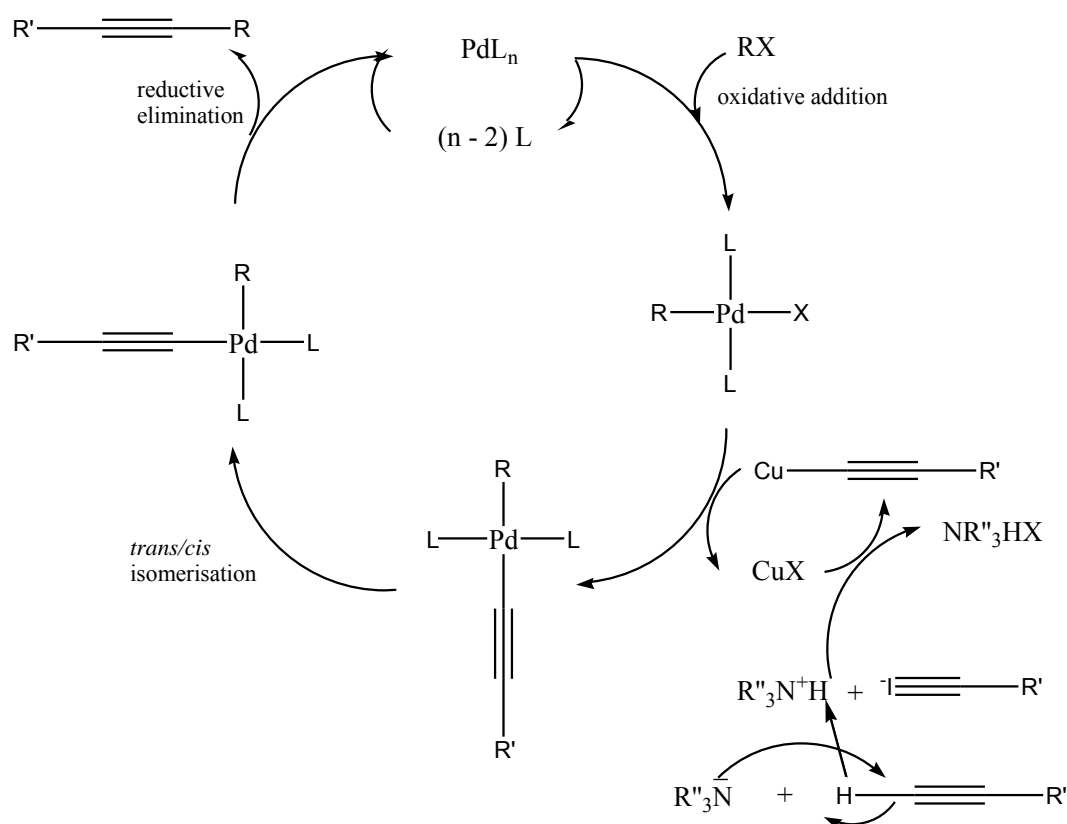
Many recent studies in organometallic chemistry involve transition metals and  $\pi$ -conjugated systems. Some of the most widely used synthetic methods to produce these desired  $\pi$ -conjugated systems are of the Sonogashira-Hagihara type which involve palladium catalysis with a copper co-catalyst to form a C-C bond. It also often includes the presence of phosphine as a ligand for palladium during the reaction mechanism. This type of C-C bond forming reaction is often referred to as cross coupling. Other important cross-coupling reactions include the Negishi,<sup>36</sup> Suzuki-Miyaura,<sup>37,38</sup> Heck<sup>39</sup> and Stille<sup>40</sup> reactions but for the purpose of this study Sonogashira coupling reactions are the most important and will be discussed further. Sonogashira coupling involves the coupling of a terminal alkyne with an aryl, or vinyl, halide (Reaction 1.4). It is a widely used reaction for the formation of C-C bonds. This mechanism was first proposed by K. Sonogashira and N. Hagihara in 1975<sup>41</sup> and the reaction method used has barely changed to date. The reaction is generally carried out using a palladium catalyst, and a copper<sup>I</sup> co-catalyst in the presence of an amine base (e.g. Et<sub>3</sub>N, *i*Pr<sub>2</sub>-NH<sub>2</sub>). This particular method of C-C triple bond formation was based on the decidedly difficult Stephens- Castro coupling of arylacetylenes with iodoarenes or iodoalkenes, which required harsh temperatures and reaction conditions such as 4 day reflux in pyridine (115°C) or DMF (153°C).<sup>42</sup> The Sonogashira method proposed much milder reaction conditions, and greater yields of up to 85% were obtained when reacting simple molecules such as 1-iodobenzene with an acetylene molecule. A comprehensive review of palladium catalysed alkylation reactions has been published.<sup>43</sup>



**Reaction 1.4- The Sonogashira Coupling Reaction.**

There are two types molecules required for this reaction, a Pd<sup>0</sup> catalyst and the halide of a Cu<sup>I</sup> salt as a co-catalyst. The exact mechanism for the Sonogashira coupling is unknown as it is very hard to isolate the intermediate organometallic complexes but

there have been proposed mechanisms mainly based on the schematic below (Scheme 1.1)



**RX** = Aryl halide.

**CuX** = Copper halide.

**PdLn** = Palladium Catalyst.

**Scheme 1.1 - Proposed Mechanism of the Sonogashira Coupling Reaction.**

The first step of the reaction is the palladium complex activation of the organic halide by oxidative addition into the carbon-halogen bond. Here the palladium<sup>0</sup> proceeds from a 16 electron system to an 18 electron system palladium<sup>II</sup> molecule.

Transmetalation occurs with the copper acetylide produced from the base reaction with the terminal alkyne and the copper halide ( $\text{CuX}$ ). Here the copper halide co-catalyst is reformed as a bi-product.

Next the palladium<sup>II</sup> molecule is trans/cis isomerised, converting a trans orientation into a cis molecule. Finally the desired product is released by reductive elimination, regenerating the palladium catalyst as a by-product. Basic conditions are required to neutralise the hydrogen halide also produced as a by-product in the reaction. An

excess of an amine serves two purposes in this reaction: it acts as a base to trap the halide and as a reducing agent for palladium.

The reaction works best with vinyl iodide > vinyl triflate > vinyl bromide > vinyl chloride > aryl iodide > aryl triflate > aryl bromide > aryl chloride. Highest yields for desired product were produced when using the more expensive vinyl-iodides. Much research has gone into using the cheaper bromides and chlorides to produce similar yields.<sup>44</sup>

Since its discovery there have been many modifications proposed including Pd free,<sup>45,46,47,48,49</sup> CuI co-catalyst free,<sup>50,51</sup> utilising microwave,<sup>52</sup> which make the reaction cheaper, due to the high cost of palladium, also faster in most cases, however yields are often lower and the harsher conditions needed mean that these methods may not be ideal when compared with the current traditional methods.

In general the methods which have been developed which do not require the use of a palladium catalyst, which can be expensive, often need higher temperatures or a higher percentage of the catalyst used. Beletskaya *et al.*<sup>45</sup> have reported using a nickel catalyst,  $[\text{Ni}(\text{PPh}_3)_2\text{Cl}_2]$ , which is very similar to the traditional palladium catalyst, to successfully synthesise a series of bi-aryl compounds containing a carbon-carbon triple bond. This nickel catalyst is much cheaper than its palladium equivalent and is more readily available. The yields achieved were between 91-100%, however the reactions required reflux temperatures and a larger equivalent of CuI co-catalyst (10%) to proceed. Beletskaya has also reported that alkylacetylenes, which are generally less reactive in Sonogashira-Hagihara type coupling reactions, react very slowly however in a simple reaction between 3-bromoquinoline and phenylacetylene a low yield of 27% was achieved after 21 hours reflux.

Copper complexes have also been used as the primary catalyst in the reaction. Copper, again, is a much cheaper alternative to palladium catalysts. Kang *et al.*<sup>46</sup> have reported using CuI as primary catalyst in 10% equivalence. A yield of 85% was achieved in the reaction between phenylacetylene and diphenyliodonium tetrafluoroborate, with room temperature stirring for 30 minutes in the presence of  $\text{NaHCO}_3$  base. The high yields and mild conditions are favourable but the high equivalence of CuI needed is not favourable as CuI promotes the cross coupling of the acetylene molecules, further reducing desired yields.

Copper co-catalyst free reactions have also been reported. These reactions use a  $\text{Pd}^{\text{II}}$  catalyst instead of the traditional  $\text{Pd}^0$ . Mery *et al.*<sup>50</sup> have used bis{tert-



butylaminomethylphosphine} (Fig. 1.8) as catalyst and achieved yields of up to 100% when reacting arylhalides with substituted acetylenes. The reactions were carried out using Et<sub>3</sub>N as the base and at temperatures between -40 and 80°C.

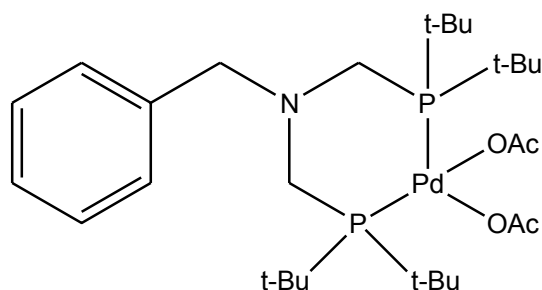


**Figure 1.8 - Pd<sup>II</sup> catalyst utilised by Mery *et al.* in copper free Sonogashira coupling reactions.<sup>50</sup>**

Erdelyi *et al.*<sup>52</sup> have reported the use of microwaves in the Sonogashira reaction and achieved yields in the range of 80-95% after only 20 mins at 120°C. They used the traditional palladium catalysts and copper co-catalysts. The yields and short time of reaction are favourable, however, high temperatures and specialised Schlenk glassware required to keep the reaction deaerated and water free make the synthesis more difficult.

### 1.2.1 Early Methods of Sonogashira Coupling

The first Sonogashira coupling reaction was reported in 1975 by Kenichi Sonogashira and Nobue Hagihara.<sup>41</sup> This reaction had many important conditions necessary for the reaction to run; the reagents must be de-aerated and completely dry before use and an inert atmosphere is required throughout the duration of the. If the catalyst comes in contact with water it renders it useless, as an alkylhalide which forms possess a  $\beta$ -hydrogen, which is unstable and readily decomposes to give palladium hydride complexes which will not catalyse the reaction<sup>53</sup>. Also oxygen promotes the formation of homo-coupled acetylenes during the Hay coupling reaction; two acetylenes coupled together, necessitating a completely air free system to be used as this would lead to an unnecessary by-product and further reduce the possible yields of the reaction. The early methods of Sonogashira coupling reactions

were quite expensive due to necessary palladium catalyst and were quite difficult to keep completely deaerated.

### 1.2.2 New Methods of Sonogashira Coupling

Raju *et al.*<sup>54</sup> have reported using water as a solvent during Sonogashira coupling reactions. The reaction involves the addition of iodothiophene to different terminal alkynes using water as a solvent. The reaction used Pd/C (Pd on carbon) catalyst in 0.026% mol. equivalence with 0.2% equivalent PPh<sub>3</sub> and 0.05% equivalent CuI as cocatalysts. This is a much lower equivalent than previously reported. The yields reported were quite high, on average 77 - 90%. The use of water as a solvent allows the reaction to be more environmentally friendly as well as economical. It does not involve the use of toxic amines as a solvent which can be expensive for use in large scale synthesis.

The use of the copper<sup>I</sup> co-catalyst has been investigated. The use of a copper salt is highly toxic to the environment as well as being difficult to recover after a reaction. It also generates homocoupling products of the terminal alkyne<sup>55</sup> which is especially deterring when the terminal alkyne is difficult to synthesise or expensive. The reaction known as copper-free Sonogashira coupling requires the use of a large amount of amine base as solvent. This is almost just as hazardous to the environment itself and somewhat diminishes the new procedure.

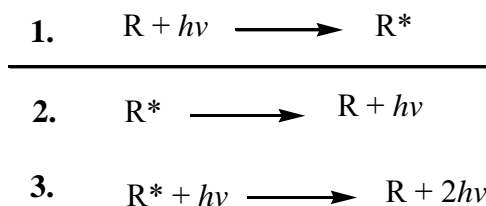
A procedure involving the use of a palladium<sup>II</sup> catalyst was proposed by Mery *et al.*<sup>50</sup>. This catalyst (Fig. 1.8) is more stable than Pd<sup>0</sup> and the use of a more bulky Pd<sup>II</sup> catalyst which is a chelating bis-tert-butylphosphine ligand coordinated to Pd<sup>II</sup> negates the need for a copper co-catalyst. The reactions carried out were one pot methods using an amine base as the solvent with temperatures between -40 to 80°C. Another advantage of this method is that the palladium catalyst was only used in 1% mol equivalent.

Reactions have been tried with the use of silver<sup>I</sup> oxide<sup>56</sup> but these reactions were sluggish and could not be carried out without the addition of copper<sup>I</sup> iodide for the reaction to proceed.

### 1.3 Principles of Photophysics

Photophysics involves the monitoring of a molecule which has absorbed a photon of light ( $h\nu$ ). When a sample is irradiated, a valence electron is usually promoted to a higher energy orbital, which induces the formation of an electronic excited state in the absorbing species (Scheme 1.2, Rxn 1.). There are two possible decay routes for this excited state;

- the excited state species can decay to the ground state through spontaneous emission (Scheme 1.2, Rxn 2.), which can occur either through the emission of light (radiative decay) or through the conversion excess energy into heat energy (non-radiative decay),
- or it can decay to ground state through stimulated emission (Scheme 1.2, Rxn 3.).



**Scheme 1.2 - Photophysical absorption and emission routes of a molecule (R).<sup>59</sup>**

The relative weight and distribution of electrons in a molecule, when compared with nuclei, mean that the electrons have a lower inertia than the nuclei. Due to this, electrons can change their position and motion almost instantaneously. The Born-Oppenheimer approximation states that nuclear and electronic motions can be treated as separate forms of motion when approximating wave functions.<sup>57</sup> This is because forces on both electrons and nuclei, due to their electric charge, are of the same order of magnitude. When these forces are applied any changes which occur in their momentum must also be the same, however, due to the mass of the nuclei being much more than that of the electrons their velocities must be much smaller. Therefore the electronic wave function depends upon the nuclear positions but not upon their velocities, i.e., the nuclear motion is so much slower than electron motion that they can be considered to be fixed.

Using the Born-Oppenheimer approximation it is assumed that the nucleus remains motionless during an electronic transition, i.e. absorption or emission. When a photon is absorbed, an excited electronic state is not only generated, but the molecule also acquires some vibrational energy. According to the Franck-Condon principle the absorption of a photon is a practically instantaneous process, since it involves only the rearrangement of inertia-free electrons.<sup>58</sup> The process of light absorption is on the femto second timescale and due to this there is insufficient time for the heavier nucleus to start any kind of motion during the absorption process but does so subsequently resulting in vibrations. The Franck-Condon principle is the approximation that an electronic transition most likely occurs without changes in the positions of the nuclei in the absorbing species and its environment. The resulting excited state is called a Franck-Condon state which is a metastable excited electron configuration where the nuclear geometry is the same as that in the ground state. After the Franck-Condon state is formed, rapid vibrational relaxation occurs to the lowest vibrational state of the electronic excited state. This is generally known as the high energy singlet excited state ( $S_n$ ).

There are several possible ways for the electronic excited state to return to its original ground state. Vibrational relaxation can occur to a lower excited state through intersystem crossing or internal conversion. Intersystem crossing occurs when non-radiative decay occurs between two states of different multiplicity, i.e. from a singlet to a triplet excited state ( $S_1-T_1$ ) whereas internal conversion occurs when non-radiative decay occurs between two states of the same multiplicity, i.e. singlet to a lower energy singlet excited state ( $S_n-S_1$ ,  $S_1-S_0$  or  $T_1-T_0$ ). Radiative decay can also occur as the excited state decays to the ground state. This is known as luminescence. It occurs when an excited state loses its excitation energy in the form of a photon of light,  $h\nu$ . There are two types of emission of this light, fluorescence and phosphorescence. Fluorescence occurs when the decay occurs between two states of the same multiplicity i.e.  $S_1-S_0$  whereas phosphorescence occurs when the decay occurs between two states of different multiplicity i.e.  $T_1-S_0$ . Kasha's rule states that emission occurs only from the lowest energy excited state of the molecule. Therefore, as with the initial Franck-Condon excited state, vibrational relaxation to the lowest energy excited state must occur by rapid internal conversion between states of the same multiplicity before emission can proceed.<sup>59</sup> It is mainly the

efficiency at which internal conversion occurs which controls the type of emission which occurs.

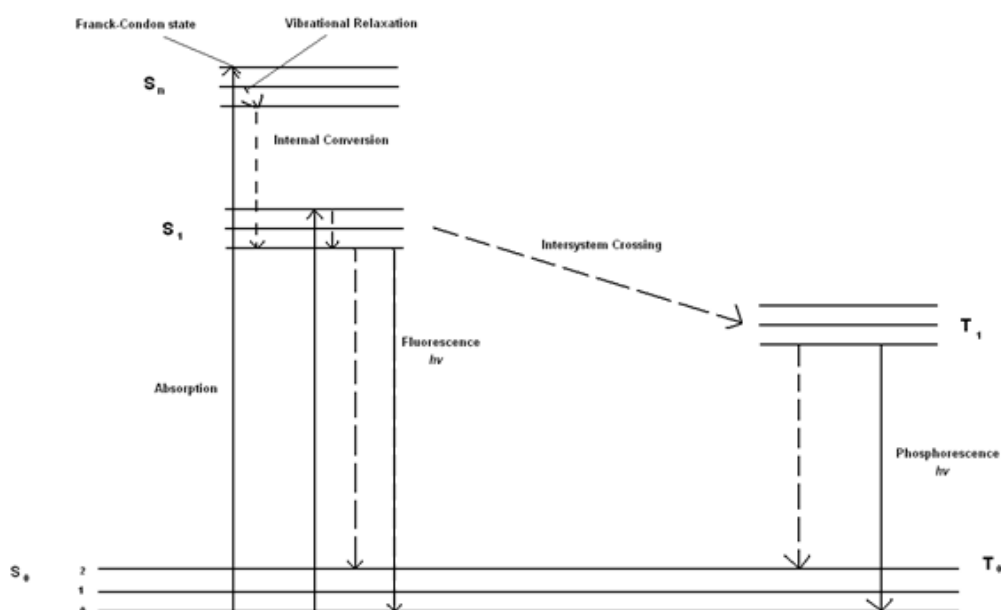


**Figure 1.9 - Jablonski Diagram.**

Fluorescence is a spontaneous and short lived process with lifetimes in the range of 1 ps to 1  $\mu$ s as this process is “spin allowed”, meaning that the electron does not need to change direction before decaying back to the ground state. Generally the emitted light is of a lower energy than that of the absorbed incident photon as the internal conversion(s) required to relax to the first excited state, consumes some of this energy. The energy loss results in the emission occurring at longer wavelengths compared to the ground state absorption. This difference in energy absorbed and energy emitted is known as a Stokes shift. A Stokes shift is defined as the difference in the absorbance and emission maxima of a given molecule.<sup>59</sup>

Phosphorescence is a long lived process with lifetimes ranging from 1  $\mu$ s up to several seconds. This is due to the process being “spin forbidden”, meaning that the electron needs to undergo spin conversion before decaying back to the ground state as it is decaying from a triplet state to a singlet state. As the  $T_1$  excited state is lower in energy than the  $S_1$  excited state phosphorescence will occur at longer wavelengths than fluorescence. Intersystem crossing to the triplet state will only occur where vibrational coupling occurs between the singlet and triplet excited states. This

vibrational coupling allows the “spin forbidden” nature of the intersystem crossing be overcome.

Molecular orbital theory is used to describe the electronic transitions which occur during photoexcitation. The location (or distribution) of electrons about the nucleus will greatly affect the possible transitions which occur during photoexcitation.

Charge transfer transitions are transitions of electrons between the orbitals of the metal and the orbitals of the ligands. There are two types; metal to ligand (MLCT,  $d-\pi^*$ ) and ligand to metal (LMCT,  $\sigma$  or  $d-\pi$ ) charge transfer transitions, which depend on where the excited electron originates. These types of transitions cause a radial redistribution of electron density between the metal and ligand orbitals. MLCT involves the movement of an excited electron in an orbital on the metal centre to an orbital on the ligand. This will leave the metal centre open to nucleophilic attack by other ligands. LMCT involves the movement of an excited electron from an orbital on the ligand to an orbital on the metal centre. This electron will usually transfer to a metal antibonding orbital.

Ligand field transitions (or d-d transitions) arise from the transition of electrons between d-orbitals. These transitions cause an angular rearrangement of electron density. There is no change to the electron distribution between the metal and the ligands. This type of transition will not affect internal redox processes however it will affect the reactivity of the metal in relation to ligand substitution or isomerisation reactions.

Intra-ligand transitions occur when an excited electron is transferred to two molecular orbitals which are centred on the ligand. These transitions do not effect charge distribution between the metal and ligands however they do affect the donor-acceptor properties and dipole moment of the ligand.

## **1.4. Electrochemistry**

Electrochemistry involves the study of chemical changes caused by the passage of electric current and the production of electrical energy by chemical reactions.<sup>60</sup> As early as the 1800's Nicholson and Ritter had developed a method to split water into hydrogen and oxygen by electrolysis and Ritter discovered the process of electroplating. It was when Michael Faraday proposed his two laws of

electrochemistry in 1832, that the field of electrochemistry began to grow exponentially.

An electrochemical experiment will usually consist of a working electrode, a counter electrode, a reference electrode and a supporting electrolyte. The working electrode and the counter electrode are connected by a series of wires.

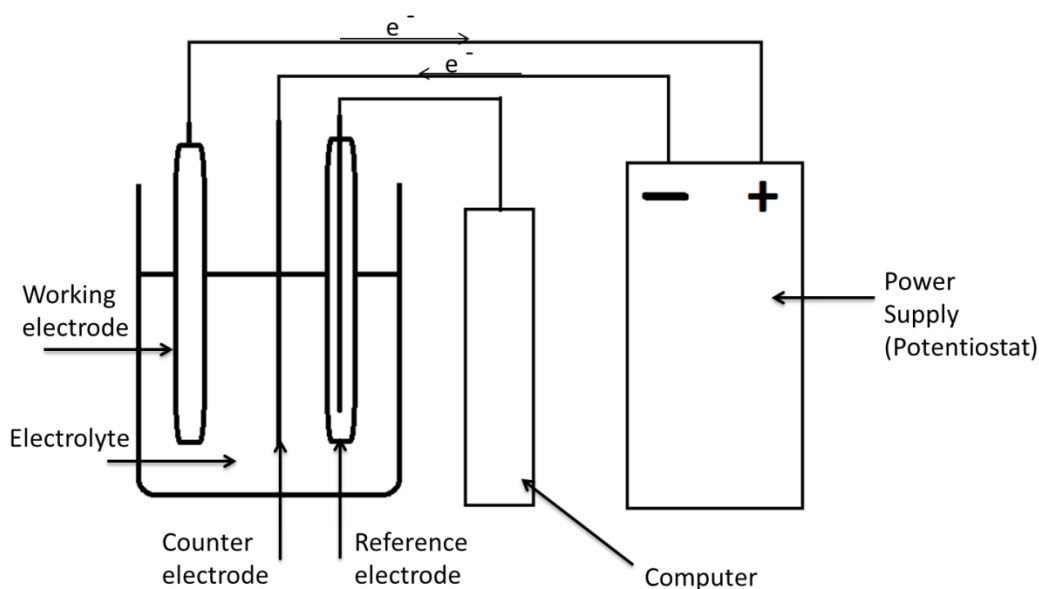


**Figure 1.10- Schematic of an electrochemical cell.**

The potential of the working electrode is controlled with respect to the reference electrode. This is achieved by connecting the cell to a power supply, a potentiostat, which will maintain the potential of the working electrode. Due to the tightly packed metal atoms within the electrode surface, overlap is present between adjacent atomic orbitals. This leads to poorly defined electronic energy levels in the metal atoms. The Fermi level within the metal electrode surface refers to the energy level at which the available electrons lie. This energy level is not fixed and can therefore be increased or decreased by applying electrical energy, in the form of potential. By applying more negative potentials to the electrochemical cell, the energy of the electrons in the working electrode are raised. Once they reach a high enough level they can then transfer to vacant electronic states in the sample dissolved in the electrolyte. This generates a reduction current within the cell. By applying a more positive potential,

the energy of the electrons in the working electrode are now lowered. Once the electrodes achieve a suitable low energy it becomes favourable for the electrons in the solution to transfer to the working electrode. This process generates an oxidation current within the cell.

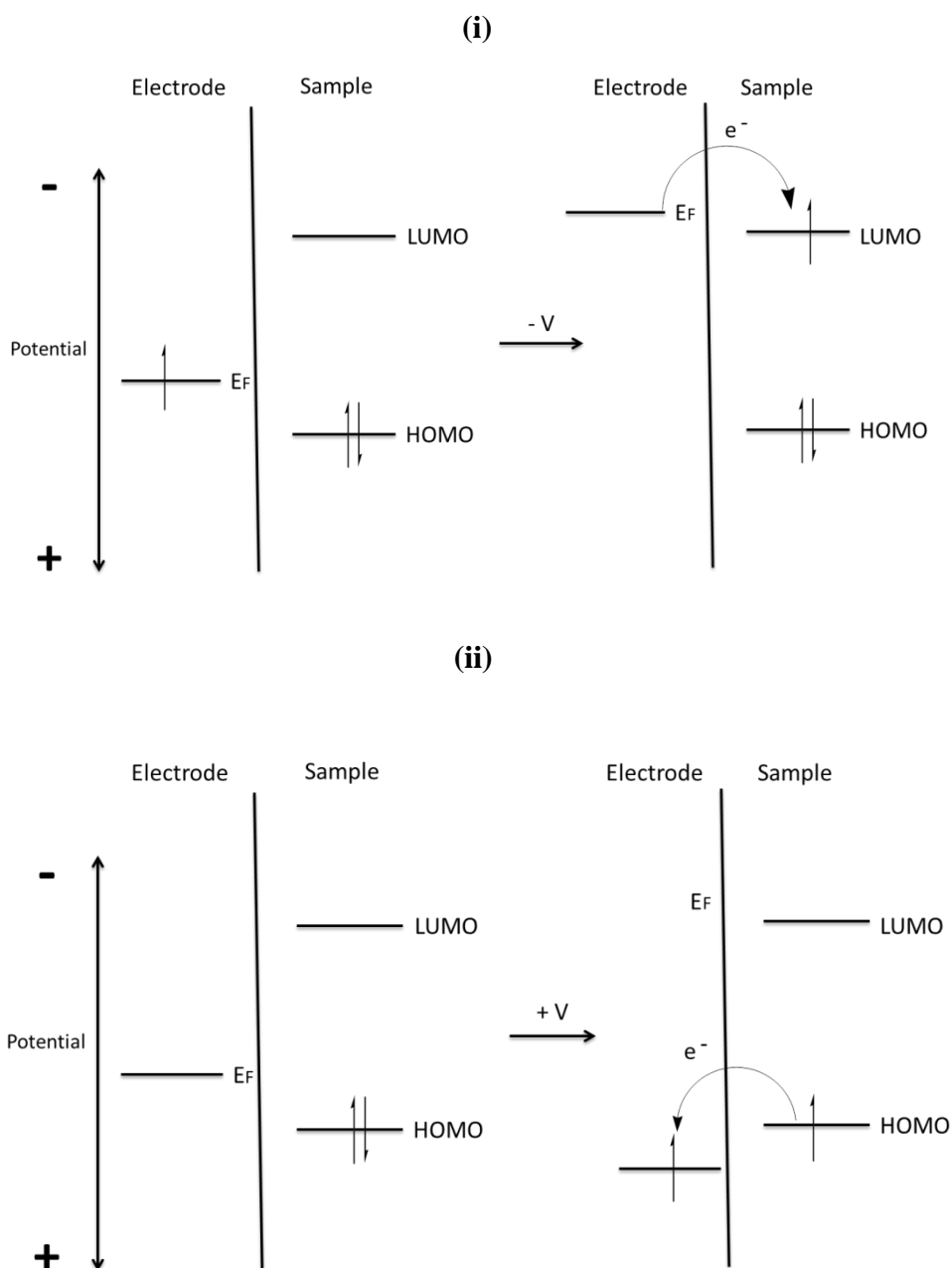


**Figure 1.11 - Representation of (i) a reduction process and (ii) an oxidation process.  $E_F$  refers to the Fermi level within the metal electrode surface.<sup>61</sup>**



By varying the potential difference between the working and the counter electrode an electrical current can be produced in the external circuit as the electrons flow between the surface and solution interface. The reference electrode is an electrode with a constant electrochemical potential and measures this current flow between the working and the counter electrodes.

Two types of reaction can occur at an electrode. The first types are known as Faradaic processes. Faraday's first law states that the amount of electricity passed through a cell is directly proportional to the amount of chemical reaction caused by the flow of current.<sup>61</sup> The example given above, where charge transfer reactions occur between the electrode/ solution interface, is known as a Faradaic process as it is governed by Faraday's first law. There are ranges of potential where no faradaic processes will occur as the charge transfer reactions are not thermodynamically or kinetically favoured. Within these regions no electrons will pass between the electrode and the solution however processes such as adsorption or desorption may occur causing the structure of the electrode-solution interface to change as the potential changes which may alter solution composition. These changes cause external current to flow even though charge does not cross the electrode- solution interface. Such processes are referred to as nonFaradaic processes.<sup>60</sup> Electrode reactions may result in both faradaic and nonFaradaic processes taking place.

The two techniques employed during this study are cyclic voltammetry and bulk electrolysis and will be discussed further in sections 1.4.4 and 1.4.5.

### **1.4.1 The Electrode- Solution Interface**

The interfacial region between the electrode and the solution is often referred to as the double layer. This double layer consists of charged species which exist at the region of the electrode- solution interface. During an experiment the charge of the metal electrode is positive or negative in relation to the solution. This charge represents an excess of electrons within the metal and is only found in a very thin layer ( $< 1\text{\AA}$ ) on the surface of the electrode. The charge in the solution is made up of an excess of cations or anions in the region of the electrode surface. The bulk of the solution is in an isotropic environment where an electrical field does not influence however the solution which is in the region of the electrode- solution interface experiences anisotropy due to the electrical field caused by the polarisation of

solvent dipoles, leading to their orientation at the solution side of the interface. Due to this a net ionic charge builds up at the interface. Once this occurs a layer of ions are attracted to the electrode surface with an equal quantity and opposite sign. The result is a charge separation produced by the local ordering of the ions at the electrode/solution interface.<sup>62</sup>

The model of the double layer was first proposed by Helmholtz in 1879. He proposed that the charged surface of the electrode would attract and immobilise a layer of counter ions using electrostatic attractions, until the charge on the surface had been neutralised. This model proposed that the electric potential falls from its value at the surface to zero in the bulk solution (Fig. 1.12). The Gouy-Chapman model, proposed in 1910-1913, recognised that ions are subject to random thermal motion and therefore could not be immobilised on the surface. To solve this problem they proposed that a diffuse double layer is formed in which the charge needed to neutralise the surface charge is spread out into solution. Using this model it was suggested that the electric potential falls more slowly to zero in the bulk solution with the distance from the surface. In 1924, realising that the two previously proposed models failed to adequately account for the properties of the ions behaviours within the double layer, Stern suggested that a combination of both models was the ideal answer. He advised that it was correct to propose that some ions would be immobilised onto the surface (specifically adsorbed) but not enough to neutralise the charge of the surface. This region is referred to as the Helmholtz layer. To neutralise the remainder of the charge a diffuse layer of ions (non-specifically adsorbed) is present which extend out into the solution and dissipates due to Brownian motion.<sup>63</sup>

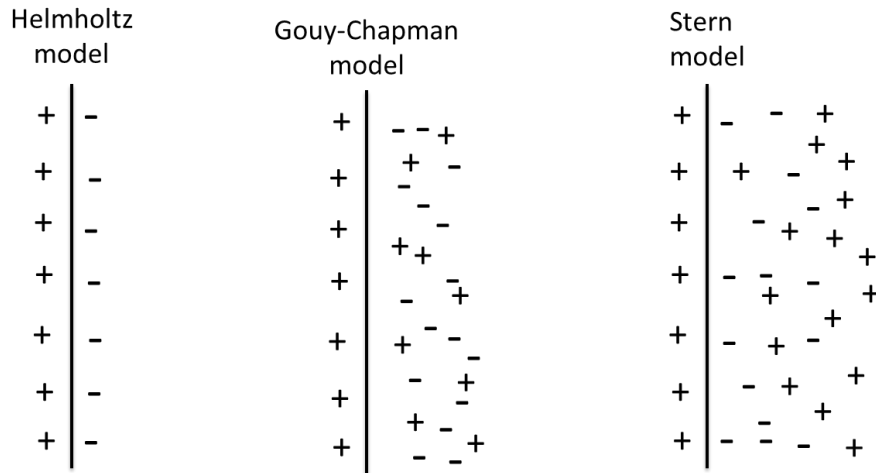


**Figure 1.12- Models of the electric double layer proposed by (a) Helmholtz, (b) Gouy and Chapman and (c) Stern.<sup>61</sup>**

### 1.4.2. Double-Layer Capacitance and Charging Current

The behaviour of the electrode-solution interface is often compared to that of a capacitor. A capacitor is an element of an electrical circuit comprising of two metal sheets separated by a dielectric material. Capacitors activities are defined by the equation 1.1:

$$\frac{q}{E} = C$$

**Equation 1.1**

Where  $q$  is the charge which is stored on the capacitor (C),  $E$  is the potential across the capacitor (V), and  $C$  refers to the capacitance of the element (F). When a potential is applied across a capacitor, charge will accumulate on its metal plates until  $q$  satisfies equation above.<sup>60</sup> The charge forms due to an excess of electrons on one plate of the capacitor and an excess of protons on the opposite plate. While this charge accumulates a current is flowing which is known as charging current.

The interfacial region in an electrochemical cell, the double layer, can be said to behave in a similar fashion to a capacitor. At an applied potential there will exist a charge on the electrode surface and an equal but opposite charge in the solution.

Changes to the applied potential across the interfacial region will modify the capacitance of the double layer. At a given potential, the electrode- solution interface is characterised by a double-layer capacitance. However, unlike real capacitors, changes in the applied potential across the double layer adjust the orientation of the solvent dipoles. This leads to adsorption and desorption of ions from the surface, which leads to a change in the charge stored across the interface. Therefore the capacitance observed in the double layer is more suitably referred to as differential capacitance ( $C_d$ ) as this definition takes into account the voltage dependant nature of the capacitance in the double layer. By measuring the charging current over a given experiment, where no redox couples are present, we can calculate the capacitance of a system using the equation 1.2:

$$i = C\nu$$

**Equation 1.2.**

Where  $i$  refers to the current and  $\nu$  is the potential scan rate.

### **1.4.3. Mass Transfer**

Mass transfer refers to the movement of material from one location to another in the solution. In general it refers to the movement of ions or cations to and from the interfacial region in the cell. Faraday's law relates the charge passed during an experiment to the number of moles of species electrolysed according to equation 1.3.:

$$Q = nFN$$

**Equation 1.3.**

Where  $Q$  is the charge,  $N$  is the number of moles of species electrolysed,  $F$  is Faraday's constant and  $n$  is the number of valence ions in the species.<sup>63</sup> The differential form of this equation relates to current:

$$\frac{dQ}{dt} = i = nF \frac{dN}{dt}$$

**Equation 1.4.**

Therefore the current ( $i$ ) is directly proportional to the rate of electrolysis. Once molecules have been electrolysed they must be transported back to the bulk solution in order to maintain electrolysis. This means that the rate of electrolysis and the current directly depend on the rate of mass transfer between the interfacial region and the bulk solution. This means that mass transfer can have a large effect on the rate of the reaction occurring at the electrode surface and is quite often the rate determining step in the reaction itself. The three principal modes of mass transfer are:

- Migration: The movement charged ion or cation due to the presence of an electrical field.
- Diffusion: The movement of material under the influence of a gradient of potential, such as concentration. During electrolysis a large excess of inert electrolyte is present in the solution so the current through the external circuit will be balanced by the passage of ions through the solution between the working and the counter electrodes.
- Convection: The movement of species due to mechanical (hydrodynamic) processes such as stirring inducing motions in the liquid.

The effects of mass transfer can be minimised through experimental technique. For example migrational mass transfer can be limited by using an inert supporting electrolyte at a concentration much higher than that of the electroactive compound and convection mass transfer can be minimised by preventing any vibrations within the electrochemical cell during an experiment.

#### **1.4.4. Cyclic Voltammetry**

Cyclic voltammetry is an electrochemical technique which can be used to investigate the chemical reactivity of a given species. In a cyclic voltammetry experiment the working electrode potential is raised or lowered linearly as a function of time. When a set potential is reached, the working electrode's potential incline, or decline, is

inverted to another set potential. The current at the working electrode is plotted versus the applied voltage to give a cyclic voltammogram. When a given sample is dissolved in a suitable electrolyte, this method can be used to investigate the electrochemical properties of the sample as this experiment results in the occurrence of oxidation or reduction reactions in electroactive species according to the potential, and a capacitive current due to double layer charging.<sup>64</sup> During an experiment the potential applied between the working electrode and the counter electrode is ramped to a set potential. During this time the current induced is measured between the working electrode and the counter electrode. The current measured will increase as it reaches the reduction potential of the sample and will then decrease as the concentration of sample close to the interface is diminished.

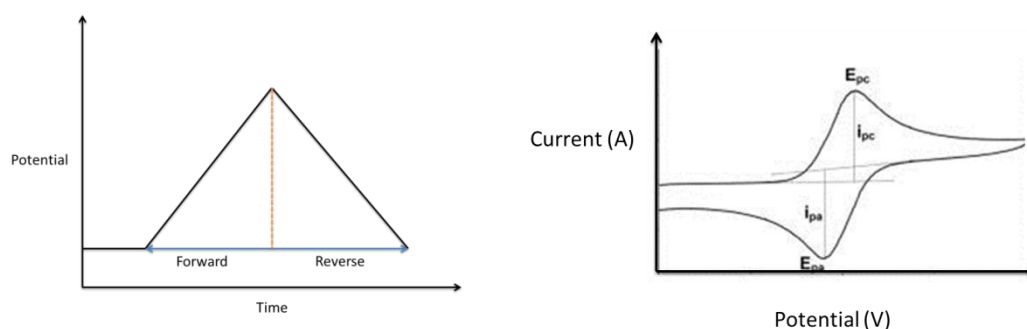
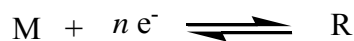


**Figure 1.13 –A cyclic voltammogram waveform and a typical cyclic voltammogram showing the location of the reduction/ oxidation peak maximum ( $E_p$ ) and the peak current of the process ( $I_p$ ).**

#### ***1.4.4.1. Reversible and Irreversible Systems:***

If an electrochemical process is considered to be reversible, the rate at which the electron transfer occurs between the working electrode and the solution redox species must occur quickly and without substantial thermodynamic barriers. As shown in the cyclic voltammogram in Fig. 1.13, once the initial sweep between the two set potentials ends a second sweep in the reverse direction begins immediately. For example, consider an electrochemical cell where a species M can be reduced (R) according to the equation (reaction 1.4):



**Reaction 1.4.**

where  $n$  represents the stoichiometric number of electrons for the process. If the reaction occurs quickly i.e. the rate of electron transfer is rapid at the electrode surface, so that species M and R immediately adjust to the ratio dictated by the Nernst equation it is said to be a reversible reaction. The Nernst equation (Eqn. 1.3) can be used to determine the equilibrium reduction potential of a half-cell in an electrochemical cell and to determine the total voltage for a full electrochemical cell. It can therefore be used to relate the half-cell potential of a process such as the one shown above to the concentrations of both species of the redox couple.

$$E = E_o + \left( \frac{RT}{nF} \right) \left( \text{Ln} \frac{[\text{Ox}]}{[\text{Red}]} \right)$$

**Equation 1.2- The Nernst Equation**

where  $E$  is the potential,  $E^o$  is the formal potential,  $R$  is the gas constant ( $\text{J mol}^{-1} \text{K}^{-1}$ ) and  $T$  is the temperature (K),  $n$  is the number of electrons transferred and  $F$  is the Faraday constant ( $96485 \text{ C mol}^{-1}$ ).

For a reversible electrochemical reaction:

- The voltage separation between the peaks must satisfy the following equation:

$$\Delta E = E_{\text{pa}} - E_{\text{pc}} = 59/n$$

**Equation 1.4.**

- The positions of the peaks must not alter when the scan rate is altered.
- The ratio of the peak currents must equal 1:

$$\left| \frac{i_{\text{pa}}}{i_{\text{pc}}} \right| = 1$$

**Equation 1.5.**

- And the peaks currents must be proportional to the square root of the scan rate.

Electron transfers reactions which are not fast because of one kind of complication or another are referred to as electrochemically irreversible reactions. The cyclic voltammogram produced from such a process will show no re-reduction/ re-oxidation peak. The process may be irreversible as the species produced may subsequently react in a chemical step after the initial oxidation/ reduction. Referred to as an EC reaction, where E is any electrode processes and C is any chemical processes. The E process leads the production of a chemically active ion, which goes on to react (in a C process), causing depletion of the initial ion produced leading to an irreversible redox process.

#### 1.4.5. Bulk Electrolysis

Bulk electrolysis involves holding the working electrode at a constant potential while the current is monitored over time. It employs coulometry which is a method which determines the amount of matter transformed during an electrolysis reaction by measuring the amount of electricity (C) consumed or produced during the experiment. The results of the experiment are presented as the total charge (C) passed, plotted versus time. Employing this technique can elucidate the number of electrons passed through the working electrode during a given reaction by relating them to Faraday's first law of electrolysis which states that the mass of a substance altered at an electrode during electrolysis is directly proportional to the quantity of electricity transferred or the charge (C) at that electrode.<sup>60</sup> Therefore the number of moles of a given substance altered during a bulk electrolysis experiment can be calculated using the equation 1.6:

$$n = (q/F)/z$$

**Equation 1.6.**

where  $n$  is the number of moles of a substance altered (mol),  $q$  is the total charge passed through the substance (C),  $F$  is Faraday's constant ( $C\ mol^{-1}$ ), and  $z$  is the valency number of ions of the substance.



## 1.5. Gas Chromatography

Gas chromatography is a technique which can be used to separate compounds due to differences in their apportioning behaviour between the mobile gas phase and a stationary phase, in the column. The instrument itself consists of a flowing gaseous carrier gas (equivalent to a mobile phase in liquid chromatography), an injection port, a column containing the stationary phase and a detector. The carrier gas is usually an inert gas such as nitrogen or helium to which the sample to be separated is introduced through the injection port. This mixture now flows through to the column using an applied pressure. The column is usually kept at a in a thermostatically controlled oven as separation is dependent on temperature as well as the affinity of the sample for the stationary phase and pressure applied.

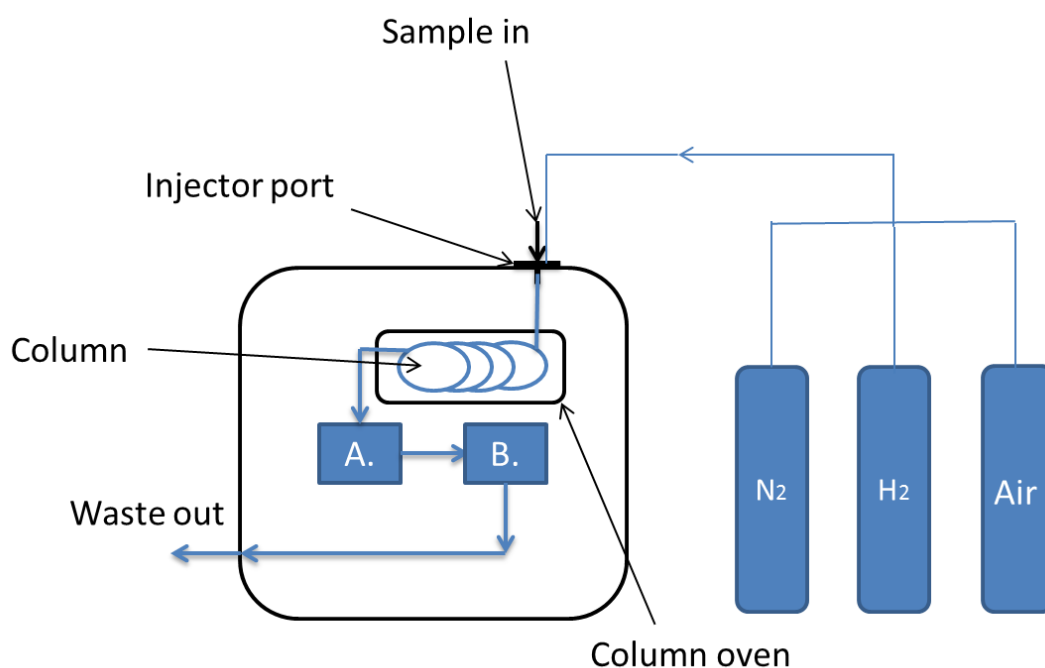


**Figure 1.14 - Simplified schematic of a gas chromatograph used in this study. A = TCD, B = FID, N<sub>2</sub> = Carrier gas, H<sub>2</sub> and Air used in FID.**

The stationary phase is located within the column. The level of interaction of the components in the sample mixture with the stationary phase of the column will lead to different retention times for each component in the sample. Once the components

have been separated, they leave the column and reach a detector where they are analysed.

A Varian GC CP-3800 was utilised in this study. Nitrogen is used as a carrier gas as it is inert and has a high chromatographic efficiency. A portion of the headspace in each sample vial, which will contain the  $H_2$ , is injected through an injection port on the GC where it is mixed with the carrier gas ( $N_2$ ). At first the two columns within the GC are arranged in parallel (Fig. 1.15). The sample firstly travels through a Hayesep porous polymeric column. The stationary phase consists of a divinyl benzene (DVB) and acrylonitrile (ACNI) copolymer. This column is used to separate  $CO_2$  and light hydrocarbons which may be present in the sample, therefore should there be smaller molecules such as  $H_2$  and  $O_2$  and  $CO$  present they are not retained on this column. As these molecules do not interact with the stationary phase they are eluted very rapidly and move to the molecular sieve column. The  $CO_2$  is retained for longer as it interacts with the stationary phase.

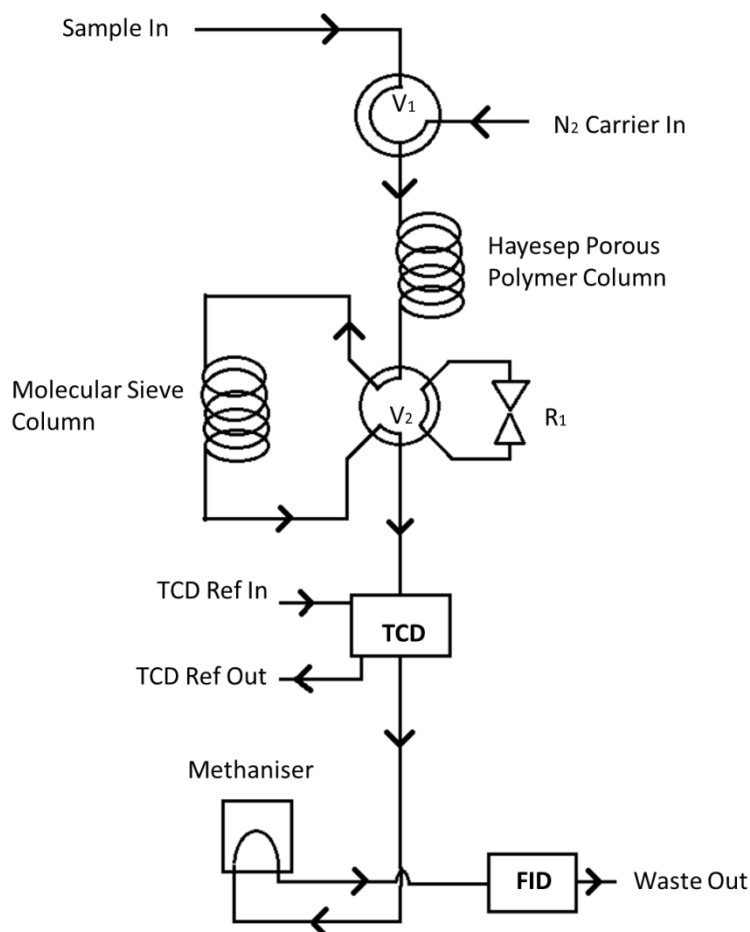


**Figure 1.15 - Schematic of GC-CP3800 in parallel mode.**

Once the smaller components have left the porous polymer column the GC switches to bypass mode (Fig. 1.16) Bypass mode involves the switching of  $V_2$  to ensure that when the  $\text{CO}_2$  elutes from the polymer column it does not flow to the molecular sieve column.  $\text{CO}_2$  is very similar in size to the  $5\text{\AA}$  pore size of the molecular sieves at  $3.23\text{\AA}$  and will become difficult to remove from this column should it be introduced. The  $\text{CO}_2$  passes through the detectors at this point.

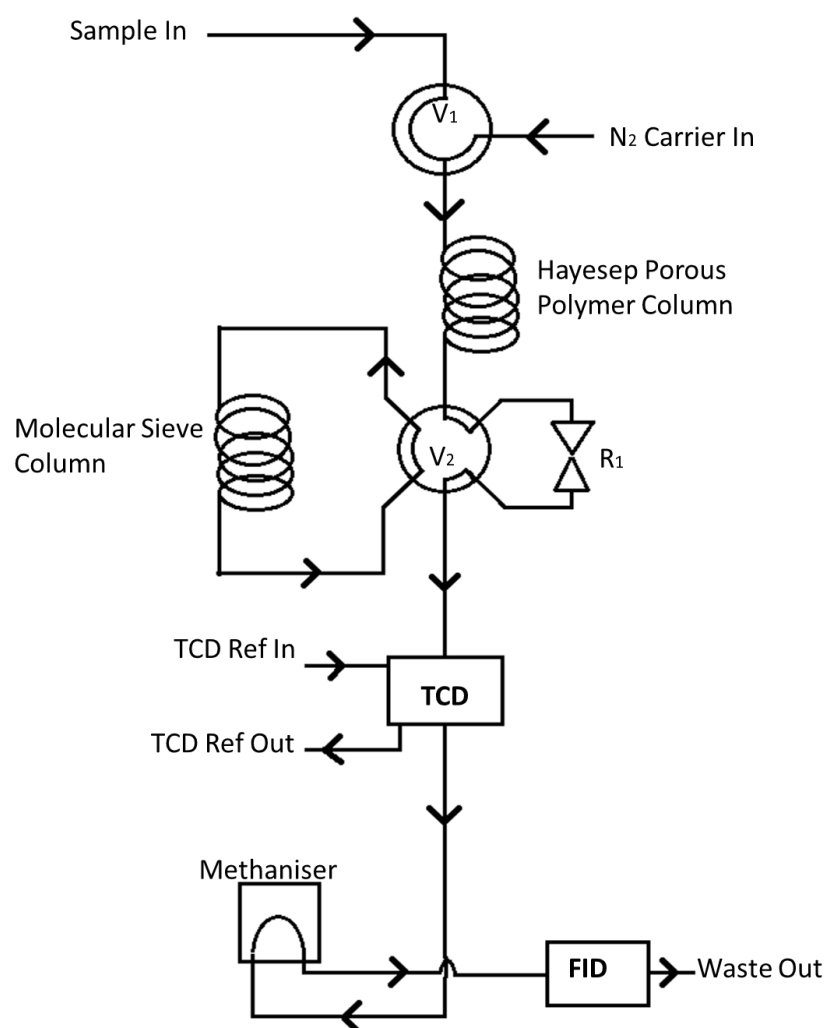


**Figure 1.16 - Schematic of GC-CP3800 in bypass mode.**

Once the  $\text{CO}_2$  has eluted the GC is switched back into “series” mode and the other gases are introduced onto the molecular sieve column. The gases now interact with the pores within the molecular sieves and are retained on the column for different amounts of time, depending on their molecular size. Once eluted from the column

the gases are analysed by two detectors. The gases first pass through a thermal conductivity detector (TCD).

### 1.5.1. TCD Detector

A TCD detector responds to changes in the thermal conductivity of the column effluent and compares it to a reference flow of the carrier gas. As everything will have its own varying thermal conductivity to that of the carrier gas, it can be used to detect all materials. It consists of an electrically heated filament which is kept in a temperature controlled cell. When the sample elutes from the column and the thermal conductivity of the column effluent changes, the filament will heat up (if the conductivity is reduced) or cool down (if the conductivity is increased) to compensate. This changes the resistance of the system. This change in resistance is identified by a wheat stone bridge circuit which produces a measurable current in response to this change. A wheat stone bridge is an electrical element used to measure an unknown electrical resistance (Fig. 1.17) by balancing two “legs” of a bridge circuit, one of which includes the unknown component.

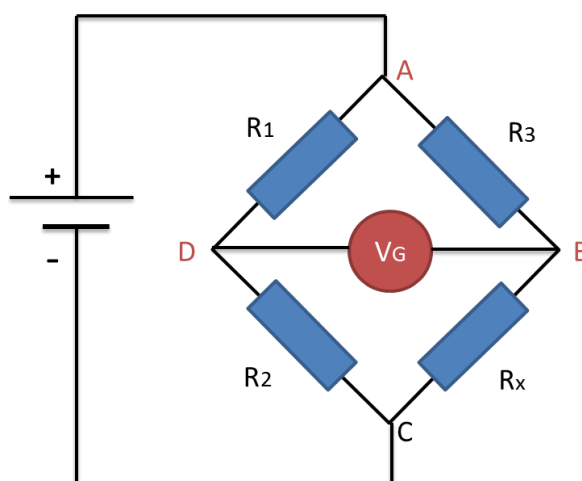


**Figure 1.17- Schematic of a wheatstone bridge.  $R_x$  = unknown resistance to be measured,  $R_1$ ,  $R_2$ ,  $R_3$  = resistors of known resistance, resistance of  $R_2$  is adjustable,  $V_G$  = galvanometer.**

The reference flow will pass across the  $R_1$ /  $R_2$  leg while the resistance generated by the column effluent will flow across the  $R_3$ /  $R_x$  leg. When the column effluent flows,

the resistance  $R_x$  changes, this change is measured as a voltage signal. If the ratio of the resistance in the  $R_1/R_2$  leg is known and equal to the resistance of the  $R_3/R_x$  leg then the voltage between the two midpoints, B and D, will be zero and therefore no current will flow through the galvanometer (Equation 1.7). If the bridge is unbalanced and  $R_1/R_2$  does not equal  $R_3/R_x$  the direction of the current flowing through  $V_G$  indicates whether  $R_2$  is too high or too low in resistance to balance the new resistance present in  $R_x$ . The resistance in  $R_2$  is then varied until the current passing through  $V_G$  is zero again. At the point of balance:

$$R_2/R_1 = R_x/R_3$$

$$\text{Therefore, } R_x = (R_2/R_1)R_3$$

**Equation 1.7.**

As this detector is a non-destructive detector the sample remains unaltered after analysing. After leaving the TCD the sample then passes through a flame ionisation detector in our GC system.

### **1.5.2. FID Detector/ Methaniser**

A flame ionisation detector (FID) is used to detect hydrocarbons. This means that it cannot detect CO or CO<sub>2</sub> should they be present in the sample. For this reason, samples studied in this thesis are first passed through a methaniser. The methaniser is a component used to convert small molecules, such as CO or CO<sub>2</sub>, into methane, ready for analysing by the FID. As this process occurs after they have eluted from the column their relative retention times will be retained. The conversion occurs with the aid of a nickel catalyst. The carbon oxides are reacted with hydrogen in the presence of Raney nickel catalysts. (Raney nickel catalysts are a fine powder of a nickel- aluminium alloy). The exact mechanism for these catalysts is not fully understood but it is thought that the reaction occurs on the surface of the catalyst and that the hydrogen atoms are bound to the metal first.

The FID detector itself is used to detect ions which are provided by burning, or ionising, the sample in a hydrogen-air flame. This flame burns at an extremely high temperature and will pyrolyse most hydrocarbons producing positively charged ions and electrons. These ions are detected by two electrodes which provide a potential difference (Fig. 1.18). The ions are therefore attracted to the collector plate and induce a current to flow. The current measured corresponds to the proportion of reduced carbon atoms in the flame. The detector then responds to the number of carbon ions (atoms) hitting the detector collector plate.

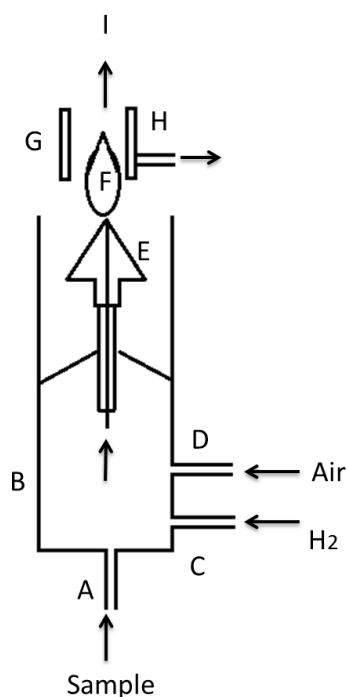


**Figure 1.18 - Schematic of a flame ionisation detector (FID).**

The eluent of the column (A) enters the detector oven (B) and is mixed with the hydrogen (C) and oxygen (D) used to fuel the flame. The mixture travels through the nozzle (E) where a positive bias is applied. The bias helps to repel the carbon ions once formed by pyrolysis. The flame (F) pyrolyses the sample and the ions are repelled towards the collector plates (G) which is connected to a highly sensitive ammeter. This ammeter detects the current induced when the ions hit the plate and sends a signal (H) to an amplifier and on to a computer. The waste is the feed out of the detector through a vent (I). An FID is a destructive detector as all sampled are completely pyrolysed during detection.

## 1.6. Laser Flash Photolysis/ Time Resolved Infra-red Spectroscopy

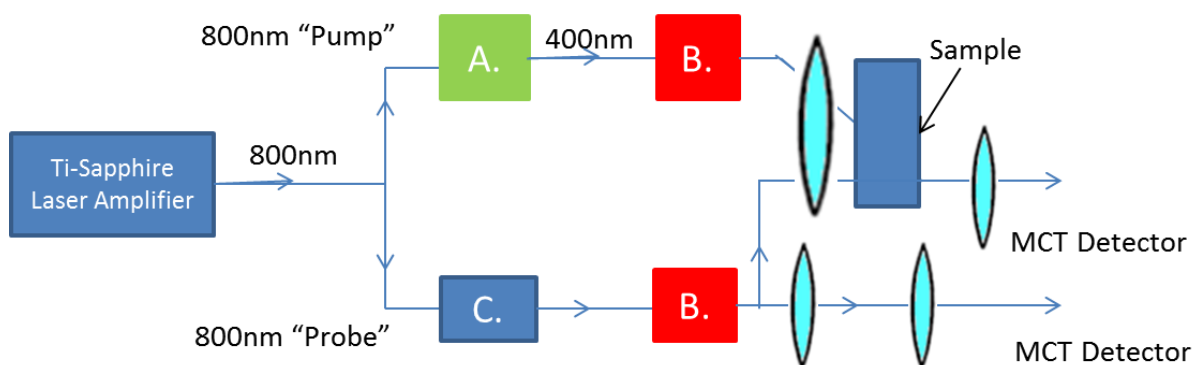
Laser flash photolysis involves the irradiation of a sample with a short, high intensity pulse of light, from a laser source or a discharge lamp. This will produce a high concentration of excited state species in the short time interval. The method was first developed by Norrish and Porter<sup>65</sup> in 1950. This technique is usually paired with either UV or IR spectroscopic monitoring, which allows the reaction kinetics to be determined. Employing UV-Vis detection, excited state species can be observed however this type of detection will not allow any structural information to be observed. When laser flash photolysis is coupled with time resolved infra-red studies the technique becomes much more comprehensive.

Time resolved infra-red spectroscopy (TRIR) involves the observation of a transient species evolving over time using IR detection. The application of laser flash photolysis, which is usually in the UV region, to a species will generate intermediates in solution and any photoproducts yielded can be monitored over time using IR spectroscopy. IR detection will allow any structural changes in the transient species over the course of the experiment to be observed. This technique is particularly useful when characterising the excited transient species of organometallic compounds as organometallic compounds contain functional groups with characteristic frequencies which are very susceptible to molecular structural changes. By monitoring these distinct frequencies (e.g. M-CO stretches), transient species can be elucidated.

TRIR involves a “pump and probe” technique where the laser pulse excites (“pumps”) the sample and the IR spectroscopy will effectively “probe” the generation of excited state transient species.

TRIR systems such as the ULTRA Laser System at the Central Laser Facility in Rutherford Appleton Laboratories (RAL) offer pump and probe spectroscopy with picosecond time resolution. This particular system allows the observation of short lived (ps) intermediates formed in solution immediately after laser flash photolysis. It utilises a cryogenically cooled Ti: Sapphire laser “pump” amplifier which provides 50 fs duration of laser pulses at a 10KHz repetition rate,<sup>66</sup> and < 1ps monitoring of mid-IR region serves as the “probe”. All TRIR studies discussed later were carried

out at RAL and a full description of the TRIR spectroscopy instrumentation is available in annual reports published by the Central Laser Facility at RAL <sup>67</sup>.



A. Second harmonic generator. B. Optical parametric amplifier. C. Difference frequency generator.

**Figure 1.19- Simple Schematic of the ULTRA Laser system in the Central Laser Facility in Rutherford Appleton Laboratories.**

The “pump” beam is generated from a Ti:sapphire laser which produces a 50 fs pulse of 800 nm light at a repetition rate of 10kHz. This beam is then split to form two beams of 800 nm light. The “pump” beam is passed through a second harmonic generator which produces a beam of twice the energy of the incident beam. This 400 nm beam then passes through an optical parametric amplifier and on through the sample exciting it.

The “probe” beam is passed through an optical parametric amplifier where it is split into variable wavelengths of light for use in the IR detection. This beam is then split into two again. One beam is passed through the sample, analysing any intermediates or photoproducts formed, while the second beam is passed straight to the detector to analyse and remove any background noise which is generated during the experiment.

### ***1.7. Time-Correlated Single Photon Counting***

Time-correlated single photon counting (TC-SPC) is a technique used to measure fluorescence lifetimes. More accurately it is used to measure fluorescence decay by measuring the precise time of emission of single fluorescent photons. In this way a measurement of how long a particular molecule takes to emit this photon can be ascertained. As different molecules within a compound will emit photons at slightly varying times following their simultaneous excitation, the decay is measured as a



rate rather than a specific length of time. Once the length of decay of these molecules has been observed and measured repeatedly, and these data points are combined, an exponential decay curve can be generated which is typical of these processes.

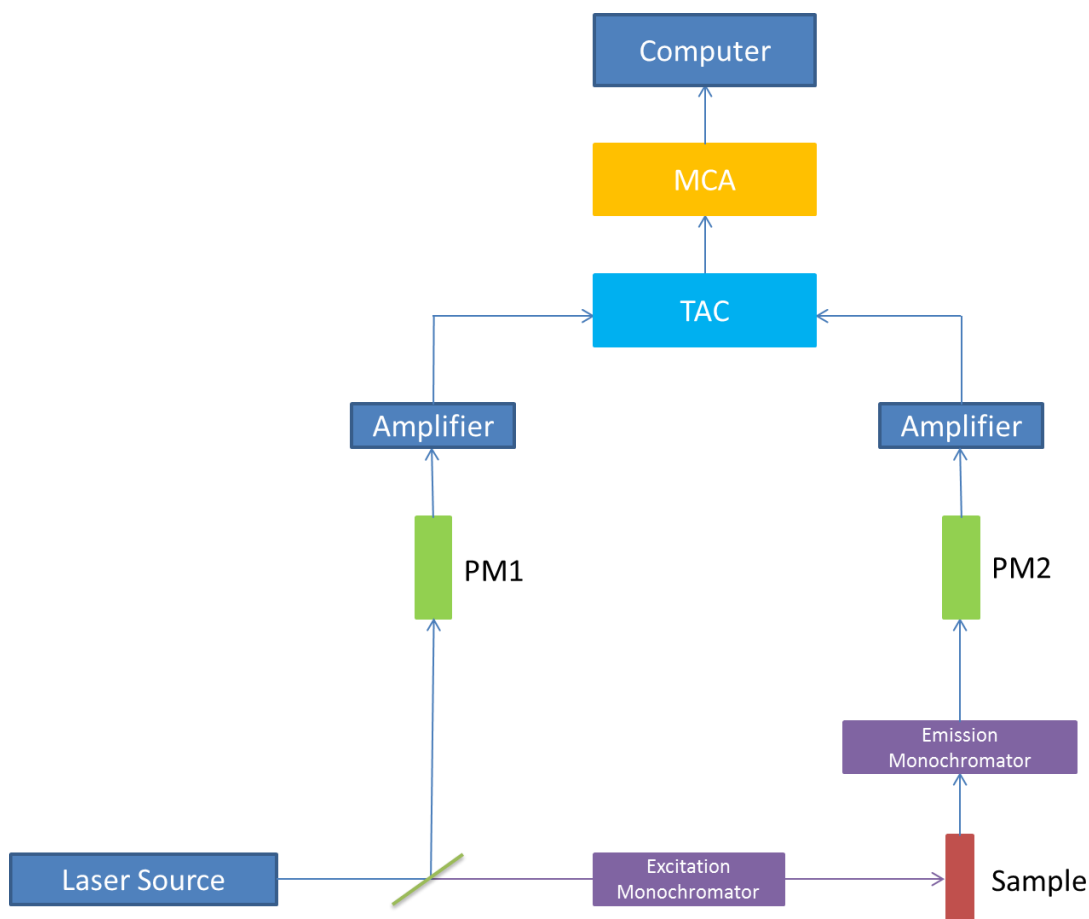


**Figure 1.20–Schematic of a simple time-correlated single-photon counting instrument.**

A laser source firstly emits a flash of light which causes the fluorescent sample to become excited and emit a photon of light from its excited state species. Two photomultiplier (PM) tubes are now employed. PM1 (Fig. 1.20) monitors the light emitted from the excitation source, once it observes a photon, which acts as the “start” signal, it begins to build up a charge on a capacitor in a time-to-analogue converter (TAC) which will only dissipate once a signal reaches it from PM2 (Fig. 1.20). This activates the time sweep of a TAC. PM2 then monitors the emitted fluorescent photons from the sample. As it is not possible to measure the length of time between signals for all photons emitted from the sample after the laser pulse, once the first photon is registered by PM2 during the sweep of the TAC it initiates a

“stop” signal in the TAC. A TAC measures the time interval between its start and stop pulses and generates an analogue output pulse precisely proportional to the measured time between signals. Thus the longer a molecule takes to emit a photon the higher the voltage released by the TAC. Therefore for a given sample we will have a precise measurement of how long it has been since the sample was excited. This process is repeated to build up the time correlation. These signals are accepted by a multi-channel pulse height analyser (MCA). The MCA converts the voltage signal received from the TAC to a time channel. Each of these time channels is a unit division on the time axis which can be varied from up to 0.2 ns down to a few microseconds per channel by the user. Each of the measurements of time between excitation and emission is referred to as a “count”. The number of counts in each channel is directly proportional to the fluorescent intensity and so a probability histogram of counts versus time is generated. The data collected consists of the sum of counts due to photon emission from the excited species and also includes counts due to random background. Deconvolution methods are required to extract the intrinsic decay information.

## ***Bibliography***

- 
- <sup>1</sup> International Energy Annual **2005**, Report Released June-October **2007**, *Energy Information Administration*.
- <sup>2</sup> A. J. Esswein, D. G. Nocera, *Chem. Rev.*, **2007**, 107, 4022.
- <sup>3</sup> M. Toledo, V. Bubnovich, A. Saveliev, L. Kennedy, *Int. J. Hydrogen Energ.*, **2009**, 1.
- <sup>4</sup> J. A. Turner, *Science*, **1999**, 285, 5428, 687.
- <sup>5</sup> M. Deminsky, V. Jivotov, B. Potapkin, V. Rusanov, *Pure Appl. Chem.*, **2003**, 74, 3, 413.
- <sup>6</sup> L. Becker, *Hydrogen Storage*, Proquest, **2001**.
- <sup>7</sup> J. A. Gilbert, D. S. Eggleston, W. R. Murphy, D. A. Geselowitz, S. W. Gersten, D. J. Hodgeson, T. J. Meyer, *J. Am. Chem. Soc.*, **1985**, 107, 3855-3864.
- <sup>8</sup> J. J. Concepcion, J. W. Jurss, M. K. Brennaman, P. G. Hoertz, A. O. T. Patrocinio, N. Y. M. Iha, J. L. Templeton, T. J. Meyer, *Acc. Chem. Res.*, **2009**, 42, 12, 1954- 1965.
- <sup>9</sup> R. Lalrempuia, N. D. McDaniel, H. Müller-Bunz, S. Bernhard, M. Albrecht, *Angew. Che. Int. Ed.*, **2010**, 49, 50, 9765.
- <sup>10</sup> A. Petronilho, M. Rahman, J. A. Woods, H. Al-Sayyed, H. Müller-Bunz, J. M. D. MacElroy, S. Bernhard, M. Albrecht, *Dalton Trans.*, **2012**, 41, 13074.

- 
- <sup>11</sup> S. Rau, B. SB. Schafer, D. Gleich, E. Anders, M. Rudolf, M. Friedrich, H. Gorls, W. Henry, J. G. Vos, *Angew. Chem. Int. Ed.*, **2006**, 45, 6215.
- <sup>12</sup> W. W. Wong, *J. Organomet. Chem.*, **2009**, 694, 2644.
- <sup>13</sup> M. Kirch, J. M. Lehn, J. P. Sauvage, *Nouv. J. Chim.*, **1977**, 1, 449.
- <sup>14</sup> T. Peng, D. Ke, P. Cai, K. Dai, L. Ma, L. Zan, *J. Power Sources*, **2008**, 180, 498.
- <sup>15</sup> F. Gao, Y. Wang, D. Shi, J. Zhang, M. Wang, X. Jing, R. Humphry-Baker, P. Wang, S. M. Zakeeruddin, M. Grätzel, *J. Am. Chem. Soc.*, **2008**, 130, 10720.
- <sup>16</sup> Z. Ning, Q. Zhang, W. Wu, H. Tian, *J. Organomet. Chem.*, **2009**, 694, 2705.
- <sup>17</sup> K. Rangan, S. M. Arachchige, J. R. Brown, K. J. Brewer, *Energ. Environ. Sci.*, **2009**, 2, 410.
- <sup>18</sup> C. Ho, W. Wong, B. Yao, Z. Xie, L. Wang, Z. Lin, *J. Organomet. Chem.*, **2009**, 694, 2735.
- <sup>19</sup> G. Sauve, M.E. Cass, S.J. Doig, I. Lauermann, K. Pomykal, N.S. Lewis, *J. Phys. Chem. B*, **2000**, 104, 3488.
- <sup>20</sup> Y. Miyaki, K. Nakajima, K. Sasaki, R. Saito, H. Nakanishi, Y. Nishibayashi, *Organometallics*, **2009**, 28, 17, 5240.
- <sup>21</sup> J. M. Lehn, R. Ziessel, *Proc. Natl. Acad. Sci. USA*, **1982**, 79, 701.
- <sup>22</sup> D. F. Watson, H. S. Tan, E. Schreiber, C. J. Mordas, A. B. Bocarsly, *J. Phys. Chem. A*, **2004**, 108, 3261.

- 
- <sup>23</sup> N. Toshime, K. Hirakawa, *Appl. Surf. Sci.*, **1997**, 121, 534.
- <sup>24</sup> B. F. DiSalle, S. Bernhard, *J. Am. Chem. Soc.* **2011**, 133, 11819.
- <sup>25</sup> A.O.T. Patrocínio, S.K. Mizoguchi, L.G. Paterno, C.G. Garcia, N.Y. Murakami Iha, *Synth. Met.*, **2009**, 159, 2342.
- <sup>26</sup> J. L. Inglis, B. J. MacLean, M. T. Pryce, J. G. Vos, *Coord. Chem. Rev.*, **2012**, 256, 21–22, 2571
- <sup>27</sup> T. Abe, G. Toda, A. Tajiri, M. Kaneko, *J. Electroanal. Chem.*, **2001**, 510, 35.
- <sup>28</sup> T. Abe, F. Taguchi, S. Tokita, M. Kaneko, *J. Mol. Catal. A: Chem.*, **1997**, 126, L89.
- <sup>29</sup> J. B. Raoof, R. Ojani, S. A. Esfeden, S. R. Nadimi, *Int. J. Hydrogen Energ.*, **2010**, 35, 3937.
- <sup>30</sup> F. Zhao, J. Zhang , T. Abe , D. Wöhrle , M. Kaneko, *J. Mol. Catal. A: Chem.*, **1999**, 145, 245.
- <sup>31</sup> Ö. A. Osmanbas, A. Kocaa, M. Kandazb, F. Karaca, *Int. J. Hydrogen Energ.*, **2008**, 33, 3281.
- <sup>32</sup> E. Lojou, M. Giudici-Orticoni, P. Bianco, *J. Electroanal. Chem.*, **2005**, 577, 79.
- <sup>33</sup> C. G. Cameron, T. J. Pittman, P. G. Pickup, *J. Phys. Chem. B*, **2001**, 105, 8838.
- <sup>34</sup> T. Abe, T. Goto, K. Ohzeki, M. Kaneko, *Electrochim. Acta*, **2000**, 45, 4009.
- <sup>35</sup> F. Zhao, J. Zhang, D. Wöhrle, M. Kaneko, *J. Porphyrins Phthalocyanines* **2000**, 4, 31.

- 
- <sup>36</sup> (a) E. Negishi, S. Baba, *J. Org. Chem. Soc., Chem. Comm.*, **1976**, 596. (b) S. Baba, E. Negishi, *J. Am. Chem. Soc.*, **1976**, 98, 6729.
- <sup>37</sup> N. Miyaoura, K. Yamada, A. Suzuki, *Tet. Lett.*, **1979**, 20, 3437. (b) N. Miyaoura, A. Suzuki, *J. Chem. Soc., Chem. Comm.*, **1979**, 866.
- <sup>38</sup> D. Canseco-Gonzalez, A. Gniewek, M. Szulmanowicz, H. Müller-Bunz, A. M. Trzeciak, M. Albrecht, *Chem. Eur. J.*, **2012**, 18, 6055.
- <sup>39</sup> R.F. Heck, J.P. Nolley, *J. Org. Chem.*, **1972**, 37, 2320.
- <sup>40</sup> (a) D. Milstein, J.K. Stille, *J. Am. Chem. Soc.*, **1978**, 100, 3636. (b) D. Milstein, J.K. Stille, *J. Am. Chem. Soc.*, **1978**, 101, 4992.
41. K. Sonogashira, Y. Tohda, N. Hagihara. *Tetrahedron Lett.*, **1975**, 16, 50, 4467.
- <sup>42</sup> R. D. Stephans, C. E. Castro, *J. Org. Chem.*, **1963**, 28, 3313.
- <sup>43</sup> E. Negishi, L. Anastasia, *Chem. Rev.*, **2003**, 103, 1979.
- <sup>44</sup> B. M. Choudary, S. Madhi, N. S. Chowdari, M. L. Kantam, B. Sreedhar, *J. Am. Chem. Soc.*, **2002**, 124, 14127.
- <sup>45</sup> I. P. Beletskaya, G. V. Latyshev, A. V. Tsvetkov, N. V. Lukashev, *Tet. Lett.*, **2003**, 44, 5011.
- <sup>46</sup> S. Kang, S. Yoon, Y. Kim, *Org. Lett.*, **2001**, 3, 17, 2697.
- <sup>47</sup> S. Cacchi, G. Fabrizi, L. M. Parisi, *Org. Lett.*, **2003**, 5, 21, 3843.
- <sup>48</sup> R. K. Gujadhur, C. G. Bates, D. Venkataraman, *Org. Lett.*, **2001**, 3, 26, 4315.

- 
- <sup>49</sup> K. Okuro, M. Furuune, M. Enna, M. Miura, M. Nomura, *J. Org. Chem.*, **1993**, 58, 4716.
- <sup>50</sup> D. Mery, K. Heuze, D. Astruc, *Chem. Comm.*, **2003**, 1934.
- <sup>51</sup> N. E. Leadbeater, B. J. Tominack, *Tet. Lett.*, **2003**, 44, 8653.
- <sup>52</sup> M. Erdelyi, A. Gogoll, *J. Org. Chem.*, **2001**, 66, 4165.
- <sup>53</sup> H. Nakako, R. Nomura, T. Masuda, *Polym. Bull.*, **2001**, 46, 147.
- <sup>54</sup> S. Raju, P. Rajender Kumar, K. Mukkanti, P. Annamalai, M. Pal. *Bioorg. Med. Chem. Lett.*, **2006**, 16, 6185.
- <sup>55</sup> R. Chinchilla, C. Najera. *Chem. Rev.*, **2007**, 107, 874.
- <sup>56</sup> Mori A., Kawashima J., Shimada T., Suguro M., Harabayashi K., Nishihara Y. *Org Lett.*, **2000**, 2, 2935.
- <sup>57</sup> V. Balzani, F. Scandola, *Supramolecular Photochemistry*, Ellis Horwood, **1991**.
- <sup>58</sup> M. Montalti, A. Credi, L. Prodi, M. T. Gandolfi, *Handbook of Photochemistry Third Edition*, Taylor and Francis, **2006**.
- <sup>59</sup> P. Suppan, *Chemistry and Light*, The Royal Society of Chemistry, Cambridge, **1994**
- <sup>60</sup> A. J. Bard, L. R. Faulkner, *Electrochemical Methods: Fundamentals and Applications, Second Edition*, Wiley, **2001**.

---

<sup>61</sup> D. B. Hibbert, *Introduction to Electrochemistry*, MacMillan Physical Science, **1993**.

<sup>62</sup> Forster, R.J., Keyes, T.E., Vos, J.G., *Interfacial Supramolecular Assemblies*, Wiley, **2003**.

<sup>63</sup> P. H. Rieger, *Electrochemistry*, Springer, **1987**.

<sup>64</sup> C. M. A. Brett, A. M. O. Brett, *Electrochemistry: Principles, Methods and Applications*, **1993**.

<sup>65</sup> R.G. Norrish, G. Porter, *Nature*, **1950**, 164, 685.

<sup>66</sup> I.P. Clarke, M. W. George, G. M. Greetham, E. C. Harvey, C. Long, J. C. Manton, M. T. Pryce, *J. Phys. Chem A*, **2010**, 114, 43, 11425.

<sup>67</sup> *Central Laser Facility Annual Report*, **2008-2009**.



## **Chapter 2**

### **$\mu_2$ -Alkyne-Cobalt**

### **Carbonyl Complexes**

Chapter 2 gives a brief introduction to the chemistry of metal carbonyl complexes. This is followed by a more in-depth look at cobalt carbonyl complexes, including their uses, photochemistry and electrochemistry. Some examples of the use of cobalt systems and carbonyl complexes in hydrogen production experiments are examined. The UV-Vis, emission, IR, picosecond time resolved IR studies, quantum yields of CO loss and cyclic voltammetry using the compounds synthesised in this chapter are also discussed. The chapter concludes with both photocatalytic and electrocatalytic generation of hydrogen studies.

## Aim

With an aim to develop novel non-noble metal containing complexes capable of generating H<sub>2</sub> photochemically and/ or electrochemically ( $\mu^2$ -alkyne) cobalt carbonyl complexes were synthesised and tested for their H<sub>2</sub> producing efficacies. With the aim of shifting the absorbances of the complexes further towards the visible region of the spectrum highly conjugated ligands were produced and coordinated to cobalt hexacarbonyl and tetracarbonyl metal centres with the hopes that the metal centre would efficiently catalyse the water splitting reaction. The addition of diphenylphosphino moieties allowed for further stability of the complexes.

The photochemistry of the complexes was investigated through UV-Vis, IR and picosecond time resolved IR studies. Two complexes  $\mu_2$ -ethynylpyrene Co<sub>2</sub>(CO)<sub>6</sub> and  $\mu_2$ -pyrene-ethynylferrocene Co<sub>2</sub>(CO)<sub>6</sub> showed evidence of CO loss during picosecond time resolved IR studies, which is the first time this process has been reported in solution using time resolved IR techniques. The quantum yields of CO loss for these two complexes were determined at various wavelengths. Their electrochemistry was also investigated using cyclic voltammetry.

## 2.1. Introduction

Organometallic chemistry is a branch of chemistry which links both organic and inorganic chemistry, and focuses on molecules containing a metal-carbon bond. The metal component of the bond can generally be a lanthanide, actinide or a transition metal from groups 3-12 of the periodic table but group 1 complexes are also possible. This type of bonding can introduce new and unique excited states which can lead to different reactivity and photochemical properties of a molecule.

During excitation, various absorptions can be observed which are specific to organometallic molecules<sup>1</sup>. Examples of these absorptions include metal to ligand charge transfer (MLCT), which are electronic transitions which occur when an excited electron is donated from the metal centre, which is acting as a reducing agent, to a lower energy excited state on the coordinated ligand. This can only occur when the energy of the excited state accepting the electron on the ligand is sufficiently lower in energy than that of the donating metal orbital. Another possible transition is ligand to metal charge transfer (LMCT). This is the opposite of MLCT, i.e. the ligand acts as the donor molecule, donating an electron to a lower energy excited state on the metal centre.

These transition metal complexes, due to their partially filled d-sublevels, give rise to unique properties such as variable valencies which often produce highly coloured compounds. They also exhibit unusual magnetic properties such as paramagnetism due to unpaired d-electrons. Another very important property of transition metals, which is utilised in this study, is the ability of these partially filled d-orbitals to bond to neutrally charged ligands.

### 2.1.1. Metal Carbonyls

The CO (carbonyl) group is an unsaturated ligand, with a carbon oxygen multiple bond, capable of forming organometallic complexes when coordinated with transition metals. It has a filled  $\sigma$  orbital and two filled  $\pi$  orbitals with two lone pairs of electrons. It is known as a soft ligand as it is

quite easy to polarise and predominantly undergoes covalent bonding. It also undergoes back bonding with metal  $d_{\pi}$  electrons using its unoccupied CO  $\pi^*$  orbital. These two orbitals overlap to form the M-C  $\pi$  bond.<sup>2</sup> Carbon monoxide is known as an  $\sigma$  donor,  $\pi$  acceptor ligand as it has the ability to accept electron density from metal centres and this stabilises its bonding with metals which have low oxidation states (highly electron rich). The complexes formed may be stable as homoleptic compounds, which means that they contain only -CO ligands such as cobalt carbonyl (e.g.  $\text{Co}(\text{CO})_8$ ), but the more common metal carbonyls contain a mix of different ligands, like  $[\text{Ru}(\text{CO})_3\text{Cl}(\text{glycinate})]$ .

#### **2.1.1.1. The Bonding of Metal Carbonyls:**

The bonding of metal carbonyls consists of two components which gives rise to a partial triple bond  $(\sigma)^2(\pi_x)^2(\pi_y)^2$ . The first component occurs when the two electrons in the lone pair of the carbon are coordinated directly to a d-orbital of the transition metal centre in a  $\sigma$  bond. Due to the addition of these two electrons to the metal centre, the metal centre itself becomes more electron rich.

The second component is known as  $\pi$ - back-bonding. Due to the electron rich nature of the metal, as a result of  $\sigma$  bonding, a filled metal d-orbital may now interact with an empty  $\pi$ -orbital ( $-\text{CO } \pi^*$ ) of the carbonyl ligand. Due to the symmetry within the molecule this means that some of the electrons which had previously been located in a metal orbital can now move to the ligand's antibonding orbital which reduces the electron density on the metal. This type of bonding is very important in the metal-ligand bonding where there is an unsaturated ligand involved.

Backbonding in CO increases the ligand field splitting parameter  $\Delta$ , which means that the bond between the M-L is very strong. The components involved in M-CO bonding are illustrated below (Fig. 2.1).

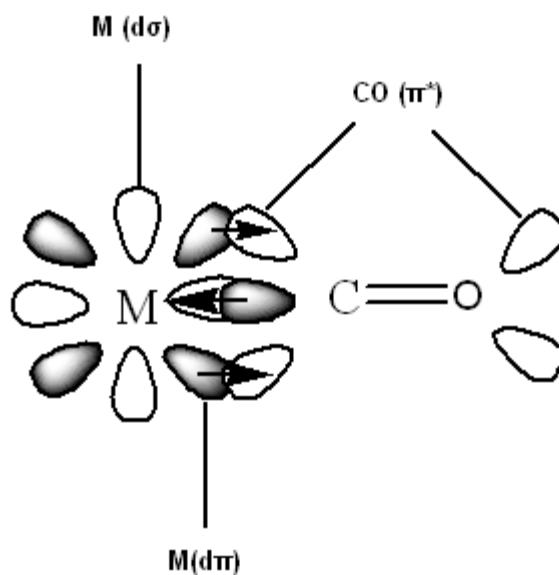


**Figure 2.1-** Schematic representation of the bonding in metal carbonyls, arrows indicate the migration of electrons.

As well as the previously discussed M-CO bond, many metal carbonyl complexes will have a carbon monoxide group bound between two metal centres. This bridging of the CO ligand is generally limited to the first row transition metals. When this occurs it is generally accepted that the bridging CO ligand will donate only one electron to each of the metal centres, forming a  $\sigma$  bond with each.

#### **2.1.1.2. Variants of CO Bridging:**

Organometallic complexes prefer to have an 18 electron configuration. Due to this they will form single or double bonds with a ligand to achieve this configuration.

CO has three principal coordination modes (Fig. 2.2).

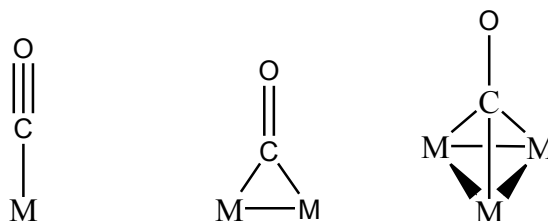


**Figure 2.2 - Coordination modes of M-CO bonding**

Larger metals generally prefer the terminal, unbridged coordination of the carbonyl to the metal. This is due to the bond distance between the metal centres and the angle of the metal to carbon to metal bond of a CO-bridge .

Unsymmetrical/ semi bridging of the CO group is also possible with the M-C bond which is like an intermediate between the terminal and bridging coordination modes.

This can be due to the presence of sterically hindering bulky constituents distorting the bond angles of the CO-bridges. These large substituents force the CO bridge to move to a distorted position to allow space.

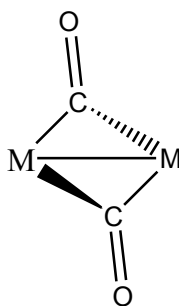


**Figure 2.3 - Unsymmetrical M-CO Bonding**

Each metal centre can coordinate with other metal centres and carbonyl species in different ways, as shown in Fig. 2.4.

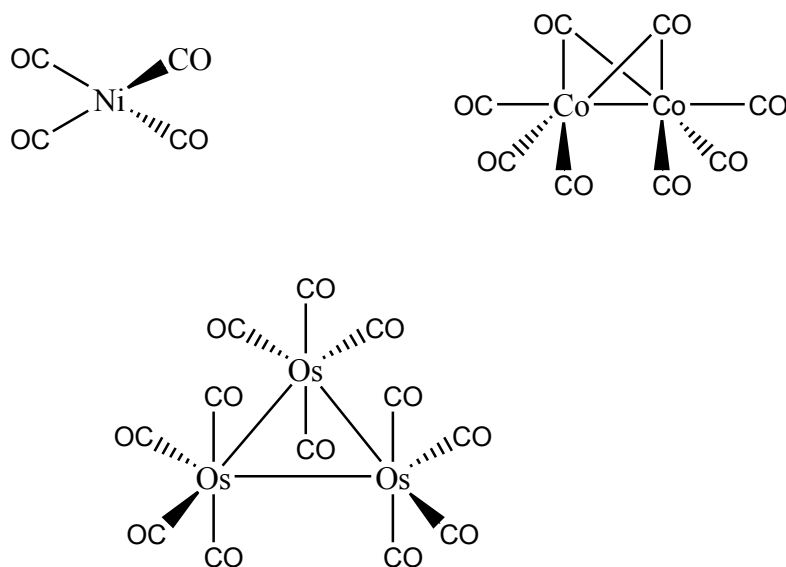


Figure 2.4 - Examples of coordination of -CO in various metals

### 2.1.2. Cobalt Carbonyl

Dicobalt octacarbonyl is the simplest closed shell cobalt carbonyl which exists in its solid state in the form shown below (Fig. 2.5, **1**) with two bridging carbonyl bonds and three terminal carbonyl groups on each Co centre, however when in solution it exists in equilibrium in the structure shown below<sup>18</sup> (Fig. 2.5, **2**) with no CO bridging ligands.

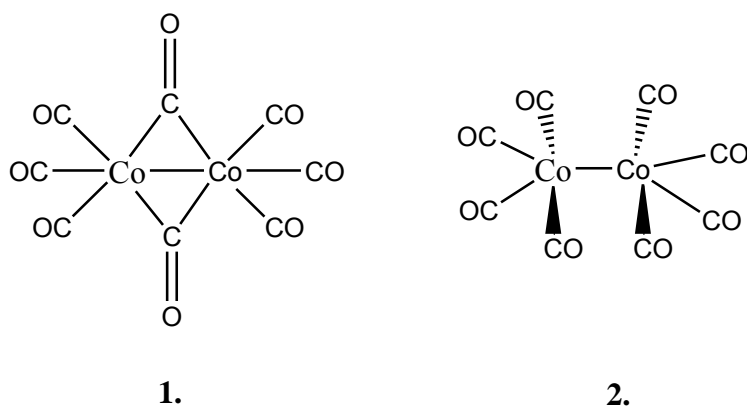


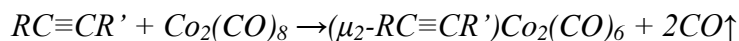
Figure 2.5 - Cobalt carbonyl bonding, 1. solid state, 2. in solution.

Cobalt carbonyls have been the source of much research in the area of carbon monoxide-releasing molecules (CORMs). The therapeutic effects of CO in the body include vasodilation of veins and arteries<sup>3</sup>, inhibition of apoptosis<sup>4</sup>, preventing inflammation<sup>5</sup> as well as others<sup>6,7</sup>. They have also been utilised as catalysts in ring forming reactions such as a precursor in the Pauson- Khand reaction. The Pauson-Khand reaction is a cobalt mediated cycloaddition reaction involving co-cyclisation of an alkyne, an alkene and carbon monoxide. The reaction was originally carried out by simply heating a mixture of a  $\text{Co}_2(\text{CO})_8$ (alkyne) and alkene in a hydrocarbon solvent, however increasing interest has been shown for the mechanism and enantioselectivity of this reaction.<sup>8,9</sup> Although it is generally accepted that the first step in the Pauson-Khand reaction involves loss of CO and subsequent alkene coordination to one of the two enantiotopic Co atoms, the full and exact mechanism is yet to be elucidated. However, it has been generally observed<sup>10</sup> that the coordinating alkene will position itself nearest the less sterically hindering and therefore less bulky ethynyl substituent and that C-C bond formation occurs between this ethynyl carbon and the alkene. This generally results in the bulky ethynyl substituent in the  $\alpha$ -position of the formed cyclopentanone, next to the C=O bond. Use of cobalt carbonyls as pure catalysts in the Pauson-Khand reaction have also been investigated.<sup>11,12</sup>

### 2.1.3. Alkyne Bonding with Cobalt Carbonyl

Alkyne bonds consist of a carbon-carbon triple bond. This triple bond consists of a  $\sigma$ -bond and two  $\pi$ -bonds localised between the two carbon atoms in the bond and also two  $\pi^*$  orbitals which are directed away from the triple bond. Alkyne bonds are often utilised in organometallic chemistry for the complexation of metal carbonyl complexes. When bonding, the alkyne has a perpendicular arrangement in relation to the metal-alkyne bond (Fig. 2.6).<sup>1</sup> Due to the two perpendicular mutually degenerate  $\pi$ -orbitals, which are located at right angles to one another on the ligand, two cobalt molecules can bond to the ligand at once, hence the bonding will occur in the bridging fashion shown below (Fig. 2.6)<sup>1</sup>. The reaction of an alkyne with the dicobalt octacarbonyl complex results in the replacement of the two bridging carbonyl groups to form the organometallic complex.





**Reaction 2.1- Reaction of an alkyne with dicobalt octacarbonyl.**

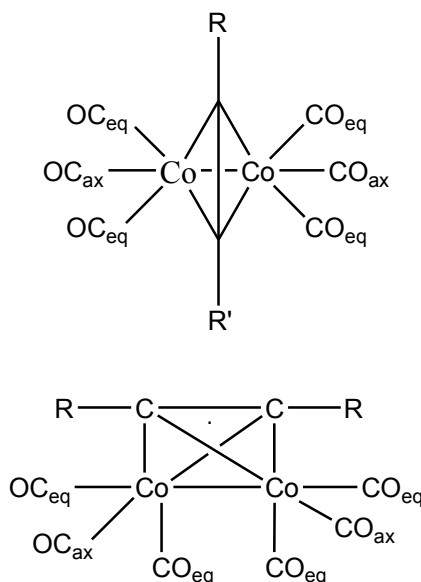


**Figure 2.6- Coordination of dicobalt hexacarbonyl,  $Co_2(CO)_6$  (showing axial and equatorial ligands), to an alkyne bond releasing carbon monoxide.**

This bridging arises due to a donation of electrons from the two bonding  $\pi$  orbitals of the alkyne group to the unfilled metal d-orbitals of the cobalt metal centres and also the donation of electrons from the filled metal d-orbitals into the empty anti-bonding  $\pi$  molecular orbitals of the alkyne.<sup>13</sup>

The structure of  $(\mu_2\text{-alkyne})Co_2(CO)_6$  complexes is based on a tetrahedrane  $Co_2C_2$  core with external R groups on each carbon and three terminal carbonyl groups on each cobalt centre. The  $(\mu_2\text{-alkyne})Co_2(CO)_6$  complex has 12 skeletal electrons required for localised bonds along its six bonds which include four Co-C bonds, one C-C bond and one Co-Co bond. In this localised bonding model the Co-Co bond can be considered to be a formal single bond however it shows some singlet diradical character in ab initio and DTF calculations.<sup>14</sup>

Sly<sup>15</sup> reported the first x-ray crystallography study on diphenylacetylene dicobalt hexacarbonyl which is one of the first molecules to be studied which exhibits multi-point attachment of a single organic molecule to more than one metal atom. The study revealed that the diphenylacetylene dicobalt hexacarbonyl molecule has a six fold coordination about the cobalt atoms in a distorted octahedral configuration with the C-C bond of the acetylene approximately normal to the Co-Co bond in a distorted tetrahedral arrangement. This gives the molecule an approximate  $C_{2v}$  symmetry except for the benzene rings.

More recently a theoretical study of the alkyne-bridged complex,  $(\mu_2-C_2H_2)Co_2(CO)_6$ , indicated a large electron density about a Co-Co antibonding orbital and also Co- $\pi^*$  back bonding.<sup>16</sup> Previous attempts to explain the bonding in the molecule using quantum theory of atoms in molecules (QTAIM), although useful, had given only a partial picture. To further describe the molecule restricted Hartree-Fock (RHF), Kohn-Sham (RKS) and complete active space (CAS) measurements were employed. The occupation of bonding and antibonding orbitals in the CAS wavefunction suggests that the Co-Co and Co-CO bonding may be more complex than initially inferred. Utilising QTAIM analysis on the ground state singlet CAS, Platts *et al.*<sup>16</sup> discovered that, surprisingly, there is no bond critical point (bcp) in the region between the Co nuclei. Four Co-C<sub>alkyne</sub> bonds were present along with all expected Co-C<sub>CO</sub>, C-C, C-O and C-H bcps. These measurements indicated the presence of two 3-membered metallocycles in the Co<sub>2</sub>C<sub>2</sub> core, sometimes referred to as a “butterfly arrangement”. A value for  $\delta(\text{Co},\text{Co})$  of 0.26 was calculated from the CAS wavefunction, where a value of 1 would indicate a single bond. Thus, the atomic overlap data suggests a weak but nonzero overlap between cobalt atoms.

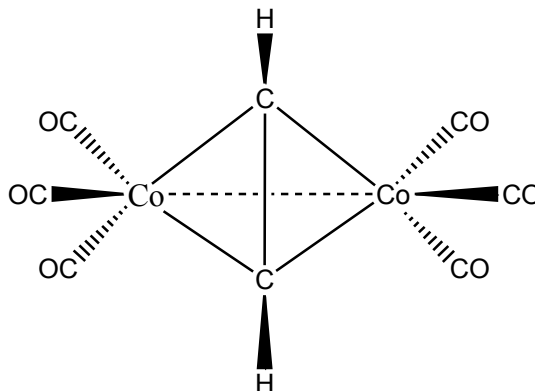


**Figure 2.7 - "Butterfly arrangement" in  $\mu_2$ -C<sub>2</sub>H<sub>2</sub>Co<sub>2</sub>(CO)<sub>6</sub> complexes indicating two 3-membered metallocycles in the tetrahedrane Co<sub>2</sub>C<sub>2</sub> core.**

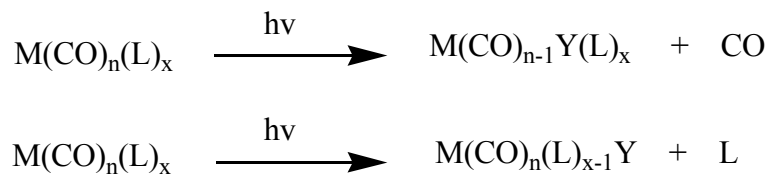
Based on the work of Espinosa<sup>17</sup> in which they employed a diagnostic tool to explore bonding interactions based on energy densities, the ratio of potential to kinetic energy densities was calculated at bond critical points. A value of greater than two indicated shared or covalent interaction, while a value of less than one indicated closed-shell interaction. Between these extremes, a "transit" region of incipient covalent bonding is proposed. Using the CAS wavefunction measurements, Platts *et al.*<sup>16</sup> calculated values for this ratio of 1.34 at the midpoint of the Co-Co vector, a value within the "transit" region described, which they suggested was due to some covalent character in the metal-metal region. They concluded that the ab initio and DFT calculations indicated that the ground state electronic structure of the alkyne-bridged complex was again, best described as a singlet diradical, with partial occupation of both bonding and antibonding orbitals between the two Co atoms.

#### **2.1.4. Photochemistry of $\mu_2$ -Alkyne Cobalt Carbonyl Complexes**

Photochemistry is the study of the reactions which occur within a molecule or group of molecules following irradiation or photoexcitation. This involves the use of light, whether ultraviolet, visible or infra-red, to excite electrons within a molecule's ground state into higher energy excited states. The excess energy now within the molecules

before they return to the ground state can meet the activation energy required for various reactions to occur.

Metal carbonyl complexes are among the most photoreactive transition metal complexes known<sup>18</sup>. The most common photoreactions which occur in metal carbonyl molecules are ligand substitutions of either the larger ligand (L) or the CO itself with a new substituent (Y)<sup>18</sup>.



**Scheme 2.1 - Ligand substitution reactions in metal carbonyls<sup>18</sup>.**

The new substituents (Y) should be good  $\pi$ -acceptors as with the loss of  $-\text{CO}$ , which itself has a great stabilising effect on the metal centre, the bonding could become very unstable if the new substituent is not a good  $\pi$ -acceptor. The quantum yield of this substitution reaction may also be wavelength dependant, leading to different quantum yields of CO loss at various wavelengths of irradiation.

It is well known that  $(\mu_2\text{-C}_2\text{H}_2)\text{Co}_2(\text{CO})_6$  compounds undergo replacement of one or both axial CO groups upon heating with monodentate tertiary phosphines, phosphites and arsines<sup>19</sup>. Upon reaction with bidentate ligands such as fluorocarbon and hydrocarbon bridged compounds a similar reaction occurs but with loss of two or four CO equatorial molecules. They coordinate about the metal atoms either by bridging two cobalt atoms in the same molecule or by chelating to one of them (Fig. 2.8).

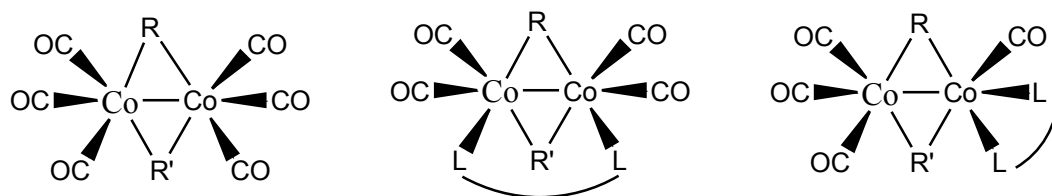
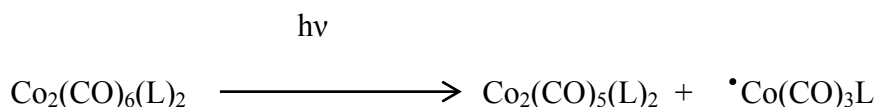


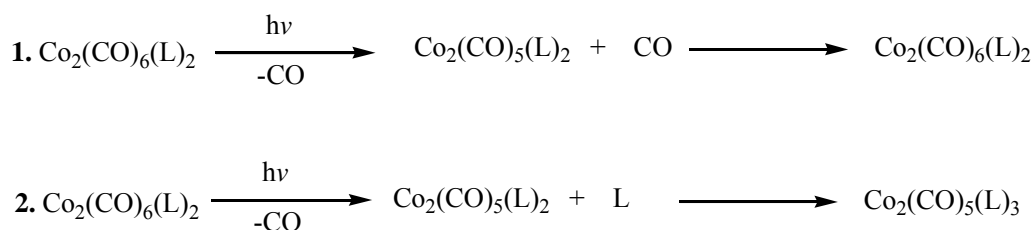
**Figure 2.8 - Coordination of ligands with cobalt carbonyl following heating.**

TRIR (time resolved infra-red) studies were carried out to investigate the reactive photoproducts upon laser flash photolysis of the cobalt hexacarbonyl complex,  $\text{Co}_2(\text{CO})_6(\text{PMePh}_2)_2$  by Marhenke *et al.*<sup>20</sup> Upon photolysis at wavelengths between 308 and 365nm two photoproducts were formed. The first was a loss of a single CO molecule which resulted in the formation of  $\text{Co}_2(\text{CO})_5(\text{PMePh}_2)_2$  through dissociation. The other was homolytic cleavage of the metal-metal bond which resulted in the formation of a  $\cdot\text{Co}(\text{CO})_3(\text{PMePh}_2)$  radical (Rxn. 2.2).



**Reaction 2.2 - Two photoproducts produced from the irradiation of  $\text{Co}_2(\text{CO})_6(\text{L})_2$ ,  $\text{L} = \text{PMePh}_2$ .**<sup>20</sup>

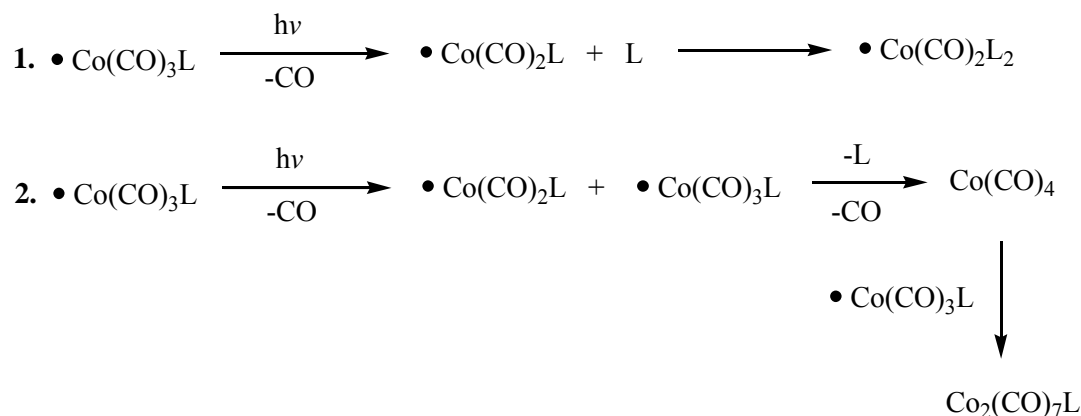
There are two possible routes for the  $\text{Co}_2(\text{CO})_5(\text{L})_2$  ( $\text{L} = \text{PMePh}_2$ ) photoproduct to follow. Under an atmosphere of CO, upon irradiation the photogenerated CO loss product  $\text{Co}_2(\text{CO})_5(\text{L})_2$  recombines with CO to reform the starting material;  $\text{Co}_2(\text{CO})_6(\text{L})_2$ . An alternative route is when an excess of ligand (L) is present in the experiment. Under these conditions  $\text{Co}_2(\text{CO})_5(\text{L})_2$  is again formed and the CO removed is replaced by another ligand resulting in the formation of  $\text{Co}_2(\text{CO})_5(\text{L})_3$ .



**Scheme 2.2 – Two possible reaction routes of  $\text{Co}_2(\text{CO})_5(\text{L})_2$ ,  $\text{L} = \text{PMePh}_2$ .**<sup>20</sup>

When the second product; the  $\cdot\text{Co}(\text{CO})_3\text{L}$  radical is formed there are also a number of possible photoproducts which can be formed when it is involved in further reactions. In the presence of excess ligand (L) this species can produce  $\cdot\text{Co}(\text{CO})_2(\text{L})_2$  via a ligand substitution reaction. This product can then react with another  $\cdot\text{Co}(\text{CO})_3\text{L}$  radical to produce  $\text{Co}_2(\text{CO})_5(\text{L})_3$ . Under an atmosphere of CO the  $\cdot\text{Co}(\text{CO})_3\text{L}$  radical can produce

a tetracarbonyl species;  $\cdot\text{Co}_2(\text{CO})_4$ . This tetracarbonyl can then undergo a combination reaction with the initial radical species  $\cdot\text{Co}(\text{CO})_3\text{L}$  to form the complex  $\text{Co}_2(\text{CO})_7\text{L}$ .



**Scheme 2.3 - Two possible reaction routes of  $\cdot\text{Co}(\text{CO})_3(\text{L})$ ,  $\text{L} = \text{PMePh}_2$ .**<sup>20</sup>

Photolysis experiments have been reported by Moskovich *et al.*<sup>21</sup> which indicates that when  $\text{Co}_2(\text{CO})_8$  is subjected to a microsecond UV pulse at room temperature, TRIR studies in heptane show the formation of both  $\text{Co}(\text{CO})_4$  and  $\text{Co}_2(\text{CO})_7$  solvated species which decay over short periods of time ( $\sim 40 \mu\text{s}$ ).

Draper *et al.*<sup>22</sup> investigated the photochemistry of a cobalt carbonyl system and have reported the importance of the wavelength of excitation on the photoproducts produced. Pulsed photolysis of a  $(\mu_2\text{-RC}_2\text{H})\text{Co}_2(\text{CO})_6$  ( $\text{R} = \text{H}, \text{C}_6\text{H}_5$ ) species with an excitation wavelength of 340 nm in the presence of a trapping ligand (trapping ligand =  $\text{C}_5\text{H}_5\text{N}$  or  $\text{PPh}_3$ ) showed the formation of the appropriate pentacarbonyl species. Upon prolonged photolysis of this pentacarbonyl the disubstituted tetracarbonyl was also produced. These experiments concluded that photochemical CO loss is achievable.

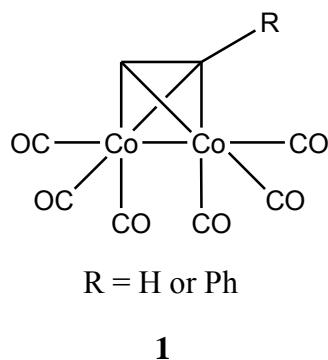


**Figure 2.9 - General structure of a  $(\mu_2\text{-RC}_2\text{H})\text{Co}_2(\text{CO})_6$  compounds.**<sup>22</sup>

Upon irradiation with monochromatic light at 355 nm there was no evidence of  $-\text{CO}$  loss in the spectra. However there was a depletion was observed in the parent absorption spectra following excitation.

When irradiated with monochromatic light at 532nm in the presence of a trapping ligand there was evidence for the loss of CO, with confirmation of the pentacarbonyl photoproduct through IR spectroscopy.

Coleman *et al.*<sup>23</sup> synthesised a series of pyrene-thiophene dyads along with their  $\text{Co}_2(\text{CO})_6$  derivatives (Fig. 2.10)

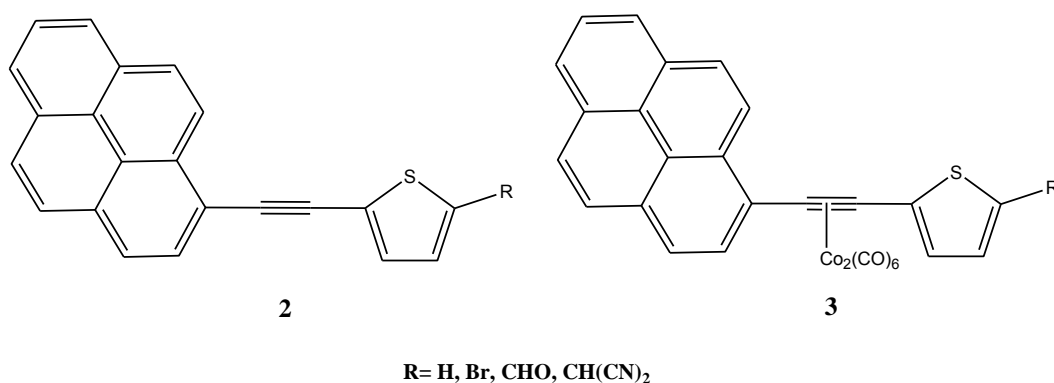


**Figure 2.10 - Pyrene-thiophene dyads and  $\text{Co}_2(\text{CO})_6$  derivatives synthesised by Coleman *et al.***<sup>23</sup>

The UV-Vis spectra of these compounds showed strong absorbances in the region 320 - 450 nm. These absorptions were attributed to  $\pi\text{-}\pi^*$  transitions by the authors. Weaker less defined absorptions were observed in the region of 580 - 600 nm, with the dicyano

derivative absorbing further towards the red  $\sim 700$  nm, and these absorption bands were attributed to weak d – d transitions.

Room temperature emission studies showed that complexation with the  $\text{Co}_2(\text{CO})_6$  moiety results in significant quenching of the ligand based emission bands, which was assigned to energy transfer from the luminescent pyrene moiety to the non-luminescent cobalt metal centre. When low temperature (77 K) emission studies were carried out this quenching process was much less efficient. Steady state photolysis experiments were carried out with  $\lambda_{\text{ex}} > 520$  nm for 10 min in the presence of a  $\text{PPh}_3$  (used as a trapping agent). The experiment resulted in the bleaching of the parent absorption bands concomitant with the generation of new product bands which were assigned to the pentacarbonyl photoproduct  $(\mu_2\text{-C}_2\text{H}_2)\text{Co}_2(\text{CO})_5\text{PPh}_3$ . Subsequent irradiation with  $\lambda_{\text{ex}} > 400$  nm for 15 min resulted in further bleaching of the parent bands and an increase in the absorbance of the new bands formed which correspond to the pentacarbonyl species. Bands were also observed at 1984, 1968 and 1941  $\text{cm}^{-1}$  which were attributed to the tetracarbonyl species  $\mu^2\text{-C}_2\text{H}_2(\text{Co}_2(\text{CO})_4(\text{PPh}_3)_2)$ .

Boyle *et al.*<sup>24</sup> utilised picosecond time resolved IR (TRIR) to probe the photochemistry of three  $(\mu_2\text{-alkyne})\text{Co}_2(\text{CO})_6$  complexes (Fig 2.11). Upon photolysis at 400 nm and 532 nm it was proposed that each of the complexes formed a triplet diradical species with lifetimes in the range of 38 - 71ps, after which time the original parent complex was reformed. In these picosecond TRIR studies no evidence was obtained for a CO loss species. Hence to ensure that any possible CO loss photoproducts, which may be produced in the time resolved IR experiment, were not absorbing in either a region similar to that of the photoproduct or under the new bands formed due to the triplet diradical species.  $\text{PPh}_3$  was added to the solutions used in the time resolved IR experiment as a trapping agent for the pentacarbonyl species, if produced. However this experiment yielded the same previously observed triplet diradical excited state and once again yielded no CO loss products.



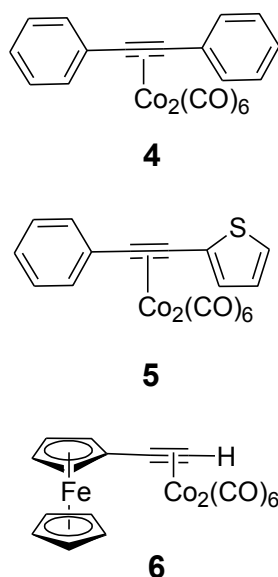


**Figure 2.11 -  $(\mu_2\text{-alkyne})\text{Co}_2(\text{CO})_6$  complexes studied by Boyle *et al.*<sup>24</sup>**

Results from steady-state photolysis experiments, using a triphenylphosphine ( $\text{PPh}_3$ ) as a trapping ligand, however showed evidence for CO loss photoproduct  $(\mu_2\text{-alkyne})\text{Co}_2(\text{CO})_5\text{PPh}_3$ .

Bitterwolf *et al.*<sup>25</sup> synthesised a series of  $\text{Co}_2(\text{CO})_6(\text{alkyne})$  complexes where the alkyne = **(I)**  $\text{H}_2\text{C}_2$ , **(II)**  $(\text{C}_2\text{H}_5)_2\text{C}_2$ , **(III)**  $(\text{C}_6\text{H}_5)_2\text{C}_2$  and **(IV)**  $\text{C}_6\text{H}_5\text{C}_2\text{H}$ . They have shown that photolysis of these compounds in frozen Nujol at 90 K results in loss of CO to give  $\text{Co}_2(\text{CO})_5(\text{alkyne})$  in which CO loss appears to be from the axial position. Upon annealing to 140 K a second isomer was observed, which was presumed to have a vacancy in the equatorial position, or regeneration of the starting material.  $\text{PPh}_3$  trapping ligands were used and the loss of CO ligands from the molecules were measured using low temperature IR. Photolysis into the MLCT or ligand field bands of the cobalt tetrahedrane compounds studied resulted in the loss of CO to form one or two species in which the tetrahedrane core was retained. Hexacarbonyl compounds were found to generate one species upon photolysis which results in the reduction of symmetry of the molecule from  $\text{C}_{2v}$  symmetry to **7**,  $\text{C}_s$  (axial loss of CO) or **8**,  $\text{C}_1$  (equatorial loss). Upon photolysis it was apparent that axial CO loss occurred forming the  $\text{Co}_2(\text{CO})_5(\text{alkyne})$  photoproduct. Upon annealing to 140 K isomerisation to a structure where the CO loss was apparently equatorial was observed (Table 2.1). Pentacarbonylphosphine species

appear to give two photoproducts; both the axial and equatorial CO loss products **9**, **10** (Fig. 2.12).

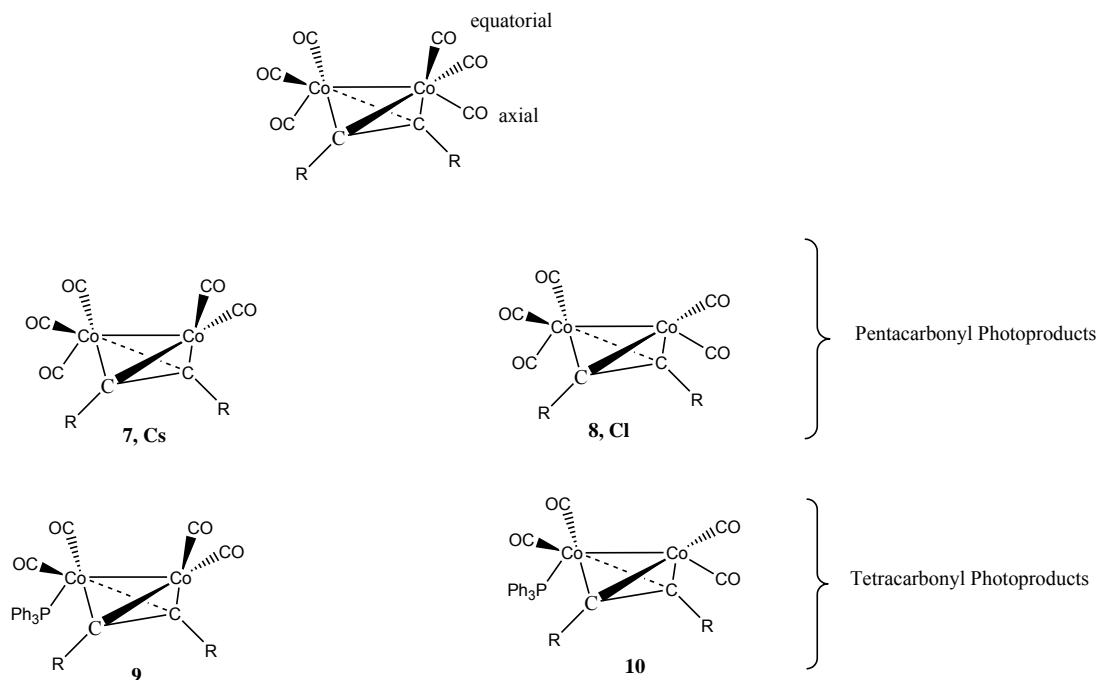


**Figure 2.12 - Photoproducts of  $\text{Co}_2(\text{CO})_6(\text{alkyne})$  and  $\text{Co}_2(\text{CO})_5(\text{alkyne})$  complexes proposed by Bitterwolf *et al.*<sup>25</sup>**

Compound*	Parent Spectrum ( $\text{cm}^{-1}$ )	Photoproduct ( $\text{cm}^{-1}$ )	Annealed Photoproduct ( $\text{cm}^{-1}$ )
<b>7</b>	2099, 2058, 2032, 2027, 2016	2084, 2080, 2034, 2019, 2011, 1980	2084, 2043, 2019, 2014, 2000
<b>8</b>	2088, 2047, 2023, 2013, 2002	2070, 2018, 2004, 1999, 1996	2073, 2032, 2006, 2001, 1988
<b>9</b>	2095, 2057, 2030, 2026	2077, 2029, 2015, 1976	2080, 2042, 2018, 1998
<b>10</b>	2091, 2056, 2028, 2025	2073, 2028, 2013, 2005, 1975	2076, 2042, 2017, 2012

**Table 2.1 - IR spectral data for the  $\text{Co}_2(\text{CO})_6(\text{alkyne derivatives})$  ( $\text{cm}^{-1}$ ) in a frozen Nujol matrix at 90 K. (Note: a free CO band was observed at  $2032\text{cm}^{-1}$  in all cases). \* See Fig 2.12 for structures of compounds **7** – **10**.**

Campeil *et al.*<sup>26</sup> have reported the synthesis of a series of cobalt hexacarbonyl ferrocenylalkynes complexes and their phosphine derivatives. Ferrocene itself has established synthetic versatility and is an electron donating group which is linked *via* an electron rich backbone to a polyaromatic acceptor moiety. When the ferrocene moiety was linked *via* an alkyne groups to an adjacent organometallic moiety it resulted in electronic interactions between the two metal centres which illustrates potential for tuneable redox chemistry within the complexes. The incorporation on one or two Co<sub>2</sub>(CO)<sub>6</sub> units along the alkyne backbone lead to a reduction in triple bond character, which was observed through a downfield shift in the proton and carbon NMR spectra of the products. The coordination of phosphine derivatives resulted in the replacement of two carbonyl groups from the cobalt centre. The use of 1,1-bis(diphenyldiphosphino)methane (dppm) resulted in coordination of the molecule through the two phosphine moieties. This coordination with the poorer  $\pi$ -accepting phosphines resulted in a shift of the carbonyl bands to lower frequencies in the IR spectrum.

### 2.1.5. Cobalt Systems Used in Photocatalytic Hydrogen Generation

A new area of research in hydrogen generation is the use of cheaper, more abundant metals coordinated to dyes, such as cobalt phthalocyanines (CoPc) which when irradiated with high energy photons are capable of catalytically generating H<sub>2</sub> from water. Cobalt is a very attractive metal for use as the catalytic centre in hydrogen generation experiments due to the fact that it is relatively cheap and also it readily coordinates to a wide variety of ligands.

Cobalt catalysis for hydrogen generation over the last decade has been primarily focused on releasing hydrogen from sodium borohydride<sup>27,28</sup> due to its high storage capacity for hydrogen, about 10 wt% of H<sub>2</sub> stored in a NaBH<sub>4</sub> system at ambient temperature and atmospheric pressure<sup>28</sup>, and its great stability in alkaline solution. The catalyst themselves which have been reported have been mainly based on Co<sub>3</sub>O<sub>4</sub><sup>29</sup> or cobalt-boride<sup>30, 31</sup>.

However, the main focus of this study is to generate hydrogen from the widely available and environmentally sound source; water. The use of cobalt carbonyl complexes to yield hydrogen from water has not been widely explored to date, however there have been a few reported cases of the use of cobalt derivatives to yield reasonably high turnover number (TON) of hydrogen, where TON refers to the number of moles of H<sub>2</sub> produced divided by the number of moles of catalyst (or photosensitiser) used in the experiment. A comprehensive review of cobalt complexes used in the production of hydrogen has been recently published.<sup>32</sup>

Lehn *et al.*<sup>33</sup> investigated the intermolecular photocatalytic efficiency of a simple catalyst; CoCl<sub>3</sub> under visible light irradiation using the photosensitiser [Ru(Bpy)<sub>3</sub>]<sup>2+</sup> (bpy = 2,2'-bipyridine) (Fig. 2.13 ) in aqueous solution. The reduction of CO<sub>2</sub> to CO and H<sub>2</sub> formation were examined.

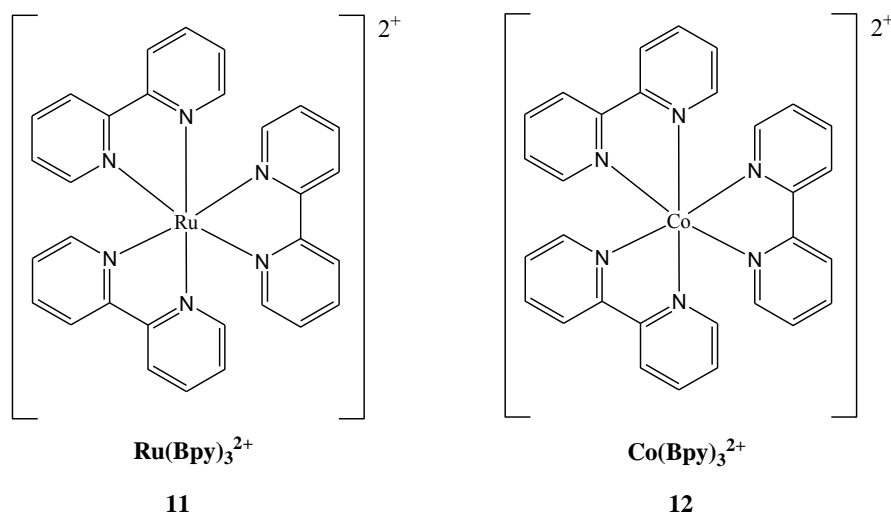


**Figure 2.13- Photosensitiser molecules tested by Lehn and co-workers.<sup>33</sup>**

CoCl<sub>3</sub> and [Ru(Bpy)<sub>3</sub>]<sup>2+</sup> were dissolved in a solution of acetonitrile/water and a tripropylamine electron donor, in a 3:1:1 ratio. This mix successfully reduced CO<sub>2</sub> to yield CO and water to yield H<sub>2</sub>. H<sub>2</sub> TONs of 9 were achieved based on CoCl<sub>3</sub> after 20 hours of irradiation at  $\lambda < 400$  nm. When a 10% (in relation to CoCl<sub>3</sub>) equivalent of bpy was added to the solution, [Co(Bpy)<sub>3</sub>]<sup>2+</sup> is generated *in situ* which promotes the production of hydrogen and hinders the reduction of CO<sub>2</sub>. The generation of a Co<sup>I</sup>

species is a key intermediate in the reduction reaction and is most likely formed upon reduction of  $\text{Co}^{\text{II}}$  by the photoreduced ruthenium photosensitiser. The hinderance of  $\text{CO}_2$  reduction shows the prominence that occupation of the coordination sites of the cobalt centre has on the process.

McNamara *et al.*<sup>34</sup> have demonstrated that cobalt-dithiolene complexes (Fig. 2.14) are capable of producing  $\text{H}_2$  generation TONs > 2700 photocatalytically upon irradiation using visible light, and also possess a strong electrocatalytically induced current at minimal overpotentialsof  $\sim 0.4$  V and a Faradaic yield of > 95% for all complexes.

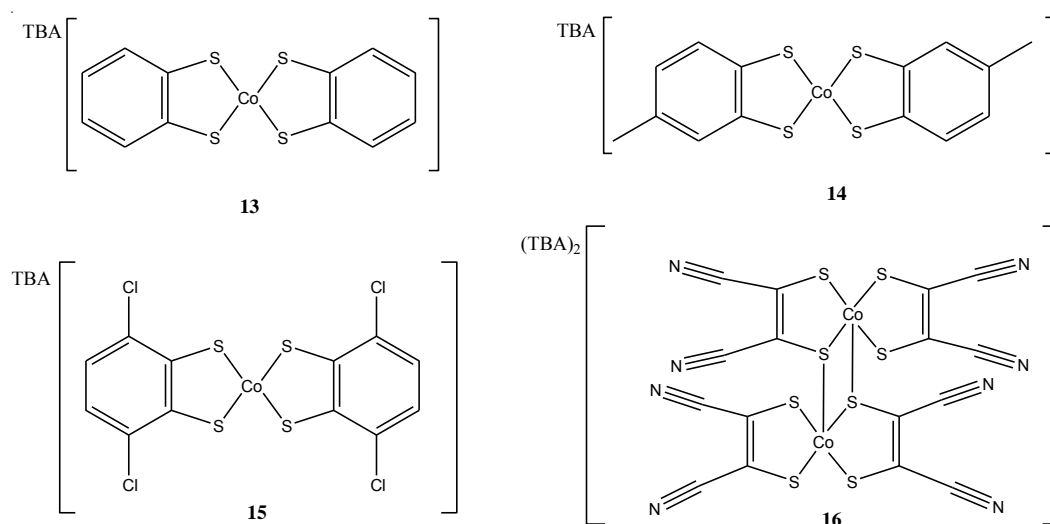


**Figure 2.14 – Cobalt dithiolene complexes studied by McNamara *et al.*<sup>34</sup>**

Photocatalytic hydrogen generation experiments were carried out using  $\text{Ru}(\text{Bpy})_3^{2+}$  as a photosensitiser group and ascorbic acid as the sacrificial donor using 520 nm LEDs for irradiation. TONs of 2700, 2300, 6000 and 9000 were achieved after 20 hours irradiation for **13**, **14**, **15**, and **16**, respectively with the activity of **16** placing it among the most active  $\text{H}_2$  generating photocatalysts reported. The systems were highly active for 6 – 10 hours before decomposition of the catalyst and the chromophore alike resulted in a gradual decrease in the rate of hydrogen generation. While decomposing continues throughout the photolysis experiment leading to system activity decline at higher catalyst concentrations  $\text{H}_2$  is still being produced after 20 hours. In general, total system cessation was observed after 24 hours of irradiation.

Singh *et al.*<sup>35</sup> successfully synthesised a cobalt complex of N,Nbis(2-pyridinylmethyl)-2,2'-bipyridine-6-methanamine (DPA-Bpy) (Fig. 2.15) and studied both its electrocatalytic and photocatalytic hydrogen production efficiencies in aqueous media.

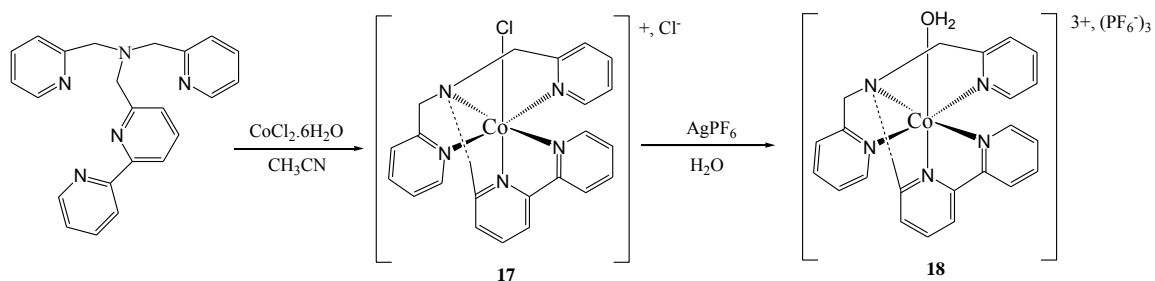


**Figure 2.15- Cobalt DPA-Bpy complexes studied by Singh *et al.*<sup>35</sup>**

The photocatalytic generation of  $\text{H}_2$  using complex **18** was also measured using a 450 nm LED light strip. 1.0M acetate buffer at pH 4.0 with 0.1M ascorbic acid, 0.5 mM  $[\text{Ru}(\text{bpy})_3]^{2+}$  and 5.0 mM complex at  $22^\circ\text{C}$ .  $\text{Ru}(\text{Bpy})\text{Cl}_3$  was added to act as a photosensitiser molecule. The generation of  $\text{H}_2$  ceased after 3 hours and a TON of  $>1600$  was measured relative to the catalyst concentration. About 90% of the  $\text{H}_2$  was produced in the first hour and a TOF of  $1500 \text{ h}^{-1}$  was measured.

More examples of cobalt complexes used in the photocatalytic generation of hydrogen will be discussed in Chapter 3 and Chapter 4.

### 2.1.6. Carbonyl Systems Used in Photocatalytic Hydrogen Generation

No literature has appeared on the use of cobalt carbonyl compounds for the photocatalytic generation of hydrogen, which are the compounds used in this study. Numerous studies have focused on the use of  $\text{Fe}^{36,38,39}$  and  $\text{Rh}^{37}$  carbonyl compounds for  $\text{H}_2$  generation and furthermore reasonable turnover numbers have been shown.

Iron carbonyl compounds have been investigated as possible biomimetic photocatalytic centres for the generation of hydrogen as they resemble the active sites in  $[\text{FeFe}]$

hydrogenases, catalysts which are used in the reduction of hydrogen in the microorganisms. Na *et al.* demonstrated that hydrogen could be intermolecularly produced using visible light with a ruthenium photosensitiser and an iron carbonyl catalytic centre, **19** (Fig. 2.16)<sup>36</sup>.

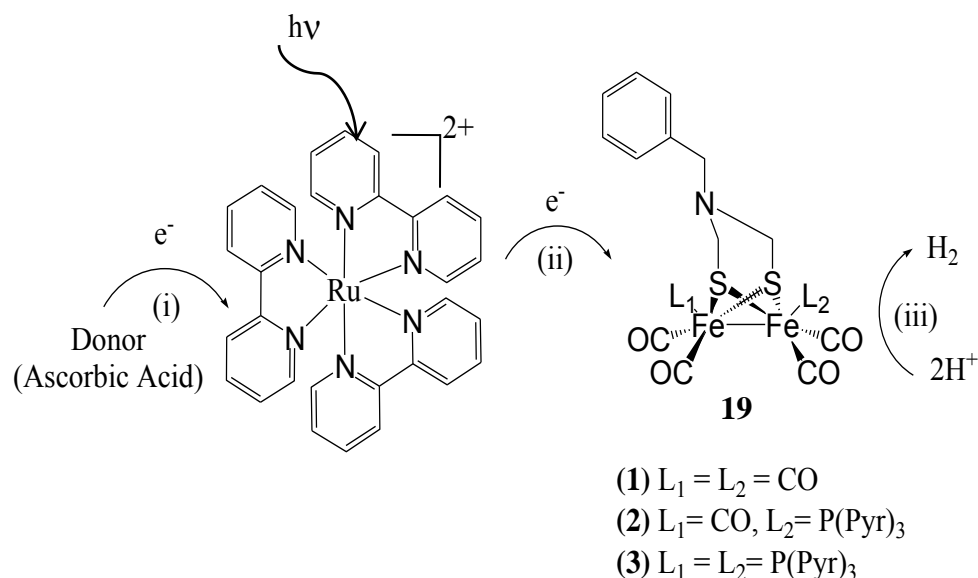


**Figure 2.16 - Fe-CO based catalytic system and  $\text{Ru}(\text{bpy})_3$  used by Na *et al.*<sup>36</sup>. (i) Reductive quenching, (ii) Intermolecular electron transfer, (iii) Catalytic proton reduction.**

A  $[\text{Ru}(\text{bpy})_3]^{2+}$  photosensitiser was used along with ascorbic acid which acted as a sacrificial donor as well as a reducing agent to regenerate the  $[\text{Ru}(\text{bpy})_3]^{2+}$ . Using IR detection it was observed that following irradiation, the catalytic centre in **19(1)** decomposed after 1 hour. A phosphine ligand, *tris*(*N*-pyrrolyl)phosphine ( $\text{P}(\text{Pyr})_3$ ), was introduced to the iron carbonyl centre for compounds **19(2)** and **19(3)** which improved the photostability of the catalytic centre. Laser flash photolysis was used to verify photoinduced electron transfer processes of the three-component systems. A TON of 0.78 was observed for **19(1)** after 3 hours when irradiated at 25 °C using an Xe lamp (500 W) with a Pyrex-glass filter ( $\lambda > \text{ca. } 400 \text{ nm}$ ) in a 1:1 ACN/  $\text{H}_2\text{O}$  solution. **19(2)** and **19(3)** were monitored under the same conditions and yielded TONs of 4.3 and 1.7 respectively. IR monitoring of **19(2)** and **19(3)** showed that they were more photostable than **19(1)** however they were found to decompose after 2.5 hours of irradiation. These

results indicate that not only did the addition of a phosphine ligand to the iron carbonyl catalytic centre improve the compounds photostability but also increased its catalytic activity.

An attractive alternative to the expensive Ru photosensitisers mentioned above are porphyrin systems as they are free from noble metals, and both catalyst and photosensitiser are biologically inspired. Some compounds which fit this description have been synthesised by Song and his co-workers.<sup>38</sup> Within these complexes the Fe-CO catalytic centre is covalently linked to the tetraphenylporphyrin (TPP) or zinctetraphenylporphyrin (ZnTPP) ring, **20**. They observed that there was a marked quenching of the fluorescence emission when the Fe-CO catalytic centre was coordinated to the TPP ring when compared to the spectra obtained for the porphyrins on their own. They believe that this is most likely due to strong intramolecular electron transfer from the photoexcited state of the porphyrin macrocycle to the covalently bonded Fe-CO moiety.

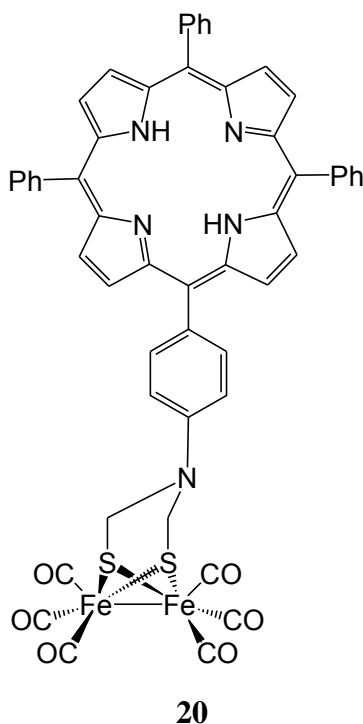
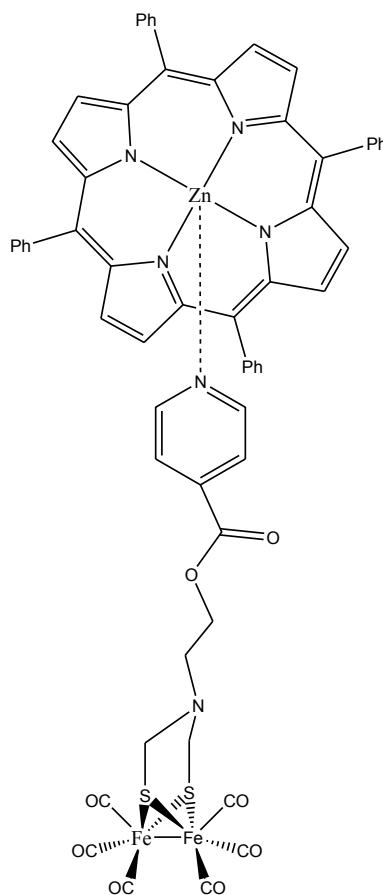


Figure 2.17- Covalently linked porphyrin and Fe-CO catalytic centre synthesised by Song *et al.*<sup>38</sup>



Recently Li *et al.* have reported the synthesis of datively linked Fe-CO catalytic centre with a ZnTPP ring<sup>39</sup>.



21

Figure 2.18 - Porphyrin photosensitisers and Fe-CO catalytic centres used by Li et al<sup>39</sup>.

Due to the strong fluorescent emission from ZnTPP it was employed as a sensitive probe for excited-state quenching, which would be due to an electron or energy transfer occurring from the singlet excited state of ZnTPP ( $^1\text{ZnTPP}^*$ ) to the Fe-CO catalytic centre. The addition of the Fe-CO centre to the ZnTPP photosensitiser did in fact quench the fluorescence significantly when compared to ZnTPP on its own. The design of this complex is such that once electron transfer has occurred intramolecularly the ZnTPP and the Fe-CO complex can separate as they are not covalently linked. This will aid the reduction of the charge recombination and energy transfer when compared with similar covalently linked dyads such as those synthesised by Song and co-workers.

Rhodium carbonyls (Rh-COs) have been used as catalytic centres for the photoinduced generation of hydrogen when bound to an osmium bis(terpyridyl) light harvesting chromophore through the diphosphine ligand.<sup>36</sup> The Rh-CO centre binds to the diphosphine ligands in a bidentate manner (Fig. 2.19).

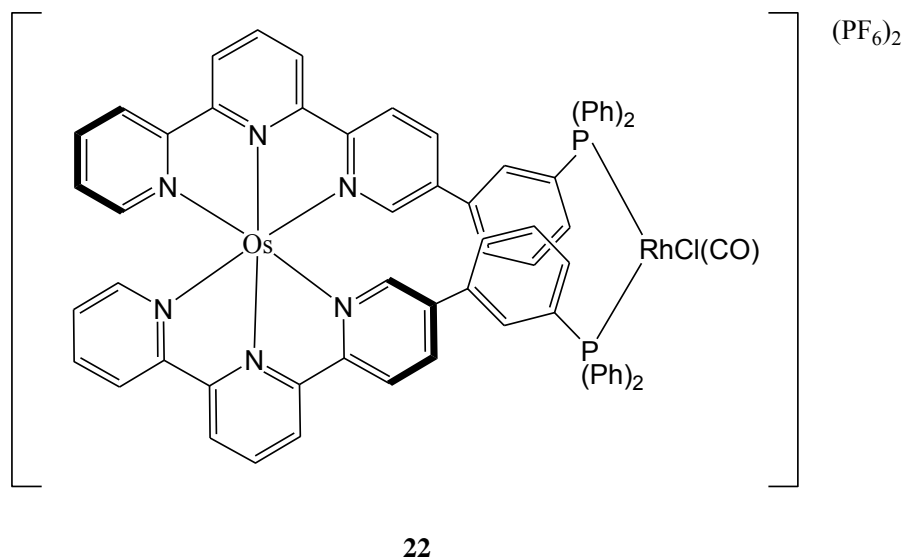


**Figure 2.19 - Rhodium carbonyl catalytic centre synthesised by Miyake *et al.*<sup>36</sup>**

When a solution of trifluoromethanesulfonic acid (HOTf) and sodium ascorbate (NaHA) and the compound in 1:1 ACN/ H<sub>2</sub>O was irradiated with visible light ( $\lambda > 380$  nm) for 18 hours a TON of 36 was observed.

### 2.1.7. Electrochemistry of $\mu_2$ -Alkyne Cobalt Carbonyl Complexes

The presence of alkynyl bridges is known to facilitate long distance electronic interactions through  $\pi$  delocalisation and the degree of these interactions between substituent ligands can be measured by electrochemical methods.<sup>40</sup> When Co<sub>2</sub>(CO)<sub>6</sub> moieties are integrated in a bidentate fashion to these alkynyl groups they are known to undergo an irreversible reduction (of the type electrochemical-chemical (EC)) forming the radical anion  $[\mu_2\text{-C}_2\text{H}_2\text{Co}_2(\text{CO})_6]^\cdot$  which results in the decomposition of the parent species.<sup>41</sup> This leads to metal-metal bond cleavage and the formation of a variety of

decomposition products. These products can give rise to oxidation peaks after this first  $1e^-$  reduction. However, reversibility of these reductions has been achieved, through increasing the scan rate of the experiment or decreasing the temperature of the experiment.<sup>41,42</sup> Some of the decomposition products are assumed to be  $\text{Co}_2(\text{CO})_4^-$ ,  $\text{RC}_2\text{R}'\text{Co}(\text{CO})_3$  and free cobalt however these products have been difficult to isolate and study as the electrode often becomes fouled with these products which renders it unusable.<sup>41</sup> The nature of the ligand substituent on the alkynyl bridge can also greatly influence the reversibility of this process. As the electron withdrawing capability of the capping group decreases, the reduction potential of the process shifts more negative leading to the lifetime of the primary radical anion increasing and the redox process approaches chemical reversibility.<sup>43</sup> Oxidation processes in  $(\mu_2\text{-C}_2\text{H}_2)\text{Co}_2(\text{CO})_6$  complexes are reasonably well understood.<sup>40,41,42</sup> An irreversible oxidation is known to occur at potentials  $\sim 1.0\text{V}$  vs. SCE at room temperature. When temperatures are lowered to  $-30^\circ\text{C}$  this wave becomes partially reversible at faster scan rates. Again, as with the reduction process, the generation of the radical cation  $[(\mu_2\text{-C}_2\text{H}_2)\text{Co}_2(\text{CO})_6]^+$  leads to fouling of the electrode, rendering it unusable.<sup>44</sup>

The addition of electron donating phosphino moieties (DPPM, DPPA etc.) to the Co-Co metal centre increases the stability of the metal-metal bond through controlling electron density at the metal centres also increasing the lifetimes of the radical anions and cations.<sup>44</sup> As this type of group donates electrons to the metal centre it also allows for easier oxidation at lower potentials, however in contrast it increases the potential at which the metal can become reduced. It has been reported it is necessary to apply more negative potentials of up to  $0.5 - 0.6\text{ V}$  to observe a reduction when compared to a  $(\mu_2\text{-C}_2\text{H}_2)\text{Co}_2(\text{CO})_6$  complex.<sup>44</sup> The increase in stability of the Co-Co metal bond and increased lifetimes of the radical cations and radical anions has been known to lead to reversibility of both the reduction and oxidation processes.

A study by Marcos *et al.*<sup>41</sup> has been published investigating the effects of various phosphino ligands on the electrochemistry of  $(\mu_2\text{-C}_2\text{H}_2)\text{Co}_2(\text{CO})_x\text{-L}$  complexes using a polycrystalline Pt working electrode, a Pt gauze counter electrode, a silver wire quasi-reference electrode and a  $0.2\text{ M TBAPF}_6$  in THF solution as supporting electrolyte. Owing to the electron donating nature of the phosphino ligand it was noted that the  $E_{1/2}$

of the reduction processes in the series occurred at increasingly lower potentials in the order  $L = \mathbf{24} > \mathbf{25} > \mathbf{27} > \mathbf{28} > \mathbf{26}$  (Fig. 2.20). However it was observed that the reduction processes for **25** and **26** are irreversible at room temperature ( $0.1 \text{ Vs}^{-1}$  scan rate) but dppa and dppm complexes are almost reversible. It was concluded that the EC mechanism that follows reduction in each of the complexes is much slower in dppa/dppm as  $i_a/i_c \approx 0.95$  at  $0.1 \text{ Vs}^{-1}$  scan rate. As the basicity of the two phosphines on **26** and **28** are similar ( $\text{p}K_a \mathbf{26} = 4.57$  and  $\text{p}K_a \mathbf{28} = 4.31$ ) it was observed that the chelation by **28** produces a less effective donation of electrons from the phosphine leading to  $E_{1/2}^{\text{ox}} = 0.51 \text{ V}$  for **26** and  $E_{1/2}^{\text{ox}} \mathbf{28} = 0.75 \text{ V}$ .

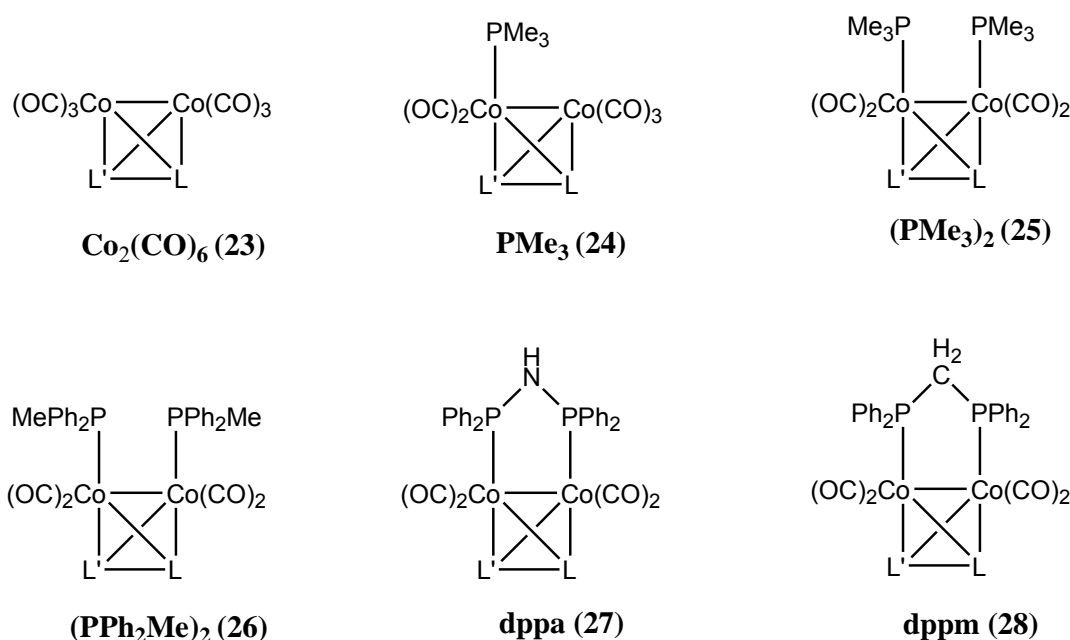
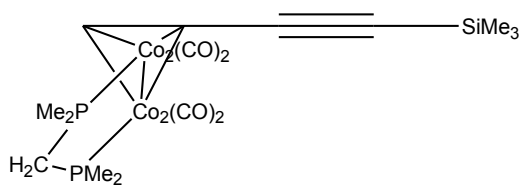


**Figure 2.20-**  $\mu_2\text{-C}_2\text{H}_2\text{Co}_2(\text{CO})_x\text{-L}$  complexes investigated by Marcos *et al.*<sup>41</sup>  $L = \text{CSiMe}_3$ ,  $L' = \text{C}\equiv\text{CSiMe}_3$ .

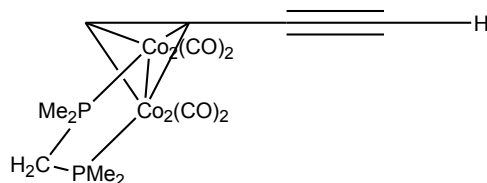
The addition of two phosphino ligands will increase the stability of the Co-Co bond more than the substitution of a single metal centre and this was observed by Marcos as the disubstituted complexes gave a more reversible process during oxidation at room

temperature. **25** and **26** produced  $i_a/i_c \approx 0.8$  V at  $0.1 \text{ V s}^{-1}$  scan rate and **27** and **28** produced  $i_a/i_c = 1$  at the same scan rate.

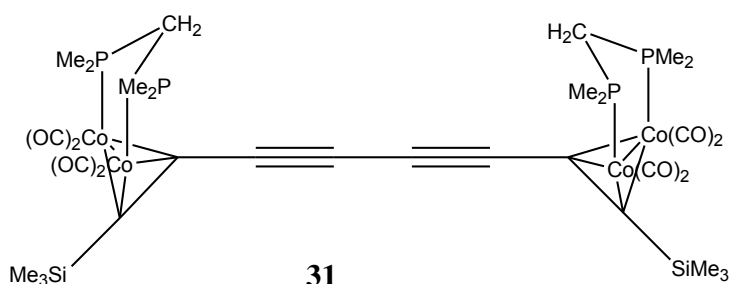
The nature of the phosphino ligand can greatly alter the electrochemical activity of the cobalt carbonyl complex, as previously mentioned, but it can also affect the electronic coupling between the two Co centres. Complexes with more than one dicobalt unit have been studied.<sup>45</sup> Two complexes with only one dicobalt (**29** and **30**) unit were compared to two complexes with two dicobalt units (**31** and **32**) (Fig. 2.21) in 0.2 M TBAPF<sub>6</sub> in DCM. The oxidations in all complexes were reversible at room temperature however it was found that complexes **29** and **30** must be cooled to  $-30^\circ\text{C}$  for their reduction processes to become reversible. When two dicobalt processes are present on the one complex such as with **31** and **32** two distinctive oxidation and two distinctive reduction processes are observable. The greater the separation between these two oxidation/reduction peaks is indicative of a greater interaction between the two metal centres. It was noticed that the more basic and less sterically hindering dmpm ligand seemed to decrease these interactions when directly compared to the dppm ligand complex. It was concluded that the dmpm group hindered efficient mixing of the filled metal fragments and the alkyne-based orbitals.



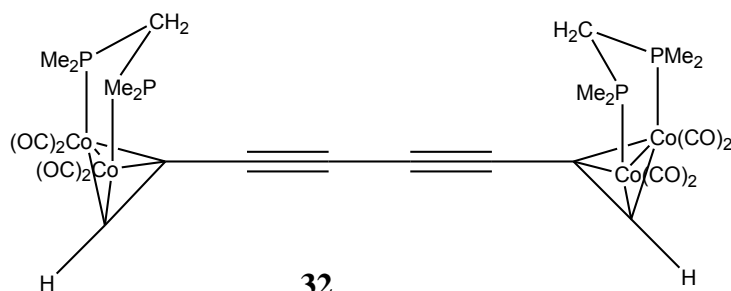
**29**



**30**



**31**



**32**

**Figure 2.21-** Complexes with one dicobalt centre (29, 30) and two dicobalt centres (31, 32) studied by Macazanga *et al.*<sup>45</sup> Phosphino group;  $\text{PMe}_2 = \text{dmpm}$ ,  $\text{PPh}_2 = \text{dppm}$ .

The nature of the alkynyl substituents can also greatly affect the reversibility of the reduction process also. Marcos *et al.*<sup>41</sup> established that the  $\text{SiMe}_3$  capping ligand, when coupled with a dppm ligand on the Co metal centre experiences a nearly completely reversible reduction at room temperature showing that it also influences the stability of

the metal carbonyl and influences the length of the lifetime of the radical anion. In contrast McAdam and his group<sup>46</sup> reported an irreversible reduction in complexes of the formula  $(\mu_2\text{-RC}\equiv\text{CH})\text{Co}_2(\text{CO})_4(\text{dppm})\text{R}$ , where  $\text{R} = \text{Ph}, \text{Fc}$ , at 25°C despite employing the same phosphino group.

### 2.1.8. Cobalt Systems Used in Electrocatalytic Hydrogen Generation

The use of cobalt for electrocatalytic hydrogen generation is at the forefront of much research. Due to its well established redox chemistry and relative ease of reduction, incorporating cobalt into various ligand structures is a step towards a sustainable hydrogen production system.

As mentioned previously, Singh *et al.*<sup>35</sup> have successfully synthesised a cobalt complex of N,Nbis(2-pyridinylmethyl)-2,2'-bipyridine-6-methanamine (DPA-Bpy) (Fig. 2.15) and studied both its electrocatalytic and photocatalytic hydrogen production efficiencies in aqueous media. Using a three electrode set up in pH 7.0, 1.0 M  $\text{NaH}_2\text{PO}_4$  buffer with a glassy carbon working electrode, an Ag/AgCl reference electrode, and a Pt wire counter electrode, three reversible redox processes are observed at 0.35 V, -0.94 V, and -1.53 V (vs. SHE) in the cyclic voltammogram of complex **17** in  $\text{CH}_3\text{CN}$  which are assigned to  $\text{Co}^{\text{III/II}}$ ,  $\text{Co}^{\text{II/I}}$ , and  $\text{Co}^{\text{I/0}}$  respectively, while in this region the ligand does not show any electrochemical behaviour. Complex **2** shows two reversible processes at 0.15 V and -0.90 V (vs. SHE) corresponding to  $\text{Co}^{\text{III/II}}$  and  $\text{Co}^{\text{II/I}}$  respectively. When the working electrode was changed to a mercury pool electrode the CV showed no significant current at potentials more positive than -1.6 V vs. SHE for a bare electrode experiment. The modification of the electrode with complex **18** induced a strong current at -1.2 V concomitant with the formation of hydrogen bubbles. This demonstrates that complex **18** is capable of generating hydrogen at a neutral pH and that the  $\text{Co}^{\text{II/I}}$  reduction must occur for water to be split. Bulk electrolysis experiments were carried out at a potential of -1.4 V vs. SHE and a current efficiency of  $99 \pm 1\%$  was achieved, while when electrolysis was carried out at -1.3 V the current efficiency measured was  $98 \pm 2\%$  after 1 hour.

Cobalt phthalocyanines (CoPc) have been at the centre of a great deal of research in recent times due to their absorbances in the visible spectrum and their highly efficient intermolecular electron transfer processes. When cobalt is incorporated into the ring structure both metal and ring based redox processes are observed (addition of Zn or Cu results in only ring based processes). Varying the substituents on the ring can vary the redox chemistry of the complexes. The addition of an electron withdrawing substituent can facilitate an easier reduction of the complex, with the opposite effect occurring when an electron donating group is attached. Koca *et al.*<sup>47</sup> have reported a study on the addition of various substituents to the ring of a cobalt phthalocyanine. They have synthesised a number of fluorinated aryloxy phthalocyanine metal derivatives. The addition of these fluorinated aryloxy groups to the phthalocyanine ring improves their solubility in organic solvents as it is well documented that phthalocyanines are sparingly soluble in many solvents.<sup>48</sup>

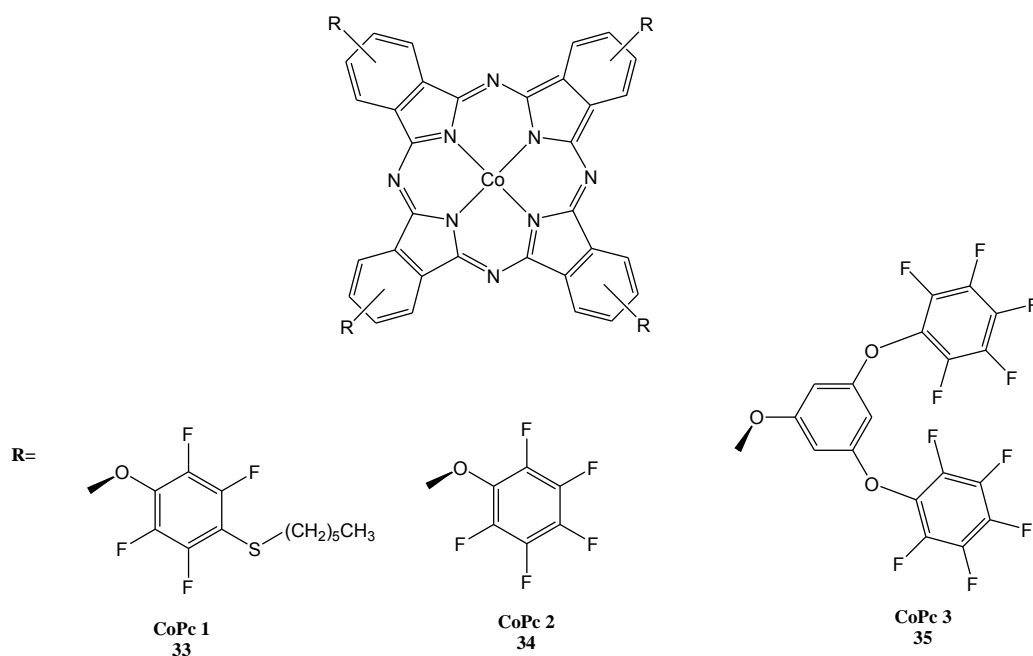


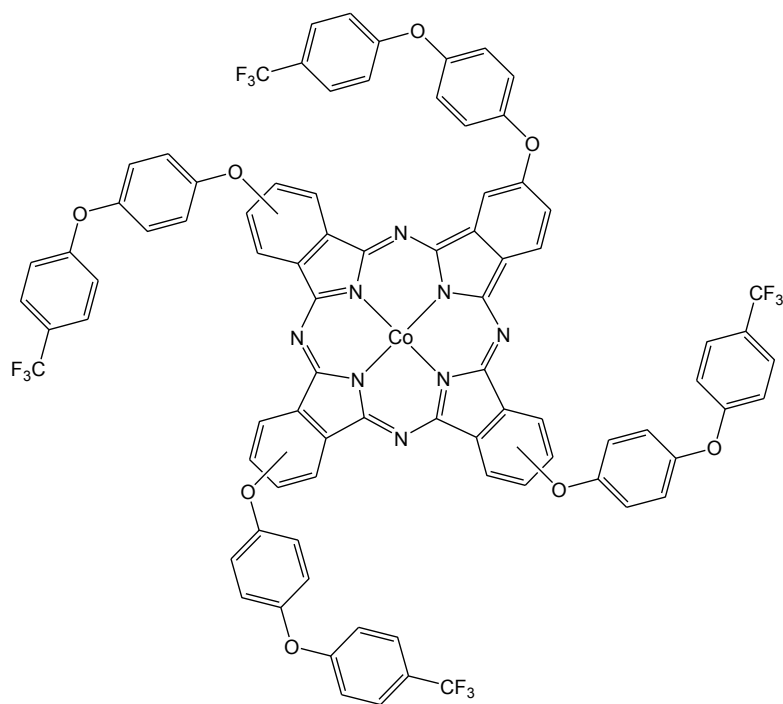
**Figure 2.23 - CoPc complexes studied by Koca *et al.*<sup>47</sup>**

The addition of the fluoro substituents resulted in small changes in the reduction potentials observed with **CoPc2**'s first reduction occurring at -0.21 V vs. SCE compared



to **CoPc1** at -0.28 V due to the more electron withdrawing nature of the pentafluoro groups on **CoPc2**. Due to the distance between the Co metal centre and the decafluoro groups in **CoPc3** the electron withdrawing ability is somewhat diminished resulting in a reduction at -0.39 V. The CoPc complexes were incorporated into Nafion polymer on the surface of the glassy carbon electrode. The addition of HClO<sub>4</sub> into the **CoPc1/2/3** cell triggers the appearance of a new irreversible cathodic wave which is attributed to the electrocatalytic hydrogen evolution reaction. For electrocatalytic measurements a glassy carbon working electrode was employed along with a platinum wire counter electrode and an SCE reference electrode. An aqueous phosphate buffer was employed as supporting electrolyte. A catalytic current was induced at -0.90 V, -1.00 V and -1.02 V for **CoPc1**, **CoPc2** and **CoPc3** respectively while this current was not seen for the electrode coated in Nafion alone until -1.25 V at pH 4.2. **CoPc1** demonstrated the greatest efficacy with **CoPc2** producing a slightly smaller catalytic current. **CoPc3** produced a catalytic current  $\sim 1/3$  less strong than that of **CoPc1** and **CoPc2**. This may be due to its aggregation tendencies preventing the protonation of the complex.

CoPcs bearing tetrakis-[4-((4'-trifluoromethyl)phenoxy)phenoxy] groups have also been investigated.<sup>49</sup> These tetrakis-[4-((4'-trifluoromethyl)phenoxy)phenoxy] groups are electron withdrawing substituents and greatly affect the reduction potentials of the processes in the Pc (Fig. 2.24).



36

**Figure 2.24 - CoPcs bearing tetrakis-[4-((4'-trifluoromethyl)phenoxy)phenoxy] groups investigated by Koca *et al.*<sup>49</sup>**

This CoPc was compared to its H<sub>2</sub>, Zn and Cu counterparts (however all redox processes were assigned to the ring in these complexes). CoPc undergoes one two-electron reduction and two one-electron reductions at  $-0.26$  V,  $-0.63$  V and  $-1.44$  V vs. SCE respectively using a platinum electrode in DCM (TBAP supporting electrolyte) with the reduction at  $-0.63$  V assigned to an aggregated species and the process at  $-0.26$  V assigned to Co<sup>II/I</sup> and the final reduction at  $-1.44$  V is a ring based, generating CoPc<sup>•-</sup>. While the hydrogen generating catalytic current starts at  $-1.31$  V and  $-1.25$  V respectively using a bare glassy carbon electrode and with the ZnPc derivative in aqueous phosphate buffer at pH 9.20 containing HClO<sub>4</sub>, it starts at  $-0.88$  and  $-1.08$  V using CuPc and CoPc modified electrodes. Both CuPc and CoPc show strong catalytic currents at these potentials, however CoPc induces a current almost twice as strong as its copper counterpart. This strong catalytic current together with the overpotential decrease

of the catalysis,  $\Delta E_{OP}$  = 0.43V for CuPc, and 0.23V for CoPc, these complexes show great potential for use in the commercial generation of hydrogen.

A tetradentate polypyridyl ligand supported  $Co^{II}$  complex has been synthesised by Bigi *et al.*<sup>50</sup> The complex exhibits a reversible reduction wave at -0.81 V vs. SCE which is assigned to the  $Co^{II/I}$  process. When TFA is added to the solution a catalytic current is triggered near this  $Co^{II/I}$  process which yields  $H_2$  with 99% efficiency indicating that the increase in current is due to a catalytic  $H_2$  generating process. The turnover frequency (TOF- which refers to the TON per unit time) calculated for this complex was  $40\ h^{-1}$  with an overpotential of 0.4 V measured.

Utilising cobalt-dithiolene complexes (Fig. 2.14) McNamara and his group have demonstrated that they are capable of producing TONs of >9000 photocatalytically and these complexes possess a strong  $H_2$  generating electrocatalytic current induced at minimal overpotentials with Faradaic yields of >95% for all complexes.<sup>34</sup> All of the complexes were active as electrocatalysts when electrolysed in a solution of p-toluene sulfonic acid (65 mM) and 0.1 M  $KNO_3$  in a 1:1 solution of  $CH_3CN:H_2O$ . 0.2 mM of catalyst was electrolysed for 1 hour at -1.0 V vs. SCE. A catalytic current is observed at a more cathodic potential than the reversible redox couple for  $CoL_2^- / CoL_2^{2-}$  which generates the active species.

Complex	$E_{1/2}$ (V)	$E_{pc}$ (V)	$\Delta E_{op}$ (V)
<b>13</b>	-0.64	-1.21	0.57
<b>14</b>	-0.70	-1.32	0.62
<b>15</b>	-0.51	-0.97	0.46
<b>16</b>	-0.04	-1.37	1.33

**Table 2.2-** Electrochemical results presented by McNamara *et al.*<sup>34</sup> (V vs. SCE) determined from cyclic voltammetry in 1:1  $CH_3CN:H_2O$  at a glassy carbon electrode with 0.1 M  $KNO_3$ . Catalytic experiments were achieved using  $CH_3CN$  and TFA as a proton source. See Fig. 2.14 for structures of complexes.

The results in Table 2.2. show the  $E_{1/2}$  values of the  $\text{CoL}_2^-/\text{CoL}_2^{2-}$  couples for each complex. The overpotential between the reduction process and the top of the catalytic wave was measured and it is clear that although **16** required the least potential to be reduced the onset of the catalytic curve begins at the most negative potential. In contrast **15** is deemed to be the most efficient electrocatalyst as the onset of the catalytic curve is at less negative potential and the overpotential is the smallest of all 4 complexes at 0.46 V.

More examples of cobalt complexes used in the electrocatalytic generation of hydrogen will be discussed in Chapter 3.

### 2.1.9. Carbonyl Systems Used in Electrocatalytic Hydrogen Generation

No literature has appeared on the use of cobalt carbonyl compounds for the electrocatalytic generation of hydrogen which is the basis of this chapter however a few groups have studied related carbonyl complexes that may be used as electrocatalysts. Donovan *et al.*<sup>51</sup> have employed cyclopentadienyl metal carbonyl dimer complexes incorporating a variety of metals (M = Fe, Ru, Mo, W) to investigate the effect of these different metals on the electrocatalytic abilities of the complexes to reduce protons from weak acids (Fig. 2.25).

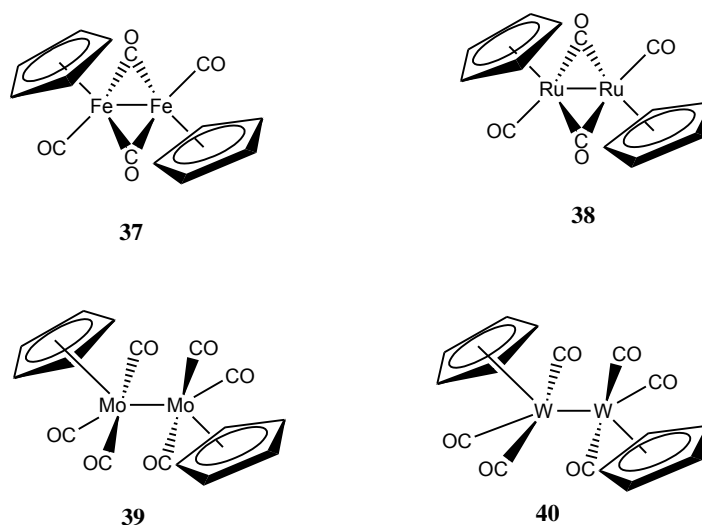
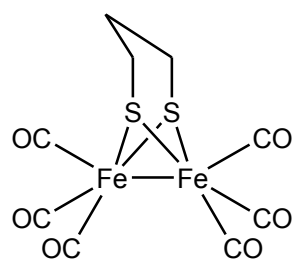


Figure 2.25- Cyclopentadienyl metal carbonyl dimer complexes studied by Donovan *et al.*<sup>51</sup>

A three electrode system was employed including a glassy carbon working electrode, platinum wire counter electrode and silver external reference electrode (10 mM AgNO<sub>3</sub> in electrolyte solution). 0.10 M tetra-n-butylammonium hexafluorophosphate (Bu<sub>4</sub>NPF<sub>6</sub>) in anhydrous acetonitrile was used as supporting electrolyte and 0.01 M of various acids. Electrolysis was carried out at -2.4 V. The iron metallocentre was deemed to be the best candidate as an electrocatalysts as it succeeded in reducing acids as weak as 4-tert-butylphenol with a pK<sub>a</sub> of 27.5 in acetonitrile. The iron complex underwent an irreversible two electron reduction at -1.91 V (vs Fc<sup>+</sup>/Fc) forming [CpFe(CO)<sub>2</sub>]<sup>-</sup>. Turnover numbers were not reported for these catalysts as they were assumed to be quite low due to the rate of decomposition of the carbonyls, catalyst peak height during cyclic voltammetry is employed to gauge the quality of the catalyst. It is reported that the peak height of the Fe dimer is roughly <sup>1</sup>/<sub>3</sub> higher than that produced by the Ru dimer indicating a larger flow of electrons in the Fe complex.

[Fe,Fe] hydrogenase complexes which are derived from nature have been used as model complexes of a system for use in the electrocatalytic generation of hydrogen using a variety of weak acid as the proton source.<sup>52</sup> bis(Thiolate) and dithiolate-bridged diiron carbonyl complexes based on these model systems have been synthesised (Fig. 2.26). Electrochemical experiments were carried out using a vitreous carbon working electrode, a platinum counter electrode, and jacketed silver wire reference electrode using both tetra-butylammonium perchlorate (TBAClO<sub>4</sub>) and TBAPF<sub>6</sub> in THF as supporting electrolytes. The first reduction of the complexes in an Ar purged solution showed that for both the bis(thiolate) and dithiolatebridged complexes that the process was only partly reversible. When the reduction was repeated in a CO purged solution this process becomes reversible suggesting this process involves CO dissociation. The following two reductions were irreversible in both cases and lead to the formation of daughter products, observed through re-oxidation. Using **41** (Fig. 2.26), H<sub>2</sub> formation using p-toluene sulfonic acid (HOTs) as the proton source was deemed to be the most efficient as the acid is strong enough to protonate the **41**<sup>-</sup> after the first reduction. Varying the acid concentration of from 0 to 10 mM increased the catalytic current intensity.



**41**

**Figure 2.26-** bis(thiolate) bridged diiron carbonyl complex studied by Borg *et al.*<sup>52</sup>

## 2.2. Experimental

### 2.2.1. Materials

All experiments were carried out under an atmosphere of nitrogen using standard Schlenk techniques. All solvents were supplied by the Aldrich Chemicals Co. Dichloromethane, chloroform, pentane, heptane and hexane were dried over  $\text{MgSO}_4$  prior to use. Methanol used was distilled over magnesium turnings and iodine before use. Diisopropylamine was distilled over sodium hydroxide prior to use. All solvents used in UV-vis absorption, Fluorescence, IR and TRIR and cyclic voltammetry (CV) experiments were of spectrophotometric grade and were used without further purification. Photocatalytic experiments were carried out in anhydrous THF or ACN distilled over  $\text{CaH}_2$  and all triethylamine dried over sodium before use. All electrochemistry experiments were carried out in anhydrous DCM and all solutions were purged with argon for 20 min prior to use. All mobile phases for column chromatography were dried over  $\text{MgSO}_4$  before use. Column chromatography was carried out using neutral silica gel pH 6.5 – 7.5 or neutral aluminium oxide. Silica Gel (Merck) was used as received. All other chemicals were obtained commercially and were used without further purification. All solutions were deoxygenated by purging with argon or nitrogen for ~5-10 min before synthesis. Argon gas used to degas samples for CV and electrocatalytic studies was purchased from BOC Ltd.

### 2.2.2 Equipment

IR spectra were recorded on a Perkin-Elmer 2000 FT-IR spectrophotometer ( $2\text{ cm}^{-1}$  resolution) in a 0.1 mm sodium chloride liquid solution cell using spectrophotometric grade hexane or dichloromethane.  $^1\text{H}$ -NMR and  $^{13}\text{C}$ -NMR were recorded on a Bruker AC 400 spectrophotometer in  $\text{CDCl}_3$  and were calibrated according to the deuterated solvent peak. All UV spectra were measured on an Agilent 8453 UV-Vis

spectrophotometer in a 1 cm quartz cell using spectrophotometric grade solvents. Emission spectra were recorded using a LS50B luminescence spectrophotometer using a 1 cm quartz cuvette and spectrophotometric grade solvents. All cyclic voltammetry or bulk electrolysis experiments were carried out using a CH Instruments CHI600a potentiostat. The electrode used during the experiments were a glassy carbon working electrode, a platinum wire counter electrode and an Ag/ AgCl reference electrode, all purchased from CH Instruments also. All hydrogen TON were measured using a Varian GC-P-3800 equipped with both a Hayesep C polysiloxane column and a 5Å molecular sieve column and with both a thermal conductivity detector and a flame ionisation detector.

### **2.2.3 Photocatalytic Hydrogen Generation Experiments**

All experiments to test for the photocatalytic generation of H<sub>2</sub> from water were carried out in triplicate. All solvents used were completely dried and deaerated before use. ACN was distilled over CaH<sub>2</sub> before use. Water used was deionised. Triethylamine was distilled over NaOH before use. All experiments were carried out under an argon atmosphere. For the photolysis experiment a 5 x 10<sup>-5</sup> M solution of the complex to be tested was made up in ACN. 1.2 ml of this solution was added to a 5 ml septa capped gas tight vial. 0.6 ml of the sacrificial donor triethylamine (30 % (v/v)) was added along with 0.2 ml of deionised water (10 % (v/v)) as proton source or 0.2 ml ACN to make a 0% water mixture. The solutions were photolysed for 20 hours using a blue (470 nm) or a UV (350 nm) LED light array. After 20 hours a 0.5 ml sample of the headspace in the reaction vial was collected using a gas-tight syringe. These samples were injected into a series CP-3800 gas chromatograph with both TCD and FID detectors in use in conjunction with one another. The peak area response was measured and compared to a series of standards to elucidate the number of moles of H<sub>2</sub> produced during the experiment. The GC was calibrated for H<sub>2</sub> using standard gas mixtures obtained from of 0.01% (100 ppm), 0.1% (1000 ppm), 1% (10000 ppm) and 5% (50000ppm). Full details of experimental conditions are found in appendix B1 and B2.



## 2.2.4 Cyclic Voltammetry

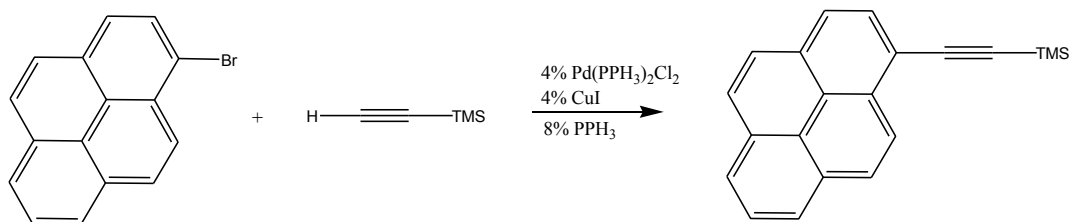
Cyclic voltammetry experiments were carried out at room temperature in a sealed two-necked v-shaped cell.  $\sim 1$  mmol solutions of the compound were prepared in spectrophotometric grade dichloromethane (exact concentrations were not known as there were some solubility issues with the compounds), using tetrabutylammonium hexafluorophosphate (0.1 M) as the supporting electrolyte. All solutions were purged with argon for 20 min prior to each experiment, and were then kept under an argon atmosphere throughout the experiment. Glassy carbon was used as the working electrode, a platinum wire was used as the counter electrode and Ag/AgCl (filled with 1 M TBAPF<sub>6</sub> and 0.1 M AgNO<sub>3</sub> in DCM) was used as reference electrode. The cyclic voltammograms were obtained at a scan rate of 0.1 Vs<sup>-1</sup> unless otherwise stated. The reference electrode was calibrated versus the ferrocene/ferrocenium redox couple; Fc/Fc<sup>+</sup> which has a potential  $E_{1/2} = 0.53$  V vs. saturated calomel electrode (SCE).

## 2.2.5 Electrocatalytic Hydrogen Generation Experiments

Electrocatalytic hydrogen generation experiments were carried out at room temperature in a sealed two-necked v-shaped cell.  $1 \times 10^{-4}$  M solutions of each compound to be tested were prepared in DMF and 1.5  $\mu$ L of each were drop-cast using a Gilson Pipetman P20 pipette on to the surface of a glassy carbon electrode (0.07 cm<sup>3</sup>) and left to evaporate overnight in darkness in a 22°C oven. A 0.1 M solution of sodium hydrogen phosphate (NaH<sub>2</sub>PO<sub>4</sub>) was prepared and brought to pH 2.0 using *ortho*-phosphoric acid. 15 ml of the buffer solution was added to the v-shaped cell. All solutions were purged with argon for 20 minutes prior to each experiment, and were then kept under an argon atmosphere throughout the length of the experiment. Glassy carbon was used as the working electrode, a platinum wire was used as the counter electrode and Ag/AgCl (filled with 3 M KCl) was used as reference electrode. See Appendix C1 and C2 for full experimental conditions. Each experiment was run in triplicate and the average values obtained.

## 2.2.6 Synthesis

### 2.2.6.1 Synthesis of 1-trimethylsilylethynylpyrene (PyrTMS)



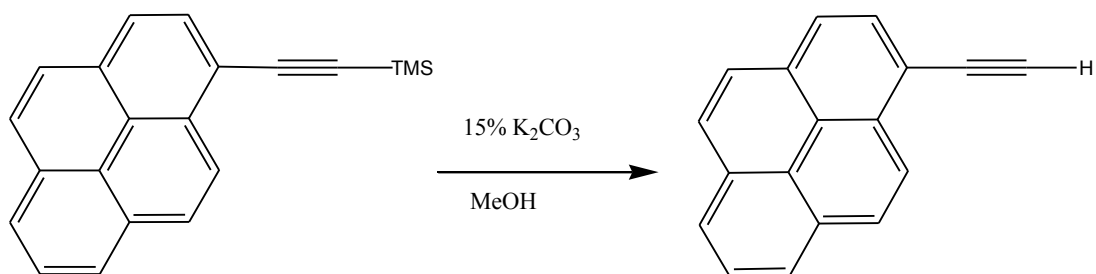
To a clean, dry round bottomed flask, 25ml of diisopropylamine was added and the solution was purged with nitrogen for 10 minutes. 0.5g (1.77 mmol) of 1-bromopyrene was added and the mixture was purged with nitrogen for a further 10 minutes. 0.05g (0.071 mmol) of Pd(PPh<sub>3</sub>)<sub>2</sub>Cl<sub>2</sub>, 0.035g (0.071 mmol) CuI and 0.037g (0.142 mmol) PPh<sub>3</sub> were added to the reaction vessel. 0.37 ml (2.66 mmol) of ethynyltrimethylsilane was added and the reaction vessel was sealed and allowed to reflux (88°C) overnight under nitrogen.

The solvent was removed under reduced pressure. The crude product was extracted from the resulting solid by adding portions of a mixture of dichloromethane and hexane (4 ml and 20 ml respectively). After each addition the liquid layer was decanted off until it ran clear. The organic phase was dried over MgSO<sub>4</sub>. The solvent was removed. The product was purified using column chromatography on silica, hexane: DCM, 25:75 to yield a yellow solid.<sup>53</sup>

% Yield: 0.509g, 1.7054 mmol, 96%

<sup>1</sup>H NMR: (400 MHz, CDCl<sub>3</sub>), 8.53 ppm (d, J = 9.08 Hz, 1H), 8.1 ppm (m, 8H), 0.36 ppm (s, 9H)

### 2.2.6.2 Synthesis of 1-ethynylpyrene (PyrH)

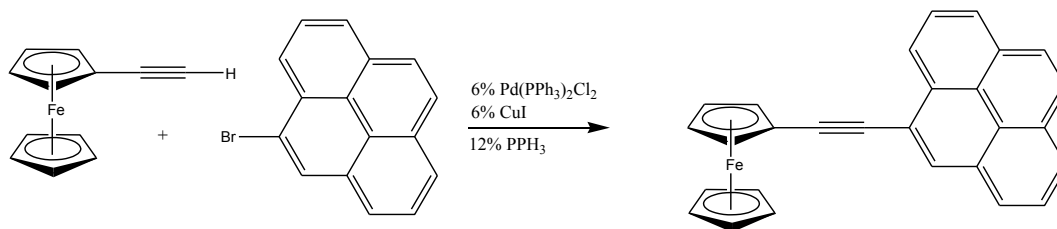


20 ml of freshly distilled methanol was added to a clean, dry round bottomed flask and the solution was purged with nitrogen for 10 minutes. 0.4g (1.3 mmol) of 1-trimethylsilylethynlpyrene was added and allowed to dissolve. 0.024g (0.17 mmol) of K<sub>2</sub>CO<sub>3</sub> was added and the solution was allowed to stir under nitrogen for 4 hours. The solvent was removed under reduced pressure. The residue was dissolved in ~100 ml of dichloromethane and washed with 4 x 25 ml of 5% (w/v) aqueous NaHCO<sub>3</sub>. The organic phase was dried over MgSO<sub>4</sub>. The solvent was removed. The product was purified using silica, hexane: DCM, 25:75 to yield a light brown solid.<sup>54</sup>

% Yield: 0.2068g, 0.9139 mmol, 70%

<sup>1</sup>H NMR: (400 MHz, CDCl<sub>3</sub>), 8.5 ppm (d, J = 8.8 Hz, 1H), 8.15 ppm (m, 8H), 3.6 ppm (s, 1H)

### 2.2.6.3 Synthesis of Pyrene-ethynylferrocene (PyrFc)



15 ml of dry, distilled diisopropylamine was purged with N<sub>2</sub> for 10 min. 0.2g (0.71 mmol) of 1-bromopyrene was added to the 15 ml of dry, distilled diisopropylamine and the solution was purged with N<sub>2</sub> for a further 10 min. 0.03g (0.042 mmol) Pd(PPh<sub>3</sub>)<sub>2</sub>Cl<sub>2</sub>, 0.023g (0.85 mmol) PPh<sub>3</sub>, and 0.008g (0.042 mmol) CuI were added as catalysts and immediately followed by 0.15g (0.71 mmol) 1-ethynylferrocene. The reaction vessel was sealed and the reaction mixture was allowed to reflux (84°C) under inert conditions overnight.

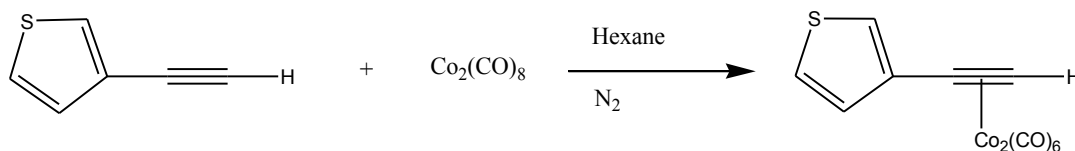
The solvent was removed under reduced pressure. Purification was carried out using silica and hexane: DCM, 1:1 as solvent. A bright orange solid resulted.<sup>53</sup>

% Yield: 0.277g, 0.70 mmol, 98%

<sup>1</sup>H NMR: (400 MHz, CDCl<sub>3</sub>) 8.62 ppm (d, J= 9.2 Hz, 1H), 7.9 ppm (m, 8H), 4.665 ppm (dd, J<sub>a</sub>= 1.6 Hz, J<sub>b</sub>= 1.6 Hz, 2H), 4.33 ppm (s, 7H)

#### 2.2.6.4 Synthesis of $\mu_2$ -3-ethynylthiophene $\text{Co}_2(\text{CO})_6$

$((\mu_2\text{-ThioH})\text{Co}_2(\text{CO})_6)$



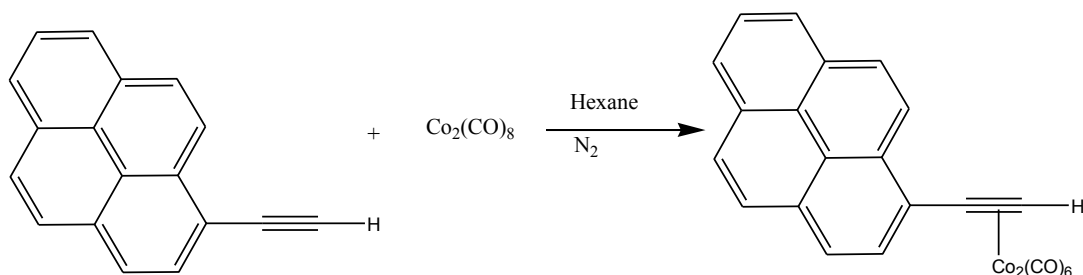
25 ml of hexane was purged with  $\text{N}_2$  for 10 min. 0.394 ml (0.2 mmol) of 3-ethynylthiophene (ThioH) was added to the 25 ml of hexane and the solution was purged with  $\text{N}_2$  for a further 10 min. 0.0684g (0.2 mmol) of cobalt octacarbonyl was added to the reaction mixture and the vessel was sealed immediately. The reaction mixture was allowed to stir overnight under inert conditions. The solvent was removed and the pure product was obtained through column chromatography using a silica solid phase and DCM: Hexane, 1:1 as the solvent. This resulted in a red solid.<sup>55</sup>

% Yield: 0.077g, 0.982 mmol, 98%

$^1\text{H}$  NMR: (400 MHz,  $\text{CDCl}_3$ ), 7.4 ppm (d,  $J = 1.24$  Hz, 1H), 7.29 ppm (d,  $J = 3.0$  Hz, 1H), 7.15 ppm (d,  $J = 1.24$  Hz, 1H), 6.28 ppm (s, 1H)

IR: ( $\text{CH}_2\text{Cl}_2$ ), 2093, 2056, 2026  $\text{cm}^{-1}$

**2.2.6.5 Synthesis of  $\mu_2$ -1-ethynylpyrene  $\text{Co}_2(\text{CO})_6$   
 $((\mu_2\text{-PyrH})\text{Co}_2(\text{CO})_6)$**



25 ml of hexane was purged with  $\text{N}_2$  for 10 min. 0.102g (0.45 mmol) of 1-ethynylpyrene was added to the 25 ml of hexane and the solution was purged with  $\text{N}_2$  for a further 10 min. 0.307g (0.9 mmol) of cobalt octacarbonyl was added to the reaction mixture and the vessel was sealed immediately. The reaction mixture was allowed to stir overnight under inert conditions. The solvent was removed and the pure product was obtained through column chromatography using a silica solid phase and DCM: hexane, 1:1 as the solvent. This resulted in a dark brown solid.<sup>55</sup>

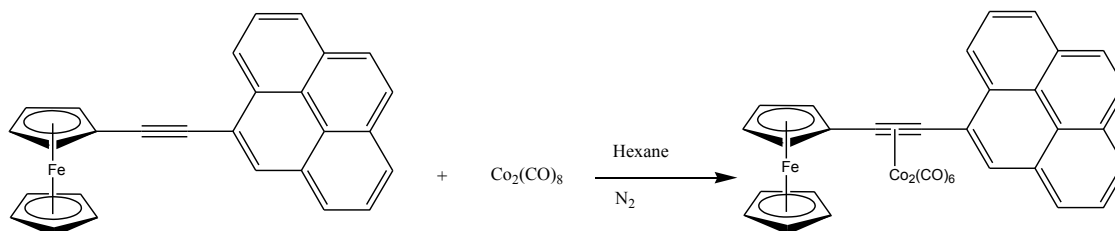
% Yield: 0.180g, 0.351 mmol, 78%

$^1\text{H}$  NMR: (400 MHz,  $\text{CDCl}_3$ ), 8.55 ppm (d,  $J = 9.2$  Hz 1H), 8.15 ppm (m, 8H), 6.95 ppm (s, 1H)

IR: ( $\text{CH}_2\text{Cl}_2$ ) 2088, 2073, 2030  $\text{cm}^{-1}$

#### 2.2.6.6 Synthesis of $\mu_2$ -Pyrene-ethynylferrocene $\text{Co}_2(\text{CO})_6$

##### $((\mu_2\text{-PyrFc})\text{Co}_2(\text{CO})_6)$



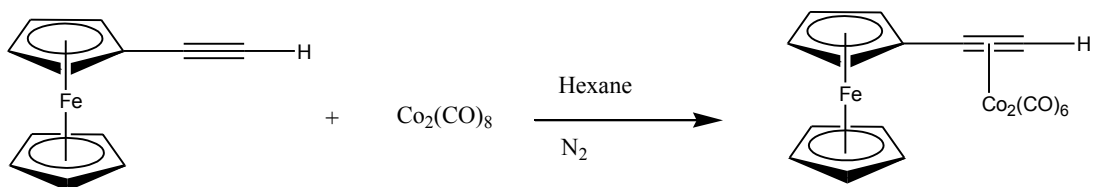
25 ml of hexane was purged with  $\text{N}_2$  for 10 min. 0.15g (0.37 mmol) of 1-pyreneethynylferrocene was added to the 25 ml of hexane and the solution was purged with  $\text{N}_2$  for a further 10 min. 0.127g (0.37 mmol) of cobalt octacarbonyl was added to the reaction mixture and the vessel was sealed immediately. The reaction mixture was allowed to stir overnight under inert conditions. The solvent was removed and the pure product was obtained through column chromatography using a silica solid phase and DCM: hexane, 1:1 as the solvent. This resulted in a dark brown solid.<sup>55</sup>

% Yield: 0.15g, 0.219 mmol, 59%

$^1\text{H}$  NMR: (400 MHz,  $\text{CDCl}_3$ ), 8.7 ppm (d,  $J = 8.08$  Hz 1H), 8.24 ppm (m, 8H), 4.6 ppm (dd,  $J_a = 1.84$  Hz,  $J_b = 1.84$  Hz, 2H), 4.48 ppm (dd,  $J_a = 1.84$  Hz,  $J_b = 1.84$  Hz 2H), 4.32 ppm (s, 5H)

IR: ( $\text{CH}_2\text{Cl}_2$ ), 2085, 2048, 2023  $\text{cm}^{-1}$

### 2.2.6.7 Synthesis of $\mu_2$ -1-ethynylferrocene $\text{Co}_2(\text{CO})_6$ ( $(\mu_2\text{-FcH})\text{Co}_2(\text{CO})_6$ )



25 ml of hexane was purged with  $\text{N}_2$  for 10 min. 0.420g (0.2 mmol) of 1-ethynylferrocene (FcH) was added to the 25 ml of hexane and the solution was purged with  $\text{N}_2$  for a further 10 min. 0.0684g (0.2 mmol) of cobalt octacarbonyl was added to the reaction mixture and the vessel was sealed immediately. The reaction mixture was allowed to stir overnight under inert conditions. The solvent was removed and the pure product was obtained through column chromatography using a silica solid phase and DCM: hexane, 1:1 as the solvent. This resulted in a dark green solid.<sup>55</sup>

% Yield: 0.094g, 0.1902 mmol, 95%

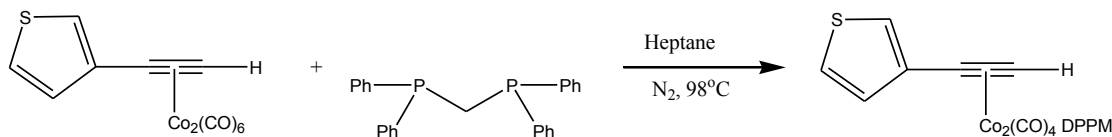
$^1\text{H}$  NMR: (400 MHz,  $\text{CDCl}_3$ ), 6.28 ppm (s, 1H), 4.33 ppm (d,  $J_a = 1.84$  Hz,  $J_b = 1.84$  Hz 4H), 4.15 ppm (s, 5H)

IR: ( $\text{CH}_2\text{Cl}_2$ ), 2090, 2051, 2023  $\text{cm}^{-1}$



### 2.2.6.8 Synthesis of $\mu_2$ -3-ethynylthiophene $\text{Co}_2(\text{CO})_4\text{DPPM}$

#### $((\mu_2\text{-ThioH})\text{Co}_2(\text{CO})_4\text{DPPM})$



100 ml of heptane was purged with  $\text{N}_2$  for 10 min. 0.177g (0.45 mmol) of 3-ethynylthiophene  $\text{Co}_2(\text{CO})_6$  was added to the 100 ml of heptane and the solution was purged with  $\text{N}_2$  for a further 10 min. 0.346g (0.9 mmol) of diphenylphosphinomethane was added to the reaction mixture and the vessel was sealed. The reaction mixture was allowed to reflux ( $98^\circ\text{C}$ ) for 40 min under inert conditions while being monitored by IR. The solvent was removed under reduced pressure and the pure product was isolated through column chromatography using silica and DCM: hexane, 1:1 as solvent. A dark brown solid results.<sup>22</sup> This complex is novel to the best of our knowledge, and all spectral data are in agreement with their formulation and compare well to similar compounds which have been previously reported in literature.<sup>58</sup>

% Yield: 0.136g, 0.187 mmol, 42%

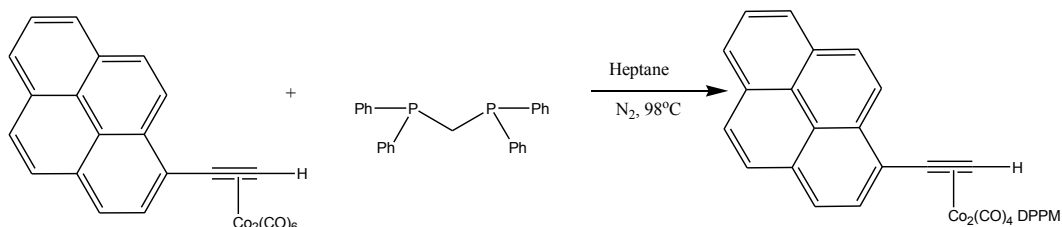
$^1\text{H}$  NMR: (400 MHz,  $\text{CDCl}_3$ ), 7.45 ppm (d,  $J = 2.0$  Hz, 8H), 7.2 ppm (m, 12H), 5.72 ppm (t, 1H), 5.66 ppm (dd,  $J_a = 6.8$  Hz,  $J_b = 6.8$  Hz, 1H), 5.23 ppm (s, 1H), 4.61 ppm (s, 1H), 3.54 ppm (m, 1H), 3.0 ppm (m, 1H)

IR: ( $\text{CH}_2\text{Cl}_2$ ) 2022, 1993,  $1966\text{ cm}^{-1}$

Elemental Analysis: Anal. Calcd. For  $\text{C}_{36}\text{H}_{29}\text{Co}_2\text{O}_4\text{P}_2\text{S}$ : C 58.63, H 3.96. Found: C 58.18, H 3.54.

### 2.2.6.9 Synthesis of $\mu_2$ -1-ethynylpyrene $\text{Co}_2(\text{CO})_4$ DPPM

#### $((\mu_2\text{-PyrH})\text{Co}_2(\text{CO})_4\text{DPPM})$



100 ml of heptane was purged with  $\text{N}_2$  for 10 min. 0.75g (0.1 mmol) of 1-ethynylpyrene  $\text{Co}_2(\text{CO})_6$  was added to the 100 ml of heptane and the solution was purged with  $\text{N}_2$  for a further 10 min. 0.77g (0.2 mmol) of diphenylphosphinomethane was added to the reaction mixture and the vessel was sealed. The reaction mixture was allowed to reflux ( $98^\circ\text{C}$ ) overnight under inert conditions while being monitored by IR.

The solvent was removed under reduced pressure and the pure product was isolated through column chromatography using silica and DCM: hexane, 1:1 as solvent.<sup>22</sup> This complex is novel to the best of our knowledge, and all spectral data are in agreement with their formulation and compare well to similar compounds which have been previously reported in literature.<sup>58</sup>

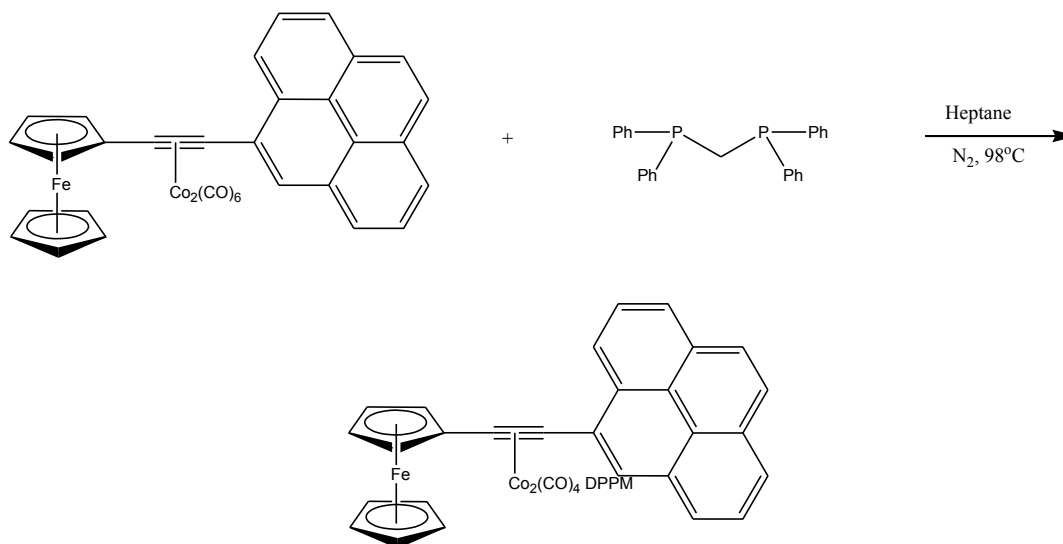
% Yield: 0.061, 0.072 mmol, 72%

$^1\text{H}$ NMR: (400 MHz,  $\text{CDCl}_3$ ), 8.6 ppm (d, 1H), 8.05 ppm (m, 8H), 7.2 ppm (m, 12H), 7.15 ppm (dd, 8H), 5.42 ppm (dd, 1H), 3.14 ppm (m, 2H)

IR: ( $\text{CH}_2\text{Cl}_2$ ) 2088, 2073,  $1950\text{ cm}^{-1}$

Elemental Analysis: Anal. Calcd. For  $\text{C}_{48}\text{H}_{35}\text{Co}_2\text{O}_4\text{P}_2$ : C 67.42, H 4.13. Found: C 69.54, H 4.47.

**2.2.6.10 Synthesis of  $\mu_2$ -Pyrene-ethynylferrocene  $\text{Co}_2(\text{CO})_4\text{DPPM}$   
 $((\mu_2\text{-PyrFc})\text{Co}_2(\text{CO})_4\text{DPPM})$**



100 ml of heptane was purged with  $\text{N}_2$  for 10 min. 0.75g (0.1 mmol) of ferrocenylacetylene pyrene  $\text{Co}_2(\text{CO})_6$  was added to the 100 ml of heptane and the solution was purged with  $\text{N}_2$  for a further 10 min. 0.77g (0.2 mmol) of diphenylphosphinomethane was added to the reaction mixture and the vessel was sealed. The reaction mixture was allowed to stir overnight under inert conditions while being monitored by IR. The solvent was removed under reduced pressure and the pure product was isolated through column chromatography using silica and DCM: hexane, 1:1 as solvent. A dark brown solid results.<sup>22</sup> This complex is novel to the best of our knowledge, and all spectral data are in agreement with their formulation and compare well to similar compounds which have been previously reported in literature.<sup>58</sup>

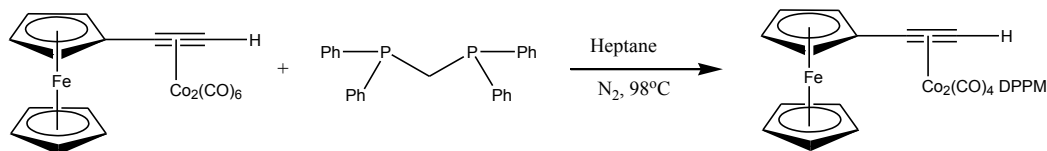
% Yield: 0.029g, 0.0286 mmol, 29%

$^1\text{H}$  NMR: (400 MHz,  $\text{CDCl}_3$ ), 8.87 ppm (d,  $J = 9.1$  Hz, 1H), 8.1 ppm (m, 8H), 7.2 ppm (m, 6H), 7.0 ppm (dd,  $J_a = 7.4$  Hz,  $J_b = 7.6$  Hz, 4H), 6.96 ppm (m, 6H), 6.82 ppm (dd,  $J_a = 7.2$  Hz,  $J_b = 7.2$  Hz, 4H), 4.62 ppm (s, 2H), 4.27 ppm (s, 2H), 3.92 ppm (s, 5H), 3.14 ppm (m, 2H)

IR: ( $\text{CH}_2\text{Cl}_2$ ) 2017, 1990, 1964  $\text{cm}^{-1}$

### 2.2.6.11 Synthesis of $\mu_2$ -1-ethynylferrocene $\text{Co}_2(\text{CO})_4$ DPPM

#### $((\mu_2\text{-FcH})\text{Co}_2(\text{CO})_4\text{DPPM})$



100 ml of heptane was purged with  $\text{N}_2$  for 10 min. 0.22g (0.45 mmol) of 1-ethynylferrocene  $\text{Co}_2(\text{CO})_6$  was added to the 100 ml of heptane and the solution was purged with  $\text{N}_2$  for a further 10 min. 0.346g (0.9 mmol) of diphenylphosphinomethane was added to the reaction mixture and the vessel was sealed. The reaction mixture was allowed to reflux ( $98^\circ\text{C}$ ) for 40 min under inert conditions while being monitored by IR. The solvent was removed under reduced pressure and the pure product was isolated through column chromatography using silica and DCM: hexane, 1:1 as solvent. A dark brown solid results.<sup>22</sup> This complex is novel to the best of our knowledge, and all spectral data are in agreement with their formulation and compare well to similar compounds with have been previously reported in literature.<sup>58</sup>

% Yield: 0.227g, 0.275 mmol, 61%

$^1\text{H}$  NMR: (400 MHz,  $\text{CDCl}_3$ ), 7.33 ppm (m, 8H), 7.2 ppm (m, 12H), 5.75 ppm (dd,  $J_a = 6.4$  Hz,  $J_b = 6.4$  Hz, 1H), 4.37 ppm (dd,  $J_a = 1.8$  Hz,  $J_b = 2.0$  Hz, 2H), 4.21 ppm (dd,  $J_a = 1.8$  Hz,  $J_b = 2.0$  Hz, 2H), 4.16 ppm (s, 5H), 3.5 ppm (m, 1H), 3.1 ppm (m, 1H)

IR: ( $\text{CH}_2\text{Cl}_2$ ) 2018, 1989,  $1962\text{ cm}^{-1}$

Elemental Analysis: Anal. Calcd. For  $\text{C}_{48}\text{H}_{35}\text{Co}_2\text{O}_4\text{P}_2$ : C 60.24, H 3.97. Found: C 59.44, H 3.77.

## 2.3. Results

### 2.3.1. UV-Vis Spectroscopy

Room temperature absorption spectra were obtained for all compounds in this study. Table 1 illustrates the absorption maxima ( $\lambda_{\text{max}}$ ) for all compounds. All UV-Vis spectra were carried out in spectrophotometric grade dichloromethane (DCM).

<b>Compound</b>	<b><math>\lambda_{\text{max}}</math> (nm), <math>\epsilon</math> (<math>\times 10^3 \text{ M}^{-1} \text{ cm}^{-1}</math>)</b>
$(\mu_2\text{-ThioH})\text{Co}_2(\text{CO})_6$	266 (9.08), 358 (1.9), 428 (0.6), 540 (0.3)
$(\mu_2\text{-ThioH})\text{Co}_2(\text{CO})_4\text{DPPM}$	290 (5.1), 340 (2.9), 533 (0.27)
$(\mu_2\text{-PyrH})\text{Co}_2(\text{CO})_6$	274 (20.5), 392 (19.1), 577 (1.1)
$(\mu_2\text{-PyrH})\text{Co}_2(\text{CO})_4 \text{DPPM}$	269 (10.1), 368 (8.3), 438 (5.9), 536 (0.92)
$(\mu_2\text{-FcH})\text{Co}_2(\text{CO})_6$	290 (17.1), 361 (4.4), 430 (1.8), 614 (1.14)
$(\mu_2\text{-FcH})\text{Co}_2(\text{CO})_4 \text{DPPM}$	341 (7.48), 579 (0.87)
$(\mu_2\text{-PyrFc})\text{Co}_2(\text{CO})_6$	279 (18.7), 389 (11.7), 574 (1.3)
$(\mu_2\text{-PyrFc})\text{Co}_2(\text{CO})_4 \text{DPPM}$	274 (16.2), 346 (7.9), 386 (4.1), 574 (0.63)

**Table 2.3- UV-vis absorption data for all compounds in this study. All spectra were recorded in dichloromethane.**

All of the compounds in this study exhibit strong absorptions in the UV-Vis region of the spectrum, which are assigned to ligand localised  $\pi$ -  $\pi^*$  transitions.<sup>56</sup> The absorbance between 380- 420nm in each of the hexacarbonyl and tetracarbonyl compounds listed are generally attributed to a common  $\sigma$  –  $\sigma^*$  (Co – Co) electronic transition.<sup>20</sup> Also in the hexa- and tetracarbonyl species there is a broad and weak absorbance further into the

red region at ~540-600 nm. This is generally attributed to a metal to ligand charge transfer (MLCT) of Co ( $d\pi$ ) – ligand ( $\pi$ ) transition.<sup>23</sup>

### 2.3.2. IR Spectroscopy

All compounds give rise to metal carbonyl stretching vibrations in the region 1900-2200  $\text{cm}^{-1}$ . Table 2 illustrates the vibrational frequencies  $\nu_{\text{CO}}$  for all compounds. All IR spectra were measured in spectrophotometric grade DCM.

Compound	$\nu_{\text{CO}}$ ( $\text{cm}^{-1}$ )
$(\mu_2\text{-ThioH})\text{Co}_2(\text{CO})_6$	2093, 2056, 2026
$(\mu_2\text{-ThioH})\text{Co}_2(\text{CO})_4\text{DPPM}$	2022, 1993, 1966
$(\mu_2\text{-PyrH})\text{Co}_2(\text{CO})_6$	2092, 2056, 2030
$(\mu_2\text{-PyrH})\text{Co}_2(\text{CO})_4\text{DPPM}$	2006, 1974, 1953
$(\mu_2\text{-FcH})\text{Co}_2(\text{CO})_6$	2090, 2051, 2023
$(\mu_2\text{-FcH})\text{Co}_2(\text{CO})_4\text{DPPM}$	2018, 1989, 1962
$(\mu_2\text{-PyrFc})\text{Co}_2(\text{CO})_6$	2085, 2048, 2023
$(\mu_2\text{-PyrFc})\text{Co}_2(\text{CO})_4\text{DPPM}$	2017, 1990, 1964

**Table 2.4-  $\nu_{\text{CO}}$  for all compounds in this study. All spectra were recorded in dichloromethane.**

The IR spectrum for  $(\mu_2\text{-PyrH})\text{Co}_2(\text{CO})_6$  which is typical for these compounds is shown in Fig. 2.27 below.

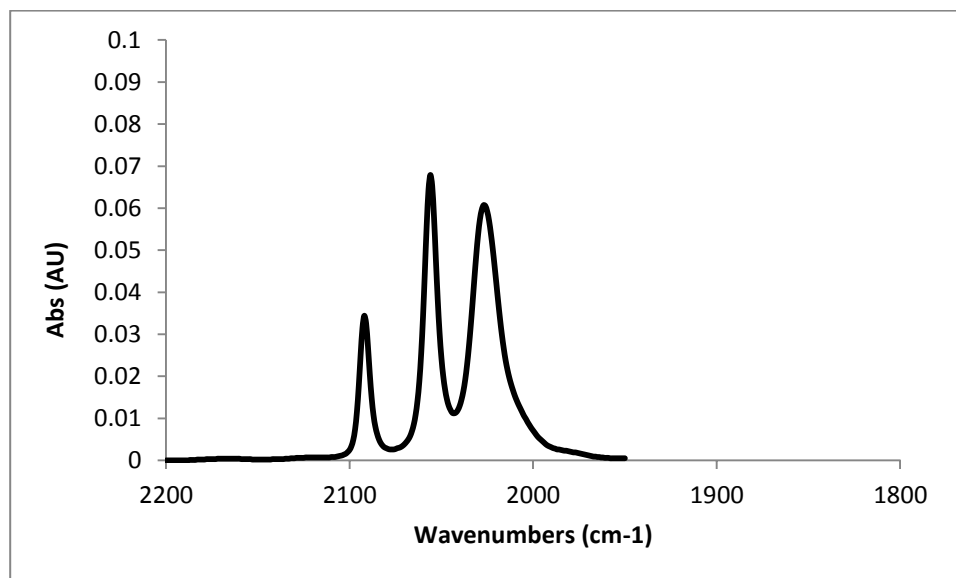


**Figure 2.27 - IR spectrum of  $(\mu_2\text{-PyrH})\text{Co}_2(\text{CO})_6$  in  $\text{CH}_2\text{Cl}_2$ .**

The addition of the DPPM group to the cobalt carbonyl species shows a shift of CO stretches to lower frequencies which indicates the DPPM is an electron donating ligand with respect to the cobalt centre thus there is more electron density involved in the CO backbonding (Fig. 2.28).

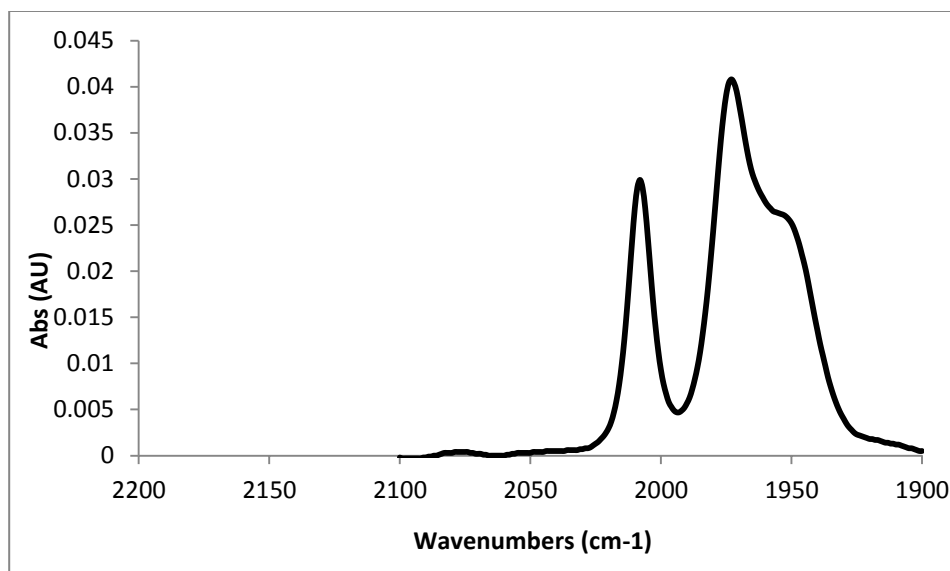
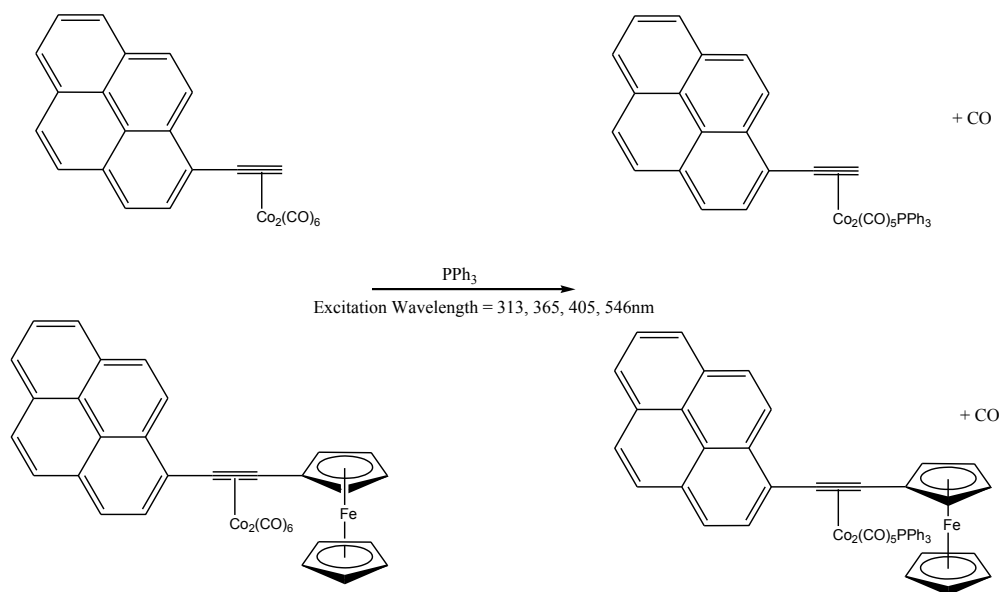


**Figure 2.28 - IR  $\nu_{\text{CO}}$  stretches of  $(\mu_2\text{-PyrH})\text{Co}_2(\text{CO})_4\text{DPPM}$  in  $\text{CH}_2\text{Cl}_2$ .**

### ***2.3.3. Quantum Yields of CO Loss***

The photochemical quantum yield for CO loss was determined using potassium ferrioxalate actinometry (full details of experiment are available in Appendix A1). The quantum yield of CO loss was calculated at various wavelengths for both  $(\mu_2\text{-PyrH})\text{Co}_2(\text{CO})_6$  and  $(\mu_2\text{-PyrFc})\text{Co}_2(\text{CO})_6$  to investigate if a wavelength dependency exists for this photochemical process. The quantum yields of CO loss were determined at 313, 365, 405 and 546 nm in heptane. Triphenylphosphine was used as a trapping ligand for the pentacarbonyl intermediate generated (Scheme 2.4).





**Scheme 2.4 – Quantum yields for CO loss ( $\Phi_{\text{CO}}$ ) were studied for the compounds shown.**

The UV-vis absorbance spectra for both hexacarbonyl complexes show an intense absorbance in the UV region up to 400 nm with a broad weak absorbance in the visible region extending to 600 nm. The isolated triphenylphosphine pentacarbonyl species,  $(\mu_2\text{-PyrH})\text{Co}_2(\text{CO})_5(\text{PPh}_3)$  and  $(\mu_2\text{-PyrFc})\text{Co}_2(\text{CO})_5(\text{PPh}_3)$ , both showed a bathochromic shift in this absorbance band to approximately 430 nm, thus the photoreaction was monitored by the change in absorbance at 430 nm (Fig. 2.29). Following photolysis of the complexes a new band was evident in the UV-vis spectra in the range 400 – 450 nm which indicated photosubstitution of a carbonyl ligand with a triphenylphosphine moiety.

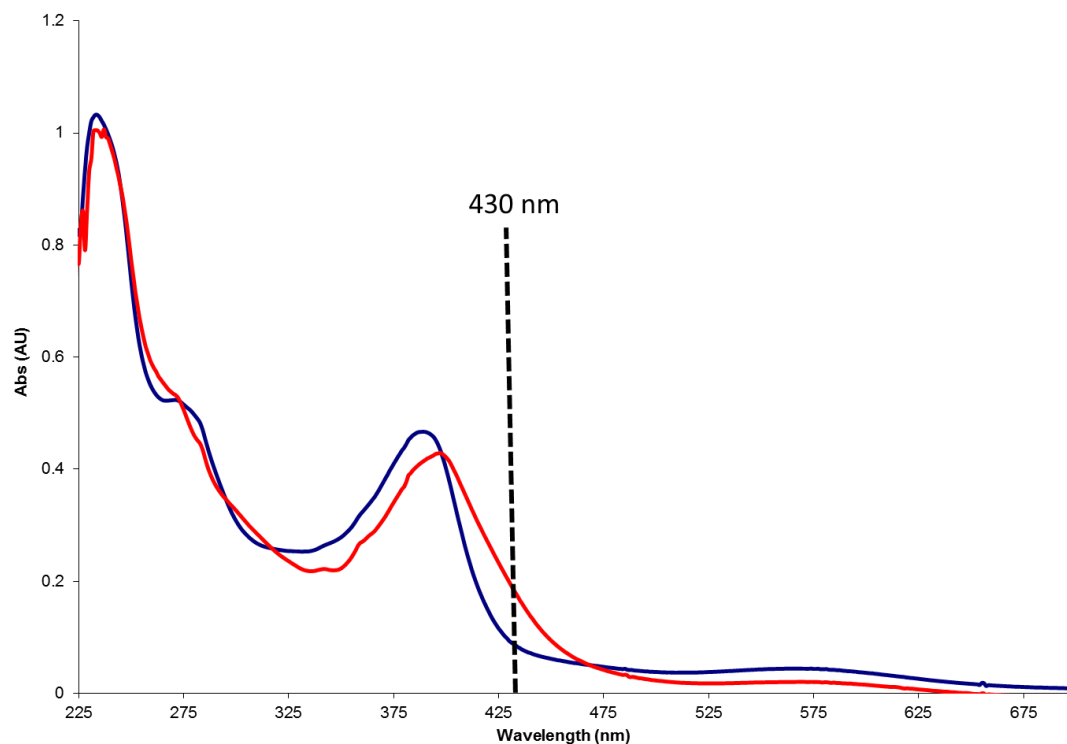


**Figure 2.29 - Absorbance spectra of  $(\mu_2\text{-PyrH})\text{Co}_2(\text{CO})_6$  (1) (blue line) and  $(\mu_2\text{-PyrH})\text{Co}_2(\text{CO})_5\text{PPh}_3$  (red line) recorded in heptane.**

The photosubstitution reaction was monitored by UV-vis spectroscopy. A comparison of the UV-Vis spectra before and after irradiation determined the number of photolysed molecules (Appendix A). The conversion to photoproduct was limited to 10%, which minimises the effect of this product absorbance at the excitation wavelength.

The mean values of all quantum yield experiments are given in Table 2.5. The results show that the photochemical quantum yield of CO dissociation was dependent on both the excitation wavelength and also the structure of complex.

Wavelength (nm)	( $\mu_2$ -PyrH) Co <sub>2</sub> (CO) <sub>6</sub>	( $\mu_2$ -PyrFc) Co <sub>2</sub> (CO) <sub>6</sub>
313	25%	8%
365	10%	19%
405	9%	13%
546	4%	10%

**Table 1.5-** Quantum yields of CO loss for ( $\mu_2$ -PyrH)Co<sub>2</sub>(CO)<sub>6</sub> and ( $\mu_2$ -PyrFc)Co<sub>2</sub>(CO)<sub>6</sub> in heptane.

From the results it is evident that a wavelength dependency exists, and also the  $\Phi_{\text{CO}}$  loss varies between the two cobalt complexes. For instance the quantum yield for  $\Phi_{\text{CO}}$  loss for the ( $\mu_2$ -PyrH)Co<sub>2</sub>(CO)<sub>6</sub> complex varied from 4 to 25% depending upon the wavelength. Furthermore for this complex the quantum yield for  $\Phi_{\text{CO}}$  loss increased with increasing wavelength. In the case of the ferrocene analogue the highest quantum yield value for CO loss was observed following irradiation at 365nm ( $\Phi_{\text{CO}} = 19\%$ ).

### **2.3.4. Picosecond Time Resolved Infra-Red (TRIR) Spectroscopy**

Picosecond time resolved infra-red studies were used to probe the photochemical pathways for a number of ( $\mu_2$ -alkyne)Co<sub>2</sub>(CO)<sub>6</sub> complexes; ( $\mu_2$ -PyrH) Co<sub>2</sub>(CO)<sub>6</sub>, ( $\mu_2$ -PyrFc)Co<sub>2</sub>(CO)<sub>6</sub>, ( $\mu_2$ -FcH)Co<sub>2</sub>(CO)<sub>6</sub>, ( $\mu_2$ -PyrH)Co<sub>2</sub>(CO)<sub>4</sub>DPPM, ( $\mu_2$ -PyrFc)Co<sub>2</sub>(CO)<sub>4</sub>DPPM and ( $\mu_2$ -FcH)Co<sub>2</sub>(CO)<sub>4</sub>DPPM. Experiments were carried out in spectrophotometric grade DCM for all DPPM derivatives however the experiments involving the Co<sub>2</sub>(CO)<sub>6</sub> derivatives were carried out in spectrophotometric grade heptane as the samples decomposed over the course of the experiment when DCM was used as the solvent. Photolysis was carried out with  $\lambda_{\text{ex}}$  400nm, and  $\tau_{\text{FWHM}} = 150\text{fs}$ . The laser system used in this study, known as ULTRA, is capable of emitting a pump beam and monitoring any changes in the species being probed at pico-second timescales, in the infra-red region.<sup>65</sup>

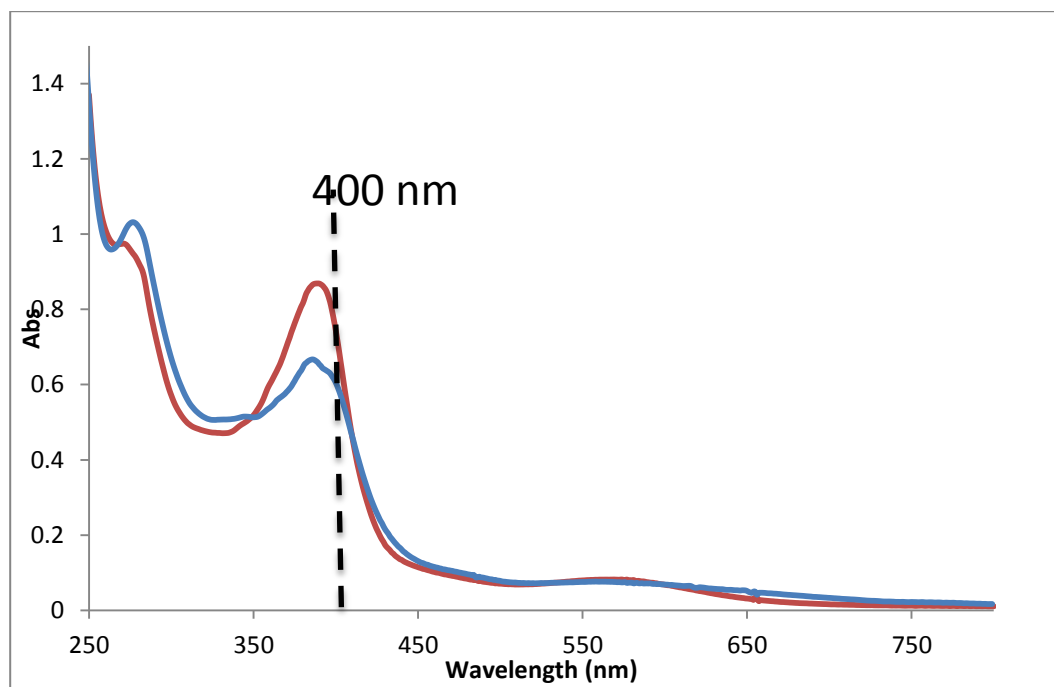


**Figure 2.30 - Overlay of the absorbance spectra of  $(\mu_2\text{-PyrH})\text{Co}_2(\text{CO})_6$  (red line) and  $(\mu_2\text{-PyrFc})\text{Co}_2(\text{CO})_6$  (blue line) recorded in heptane.**

Photolysis ( $\lambda_{\text{exc}} = 400 \text{ nm}$ ) of  $(\mu_2\text{-PyrH})\text{Co}_2(\text{CO})_6$  resulted in bleaching of the parent  $\nu_{\text{CO}}$  bands at 2092, 2056, and 2030  $\text{cm}^{-1}$  within the laser pulse, together with the generation of three new metal-carbonyl bands at 2078, 2046 and 2012  $\text{cm}^{-1}$ . These bands undergo vibrational cooling (over the following  $\sim 10 \text{ ps}$ ) and shift to higher frequency; 2081, 2048, and 2016  $\text{cm}^{-1}$  respectively, and then decay within the subsequent 200 ps.

Boyle et. al.<sup>24</sup> used picosecond TRIR studies to study similar compounds. In their studies they assigned the short lived species to a di-radical intermediate which formed as a result of cleavage of the Co-Co metal bonds as shown in Fig. 2.31.

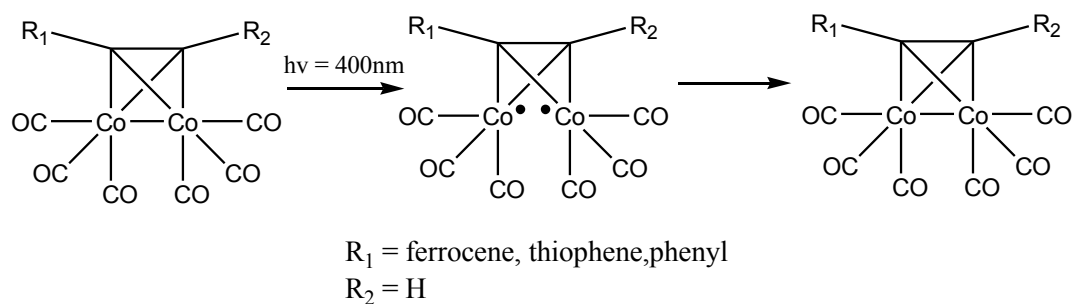


**Figure 2.31 - Homolytic cleavage of a Co-Co bond upon photolysis at  $\lambda_{\text{exc}}$  400nm<sup>24</sup>**

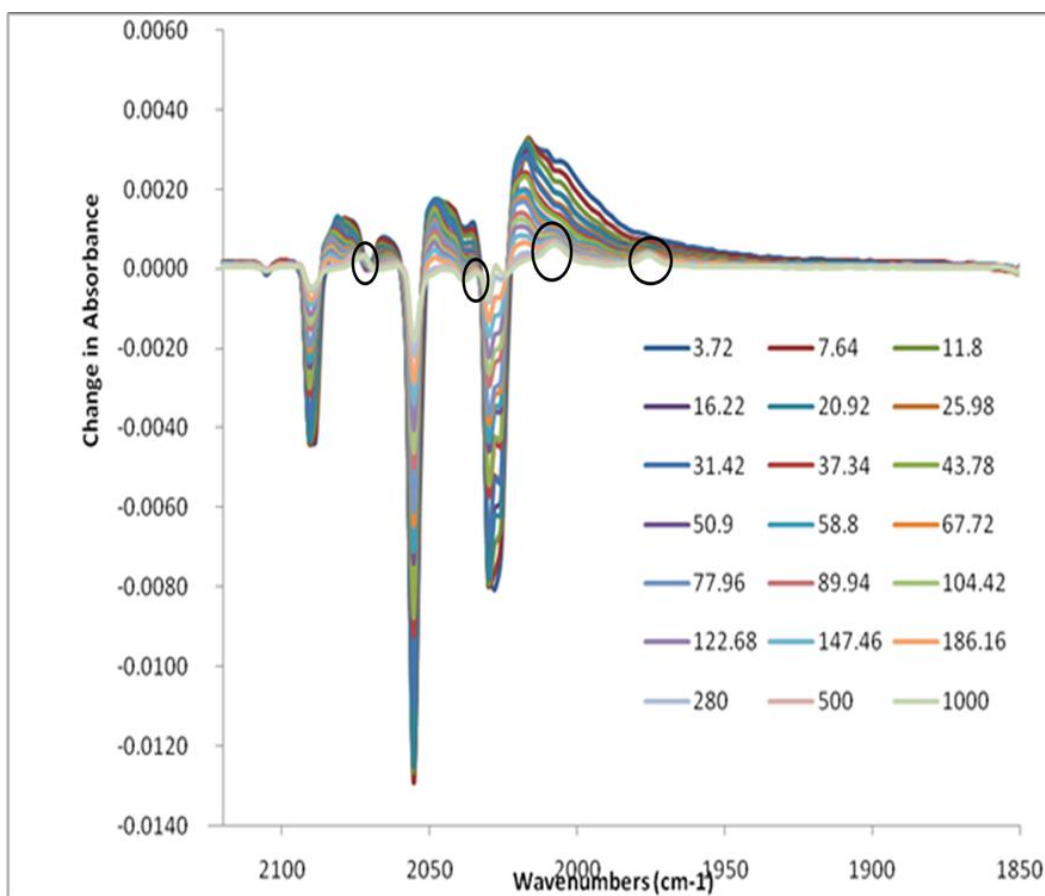


**Figure 2.32 - Time resolved infra-red difference spectra following laser photolysis ( $\lambda_{\text{exc}} = 400\text{nm}$ ) for  $(\mu_2\text{-PyrH})\text{Co}_2(\text{CO})_6$  in heptane. Legend indicates time in ps. Circled are the new bands formed due to the CO loss photoproduct.**

In addition to the bands which decay on the picosecond timescale, four additional bands were apparent at 2074, 2034, 2007 (underneath the parent depletion), and 1977  $\text{cm}^{-1}$  (Fig. 2.32). The bands observed in this study compare well to those previously reported in the literature for CO loss in other types of metal carbonyls<sup>57</sup> which were carried out in a matrix study at 20 K. These bands are evident directly after the laser pulse and persist on the time scale of the experiment (1 ns), and furthermore the parent bands do not fully recover. These bands are assigned to the solvated CO loss product  $(\mu_2\text{-PyrH})\text{Co}_2(\text{CO})_5(\text{heptane})$ . As the  $(\mu_2\text{-PyrH})\text{Co}_2(\text{CO})_5(\text{heptane})$  stretches are visible directly after the laser pulse it is proposed that the generation of this species is not formed due to the excited state generated when the parent bands deplete but is an independent photoproduct. From measurement of the recovery of the parent bands after the length of the experiment (1 ns) the quantum yield for CO loss was estimated to be  $\sim 10\%$ . This result is comparable that determined (9%) at 405 nm during the ferrioxalate actinometric quantum yield studies.

Similar results were observed for  $(\mu_2\text{-PyrFc})\text{Co}_2(\text{CO})_6$  in heptane solution following photolysis at  $\lambda_{\text{exc}}$  400 nm. Bleaching of the parent ground state  $\nu_{\text{CO}}$  bands at 2085, 2048, and 2023  $\text{cm}^{-1}$  was observed together with the formation of three new strong bands at 2067, 2034 and 2003  $\text{cm}^{-1}$  (Fig. 2.33). Again the bands undergo vibrational cooling (over the following  $\sim 10$  ps) and shift to higher frequencies of 2076, 2041, and 2012  $\text{cm}^{-1}$  respectively. These bands, which decay in less than 300 ps are assigned to the triplet diradical species. The decay of these bands, again, corresponds to partial recovery of the parent bands.

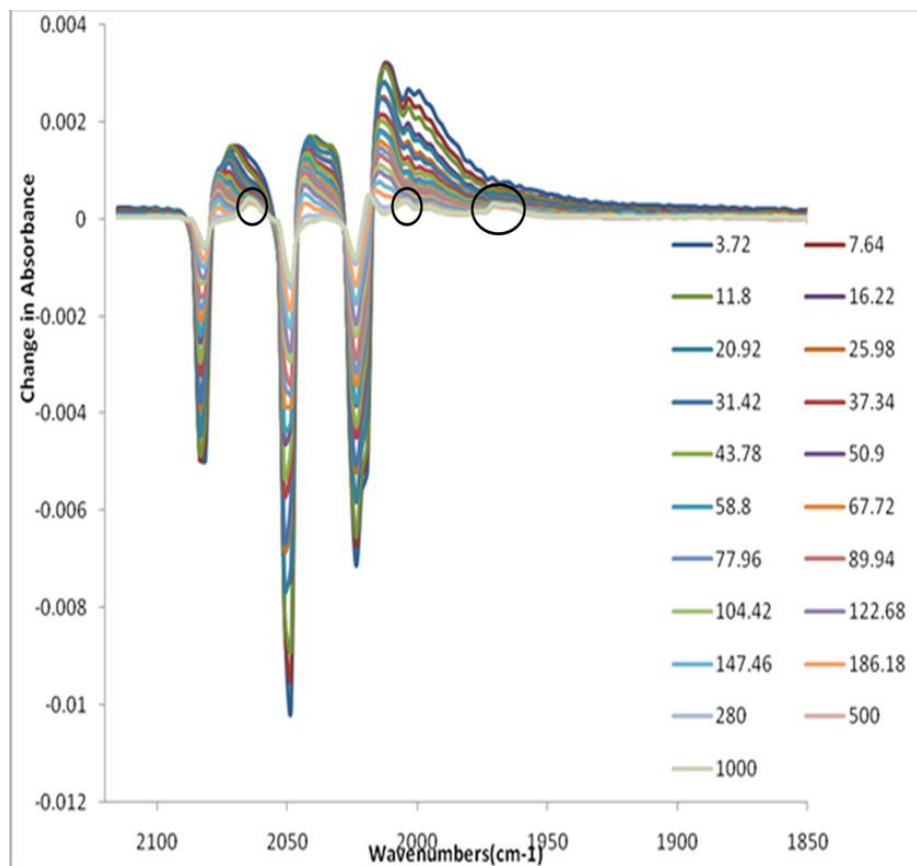


**Figure 2.33 - Time resolved infra-red difference spectra following laser photolysis ( $\lambda_{\text{exc}} = 400\text{nm}$ ) of  $(\mu_2\text{-PyrFc})\text{Co}_2(\text{CO})_6$  in a heptane solution (legend indicates time in ps). Circled are the new bands formed due to the CO loss photoproduct.**

In addition three further bands are observed at 2064, 2004 and 1970  $\text{cm}^{-1}$ . As similarly discussed above for  $(\mu_2\text{-PyrH})\text{Co}_2(\text{CO})_6$ , these bands are assigned to the CO loss solvated photoproduct  $(\mu_2\text{-PyrFc})\text{Co}_2(\text{CO})_5(\text{heptane})$ . There was no evidence for these bands decaying on the timescale of the experiment (1 ns). Furthermore the parent bands did not fully recover over the course of the experiment. From measurement of the recovery of the parent bands after the length of the experiment (1 ns) the quantum yield for CO loss was estimated to be  $\sim 15\%$ . This result is comparable to the 13% which was determined at 405 nm using the ferrioxalate actinometric quantum yield studies.

Laser flash photolysis experiments ( $\lambda_{\text{exc}} = 400\text{nm}$ ) were also carried out on the DPPM compounds in spectrophotometric grade DCM. For all compounds of this type similar results were observed. Following photolysis of  $(\mu_2\text{-PyrFc})\text{Co}_2(\text{CO})_4\text{DPPM}$  in DCM at

room temperature, bleaching of the parent  $\nu_{\text{CO}}$  bands at 2017, 1990, and 1964  $\text{cm}^{-1}$  occurred within the laser pulse, together with the formation of three new metal-carbonyl bands at 2003, 1975 and 1949  $\text{cm}^{-1}$ . There was little evidence of vibrational cooling and these bands decayed within 500ps together with  $\sim 90\%$  recovery of the parent bands. Due to the similarity of these results to those observed following photolysis of the dicobalt hexacarbonyl complexes, the transient species were assigned to the triplet diradical previously discussed (Fig.2.31).<sup>24</sup>

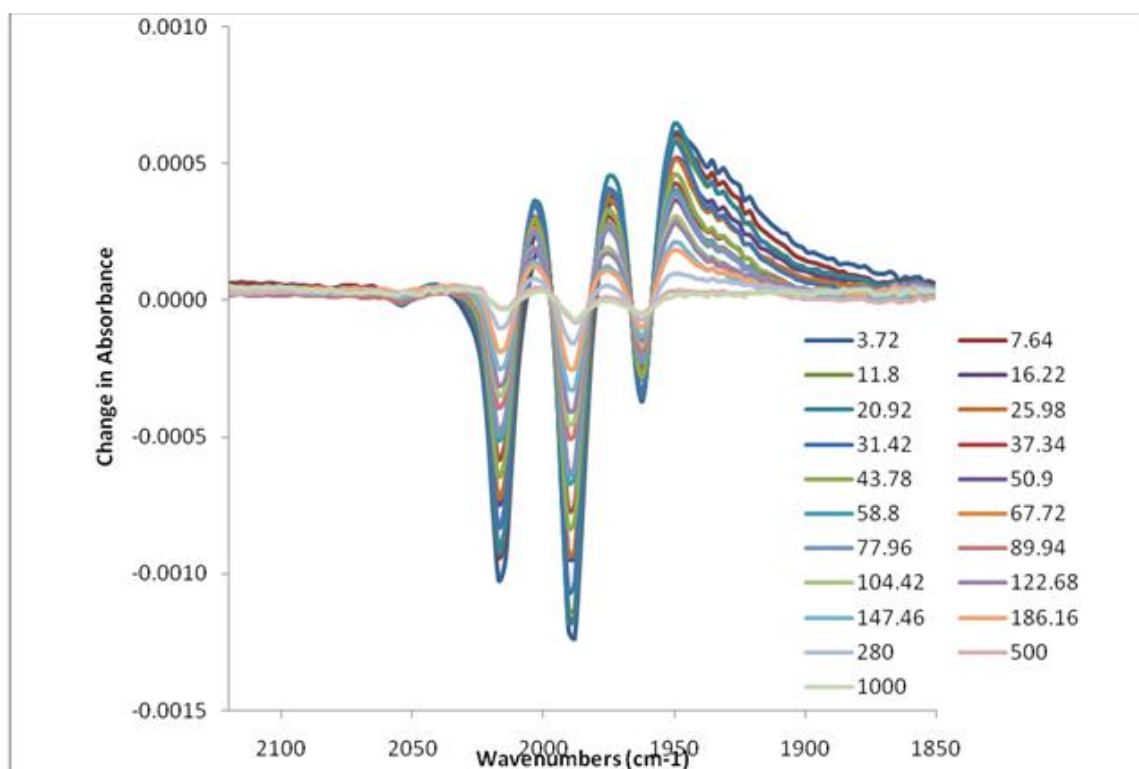


**Figure 2.34 - Time resolved infra-red difference spectra following laser flash photolysis ( $\lambda_{\text{exc}} = 400\text{nm}$ ) of  $(\mu_2\text{-PyrFc})\text{Co}_2(\text{CO})_4\text{DPPM}$  in DCM (legend shows time in ps).**

### ***2.3.5. Photocatalytic Hydrogen Generation Experiments***

Each of the complexes in this study were tested under the conditions (1 - 4) listed in Table 2.6.



Exp . No.	Conc. Complex (M)	TEA (%)	Water (%)	Irradiation $\lambda$ (nm)	Irradiation length (hr)
1	$5 \times 10^{-5}$	16.6	10	350	20
2	$5 \times 10^{-5}$	16.6	0	350	20
3	$5 \times 10^{-5}$	16.6	10	470	20
4	$5 \times 10^{-5}$	16.6	0	470	20

**Table 2.6- Experimental conditions for photocatalytic studies.**

No H<sub>2</sub> was detected in the headspace of the sample vials via GC analysis. This may be either because none was produced during the experiments or the amount produced was less than the limit of detection of the GC.

### ***2.3.6 Cyclic Voltammetry***

#### **2.3.6.1: Reductive Electrochemistry**

Reductive electrochemistry was carried out on the all cobalt hexacarbonyl and cobalt tetracarbonyl DPPM complexes in the range 0V to -2.0 V. The potential window of DCM is between 0 and -2.0 V for reduction processes so experiments were not carried out at lower potential limits. Within this range several reduction process were observed and have been summarised in Table 2.7.

Cyclic Voltammetry Reduction Processes							
( $\mu_2$ -alkyne) $\text{Co}_2(\text{CO})_6$ Complexes	$E_{\text{pa}}$ (V)	$E_{\text{pc}}$ (V)	$E_{1/2}$ (V)	( $\mu_2$ -alkyne) $\text{Co}_2(\text{CO})_4$ DPPM Complexes	$E_{\text{pa}}$ (V)	$E_{\text{pc}}$ (V)	$E_{1/2}$ (V)
( $\mu_2$ -FcH) $\text{Co}_2(\text{CO})_6$		-1.22 <sup>a</sup>		( $\mu_2$ -FcH) $\text{Co}_2(\text{CO})_4$ DPPM	-	-	-
( $\mu_2$ -ThioH) $\text{Co}_2(\text{CO})_6$		-1.20 <sup>a</sup>		( $\mu_2$ -ThioH) $\text{Co}_2(\text{CO})_4$ DPPM	-	-	-
( $\mu_2$ -PyrH) $\text{Co}_2(\text{CO})_6$		-1.16 <sup>a</sup>		( $\mu_2$ -PyrH) $\text{Co}_2(\text{CO})_4$ DPPM	-	-	-
( $\mu_2$ -PyrFc) $\text{Co}_2(\text{CO})_6$		-1.07 <sup>a</sup>		( $\mu_2$ -PyrFc) $\text{Co}_2(\text{CO})_4$ DPPM	-	-	-

**Table 2.7 - The cyclic voltammetry results for the reduction processes of all  $\text{Co}_2(\text{CO})_6$  and  $\text{Co}_2(\text{CO})_4$ DPPM complexes. <sup>a</sup> indicates an irreversible reduction wave.**

All ( $\mu_2$ -C<sub>2</sub>R<sub>2</sub>) $\text{Co}_2(\text{CO})_6$  complexes exhibited one irreversible reduction which is in agreement with the literature.<sup>41</sup> Addition of the electron withdrawing DPPM moiety lead to there being no observable reduction processes within the electrochemical window.<sup>42,45,67</sup>

### 2.3.6.2: Oxidative Electrochemistry

Oxidative electrochemistry was carried out on all of the cobalt hexacarbonyl and cobalt tetracarbonyl DPPM complexes in the range 0 V to 2.0 V. Within this range several oxidation process were observed and have been summarised in Table 2.8.

Cyclic Voltammetry Oxidation Processes							
( $\mu_2$ -alkyne) $\text{Co}_2(\text{CO})_6$ Complexes	$E_{\text{pa}}$ (V)	$E_{\text{pc}}$ (V)	$E_{1/2}$ (V)	( $\mu_2$ -alkyne) $\text{Co}_2(\text{CO})_4$ DPPM Complexes	$E_{\text{pa}}$ (V)	$E_{\text{pc}}$ (V)	$E_{1/2}$ (V)
( $\mu_2$ -FcH) $\text{Co}_2(\text{CO})_6$	0.4 <sup>b</sup>	0.64 <sup>b</sup>	0.52	( $\mu_2$ -FcH) $\text{Co}_2(\text{CO})_4$ DPPM	0.36 <sup>b</sup>	0.22 <sup>b</sup>	0.28
	1.45 <sup>a</sup>				0.93 <sup>a</sup>		
( $\mu_2$ -ThioH) $\text{Co}_2(\text{CO})_6$	1.41 <sup>a</sup>			( $\mu_2$ -ThioH) $\text{Co}_2(\text{CO})_4$ DPPM	0.47 <sup>b</sup>	0.25 <sup>b</sup>	0.36
					1.3 <sup>a</sup>		
( $\mu_2$ -PyrH) $\text{Co}_2(\text{CO})_6$	1.22 <sup>a</sup>			( $\mu_2$ -PyrH) $\text{Co}_2(\text{CO})_4$ DPPM	0.23 <sup>b</sup>	0.13 <sup>b</sup>	0.18
					1.14 <sup>a</sup>		
( $\mu_2$ -PyrFc) $\text{Co}_2(\text{CO})_6$	0.71 <sup>b</sup>	0.52 <sup>b</sup>	0.49	( $\mu_2$ -PyrFc) $\text{Co}_2(\text{CO})_4$ DPPM	0.29 <sup>b</sup>	0.18 <sup>b</sup>	0.24
	1.41 <sup>a</sup>				0.48 <sup>b</sup>	0.38 <sup>b</sup>	0.43
					0.85 <sup>b</sup>	0.74 <sup>b</sup>	0.795

**Table 2.8 - The cyclic voltammetry results for the oxidation processes of all  $\text{Co}_2(\text{CO})_6$  and  $\text{Co}_2(\text{CO})_4\text{DPPM}$  complexes. <sup>a</sup> indicates an irreversible reduction, <sup>b</sup> indicates a reversible wave.**

One irreversible oxidation was observed for all  $(\mu_2\text{-C}_2\text{R}_2)\text{Co}_2(\text{CO})_6$  complexes, attributed to the formation of the cation radical  $[\mu_2\text{-C}_2\text{H}_2\text{Co}_2(\text{CO})_6]^+$ .<sup>40-42</sup> These oxidations were moved to more cathodic potentials through the addition of the electron withdrawing DPPM unit.

### 2.3.7. Electrocatalytic Hydrogen Generation Experiments

Electrocatalytic hydrogen generation experiments were carried out using glassy carbon electrode surfaces modified with each of the compounds synthesised in this study. The surfaces were modified using the dropcast method where a known amount of sample is dissolved in a suitable solvent, in this case DMF, and a known amount of this solution is

applied to the surface using an autopipette. The solvent is then allowed to evaporate overnight in darkness leaving a thin film of solid sample on the surface of the electrode. Using this method the number of moles of sample on the electrode surface can be calculated, however this may not be an accurate measurement of the number of moles of the “active” sample, or participating in the process, on the surface during the experiment. It is possible to calculate the active catalyst on the surface by measuring the area under the curve of an electrochemical process during cyclic voltammetry and dividing this value by Faradays constant ( $96485 \text{ C mol}^{-1}$ ) according to Faradays law of electrolysis. Generally the active catalyst on the surface has been calculated to be between 2 and 5 % using this method with any inactivity being attributed to stacking, poor electronic communication through space and even to some of the sample drying on the plastic surround of the electrode surface itself. Traditionally TONs have been calculated based upon the number of moles of active catalyst on the electrode surface, however, during the experiments completed during this study no discernable process was visible during cyclic voltammogram sweeps and therefore the number of moles of active catalyst could not be accurately measured. Therefore each TON calculated has been based upon the number of moles of sample dropcast on to the surface initially and it is estimated that the TONs quoted are in fact an order of magnitude less than their true values.

#### **2.3.6.1. Onset of Catalytic Current**

A series of cyclic voltammogram experiments were carried out using both the bare glassy carbon electrode and glassy carbon electrodes with modified surfaces. The scans were performed at  $0.1 \text{ Vs}^{-1}$  from 0V to -1.2 V in pH 2.0, 0.1 M  $\text{NaH}_2\text{PO}_4$  buffer. An additional process is visible in these CVs when the cyclic voltammograms produced were compared to similar CVs run in pH 7.0, 0.1 M  $\text{NaH}_2\text{PO}_4$  buffer or ACN. This process is assigned to the catalytic production of  $\text{H}_2$  in aqueous media and was confirmed through GC analysis of the headspace after the experiment. Table. 2.9 details the onset of current induced by this process according to the complex used to modify the surface (Fig 2.47 to 2.50 show these processes). ThioH was not measured as it is a liquid at room temperature.

Complex	Onset of Catalytic Current (V)
Bare Electrode	-1.15
FcH	-0.85
( $\mu_2$ -FcH)Co <sub>2</sub> (CO) <sub>6</sub>	-1.01
( $\mu_2$ -FcH)Co <sub>2</sub> (CO) <sub>4</sub> DPPM	-1.00
ThioH	N/A
( $\mu_2$ -ThioH)Co <sub>2</sub> (CO) <sub>6</sub>	-0.96
( $\mu_2$ -ThioH)Co <sub>2</sub> (CO) <sub>4</sub> DPPM	-0.85
PyrH	-0.90
( $\mu_2$ -PyrH)Co <sub>2</sub> (CO) <sub>6</sub>	-1.05
( $\mu_2$ -PyrH)Co <sub>2</sub> (CO) <sub>4</sub> DPPM	-0.89
PyrFc	-0.85
( $\mu_2$ -PyrFc)Co <sub>2</sub> (CO) <sub>6</sub>	-1.10
( $\mu_2$ -PyrFc)Co <sub>2</sub> (CO) <sub>4</sub> DPPM	-0.90

**Table 2.9-** Potential of the onset of electrocatalytic H<sub>2</sub> generation through modification of the glassy carbon electrode surface with the complexes utilised in this study. All potentials are referenced vs. Ag/AgCl. Experiments were carried out in pH 2.0, 1 mM NaH<sub>2</sub>PO<sub>4</sub> buffer at 25°C.

The onset of the catalytic current greatly influenced the intensity of the catalytic current induced when the CV was measured over a potential window of 0 to -1.2 V. The complexes with the least negative onset of this current presented the most enhanced currents when compared with the unmodified bare electrode. All ( $\mu_2$ - alkyne)Co<sub>2</sub>(CO)<sub>6</sub> complexed presented only slightly enhanced catalytic currents which may be due to decomposition of the complexes following reduction as was evident in the cyclic voltammetry carried out in ACN in section 2.3.6.1.

### 2.3.6.2. H<sub>2</sub> Generation TONs

Each compound was tested for its electrocatalytic H<sub>2</sub> generation efficacy using an applied potentiostatic potential of -1.2 V for 1 hour. A 1ml sample of the headspace was injected into a GC to analyse the H<sub>2</sub> content. The TONs calculated electrochemically vs.

GC were compared so as to measure the overall efficiency of the electrochemical reaction (Table 2.10). Full details of calculations are available in appendix C. ThioH was not measured as it is a liquid at room temperature.

Compound	Charge Passed After 1 Hr (C)	Electrochemical TON ( $\times 10^3$ )	GC TON ( $\times 10^3$ )	*Efficiency %	Avg current during bulk electrolysis	Current Density ( $\text{mA}/\text{cm}^2$ )
FcH	0.622	21.5	14.4	67	$1.76 \times 10^{-4}$	2.52
( $\mu_2$ -FcH) $\text{Co}_2(\text{CO})_6$	0.154	5.3	2.6	48	$4.28 \times 10^{-5}$	0.64
( $\mu_2$ -FcH) $\text{Co}_2(\text{CO})_4$ DPPM	0.397	13.7	8.9	65	$1.18 \times 10^{-4}$	1.69
PyrH	0.306	10.6	6.9	66	$1.09 \times 10^{-4}$	1.56
( $\mu_2$ -PyrH) $\text{Co}_2(\text{CO})_6$	0.136	4.7	4.0	85	$4.48 \times 10^{-5}$	0.64
( $\mu_2$ -PyrH) $\text{Co}_2(\text{CO})_4$ DPPM	0.333	11.5	10.0	87	$1.19 \times 10^{-4}$	1.70
ThioH	N/A	N/A	N/A	N/A	N/A	N/A
( $\mu_2$ -ThioH) $\text{Co}_2(\text{CO})_6$	0.221	7.6	5.8	76	$5.98 \times 10^{-5}$	0.85
( $\mu_2$ -ThioH) $\text{Co}_2(\text{CO})_4$ DPPM	0.278	9.6	5.7	59	$6.43 \times 10^{-5}$	0.92
PyrFc	0.322	11.1	7.2	65	$1.16 \times 10^{-4}$	1.65
( $\mu_2$ -PyrFc) $\text{Co}_2(\text{CO})_6$	0.145	5.0	3.0	60	$4.51 \times 10^{-5}$	0.65
( $\mu_2$ -PyrFc) $\text{Co}_2(\text{CO})_4$ DPPM	0.303	10.5	6.7	64	$1.14 \times 10^{-4}$	1.63

**Table 2.10- Results of electrocatalytic studies for all ( $\mu_2$ -C<sub>2</sub>R<sub>2</sub>)cobalt carbonyl complexes and ligands. \* refers to  $(\text{TON}_{\text{GC}}/\text{TON}_{\text{electro}}) \times 100$ . All TON are quoted  $\pm 30\%$ .**

## 2.4. Discussion

**Synthesis.** All ligands and cobalt hexacarbonyl carbonyl complexes discussed in this chapter were synthesised using Sonogashira coupling and all spectral data are in good agreement with reported data.<sup>57</sup> Catalysis was achieved using  $\text{Pd}(\text{PPh}_3)_2\text{Cl}_2$ ,  $\text{PPh}_3$  and a  $\text{CuI}$  co-catalyst. The  $\text{Pd}^0$  catalyst needed for this type of reaction is formed in situ following the coupling of  $\text{Pd}(\text{PPh}_3)_2\text{Cl}_2$  and  $\text{PPh}_3$ . The yield achieved during the synthesis of  $\text{PyrFc}$  was very high 98%, which is expected during this type of reaction using bulky groups such as pyrene and ferrocene. Similarly the synthesis of  $\text{PyrTMS}$  achieved a 96% yield; however the deprotection step only yielded 70% following stirring with  $\text{K}_2\text{CO}_3$ .

The addition of the cobalt carbonyl moiety was achieved through stirring overnight in hexane. Yields of between 78 and 98% were achieved for this step of synthesis with the lowest yield achieved following purification of  $\mu_2\text{-PyrFcCo}_2(\text{CO})_6$  presumable due to the large bulk of the pyrene and ferrocene group sterically hindering the coordination of the  $\text{Co}_2(\text{CO})_6$  moiety.

The  $(\mu_2\text{-C}_2\text{R}_2)\text{Co}_2(\text{CO})_4\text{DPPM}$  derivatives synthesised are all novel to the best of our knowledge, and all spectral data are in agreement with their formulation and compare well to similar compounds which have been previously reported in literature.<sup>58</sup> The yields achieved during this synthesis were quite low which may be expected due to the unstable nature of the  $(\mu_2\text{-C}_2\text{R}_2)\text{Co}_2(\text{CO})_6$  complexes and the harsh conditions of the DPPM addition reaction; reflux at 98 °C, leading to possible degradation of the starting material which was confirmed following the reaction using TLC.

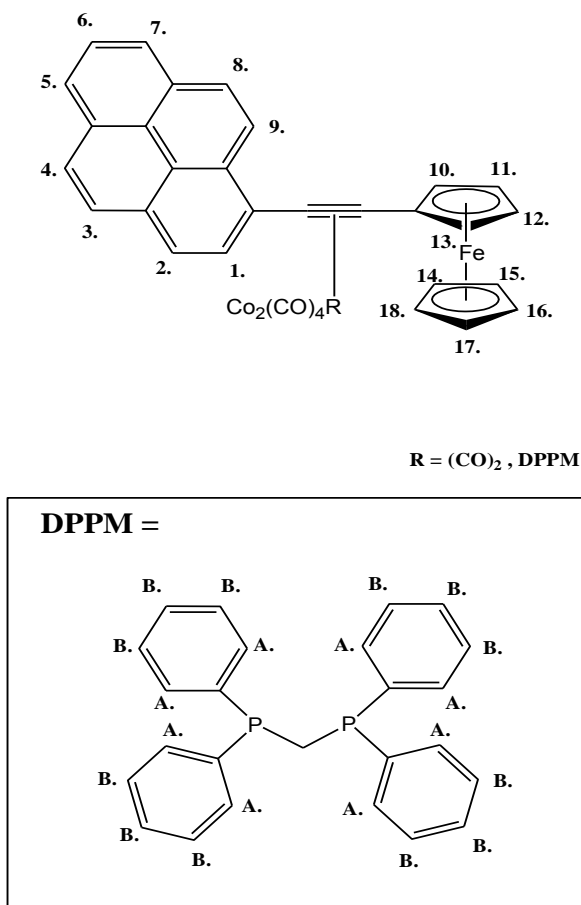


Figure 2.35- Numbering of protons in pyrene-ethynylferrocene complexes.

**NMR Spectra.** The  $^1\text{H}$  NMR resonances for the pyrene protons (1-9) occur in the range 8.6 to 8ppm with the signal due to the proton closest to the alkyne bridge (1) producing a doublet signal at  $\sim 8.6\text{ppm}$ . The ferrocynyl protons (10-18) appear between 4.8 and 5.2 ppm in the  $(\mu_2\text{-alkyne})\text{Co}_2(\text{CO})_6$  derivative but these signals shift to between 3.8 and 4.7ppm in the  $(\mu_2\text{-alkyne})\text{Co}_2(\text{CO})_4\text{DPPM}$  complexes. The signals due to the DPPM moiety (A and B) also appear in the aromatic region between 6.8 and 7.25ppm. Also visible are the protons due to the methane bridge in the DPPM ligand at 3.15ppm. Sample  $^1\text{H}$ NMR are available in appendix D1.

**Electronic Absorption Spectroscopy.** All compounds synthesised in this study showed strong absorbances in the UV-vis region which are usually associated with ligand based  $\pi - \pi^*$  transitions.<sup>56</sup> For all ligands and complexes in this study, spectra contained strong absorbances in the region between 250 and 300 nm, which are attributed to ligand field



$\pi - \pi^*$  transitions on the pyrene, thiophene and ferrocene groups.<sup>54</sup> The addition of a pyrene moiety to the alkyne bridge gives rise to a strong absorbance in the region of 320- 450 nm.<sup>23</sup> This is evident from the spectra in Fig. 2.36 as both  $(\mu_2\text{-1-ethynylpyrene})\text{Co}_2(\text{CO})_6$  and  $(\mu_2\text{-pyrene-ethynylferrocene})\text{Co}_2(\text{CO})_6$  exhibit this absorption band which is not present in  $(\mu_2\text{-3-ethynylthiophene})\text{Co}_2(\text{CO})_6$  and  $(\mu_2\text{-ethynylferrocene})\text{Co}_2(\text{CO})_6$ . This is due to the strong double bond character introduced by the highly conjugated pyrene group. This strong absorbance is in agreement with similar results reported by Coleman et. al.<sup>23</sup> Low-lying metal to ligand charge transfer (MLCT) bands of Co ( $d\pi$ ) – ligand ( $\pi$ ) were also observed in the visible region from approximately 420 to 600 nm associated with cobalt carbonyl moiety. A small contribution to these low energy transitions may be assigned to weak d- d transitions between the two Co metal centres.

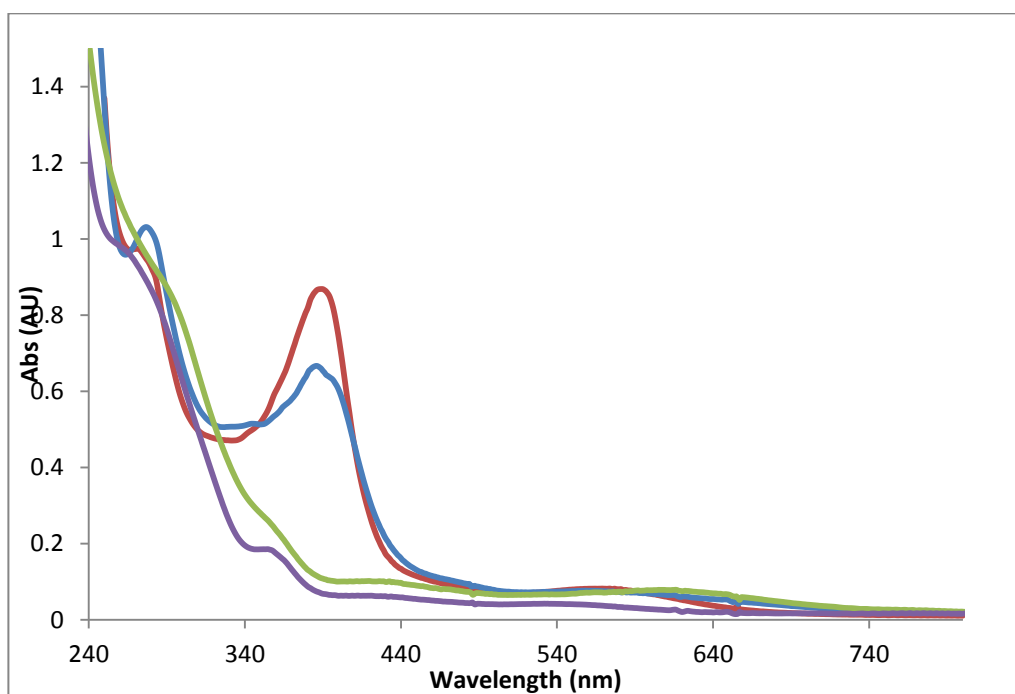


**Figure 2.37 – Overlay of electronic absorbance spectra of  $(\mu_2\text{-alkyne})\text{-Co}_2(\text{CO})_6$  complexes in DCM.  $(\mu_2\text{-1-ethynylpyrene})\text{Co}_2(\text{CO})_6$  (red line),  $(\mu_2\text{-pyrene-ethynylferrocene})\text{Co}_2(\text{CO})_6$  (blue line),  $(\mu_2\text{-ethynylferrocene})\text{Co}_2(\text{CO})_6$  (green line) and  $(\mu_2\text{-3-ethynylthiophene})\text{Co}_2(\text{CO})_6$  (purple line). Concentrations range between  $1.6 \times 10^{-2}$  and  $1.3 \times 10^{-2}$  M.**

The addition of the DPPM group to each system resulted in a broadening of absorbance bands as is evident in Fig. 2.38. Substitution of the carbonyl groups with DPPM induced a small hypsochromic shift in the absorbances (See Table 2.3).

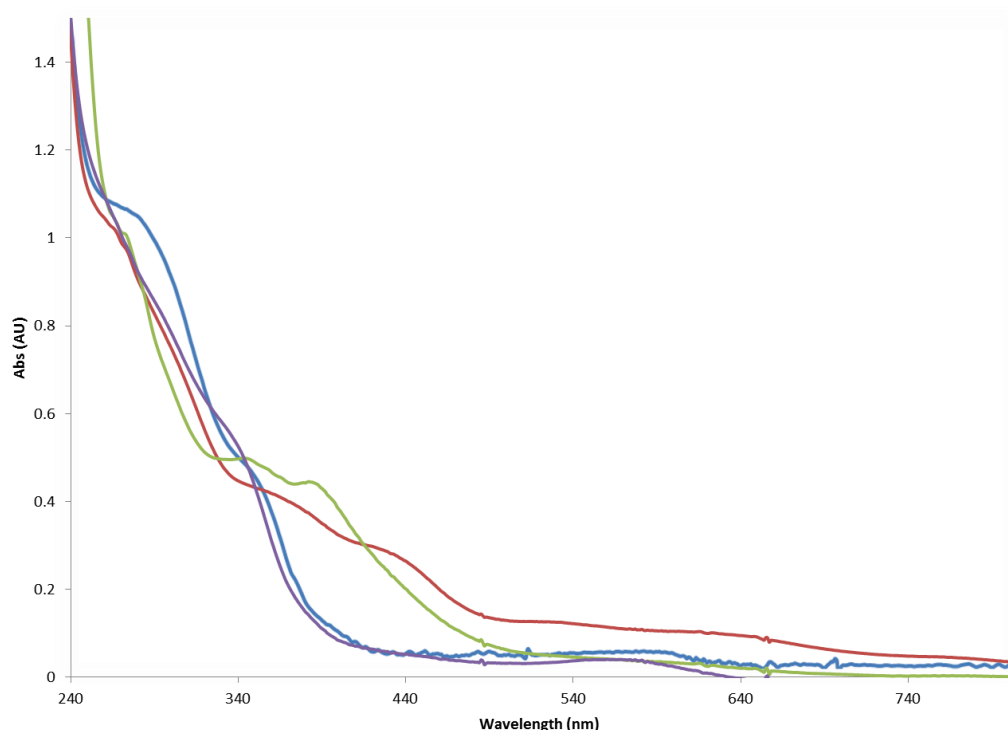


**Figure 2.38 – Overlay of electronic absorbance spectra of  $\text{Co}_2(\text{CO})_4\text{DPPM}$  complexes in DCM. .  $\mu_2$ -1-ethynylpyrene  $\text{Co}_2(\text{CO})_4\text{DPPM}$  (red line),  $\mu_2$ -pyrene-ethynylferrocene  $\text{Co}_2(\text{CO})_4\text{DPPM}$  (green line),  $\mu_2$ -ethynylferrocene  $\text{Co}_2(\text{CO})_4\text{DPPM}$  (purple line) and  $\mu_2$ -3-ethynylthiophene  $\text{Co}_2(\text{CO})_4\text{DPPM}$  (blue line). Concentrations are between  $2.9 \times 10^{-2}$  and  $1.3 \times 10^{-2}$  M.**

**Quantum Yields for CO loss ( $\Phi_{\text{CO}}$ ).** To determine the efficiency for CO loss in the hexacarbonyl compounds the quantum yield for CO loss ( $\Phi_{\text{CO}}$ ) was determined at a number of wavelengths. In these experiments the conversion of  $(\mu_2\text{-alkyne})\text{Co}_2(\text{CO})_6$  to  $(\mu_2\text{-alkyne})\text{Co}_2(\text{CO})_5(\text{PPh}_3)$  was measured. For the photoproducts,  $(\mu_2\text{-PyrH})\text{Co}_2(\text{CO})_5(\text{PPh}_3)$  and  $(\mu_2\text{-PyrFc})\text{Co}_2(\text{CO})_5(\text{PPh}_3)$ , an absorbance maximum is centred at  $\sim 430$  nm, thus the photoreaction was monitored by noting the changes in absorbance at this wavelength (Fig. 2.29). UV-vis photolysis was used to monitor the

reaction. Displayed in Table 2.5 are the mean values for each quantum yield experiment at each excitation wavelength. The values obtained demonstrate that the  $\Phi_{\text{CO}}$  loss is dependent on the excitation wavelength, and also varies with the complex. It is apparent that the quantum yield of CO loss for  $(\mu_2\text{-PyrH})\text{Co}_2(\text{CO})_6$  (**1**) increases on moving from low to high energy (546 – 313 nm). For instance at 546 nm  $\Phi_{\text{CO loss}} = 4 \%$ , and on moving to 313 nm this value increases with  $\Phi_{\text{CO loss}} = 25 \%$ . In the case of  $(\mu_2\text{-PyrFc})\text{Co}_2(\text{CO})_6$  there is no specific trend for  $\Phi_{\text{CO loss}}$ . Similar values were obtained following excitation at both 313 and 546 nm, and these values increased on moving to 365 and 405 nm. The values obtained in this study are relatively low compared to organometallic compounds such as  $\text{Cr}(\text{CO})_6$  or  $(\eta^6\text{-benzene})\text{Cr}(\text{CO})_3$  where  $\Phi_{\text{CO}} < 0.68$  have been reported.<sup>59</sup> Furthermore the  $\Phi_{\text{CO loss}}$  values obtained here following excitation at 405 nm agree with the results obtained in the TRIR studies following excitation at 400 nm.

**Time Resolved Infra-red Studies.** The IR spectra for the cobalt carbonyl complexes presented here have cobalt carbonyl stretching vibrations in the range  $1900 - 2200 \text{ cm}^{-1}$ . These spectral patterns are similar to those observed for previously reported alkyne dicobalt carbonyl complexes.<sup>22,23</sup> The absence of the alkyne stretch,  $\nu(\text{C}\equiv\text{C})$ , in the region of  $2200 \text{ cm}^{-1}$  indicated that the alkynyl bond has lost its triple bond character as it is coordinated to the  $\text{Co}_2(\text{CO})_6$  metal centres. The addition of a diphenylphosphinomethane (DPPM) moiety to the metal centre shifts the  $\nu_{\text{CO}}$  stretches to lower frequencies. One such example is shown for  $(\mu_2\text{-PyrH})\text{Co}_2(\text{CO})_6$  and  $(\mu_2\text{-PyrH})\text{Co}_2(\text{CO})_4\text{DPPM}$  in Fig. 2.39.

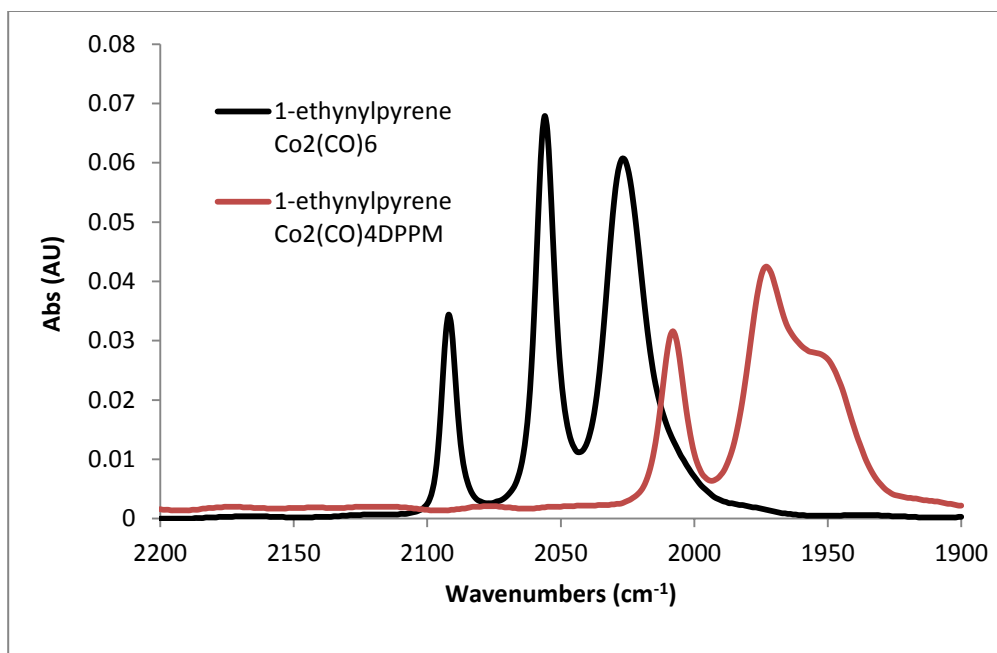


**Figure 2.39 – Overlay of IR spectra of  $(\mu_2\text{-PyrH})\text{Co}_2(\text{CO})_6$  (black line) and  $(\mu_2\text{-PyrH})\text{Co}_2(\text{CO})_4\text{DPPM}$  (red line), spectrum recorded in DCM.**

TRIR measurements showed that photoexcitation ( $\lambda_{\text{exc}} = 400 \text{ nm}$ ) of all of the complexes in the study resulted in depletion of the parent  $\nu_{\text{CO}}$  bands, together with the generation of three new bands in the carbonyl region within the laser pulse. The IR bands generated initially corresponded to a vibrationally “hot” species and these bands shifted to higher wavenumber over 10 ps due to vibrational cooling. This cooling has previously been observed on a ps timescale and reported by Busby *et al.* for a number of metal carbonyl systems.<sup>60</sup> The new bands formed within the laser pulse were tentatively assigned to an  $(\mu_2\text{-alkyne})\text{Co}_2(\text{CO})_6$  diradical which is formed due to cleavage of the Co-Co metal bond.<sup>24</sup> It has also been reported using density functional theory (DFT) that the Co-Co bond in  $(\mu_2\text{-HC}\equiv\text{CC}_6\text{H}_{10}\text{OH})\text{Co}_2(\text{CO})_6$  complexes is very weak<sup>14</sup>. This supports the hypothesis that a  $(\mu_2\text{-alkyne})\text{Co}_2(\text{CO})_6$  diradical is formed (Fig. 2.31). These diradical bands decay within the subsequent 300 ps.

For instance; in the case of  $(\mu_2\text{-FcH})\text{Co}_2(\text{CO})_6$  bleaching of each of the parent  $\nu_{\text{CO}}$  bands at 2090, 2051, and 2023  $\text{cm}^{-1}$  occurred within the laser pulse, giving rise to new stretching vibrations at 2069, 2039 and 1999  $\text{cm}^{-1}$ , which undergo vibrational cooling (over the following  $\sim 10$  ps) with a shift to higher frequency with bands at 2081, 2041,

and  $2007\text{ cm}^{-1}$ . This cooling process has been previously reported on a ps timescale by Vlček *et al.* for a number of metal carbonyl systems.<sup>62</sup> These bands then decay in  $\sim 300$  ps which correspond to the recovery of the parent bands, which almost fully recover by the end of the experiment (Fig.2.40).

Similarly results were obtained for the DPPM derivative  $(\mu_2\text{-FcH})\text{Co}_2(\text{CO})_4(\text{DPPM})$  following laser flash photolysis ( $\lambda_{\text{exc}} = 400\text{ nm}$ ). Following photolysis of  $(\mu_2\text{-FcH})\text{Co}_2(\text{CO})_4(\text{DPPM})$ , bleaching of the parent  $\nu_{\text{CO}}$  bands occurred at  $2017$ ,  $1990$ , and  $1964\text{ cm}^{-1}$  within the laser pulse. Three new metal-carbonyl bands were generated at  $2003$ ,  $1975$  and  $1949\text{ cm}^{-1}$ . There was little evidence of vibrational cooling and these bands decayed within  $500\text{ ps}$  together with  $\sim 90\%$  recovery of the parent bands. Due to the similarity of these results to those observed following photolysis of the dicobalt hexacarbonyl complexes, the transient species was tentatively assigned to the triplet diradical.

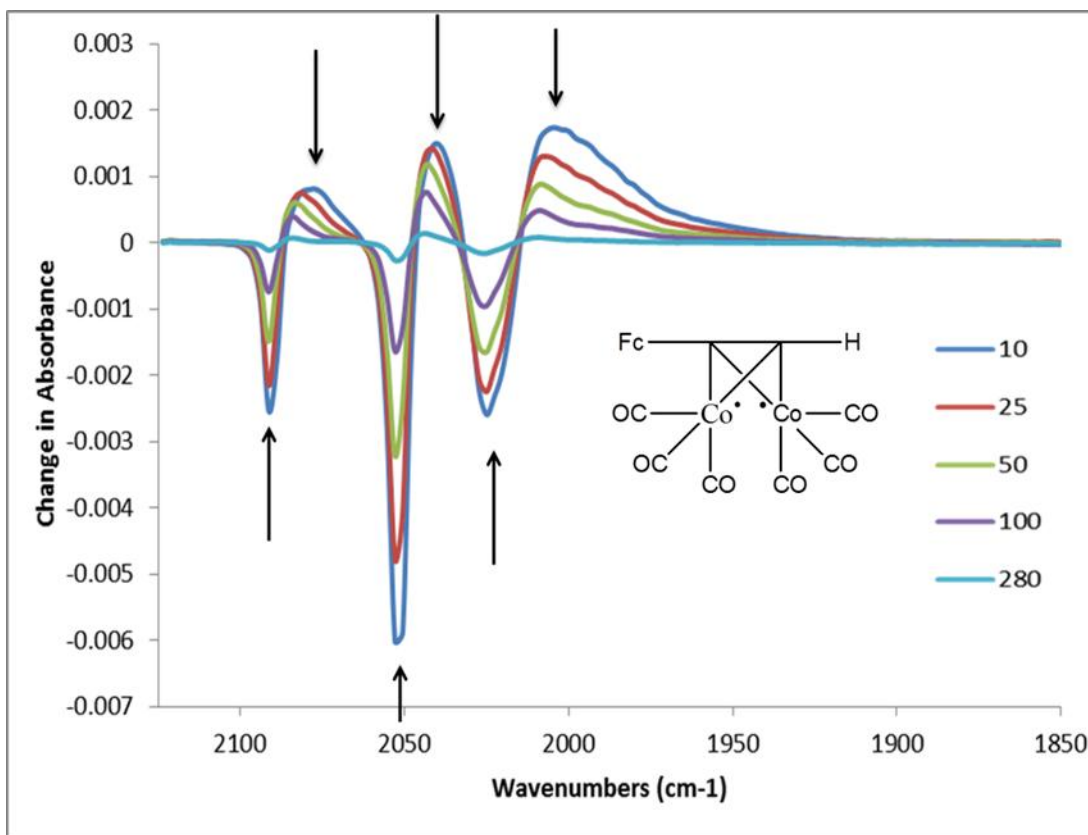


**Figure 2.40-** Transient absorption difference spectrum of  $(\mu_2\text{-FcH})\text{Co}_2(\text{CO})_6$  in heptane at 10, 25, 50, 100 and 280ps following excitation at 400nm. (Legend indicates time in ps)

In the case of  $(\mu_2\text{-PyrH})\text{Co}_2(\text{CO})_6$  and  $(\mu_2\text{-PyrFc})\text{Co}_2(\text{CO})_6$  in addition to the triplet diradical species there was evidence for a second species that persisted on the nanosecond timescale. In the case of  $(\mu_2\text{-PyrH})\text{Co}_2(\text{CO})_6$  these bands were observed at 2074, 2034, 2007 (obscured by depleted parent bands) and  $1977\text{ cm}^{-1}$  (Fig. 2.32) and in the case of  $(\mu_2\text{-PyrFc})\text{Co}_2(\text{CO})_6$  at 2064, 2004,  $1970\text{ cm}^{-1}$  (Fig. 2.33) These bands are assigned to the solvated CO loss species,  $(\mu^2\text{-PyrH-})\text{Co}_2(\text{CO})_5(\text{heptane})$  and  $(\mu_2\text{-PyrFc})\text{Co}_2(\text{CO})_5(\text{heptane})$  respectively. A coordinatively unsaturated intermediate is generated due to the loss of one CO group from the cobalt centre following irradiation. This vacant site is most likely coordinated with a solvent molecule. Other carbonyl systems have been shown to undergo CO loss followed by coordination of a solvent molecule;  $\text{Cr}(\text{CO})_6$  has been shown to undergo solvation following irradiation in THF and cyclohexane,<sup>61,62</sup>  $\text{Ru}^{\text{I}}$  and  $\text{Re}^{\text{II}}(\text{CO})_3$  diimine complexes are known to undergo solvation following irradiation in toluene.<sup>63</sup> Similar experiments using  $\text{Co}_2(\text{CO})_8$  have also resulted in the formation of the solvated photoproduct,  $\text{Co}_2(\text{CO})_7\text{heptane}$ , following UV irradiation.<sup>21</sup> However this is the first time that this solvated pentacarbonyl species has been observed in TRIR studies for an  $(\mu_2\text{-alkyne})\text{Co}_2(\text{CO})_6$  complex in solution and the bands observed in this study also compare well to those previously reported in the literature for  $(\mu_2\text{-alkyne})\text{Co}_2(\text{CO})_5$  which was observed in a frozen matrix at 20K.<sup>57</sup> CO loss is a well-studied process in metal carbonyl compounds and TRIR has been extensively used for chromium carbonyl complexes,<sup>64,65</sup> however these processes have been slow at  $\sim 150\text{ps}$ . It is evident from Fig. 2.41, that the generation of the solvated carbonyl species,  $(\mu_2\text{-PyrH})\text{Co}_2(\text{CO})_5\text{heptane}$ , occurs at a very fast rate ( $<4\text{ ps}$ ) when  $(\mu_2\text{-PyrH})\text{Co}_2(\text{CO})_6$  is irradiated at  $\lambda = 400\text{ nm}$  in heptane. Two of the stretches assigned to this solvated species at 2074 and  $2034\text{ cm}^{-1}$  are visible after 4 ps, while the other two stretches assigned to this species are obscured by the strong bands generated by the Co-Co bond homolysis photoproduct. As the CO loss photoproduct forms within the pulse, at the same time as the diradical photoproduct, the two processes can be said to occur independently of each other.

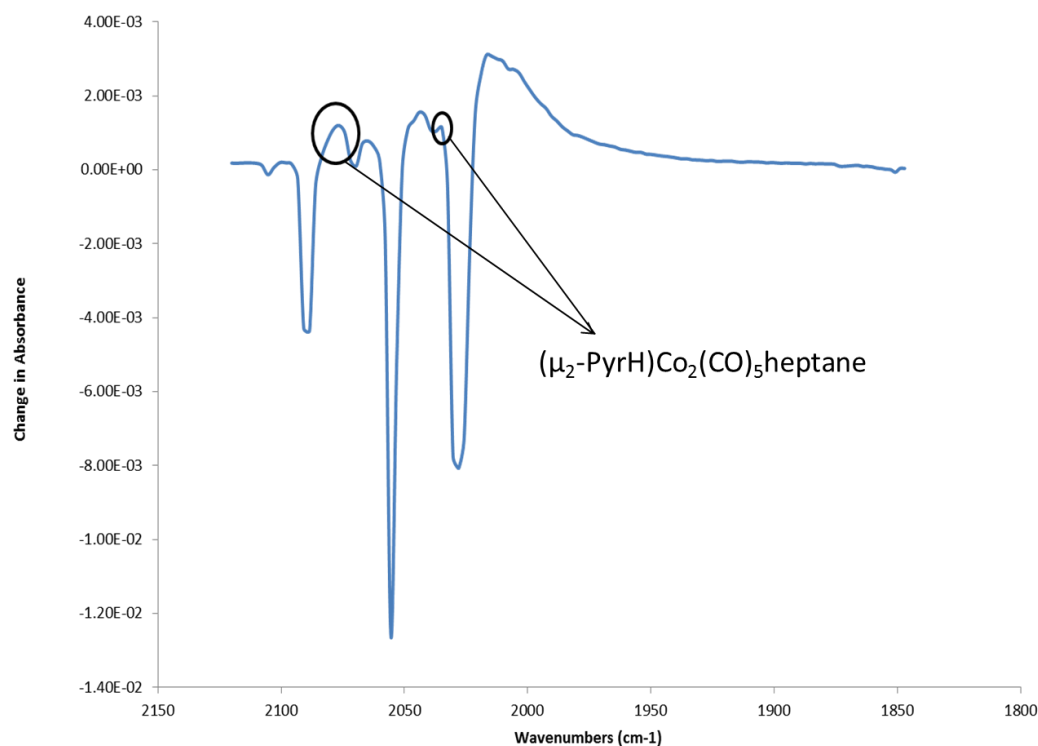


**Figure 2.41- TRIR difference spectrum following excitation (400 nm) of  $(\mu_2\text{-PyrH})\text{Co}_2(\text{CO})_6$  in heptane at 3.72ps. The negative bands correspond to depletion of parent material while the positive bands correspond to photoproduct.**

Fast CO release has been reported by Vlček *et al.*<sup>62,63</sup> was reported to occur in  $< 30$  ns in Cr, Ru and Re carbonyl complexes yielding a free coordination site on the metal centre. In these studies Vlček and his co-workers also observed the coordination of a solvent molecule at this free site using time resolved transient absorption. The solvated photoproduct of  $\text{Cr}(\text{CO})_4(\text{bpy})$  recorded in DCM was also reported in later work by the same research group using TRIR.<sup>66</sup> Following a laser pulse at  $\lambda = 355$  nm, three new  $\nu_{\text{CO}}$  stretches are observed in the TRIR spectrum after  $\sim 50$  ps which the author assigns to the solvated photoproduct  $\text{Cr}(\text{CO})_3(\text{bpy})(\text{DCM})$ .

Unfortunately the generation of the Co-Co bond homolysis intermediate following excitation of  $(\mu_2\text{-PyrFc})\text{Co}_2(\text{CO})_6$  obscures any IR stretching vibrations that may be present in the first 500 ps. Vibrations which have been assigned to the solvated species are not visible until  $\sim 500$  ps. The bands assigned to the CO loss photoproducts

following irradiation of  $(\mu_2\text{-PyrH})\text{Co}_2(\text{CO})_6$  and  $(\mu_2\text{-PyrFc})\text{Co}_2(\text{CO})_6$  persist on the time scale of the experiment (1ns). Furthermore as expected the parent bands do not fully recover (Fig. 2.42).

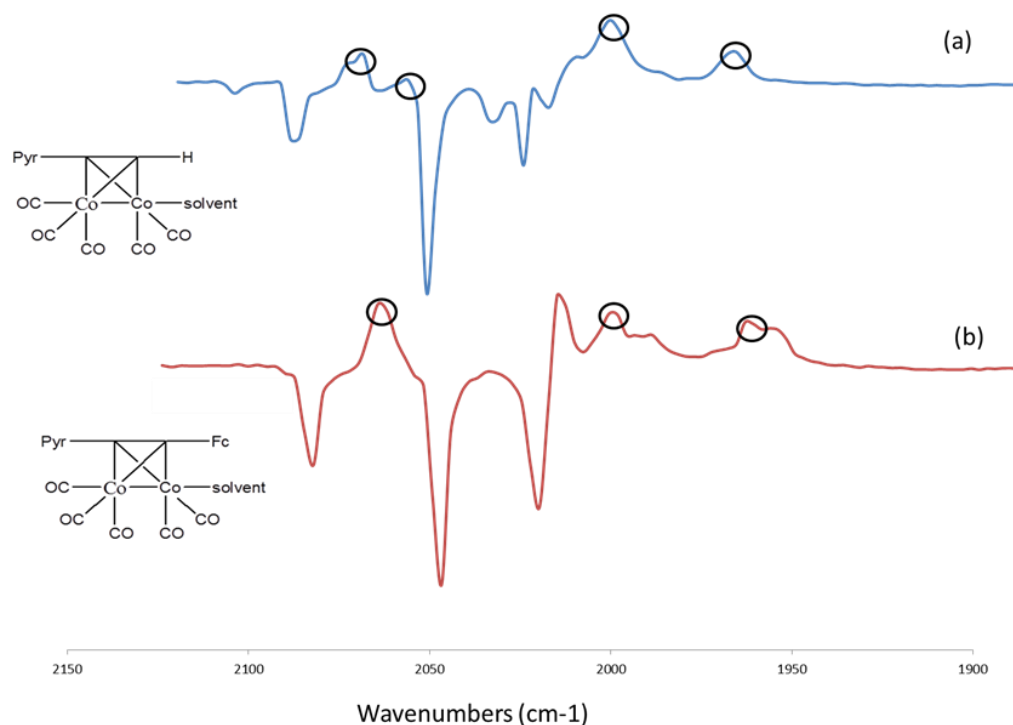


**Figure 2.42 – Transient absorption spectra of  $(\mu_2\text{-PyrH})\text{Co}_2(\text{CO})_6$  (a) and  $(\mu_2\text{-PyrFc})\text{Co}_2(\text{CO})_6$  (b) in heptane at 500ps showing the new IR absorbance peaks assigned to CO loss solvated species  $\mu_2\text{-(C}_2\text{R}_2\text{)Co}_2(\text{CO})_5\text{heptane}$ .**

The parent bands recover to approximately 85% of the initial depletion which correlates well with the measured quantum yield for CO-loss from  $(\mu_2\text{-PyrFc})\text{Co}_2(\text{CO})_6$  of 13% (see Fig. 2.26), and in the case of  $(\mu_2\text{-PyrH})\text{Co}_2(\text{CO})_6$ , the parent bands recover to approximately 90 %, and a quantum yield for CO-loss from  $(\mu_2\text{-PyrH})\text{Co}_2(\text{CO})_6$  of 9% was measured (Table 2.5).



Complex	Parent Spectrum (cm <sup>-1</sup> )	Vibrationally "hot" species (cm <sup>-1</sup> )	Diradical species (cm <sup>-1</sup> )	CO loss photoproduct (cm <sup>-1</sup> )
( $\mu_2$ -PyrH) Co <sub>2</sub> (CO) <sub>6</sub>	2092, 2056, 2030	2078, 2046, 2012	2081, 2048, 2016	2074, 2034, 2007, 1977
( $\mu_2$ -PyrFc) Co <sub>2</sub> (CO) <sub>6</sub>	2085, 2048, 2023	2067, 2034, 2003	2076, 2041, 2012	2064, 2004, 1970
( $\mu_2$ -FcH) Co <sub>2</sub> (CO) <sub>6</sub>	2090, 2051, 2023	2069, 2039, 1999	2081, 2041, 2007	N/A
( $\mu_2$ -PyrH) Co <sub>2</sub> (CO) <sub>4</sub> DPPM	2006, 1974, 1953	N/A	2004, 1954, 1927	N/A
( $\mu_2$ -PyrFc) Co <sub>2</sub> (CO) <sub>4</sub> DPPM	2017, 1990, 1964	N/A	2003, 1975, 1949	N/A
( $\mu_2$ -FcH) Co <sub>2</sub> (CO) <sub>4</sub> DPPM	2018, 1989, 1962	N/A	2006, 1973, 1947	N/A

**Table 2.11 : TRIR spectral data for all complexes in this study. TRIR for ( $\mu_2$ -alkyne)Co<sub>2</sub>(CO)<sub>6</sub> complexes were carried out in spectrophotometric grade heptane. TRIR for ( $\mu_2$ -alkyne)Co<sub>2</sub>(CO)<sub>4</sub> DPPM complexes were carried out in spectrophotometric grade DCM.**

**Electrochemistry.** Due to solubility issues accurate concentrations of samples was not possible, however, samples prepared were  $\sim 1$  mmol concentration. Reductive electrochemistry measurements were carried out on all complexes in this study. Cyclic voltammograms of all ( $\mu_2$ -alkyne)Co<sub>2</sub>(CO)<sub>6</sub> complexes exhibited a single reduction between -1.07 V and -1.22 V which corresponds to the formation of the [( $\mu_2$ -alkyne)Co<sub>2</sub>(CO)<sub>6</sub>]<sup>•-</sup> radical anion.<sup>41</sup> This EC type reduction results in the decomposition of the parent species and leads to metal-metal (Co-Co) bond cleavage which results in the formation of a variety of decomposition products such as Co<sub>2</sub>(CO)<sub>4</sub><sup>-</sup> RC<sub>2</sub>R'Co(CO)<sub>3</sub> and free cobalt, some of which are electroactive themselves.<sup>42</sup> These decomposition products result in an oxidation wave appearing at  $\sim 0.4$  V following reduction in the anodic sweep (Fig. 2.42) and result in eventual fouling of the electrode.

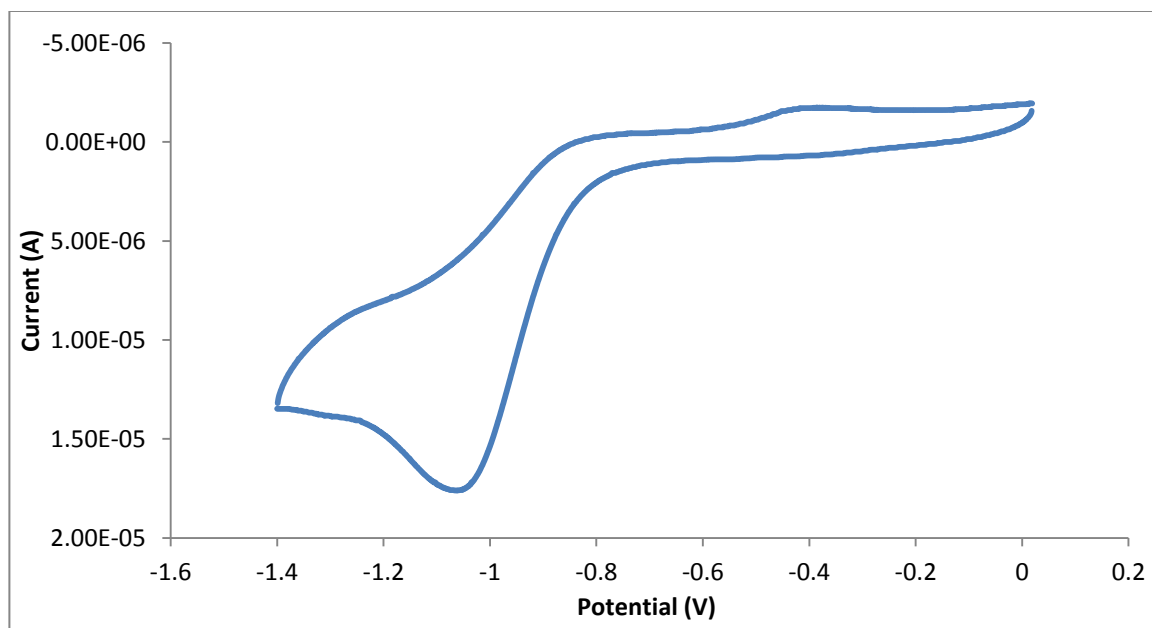
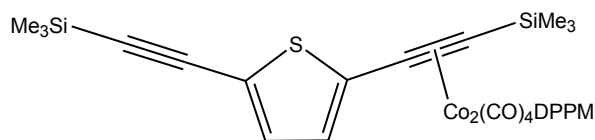
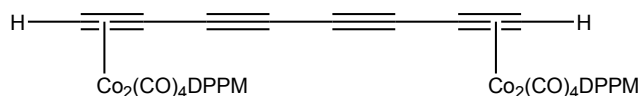


**Figure 2.42-** Cyclic voltammogram of  $(\mu_2\text{-PyrFc})\text{Co}_2(\text{CO})_6$  in 0.1 M TBAPF<sub>6</sub>/ DCM illustrating the reduction process and consequential oxidation formed due to decomposition products. Scan rate 0.1 Vsec<sup>-1</sup>.

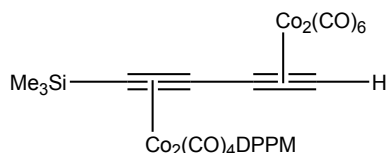
With respect to all  $(\mu_2\text{-alkyne})\text{Co}_2(\text{CO})_4\text{DPPM}$  complexes, reduction processes were not found to occur within the solvent potential window limit of 0 V to -2.0 V. This lack of visible reduction processes can be ascribed to the electron donating nature of the DPPM ligand. This makes reduction more difficult within the complex necessitating more negative potentials to gain an electron forming the anionic species described above. This effect has been previously reported in the literature for ethynyl complexes of cobalt such as  $2\text{-}[\text{Co}(\text{CO})_4(\text{dppm})\{\mu_2\text{-}\eta^2\text{-(SiMe}_3\text{)}_2\text{C}_2\}]\text{-5-(Me}_3\text{SiC}\equiv\text{C)C}_4\text{H}_2\text{S}$  (Fig. 2.43, **42**),<sup>41</sup>  $[\text{Co}_2(\text{CO})_4(\mu\text{-dppm})]_2(\mu\text{-}\eta^2\text{-HC}_2(\text{C}\equiv\text{C})_2\text{C}_2\text{H})$  (Fig. 2.43, **43**),<sup>44</sup> and  $[\text{Co}_2(\text{CO})_4(\text{dppm})][\text{Co}_2(\text{CO})_6](\text{MeSiC}_2\text{C}_2\text{H})$  (Fig. 2.43, **44**).<sup>67</sup>



42



43



44

**Figure 2.43- ( $\mu_2$ -alkyne) $\text{Co}_2(\text{CO})_4\text{DPPM}$  complexes which exhibit a large cathodic shift in reduction potentials due to the electron donating nature of the DPPM ligand.**

( $\mu_2$ -alkynyl) $\text{Co}_2(\text{CO})_6$  and  $\text{Co}_2(\text{CO})_4\text{DPPM}$  complexes are known to undergo a one-electron oxidation process to yield the corresponding cation radical  $[(\mu_2\text{-C}_2\text{H}_2)\text{Co}_2(\text{CO})_6]^+$ .<sup>40-42</sup> The formation of this radical often leads to fouling of the electrode, therefore an accurate oxidation study can be quite difficult with such compounds.<sup>44</sup> Both the ( $\mu_2$ -PyrH) $\text{Co}_2(\text{CO})_6$  and ( $\mu_2$ -PyrFc) $\text{Co}_2(\text{CO})_6$  complexes exhibit an oxidation at 1.22 V and 1.41 V respectively. The irreversible oxidation wave can be assigned to oxidation of the pyrene unit based upon comparison with literature, utilising ethynylpyrene complexes, where this oxidation is reported to occur between 1.28 V and 1.44 V vs. SCE.<sup>57,68</sup> The addition of the electron withdrawing ferrocene unit to the alkynyl bridge shifts the oxidation potential of the pyrene group to more positive potentials. In the case of the thienyl and ferrocenyl  $\text{Co}_2(\text{CO})_6$  complexes irreversible ring based oxidations can be observed at 1.41 V and 1.45 V respectively and correspond

to oxidation of the thienyl ring and the ferrocene rings in the complexes. In addition to these ligand based oxidations, the ferrocene complexes,  $(\mu_2\text{-FcH})\text{Co}_2(\text{CO})_6$  and  $(\mu_2\text{-PyrFc})\text{Co}_2(\text{CO})_6$ , exhibit an 2 electron Fe based reversible oxidation at 0.52 V and 0.49 V vs. Ag/AgCl respectively (Fig. 2.44). This process is due to the oxidation and consequential re-reduction of the  $\text{Fe}^{2+}/\text{Fe}^{3+}$  oxidation couple on the terminal ferrocene unit. Oxidation occurs in the pyrene appended complex at a lower potential of 0.03 V due to the electron donating nature of the appended pyrene moiety. This process has been reported in (ferrocenylethynyl)phosphanes at similar potentials such as  $E_{1/2} = 0.48$  V vs. SCE in  $\text{TBAPF}_6/\text{DCM}$  solution.<sup>69</sup> and in ferrocene itself at 0.46 V vs. SCE in DCM.<sup>70</sup> These oxidations also occur at similar potentials to the  $\text{Fc}/\text{Fc}^+$  redox couple used to calibrate the system under comparable experimental condition occurring at higher potentials of  $\sim 0.12$  V.

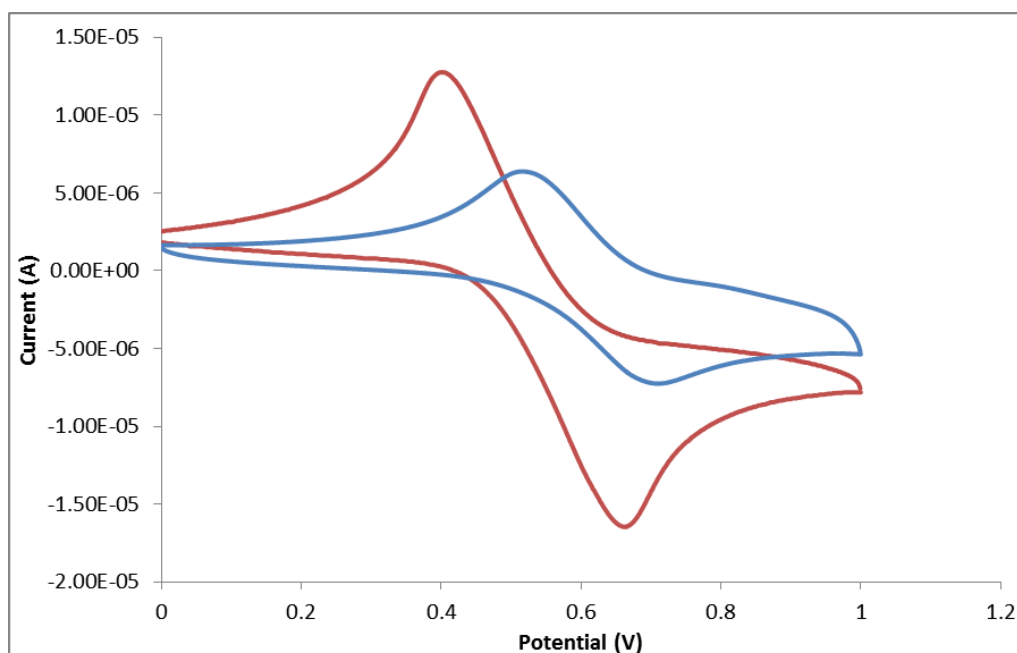


**Figure 2.44-** Cyclic voltammograms of the Fe based oxidation process in  $\mu_2\text{-FcHCo}_2(\text{CO})_6$  (blue line) and  $\mu_2\text{-PyrFcCo}_2(\text{CO})_6$  (red line) in 0.1 M  $\text{TBAPF}_6/\text{DCM}$  vs. Ag/AgCl. Scan rate  $0.1 \text{ Vsec}^{-1}$ .

The cyclic voltammograms of  $(\mu_2\text{-PyrH})\text{Co}_2(\text{CO})_6$  and the DPPM derivatives yielded the irreversible pyrene based oxidation at 1.22 v and 1.14 V respectively however the addition of the DPPM group allows the oxidation at slightly more cathodic potentials

due the DPPM group being electron donating in nature which helps stabilise the HOMO (Fig. 2.45). Oxidation of  $(\mu_2\text{-PyrH})\text{Co}_2(\text{CO})_4\text{DPPM}$  resulted in a reversible oxidation wave at  $E_{1/2} = 0.18 \text{ V}$  ( $I_a/I_c = 1.0$ ), which can be attributed to a 1 electron oxidation process on the DPPM unit.

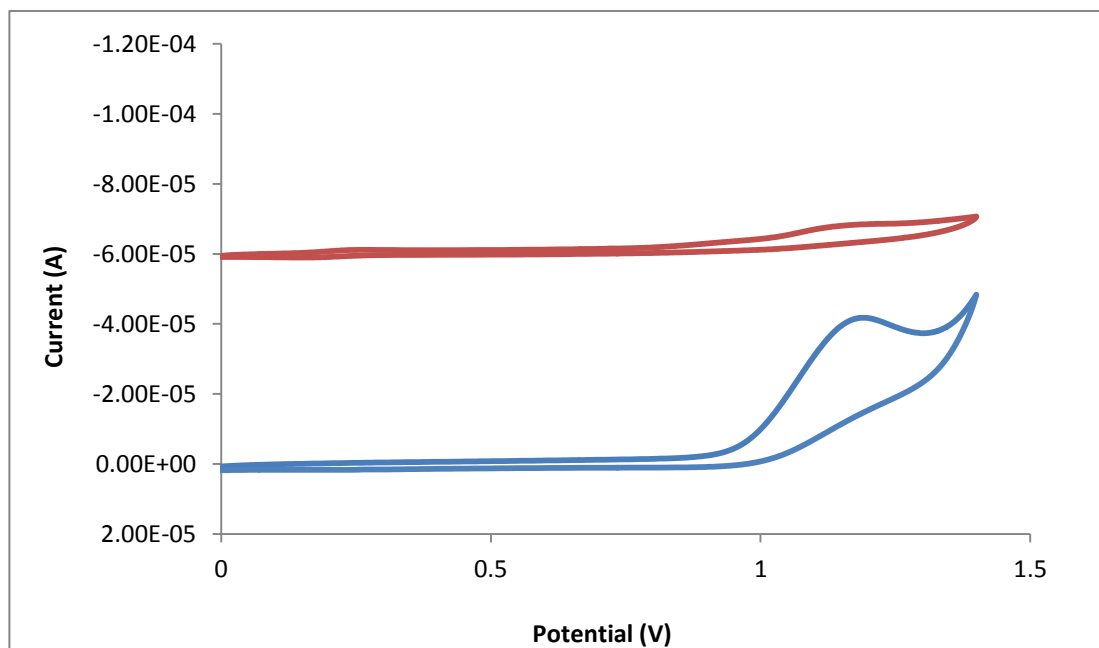


**Figure 2.45-Cyclic voltammograms of the oxidation process in  $(\mu_2\text{-PyrH})\text{Co}_2(\text{CO})_6$  (blue line) and  $(\mu_2\text{-PyrH})\text{Co}_2(\text{CO})_4\text{DPPM}$  (red line) in 0.1M TBAPF6/DCM vs. Ag/ AgCl.  $\mu_2\text{-PyrH}(\text{Co}_2(\text{CO})_4\text{DPPM}$  is offset along the coordinate for ease of comparison. Scan rate  $0.1 \text{ Vsec}^{-1}$ .**

A similar trend was observed for the oxidation of  $(\mu_2\text{-ThioH})\text{Co}_2(\text{CO})_6$  and  $(\mu_2\text{-ThioH})\text{Co}_2(\text{CO})_4\text{DPPM}$ . The addition of the DPPM unit shifted the ring based oxidation from 1.41 V to a lower potential, 1.13 V due to electron donation from the DPPM moiety allowing oxidation to occur more easily. A reversible peak at  $E_{1/2} = 0.36 \text{ V}$  is present during oxidation of  $(\mu_2\text{-ThioH})\text{Co}_2(\text{CO})_4\text{DPPM}$ , which is attributed to oxidation of the DPPM unit yielding a  $[(\mu_2\text{-ThioH})\text{Co}_2(\text{CO})_4\text{DPPM}]^{\bullet+}$  radical cation. The thiophene unit is clearly less electron donating than the pyrene unit discussed previously as the oxidation in the pyrene derivatives occurs at a lower potential when compared with the thiophene appended analogues (See Table 2.8).

When DPPM is coordinated to the ferrocenyl complexes the Fe based oxidation,  $\text{Fe}^{2+}/\text{Fe}^{3+}$ , is shifted to the more cathodic potential of 0.28 V vs. Ag/ AgCl for  $(\mu_2\text{-FcH})\text{Co}_2(\text{CO})_4\text{DPPM}$  from 0.52 V for  $(\mu_2\text{-FcH})\text{Co}_2(\text{CO})_6$ . An irreversible oxidation is also shifted significantly from 1.45 V to 0.93 V (Fig. 2.46). The third oxidation which is generally attributed to oxidation of the DPPM moiety is not visible for  $(\mu_2\text{-PyrFc})\text{Co}_2(\text{CO})_4\text{DPPM}$  which is perhaps due to the strong current induced during the  $\text{Fe}^{2+}/\text{Fe}^{3+}$  oxidation process obscuring the observation of this DPPM oxidation.

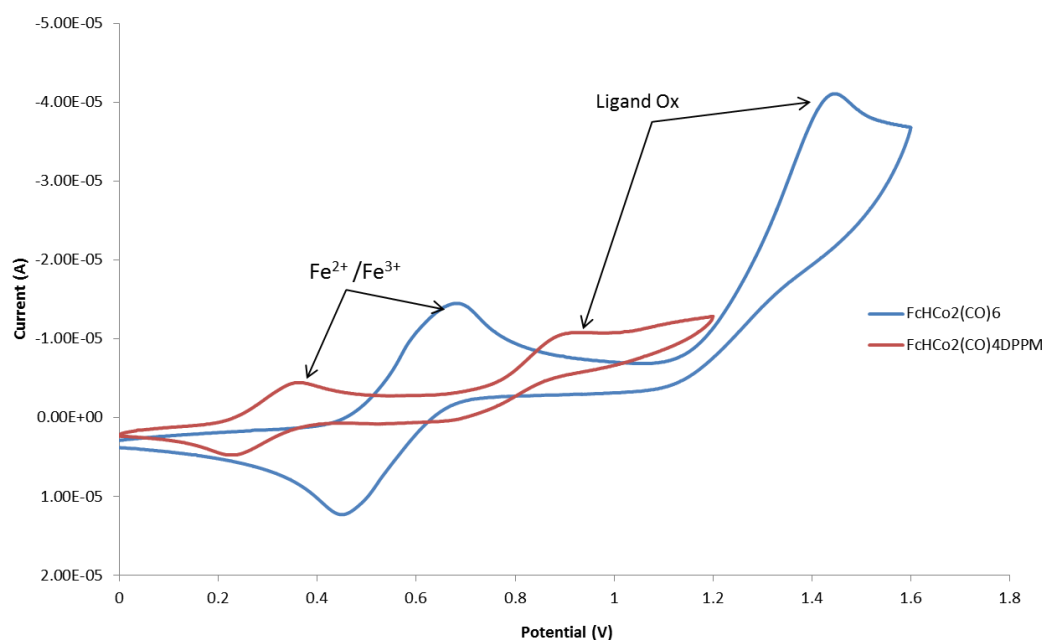


**Figure 2.46-** Cyclic voltammograms of  $(\mu_2\text{-FcH})\text{Co}_2(\text{CO})_6$  and  $(\mu_2\text{-FcH})\text{Co}_2(\text{CO})_4\text{DPPM}$  in 0.1 M TBAPF<sub>6</sub>/ DCM showing the cationic shift of processes following coordination of DPPM moiety. Scan rate 0.1 Vsec<sup>-1</sup>.

The  $\text{Fe}^{2+}/\text{Fe}^{3+}$  oxidation of  $(\mu_2\text{-PyrFc})\text{Co}_2(\text{CO})_6$  is observed at 0.49 V, however addition of the DPPM unit leads to this oxidation appearing at 0.24 V which represents a shift in the oxidation potential. The ligand based oxidation on  $(\mu_2\text{-PyrFc})\text{Co}_2(\text{CO})_6$  is also significantly shifted to lower potential when complexation with DPPM occurs. Oxidation of  $(\mu_2\text{-PyrFc})\text{Co}_2(\text{CO})_4\text{DPPM}$  results in the appearance of the irreversible ring based oxidation at 0.795 V, whereas the equivalent oxidation occurs at 1.41 V in the  $\text{Co}_2(\text{CO})_6$  derivative. As these cathodic shifts are far greater than those measured

with the pyrene and thiophene appended complexes, the significant shifts in the  $E_{1/2}$  values in the ferrocenyl complexes imply that strong electronic communication between the DPPM moiety and the ferrocenyl unit exists through the alkyne group. The appearance of a third oxidation at  $E_{1/2} = 0.43$  V is attributed to oxidation of the DPPM moiety.

**Electrocatalytic Studies.** Following on from CV studies electrocatalytic generation of  $H_2$  measurements were carried out using the same electrode set up but in aqueous buffer solutions. No catalytic current was observed when glassy carbon electrode surfaces were modified with any of the compounds used in this study in pH 7.0, 0.1 M  $NaH_2PO_4$  buffer. Electrocatalytic  $H_2$  production was observed at pH 2.0 in 0.1 M  $NaH_2PO_4$  buffer solution. In Fig. 2.47 the cyclic voltammogram produced by the bare electrode at pH 2.0 is compared with electrodes modified with FcH,  $(\mu_2\text{-FcH})Co_2(CO)_6$  and  $(\mu_2\text{-FcH})Co_2(CO)_4DPPM$ . As is evident from the graph that the catalytic current producing  $H_2$  is generated at -1.15 V vs. Ag/AgCl using a bare electrode. Modification of this electrode surface with FcH induces a greatly enhanced catalytic current with an onset of this current at -0.85 V representing an anodic shift of 0.3 V when compared with a bare electrode. Modification of the same surface with the  $(\mu_2\text{-FcH})Co_2(CO)_6$  complex shows significant drop in current induced and the onset occurs at a more negative potential, -1.01 V, than FcH. The addition of the DPPM moiety to the cobalt carbonyl slightly improves the catalytic current generated but the onset is also at -1.00 V.

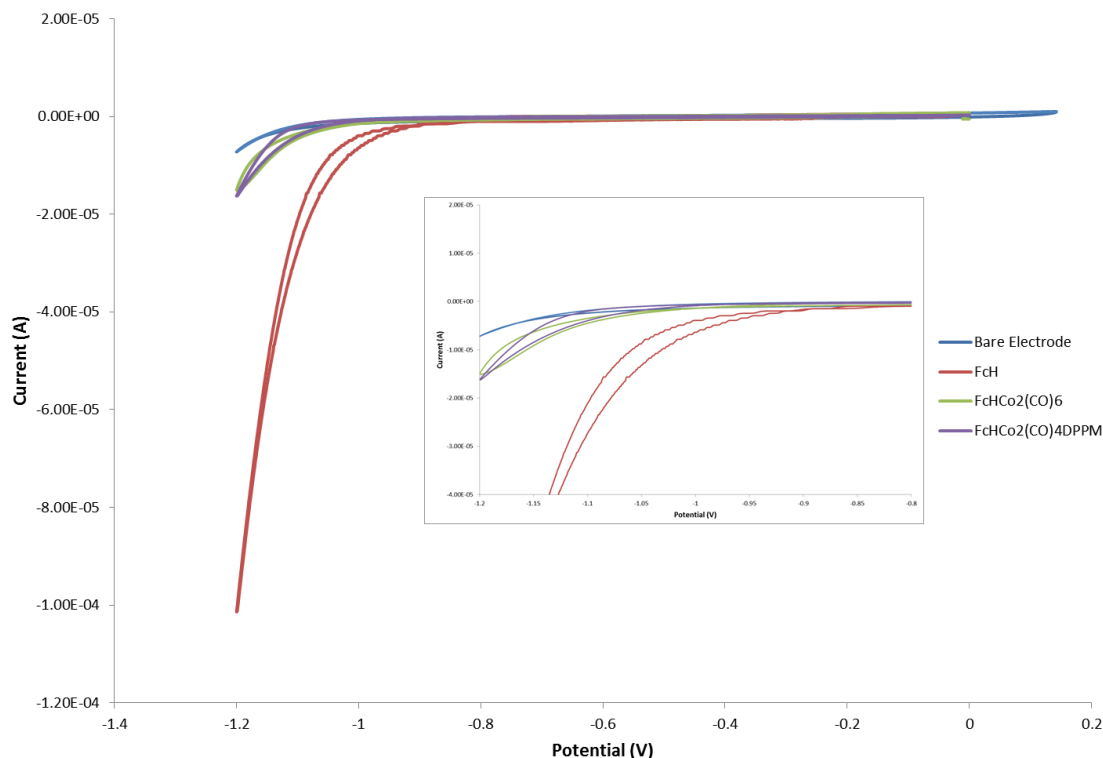


**Figure 2.47-** Typical cyclic voltammogram of a electrode modified with FcH (red line),  $(\mu_2\text{-FcH})\text{Co}_2(\text{CO})_6$  (green line),  $(\mu_2\text{-FcH})\text{Co}_2(\text{CO})_4\text{DPPM}$  (purple line) and a bare electrode (blue line), in pH 2.0, 0.1 M  $\text{NaH}_2\text{PO}_4$  buffer. (Scan rate =  $0.1 \text{ Vs}^{-1}$ ). Inset is a closer view of the onset of the catalytic current.

The TON values generated upon modification of the glassy carbon electrode with these complexes followed the trend observed for the intensity of the catalytic current induced. The current density measured over the course of the hour long bulk electrolysis experiment at -1.2 V was measured as  $2.52 \text{ mA/cm}^2$ , producing an electrochemically determined TON of  $215 \times 10^3$  when using FcH, while the current density measured when using  $(\mu_2\text{-FcH})\text{Co}_2(\text{CO})_6$  was only  $0.64 \text{ mA/cm}^2$  and a TON of  $5.3 \times 10^3$ , implying a higher catalytic activity utilising the FcH ligand. The DPPM complex produced a current density of  $1.69 \text{ mA/cm}^2$  and a TON of  $13.7 \times 10^3$ , showing that it is more efficient at catalysing the proton reduction reaction yielding  $\text{H}_2$  than its hexacarbonyl counterpart. The efficiency of the process was determined by dividing the GC TON value with the electrochemical TON value. The efficiencies of the systems were calculated by injecting a portion of the headspace in the reaction vessel on to a GC and analysing it for its  $\text{H}_2$  content. This GC generated TON is a more accurate



measurement of the number of moles of  $\text{H}_2$  produced as it does not take background charging into account as the electrochemically generated TON does. The FcH and DPPM systems presented the greatest efficiencies at  $\sim 66\%$ .  $(\mu_2\text{-FcH})\text{Co}_2(\text{CO})_6$  produced a low efficiency at 48%. This is possibly due to the decomposition of the unstable reduced anion formed during the experiment. This decomposition was also noted during cyclic voltammogram experiments in ACN (section 2.3.6.1).

In Fig. 2.48 the cyclic voltammograms of the bare electrode (blue line) is compared with the electrodes modified with  $(\mu_2\text{-ThioH})\text{Co}_2(\text{CO})_6$  (red line) and  $(\mu_2\text{-ThioH})\text{Co}_2(\text{CO})_4\text{DPPM}$  (blue line). The ligand ThioH was not tested as it is a liquid at room temperature and therefore could not be adsorbed onto the electrode surface. The onset of the catalytic current significantly different for both of the modified surfaces and the bare electrode and was measured occur at 0.85 V, 0.96 V and 1.15 V for  $(\mu_2\text{-ThioH})\text{Co}_2(\text{CO})_4\text{DPPM}$ ,  $(\mu_2\text{-ThioH})\text{Co}_2(\text{CO})_6$  and the bare electrode respectively. As the onset of the catalytic current occurs at the least negative potential when using  $(\mu_2\text{-ThioH})\text{Co}_2(\text{CO})_4\text{DPPM}$  the catalytic current induced greatly enhanced when compared to both the bare electrode and  $(\mu_2\text{-ThioH})\text{Co}_2(\text{CO})_6$ .

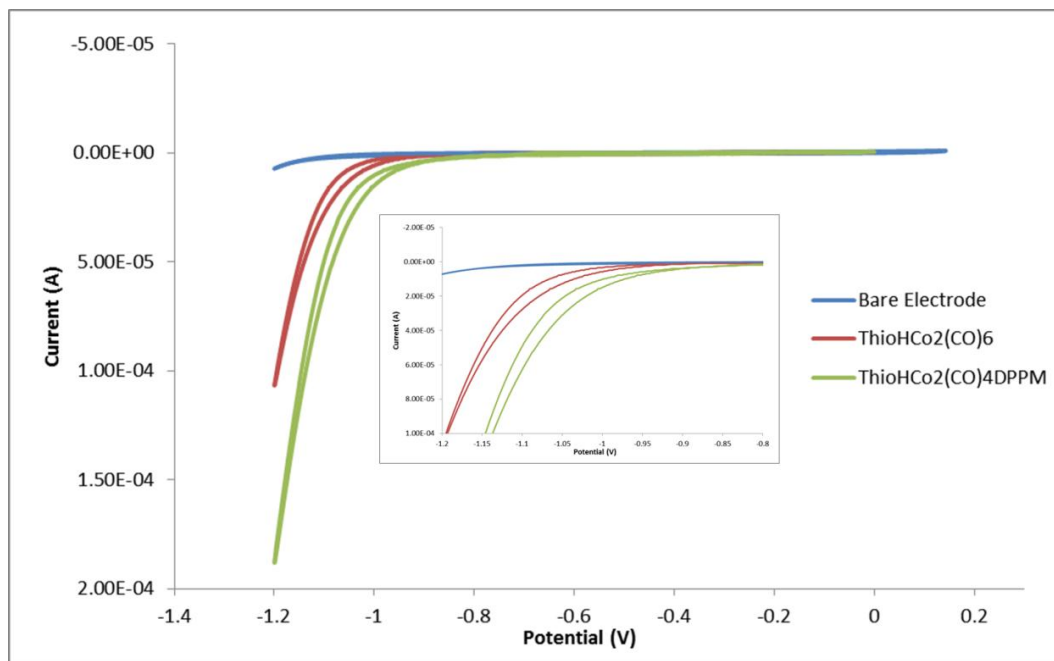


**Figure 2.48-** Typical cyclic voltammogram of a electrode modified with  $(\mu_2\text{-ThioH})\text{Co}_2(\text{CO})_6$  (red line),  $(\mu_2\text{-ThioH})\text{Co}_2(\text{CO})_4\text{DPPM}$  (green line) and a bare electrode (blue line), in pH 2.0, 0.1 M  $\text{NaH}_2\text{PO}_4$  buffer. (Scan rate =  $0.1 \text{ Vs}^{-1}$ ). Inset is a closer view of the onset of the catalytic current.

Modification of the electrode with  $(\mu_2\text{-ThioH})\text{Co}_2(\text{CO})_4\text{DPPM}$  yielded an electrocatalytically determined TON of  $9.6 \times 10^3$  following bulk electrolysis at -1.2 V. The current density measured for this system was  $0.92 \text{ mA/cm}^2$  which shows slightly enhanced catalytic activity when compared with  $(\mu_2\text{-ThioH})\text{Co}_2(\text{CO})_6$  which exhibited a current density of  $0.85 \text{ mA/cm}^2$ . The electrochemically determined TON for the  $(\mu_2\text{-ThioH})\text{Co}_2(\text{CO})_6$  system was calculated to be  $7.6 \times 10^3$  which represents a loss of activity when compared to the DPPM analogue. However, the efficiency of the hexacarbonyl system was observed to be much higher than the tetracarbonyl system at 76% and 59% respectively.

A similar trend was observed when CVs of electrodes modified with PyrH,  $(\mu_2\text{-PyrH})\text{Co}_2(\text{CO})_6$  and  $(\mu_2\text{-PyrH})\text{Co}_2(\text{CO})_4\text{DPPM}$  were examined. As is evident from Fig. 2.49, modification of the electrode surface with  $(\mu_2\text{-PyrH})\text{Co}_2(\text{CO})_4\text{DPPM}$  presented a substantial enhancement of the catalytic current.  $(\mu_2\text{-PyrH})\text{Co}_2(\text{CO})_4\text{DPPM}$  exhibits an onset of catalytic current at - 0.89 V. Upon modification with PyrH the catalytic current is greatly increased when compared to the bare electrode. The onset of the catalytic current on the bare electrode (1.15 V) is very similar to the onset observed for the  $(\mu_2\text{-PyrH})\text{Co}_2(\text{CO})_6$  modified electrode (1.05 V) however the  $(\mu_2\text{-PyrH})\text{Co}_2(\text{CO})_6$  complex exhibits a slightly enhanced catalytic current. Modification of the electrode surface with PyrH prompts the onset of a catalytic current at - 0.9 V inducing a greatly enhanced catalytic current.

As with the ferrocene and thiophene complexes the TONS generated upon modification of the glassy carbon electrode with these complexes followed the trend observed for the intensity of the catalytic current induced. The current density measured over the course of the hour long bulk electrolysis experiment at -1.2 V was measured to be  $1.56 \text{ mA/cm}^2$ , producing an electrochemically determined TON of  $10.6 \times 10^3$  when using PyrH, while the current density measured when using  $(\mu_2\text{-PyrH})\text{Co}_2(\text{CO})_6$  was only  $0.64 \text{ mA/cm}^2$  and a TON of  $4.7 \times 10^3$ , implying a higher catalytic activity utilising the PyrH ligand.  $(\mu_2\text{-PyrH})\text{Co}_2(\text{CO})_4\text{DPPM}$  exhibited a greater current density of  $1.70 \text{ mA/cm}^2$  during the experiment, yielding an electrochemically determined TON of  $11.5 \times 10^3$ . The current efficiencies measured in the systems were 87, 85 and 66 % for  $(\mu_2\text{-$

PyrH)Co<sub>2</sub>(CO)<sub>4</sub>DPPM, (μ<sub>2</sub>-PyrH)Co<sub>2</sub>(CO)<sub>6</sub> and PyrH respectively implying that though the PyrH ligand produces a larger TON and more efficient current density when compared with (μ<sub>2</sub>-PyrH)Co<sub>2</sub>(CO)<sub>6</sub> it does not yield H<sub>2</sub> as efficiently as the hexacarbonyl complex.

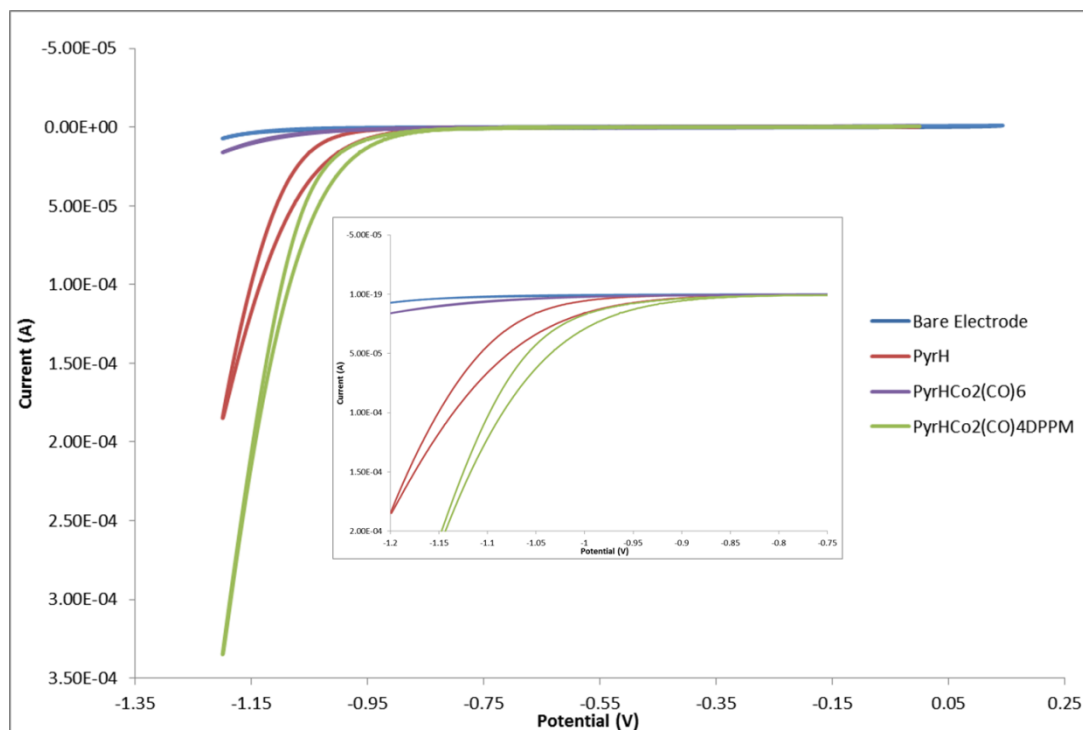


**Figure 2.49-** Typical cyclic voltammogram of a electrode modified with PyrH (red line), (μ<sub>2</sub>-PyrH)Co<sub>2</sub>(CO)<sub>6</sub> (purple line), (μ<sub>2</sub>-PyrH)Co<sub>2</sub>(CO)<sub>4</sub>DPPM (green line) and a bare electrode (blue line), in pH 2.0, 0.1 M NaH<sub>2</sub>PO<sub>4</sub> buffer. (Scan rate = 0.1 Vs<sup>-1</sup>). Inset is a closer view of the onset of the catalytic current.

In Fig. 2.50 the cyclic voltammogram produced by the bare electrode is compared with electrodes modified with PyrFc, (μ<sub>2</sub>-PyrFc)Co<sub>2</sub>(CO)<sub>6</sub> and (μ<sub>2</sub>-PyrFc)Co<sub>2</sub>(CO)<sub>4</sub>DPPM. As is evident from the graph the catalytic current producing H<sub>2</sub> is generated at -1.15 V vs. Ag/AgCl using a bare electrode. Modification of this electrode surface with PyrFc induces a greatly enhanced catalytic current with an onset of this current at -0.85 V representing an anodic shift of 0.3 V when compared with a bare electrode. Modification of the same surface with the (μ<sub>2</sub>-PyrFc)Co<sub>2</sub>(CO)<sub>6</sub> complex shows a significant drop in current and the onset occurs at a more negative potential, -1.1 V, than

PyrFc. The addition of the DPPM moiety to the cobalt carbonyl slightly improves the catalytic current generated but the onset is more negative than PyrFc also at -0.95 V.

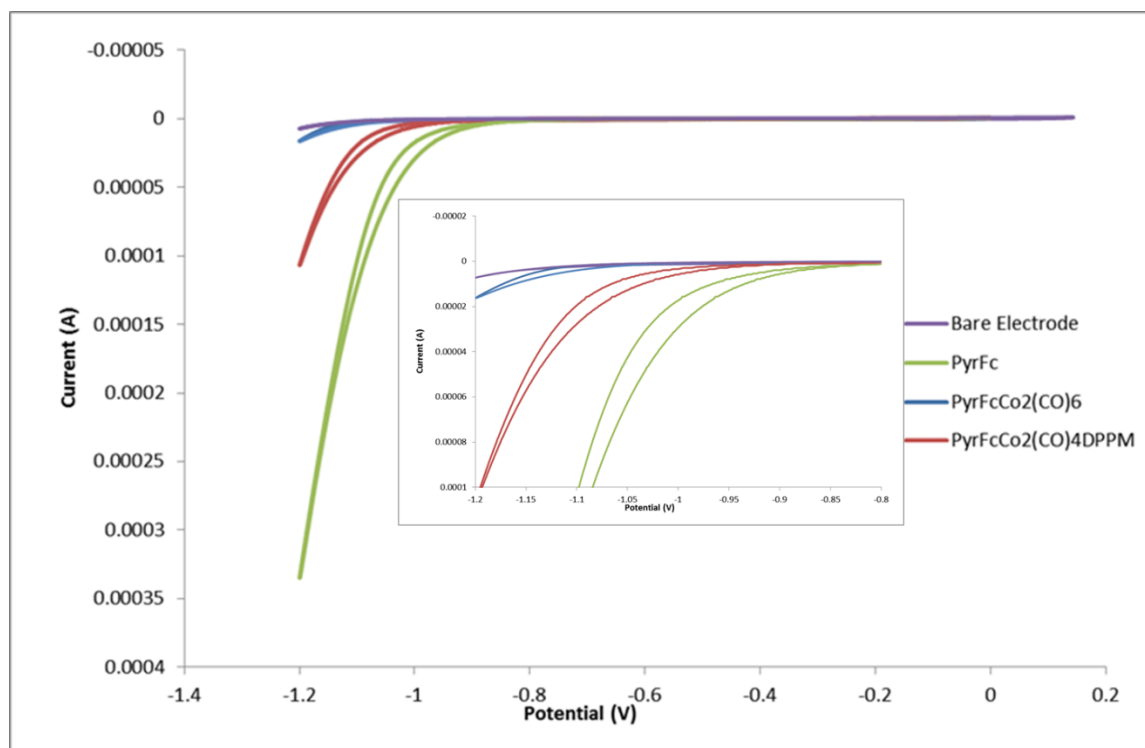


**Figure 2.50-** Typical cyclic voltammogram of a electrode modified with PyrFc (green line), ( $\mu_2$ -PyrFc) $\text{Co}_2(\text{CO})_6$  (blue line), ( $\mu_2$ -PyrFc) $\text{Co}_2(\text{CO})_4\text{DPPM}$  (red line) and a bare electrode (purple line), in pH 2.0, 0.1 M  $\text{NaH}_2\text{PO}_4$  buffer. (Scan rate =  $0.1 \text{ Vs}^{-1}$ ). Inset is a closer view of the onset of the catalytic current.

The TONS generated upon modification of the glassy carbon electrode with these complexes followed the trend observed for the intensity of the catalytic current obtained. The current density measured over the course of the hour long bulk electrolysis experiment at -1.2 V was measured as  $1.65 \text{ mA/cm}^2$ , generating an electrochemically determined TON of  $11.1 \times 10^3$  when using PyrFc, while the current density measured when using ( $\mu_2$ -PyrFc) $\text{Co}_2(\text{CO})_6$  was only  $0.65 \text{ mA/cm}^2$  and a TON of  $5.0 \times 10^3$ , implying a higher catalytic activity utilising the PyrFc ligand. The DPPM complex generated a current density of  $1.63 \text{ A/m}^2$  and a TON of  $10.5 \times 10^3$ , showing that it is

more efficient at catalysing the proton reduction reaction yielding  $H_2$  than its hexacarbonyl counterpart. The PyrFc system presented the greatest efficiency at 65% while  $(\mu_2\text{-FcH})Co_2(CO)_4DPPM$  produced a 64% efficiency.  $(\mu_2\text{-FcH})Co_2(CO)_6$  produced a lower efficiency at 60%. This is possibly due to the decomposition of the unstable reduced anion formed during the experiment. This decomposition was also noted during cyclic voltammogram experiments in ACN (section 2.3.6.1).

Overall FcH has produced the largest GC determined TON over the course of the bulk electrolysis experiment at  $14.4 \times 10^3$  however the efficiency of the system was measured to be only 67%. The  $(\mu_2\text{-PyrH})Co_2(CO)_4DPPM$  catalyst yielded the highest efficiency within the system for yielding molecular  $H_2$  at 87% with only a slightly diminished TON of  $11.5 \times 10^3$ .

As there has been no reported use of this  $(\mu_2\text{-alkyne})cobalt$  carbonyl complexes for electrocatalytic  $H_2$  generation studies direct comparison to literature cannot be presented however bis(thiolate) bridged diiron carbonyl and cyclopentadienyl metal carbonyldimers have been successfully utilised to modify electrode surfaces and induce catalytic currents in acidic media at potentials  $\sim -2.0$  V vs.  $Fc^+/Fc$ .<sup>51,52</sup> This represents a significant shift in reduction potential needed when compared with the results presented in this chapter indicating that a  $(\mu_2\text{-alkyne})cobalt$  carbonyl complex may be an efficient system for electrocatalytic hydrogen production. Other cobalt complexes have been shown to produce catalytic currents at as low as  $-1.0$  V vs. SCE producing a TON of 9000.<sup>34</sup> These results are analogous with the results presented here however, it is unclear how the TON was calculated making it difficult for direct comparison.

One possible reason for the lower catalytic activity observed for the  $(\mu_2\text{-alkyne})Co_2(CO)_6$  complexes is the irreversibility of the 1<sup>st</sup> reduction within these complexes. As observed in the CVs of these complexes (Section 2.3.6.), the reduction of  $Co_2(CO)_6$  complexes leads to decomposition products and eventual fouling of the electrode which means that the radical anions formed during reduction are not stable enough to catalyse the  $H_2$  production reaction.

**Photocatalytic Studies.** These compounds were also tested for photocatalytic generation of hydrogen. The cobalt carbonyl complexes present here have never been

used in this type of experiment before but low TONs of H<sub>2</sub> production have been reported for a few carbonyl complexes. A TON of 0.78 was observed for biomimetic [FeFe] hydrogenase complex, which contains an iron carbonyl catalytic centre, after 3 hours when irradiated at 25 °C using an Xe lamp (500 W) with a Pyrex-glass filter ( $\lambda >$  ca. 400 nm) in a 1:1 ACN/ H<sub>2</sub>O solution.<sup>36</sup> When a rhodium carbonyl bound to an osmium bis(terpyridyl) light harvesting chromophore through the diphosphine ligand in a 1:1 ACN/ H<sub>2</sub>O solution in the presence of trifluoromethanesulfonic acid (HOTf) and sodium ascorbate (NaHA) of the compound in 1:1 ACN/ H<sub>2</sub>O was irradiated with visible light ( $\lambda >$  380 nm) for 18 hours a TON of 36 was observed. No H<sub>2</sub> was detected in the headspace of any of the vials during the photocatalytic experiments performed in this study. The reasons for the lack of hydrogen produced by these intramolecular systems are at present not clear, however, it is proposed that either no H<sub>2</sub> has been produced photochemically or the amount produced was below the limit of detection for our instrument. The absorption features of the ligand complexes are tuned to absorb in the region of the 350 nm light source, and the MLCT bands in the absorbance spectra of all carbonyl complexes are in the region of 470 nm, so absorption of light should not be a problem. The excited state lifetime may be short not allowing enough time for the catalytic water splitting to occur or the complexes may simply decompose following irradiation. In addition the regeneration of the photosensitiser by the sacrificial agents may have proven difficult due to the aggressive nature of the radicals formed from TEA during the regenerating process.

## 2.5. Conclusion

This chapter discussed the synthesis, characterisation, electrochemistry and photochemistry of  $\mu_2$ -alkyne cobalt carbonyl compounds and their corresponding DPPM complexes. All synthesised complexes were characterised using  $^1\text{H}$  NMR, UV-Vis spectroscopy and IR spectroscopy. Picosecond TRIR studies were carried out on a number of the carbonyl complexes.

Synthesis of the ligands PyrTMS, PyrH and PyrFc were accomplished using Sonogashira coupling achieving yields of up to 98%. Addition of the  $\text{Co}_2(\text{CO})_6$  moiety involved stirring of the reactants overnight and yields of up to 98% were obtained. The  $(\mu_2\text{-C}_2\text{R}_2)\text{Co}_2(\text{CO})_4\text{DPPM}$  derivatives synthesised are all novel to the best of our knowledge, and all spectral data are in agreement with their formulation and compare well to similar compounds which have been previously reported in literature.<sup>58</sup>

The UV-vis spectra of the ligands show strong absorbances in the UV-Vis region of the spectrum. This indicates ligand localised  $\pi$ -  $\pi^*$  transitions.<sup>23</sup> The corresponding hexacarbonyl and tetracarbonyl complexes show strong absorbances in the region of 380- 420nm which is attributed to a common  $\sigma$  –  $\sigma^*$  (Co – Co) electronic transition. They also possess absorbances more into the red, with a broad and weak absorbance in the region of ~540-600nm is also observed which is generally attributed to a metal to ligand charge transfer (MLCT) of Co ( $d\pi$ ) – ligand ( $\pi$ ) transition.

The IR spectra of the carbonyl complexes have metal carbonyl stretching vibrations in the appropriate region for cobalt carbonyl complexes, 1850-2050  $\text{cm}^{-1}$ . The addition of a DPPM group to the hexacarbonyl complexes to form a tetracarbonyl compound causes the  $\nu_{\text{CO}}$  to move to lower frequencies due to electron donation from the DPPM group to the Co centre.

Quantum yields for CO loss demonstrated that CO loss was both wavelength and complex dependent. Picosecond TRIR studies indicate that Co-Co bond homolysis occurs for all cobalt carbonyls upon laser flash photolysis at  $\lambda_{\text{exc}}$  400nm. However, in addition to Co-Co bond homolysis,  $(\mu_2\text{-1-ethynylpyrene})$  and  $(\mu_2\text{-1-pyreneethynylferrocene})\text{Co}_2(\text{CO})_6$  gave rise to changes in their IR spectra which indicated CO loss giving rise to the solvated intermediate;

$(\mu_2$ -1-ethynylpyrene) $\text{Co}_2(\text{CO})_5$ (heptane) and  $(\mu_2$ -1-pyrene-ethynylferrocene) $\text{Co}_2(\text{CO})_5$ (heptane).

Cyclic voltammetry indicated that the addition of a DPPM moiety to a dicobalt carbonyl complex results in a cathodic shift of both the oxidation and reduction process potentials due to the electron donating properties of this ligand. In fact there were no observable reduction processes within the potential window of the DCM solvent for the tetracarbonyl species. Along with a cathodic shift in the ring (and Fc) based oxidations another new oxidation is introduced between 0.18 V and 0.43 V which is attributed to a DPPM based oxidation forming a  $[\mu_2\text{-alkyne-Co}_2(\text{CO})_4\text{DPPM}]^{++}$  radical cation.

During electrocatalytic  $\text{H}_2$  generation experiments FcH produced the largest TON for  $\text{H}_2$  generation (determined using the GC) over the course of the bulk electrolysis experiment at  $14.4 \times 10^3$  however the efficiency of the system was measured to be only 67%. The  $(\mu_2\text{-PyrH})\text{Co}_2(\text{CO})_4\text{DPPM}$  catalyst yielded the highest efficiency of 87%. The hexacarbonyl complexes did not exhibit high efficiencies or yield high TONs presumably due to decomposition of the catalysts following reduction.

Any  $\text{H}_2$  produced photocatalytically was not detected either because none was generated or, it was lower than the detection limit of the instrument.



## Bibliography

---

- <sup>1</sup> G. L. Gregory, M. S. Wrighton, *Organometallic Photochemistry*, **1979**.
- <sup>2</sup> The Organometallic Chemistry of Transition Metals. 2nd Edition. Robert H. Crabtree.
- <sup>3</sup> W. Durante, F. K. Johnson, R. R. Johnson. *J. Cell. Mol. Med.*, **2006**, 10, 3: 1-12
- <sup>4</sup> A. Nakao, A. M. K. Choi, N. Murase. *J. Cell. Mol. Med.*, **2006**, 10, 3, 1-17.
- <sup>5</sup> E. Fiumana, H. Parfenova, J. H. Jaggar, C. W. Leffler. *Am. J. Physiol. Heart; Circ. Physiol.*, **2003**, 284, H1073 – H1079.
- <sup>6</sup> R. Alberto, R. Motterlini, *Dalton Trans.*, **2007**, 17, 1651- 1660.
- <sup>7</sup> B. E. Mann, R. Motterlini, *Chem. Commun.*, **2007**, 41, 4197- 4208.
- <sup>8</sup> C. M. George, M. Kiszka, I. R. Dunkin, W. J. Kerr, J. S. Scott, J. Gebicki, *J. Organomet. Chem.* **1998**, 554, 147-154.
- <sup>9</sup> X. Verdaguer, A. Moyano, M. A. Pericas, A. Riera, V. Bernardes, A. E. Greene, . Alvarez-Larena, J. Francesc Piniella, *J. Am. Chem. Soc.* ,**1994**, 116, 2153.
- <sup>10</sup> F. Robert, A. Milet, Y. Gimbert, D. Konya, A.E. Greene, *J. Am. Chem. Soc.*, **2001**, 123, 5396-5400
- <sup>11</sup> B. L. Pagenkopf, T. Livinghouse, *J. Am. Chem. Soc.* **1996**, 118, 2285-2286.

- 
- <sup>12</sup> N. Jeong, S. H. Hwang, Y. Lee, *J. Am. Chem. Soc.*, **1994**, 116, 3159-3160.
- <sup>13</sup> R. S. Dickson, D. B. W Yawney, *Aust. J. Chem.*, **1968**, 21, 97 – 102.
- <sup>14</sup> J. Overgaard, H.F. Clausen, J.A. Platts, B.B. Inversen, *J. Am. Chem. Soc.*, **2008**, 130, 3834.
- <sup>15</sup> W. G. Sly, *J. Am. Chem. Soc.* **1959**, 81, 18.
- <sup>16</sup> J. A. Platt, G. J. S. Evans, M. P. Coogan, J. Overgaard, *Inorg. Chem.* **2007**, 46, 16, 6291.
- <sup>17</sup> E. Espinosa, I. Alkorta, J. Elguero, E. Molins, *J. Phys. Chem.* **2002**, 117, 5529.
- <sup>18</sup> M. Wrighton, *Chem. Rev.*, **1974**, 74, 401-430.
- <sup>19</sup> L. S. Chia, W. R. Cullen, M. Franklin, A. R. Manning, *Inorg. Chem.* **1975**, 14, 2521.
- <sup>20</sup> J. Marhenke, S. M. Massick, P. C. Ford, *Inorganica Chimica Acta*, **2007**, 360, 825- 836
- <sup>21</sup> S. Mosokovich, D. Reuvenov, R. H. Schultz, *Chem. Phys. Lett.*, **2006**, 431, 62-66.
- <sup>22</sup> S. M. Draper, C. Long, B. M. Myers, *J. Organomett. Chem.*, **1999**, 588, 195-199.
- <sup>23</sup> A. Coleman, M. T. Pryce, *Inorg. Chem*, **2008**, 47, 10980.

- 
- <sup>24</sup> N. M. Boyle, A. C. Coleman, C. Long, K. L. Ronayne, W. R. Browne, B. L. Feringa, M. T. Pryce, *Inorg. Chem.*, **2010**, 49, 10214–10216.
- <sup>25</sup> T.E. Bitterwolf, W. B. Scallorn, C. A. Weiss, *J. Organomet. Chem.* **2000**, 605, 7.
- <sup>26</sup> E. Campeil, S. M. Draper, *J. Chem. Soc. Dalton. Trans.* **2001**, 1440.
- <sup>27</sup> C. Liu, B. Chen, C. Hseuh, J. Ku, F. Tsau, K. Hwang, *Applied Catalysis B: Environmental*, **2009**, 91, 368-379.
- <sup>28</sup> S. Bennicini, A. Garron, A. Auroux, *Int. J. of Hydrogen Energy*, **2010**, 35, 8621-8625
- <sup>29</sup> P. Krishnan, K. Hsueh, S. Yim, *App. Catal. B: Environ.*, **2007**, 77, 206-214.
- <sup>30</sup> J. Zhao, H. Ma, J. Chen, *Int. J. of Hydrogen Energy*, **2007**, 32, 4711-4716.
- <sup>31</sup> C. Wu, F. Wu, Y. Bai, B. Yi, H. Zhang, *Mater. Lett.*, **2005**, 59, 1748-1751.
- <sup>32</sup> S. Losse, J. G. Vos, S. Rau, *Coord. Chem. Rev.*, **2010**, 254, 2492.
- <sup>33</sup> J.M. Lehn, R. Ziessel, *Proc. Natl. Acad. Sci. U.S.A.*, **1982**, 79, 701.
- <sup>34</sup> W. R. McNamara, Z. Han, C. Yin, W. W. Brennessel, P. L. Holland, R. Eisenberg, *J. Am. Chem. Soc.*, **2011**, 133, 39, 15368.
- <sup>35</sup> W. M. Singh, T. Baine, S. Kudo, S. Tian, X. A. N. Ma, H. Zhou, N. J. DeYonker, T. C. Pham, J. C. Bollinger, D. L. Baker, B. Yan, C. E. Webster, X. Zhao, *Angew. Chem. Int. Ed.*, **2012**, 51, 5941.

- 
- <sup>36</sup> Y. Na, M. Wang, J. Pan, P. Zhang, B. A. Kermack, L. Sun, *Inorg. Chem.* **2008**, 47, 2805.
- <sup>37</sup> Y. Miyake, K. Nakajima, K. Sasaki, R. Saito, H. Makanishi, Y. Mishibayashi, *Organomet.*, **2009**, 28, 17, 5240-5243.
- <sup>38</sup> L. C. Song, M. Y. Tang, F. H. Su, Q. M. Hu, *Angew. Chem. Int. Ed.* **2006**, 45, 1130.
- <sup>39</sup> X. li, M. Wang, S. Zhang, J. Pan, Y. Na, J. Liu, B. A. Kermack, L. Sun, *J. Phys. Chem. B*, **2008**, 112, 8198.
- <sup>40</sup> C. Moreno, M. Marcos, G. Domínguez, A. Arnanz, D. H. Farrar, R. Teeple, A. Lough, J. Gonzalez-Velasco, S. Delgado, *J. Organomet. Chem.*, **2001**, 631, 19.
- <sup>41</sup> M. L. Marcos, M. J. Macazaga, R. M. Medina, C. Moreno, J. A. Castro, J. L. Gomez, S. Delgado, J. Gonzalez-Velasco, *Inorg. Chim. Acta*, **2001**, 312, 249.
- <sup>42</sup> A. Arnanz, M. Marcos, S. Delgado, J. Gonzalez-Valesco, C. Moreno, *J. Organomet. Chem.*, **2008**, 693, 3457.
- <sup>43</sup> N. W. Duffy, C. J. McAdam, B. H. Robinson, J. Simpson, *J. Organomet. Chem.*, **1998**, 565, 19.
- <sup>44</sup> A. Arnanz, M. Marcos, C. Moreno, D. H. Farrar, A. J. Lough, J. O. Yu, S. Delgado, J. Conzalez-Valesco, *J. Organomet. Chem.*, **2004**, 689, 3218.
- <sup>45</sup> M. J. Macazaga, M. L. Marcos, C. Moreno, F. Benito-Lopez, J. Gomez-Gonzalez, J. Gonzalez- Velasco, R. M. Medina, *J. Organomet. Chem.*, **2006**, 691, 138.

- 
- <sup>46</sup> C. J. McAdam, N. W. Duffy, B. H. Robinson, J. Simpson, *Organometallics*, **1996**, 15, 3935.
- <sup>47</sup> A. Koca, M. Özçeşmeci, E. Hamuryudanb, *Electroanal.*, **2010**, 22, 14, 1623.
- <sup>48</sup> M. Tian, T. Wada, H. Sasabe, *J. Heterocycl. Chem.* **1997**, 34, 171.
- <sup>49</sup> A. Koca, A. Kalkanb, Z. A. Bayır, *Electrochim. Acta.*, **2011**, 56, 5513.
- <sup>50</sup> J. P. Bigi, T. E. Hanna, W. Hill Harman, A. Changa, C. J. Chang, *Chem. Commun.*, **2010**, 46, 958.
- <sup>51</sup> E. S. Donovan, G. A.N. Felton, *J. Organomet. Chem.*, **2012**, 711, 25.
- <sup>52</sup> S. J. Borg, S. K. Ibrahim, C. J. Pickett, S. P. Best, *C. R. Chimie*, **2008**, 11, 852.
- <sup>53</sup> K. Sonogashira, Y. Tohda, N. Hagihara. *Tetrahedron Lett.*, **1975**, 16, 50, 4467.
- <sup>54</sup> W. B. Austin, N. Bilow, W. J. Kelleghan, Kreisler S. Y. Lau., *J. Org. Chem.*, **1981**, 46, 2280.
- <sup>55</sup> N. Boyle, PhD Thesis, *Dublin City University*, **2011**.
- <sup>56</sup> A. C. Benniston, A. Hariman, D. J. Lawrie, S. A. Rostron, *Tetrahedron Lett.*, **2004**, 45, 2503- 2506.
- <sup>57</sup> A. Coleman. PhD Thesis, *Dublin City University*, **2007**.
- <sup>58</sup> E. Campiel, S. Draper, *Dalton Trans.* **2001**, 9, 1440.

- 
- <sup>59</sup> M. A. H. Alamiry, N. M. Boyle, C.R M. Brookes, M. W. George, C. Long, P. Portius, M. T. Pryce, K. L. Ronayne, X.Sun, M. Towrie, K. Q. Vuong, *Organomett.*, **2009**, 28, 1461.
- <sup>60</sup> M. Busby, P. Matousek, M. Towrie, A. Vlček, *J. Phys. Chem. A*, **2005**, 109, 3000.
- <sup>61</sup> M. Lee, C. B. Harris, *J. Am. Chem. Soc.*, **1989**, 111, 24, 8963.
- <sup>62</sup> A. Vlček Jr, *Inorg. Chem.* **1986**, 25, 522.
- <sup>63</sup> D. J. Stufkens, A. Vlček Jr, *Coord. Chem. Rev.*, **1998**, 177, 127.
- <sup>64</sup> I.P. Clarke, M. W. George, G. M. Greetham, E. C. Harvey, C. Long, J. C. Manton, M. T. Pryce, *J. Phys. Chem A*, **2010**, 114, 11425.
- <sup>65</sup> I.P. Clarke, M. W. George, G. M. Greetham, E. C. Harvey, C. Long, J. C. Manton, M. T. Pryce, *J. Phys. Chem A*, **2011**, 115, 2985.
- <sup>66</sup> I. G. Virrels, M. W. George, J. J. Turner, J. Peters, A.Vlček Jr., *Organometallics*, **1996**, 15, 4089.
- <sup>67</sup> R. M. Medina, C. Moreno, M. L. Marcos, J. A. Castro, F. Benito, A. Arnaz, S. Delgado, J. Gonzalez-Velasco, M. J. Macazaga, *Inorgan. Chim. Acta*, **2004**, 357, 2069.
- <sup>68</sup> R. Ziessel, C. Goze, G. Ulrich, M.Cosario, P. Retailleau, A.Harriman, J. P. Rostron, *Chem. Eur. J.*, **2005**, 11, 7366.
- <sup>69</sup> T. Baumgartner, M. Fiege, Fl. Pontzen, R. Arteaga-Müller, *Organometallics*, **2006**, 25, 5657.

---

<sup>70</sup> N. G. Connelly, W. E. Geiger, *Chem. Rev.*, **1996**, 96, 877.

## Chapter 3

# Boron Dipyrromethene- Cobaloxime Complexes

A concise literature survey concerning boron-dipyrromethene (BODIPY) dyes and bis(dimethylglyoximate)cobalt<sup>III</sup> (cobaloxime) complexes is presented at the beginning of chapter three. The synthetic procedures employed to prepare the compounds are discussed in addition to cyclic voltammetry, UV-Vis, fluorescence spectroscopy and the fluorescence lifetimes of the complexes. Compounds were studied for their ability to produce hydrogen both photochemically and electrochemically, the results of which are presented.



## Aim

The main objective of this section of research was to synthesise a series of BODIPY dyes, for use as photosensitisers, and their cobaloxime derivatives, where cobalt functions as a catalytic centre for use in both the photocatalytic and electrocatalytic generation of H<sub>2</sub>. BODIPY dyes are known to have strong absorbances in the long wavelength, yellow - green region of the spectrum which could facilitate efficient H<sub>2</sub> generation following irradiation with lower energy light sources. The photochemistry of the complexes was investigated through UV-Vis and fluorescence studies. The electrochemistry was also investigated using cyclic voltammetry.

### 3.1 Introduction

#### 3.1.1. Photochemistry of Boron-Dipyrromethene Complexes (BODIPYs)

Boron-dipyrromethene, which is derived from 4,4-difluoro-1,3,5,7-tetramethyl-4-bora-3a,4a-diaza-*s*-indacene, is a highly fluorescent dye which has found applications in imaging,<sup>1,2</sup> DNA labelling<sup>3</sup> and as fluorescence indicators.<sup>4,5</sup> Originally prepared in 1968 by Triebs and Kreuzer,<sup>6</sup> it is based on a half-porphyrin design with the chelation of a difluoroboron moiety to the two nitrogen groups which helps the molecule maintain structural rigidity (Fig. 3.1).

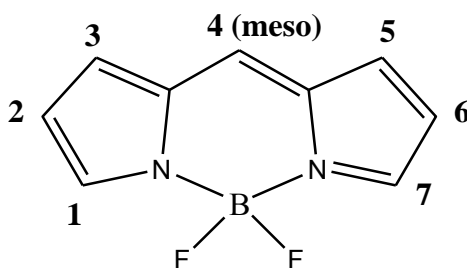


Figure 3.1- BODIPY Dyes indicating the points of substitution.

Freebase dipyrins exhibit very little fluorescence in liquid medium. It has been shown that when locked in frozen matrices the dipyrins exhibit high fluorescence yields, which is attributed to the rigidifying of the structure of the molecule.<sup>7</sup> Most importantly for this study BODIPYs have been used as energy absorbing and transferring antennae which indicate a use in the photocatalytic generation of hydrogen. Addition of the BF<sub>2</sub> group adds rigidity to the dipyrromethene structure affording a fluorescent complex. As with porphyrins they absorb strongly in the blue-green region closely matching that of the light harvesting chlorophyll used during natural photosynthesis. Complexes employing BODIPY appendages show attractive characteristics including sharp (full width at half maximum (fwhm) ~ 25nm) and moderately strong absorbances near 500 nm ( $\epsilon = 40000 - 100000 \text{ M}^{-1}\text{cm}^{-1}$ ), large quantum yields, long excited state lifetimes and good stability in organic solvents.<sup>8</sup> Singlet lifetimes have been measured to be between 2 and 5 ns.<sup>9,10</sup> A sharp absorbance in the blue-green region has been assigned to an S<sub>0</sub>→S<sub>1</sub> ( $\pi$ - $\pi^*$ ) transition. A second weaker and broader absorbance has also been observed and is due to the S<sub>0</sub>→S<sub>2</sub> ( $\pi$ - $\pi^*$ ) transition within the dipyrromethene ligand.<sup>45</sup> BODIPYs are generally recognised to also emit in the visible green-yellow region of the spectrum and to possess small stokes shifts, typically 5 – 15 nm for simple BODIPY complexes. This small stokes shift results in the differentiation between the excitation and the fluorescence wavelength becoming quite difficult. Small structural changes in the assembly of BODIPY dyes greatly influence their photophysical properties, as the extent of electron delocalisation around the central cyanine framework and the donor and acceptor characteristics of the pyrrole substituents greatly influence the absorbance and therefore emission of the complexes. Therefore changing the location and nature of the substituents on the core will allow tuneable absorbance and emission spectra.

Extending the absorbance spectrum of a BODIPY complex requires the addition of a conjugated delocalised substituent. The coordination of thiophene subunits onto BODIPY dyes results in a bathochromatic shift of the absorption and emission wavelengths, allowing absorption far into the green region and emit in the red (Fig. 3.2).<sup>11</sup>

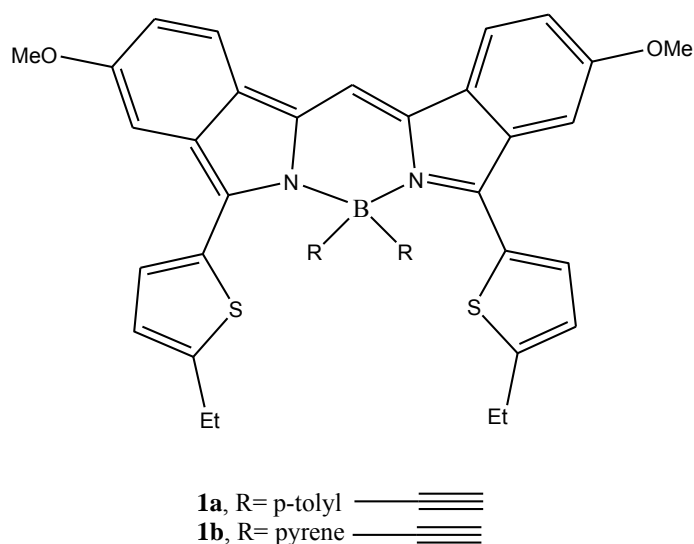
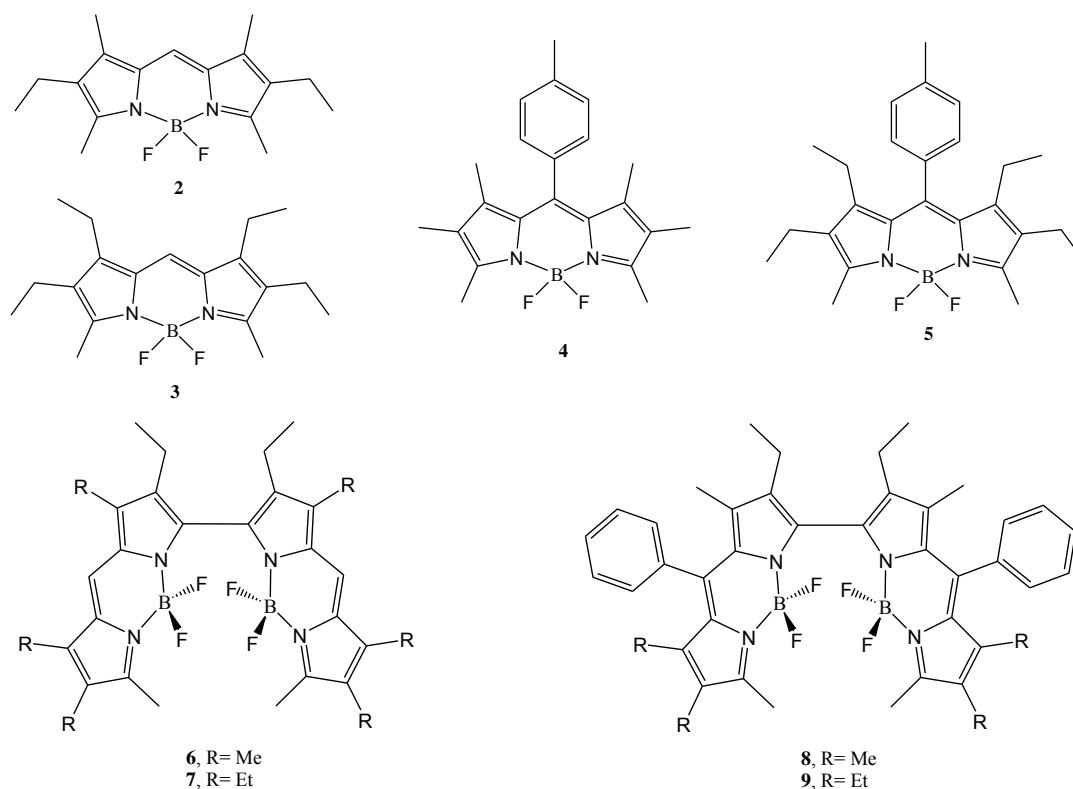


Figure 3.2 - Extension of BODIPY dyes studied by Ulrich *et al.*<sup>11</sup>

The addition of phenyl residues at the  $\beta$ -positions and the extension of the conjugation of the system through replacing the fluoro substituents with ethynyl p-tolyl and pyrene groups afforded enhanced stokes shifts also. The addition of the ethynyl moieties afforded absorbances between 707 (**1a**) and 720 nm (**1b**) attributed to the  $\pi$ - $\pi^*$  transition in the BODIPY chromophore. Emissions of 746 (**1a**) and 754 (**1b**) nm were detected generating stokes shifts of 39 and 34 nm respectively, significantly larger than those afforded by unsubstituted dyes.

Bis-BODIPY complexes have been developed by Broring *et al.*<sup>12</sup> When compared with similar complexes with a single chromophore (**2** – **5** Fig. 3.3) with stokes shifts between 6 and 9 nm, the bis-BODIPY complexes (**6** – **9**) possess stokes shifts between 79 and 83 nm.



**Figure 3.3 - BODIPY and bis-BODIPY complexes analysed by Bröring *et al.*<sup>12</sup>**

The incorporation of two chromophores in the bis-BODIPY complexes (**6 – 9**) resulted in excited species splitting in the absorbance spectra. This two component absorbance was expected due to the close spacial relationship of the two dyes. The emission spectra of the bis-BODIPY complexes exhibit a strong, broad band and excitation into this emission generates an excitation spectrum which matches the original absorbance spectrum indicating a genuine emission from the dimeric system. The broad shape of the emission band and the large stokes shift compared to the monomeric dyes point to a large geometric displacement of the excited state with respect to the ground state in the complexes and of some excimer-like character in the excited state.

Based on the principals of light harvesting antennae in natural photosynthesis Li *et al.*<sup>13</sup> have measured energy migration in a multi-pigment array incorporating both porphyrin and one, two or eight BODIPY moieties (Fig. 3.4). These complexes were studied using time resolved absorption and fluorescence techniques to probe the dynamics of electron transfer and to measure estimates for the energy-transfer yields.

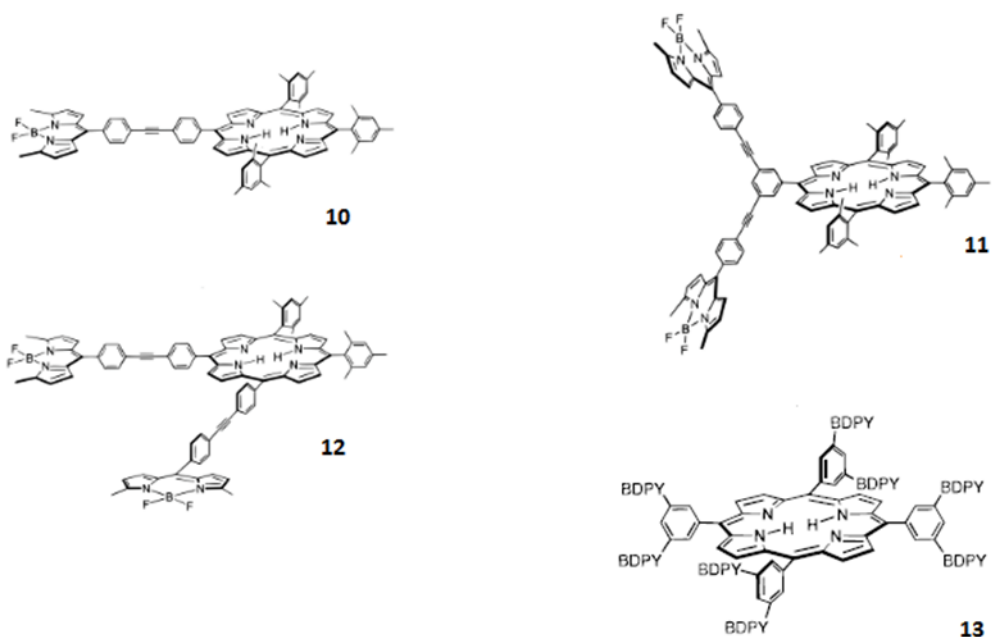
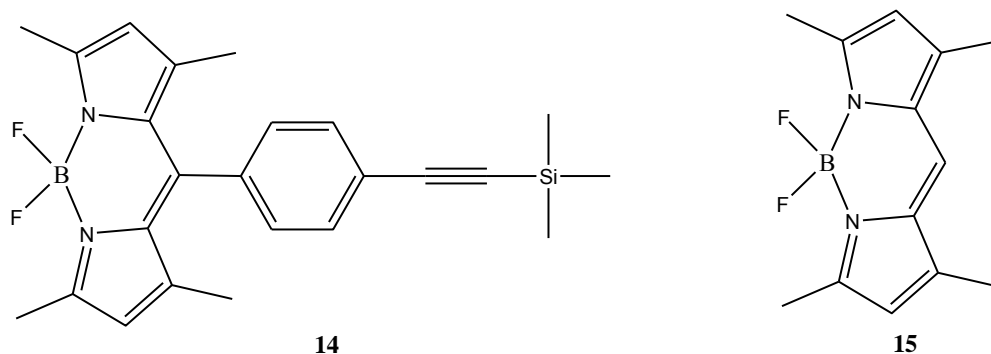


Figure 3.4- Porphyrins bearing one, two and eight BODIPY substituents studied by Li *et al.*<sup>11</sup>

The excited state lifetimes of the BODIPY and porphyrin chromophores in the arrays were monitored over time following a 513 nm laser flash. The transient absorption spectrum of **10** in toluene exhibits an initial bleaching of the parent BODIPY absorbance band at 515 nm directly after the laser pulse, whereas no bleaching of the porphyrin absorbance bands are reported at 0.1 ps. As time proceeded it was reported that the bleaching of the BODIPY bands diminishes back towards baseline corresponding to the concomitant bleaching in the ground state of the porphyrin bands. The decay of the BODIPY constituent consists of two-components, reflected in the changing of the bleaching over time at 515 nm. Following a fit of this decay, time constants of  $2.4 \pm 0.4$  and  $23 \pm 2$  ps with relative amplitudes of 36/64 were obtained. The bleaching of the porphyrin bands exhibit this same two-component decay and following a fit time constants of  $1.8 \pm 0.7$  and  $30 \pm 6$  ps were obtained with about the same amplitude. Dyes containing multiple BODIPY units showed much the same time-resolved absorption data, however slight differences were noted; in systems **11** and **12** the fast component of the decay in the BODIPY absorbance has a slightly smaller amplitude than on **10**, and in system **13** the fast component of the decay in the BODIPY absorbance has a slightly larger amplitude than on **10**, **11** and **12**. Energy transfer rates and the efficiencies of electron transfer

within the systems were calculated to be  $\sim (2 \text{ ps})^{-1}$  and  $\Phi_{\text{trans (R)}} = 83\text{-}90\%$  for the smaller component and  $\sim (20 \text{ ps})^{-1}$  and  $\Phi_{\text{trans (M)}} = 90\text{-}97\%$  for the larger more long lived component.



**Figure 3.5- BODIPY ligands studied by Li *et al.*<sup>13</sup>**

The decay rates were also measured for complex **14** yielding lifetimes of  $17 \pm 2$  and  $440 \pm 60 \text{ ps}$  and **15** yielding lifetimes of  $15 \pm 4$  and  $520 \pm 60 \text{ ps}$ . When these results are compared it is evident that the shorter decay rates seen for the porphyrin appended BODIPYs are due to energy transfer from the BODIPY to the porphyrin moieties. As the rates are so much shorter for **10-13** when compared to **14** and **15** these energy transfer rates are deemed to be highly efficient.

The energy transfer efficiencies of BODIPY dyes coordinated to oligo(p-phenyleneethynylene)s (OPEs) have been measured.<sup>14</sup>  $\Phi_{\text{ET}}$  of between 98.6 and 99.9% in THF were reported with the shorter chain length of OPE showing the highest electron transfer yield. A study by Harriman *et al.*<sup>15</sup> proposed that the change in electron transfer over the length of chains is affected by disparate spectral overlap of orbitals within the molecule. They have reported that the rate of electronic energy transfer from the spacer to each terminal is dependent on the molecular length of the chain, with the tendency to populate the BODIPY dye changing from 65% for  $n = 0$  to 45% for  $n = 2$ , where  $n$  refers to the number of ethynyl groups employed. Similarly to work done by Li *et al.*<sup>11</sup>, Harriman measured time-resolved fluorescence spectra of the complexes and observed initial depletion of the BODIPY dye fluorescence spectra after the laser pulse (310 nm) and relaxation over time concomitant with the depletion of the acceptor unit's fluorescence, indicating energy transfer between from the BODIPY dye to the porphyrin.

BODIPY complexes are known to show very little triplet excited state population. Attachment of a Pt<sup>II</sup> centre directly onto the BODIPY core through ethynyl bonds, rather than on the periphery, has been shown to maximise the heavy-atom effect of the Pt<sup>II</sup>.<sup>16</sup> The Pt complex, with ethynyl Pt<sup>II</sup> groups attached to the boron metal directly, exhibited strong absorption bands at 406 and 574 nm in toluene and the longest-lived T<sup>1</sup> excited state reported to date, 128.4  $\mu$ s, as well as room temperature phosphorescence from the BODIPY. The Pt complex produced dual emission with two narrow bands centred at 660 and 770 nm. The band at 660 nm was sensitive to O<sub>2</sub> and was significantly quenched in air and when the experiment was repeated at 77 K only the 770 nm emission band was observed; therefore the 660 nm band was assigned to phosphorescence. It was proposed that the dual emissions are due to <sup>3</sup>MLCT (660 nm) and the <sup>3</sup>IL (770 nm) emissive state, respectively, and that these two triplet excited states are in equilibrium at room temperature. The population of the BODIPY-localized <sup>3</sup>IL excited state for complex investigated by nanosecond time-resolved transient absorption difference spectroscopy, emission spectroscopy at 77 K.

### 3.1.1.2. Electrochemistry of BODIPY complexes

Completely substituted BODIPY dyes possess one nernstian oxidation and one nernstian reduction.<sup>13,17</sup> When BODIPYs are unsubstituted in the 2 and 6 position they often tend to form dimers upon oxidation. Importantly for this study, BODIPY dyes which are unsubstituted at the meso position do not form stable radical ions leading to decomposition of the dye after reduction rendering them useless for catalysis. To stabilise the radical anions the meso-position of the cyanine core is of crucial importance, because of the expected strong spin localisation at the meso carbon atom.<sup>18</sup> Due to this spin localisation it is thought that, following reduction, through an electrochemical-chemical (EC) pathway, the radical anions formed quickly undergo a chemical reaction to yield the dimerised form bound at the meso position. The addition of a substituent at this position would therefore stabilise the complex following reduction. Nepomnyashchii *et al.*<sup>17</sup> have reported the electrochemistry of a series of BODIPY dyes bearing substituents at different positions (Fig. 3.6.)

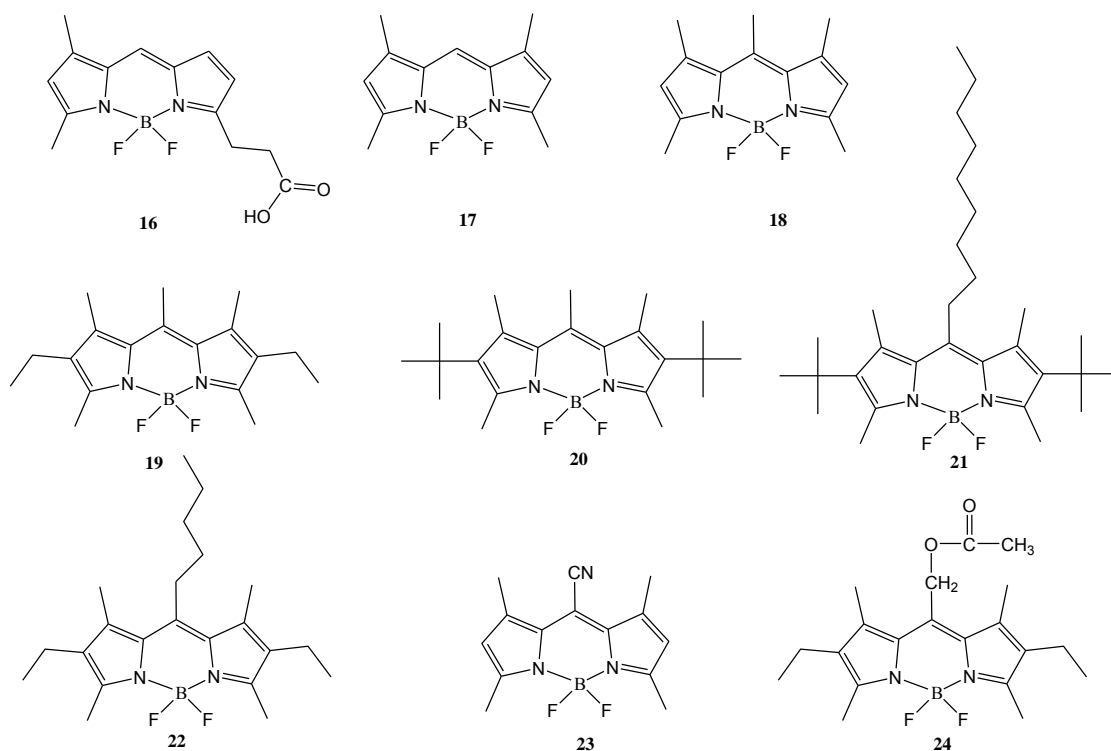


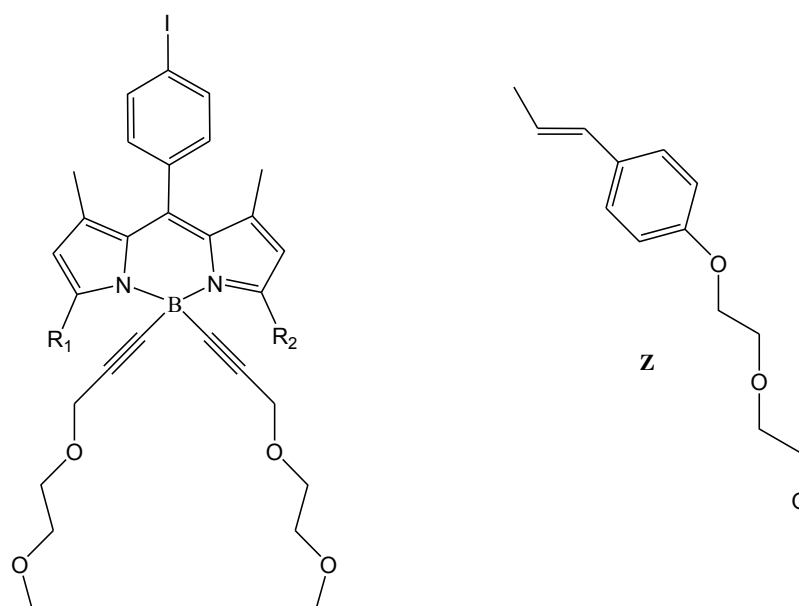
**Figure 3.6 - BODIPY dyes with varying substituents at different positions studied by Nepomnyashchii *et al.*<sup>17</sup>**

Both oxidation and reduction of dye **16** were irreversible as it is unsubstituted in positions 2, 4, 5, and 6 (Fig.3.1). Dye **17** showed a similar redox behaviour. The oxidation process was slightly more reversible due to the substitution on the 5 position. The reduction process in dye **18** is reversible due to the substitution at the meso position. The 4 dyes that were completely substituted, **19** - **22** showed reversible waves for both oxidation and reduction near 1.3 V and -1.4 V (vs SCE), respectively, in DCM with a platinum working electrode and a platinum wire counter electrode. Thus both the radical cation and radical anion formed are stabilised by the substituents blocking dimerization by nucleophilic and electrophilic species. The addition of electron withdrawing cyano groups in compound **23** allows the reduction to occur easier and therefore at a higher potential of -0.82 V. Dye **24** shows reversibility of the oxidation process; however the reduction process is unstable due to electron transfer to the electron withdrawing carboxylic acid substituent.

Suk *et al.*<sup>19</sup> have studied a series of long chained BODIPY derivatives with substitution at the boron centre (Fig. 3.7). The addition of long chained groups at the



boron centre allowed for further investigations into the effect of substitution at varying positions on the electrochemistry of BODIPY complexes.



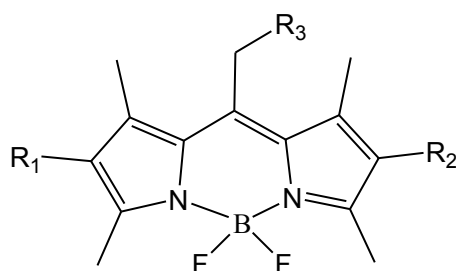
(25) PB:  $R_1 = \text{CH}_3$ ,  $R_2 = \text{CH}_3$   
 (26) MCPB:  $R_1 = \text{Z}$ ,  $R_2 = \text{CH}_3$   
 (27) DCPB:  $R_1 = \text{Z}$ ,  $R_2 = \text{Z}$

Figure 3.7 - BODIPY derivatives substituted at the boron group, studied by Suk *et al.*<sup>17</sup>

Cyclic voltammetry of all three derivatives (**25** - **27**) shows that at low scan rates a nernstian, reversible reduction wave between -1.29 and -1.05 V (vs. SCE) and a somewhat irreversible oxidation wave between 1.05 and 0.72 V (vs. SCE) present which is consistent with lack of substitution in the 2 and 6 positions (Fig. 3.1). When studying the cyclic voltammetry of **26** it was found that its oxidation process was less chemically reversible than that of **25**. Due to the large size of the Z group it was assumed that it would terminate the formation of dimers following oxidation however, in this molecule, the 2-position is unblocked and it was deduced that the substitution in the 5-position increases the positive charge density at the 2 position leading to increased dimer formation. **27** showed a nernstian reversible oxidation processes as the 2 and 6 positions are somewhat blocked by the Z substitution group when compared with **25** indicating stability of the radical cation. As the substitution is varied from **25** to **26** to **27** the electron withdrawing nature of the Z group causes

the reduction potentials of the dyes to move to more positive potentials however the oxidation potentials also become more negative possibly due to greater  $\pi$ -conjugation reducing the HOMO-LUMO energy gap and **27** is more easily oxidized than both **26** and **25**. Although the addition of the long chained substituents at the boron did not appear to have a great effect on the electrochemistry of the BODIPY dyes it was shown that long chained substituents at the R<sub>1</sub> and R<sub>2</sub> positions can block dimerisation through steric hindrance and/ or stabilisation of the radicals formed during oxidation.

The redox potentials of BODIPY dyes can be fine-tuned through the addition of electron withdrawing or electron donating groups. Whether electron withdrawing substituents are bound to the  $\alpha$ ,  $\beta$  or meso position they will lead to a strong anodic shift, to more positive potentials, of the reduction processes. This will also lead to a strong anodic shift of the oxidation potentials. The opposite is true for electron donating groups. They will induce a cathodic shift in both the reduction and oxidation potentials. The redox potential of a series of BODIPY dyes with either electron donating or electron withdrawing substituents measured by Krumova et al.<sup>20</sup> When a H and/or an electron-withdrawing group (e.g. CN, Cl) were introduced at positions R<sub>1</sub> and R<sub>2</sub> an increase in both the reduction and the oxidation potentials were observed with respect to Et-substituted counterparts which is an electron donating group. The changing of the groups at position R<sub>1</sub> and R<sub>2</sub> had no substantial effect on the HOMO-LUMO energy gap as measured through absorption and emission spectroscopy. In contrast substitution at the R<sub>3</sub> position with acetoxymethyl groups or formyl groups proved to induce the first reduction and first oxidation process at lower potentials due to their electron donating nature. The acetoxymethyl substituted BODIPY dyes (**28** – **31**) showed high extinction coefficients (50,000 – 100,000) and high fluorescence quantum yields (0.7 – 1) however the formyl substituted dyes (**38** – **43**) showed up to a 4-fold reduction in the molar extinction coefficient and are completely non-emissive which is attributed to a forbidden  $n\text{-}\pi^*$  transition from the ground state to the lowest singlet excited state in these complexes.



Complex	R <sub>1</sub>	R <sub>2</sub>	R <sub>3</sub>
28	H	H	OAc
29	H	Cl	OAc
30	Cl	Cl	OAc
31	H	CN	OAc
32	CN	CN	OAc
33	H	H	OH
34	H	Cl	OH
35	Cl	Cl	OH
36	H	CN	OH
37	CN	CN	OH
38	Et	Et	=O
39	H	Cl	=O
40	Cl	Cl	=O
41	H	H	=O
42	H	CN	=O
43	CN	CN	=O

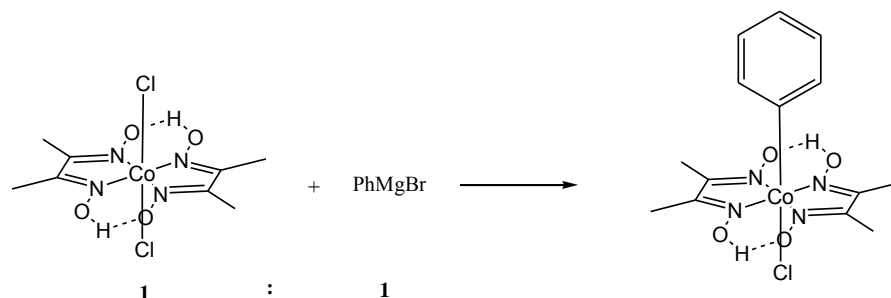
Table 3.1- Various substituted BODIPY dyes studied by Krumova *et al.*<sup>18</sup>

### 3.1.2. *bis*(dimethylglyoximato)cobalt<sup>III</sup> Complexes (Cobaloximes)

In the past cobaloxime complexes have been synthesised as model compounds for the study of the reaction processes in vitamin B<sub>12</sub>.<sup>21</sup> They were found to be air stable solids with high thermal stability that could be prepared on a macro scale from inexpensive starting materials. In the pursuit of noble metal free catalytic centres cobaloxime complexes have been considered promising model compounds due to their electrochemical ease of reduction and their high activity in photoinduced hydrogen production.<sup>22,23,24</sup> Cobalt centres in cobaloxime complexes are in the Co<sup>III</sup> oxidation state with octahedral coordination in relation to the glyoximato ligands. Synthesis of cobaloxime complexes involves the reaction of cobalt<sup>II</sup> halide with dimethyl glyoxime in the presence of a stream of air to aid the oxidation of the metal centre.<sup>25</sup> The replacement of an axial halide group is achieved through two routes; the reaction of a carbanionic reagent with the Co<sup>III</sup> halide which results in a nucleophilic displacement of one or both of the halide ions (Fig. 3.8. eq 1), or the

$\text{Co}^{\text{IV}}$  centre is converted to  $\text{Co}^{\text{I}}$  using a variety of reducing agents, the  $\text{Co}^{\text{I}}$  centre is then available to react with a variety of electrophiles (Fig. 3.8. eq. 2).

Eq. 1:



Eq. 2:

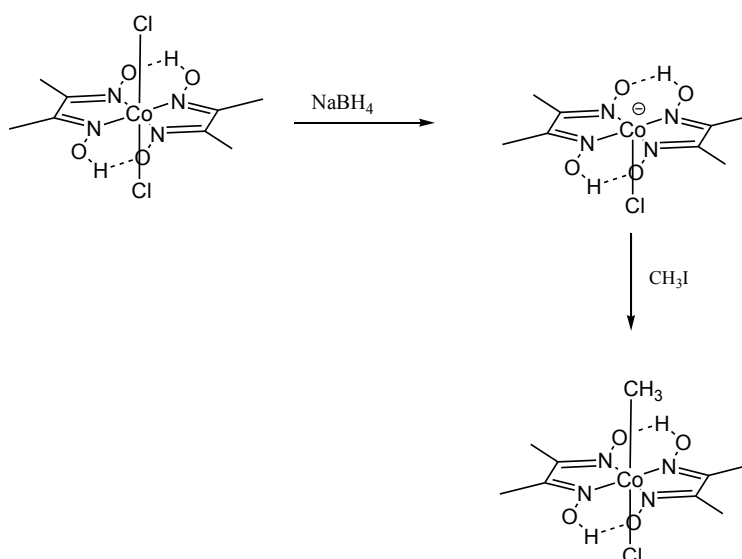


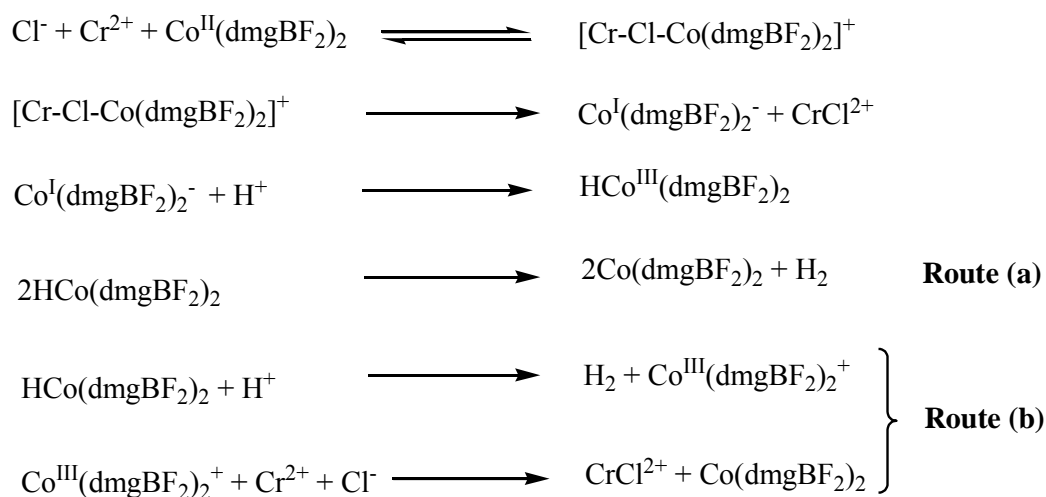
Figure 3.8 - Routes for substitution of cobaloxime complexes.<sup>25</sup>

### 3.1.2.1. Cobaloxime Complexes Used in the Photocatalytic Generation of Hydrogen

Cobaloxime complexes are known to absorb strongly in the UV-Vis spectrum which is generally attributed to  $\pi$ - $\pi^*$  transitions.<sup>27</sup> Three characteristic absorption bands appear closer to the visible region of the UV-Vis spectrum also. A ligand-metal charge transfer (LMCT) band from the axial coordinated ligand to the Co metal centre is observed around 400 nm. This absorbance is characteristic low-energy charge-transfer band which can be assigned to a transition between the highest bonding and lowest antibonding axial ligand molecular orbital's.<sup>27</sup> A singlet  $d$ - $d$

transition of  $\text{Co}^{\text{III}}$  is observed at longer wavelengths, Followed by a triplet  $d-d$  transition of  $\text{Co}^{\text{III}}$  around 600 nm.<sup>26,27</sup>

Due to their high stability, relative ease of synthesis and low cost of production, cobaloxime complexes have been realised as potential catalytic centres for photo induced hydrogen production. Large macrocycles containing cobaloximes have been shown to produce  $\text{H}_2$  through the splitting of water. Connolly and Espenson<sup>28</sup> have proposed a reaction sequence to explain how the cobalt centre behaves during the  $\text{H}_2$  evolution experiments using such cobaloxime complexes. It is illustrated in Scheme 3.1.



**Scheme 3.1 - Reaction scheme proposed by Connolly and Espenson<sup>28</sup> for the hydrogen generation experiment involving  $(\text{H}_2\text{O})_2\text{Co}(\text{dmgBF}_2)_2$  in a solution of  $\text{CrCl}_2$  in  $\text{HCl}$  (final step(s) of reaction may proceed via route (a) or route (b)).**

The mechanism involves the reduction of the initial  $\text{Co}^{\text{II}}$  (Fig. 3.9) species to a  $\text{Co}^{\text{I}}$  species. This is the rate limiting step in the reaction. The  $\text{Co}^{\text{I}}$  is protonated to become  $\text{Co}^{\text{III}}$  in a fast reaction, and the reaction then proceeds via route (a) where two of these protonated molecules react to release the desired  $\text{H}_2$ , and regenerates two of the starting  $\text{Co}^{\text{III}}$  catalysts. If the reaction proceeds via route (b) the  $\text{Co}^{\text{III}}$ -hydride intermediate reacts with  $\text{H}^+$  to yield  $\text{H}_2$  and a  $\text{Co}^{\text{III}+}$  species is reduced with  $\text{Cr}^{2+}$  to yield the starting  $\text{Co}^{\text{II}}$  catalyst and  $\text{CrCl}^{2+}$ .

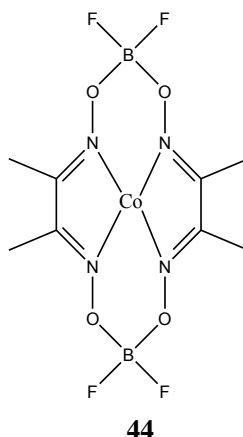


**Figure 3.9 -  $\text{Co}^{\text{II}}(\text{dmgBF}_2)_2$  catalyst used in the generation of  $\text{O}_2$  by Connolly and Espenson.<sup>28</sup>**

Du *et al.*<sup>29</sup> have run experiments using cobalt dimethylglyoximes which are similar to those which Connolly and Espenson have used and shown that these cobaloxime catalytic centres can generate high turnovers of  $\text{H}_2$  in a solvent mixture of MeCN: $\text{H}_2\text{O}$  with varying ratios, containing  $1.1 \times 10^{-5}$  M Pt chromophore,  $1.6 \times 10^{-2}$  M TEOA (as sacrificial agent) and a  $2.0 \times 10^{-4}$  M equivalent of the Co catalyst. The most successful catalyst in the study was  $[\text{Co}(\text{dmgH})_2\text{pyCl}]$  where py= pyridine in a solution of MeCN: $\text{H}_2\text{O}$  24:1, which produced a TON of 2150 after 10 hours of photolysis at  $\lambda > 410\text{nm}$ . They showed that in every system they studied that there was an “induction period” in which no  $\text{H}_2$  was produced which lasted on average 1-2 hours. During this time they witnessed a colour change in solution to a bright yellow which is indicative of a reduction of the initial  $\text{Co}^{\text{III}}$  to  $\text{Co}^{\text{II}}$ . It was also proposed that mechanistically  $\text{Co}^{\text{II}}$  undergoes a further reduction to  $\text{Co}^{\text{I}}$  during the  $\text{H}_2$  evolution process and the  $\text{Co}^{\text{I}}$  undergoes protonation to produce a  $\text{Co}^{\text{III}}$  hydride intermediate. This  $\text{Co}^{\text{III}}$  hydride intermediate is reduced and then reacts with  $\text{H}^+$  to give  $\text{H}_2$  the  $\text{Co}^{\text{II}}$  catalyst is generated. This proposed mechanism is very similar to the one proposed by Connolly and Espenson in 1986.<sup>28</sup> They also showed that the rate of  $\text{H}_2$  production is dependent on the pH of the solution (below pH 5 no  $\text{H}_2$  was produced, above pH 12 the results were low, pH 8.5 showed optimal  $\text{H}_2$  evolution), concentration of sacrificial agent (higher concentrations lead to higher TONs), ratio of MeCN:  $\text{H}_2\text{O}$  (higher concentrations of MeCN yields higher TONs), and also the concentration of the catalyst. The concentration of the catalyst showed a linear relationship with  $\text{H}_2$  generation which showed that only one Co centre is used for  $\text{H}_2$  evolution.

Fihri *et al.*<sup>22</sup> have investigated the use of a ruthenium supramolecular photosensitiser coordinated to a cobaloxime catalytic centre for its efficiencies towards photoinduced hydrogen generation. Three complexes containing ruthenium tris(diimine) moieties and cobalt centres were synthesised (Fig. 3.10).

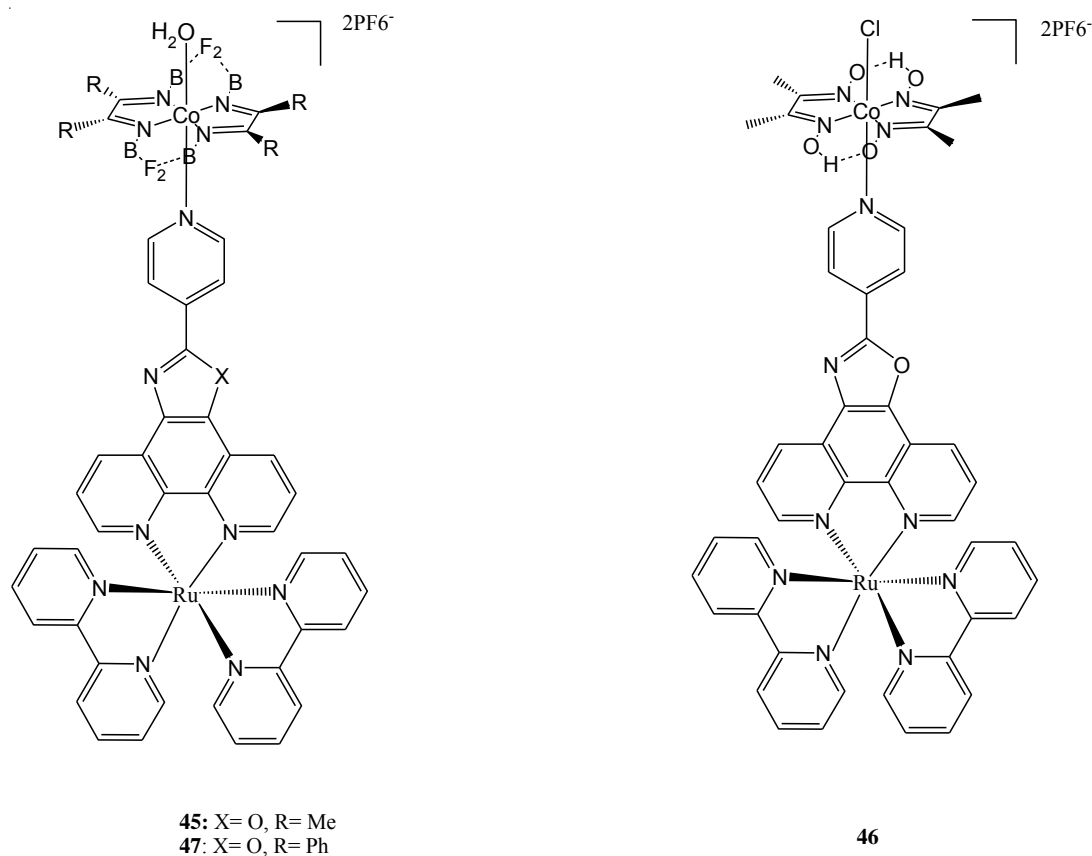


Figure 3.10- Ruthenium-Cobaloxime complexes synthesised by Fihri *et al.*<sup>22</sup>

It was found that H<sub>2</sub> was produced when solutions of **45- 47** were irradiated ( $\lambda > 350$  nm) in acetone in the presence of 100 equivalents of TEA as the sacrificial electron donor and 100 equivalents of Et<sub>3</sub>NHBF<sub>4</sub> as the proton source. Complex **45** yielded a TON of 56 after 4 hours of irradiation while complex **46** achieved a TON of 17 and **47** yielded only 12. Fihri noted that increasing the amount of TEA and Et<sub>3</sub>NHBF<sub>4</sub> to 300 equivalents had a minimal effect on the TONs observed. Also when the reaction was carried out using water as the proton source the TONs for all 3 complexes were negligible which they ascribe to the high pH (7.0). Most of the H<sub>2</sub> generated was observed during the first hour of irradiation but was continual for the following 3 hours yielding a TOF of 7–8 h<sup>-1</sup> for complex **45**. Complexes **45** and **46** produced H<sub>2</sub>

when a UV cut-off filter was employed. The TON yielded using complex **45** and the UV cut-off filter was only 16 after the first hour but 103 after 15 hours irradiation implying that both visible and UV light are necessary for the photocatalytic reaction to occur.

In the same year Fihri *et al.*<sup>30</sup> proposed ruthenium, iridium and rhenium based photosensitisers coupled with cobaloxime catalytic centres to compete with TON and TOF achieved by platinum and palladium catalysed H<sub>2</sub> production as after publishing the first paper they discovered that systems **47** - **49** required near-UV irradiation and were almost inactive under visible irradiation ( $\lambda > 380$  nm). A series of new complexes (Fig. 3.11) were irradiated with  $\lambda > 380$  nm and 300 equivalents of TEA, as well as 300 equivalents of Et<sub>3</sub>NH<sup>+</sup> as the proton source.

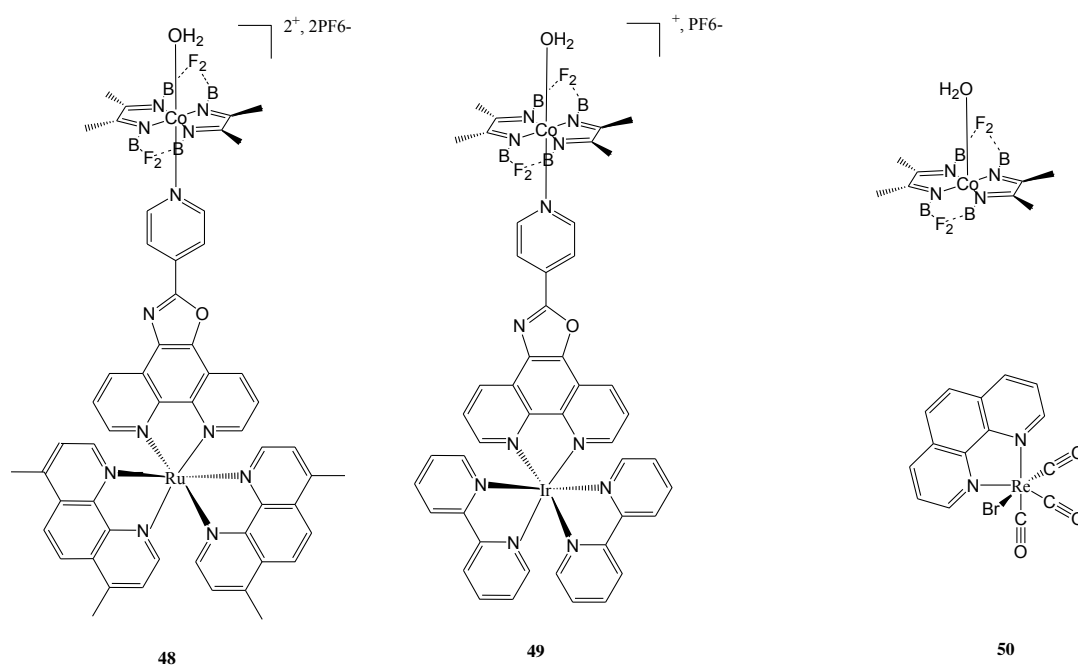


Figure 3.11- Cobaloxime complexes used for the visible light drive generation of H<sub>2</sub> by Fihri *et al.*<sup>30</sup>

Complex **48**, which only differs from the complexes previously reported by the replacement of the two bpy (bipyridine) ligands on the Ru centre with phenanthroline moieties, achieved a TON = 9 after a 4 hour irradiation  $\lambda > 380$  nm. Replacing the Ru centre with Ir (complex **49**) afforded TON = 140 after 8 hour irradiation  $\lambda > 380$  nm, which equated to a TOF of 42 h<sup>-1</sup>. The mixed intermolecular



system **50** achieved TON = 140 following 4 hours irradiation. During the first hour of irradiation **50**, TOF = 53 was obtained which is comparable to that of **49**. It was proposed that the enhanced activity of **50** is due to the stability of the complex which was confirmed by the observance of a TON = 273 after 15 hours irradiation.

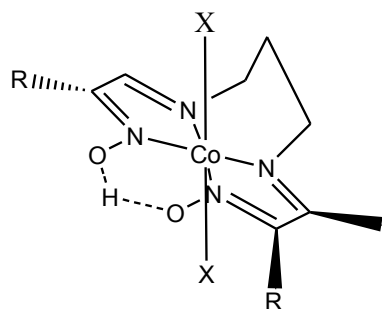
Utschig *et al.*<sup>31</sup> have derived inspiration directly from nature and utilised the photosystem I protein (PSI) to harness light and drive the catalytic splitting of water using a cobaloxime metal centre. They have reported that PSI and the cobaloxime catalyst Co(dmgh)<sub>2</sub>pyCl (where dmgh = dimethylglyoximate, py = pyridine) self-assemble, and the resultant complex rapidly produces hydrogen in aqueous solution upon exposure to visible light. PSI itself has an exceptionally long-lived charge-separated state P700<sup>+</sup> FB<sup>-</sup> (~60 ms), where P700 is the primary electron donor and FB is an [4Fe-4S] cluster in PSI, and a low reduction potential of -0.58 V (vs. NHE) which is associated with the FB cluster in the molecule. The complexes were found to produce hydrogen upon irradiation with visible light at a pH of 6.4 using sodium ascorbate as a sacrificial donor. A maximum TOF = 170 mol H<sub>2</sub> (mol PSI)<sup>-1</sup> min<sup>-1</sup> was observed within 10 min of illumination and the H<sub>2</sub> production leveled off after 1.5 hours yielding a TON = 1500. Metal analysis of PSI was carried out after photocatalysis and showed that > 90% of the cobaloxime had dissociated from PSI during the experiment explaining the initial high TOF which slowed after 1.5 hours. Further cobaloxime photocatalysts will be discussed in chapter 4.

### 3.1.2.2. Electrochemistry of Cobaloxime Complexes

Cobaloxime complexes are known to undergo two reduction processes which are attributed to Co<sup>III/II</sup> and Co<sup>II/I</sup>. The introduction of both electron donating and electron withdrawing substituents on the dioxime “ring” can greatly affect the redox potentials of the complexes. Razavet *et al.*<sup>32</sup> investigated the substitution of hydrogen or phenyl for methyl at the glyoxime ligands and found that it significantly increases the electrochemical potentials required to reduce the Co<sup>II/I</sup> couple. This is due to the fact that the conjugated ring systems are less electron donating. The exchange of the proton linker in the ring for a BF<sub>2</sub> moiety was observed to have the opposite effect on the reduction, allowing it to occur at a less negative potential

allowing the  $\text{Co}^{\text{III/I}}$  redox couple to occur at -0.55 V vs. Ag/AgCl rather than at -0.98 V for the proton linked analogue.

Jacques and his group measured the redox potentials of cobalt diimine-dioxime complexes in ACN.<sup>24</sup> The addition of an imine ligand rather than two glyoxime groups allowed reduction to occur at less negative potentials of  $\sim 0.2$  V. When the proton linkers in the ring structure of these complexes were exchanged for a  $\text{BF}_2$  moiety the group observed the same anodic shift in the negative potential that must be applied for the  $\text{Co}^{\text{III/I}}$  redox process. It was proposed that the  $\text{BF}_2$  moiety moves electron density away from the metal centre allowing reduction to occur more easily. The oxime substituent also greatly affects the electron density on the metal centre and when exchanging a Cl group in  $[\text{Co}(\text{MO})(\text{MOH})\text{pnCl}_2]$  for a Br group to yield  $[\text{Co}(\text{DO})(\text{DOH})\text{pnBr}_2]$  **51** (Fig. 3.12), with a anodic shift of 0.08 V of the redox couple due to the more electron withdrawing nature of Br.

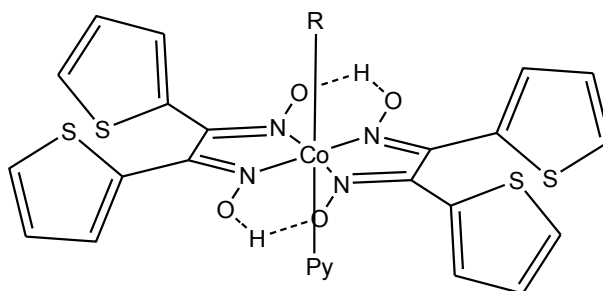


**(51)**  $[\text{Co}(\text{DO})(\text{DOH})\text{pnBr}_2]$ : R= Me, X= Br

**(52)**  $[\text{Co}(\text{MO})(\text{MOH})\text{pnCl}_2]$ : R=H, X= Cl

Figure 3.12- Cobalt complexes with varying imine-oxime substitution studied by Jaques *et al.*<sup>24</sup>

Kumar and Ghupta<sup>33</sup> reported exchanging the methyl groups on the ring periphery for thiophene groups which afforded complexes which can be significantly more easily reduced than those produced by Razavet *et al.*<sup>23</sup> (Fig. 3.13), which had Me groups in these positions. The first reduction,  $\text{Co}^{\text{III/II}}$ , occurred at -0.239 V vs. Ag/AgCl whereas Razavat reported this process to occur at -0.59 V vs. Ag/AgCl in the Me derivatives, while the second reduction,  $\text{Co}^{\text{II/I}}$ , was reported to occur at -0.643 V in the thiophene complexes and -0.98 V in the Me derivatives.

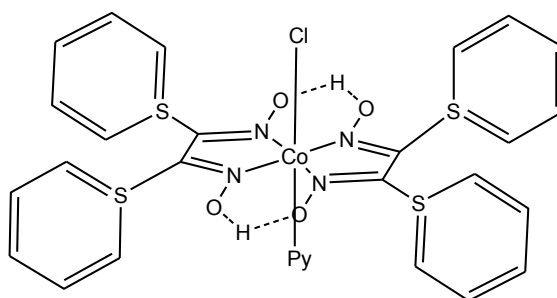


**R** = Cl (**53**), Et (**54**), Bn (**55**).

**Figure 3.13-** Cobaloximes with dithienylglyoxime ligands synthesised and studied by Kumar and Ghupta.<sup>33</sup>  
Py = pyridine.

In addition it was noted that due to the  $\sigma$  donating ability of the alkyl groups in **54** and **55** the second redox couple,  $\text{Co}^{\text{II/I}}$  was not visible in the reduction window, even when potentials as negative as -1.6 V were viewed.

An investigation regarding SPhenyl (SPh) groups incorporated as axial ligands on the oxime ring was carried out (Fig. 3.14).<sup>34</sup> The possibility of the SPh group acting as an electron donating group, due to the lone pair on the sulphur, or electron withdrawing group, due to the higher electronegativity of the sulphur when compared with a carbon or hydrogen atom, was explored.



**56**

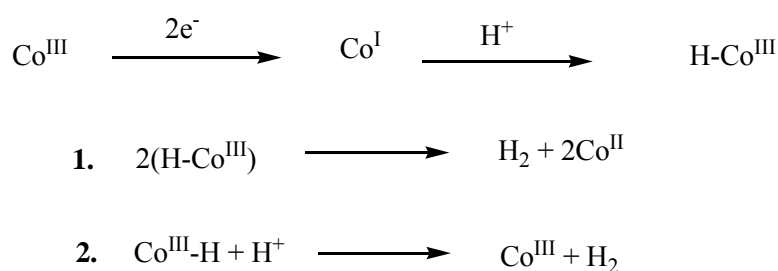
**Figure 3.14-** SPh appended cobaloxime  $[\text{Co}(\text{dSPhgH})_2\text{Py}]$  complex investigated by Dutta *et al.*<sup>34</sup>

When compared to  $[\text{Co}(\text{dmgH})_2\text{Py}]$  the two reductions at the cobalt centre experienced an anodic shift of 0.14 V indicating that the SPh groups are acting as electron withdrawing complexes.

By incorporating both an electron withdrawing acetonitrile group on the Co centre along with BF<sub>2</sub> linked glyoxime units on the ring Hu et al have achieved reductions at 0.3 V and -0.28 V for the Co<sup>III/II</sup> and Co<sup>II/I</sup> redox pairs respectively representing a huge anodic shift.<sup>36</sup>

### 3.1.2.3. Cobaloxime Complexes Used in the Electrocatalytic Generation of Hydrogen

Hydrogen production through the reduction of water can be achieved using electrode surfaces modified with cobaloxime electrocatalysts. Much research has been centred on the incorporation of various electron withdrawing groups around the glyoxime ligand to facilitate proton reduction at a less negative applied potential. When in the Co<sup>I</sup> oxidation state, cobaloxime complexes are known to be great nucleophiles. The Co<sup>I</sup> metal can become protonated and it is believed that these metal hydrides are the first step in hydrogen generation and either the hydride moiety is then protonated (1., Scheme 3.2) or a bimolecular reductive elimination occurs to evolve hydrogen (2., Scheme 3.2). The mechanism for the hydrogen evolution process is illustrated in Scheme 3.2.



**Scheme 3.2-** The possible mechanistic pathways for H<sub>2</sub> evolution showing the homolytic process (1) and the heterolytic process (2).<sup>24</sup>

Pantani *et al.*<sup>35</sup> have reported the use of both cobalt glyoximes and nickel glyoximes incorporated in a Nafion polymer in the electrocatalytic production of hydrogen. Both the cobaloxime and nickel glyoxime complexes produced two reversible reduction processes which are attributed to the Co<sup>III/II</sup> and Co<sup>II/I</sup> and the Ni<sup>III/I</sup> and Ni<sup>I/0</sup> processes respectively. No TON are reported however it is reported that catalytic activity for both types of complex increases upon addition of more HClO<sub>4</sub> when

using a glassy carbon working electrode in ACN for cobaloximes and DMF for nickel glyoximes.

Similarly Jaques *et al.*<sup>24</sup> have synthesised a series of electrocatalysts based on the ligand N2,N2'-propanediylbis(2,3-butandione-2-imine-3-oxime) utilising both cobalt and nickel as the metal centre. (Fig 3.15.) These systems are active in producing H<sub>2</sub> in non-aqueous conditions at low overpotentials.

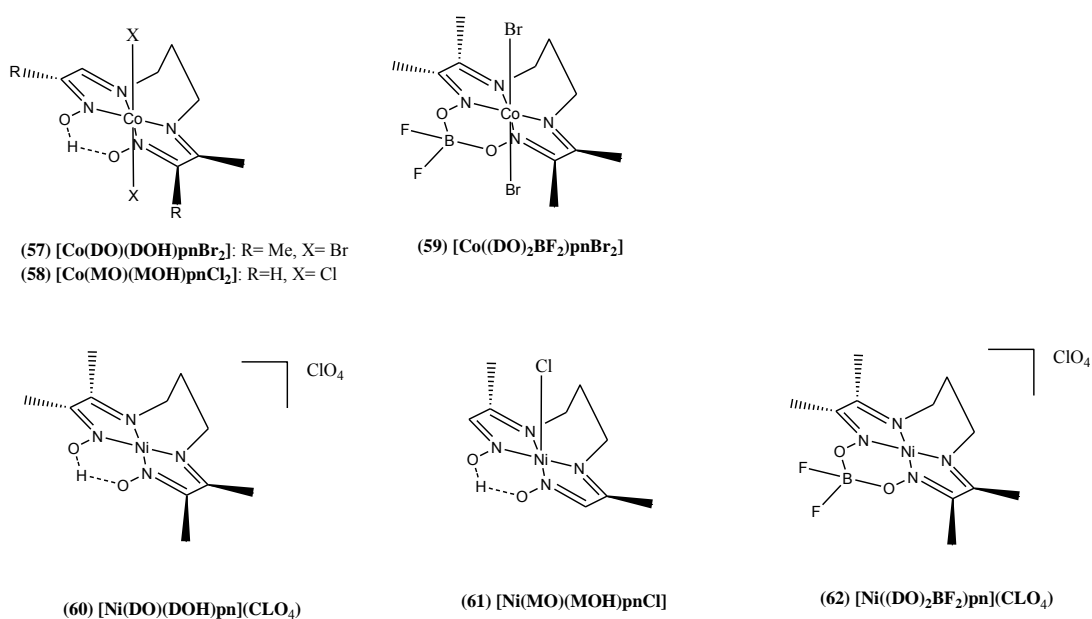


Figure 3.15- Structures of Co and Ni diimine-dioxime complexes studied by Jaques *et al.*<sup>24</sup>

The proton linked diimine-dioxime complexes were seen to undergo the Co<sup>II/I</sup> reduction at much more positive potentials than their cobaloxime counterparts indicating lower electron density on the metal centre. The highest potential for this process was seen for [Co(MO)(MOH)pnCl<sub>2</sub>] at -0.96 V vs. Fc<sup>+/0</sup>. The nickel complexes had a reversible process attributed to the Ni<sup>II/I</sup> reduction at approximately 0.1 V more negative than the corresponding Co<sup>II/I</sup> process due to the higher electron density on the metal centre. Electrocatalytic studies were carried out using graphite rod working electrode in a 0.1 M TBABF<sub>4</sub> solution in acetonitrile containing 50 mM of oxime and 50 mM acid and it was observed that the overpotential required to produce H<sub>2</sub> for all compounds was larger when weaker acids were employed, such as p-cyanoanilinium and tosic acid, when compared with the stronger anilinium and

TFA acids. TONs of up to 40 (for **57** - [Co(DO)(DOH)pnBr<sub>2</sub>] with p-cyanoanilinium) for the cobalt complexes and 20 (for **61** - Ni(MO)MOH)PnCl] with p-cyanoanilinium) for the nickel complexes were obtained after 3 hours bulk electrolysis. Also the cobalt complexes achieved Faradaic yields of up to 100% while the nickel complexes achieved efficiencies of between 30 and 70%.

Hu *et al.*<sup>36</sup> have reported the electrocatalytic behaviour of a series of cobalt complexes having BF<sub>2</sub>-bridged diglyoxime or propane-bridged macrocyclic tetraimine ligands (Fig. 3.16).

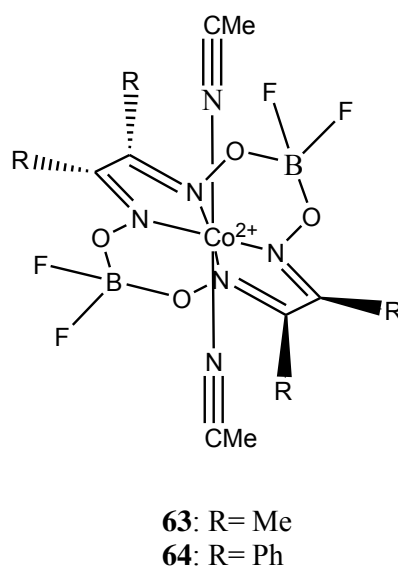


Figure 3.16- Cobaloximes bearing MeCN ligands and BF<sub>2</sub> linkers studied by Hu *et al.*<sup>36</sup>

The incorporation of MeCN ligands at the cobalt centre afforded less negative reduction potentials for the Co<sup>III/I</sup> process at -0.55 V vs. SCE for **63** and at -0.28 V for **64**. The production of hydrogen in acidic ACN with HCl or HBF<sub>4</sub>·Et<sub>2</sub>O required potentials between -0.55 V and -0.20 V vs. SCE respectively with a maximum TON > 5 with minimal decomposition of the catalyst. The overpotentials relative to the potentials for H<sub>2</sub> evolution in acidic ACN, were estimated to be ~ 0.4 V for **63** and ~ 0.5 V for **64**.

Electrocatalytic hydrogen evolution by cobalt tetraimine catalysts modified with carboxylic acid groups and BF<sub>2</sub> moieties have been reported by Berben *et al.*<sup>37</sup> The aim was to have the complexes adsorbed onto an ITO surface through the carboxylic acid groups. Catalytic experiments were carried out in 0.1 M TBAClO<sub>4</sub> and ACN

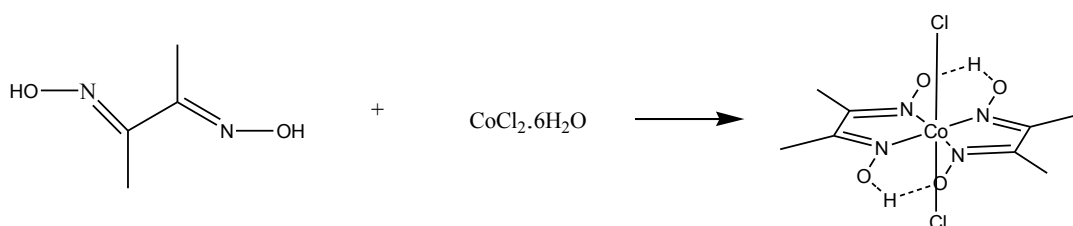
acidified with tosic acid (*p*-toluene-sulphonic acid). The increase in current occurred at -0.6 V vs. SCE at pH 2.0, which corresponded to an overpotential of 0.24 V. Following bulk electrolysis at -0.9 V at concentrations of  $1.14 \times 10^{-9} \text{ mol cm}^{-2}$ , which was calculated from the area under the cathodic peak for  $\text{Co}^{\text{II/I}}$  in a typical experiment, a TON of  $5 \times 10^5$  was obtained after 7 hours with an 80 ( $\pm 10$ ) % Faradaic yield.

## 3.2. Experimental

All materials and equipment used in this studied are detailed in chapter 2 sections 2.21 and 2.22. Details of cyclic voltammetry, electrocatalytic studies and photocatalytic studies are also available in chapter 2 sections 2.23, 2.24 and 2.25.

### 3.2.1. Synthesis

#### 3.2.1.1. Synthesis of bis(dimethylglyoximate)cobalt(IV) (cobaloxime)



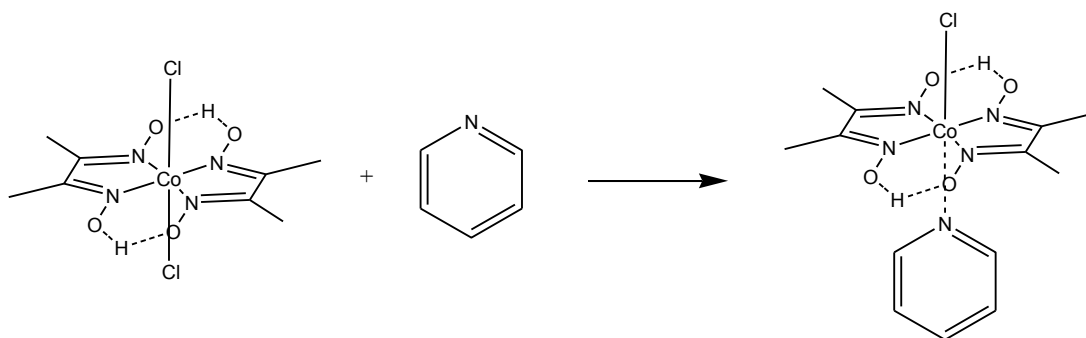
1.1g (4.62 mmol) of cobalt (II) chloride hexahydrate was dissolved in 15 ml of acetone and added to a clean, dry, 50ml round bottom flask. 1.07 g (9.24 mmol) of dimethylglyoxime was dissolved in 15 ml of acetone and added to the round bottomed flask. This solution was stirred for 30 – 60 min with a gentle stream of air passing over the reaction mixture. A dark green precipitate formed. The solution was cooled in ice then vacuum filtered & washed down with ice cold acetone.

% Yield: 1.45 g, 4.03 mmol, 87%

<sup>1</sup>H NMR: (400 MHz, CDCl<sub>3</sub>), 2.41 ppm (s, 2H), 2.33 ppm (s, 12H).



### 3.2.1.2. Synthesis of Pyridine- Cobaloxime

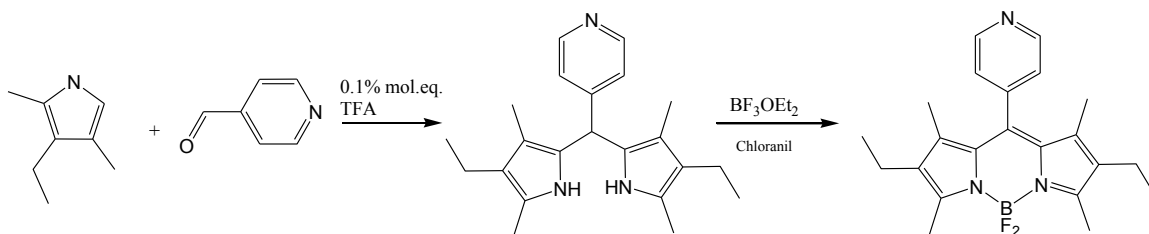


0.3g (0.833 mmol) of cobaloxime was suspended in 15 ml of methanol in a clean, dry, round bottomed flask. 0.066g (0.833 mmol) of pyridine was added to the solution and the suspension was allowed to stir for 30 min. A brown suspension results. 20 mls of deionised water was added and the solution was stirred while cooling on ice for 10 mins. The product was collected by vacuum filtration and washed with 3 x 15 ml solution 2:1 water / methanol followed by 2 x 10 ml diethyl ether. The remaining solid was dissolved in DCM and the final undissolved by-product was removed by vacuum filtration. A light brown product results.

% Yield: 0.255 g, 0.632 mmol, 76 %.

<sup>1</sup>H NMR: (400 MHz, CDCl<sub>3</sub>), 8.24 ppm (dd,  $J_a = 6.6$  Hz,  $J_b = 1.6$  Hz, 2H), 7.69 ppm (m, 1H), 7.18 ppm (dd,  $J_a = 7.4$  Hz,  $J_b = 6.4$  Hz, 2H), 2.391 ppm (s, 12H).

### 3.2.1.3. Synthesis of 4-[Bis-(4-ethyl-3,5-dimethyl-1H-pyrrol-2-yl)-methyl]-pyridine-borondifluoride (4-pyridine-BODIPY)

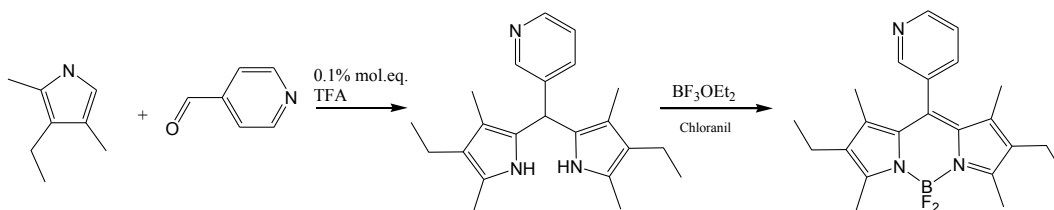


To a clean, dry 25ml round bottomed flask 15 ml of DCM followed by 0.1 ml (1.0652 mmol) of 4-pyridinecarboxaldehyde. The solution was purged with nitrogen for 10 min. 0.26 ml (2.13 mmol) of kryptopyrrole (3-ethyl-2,4-dimethylpyrrole) was added followed by 27  $\mu$ L of TFA was added to the purged solution. The reaction vessel was sealed and covered allowed to stir for 3 hours. A dark red solution is formed. 4.92 g (20 mmol) of chloranil was dissolved in  $\sim$  5 ml of DCM and added to the reaction vessel. The reaction mixture was allowed to stir for a further hour. 1 ml of triethylamine was added followed in quick succession by 1.2 ml of  $\text{BF}_3 \cdot \text{OEt}_2$ . The solution was allowed to stir for a further 4 hours. After this time the reaction mixture was separated with 3 x 10 ml portions of a saturated  $\text{NaHCO}_3$  solution. The organic layer was dried using  $\text{MgSO}_4$ . Purification was carried out using column chromatography with silica and a hexane: chloroform 97:3 mobile phase. A red solid results.<sup>38</sup>

% Yield: 0.175 g, 0.459 mmol, 43%

$^1\text{H}$  NMR: (400 MHz,  $\text{CDCl}_3$ ), 8.7 ppm (dd,  $J_a = 4.4$  Hz,  $J_b = 1.6$  Hz, 2H), 7.24 ppm (dd,  $J_a = 2.4$  Hz,  $J_b = 1.6$  Hz, 2H), 2.47 ppm (s, 6H), 2.23 ppm (q,  $J = 8.0$  Hz, 4H), 1.28 ppm (s, 6H), 0.91 ppm (t,  $J = 7.6$  Hz, 6H).

### 3.2.1.4. Synthesis of 3-[Bis-(4-ethyl-3,5-dimethyl-1H-pyrrol-2-yl)-methyl]-pyridine-borondifluoride (3-pyridine-BODIPY)

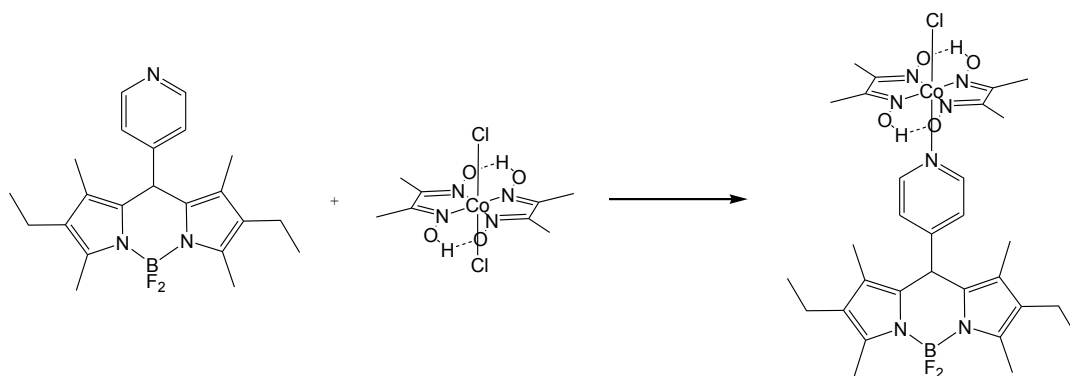


To a clean, dry 25ml round bottomed flask 15 ml of DCM followed by 0.1 ml (1.0652 mmol) of 4-pyridinecarboxaldehyde. The solution was purged with nitrogen for 10 min. 0.26 ml (2.13 mmol) of kyrptopyrrole (3-ethyl-2,4-dimethylpyrrole) was added followed by 27  $\mu\text{L}$  of TFA was added to the purged solution. The reaction vessel was sealed and covered allowed to stir for 3 hours. A dark red solution is formed. 4.92 g (20 mmol) of chloranil was dissolved in  $\sim 5$  ml of DCM and added to the reaction vessel. The reaction mixture was allowed to stir for a further hour. 1 ml of triethylamine was added followed in quick succession by 1.2 ml of  $\text{BF}_3\cdot\text{OEt}_2$ . The solution was allowed to stir for a further 4 hours. After this time the reaction mixture was separated with 3 x 10 ml portions of a saturated  $\text{NaHCO}_3$  solution. The organic layer was dried using  $\text{MgSO}_4$ . Purification was carried out using column chromatography with silica and a hexane: chloroform 97:3 mobile phase. A red solid results.<sup>38</sup>

% Yield: 0.212 g, 0.551 mmol, 52%

$^1\text{H}$  NMR: (400 MHz,  $\text{CDCl}_3$ ), 8.73 ppm (dd,  $J_a = 4.8$  Hz,  $J_b = 1.2$  Hz, 1H), 8.54 ppm (d,  $J = 1.2$  Hz, 1H), 7.63 ppm (dd,  $J_a = 6.0$  Hz,  $J_b = 2.0$  Hz, 1H), 7.44 ppm (dd,  $J_a = 7.4$  Hz,  $J_b = 4.8$  Hz, 1H), 2.519 ppm (s, 6H), 2.28 ppm (q,  $J = 7.6$  Hz, 4H), 1.24 ppm (m, 6H), 0.96 ppm (t,  $J = 7.6$  Hz, 6H).

### 3.2.1.5. Synthesis of 4-BODIPY-Cobaloxime



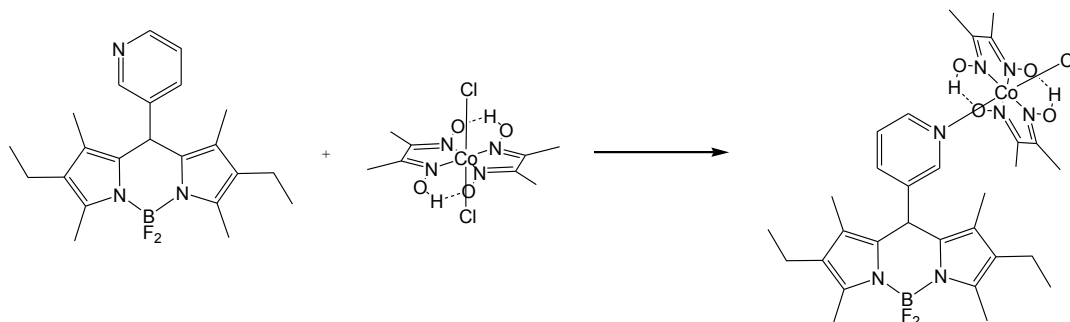
0.05g (0.131 mmol) of 4-BODIPY was dissolved in 10 ml of MeOH in a clean, dry, 2 necked round bottomed flask. 0.047g (0.131 mmol) of cobaloxime was dissolved in 10 ml of MeOH and this solution was added to the round bottomed flask. 0.0192 ml (0.262 mmol) of TEA was added to the reaction vessel. The reaction mixture was allowed to stir for 1.5 hours under a gentle stream of air. A dark red precipitate is formed. The solution was cooled in an ice bath and vacuum filtered. Purification was carried out using column chromatography with silica and a hexane: chloroform 97:3 mobile phase. A dark red solid product results.

% Yield: 0.063 g, 0.089 mmol, 68%

$^1\text{H}$  NMR: (400 MHz,  $\text{CDCl}_3$ ), 12.25 ppm (s, 2  $-\text{OH}$ ), 8.35 ppm (d,  $J = 6.4$  Hz, 2H), 7.17 ppm (d,  $J = 6.8$  Hz, 2H), 2.434 ppm (s, 6H), 2.36 ppm (s, 12H), 2.19 ppm (q,  $J = 7.6$  Hz, 4H), 0.96 ppm (s, 6H), 0.88 ppm (t,  $J = 7.6$  Hz, 6H)

Anal. Calcd. For  $\text{C}_{30}\text{H}_{41}\text{N}_7\text{BF}_2\text{CoClO}_4$ : C 50.5, H 5.85, N 13.66. Found: C 50.1, H 5.21, N. 12.92.

### 3.2.1.6. Synthesis of 3-BODIPY-Cobaloxime



0.05g (0.131 mmol) of 3-BODIPY was dissolved in 10 ml of MeOH in a clean, dry, 2 necked round bottomed flask. 0.047g (0.131 mmol) of cobaloxime was dissolved in 10 ml of MeOH and this solution was added to the round bottomed flask. 0.0192 ml (0.262 mmol) of TEA was added to the reaction vessel. The reaction mixture was allowed to stir for 1.5 hours under a gentle stream of air. A dark red precipitate is formed. The solution was cooled in an ice bath and vacuum filtered. Purification was carried out using column chromatography with silica and a hexane: chloroform 97:3 mobile phase. A dark red solid product results.

% Yield: 0.060 g, 0.085 mmol, 65%

<sup>1</sup>H NMR: (400 MHz, CDCl<sub>3</sub>), 12.125 ppm (s, 2 -OH), 8.33 ppm (d, J= 5.6 Hz, 1H), 8.175 ppm (s, 1H), 7.58 ppm (dd, J<sub>a</sub>= 7.8 Hz, J<sub>b</sub>= 1.6 Hz, 1H), 7.32 ppm (dd, J<sub>a</sub>= 7.6 Hz, J<sub>b</sub>= 6.0 Hz, 1H), 2.47 ppm (s, 6H), 2.38 ppm (s, 12H), 2.21 ppm (q, J= 7.6 Hz, 4H), 0.9 ppm (t, J= 7.6 Hz, 6H), 0.86 ppm (s, 6H).

Anal. Calcd. For C<sub>30</sub>H<sub>41</sub>N<sub>7</sub>BF<sub>2</sub>CoClO<sub>4</sub>: C 50.5, H 5.85, N 13.66. Found: C 49.95, H 5.34, N. 12.83.

### 3.3. Results

#### 3.3.1. UV-Vis Spectroscopy

Room temperature absorption spectra were obtained for all compounds. Table 3.2 illustrates the absorption maxima ( $\lambda_{\text{max}}$ ) for all compounds in this study. All UV-Vis spectra were carried out using spectrophotometric grade dichloromethane (DCM).

Compound	$\lambda_{\text{max}}$ (nm), $\epsilon$ ( $\times 10^4 \text{ M}^{-1} \text{ cm}^{-1}$ )	FWHM ( $\times 10^5 \text{ cm}^{-1}$ ) of $S_0 - S_1$ transition.
3-Pyridine BODIPY	377 (4.9), 494 (18.1), 524 (47.8)	3.85
4-Pyridine BODIPY	377 (4.3), 494 (16.2), 524 (40.3)	3.77
3-Pyridine BODIPY-Cobaloxime	285 (0.04), 379 (0.96), 501 (2.33), 534 (6.74)	2.99
4-Pyridine BODIPY-Cobaloxime	284 (0.04), 379 (0.82), 504 (2.00), 536 (4.98)	2.91
Cobaloxime	262 (0.05), 412, 503, 598	-
Pyridine-Cobaloxime	252 (0.054), 401, 501, 586	-

**Table 3.2-** UV-Vis absorption data for all compounds in this study. All spectra were recorded in spectrophotometric grade DCM.

All BODIPY complexes absorb strongly in the yellow green range of the UV-Vis spectrum around 525 nm, with a shoulder at  $\sim 496$  nm, attributed to an  $S^0 - S^1$  transition, which is typical of this type of compound.<sup>17,39,40</sup> Absorbances observed between 375 and 400 nm are attributed to  $\pi - \pi^*$  transitions localised within the pyridine unit.<sup>41</sup> Addition of the cobaloxime moiety causes a bathochromatic shift of  $\sim 7$  nm.

### 3.3.2. Fluorescence Studies

Room temperature emission spectra and fluorescence lifetimes were obtained for all compounds. Table 3.3 illustrates the excitation wavelength and emission maxima for all compounds in this study and their respective singlet lifetimes. All emission spectra and lifetimes were measured using spectrophotometric grade dichloromethane (DCM).

Compound	Excitation (nm)	Emission (nm)	Stokes Shift (cm <sup>-1</sup> )	<sup>1</sup> τ (ns) ± 5%
3-Pyridine BODIPY	377	549	865	5.94
4-Pyridine BODIPY	377	540	565	4.82
3-Pyridine BODIPY- Cobaloxime	379	550	545	4.88
4-Pyridine BODIPY- Cobaloxime	370	542	207	3.66
Cobaloxime	262	N/A	-	-
Pyridine- Cobaloxime	252	N/A	-	-

Table 3.3- Fluorescence properties and singlet lifetimes <sup>1</sup>τ of all compounds in this study. All spectra were recorded in spectrophotometric grade DCM. Singlet lifetimes are measured +/- 5%.

Excitation of each complex into the  $S_0 - S_2$  band gives rise to an emission band between 540 nm and 550 nm. Complexation of the cobaloxime moiety to the BODIPY compound resulted in a bathochromatic shift of only 1 to 2 nm in the emission wavelength suggesting that the emission is based only on the BODIPY complex. The fluorescence spectra of 3-pyridine BODIPY-cobaloxime and 4-pyridine BODIPY-cobaloxime show quenched emission when compared to their BODIPY counterparts.

The singlet lifetimes of the BODIPY ligands were measured at ~4 ns which correlate with literature values.<sup>9,10</sup> Addition of the cobaloxime unit had little effect on the lifetimes but some quenching of the emission bands were observed for the cobaloxime complexes (Fig. 3.22).

### 3.3.3. Photocatalytic Hydrogen Generation Studies

All compounds were tested to measure their photocatalytic efficiency for  $H_2$  generation. All experimental details are discussed in chapter 2, section 2.3.5, and are available in appendix B1. All complexes were tested under the conditions listed in Table 3.4.

Exp . No.	Conc. Complex (M)	TEA (%)	Water (%)	Irradiation $\lambda$ (nm)	Irradiation length (hr)
1	$5 \times 10^{-5}$	16.6	10	350	20
2	$5 \times 10^{-5}$	16.6	0	350	20
3	$5 \times 10^{-5}$	16.6	10	470	20
4	$5 \times 10^{-5}$	16.6	0	470	20

**Table 3.4- Experimental conditions for photocatalytic studies.**

No  $H_2$  was detected via GC analysis in the headspace of the sample vials either because none was produced or the amount produced was less than limit of detection of the GC.



### 3.3.4. Cyclic Voltammetry

Cyclic voltammetry experiments were carried out at room temperature. Details of experimental set up are available in chapter 2, section 2.2.4.

#### 3.3.4.1. Reductive Electrochemistry

Reductive electrochemistry was carried out on the all BODIPY and BODIPY-Cobaloxime complexes in the range 0V to -2.0V. The potential window of ACN is between 0 and -2.0V for reduction processes so experiments were not carried out at lower potential limits. Within this range several reduction process were observed and have been summarised in Table 3.5.

Cyclic Voltammetry Reduction Potentials			
	$E_{pa}$ (V)	$E_{pc}$ (V)	$E_{1/2}$ (V)
3-Pyridine-BODIPY		-1.51 <sup>a</sup>	
3-Pyridine-BODIPY-Cobaloxime		-1.1 <sup>a</sup>	
	-1.37 <sup>b</sup>	-1.5 <sup>b</sup>	-1.435
4-Pyridine-BODIPY-Cobaloxime		-0.92 <sup>a</sup>	
	-1.23 <sup>b</sup>	-1.33 <sup>b</sup>	1.28
Cobaloxime	-1.30 <sup>c</sup>	-1.38 <sup>c</sup>	-1.34
Pyridine-Cobaloxime	-1.22 <sup>b</sup>	-1.02 <sup>b</sup>	-1.205
	-1.57 <sup>b</sup>	-1.47 <sup>b</sup>	1.52

Table 3.5- The cyclic voltammetry results for the reduction processes of all BODIPY ligands and BODIPY-cobaloxime complexes vs. Ag/AgCl in 0.1M TBAPF<sub>6</sub>/ DCM. <sup>a</sup> indicates an irreversible reduction, <sup>b</sup> indicates a reversible wave, <sup>c</sup> indicates a quasi-reversible wave.

All BODIPY complexes exhibited a ligand based reduction in the range  $\sim -1.28$  to  $-1.44$  V which is attributed to the formation of a  $[\text{BODIPY}]^{\cdot-}$  radical anion. Addition of a cobaloxime unit induces a second reduction which is assigned to the  $\text{Co}^{\text{III}}/\text{Co}^{\text{II}}$  redox couple.

### 3.3.4.2. Oxidative Electrochemistry

Oxidative electrochemistry was carried out on the all BODIPY and BODIPY-cobaloxime complexes in the range 0V to 2.0 V. The potential window of ACN is between 0 and 2.0 V for oxidation processes so experiments were not carried out at higher potentials. Within this range several reduction process were observed and have been summarised in Table 3.6.

Cyclic Voltammetry Oxidation Potentials			
	$E_{pa}$ (V)	$E_{pc}$ (V)	$E_{1/2}$ (V)
3-Pyridine-BODIPY	0.82 <sup>a</sup>		
3-Pyridine-BODIPY-Cobaloxime	0.88 <sup>a</sup>		
	0.97 <sup>c</sup>	0.82 <sup>c</sup>	0.895
	1.6 <sup>a</sup>		
4-Pyridine-BODIPY-Cobaloxime	1.12 <sup>c</sup>	0.98 <sup>c</sup>	1.05
	1.73 <sup>a</sup>		
Cobaloxime	1.0 <sup>b</sup>	0.80 <sup>b</sup>	0.90
	1.39		
Pyridine-Cobaloxime	1.01 <sup>b</sup>	0.913 <sup>b</sup>	0.962
	1.66 <sup>a</sup>		

**Table 3.6 - The cyclic voltammetry results for the oxidation processes of all BODIPY ligands and BODIPY-cobaloxime complexes vs. Ag/AgCl. <sup>a</sup> indicates an irreversible oxidation, <sup>b</sup> indicates a reversible wave, c indicates a quasi-reversible wave.**

All BODIPY complexes possess an irreversible oxidation between 0.895 and 1.05 V which is attributed to the formation of a [BODIPY]<sup>•+</sup> radical cation, this process is obscured by the Co<sup>III</sup>/ Co<sup>IV</sup> process in 4-pyridine-BODIPY-cobaloxime. Addition of a cobaloxime unit leads to the observation of a quasi-reversible oxidation assigned to the Co<sup>III</sup>/ Co<sup>IV</sup> redox couple along with an oxime based irreversible oxidation at high potentials between 1.39 V and 1.73 V.

### 3.3.5. Electrocatalytic Hydrogen Generation Studies

The electrocatalytic hydrogen generation studies were carried out using pH 2.0, 0.1 M NaH<sub>2</sub>PO<sub>4</sub> buffer, a glassy carbon working electrode, a Ag/ AgCl reference

electrode filled with 3 M KCl and a platinum wire counter electrode in an airtight v-shaped electrolysis cell. Full details of the experimental set-up are available in Appendix C1/ C2.

### 3.3.5.1. Onset of Catalytic Current

A series of cyclic voltammogram experiments were carried out using both the bare glassy carbon electrode and glassy carbon electrodes with modified surfaces. The scans were performed at  $0.1 \text{ Vs}^{-1}$  from 0 V to -1.2 V in pH 2.0, 0.1 M  $\text{NaH}_2\text{PO}_4$  buffer. An additional process is visible in these CVs when the cyclic voltammograms produced were compared to similar CVs run in ACN. This process is assigned to the catalytic production of  $\text{H}_2$  in aqueous media and was confirmed through GC analysis of the headspace after the experiment. Table. 3.7 details the potential at which the onset of this process occurs according to the complex used to modify the surface.

Complex	Onset of Catalytic Current (V)
Bare Electrode	-1.15
Cobaloxime	-1.01
Pyridine-cobaloxime	-0.96
3-pyridine-BODIPY	-1.01
3-pyridine-BODIPY-cobaloxime	-0.90
4-pyridine-BODIPY	-0.95
4-pyridine-BODIPY-cobaloxime	-0.80

**Table 3.7-** The potential at which the onset of the  $\text{H}_2$  producing catalytic current is observed through modification of the glassy carbon electrode surface with the complexes utilised in this study.

The onset of the catalytic current is altered through coordination of the cobaloxime moiety to the electron withdrawing BODIPY ligand which is consistent with the CV measurements described ACN previously (Section 3.3.5.1.). The current produced by the bare electrode were greatly enhanced through modification with each of the

complexes. 4-pyridine-BODIPY-cobaloxime presented the strongest catalytic current due to the electron withdrawing properties of the BODIPY ligand allowing the Co metal reduction, necessary for the H<sub>2</sub> generating reaction, to occur at lower potentials. Also the linear coordination of the cobaloxime unit allows an ease of movement of H<sup>+</sup> ions to and from the catalytic centre due to very little steric hindrance from the bulky BODIPY moiety.

When the experiments were repeated in pH 7.0 buffer there was no evidence of the onset of a catalytic current within the potential window showing that the reaction is pH dependant and works more efficiently in more acidic conditions.

### **3.3.5.2. Varying Potentiostatic Electrolysis Potential**

3-pyridine-BODIPY, 3-pyridine-BODIPY-cobaloxime and cobaloxime were chosen as a model series and were tested at various applied electrolysis potentials.  $1.5 \times 10^{-10}$  moles of each compound was coated on the surface of a glassy carbon electrode and varying potentiostatic electrolysis potentials were applied for one hour in pH 2.0, 0.1 M NaH<sub>2</sub>PO<sub>4</sub> buffer solution. During these tests a constant potential is applied to the system over the course of a 1 hour experiment. The current passed through the system as a function of H<sub>2</sub> generation is measured and using Faraday's law of electrolysis is related to the number of moles of H<sub>2</sub> generated during the experiment.<sup>42</sup> After 1 hour a 1 ml sample of the headspace in the reaction vessel is injected in to the GC where its H<sub>2</sub> content is measured. The charge passed after one hour at the applied potential was measured and compared to the charge passed by a bare electrode under the same experimental conditions. Each experiment was repeated in triplicate and the average results are presented below. Full calculation details are available in Appendix C2.

Compound	BE Potential Applied (V)	Charge Passed after 1 hr (C)	Echem TON (x 10 <sup>3</sup> )	GC TON (x 10 <sup>3</sup> )
<u>Bare Electrode</u>	-0.7	3.37 x 10 <sup>-4</sup>	-	-
	-0.8	9.03 x 10 <sup>-4</sup>	-	-
	-1	1.90 x 10 <sup>-2</sup>	-	-
	-1.1	1.99 x 10 <sup>-2</sup>	-	-
	-1.2	2.63 x 10 <sup>-2</sup>	-	-
	-1.3	8.97 x 10 <sup>-1</sup>	-	-
<u>3-pyridine-BODIPY</u>	-1	8.90 x 10 <sup>-3</sup>	0.3	0*
	-1.1	3.13 x 10 <sup>-2</sup>	1.1	0*
	-1.2	1.60 x 10 <sup>-1</sup>	5.5	5.2
	-1.3	8.56 x 10 <sup>-1</sup>	29.6	25.5
<u>3-pyridine-BODIPY-cobaloxime</u>	-0.7	2.47 x 10 <sup>-4</sup>	0.009	0*
	-0.8	1.04 x 10 <sup>-3</sup>	0.036	0*
	-1	2.79 x 10 <sup>-1</sup>	9.6	7.1
	-1.1	6.60 x 10 <sup>-1</sup>	22.8	13.9
	-1.2	6.356 x 10 <sup>-1</sup>	22.0	18.5
	-1.3	1.02 x 10 <sup>1</sup>	35.2	29.9
<u>Cobaloxime</u>	-0.7	4.74 x 10 <sup>-4</sup>	0.016	0*
	-0.8	1.25 x 10 <sup>-3</sup>	0.043	0*
	-1	2.12 x 10 <sup>-1</sup>	7.3	6.5
	-1.1	3.80 x 10 <sup>-1</sup>	13.1	10.2
	-1.2	4.54 x 10 <sup>-1</sup>	15.7	8.0
	-1.3	9.37 x 10 <sup>-1</sup>	32.4	21.1

**Table 3.8 – Results of experiments varying the applied potential during potentiostatic electrolysis. BE = bulk electrolysis, no peaks were observed for low concentrations of H<sub>2</sub> due to the limit of detection of the GC. \*No H<sub>2</sub> detected as the quantity produced is below LOD of instrument. All TON are quoted ± 30%.**

Modification of the electrode surface allowed H<sub>2</sub> to be produced during bulk electrolysis experiments at less negative potentials. Reasonable TONs were measured for 3-pyridine-BODIPY at an applied potential of -1.2 while 3-pyridine-BODIPY-cobaloxime was capable of generating large TONs at potentials as positive as -1.0 V, which is consistent with the observed onset of the catalytic current being induced at more positive potentials when the surface is modified with this complex. Cobaloxime itself is capable of generating TONs upon application of a potential of -1.0 V however TONs generated are not as high as those observed with 3-pyridine-BODIPY-cobaloxime.

#### **3.3.5.3. H<sub>2</sub> Generation TONs**

Each compound was tested using an applied potential of -1.2 V for 1 hour and the resulting hydrogen TONs generated were compared. A 1ml sample of the headspace was injected into a GC and the GC calculated TONs were also compared to measure the overall efficiency of the electrochemical reaction (Table 3.9).

Compound	Charge Passed After 1 Hr (C)	Electrochemical TON ( $\times 10^3$ )	GC TON ( $\times 10^3$ )	Efficiency %	Avg Current During Bulk Electrolysis (mA)	Current Density (mA/cm <sup>2</sup> )
3-pyridine-BODIPY	0.160	5.5	5.2	94	0.034	0.49
4-pyridine-BODIPY	0.164	5.76	5.5	96	0.057	0.81
3-pyridine-BODIPY-cobaloxime	0.635	22.0	16.5	75	0.104	1.51
4-pyridine-BODIPY-cobaloxime	0.529	18.3	10.8	59	0.102	1.46
Cobaloxime	0.454	15.7	8.0	51	0.152	2.18
Pyridine-Cobaloxime	0.337	11.7	9.1	78	0.130	1.86

**Table 3.9- Results of electrocatalytic studies for all pyridine-BODIPY and pyridine-BODIPY-cobaloxime complexes upon bulk electrolysis at -1.2 V for 1 hour in pH 2.0, 1 mM NaH<sub>2</sub>PO<sub>4</sub> buffer. All TON are quoted  $\pm$  30%.**

### 3.4. Discussion

**Synthesis.** 3-pyridine-BODIPY, 4-pyridine-BODIPY and cobaloxime which are discussed in this chapter have been synthesised using a modified method from Ulrich and Ziessel and all spectral data for all complexes are in agreement with reported data.<sup>38</sup> The reaction progress was monitored using TLC throughout the experiments and reasonably high yields of 43 and 52 were obtained for 4-pyridine-BODIPY and 3-pyridine-BODIPY respectively through the use of kryptopyrrole as the starting material which hinders some of the mixed products which can be usually expected during dipyrromethene synthesis.

Synthesis of cobaloxime was facile and involved stirring the reactants in acetone for 1 hour. High yields of 87% were obtained following washing with cold acetone.

The BODIPY-cobaloxime derivatives are novel to the best of our knowledge, and all spectral data are in agreement with their formulation and compare well to similar compounds which have been previously reported in literature. Coordination of the cobaloxime moiety was achieved through the nitrogen group in the pyridyl substituent on the BODIPY complex following loss of a chloride group from the Co metal centre. Isolation of the products proved difficult and yields of 68 and 65% were achieved following column chromatography.



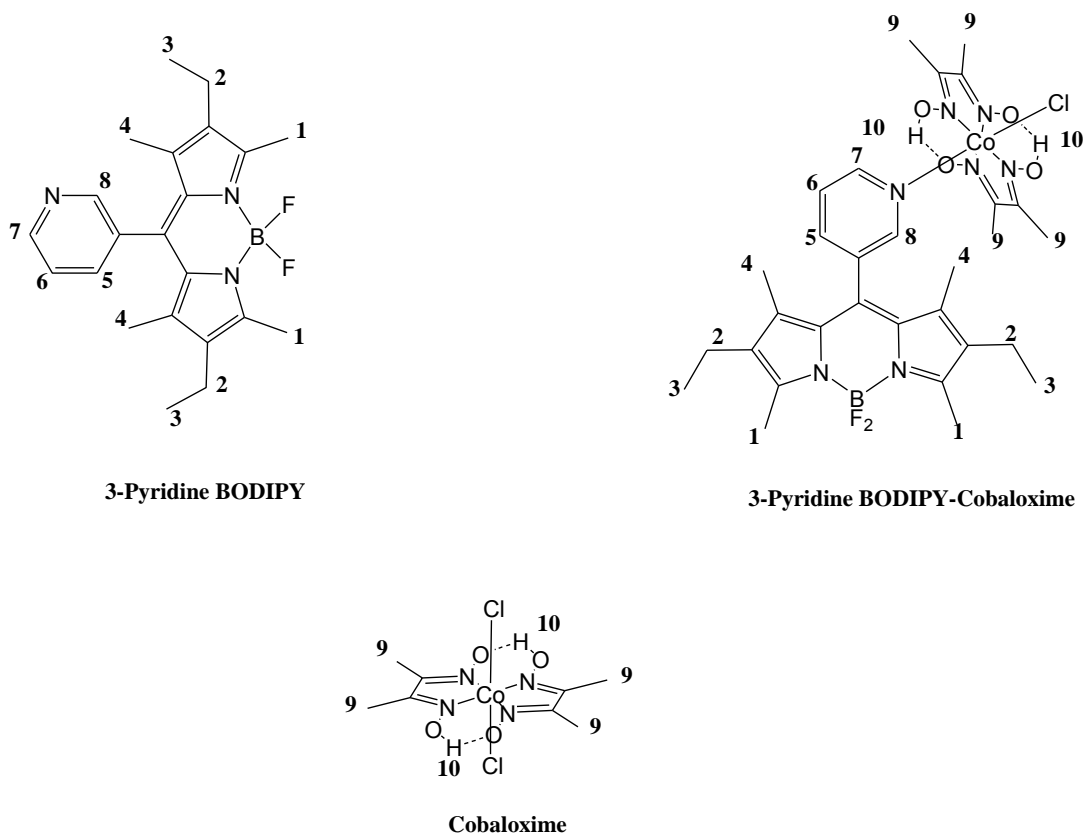


Figure 3.17- Numbering of protons in 3-pyridine-BODIPY, 3-pyridine-BODIPY-cobaloxime and cobaloxime.

**NMR Spectroscopy.** The  $^1\text{H}$ NMR spectral signals of both 3-pyridine-BODIPY and 4-pyridine-BODIPY are very similar except for the splitting in the pyridyl protons. Due to the symmetry in 4-pyridine-BODIPY two sets of resonances arise for these protons at 8.4 ppm and 7.24 ppm with the protons nearest the nitrogen appearing further downfield due to the lone pair on the nitrogen. As 3-BODIPY is more unsymmetrical 4 proton signals for the pyridyl protons are observed between 8.73 ppm and 7.44 ppm. Protons 5 and 6 appear further upfield than protons 7 and 8 due to the shielding effect of the nitrogen lone pair.

The alkyl protons (1 – 4) are present between 2.5 ppm and 1 ppm. The addition of the cobaloxime moiety shifts all of the signals slightly upfield due to the shielding effect of the cobaloxime with the pyridyl protons being the most affected. The coordination of the BODIPY ligand to the cobaloxime moiety leads to the appearance of a singlet at ~2.35 ppm (9). Proton 10, from the OH group, can be observed far downfield at ~ 12 ppm.

Examples of  $^1\text{H}$  NMR are available in appendix D1.

**Electronic Absorption Spectroscopy.** The absorbance spectra of 3-pyridine-BODIPY and 3-pyridine-BODIPY-cobaloxime are very similar however after addition of the cobaloxime group a small bathochromic shift of 7 nm is observed (Fig. 3.18). This shift is attributed to an interaction between the pyridyl-porphyrin and the cobalt centre on the cobaloxime. This effect was reported by Zhang *et al.*<sup>43</sup> when investigating the photophysics of cobaloxime linked porphyrin complexes. Freebase dipyrromethanes are known to absorb weakly in the blue-green region of the spectrum and addition of the  $\text{BF}_2$  moiety gives rise to the strong sharp absorbance in the region  $\sim 500 - 525 \text{ nm}$ .<sup>44</sup>

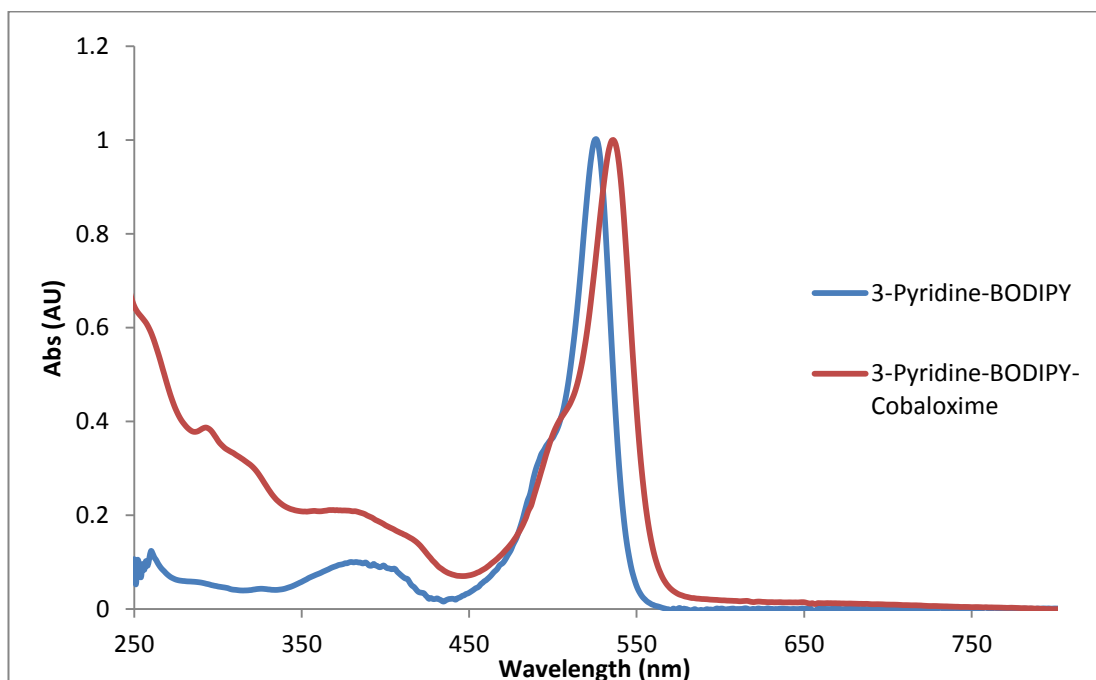
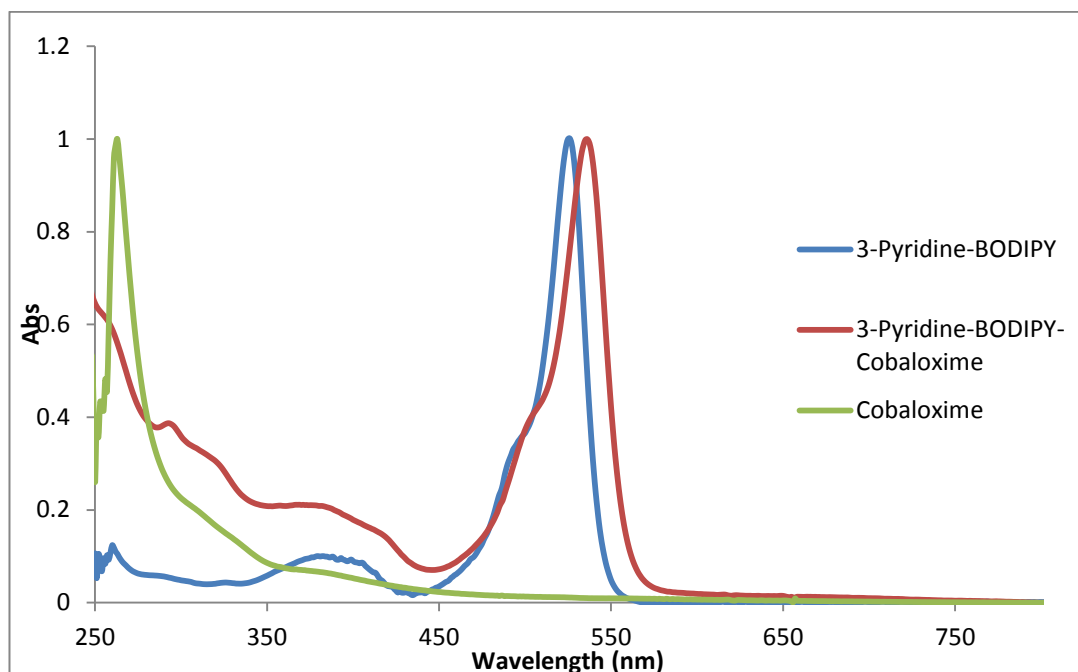


Figure 3.18- UV-Vis spectra of 3-Pyridine-BODIPY (blue line) ( $2 \times 10^{-2} \text{ M}$ ) and 3-Pyridine-BODIPY-cobaloxime (red line) ( $2 \times 10^{-3} \text{ M}$ ). All spectra were recorded in spectroscopic grade DCM.

These intense absorbances are attributed to the  $S_0 \rightarrow S_1$  ( $\pi-\pi^*$ ) transition on the dipyrromethene. A vibronic overtone of this transition appears at  $\sim 494 \text{ nm}$  and appears as a shoulder to the stronger absorbance.<sup>45</sup>

Along with this strong sharp absorbance a weaker, broader absorbance is present at shorter wavelengths centred at  $370 \text{ nm}$ . This absorbance is due to the  $S_0 \rightarrow S_2$  ( $\pi-\pi^*$ ) transition within the dipyrromethene ligand.<sup>45</sup> The addition of the cobaloxime unit

introduces a third broad band at higher energy, 285 nm, which is attributed to a  $\pi$ - $\pi^*$  transition within the cobaloxime subunit (Fig. 3.19).



**Figure 3.19-** UV-Vis spectra of 3-Pyridine-BODIPY (blue line) ( $2 \times 10^{-2}$  M), 3-Pyridine-BODIPY-cobaloxime (red line) ( $2 \times 10^{-3}$  M) and cobaloxime (green line).

The FWHM values are shown in Table 3.2, and there is some variance upon coordination of the cobaloxime complex. The  $S_0 - S_1$  transition bands are broadened when compared to the non-substituted BODIPYs. The width of the 3-pyridine-BODIPY ( $3.85 \times 10^5 \text{ cm}^{-1}$ ) and 4-pyridine-BODIPY ( $3.77 \times 10^5 \text{ cm}^{-1}$ ) absorbances are significantly broader than those of 3-pyridine-BODIPY-cobaloxime ( $2.99 \times 10^5 \text{ cm}^{-1}$ ) and 4-pyridine-BODIPY-cobaloxime ( $2.91 \times 10^5 \text{ cm}^{-1}$ ), which could suggest lower electronic and vibronic coupling between the  $\pi$ -electrons in the BODIPY dye system and the meso-substituted pyridyl groups.<sup>46</sup>

Further absorbances in the visible region of the UV-vis spectrum were observed for cobaloxime and pyridine cobaloxime. Weak broad absorbances at 412 nm and 401 nm respectively have been assigned to a ligand-metal charge transfer (LMCT) band from the axial coordinated pyridine group to the Co metal centre.<sup>26</sup> Also visible are two weaker absorbances further into the red region at 503 nm and 598 nm in cobaloxime and 501 nm and 586 nm in pyridine-cobaloxime complexes. These

transitions are assigned to a singlet  $d-d$  transition of  $\text{Co}^{\text{III}}$  followed by a triplet  $d-d$  transition of  $\text{Co}^{\text{III}}$ .<sup>26</sup> These absorbances are presumably present in the BODIPY-cobaloxime complexes also but due to the weakness of the bands they have been obscured by the strongly absorbing BODIPY based transitions.

**Fluorescence Spectroscopy.** Cobaloxime and pyridine-cobaloxime do not emit. All BODIPY complexes were excited at  $\sim 370$  nm which corresponds to the  $S_0 - S_2$  transition. As is illustrated in Fig. 3.20, BODIPY complexes exhibit one sharp emission band with a very small stokes shifts ( $207 - 865$   $\text{cm}^{-1}$ ). This is in agreement with reports of similar complexes in literature.<sup>16,43</sup>

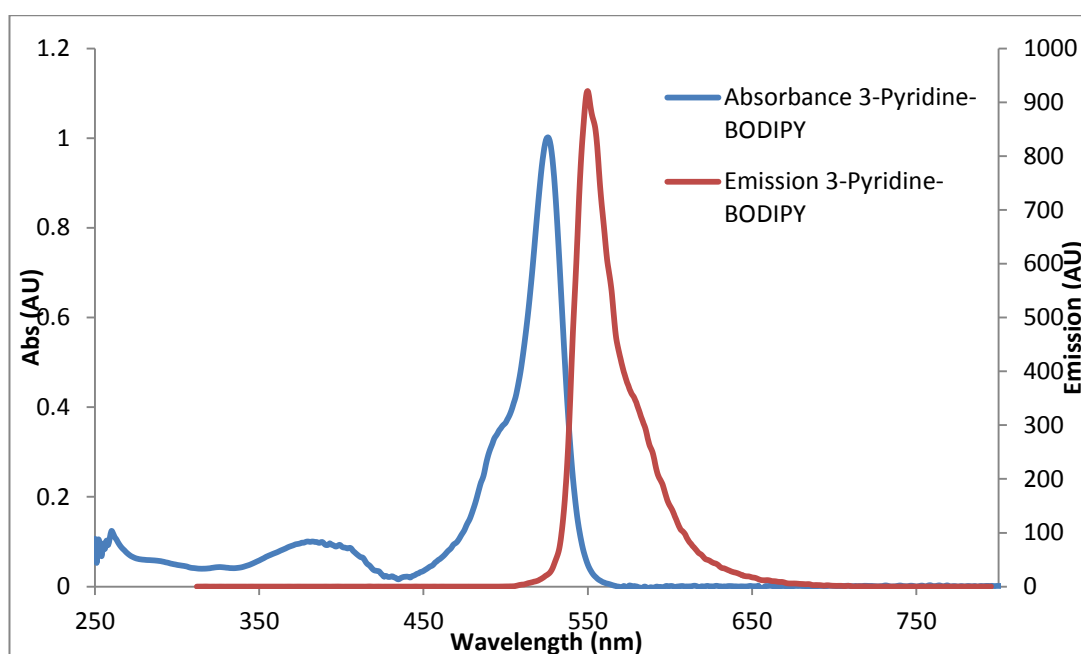


Figure 3.20 – UV-Vis spectrum and emission spectrum of 3-Pyridine-BODIPY-Cobaloxime recorded in spectrophotometric grade DCM.  $\lambda_{\text{ex}} = 370$  nm for 3-Pyridine-BODIPY.

Varying the position of the nitrogen on the meso-pyridyl group did not have a large effect on the stokes shifts with values of  $865$   $\text{cm}^{-1}$  and  $565$   $\text{cm}^{-1}$  calculated for 3-pyridine-BODIPY and 4-pyridine-BODIPY respectively. The stokes shift was only slightly effected by the coordination of the cobaloxime centre with measurements of  $545$   $\text{cm}^{-1}$  and  $207$   $\text{cm}^{-1}$  calculated for 3-pyridine-BODIPY-cobaloxime and 4-pyridine-BODIPY-cobaloxime respectively. The small stokes shifts indicate that the pyridyl-BODIPYs do not undergo considerable excited state structural distributions following excitation. As the addition of the cobaloxime moiety does not affect the

stokes shift it is proposed that the absorption and emission both occur on the BODIPY ligand.

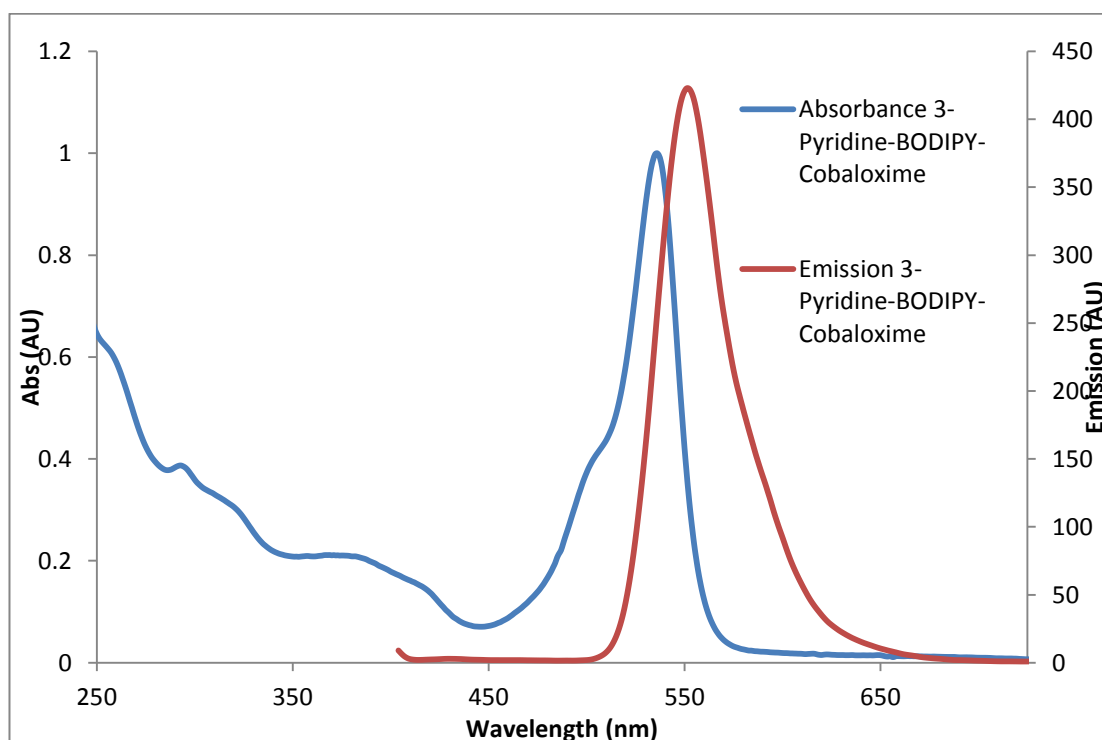
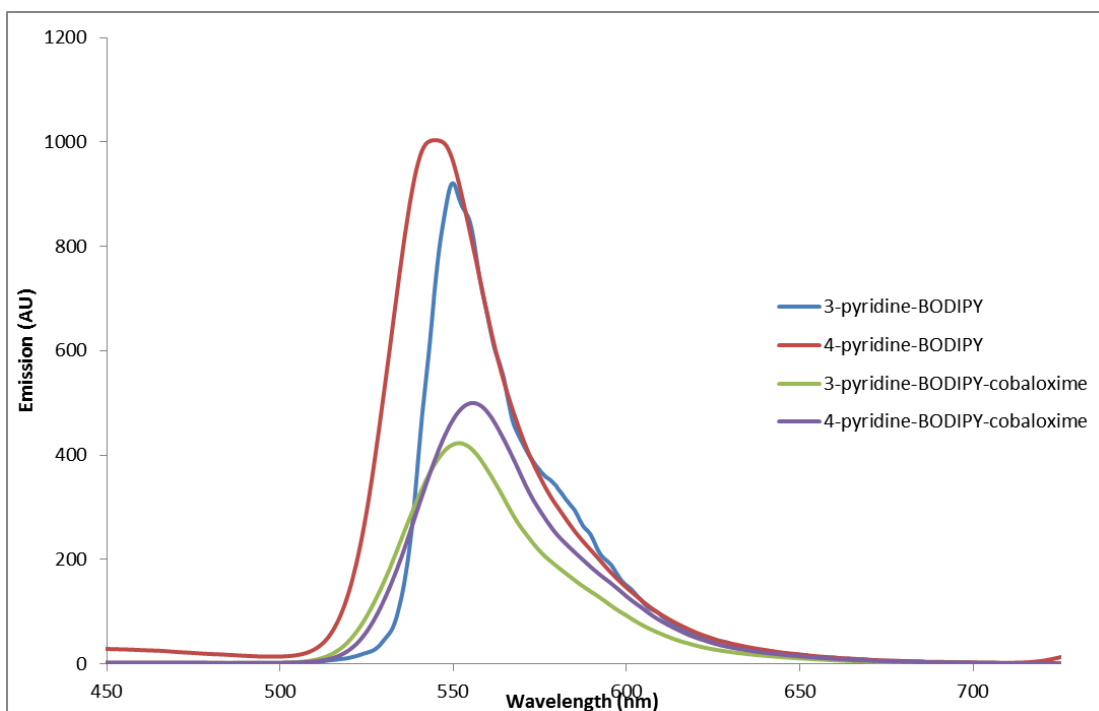


Figure 3.21 – UV-Vis spectrum and emission spectrum of 3-Pyridine-BODIPY-Cobaloxime recorded in spectrophotometric grade DCM.  $\lambda_{\text{Ex}} = 377$  nm for 3-Pyridine-BODIPY-cobaloxime.

The most obvious difference in the fluorescence spectra of the BODIPYs and the cobaloxime coordinated BODIPYs is that the emission intensity of the cobaloxime derivatives are reduced with respect to the uncoordinated BODIPY compound (Fig. 3.22). This quenching would seem to indicate electronic communication between the BODIPY ligand and the cobalt metal centre. The quenching in the emission of the cobaloxime complexes is  $\sim 50\%$  when compared to the BODIPY ligands alone, signifying that intramolecular electron or energy transfer between the  $\pi$ -BODIPY electrons and the cobalt metal centre is occurring following excitation.



**Figure 3.22-** Emission spectra for 3-pyridine-BODIPY (blue line), 4-pyridine-BODIPY (red line), 3-pyridine-BODIPY-cobaloxime (green line) and 4-pyridine-BODIPY-cobaloxime (purple line). All spectra were recorded in spectrophotometric grade DCM.

The fluorescence lifetimes ( $^1\tau$ ) were recorded in dichloromethane and are included in Table 3.3. A lifetime of  $5.94 \pm 5\%$  was observed for 3-pyridine-BODIPY and  $4.82 \pm 5\%$  for 4-pyridine-BODIPY, which is in good agreement with the literature reported values for similar BODIPY complexes of between  $2.8$  and  $5.0 \pm 5\%$ .<sup>9,10</sup> Upon complexation of the cobaloxime unit there was little difference in the lifetimes calculated ( $4.88 \pm 1$  ns and  $3.66 \pm 1$  ns for 3-pyridine-BODIPY-cobaloxime and 4-pyridine-BODIPY-cobaloxime respectively). Typical fluorescence decays observed for 3-pyridine-BODIPY and 3-pyridine-BODIPY-cobaloxime are shown in Fig. 3.23 and Fig. 3.24. As cobaloxime and pyridine-cobaloxime were non-emissive no lifetimes were measured.

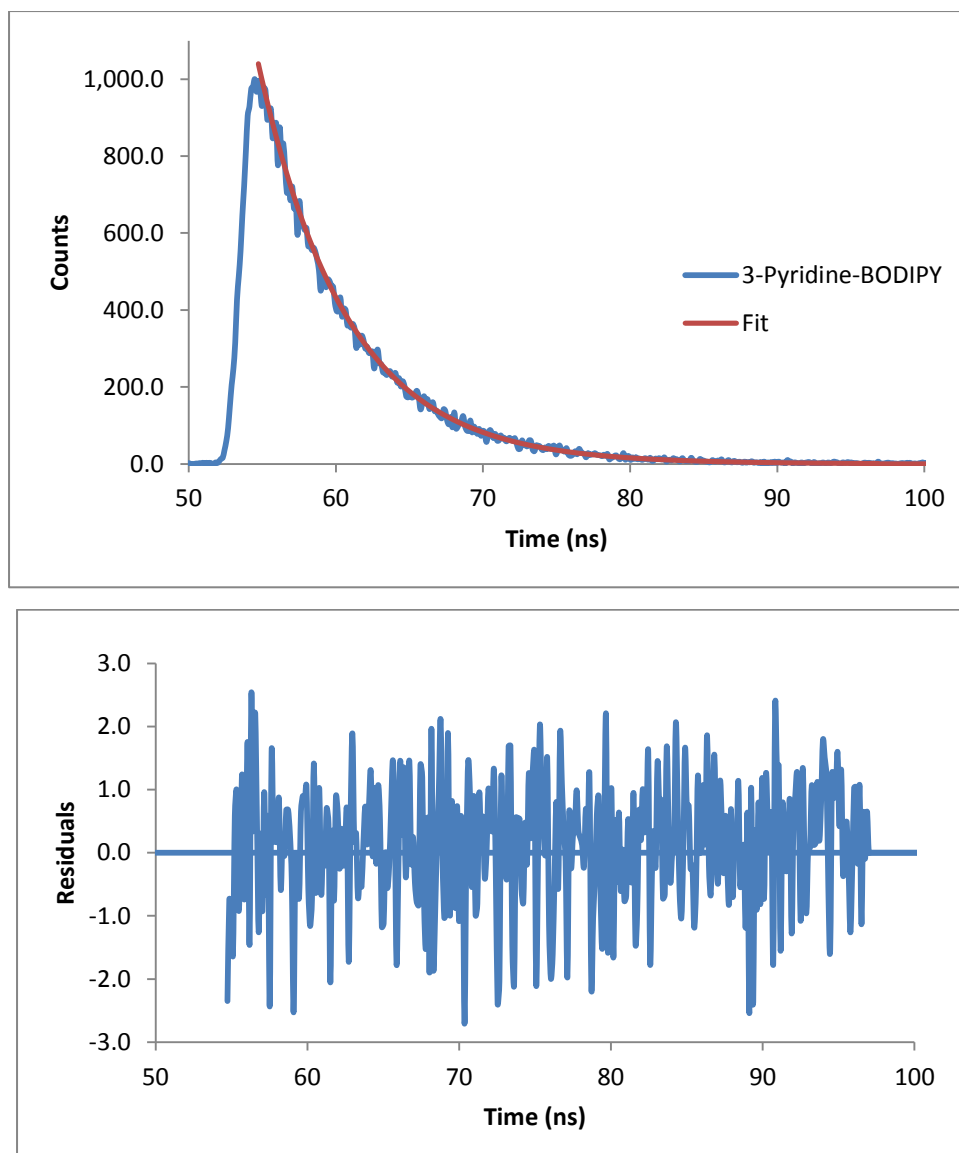


**Figure 3.23-** Typical fluorescence decay observed for 3-pyridine-BODIPY ( $^1\tau = 5.94$  ns) following excitation at 549 nm. Singlet lifetime is measured  $\pm 5\%$ .

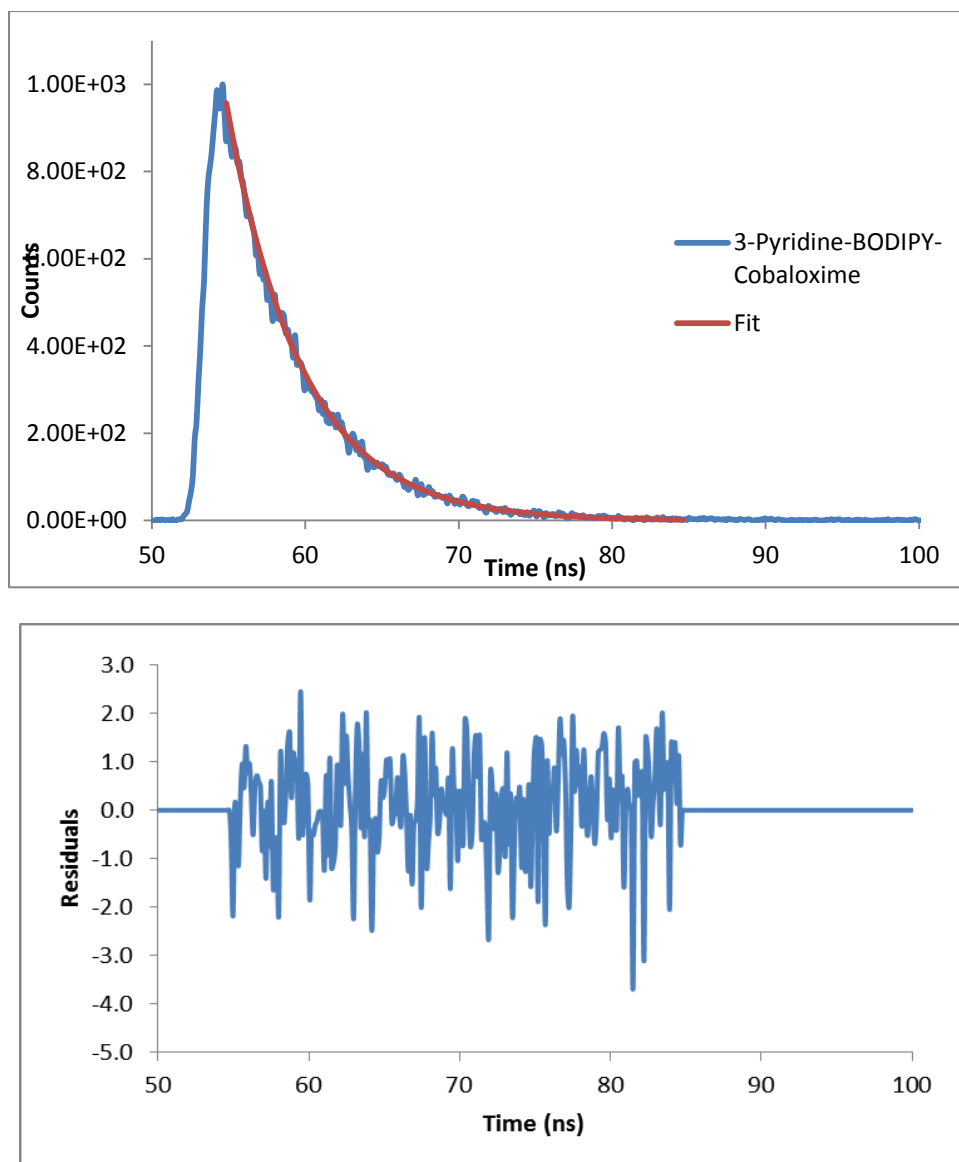


Figure 3.24-Typical fluorescence decay observed for 3-pyridine-BODIPY-cobaloxime ( $^1\tau = 4.88$  ns) following excitation at 549 nm. Singlet lifetime is measured  $\pm 5\%$ .

**Photocatalytic H<sub>2</sub> generation Experiments.** In efforts to develop novel, non-noble metal photocatalytic systems the utilisation of cobalt is an ideal alternative to expensive and rare metals. Using the BODIPY moiety as a light harvesting complex, efficient electron transfer through the meso-pyridyl ring to the cobalt catalytic centre was anticipated. BODIPY ligands are known to be efficient light absorbing complexes<sup>12-14</sup> and have been used in a variety of systems as effective electron transfer devices.<sup>13,14</sup> Cobaloxime complexes have demonstrated efficacy in the photocatalysed production of hydrogen<sup>28-31</sup> and TONs of up to  $\sim 300$  have been achieved. Here all of the complexes; 3-pyridine-BODIPY, 4-pyridine-BODIPY,



cobaloxime, 4-pyridine-cobaloxime, 3-pyridine-BODIPY-cobaloxime and 4-pyridine-BODIPY-cobaloxime were studied for their capacity to generate H<sub>2</sub> photocatalytically. Unfortunately no H<sub>2</sub> was detected in the headspace of any of the vials during the photocatalytic experiments. Low TONs for H<sub>2</sub> production have been reported for cobaloxime complexes which are similar to those reported in this study, however, BODIPY has yet to be used as a photosensitiser in this type of experiment. The reasons for the lack of hydrogen produced by these systems are at present not clear, however, it is proposed that either no H<sub>2</sub> has been produced photochemically or the amount produced was below the limit of detection for our instrument. The absorption features of BODIPY unit were tuned to be as close to the 470 nm light source as possible, while the cobaloxime derivatives absorb in the region of the UV light source used which has a wavelength of 350 nm, so absorption of light should not be a problem. Photolysis may have led to decomposition of the complexes due to the aggressive nature of the radicals formed from TEA during the regenerating process. Importantly it is also worth stating that the limit of detection of the GC used is ~100 ppm.

**Electrochemistry.** The electrochemistry of pyridyl BODIPYs and their cobaloxime coordinated counterparts have also been investigated. For comparison with the BODIPY complexes, cobaloxime and pyridine-cobaloxime have been examined under the same conditions and the data has been summarised in Table 3.3 and Table 3.4. The redox properties of the BODIPY complexes compare well with those previously reported.<sup>47</sup> Due to solubility issues accurate concentrations of samples was not possible, however, samples prepared were ~ 1 mmol.

3-pyridine-BODIPY undergoes one irreversible reduction at -1.44 V (Fig. 3.25). As the species is fully substituted in the meso and  $\beta$ - positions formation of a dimer is not expected which is common for non-substituted BODIPY dyes.<sup>13,17</sup> The process is most likely an electrochemical-chemical (EC) mechanism forming a non-electroactive species.<sup>48</sup> The coordination of a cobaloxime moiety to the BODIPY complexes produces a fully reversible wave at a similar potential, -1.435 V. The addition of a bulky cobaloxime group hinders the EC pathway which was observed using 3-pyridine-BODIPY, which most likely occurred at the meso-substituted pyridyl group.

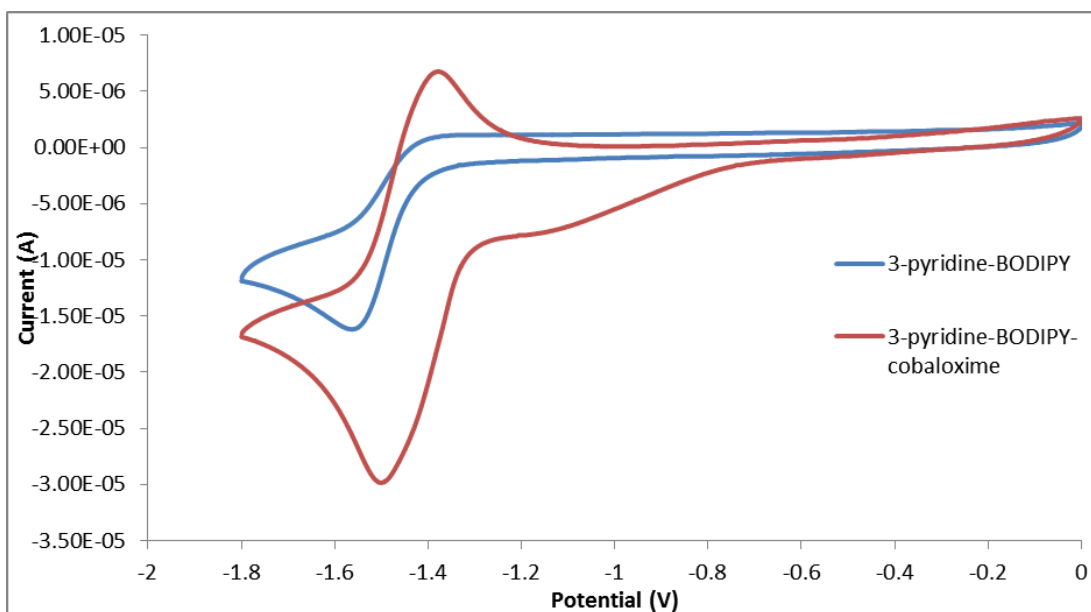


**Figure 3.25-** Cyclic voltammogram of 3-pyridine-BODIPY (blue line) and 3-pyridine-BODIPY-cobaloxime (red line) in 0.1 M TBAPF<sub>6</sub>/ACN illustrating their reduction processes. Scan rate 0.1 Vsec<sup>-1</sup>.

Cobaloxime exhibits a quasi-reversible reduction wave at -1.34 V. This is attributed to the Co<sup>2+</sup>/Co<sup>3+</sup> redox couple. Along with a reduction at the BODIPY ligand, 3- and 4-pyridine-BODIPY-cobaloxime exhibit an irreversible reduction at ~ - 1.0 V which is partially masked by the ligand based reduction (Fig. 3.26). Due to the similar potential of this reduction with that of the Co<sup>2+</sup>/Co<sup>3+</sup> redox couple in cobaloxime it is assigned to this process at the cobalt metal centre of the complex. Due to the electron withdrawing nature of the BODIPY ligand, which has been previously reported by Peña-Cabrera *et al.*,<sup>49</sup> this represents an anodic shift of 0.28 and 0.46 V for 3-pyridine-BODIPY-cobaloxime and 4-pyridine-BODIPY-cobaloxime respectively with regard to cobaloxime.

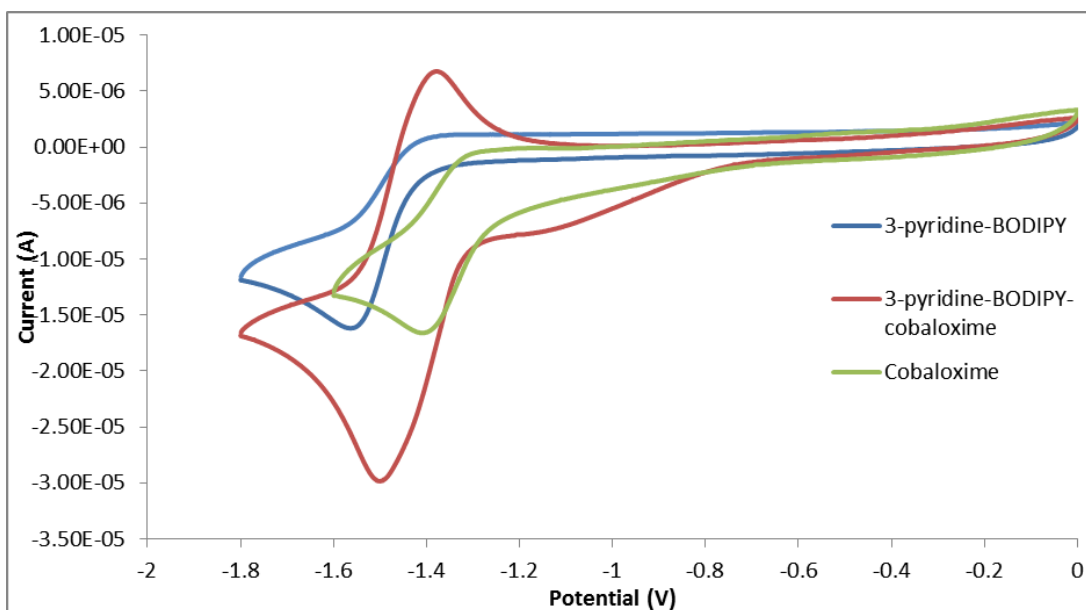


**Figure 3.26-**Cyclic voltammogram of 3-pyridine-BODIPY (blue line) and 3-pyridine-BODIPY-cobaloxime (red line) and cobaloxime (green line) in 0.1M TBAPF<sub>6</sub>/ ACN illustrating their reduction processes. Scan rate 0.1 Vsec<sup>-1</sup>.

3-pyridine-BODIPY possesses one irreversible oxidation at 0.82 V. Upon coordination of the cobaloxime unit the irreversible process is only slightly shifted by 0.06 V to 0.88 V (Fig. 3.27). 3-pyridine-BODIPY-cobaloxime possesses a irreversible oxidation at  $E_{1/2} = 0.97$  V which is directly related to the cobaloxime unit and is assigned to the  $\text{Co}^{3+}/\text{Co}^{4+}$  redox couple. Cobaloxime itself exhibits a irreversible oxidation at 0.8 V (Fig. 3.27). 4-pyridine-BODIPY-cobaloxime exhibits the same the irreversible  $\text{Co}^{3+}/\text{Co}^{4+}$  redox couple at 1.12 V, however the irreversible BODIPY based reduction is unresolved from this wave and it presumably found at a very similar potential to this process.

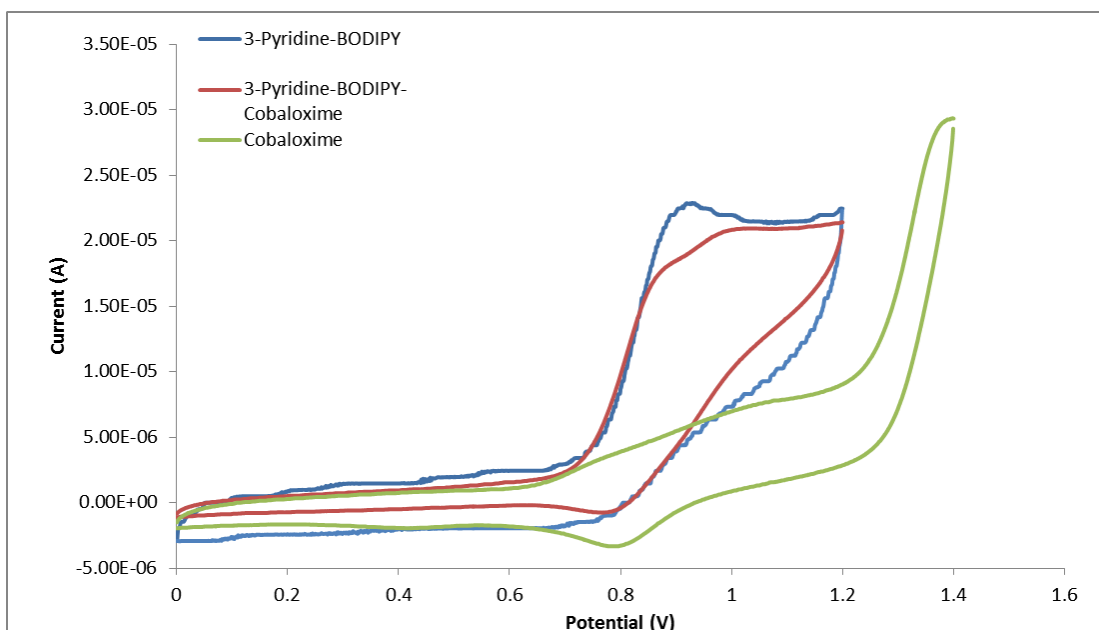


**Figure 3.27-**Cyclic voltammogram of 3-pyridine-BODIPY (blue line) and 3-pyridine-BODIPY-cobaloxime (red line) and cobaloxime (green line) in 0.1 M TBAPF<sub>6</sub>/ ACN illustrating their oxidation processes. Scan rate 0.1 Vsec<sup>-1</sup>.

In addition 3-pyridine-BODIPY-cobaloxime and 4-pyridine-BODIPY-cobaloxime exhibit another irreversible oxidation at 1.6 V and 1.73 V respectively. This process is attributed to a BODIPY based oxidation yielding the radical cation [BODIPY]<sup>•+</sup>.

Pyridine-cobaloxime exhibits the same oxidation processes as cobaloxime however these processes have been shifted to higher potentials due to the electron withdrawing effect of the pyridine moiety (Fig. 3.28.). No oxidation processes were found to occur on the pyridine group itself within the solvent potential window.

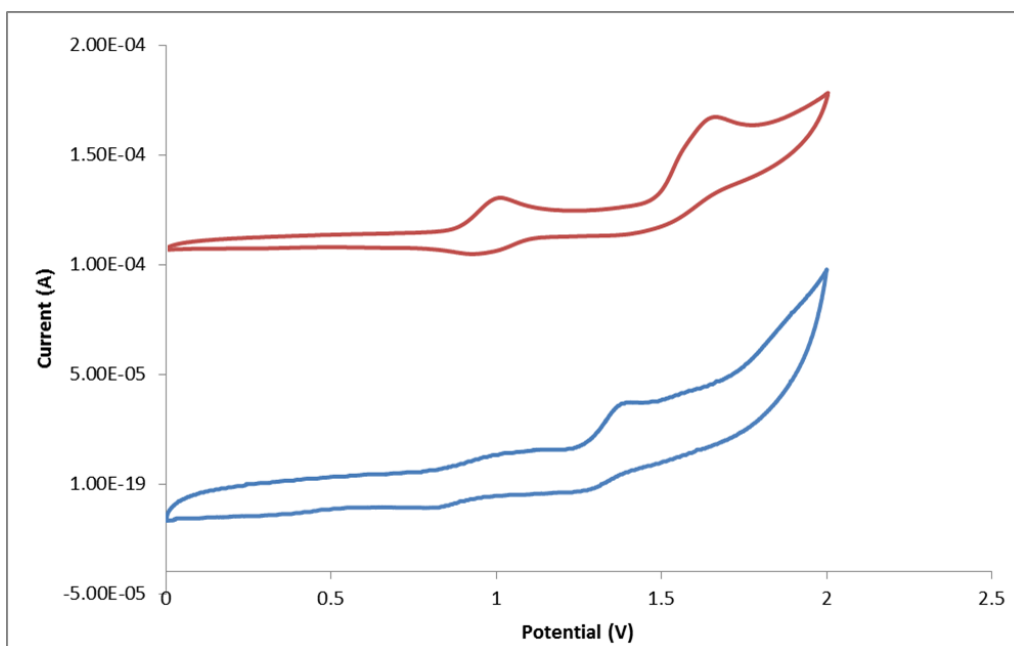


**Figure 3.28-Cyclic voltammogram of cobaloxime (blue line) and pyridine-cobaloxime (red line) in 0.1 M TBAPF<sub>6</sub>/ ACN, illustrating their oxidation processes. CV of pyridine-cobaloxime is offset along the axis for ease of viewing. Scan rate 0.1 Vsec<sup>-1</sup>.**

**Electrocatalytic H<sub>2</sub> Generation Experiments.** Following on from CV studies electrocatalytic generation of H<sub>2</sub> measurements were carried out using the same electrochemical set up but using aqueous buffer solutions. No catalytic current was observed when glassy carbon electrode surfaces were modified with any of the compounds used in this study at pH 7.0, in a 0.1 M NaH<sub>2</sub>PO<sub>4</sub> buffer. The electrocatalysis of H<sub>2</sub> production was, however, observed when the experiment was carried out in acidic media; in a pH 2.0, 0.1 M NaH<sub>2</sub>PO<sub>4</sub> buffer solution.

In Fig. 3.29 the cyclic voltammogram of the bare electrode is compared with electrodes modified with cobaloxime and pyridine-cobaloxime. As is evident from the graph, the catalytic current producing H<sub>2</sub> is generated at -1.15 V vs. Ag/AgCl using a bare electrode. Modification of this electrode surface with cobaloxime induces a greatly enhanced catalytic current, where the onset of this current occurs at -1.01 V, representing an anodic shift of 0.14 V when compared with a bare electrode. Modification of the same surface with the pyridine-cobaloxime complex also shows an improved current and the onset occurs at a lower potential, -0.96 V. The addition of the pyridine group to the cobaloxime catalytic unit moves the Co centre reduction potentials to more anodic potentials, as is evident from the cyclic voltammograms in

ACN (Section 3.3.5.1.), therefore allowing the production of H<sub>2</sub> to take place at lower potentials.

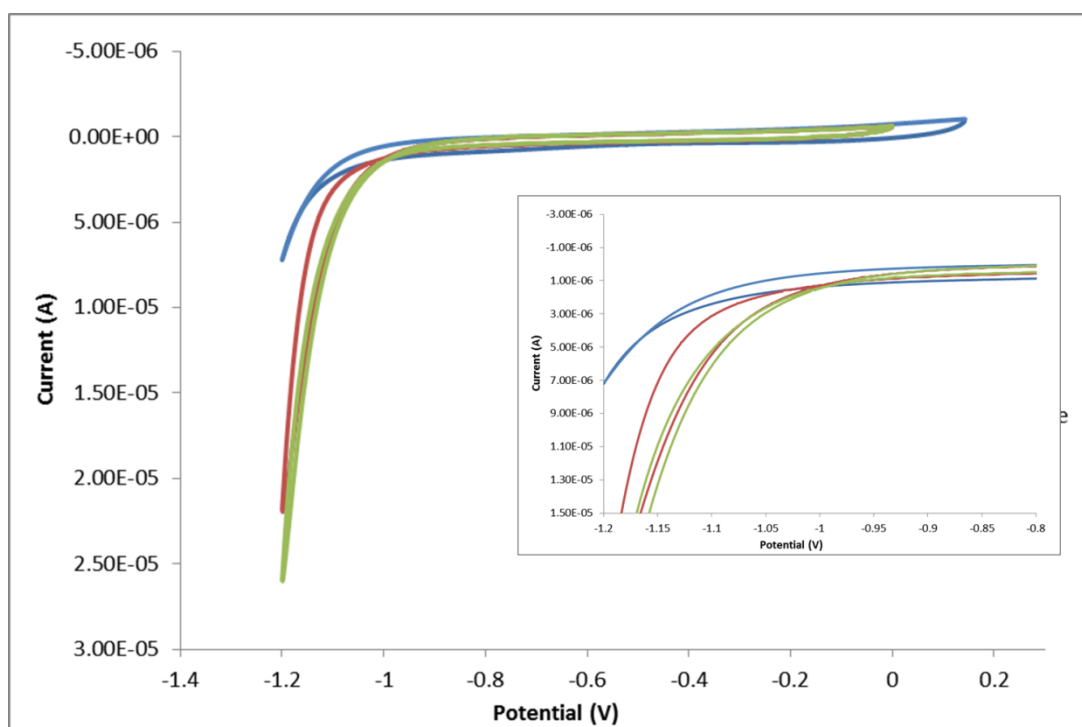


**Figure 3.29-** Typical cyclic voltammogram of a electrode modified with cobaloxime (blue line), pyridine-cobaloxime (red line) and a bare electrode (green line), in pH 2.0, 0.1 M NaH<sub>2</sub>PO<sub>4</sub> buffer. (Scan rate = 0.1 Vs<sup>-1</sup>). Inset is a closer view of the onset of the catalytic curve.

On comparing the TONs generated upon modification of the glassy carbon electrode with these two complexes in Table 3.9, the onset of the catalytic current was measured at a similar potential which is consistent with the observed intensity of the catalytic current induced using both complexes being comparable. The current density measured over the course of the hour long bulk electrolysis experiment at -1.2 V was measured as 2.18 mA/cm<sup>2</sup>, producing an electrochemically determined TON of 16.7 x 10<sup>3</sup> for cobaloxime alone, while the current density measured using the pyridine-cobaloxime complex was slightly less at 1.86 mA/cm<sup>2</sup> (TON = 11.7 x 10<sup>3</sup>), this implies higher catalytic activity for the cobaloxime modified surface. The efficiencies of the systems were calculated by comparing the GC TON with that determined electrochemically. This GC generated TON is a more accurate measurement of the number of moles of H<sub>2</sub> produced as it does not take background charging into account. The pyridine-cobaloxime system presented the greatest

efficiency at 78% while cobaloxime gave a much lower value, 51%, indicating that the pyridine-cobaloxime system produces hydrogen more efficiently despite yielding a lower TON after 1 hour.

In Fig. 3.30 the cyclic voltammograms of the bare electrode (green line) is compared with the electrodes modified with 3-pyridine-BODIPY (blue line) and 3-pyridine-BODIPY-cobaloxime (red line). A similar onset of the catalytic current was observed for 3-pyridine-BODIPY and the bare electrode at -1.0 V and -1.05 V vs. Ag/AgCl respectively however, an enhancement of this catalytic current was observed upon modification of the electrode surface.

Modification of the electrode with 3-pyridine-BODIPY-cobaloxime also showed a significant enhancement of the catalytic current, in fact the addition of the cobaloxime group allowed for and even greater improvement when compared with the 3-pyridine-BODIPY coated electrode. Also evident is a 0.25 V anodic shift in the onset of the catalytic current (at -0.90 V) when 3-pyridine-BODIPY-cobaloxime is employed. The onset is at a similar potential as was observed for the Co metal based reduction in the cyclic voltammogram in ACN (Section 3.5.5.1.), which suggests that this enhanced current is due to the presence of the Co centre on the cobaloxime moiety being involved in the reduction of H<sub>2</sub>.

The TONs generated upon modification of the glassy carbon electrode with the 3-pyridine-BODIPY and 3-pyridine-BODIPY-cobaloxime complexes followed the trend observed for the onset of the catalytic current. 3-pyridine-BODIPY produced a current density of 0.49 A/m<sup>2</sup> over the course of the hour long bulk electrolysis experiment at -1.2 V, producing an electrochemically determined TON of 5.5 x 10<sup>3</sup>, while the current density measured when using 3-pyridine-BODIPY-cobaloxime was 1.51 A/m<sup>2</sup> and a TON of 21.4 x 10<sup>3</sup> was calculated, implying a higher catalytic activity utilising the cobaloxime derivative. The 3-pyridine-BODIPY system, however, presented the greatest efficiency at 94% while 3-pyridine-BODIPY-cobaloxime achieved only 65% efficiency.

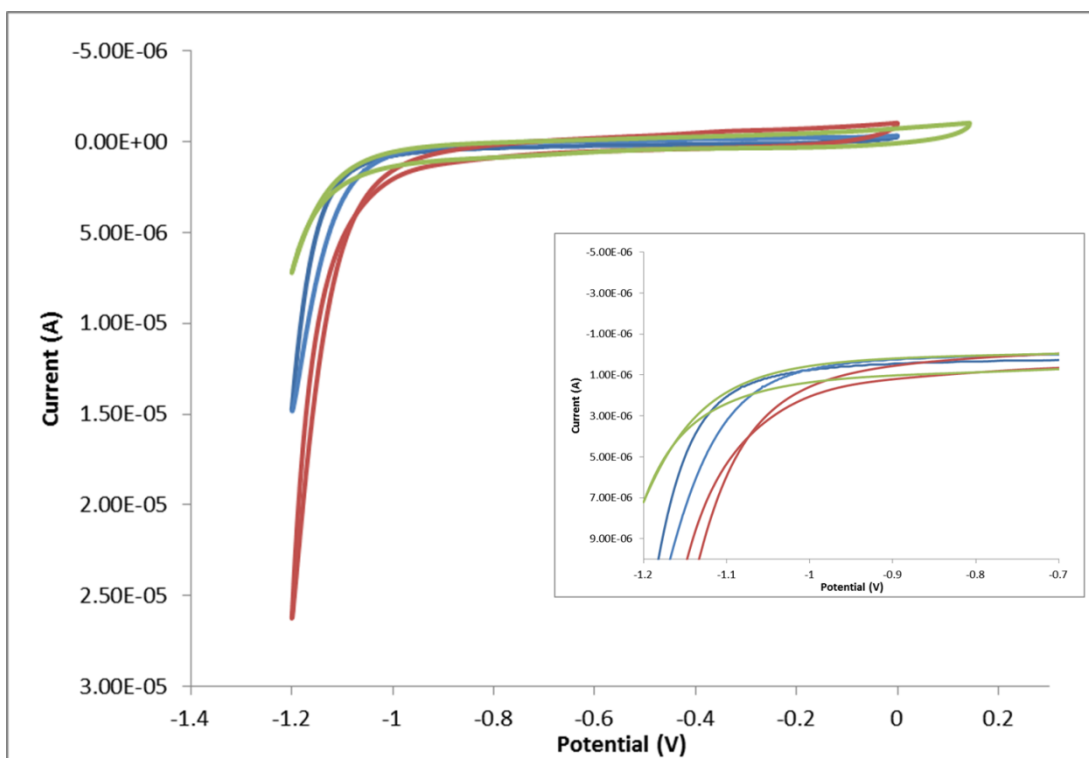


**Figure 3.30-** Typical cyclic voltammogram of a electrode modified with 3-pyridine-BODIPY (blue line), 3-pyridine-BODIPY-cobaloxime (red line) and a bare electrode (green line), in pH 2.0, 0.1 M  $\text{NaH}_2\text{PO}_4$  buffer. (Scan rate =  $0.1 \text{ Vs}^{-1}$ ). Inset is a closer view at the onset of the catalytic current.

Similar trends in catalytic current induction were observed when cyclic voltammograms of electrodes modified with 4-pyridine-BODIPY and 4-pyridine-BODIPY-cobaloxime were carried out (Fig. 3.31). Incorporating 4-pyridine-BODIPY on the electrode surface affords a greatly enhanced current when compared to the bare electrode experiment. Upon modification with 4-pyridine-BODIPY-cobaloxime onset of the catalytic current is at an even more positive potential. Again the onset of the catalytic current on the bare electrode ( $-1.15 \text{ V}$ ) is much more negative than the onset observed for the 4-pyridine-BODIPY modified electrode ( $-0.95 \text{ V}$ ). However, the onset of the current when the 4-pyridine-BODIPY-cobaloxime modified electrode is employed is observed at  $-0.8 \text{ V}$  representing an anodic shift of  $0.35 \text{ V}$  when compared with the bare electrode. The onset, as with 3-pyridine-BODIPY-cobaloxime, is at a similar potential as was observed for the Co metal based reduction in the cyclic voltammogram in ACN, which implies that this enhanced current is due to the presence of the Co centre.



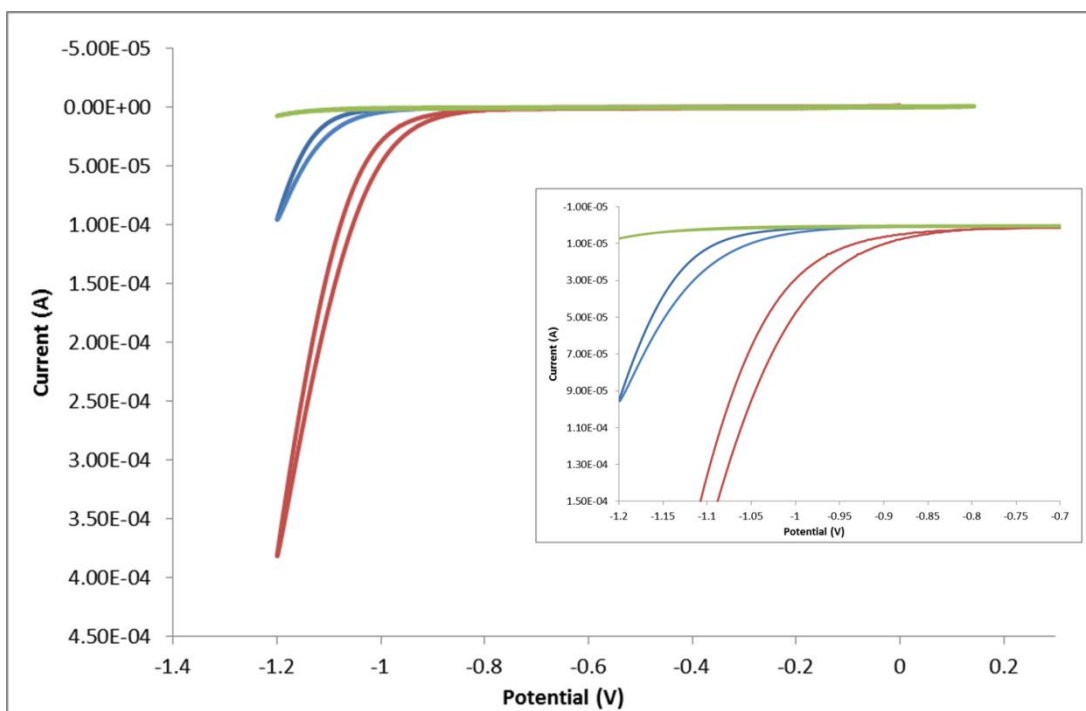


**Figure 3.31-** Typical cyclic voltammogram of a electrode modified with 4-pyridine-BODIPY (blue line), 4-pyridine-BODIPY-cobaloxime (red line) and a bare electrode (green line), in pH 2.0, 0.1 M  $\text{NaH}_2\text{PO}_4$  buffer. (Scan rate =  $0.1 \text{ Vs}^{-1}$ )

The current density measured over the course of the hour long bulk electrolysis experiment at  $-1.2 \text{ V}$  was measured as  $1.46 \text{ mA/cm}^2$ , producing an electrochemically determined TON of  $18.3 \times 10^3$  when using 4-pyridine-BODIPY-cobaloxime, while the current density measured for the 4-BODIPY ligand was only  $0.81 \text{ mA/cm}^2$  and a TON of  $5.7 \times 10^3$ . The efficiencies measured in the systems were 96 and 59 % for 4-pyridine-BODIPY and 4-pyridine-BODIPY-cobaloxime respectively implying that though the cobaloxime derivatised system produces a larger TON and more effective current density when compared with 4-pyridine-BODIPY it does not yield  $\text{H}_2$  as efficiently as the ligand alone.

When comparing the enhancement of the catalytic current between uncoordinated cobaloxime with BODIPY derivatives it is evident that the BODIPY-cobaloxime complexes show the most promise as catalytic centres for electrocatalytic  $\text{H}_2$  production. When cyclic voltammograms of the complexes were compared in ACN (Section 3.3.5.) it was evident that coordination of the BODIPY complex to the cobaloxime unit shifted the reduction potentials at the Co metal centre anodically to potentials of an average  $\sim 0.35 \text{ V}$  less negative when compared with uncoordinated

cobaloxime. The easier reduction at the metal centre means that less energy is required for the system to drive the catalytic reaction.

The results exhibited in Table 3.9 also demonstrate that the cobaloxime derivatives yielded the highest TONs for H<sub>2</sub> production. The currents passed over the course of the 1 hour experiments were also far greater for the complexes containing a cobaloxime catalytic centre. The complexation of BODIPY allows H<sub>2</sub> generation to occur at the Co metal centre on the cobaloxime moiety at these lower potentials with stronger catalytic currents produced. 3-pyridine-BODIPY-cobaloxime and 4-pyridine-BODIPY-cobaloxime yielded the highest electrochemically determined TON at  $21.4 \times 10^3$  and  $18.3 \times 10^3$  respectively which compares well with the TONs reported in the literature. The efficiency of the system, however, is greatly reduced following complexation with the cobaloxime complexes. Electrodes modified with 3-pyridine-BODIPY and 4-pyridine-BODIPY presented efficiencies of  $\sim 95\%$  respectively however upon modification with 3-pyridine-BODIPY-cobaloxime and 4-pyridine-BODIPY-cobaloxime these efficiencies dropped to  $\sim 60\%$  respectively. Cobaloxime and pyridine-cobaloxime achieved similar efficiencies  $\sim 55\%$ .

3-pyridine-BODIPY, 3-pyridine-BODIPY-cobaloxime and cobaloxime were chosen as a model system and their electrocatalytic H<sub>2</sub> generating efficacy was tested at various potentials. Presented in Table 3.8 are the TONs generated when applying various potentials during bulk electrolysis (BE). As is apparent from these results the bare glassy carbon electrode is capable of generating small amounts of H<sub>2</sub>, unmodified, at potentials above -1.2 V vs. Ag/AgCl. The currents generated by the bare electrode are quite weak; however upon applying bulk electrolysis at -1.3 V the electrode is capable of yielding a strong catalytic current at -1.15 V.

By comparison, when the electrode surface was modified with 3-pyridine-BODIPY, catalysis began at an applied potential of -1.2 V, with a current of  $1.6 \times 10^{-3}$  A being passed over the hour long experiment. An electrochemically determined TON of  $5.5 \times 10^3$  and a GC determined TON of  $5.2 \times 10^3$  were measured. Upon increasing the potential applied to -1.3 V the current passed after one hour is less than that passed by the bare electrode, implying that the modification of the surface is hindering the electrodes capabilities to catalyse the reaction at this potential. When the potential applied is less negative than -1.2 V smaller amounts of H<sub>2</sub> were generated.

As is consistent with the measured onset of the catalytic current appearing at more positive potentials, when the surface is modified with 3-pyridine-BODIPY-

cobaloxime TONs for H<sub>2</sub> generation are detectable when potentials as low as -1.0 V are applied. Electrochemically calculated TONs of 9648 and 21959 are observed following bulk electrolysis at -1.0 V and -1.2 V respectively. This displays that 3-pyridine-BODIPY-cobaloxime is capable of producing larger TONs for H<sub>2</sub> generation a -1.0 V BE than 3-pyridine-BODIPY during bulk electrolysis at -1.2 V. Similar to results obtained using 3-pyridine-BODIPY, following bulk electrolysis at -1.3 V the current passed was less than that passed by the bare electrode, implying that the modification of the surface is hindering the electrodes capabilities to catalyse the reaction at this potential itself.

Cobaloxime itself is capable of generating TONs upon application of a potential of -1.0 V however TONs generated at this potential are not as high as those produced using 3-pyridine-BODIPY-cobaloxime.

There have been no reports regarding the use of BODIPY complexes in the electrocatalytic generation of H<sub>2</sub>, however, cobaloxime complexes have been used efficiently in this process. TONs of up to 40<sup>24</sup> following potentiostat electrolysis (1 hour) at -0.96 V vs. Fc<sup>+</sup>/Fc and 5 x 10<sup>5</sup> following potentiostatic electrolysis (7 hours) at -0.6 V vs. SCE <sup>37</sup>. However, it is unclear how these TON were calculated so a direct comparison with the results presented in this study is difficult although it is clear that the complexes utilised in this study have shown potential as H<sub>2</sub> generating electrocatalysts achieving TONs of up to 2.2 x 10<sup>3</sup> after 1 hour potentiostatic electrolysis.

The onset of the catalytic current has been reported as low as -0.2 V vs. SCE using a cobaloxime complex with MeCN ligands coordinated.<sup>36</sup> However, TONs of > 5 were reported for these systems, which is significantly less than the TON reported here.

### 3.5. Conclusion

This chapter discusses the synthesis, characterisation, electrochemistry and photochemistry of *meso*-pyridine-BODIPY compounds and their corresponding cobaloxime complexes. All synthesised complexes were characterised using  $^1\text{H}$  NMR, and UV-Vis spectroscopy. Fluorescence spectroscopy was carried out along with the fluorescence lifetimes of the complexes.

Synthesis of the BODIPY photosensitiser group was achieved using a method developed by Zeissel *et al.*<sup>38</sup> and yields of ~45% were achieved which is typical for this type of compound.

The UV-vis spectra of the ligands; 3-pyridine-BODIPY and 4-pyridine-BODIPY, show strong absorbances in the UV-Vis spectrum at ~525 nm, attributed to an  $\text{S}^0 - \text{S}^1$  transition, which is typical of this type of compound.<sup>17,50,51</sup> Absorbances observed between 375 and 400 nm are attributed to  $\pi - \pi^*$  transitions localised within the pyridine unit.<sup>52</sup> Addition of the cobaloxime moiety to the ligands induced a small bathochromatic shift of ~7 nm in the strongly absorbing  $\text{S}^0 - \text{S}^1$  transition.

Due to the small Stokes shift possessed by BODIPY complexes excitation into the strongest absorbance band ( $\text{S}^0 - \text{S}^1$ ) did not yield a complete fluorescence profile. Complexation of the cobaloxime moiety to the pyridine-BODIPY complex resulted in a small bathochromatic shift of 1 to 2 nm in the emission wavelength suggesting that the emission is based only on the BODIPY complex. The fluorescence spectra of 3-pyridine BODIPY-cobaloxime and 4-pyridine BODIPY-cobaloxime showed a slightly quenched emission when compared to their BODIPY counterparts indicating electronic or energetic communication between the BODIPY to the Co metal centre.

The fluorescence lifetimes of the pyridine-BODIPY ligands were measured at 5.94 ns  $\pm$  5% and 4.82 ns  $\pm$  5% for 3-pyridine-BODIPY and 4-pyridine-BODIPY respectively. Upon complexation of the cobaloxime unit the lifetimes did not change significantly with measured values of 4.88 ns  $\pm$  5% and 3.66 ns  $\pm$  5% for 3-pyridine-BODIPY-cobaloxime and 4-pyridine-BODIPY-cobaloxime respectively.

Cyclic voltammetry of all BODIPY complexes showed that they possess an irreversible oxidation between 0.82 and 1.12 V which is attributed to the formation of a  $[\text{BODIPY}]^+$  radical cation, this process is obscured by the  $\text{Co}^{\text{III}}/\text{Co}^{\text{IV}}$  process in 4-pyridine-BODIPY-cobaloxime. Addition of a cobaloxime unit leads to the

observation of a quasi-reversible oxidation assigned to the  $\text{Co}^{\text{III}}/\text{Co}^{\text{IV}}$  redox couple along with an oxime based irreversible oxidation at high potentials between 1.39 V and 1.73 V. All BODIPY complexes also exhibited a ligand based reduction  $\sim -1.28$  v to  $-1.44$  V which is attributed to the formation of a  $[\text{BODIPY}]^{\cdot-}$  radical anion. Addition of a cobaloxime unit induces a second reduction which is assigned to the  $\text{Co}^{\text{III}}/\text{Co}^{\text{II}}$  redox couple.

During electrocatalytic  $\text{H}_2$  generation experiments 3-pyridine-BODIPY-cobaloxime and 4-pyridine-BODIPY-cobaloxime produced the largest GC determined TON over the course of the bulk electrolysis experiment at  $21.4 \times 10^3$  and  $18.3 \times 10^3$  respectively, however the efficiency of the system was measured to be only 65 and 59%. The BODIPY ligands yielded the highest efficiencies for yielding  $\text{H}_2$  at 94% for 3-pyridine-BODIPY and 96% for 4-pyridine-BODIPY but with diminished TONs of  $5.5 \times 10^3$  and  $5.8 \times 10^3$  respectively when compared with their cobaloxime analogues.

Any  $\text{H}_2$  that may have been produced photocatalytically was not detected on the GC during the studies; this is either because it was not produced or the amount produced was lower than the LOD of the GC.

## Bibliography

---

- <sup>1</sup> A. P. de Silva, H. Q. N. Gunaratne, T. Gunnlaugsson, A. J. M. Huxley, C. P. McCoy, J. T. Rademacher, T. E. Rice, *Chem. Rev.*, **1997**, 97, 1515.
- <sup>2</sup> Z. Li, T. Lin, S. Liu, C. Huang, T. W. Hudnall, F. P. Gabbaï, P. S. Conti. *Chem. Commun.*, **2011**, 47, 9324.
- <sup>3</sup> M. Cornelius, C. G. C. T. Wörth, H. C. Kliem, M. Wiessler, H. H. Schmeiser, *Electrophoresis*, **2005**, 26, 13, 2591.
- <sup>4</sup> Y. Gabe, T. Ueno, Y. Urano, H. Kojima, T. Nagano, *Anal. Bioanal. Chem.*, **2006**, 386, 3, 621.
- <sup>5</sup> N. Basari, M. Baruah, W. Qin, B. Metten, M. Smet, W. Dehaen, N. Boens, *Org. Biomol. Chem.*, **2005**, 3, 2755.
- <sup>6</sup> A. Treibs, F. Kreuzer, *Justus Liebigs Ann. Chem.* **1968**, 718, 208-223.
- <sup>7</sup> B. I. Greene, A. A. Lamola, C. V. Shank, *Proc. Natl. Acad. Sci. U.S.A.*, **1981**, 78, 2008.
- <sup>8</sup> S. Hattori, K. Ohkubo, Y. Urano, H. Sunahara, T. Nagano, Y. Wada, N. V. Tkachenko, H. Lemmetyinen, S. Fukuzumi, *J. Phys. Chem. B.*, **2005**, 109, 15368.
- <sup>9</sup> T.K. Khan, M. S. Shaikh, M. Ravikanth, *Dyes Pigm.*, **2012**, 94, 66.
- <sup>10</sup> V. R. Donuru, G. K. Vegesna, S. Velayudham, S. Green, H. Liu, *Chem. Mater.* **2009**, 21, 2130.
- <sup>11</sup> G. Ulrich, S. Goeb, A. De Nicola, P. Retailleau, R. Ziessel, *Synlett*, **2007**, 10, 1517.
- <sup>12</sup> M. Bröring, R. Krüger, S. Link, C. Kleeberg, S. Köhler, X. Xie, B. Ventura, L. Flamigni, *Chem. Eur. J.*, **2008**, 14, 2976.

- 
- <sup>13</sup> F. Li, S. I. Yang, Y. Cicingh, J. Seth, C. H. Martin, D. L. Singh, D. Kim, R. R. Birge, D. F. Bocian, D. Holton, J. S. Lindsey, *J. Am. Chem. Soc.*, **1998**, 120, 10001.
- <sup>14</sup> S. Yin, V. Leen, C. Jackers, D. Beljonne, B. Van Averbek, M. Van der Auweraer, N. Boens, W. Dehaen, *Chem. Eur. J.*, **2011**, 17, 13247.
- <sup>15</sup> A. Harriman, L. J. Mallon, K. J. Elliot, A. Haefele, G. Ulrich, R. Ziessel, *J. Am. Chem. Soc.*, **2009**, 131, 13375.
- <sup>16</sup> W. Wu, Jianzhang Zhao, H. Guo, J. Sun, S. Ji, Z. Wang, *Chem. Eur. J.*, **2012**, 18, 1961.
- <sup>17</sup> A. B. Nepomnyashchii, S. Cho, P. J. Rossky, A. J. Bard, *J. Am. Chem. Soc.*, **2010**, 132, 17550.
- <sup>18</sup> M. Kollmannsberger, T. Gareis, S. Heinl, J. Breu, J. Daub, *Angew. Chem. Ed. Engl.* **1997**, 36, 1333.
- <sup>19</sup> J. Suk, K. M. Omer, T. Bura, R. Ziessel, A. J. Bard, *J. Phys. Chem. C*, **2011**, 115, 15361.
- <sup>20</sup> K. Krumova, G. Cosa, *J. Am. Chem. Soc.*, **2010**, 132, 17560.
- <sup>21</sup> G. N. Schrauzer, *Acc. Chem. Res.*, **1968**, 1, 4, 97.
- <sup>22</sup> A. Fihri, V. Artero, M. Razavet, C. Baffert, W. Leibl, M. Fontecave, *Angew. Chem. Int. Ed.*, **2008**, 47, 564.
- <sup>23</sup> M. Razavet, V. Artero, M. Fontecave, *Inorg. Chem.*, **2005**, 44, 4786.
- <sup>24</sup> P. Jacques, V. Artero, J. Pécaut, M. Fontecave, *PNAS*, **2009**, 106, 49, 20627.

- 
- <sup>25</sup> D. L. Jameson, J. J. Grzybowski, D. E. Hammels, R. K. Castellano, M. E. Hoke, K. Freed, S. Basquill, A. Mendel, W. J. Shoemaker, *J. Chem. Ed.*, **1998**, 75, 4, 447.
- <sup>26</sup> K. Ikeda, W. Liu, Y. R. Shen, H. Uekusa, Y. Ohashi, S. Koshihara, *J. Chem. Phys.*, **2005**, 112, 141103.
- <sup>27</sup> G. N. Schrauzer, L. P. Lee, and J. W. Sibert, *J. Am. Chem. Soc.*, **1970**, 92, 2997.
- <sup>28</sup> P. Connolly, J. H. Espenson, *Inorg. Chem.*, **1986**, 25, 2684.
- <sup>29</sup> P. Du, J. Schneider, G. Lo, W. W. Brennessel, R. Eisenberg, *Inorg. Chem.*, **2009**, 48, 1, 4952.
- <sup>30</sup> A. Fihri, V. Artero, A. Pereira, M. Fontecave, *Dalton Trans.*, **2008**, 5567.
- <sup>31</sup> L. M. Utschig, S. C. Silver, K. L. Mulfort, D. M. Tiede, *J. Am. Chem. Soc.*, **2011**, 133, 16334.
- <sup>32</sup> M. Razavet, V. Artero, M. Fontecave, *Inorg. Chem.*, **2005**, 44, 4786.
- <sup>33</sup> K. Kumar, B. D. Gupta, *J. Organomet. Chem.*, **2011**, 696, 3785.
- <sup>34</sup> G. Dutta, K. Kumar, B. D. Gupta, *Organomet.*, **2009**, 28, 3485.
- <sup>35</sup> O. Pantani, E. Anxolabéhère-Mallart, A. Aukauloo, P. Millet, *Electrochem. Commun.*, **2007**, 9, 54.
- <sup>36</sup> X. Hu, B. S. Brunshwig, J. C. Peters, *J. Am. Chem. Soc.*, **2007**, 129, 8988.
- <sup>37</sup> L. A. Berben, J. C. Peters, *Chem. Commun.*, **2012**, 46, 398.
- <sup>38</sup> G. Ulrich, R. Ziessel, *J. Org. Chem.*, **2004**, 69, 2070.



- 
- <sup>39</sup> T. K. Kahn, M. Ravikanth, *Tetrahedron*, **2012**, 68, 830.
- <sup>40</sup> S. Rihn, P. Retailleau, N. Bugsaliewicz, A. De Nicola, R. Ziessel, *Tetrahedron Letters*, **2009**, 50, 7008.
- <sup>41</sup> J. Rosenthal, A. B. Nepomnyashchii, J. Kozhukh, A. J. Bard, S. J. Lippard, *J. Phys. Chem. C.*, **2011**, 115, 17993.
- <sup>42</sup> A. J. Bard, L. R. Faulkner, *Electrochemical Methods: Fundamentals and Applications, Second Edition*, Wiley, **2001**.
- <sup>43</sup> P. Zhang, M. Wang, C. Li, X. Li, J. Dong, L. Sun, *Chem. Commun.* **2010**, 46, 8806.
- <sup>44</sup> L. Yu, K. Muthukumaran, I. V. Sazanovich, C. Kirmaier, E. Hindin, J. R. Diers, P. D. Boyle, D. F. Bocian, D. Holten, J. S. Lindsey, *Inorg. Chem.*, **2003**, 42, 6629.
- <sup>45</sup> R. Ziessel, C. Goze, G. Ulrich, M. Cesario, P. Retailleau, A. Harriman, J.P. Rostron, *Chem. Eur. J.*, **2005**, 11, 7366.
- <sup>46</sup> (i) A. Harriman, J. Davila, *Tetrahedron*, **1989**, 45, 4737. (ii) N. M. Boyle, *Ph.D. Thesis*, **2010**, Dublin City University.
- <sup>47</sup> M. Kollmannsberger, T. Gareis, S. Heinl, J. Breu, J. Daub, *Angew. Chem. Int. Ed. Engl.* **1997**, 36, 1333
- <sup>48</sup> C. Engtrakul, W. J. Shoemaker, J. J. Grzybowski, *Inorg. Chem.*, **2000**, 39, 5161.
- <sup>49</sup> E. Peña-Cabrera, A. Aguilar-Aguilar, M. González-Domínguez, E. Lager, R. Zamudio-Vázquez, J. Godoy-Vargas, F. Villanueva-García, *Org. Let.*, **2007**, 9, 20, 3985.

---

<sup>50</sup> T. K. Kahn, M. Ravikanth, *Tetrahedron*, **2012**, 68, 830.

<sup>51</sup> S. Rihn, P. Retailleau, N. Bugsaliewicz, A. De Nicola, R. Ziessel, *Tetrahedron Lett.*, **2009**, 50, 7008.

<sup>52</sup> J. Rosenthal, A. B. Nepomnyashchii, J. Kozhukh, A. J. Bard, S. J. Lippard, *J. Phys. Chem. C.*, **2011**, 115, 17993.

# **Chapter 4**

## **Porphyrin-Cobaloxime**

### **Complexes**

Chapter 4 begins with a short literature survey detailing the synthetic procedures which have been employed in the synthesis of meso-substituted porphyrin dyes. Briefly discussed are the photochemical and electrochemical properties of porphyrin systems which have been previously reported. Also detailed is the use of porphyrin photosensitisers in the photocatalytic and electrocatalytic of hydrogen. The synthetic procedures employed to prepare four porphyrin dyes and the additions of cobaloxime to the ligands are discussed.  $^1\text{H}$  NMR, mass spectrometry, elemental analysis, UV-vis spectroscopy and fluorescence spectroscopy were employed, where applicable, to characterise the final products. The results of cyclic voltammetry together with both photocatalytic and electrocatalytic hydrogen generation studies are presented.

## Aim

The main objective of this section of research is to synthesise a series of porphyrin dyes, for use as photosensitisers, and their cobaloxime derivatives, utilising cobalt as a catalytic centre for use in both the photocatalytic and electrocatalytic generation of H<sub>2</sub> using no noble metals. Porphyrin dyes are known to have strong absorbances in the long wavelength, blue - green region of the spectrum which could facilitate efficient H<sub>2</sub> generation following irradiation with lower energy light sources. The complexes photochemistry will be investigated through UV-Vis and fluorescence studies. Their electrochemistry will also be investigated using cyclic voltammetry.

## 4.1 Introduction

### 4.1.1. Porphyrins

Porphyrins are large highly conjugated, macrocyclic molecules which contain four pyrrole units linked through their  $\alpha$  and  $\alpha'$  positions by four methine bridges. These pigments were originally studied due to their presence in a variety of important processes in nature. Chlorophyll A used in photosynthesis and Heme A used in transporting oxygen in blood both contain porphyrin rings leading them to be at the centre of much research since their first discovery in 1912<sup>1</sup>. They contain 22  $\pi$  electrons, 18 of which are delocalised around the ring structure. Obeying Huckle's rule they contain  $4n + 2\pi$  electrons ( $n = 4$ ). The most basic porphyrin molecule is known as porphine (Fig. 4.1, **1**) and there are two principal substitution modes (Fig. 4.2, **2** and **3**). They are planar molecules which readily undergo aggregation without bulky substituents in  $\beta$  or *meso*- positions to inhibit this process.

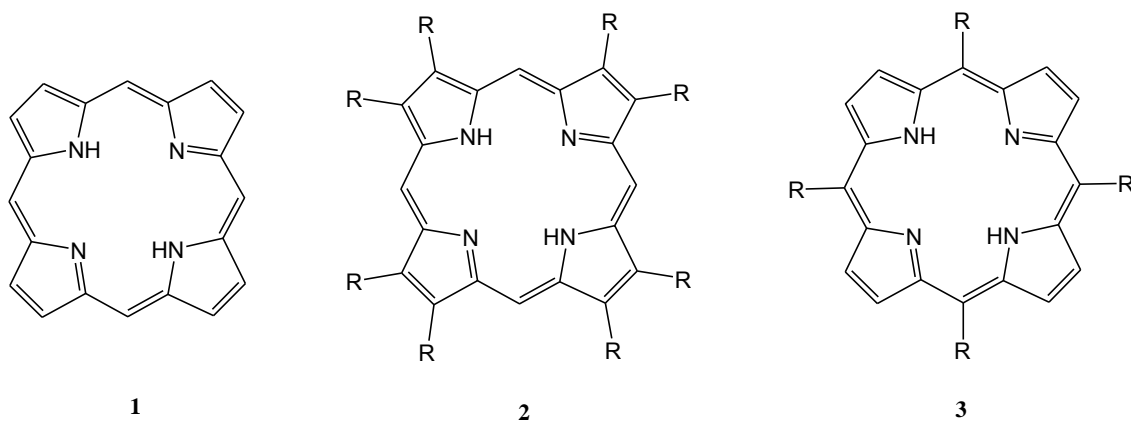


Figure 4.1- Substitution patterns in porphyrins, R= alkyl or aryl substituent.

All naturally occurring porphyrins are substituted at the  $\beta$  position (Fig. 4.1, **2**) while the majority of synthesised porphyrins are produced with substituents at the *meso*-positions (Fig. 4.2, **3**). The two nitrogen protons in the centre of the ring of the freebase porphyrin can be readily displaced by transition metal to yield the corresponding metalloporphyrin.<sup>2</sup> Porphyrins have been used as light harvesting and energy transferring groups in molecular devices. Owing to their stable and rigid structure they have been employed for a wide variety of purposes including molecular wires,<sup>3</sup> DSSCs,<sup>4</sup> photodynamic therapy,<sup>5</sup> and catalysis.<sup>6</sup> As chlorophyll molecules and Heme A molecules are complex and therefore difficult to synthesise, more simpler porphyrins have been designed to mimic the properties and uses of their much more elaborate counterparts.<sup>7</sup> It has been realised that the coordination chemistry of porphyrins is not limited to the tetrapyrrolic core, substituents on the periphery can have a profound effect on their photophysical and electrochemical properties.

#### 4.1.1.1. Synthesis of *meso*-Substituted Porphyrins

The first reported synthesis of a substituted porphyrin was reported in 1939 by Rothmund when he successfully synthesised tetraphenylporphyrin (TPP).<sup>8</sup> Benzaldehyde and pyrrole were reacted in a sealed bomb at 150°C for 24 hours producing very low yields. These reaction conditions were harsh but Rothmund

proposed that as porphyrins were aromatic and therefore stable they could survive these conditions. He reasoned that breaking the initially formed adducts of benzaldehyde and pyrrole was necessary and would therefore require very high temperatures to produce the desired porphyrin. This method was modified to use slightly less harsh conditions by Alder *et al.* in 1967.<sup>9</sup> Using propionic acid as the solvent they allowed the direct condensation of benzaldehyde with pyrrole at 141°C in the open air. The milder conditions allowed more substituted benzaldehydes to be converted to porphyrins and achieved yields of up to 20%.<sup>10</sup> Alders method was still considered problematic as it did not allow for sensitive functional groups to be incorporated into the ring structure due to the high temperatures and strongly acidic conditions. Also purification was difficult due to the large amount of “tar” produced in the reaction, however much of the methods developed in the more recent years are derived from Alder’s method of synthesis.

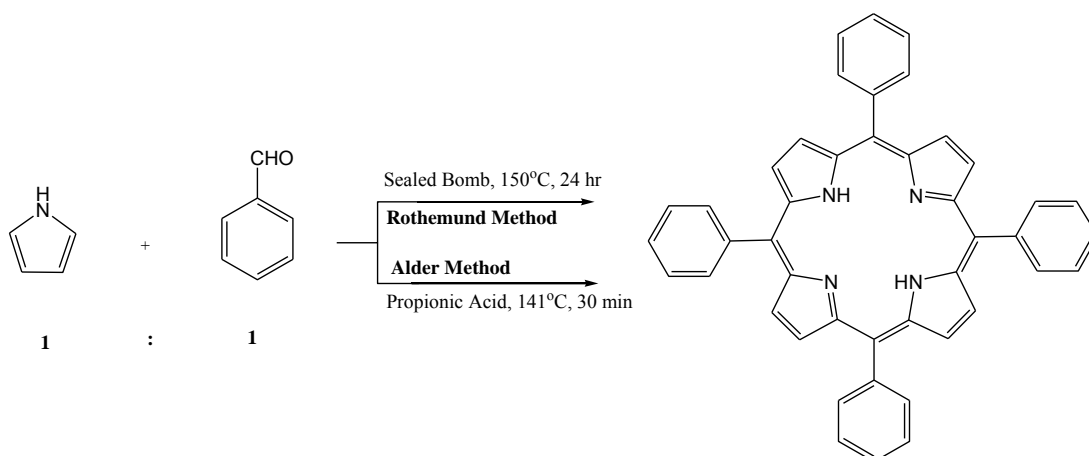


**Figure 4.2- Rothmund and Adler synthesis of meso tetraphenylporphyrin (TPP).**

Lindsey and his co-workers proposed using an acid to catalyse the synthesis of porphyrinogen from the aldehyde and pyrrole followed by oxidation to yield the desired porphyrin.<sup>11</sup> Preparing the porphyrinogen first means that the highly oxidising environments used by Rothmund and Alder can be avoided until the ring structure has been produced allowing more sensitive substituents to be incorporated. Trifluoroacetic acid (TFA) was used to catalyse the reaction while 2,3-Dichloro-5,6-dicyano-1,4-benzoquinone (DDQ) or *p*-chloranil was used as the oxidising agent,

obtaining yields of up to 55% of TPP without the harsh reaction conditions. The majority of substituted porphyrins are now synthesised according to the Lindsey method (derived from the Alder method<sup>10</sup>) as the reaction is much safer and simpler to repeat.

Arsenault *et al.*<sup>12</sup> developed a synthetic method which employed the production of dipyrromethane complexes followed by complexation to form porphyrins. The condensation of the dipyrromethane was carried out in acetic acid containing 0.4% hydrogen iodide, the subsequent oxidation was induced by aerating the solution after adding sodium acetate. Yields of up to 65% were obtained using this method. This method allowed for the more facile synthesis of mixed porphyrins, that is porphyrins where there is more than one type of substituent. Synthesising dipyrromethanes with different substituents then complexing them allows for the production of wide libraries of substituted porphyrins.

Since the development of the Lindsey method variations have been reported including the synthesis of *meso*-tetraarylporphyrins in one step without solvents or catalysts.<sup>13</sup> The reactions were carried out at temperatures 10–15 °C (up to 220°C) above the boiling point of the starting aldehydes using just air as oxidant, in doing so all reactants are reacting in the gas phase. Yields of between 7 and 23% were achieved with the simplest tetraphenylporphyrin (TPP) being formed in the greatest yield.

Shi *et al.*<sup>14</sup> reported the synthesis of very high yields of functionilised porphyrins using a commercially available porphine (Fig. 4.3). The reaction of 5,10,15,20-tetrabromoporphine magnesium complex with aryl or heteroaryl boronic acids in the presence of Pd(PPh<sub>3</sub>)<sub>4</sub> produced *meso*-substituted porphyrins in yields up to 70%. Mg(II)-5,10,15,20-tetrakisbromoporphine was synthesised from the Mg(II)-porphine through bromination. Suzuki coupling reaction conditions were employed to couple aryl boronic acid groups to the porphyrin ring. It was then possible to remove the magnesium ion to produce the freebase porphyrin.

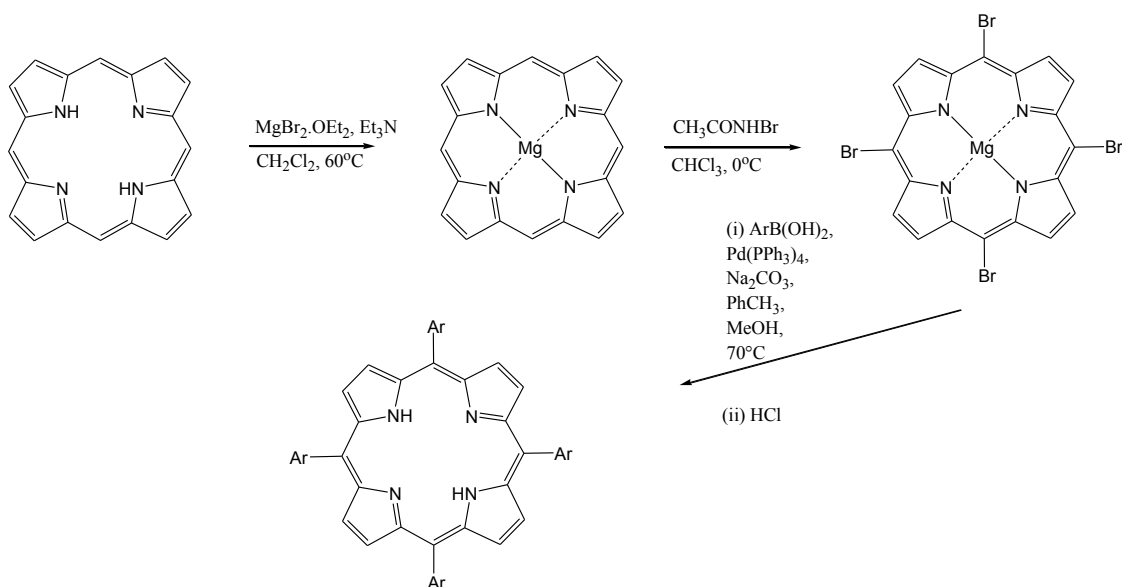


Figure 4.3- Shi procedure to produce meso functionalised porphyrins.<sup>14</sup>

However, these percentage yields are not fully comparable to other yields reported as the greatest loss of yield is in the synthesis of the porphyrin ring itself which Shi *et al.* did not produce.

#### 4.1.1.2. Photochemistry of Porphyrins

Porphyrins have very distinctive UV-Vis absorption spectra and absorb strongly in the blue and weakly in the green region which mimics the absorption properties of chlorophyll pigments in photosynthesis. There are two characteristic types of absorbance bands produced by porphyrins; the Soret band region which is generally in the UV region of the spectrum and the Q- bands region which generally stretches from the UV to the visible region of the spectrum. The Soret band is known to arise due to a strong transition to the second excited state ( $S_0 \rightarrow S_2$ ) and usually occurs between 390 – 430 nm. This is the strongest absorbance in the porphyrin spectrum and can have molar extinction coefficients up to  $10^5 \text{ M}^{-1} \text{ cm}^{-1}$ . Four more, less intense, absorptions arise in a freebase porphyrin spectrum due to the  $D_{2h}$  symmetry of the complex. These are known as quasi-allowed (Q) bands and are due to  $S_0 \rightarrow S_1$  transition to the first, lowest energy excited state and are observed between 500 and



700 nm. Metalloporphyrins only give rise to two Q-bands as they possess  $D_{4h}$  symmetry and are therefore more symmetrical than their freebase counterparts.<sup>15</sup> These Q-bands are often labelled as the following, from highest wavelength to lowest:

- $Q(0,0)$ , the excitation into the lowest energy excited state in a metalloporphyrin,
- $Q(1,0)$ , a vibrational overtone of  $Q(0,0)$ , found at a higher energy wavelength,
- $Q_x(0,0)$ ,  $Q_y(0,0)$ , the excitation into the lowest energy excited state in a freebase porphyrin split due to the change in symmetry when compared to a metalloporphyrin and
- $Q_x(1,0)$ ,  $Q_y(1,0)$ , two vibrational overtones from  $Q_x(0,0)$  and  $Q_y(0,0)$  in a freebase porphyrin.

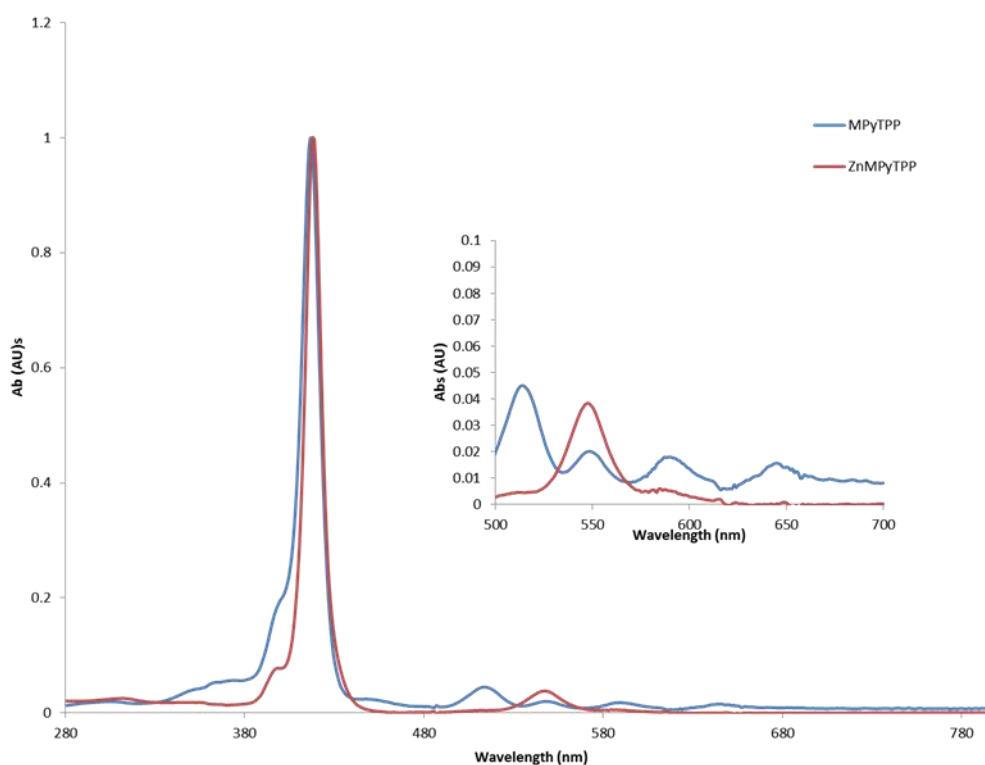


**Figure 4.4-** Example of a UV spectrum of a porphyrin illustrating the strong Soret band and (inset) the q-bands. Blue line – MPyTPP, four q-bands, red line = ZnMPyTPP, two q-bands.

The nature of the metal centre coordinated in the ring can greatly affect the absorption and emission spectra of porphyrins. Transition metals from some of the first row which have no partially filled d-orbitals such as  $\text{Zn}^{\text{II}}$  or  $\text{Ti}^{\text{IV}}$  and do not perturb the  $\pi$  conjugation of the porphyrin ring and so have little influence on the absorption and emission spectra, which are said to be *normal*. When there are strong interactions between the partially filled d-orbitals of the metal and the  $\pi$ -orbitals of the porphyrin the spectra are said to be *irregular*. Two types of *irregular* spectra are possible. *Hypso* spectra exhibit Q-bands which are blue shifted in relation to the freebase porphyrin. This shift is due to a strong mixing of the d-orbital electrons with the lowest unfilled porphyrin  $\pi^*$ -orbital. This usually occurs with metal centres such as  $\text{Fe}^{\text{II}}$  (low spin) and  $\text{Co}^{\text{II}}$ . *Hyper* spectra exhibit a red shift in the absorbance of the Q-bands. This shift of absorbances to lower energy generally occurs with coordination of high spin metals such as  $\text{Fe}^{\text{II}}$  (high spin) and  $\text{Mn}^{\text{III}}$ .<sup>16</sup>

The addition of a pyridyl-cobaloxime peripheral unit shows a slight red-shift of  $\sim 5$  nm in the absorption spectrum of the porphyrin.<sup>28</sup> These red-shifts have been attributed to a coordinate interaction between the pyridyl functionalised porphyrin unit and the cobalt centre of the cobaloxime.

Energy transfer from porphyrins has been well studied as it is a crucial step in photosynthesis. Porphyrins and metalloporphyrins are known to possess efficient electron transfer rates which make them particularly useful as photosensitiser. The electron transfer from a copper porphyrin (CuMeTPP) and its corresponding freebase porphyrin via a  $-(\text{CH}_2)_3-$  bridge was measured.<sup>17</sup> The movement of energy within the dyad is attributed to a triplet-triplet energy transfer due to a dipole-dipole interaction in the excited porphyrin dyad. The decay lifetime of emission of the dimer is 3.1 ns in toluene, while that of the monomeric free base porphyrin is 11.7 ns demonstrating that the copper porphyrin in the dimer quenches the excited free-base counterpart.

Gonen *et al.*<sup>18</sup> investigated the electron transfer rate of a ZnTPP- $\text{H}_2$ TPP dyad (Fig. 4.5) in an uniaxial liquid crystal and a glass matrix at 100K and 10K. Using EPR spectroscopy it was determined that the electron transfer rate from ZnTPP\*- $\text{H}_2$ TPP  $\rightarrow$  ZnTPP- $\text{H}_2$ TPP\* was  $[1.0 \pm 0.2] \times 10^9 \text{ s}^{-1}$  at 10K. The transfer occurs between the ZnTPP triplet excited state and the triplet state of the  $\text{H}_2$ TPP complex. Excitation into the  $\text{H}_2$ TPP component resulted in a slower electron transfer rate of  $\sim 3 \times 10^9 \text{ s}^{-1}$ . The slower rate from the  $\text{H}_2$ TPP may be due to the efficient relaxation of freebase

porphyrin. In fact emission is almost completely quenched when excitation into the H<sub>2</sub>TPP moiety is monitored by fluorescence spectroscopy.

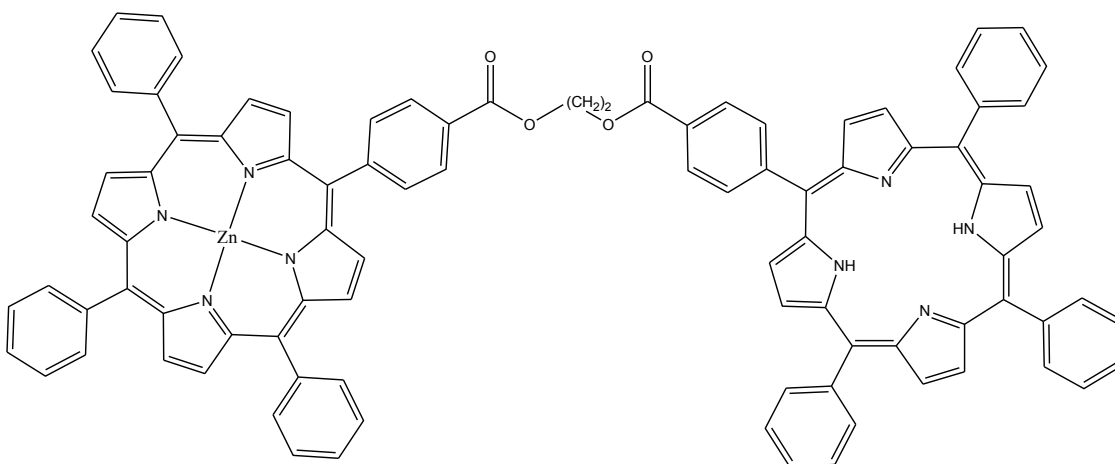


**Figure 4.5 - ZnTPP-H<sub>2</sub>TPP dyad used by Gonen *et al.*<sup>18</sup>**

Electrostatically bound porphyrin dimers have also been observed to undergo efficient electron transfer.<sup>19</sup> These dimers closely mimic the actions of porphyrins in proteins in the body which are held in space by charge distribution within the proteins themselves. The metalloporphyrin dimers zinc(II) tetrakis(4-sulfonatophenyl)porphyrin and magnesium(II) tetrakis(4-*N,N,N*-trimethylanilinium)porphyrin, i.e., **4**, [ZnTSPP-MgTTAP], and zinc(II) tetrakis(4-*N,N,N*-trimethylanilinium)porphyrin and magnesium(II) tetrakis(4-sulfonatophenyl)porphyrin, i.e., **5**, [ZnTTAP-MgTSPP] (Fig. 4.6) exhibit a high efficiency of triplet state production upon photoexcitation and the relatively long lifetime of this photoexcited triplet state allows their participation in intramolecular electron transfer and energy transfer reactions.

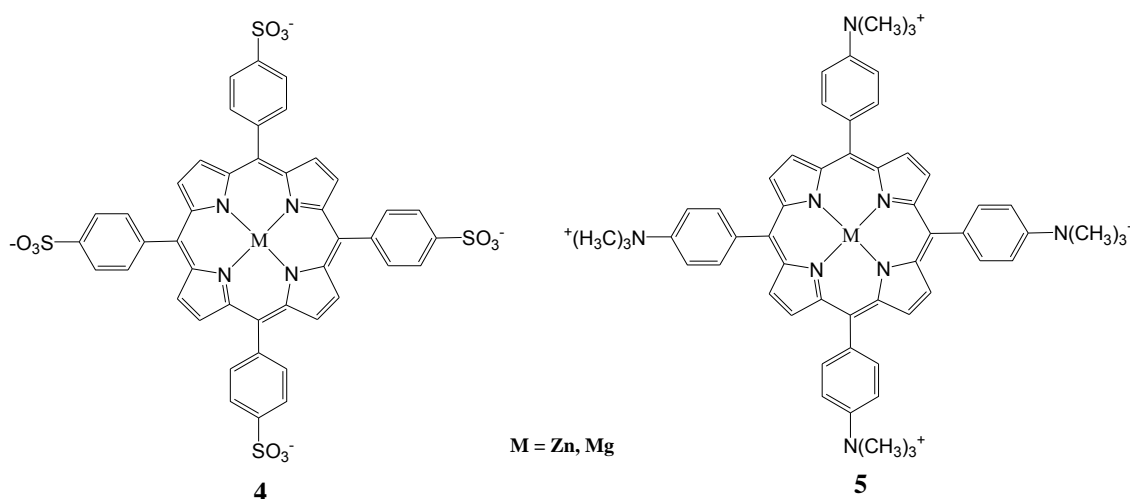
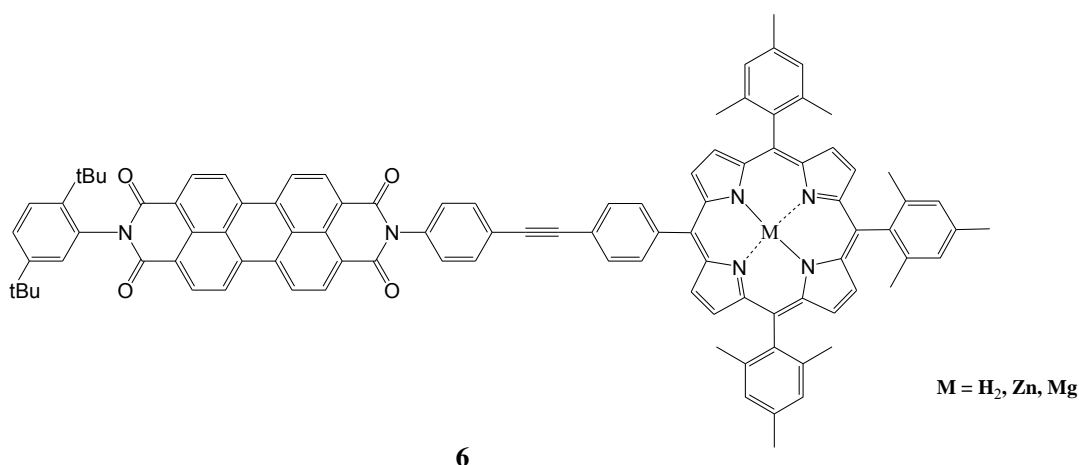


Figure 4.6- Electrostatically bound porphyrin models employed by Berg *et al.*<sup>19</sup>

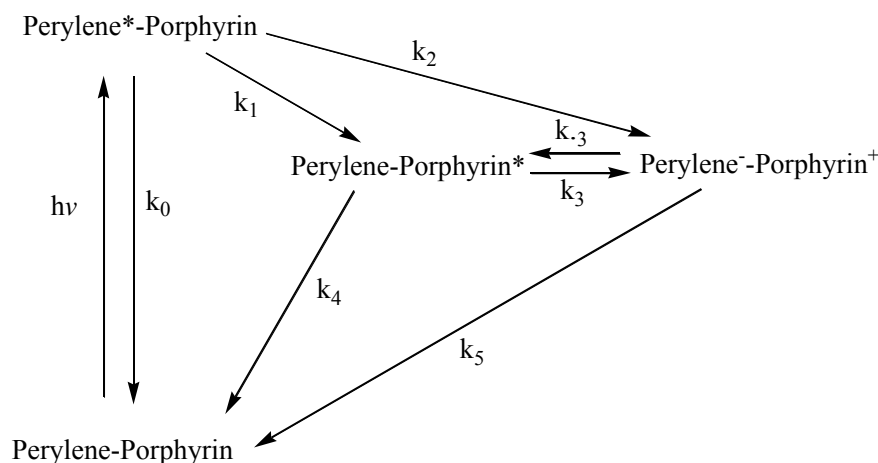
The singlet energy level of the Zn-porphyrins were found to be of an order of magnitude higher in eV than that of the Mg-porphyrins, therefore it was proposed that the intramolecular energy transfer (IEnT) occurs from the Zn-porphyrin to the Mg-porphyrin through a singlet excited state. This is then followed by intersystem crossing within the Mg-porphyrin.<sup>19</sup> Altering the meso substituents allowed not only IEnT occur but also an intramolecular electron transfer (IET) to occur in parallel. When the complex **4**, [ZnTSPP-MgTTAP], is employed, IEnT occurs from the singlet excited Zn to the Mg constituent and is the only process which occurs however when **5**, [ZnTTAP-Mg-TSPP], is employed an IET to produce the charge-separated state, [ZnTTAP<sup>•+</sup>-MgTSPP<sup>•-</sup>] occurs through a intersystem crossing on the Zn-porphyrin to yield the triplet excited porphyrin, along with an IEnT in [ZnTTAP-MgTSPP] from the singlet excited Zn-porphyrin. It was concluded that further investigations were required to fully explain the photochemical differences between the two dimers.

Yang *et al.*<sup>20</sup> studied electron transfer efficiencies from perylene-bis(imide) dye to freebase (Fb), Zn and Mg porphyrins using time resolved absorption techniques (Fig. 4.7).



**Figure 4.7-** Perylene-prophyrin dyads synthesised and studied by Yang *et al.*<sup>20</sup>

Measurements in toluene indicate that the excited perylene unit decays rapidly (Fb = 2.9 ps, Zn 2.5 ps, Mg = 2.5 ps) by energy transfer to the porphyrin forming perylene-porphyrin\* in relatively high yield (Fb = 85%, Zn = 80%, Mg = 50%) and hole transfer to the porphyrin forming perylene<sup>-</sup>-porphyrin<sup>+</sup> (Fb = 15%, Zn 20%, Mg = 50%) indicating these processes directly compete. The Fb porphyrin was found to behave differently after these processes occur. Charge recombination occurs within the perylene<sup>-</sup>-Fb<sup>+</sup>, giving rise to the energy transfer product perylene-Fb\*, which then decays to the ground state via emission. Within the Zn and Mg porphyrins predominant decay process for perylene-porphyrin\* is electron-transfer from the perylene unit producing perylene<sup>-</sup>-porphyrin<sup>+</sup> (Zn = 80%, Mg > 99%). This electron transfer is rapid and therefore quenches the emission of perylene-porphyrin\* and the non-emissive character of the perylene<sup>-</sup>-porphyrin<sup>+</sup> species means there is negligible fluorescence from the metalloporphyrin. The energy of the excited states indicated that the energy of the perylene<sup>-</sup>-porphyrin<sup>+</sup> charge separated state is higher than that of the porphyrin excited energy transfer product perylene-porphyrin\* in Fb however the opposite is true for both the Mg and Zn porphyrins.



**Scheme 4.1- Proposed state/ kinetic diagram for the perylene-porphyrin diads.<sup>20</sup>**

Measurements of the kinetics involved in the decay of the energy transfer product exposed why these differences occurred (See Scheme 4.1). In the case of all three porphyrins  $k_0$  (Scheme 4.1) occurred after 3.6 ns.  $k_1$  was measured as Fb = 3.4 ps, Zn = 3.1 ps and Mg = 5.0 ps following excitation to yield perylene-porphyrin\* while  $k_2$  was measured as Fb = 19.3 ps, Zn = 12.5 ps and Mg = 5.0 ps. The decay processes from perylene<sup>-</sup>-porphyrin<sup>+</sup> to perylene-porphyrin\* ( $k_3$ ) in Fb was measured as 0.5ns whereas decay to the ground state was measured to be less rapid at 5 ns indicating a preferred route to produce perylene-porphyrin\*. In the Zn and Mg porphyrins  $k_3$  was observed to occur much more rapidly (0.5 and 0.14 ns respectively) than  $k_4$  (2.4 and 10.0 ns) showing decay occurring mostly through the  $k_3 - k_5$  route.

#### **4.1.1.3. Porphyrins Used in the Light driven Processes**

##### **4.1.1.3.1. Solar cells**

Porphyrins have been incorporated into TiO<sub>2</sub> surfaces when producing dye-sensitised solar cells (DSSCs).<sup>21,22,23</sup> Zn-Zn porphyrin dimers have been utilised at photosensitisers chemically bound to TiO<sub>2</sub> in DSSCs by Mozer *et al.*<sup>21</sup> Both a linear anti and a 90° *syn* linked porphyrin were synthesised (Fig. 4.8) and tested for their photocurrent inducing efficiencies.

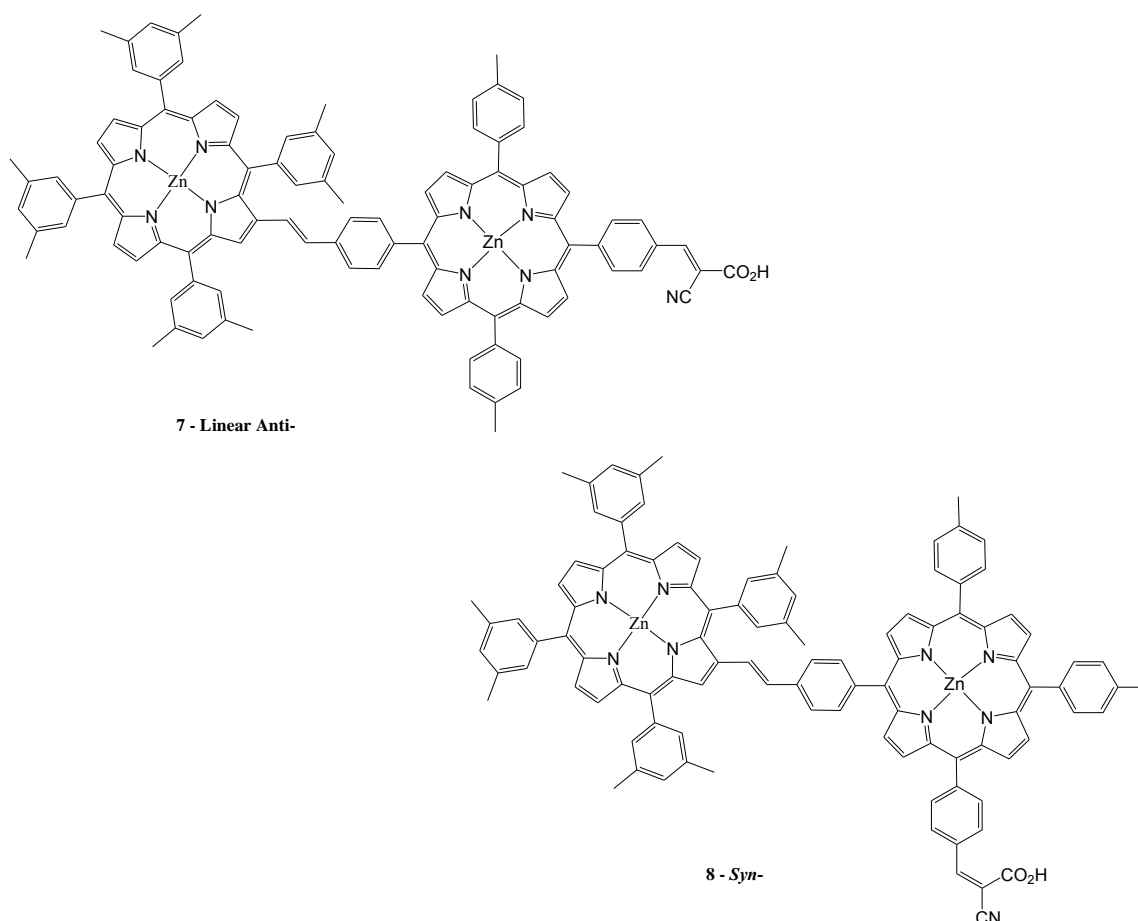


**Figure 4.8- Zn-porphyrin dyads incorporated into DSSCs by Mozer *et al.*<sup>21</sup>**

Both of the Zn-porphyrin chromophores were found to efficiently inject electrons into the TiO<sub>2</sub> surface. Up to 70% absorbed photon to current energy efficiency was achieved for both configurations were measured using fs-transient absorption spectroscopy. It was also noted that there was no significant difference in results generated by the linear anti or *syn* linked dimers suggesting that both configurations could be utilised in DSSCs equally. Dye uptake on the surface did not contribute significantly to the efficiency of the cell also, implying that steric hindrance of dye uptake does not play a major role in the current generation within these cells.

Campbell *et al.*<sup>23</sup> have reported Zn-porphyrin monomers used as photosensitiser in titania films in DSSCs achieving power conversion efficiencies  $\geq 5\%$  and absorbed photon to current efficiencies of up to 75% following irradiation with light spanning from 350 - 750 nm wavelengths. Aryl groups incorporated at the meso positions

were varied but showed little variance in the efficiencies achieved, with Ar = 4-n-butylPh yielding 6.4%.

#### 4.1.1.3.2. Hydrogen Generation

Photocatalytic splitting of water was achieved by Zhu *et al.*<sup>24</sup> using EDTA as a sacrificial electron donor and a porphyrin-functionalised platinum colloid as the photocatalyst (Fig. 4.9).  $\text{TON}_{\text{Pt}}$  and  $\text{TON}_{\text{dye}}$  were reported as 63 and 6311 respectively after irradiation with UV-Vis light for 12 hours at a pH of 6.8. As the concentration of  $\text{H}^+$  in the solution increases, the reduction of  $\text{H}^+$  was found to occur at a faster rate. However EDTA may be limiting as an electron source as the donating ability of EDTA is decreased at low pHs due to protonation. It was noted that no  $\text{H}_2$  was detected from the complex only when visible light source was employed.

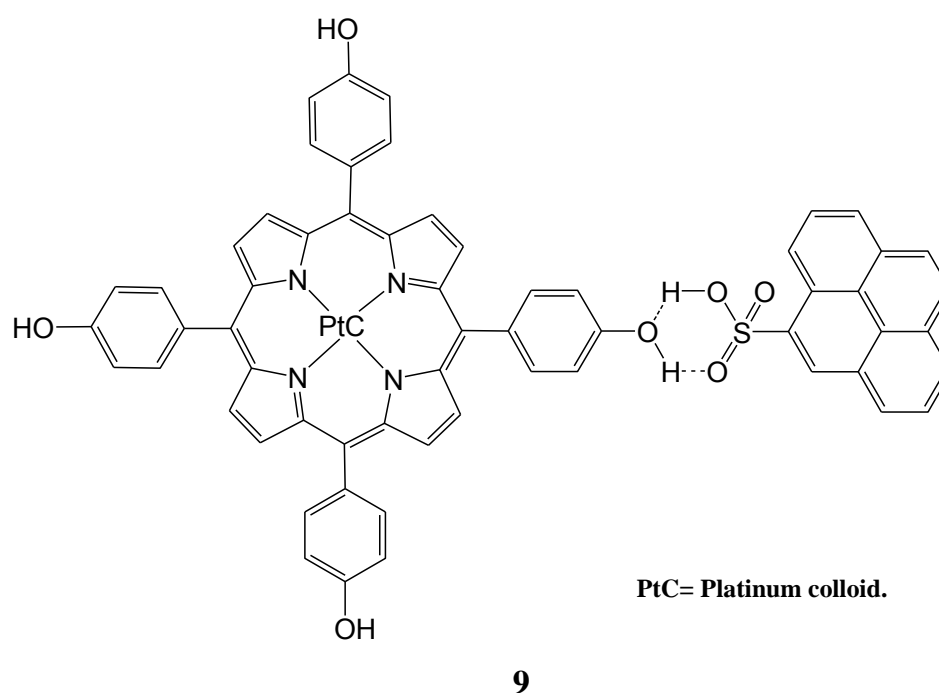
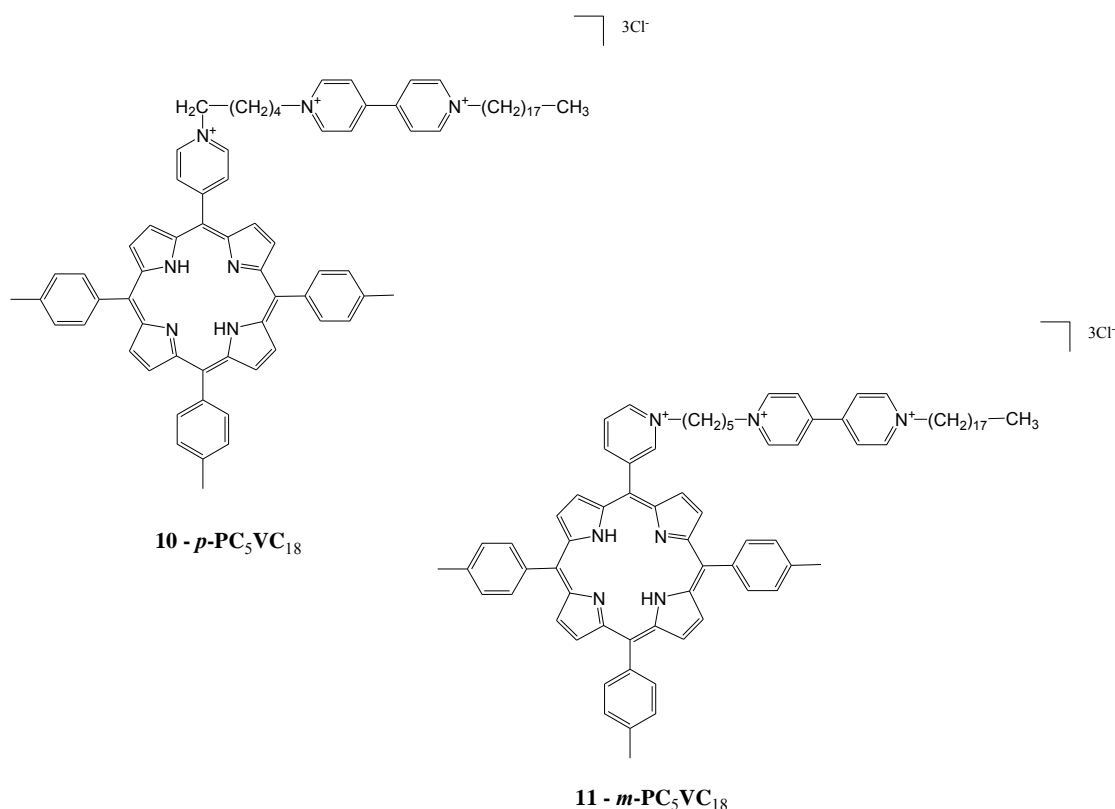


Figure 4.9- Porphyrin functionalised platinum colloid utilised by Zhu *et al.* in the photocatalytic splitting of water.<sup>24</sup>



Intermolecular photoinduced hydrogen production has been reported using viologen-linked porphyrins using EDTA as the sacrificial electron donor and  $\text{H}_2\text{PtCl}_6$  as the catalytic centre.<sup>25</sup> The complexes were incorporated as  $\text{PtCl}_6^-$  ions and porphyrin cations into Langmuir-Blodgett (LB) films and irradiated with visible light ( $720\text{nm} > \lambda < 390\text{nm}$ ) for 280 hours.



**Figure 4.10- Viologen-linked porphyrins photosensitisers used by Hosono *et al.*<sup>25</sup>**

TONs for  $\text{H}_2$  production for *p*-PC<sub>5</sub>VC<sub>18</sub> and *m*-PC<sub>5</sub>VC<sub>18</sub> (Fig. 4.10) were 5.2 and 16.8 respectively. The hydrogen evolution rate for *m*-PC<sub>5</sub>VC<sub>18</sub> was reported as almost three times greater than that of *p*-PC<sub>5</sub>VC<sub>18</sub>. This difference was attributed to the configuration of the porphyrins as the electron transfer rate and the redox potentials measured for both were almost identical. As apparent in Fig. 4.10 the orientation of the *m*-PC<sub>5</sub>VC<sub>18</sub> functional groups would be slightly more exposed to the water than those of *p*-PC<sub>5</sub>VC<sub>18</sub> and therefore is a more suitable configuration.

While studying the efficacy of CoTPP and FeTPP on the photoreduction of  $\text{CO}_2$  to CO, Dhanasekaran *et al.*<sup>26</sup> report a competing side reaction, which is the generation

of H<sub>2</sub>. A CO<sub>2</sub> saturated solution of the complexes containing 5% TEA were irradiated at  $\lambda > 300$  nm. They observed that CoTPP produced 1.6 mmol L<sup>-1</sup> and FeTPP produced 3.4 mmol L<sup>-1</sup> of H<sub>2</sub> following 20 hours irradiation. It was also found that production of H<sub>2</sub> continued using FeTPP even after the production of CO had ceased. The authors suggested that H<sub>2</sub> may have been formed following reduction of protons formed during Rxn. 4.1. Et<sub>3</sub>N<sup>•+</sup> is formed following electron transfer from Et<sub>3</sub>N to the metalloporphyrin (Rxn 4.1).



**Reaction 4.1 – Production of a reducing radical from TEA following electron transfer to an electron acceptor.<sup>26</sup>**

Grodkowski and Neta also reported the same competing reaction of CO<sub>2</sub> reduction vs. H<sub>2</sub> production when investigating cobalt corrins as vitamin B<sub>12</sub> analogues.<sup>27</sup> Corrins are very similar in structure to porphyrins however it possesses three methine bridges between its pyrrole subunits and one direct Ca–Ca bond. Photolysis ( $\lambda \geq 300$  nm) lead to production of CO and formic acid as well as H<sub>2</sub>. The corrins yielded greater amounts of H<sub>2</sub> compared to similar cobalt porphyrin counterparts. In an acetonitrile/methanol (9/1 v/v) solution containing 5% TEA, yields of up to 6.07 mmol L<sup>-1</sup> were produced using the corrin complexes. This is compared to 0.92 mmol L<sup>-1</sup> for CoTPP. Interestingly these yields were higher than that observed for the formation of CO and formate under the same conditions.

More recently hydrogen production has been reported using a porphyrin photosensitiser and a cobaloxime catalytic centre. Zhang et. al.<sup>28</sup> have synthesised a monopyridyl triphenyl porphyrin coordinated to a cobaloxime chloride catalytic centre (Fig. 4.11) which has shown photoinduced H<sub>2</sub> evolution using TEA as a sacrificial donor at 25°C using a 300W Xe lamp with a cut-off filter,  $\lambda_{\text{exc}} > 400\text{nm}$ . Using a solvent mixture of THF: H<sub>2</sub>O (8:2) yielded an optimum TON of 22 after 5 hours for the zinc metallated porphyrin-oxime complex **12**. The effect of the metallation of the porphyrin was demonstrated. Utilising the same conditions both **13** and **14** showed a far poorer yield of hydrogen with **13** producing a TON of 3 after

3 hours beyond which time the H<sub>2</sub> evolution levelled off, and **14** showed only trace amounts of H<sub>2</sub>, showing that the metal which is coordinated into the centre of the porphyrin ring is very important.

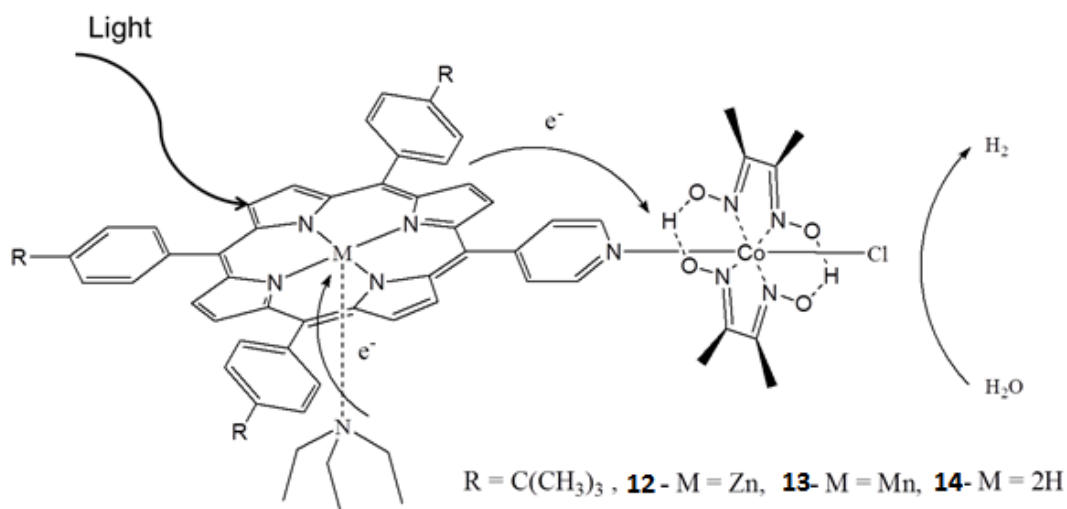


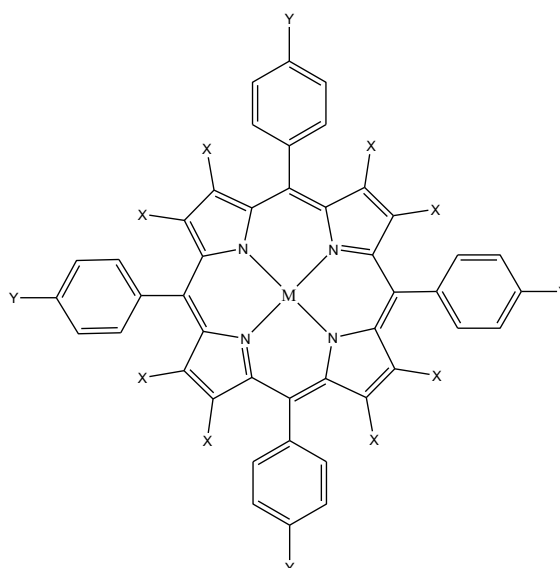
Figure 4.11 - Porphyrin photosensitizers and cobaloxime catalyst used by Zhang *et al.*<sup>28</sup>,  $\lambda_{\text{exc}} > 400\text{nm}$

The interaction of the complexes with the TEA sacrificial electron donor was studied in THF. When TEA was added to a solution of **12** there is a 2 nm red shift in the  $\lambda_{\text{max}}$  of the Soret band of each complex was observed. This indicates a weak axial coordination of the TEA to the Zn ion of the porphyrin. The addition of TEA to solutions of **13** and **14** had no effect on the UV-Vis spectra of the complexes implying no considerable interaction between these complexes and the TEA.

#### 4.1.1.4. Electrochemistry of Porphyrins

Porphyrins are a redox active species which undergo multiple oxidation and reduction processes. The number of processes and potential at which these processes occur are greatly influenced by the potential range of the solvent used, the type of macrocycle and the type of axially coordinated ligands. The ability of any porphyrin to serve as a reduction catalyst is related to its electronic structure involving the location and number of electron-withdrawing/ donating substituents on the porphyrin

ring and also by the metal ion present in the porphyrin centre. By monitoring shifts in the anodic and cathodic processes the influence of different metal centres and different ring substituents on the HOMO-LUMO energy gap can be elucidated. The simplest freebase porphyrins such as TPP are known to possess two successive one electron oxidations as well as two successive one electron reductions on the ring system which form  $\pi$ -cation radicals and dications and  $\pi$ -anion radicals and dianions respectively. Early measurements of the redox properties of TPP and other simple porphyrins demonstrated that most of the porphyrins exhibited a constant potential difference between the first and second ring based oxidations or first and second ring based reductions as well as a similar HOMO-LUMO gap of  $2.25 \pm 0.15$  V.<sup>29</sup> These redox gaps have been employed to distinguish macrocycle centered reactions from reactions involving the metal core.<sup>30</sup> The addition of electron withdrawing substituents such as a basic pyridine moiety or a cyano group leads to the ring becoming harder to reduce and therefore easier to oxidise. Likewise the addition of an electron donating group such as CHO or CH<sub>3</sub> will allow reduction to occur more easily but oxidation becomes more difficult. It has been noted that planar porphyrins such as TPP have a larger HOMO-LUMO energy gap than non-planar porphyrins such as octaethyltetraphenylporphyrin and octabromotetraphenylporphyrin which are more easily oxidised due to their bulky electron withdrawing substituents.<sup>30</sup> A study carried out by Hariprasad *et al.* investigated the effects of long chained electron-withdrawing bromo substituents, at both the *meso* and  $\beta$  positions, on the redox potentials of freebase, Zn and Cu porphyrins (Fig. 4.12).<sup>31</sup>



<b>L</b>	<b>X</b>	<b>Y</b>
<b>15- tpp</b>	H	H
<b>16- ttp</b>	H	CH <sub>3</sub>
<b>17- tctpp</b>	H	Cl
<b>18- obtpp</b>	Br	H
<b>19- obttp</b>	Br	CH <sub>3</sub>
<b>20- obtctpp</b>	Br	Cl



**Figure 4.12- Bromo substituted porphyrins studied by Hariprasad *et al.*<sup>31</sup>** tpp = 5,10,15,20-tetraphenylporphyrin, ttp = 5,10,15,20-tetra(4-methylphenyl)porphyrin, tctpp = 5,10,15,20-tetra(4-chlorophenyl)porphyrin, obtpp = 2,3,7,8,12,13,17,18-octabromo-5,10,15,20-tetraphenylporphyrin, obttp = 2,3,7,8,12,13,17,18-octabromo-5,10,15,20-tetra(4-methylphenyl)porphyrin, obtctpp = 2,3,7,8,12,13,17,18-octabromo-5,10,15,20-tetra(4-chlorophenyl)porphyrin.

All processes observed for all of the compounds, freebase, Zn<sup>II</sup> or Cu<sup>II</sup> porphyrins, were proposed to be ring based oxidations or reductions and not metal based processes as these metals are known to be non-electroactive. Experimental redox potentials are presented in Table 4.1. It is evident that the reduction potentials of the brominated porphyrin derivatives are shifted to less negative potentials of between 0.38 V - 0.72 V when compared to their non-brominated counterparts (Table 4.1). It is also evident that the corresponding shifts in the oxidation potentials are not as vast with shifts between 0.02 V to 0.2 V indicating that bromo-substitution at the  $\beta$ -position allows the reduction of the porphyrin to occur more easily but the oxidation of the ring only slightly more easier/ difficult to achieve.

$E_{1/2}$ vs. SCE				
	Ox 1 (V)	Ox 2 (V)	Red 1 (V)	Red 2 (V)
H <sub>2</sub> tpp	1	1.25	-1.23	-1.59
H <sub>2</sub> ttp	0.94	1.18	-1.27	-1.65
H <sub>2</sub> tctpp	1.1	1.28	-1.15	-1.6
Cu(tpp)	0.98	1.21	-1.33	-1.8
Cu(ttp)	0.93	1.23	-1.37	-1.83
Cu(tctpp)	1.07	1.26	-1.3	-1.75
Zn(tpp)	0.8	1.02	-1.35	-1.67
Zn(ttp)	0.77	1.01	-1.4	-1.72
Zn(tctpp)	0.83	1.16	-1.34	-1.64
H <sub>2</sub> obtpp	0.96	1.37	-0.82	-1.24
H <sub>2</sub> obttp	0.96	1.1	-0.85	-1.26
H <sub>2</sub> obtctpp	0.85	-	-0.72	-1.08
Cu(obtpp)	0.96	1.41	-0.87	-1.12
Cu(obttp)	0.89	1.41	-0.9	-1.16
Cu(obtctpp)	1.02	1.49	-0.75	-1.03
Zn(obtpp)	0.84	1.07	-0.95	-1.16
Zn(obttp)	0.74	1.01	-1.02	-1.2
Zn(obtctpp)	0.93	1.18	-0.86	-1.1

**Table 4.1-** Electrochemical redox potentials of bromo-substituted porphyrins studied by Hariprasad *et al.*<sup>31</sup> All experiments were carried out in DCM and quoted vs. SCE. tpp = 5,10,15,20-tetraphenylporphyrin, ttp = 5,10,15,20-tetra(4-methylphenyl)porphyrin, tctpp = 5,10,15,20-tetra(4-chlorophenyl)porphyrin, obtpp = 2,3,7,8,12,13,17,18-octabromo-5,10,15,20-tetraphenylporphyrin, obttp = 2,3,7,8,12,13,17,18-octabromo-5,10,15,20-tetra(4-methylphenyl)porphyrin, obtctpp = 2,3,7,8,12,13,17,18-octabromo-5,10,15,20-tetra(4-chlorophenyl)porphyrin.

Chloro-substitution at the meso-position also made reduction of the ring more difficult and oxidation slightly easier but not even close to the extent of the  $\beta$ -substitution. Hariprasad also noted that a third reversible reduction is observed for the Zn-octabromo derivatives. As previously illustrated by D'Souza *et al.*<sup>32</sup> further reduction of the singly reduced species of each of cobalt octa-bromoporphyrins lead to stepwise elimination of the bromo groups on the ring to give CoTPP as a final product in the solution. It was therefore hypothesised that this third reversible reduction observed in the Zn-octabromo derivatives is the formation of ZnTPP following the loss of the bromo groups from the ring periphery. D'Souza observed similar results from brominated Co-porphyrins in that the reduction and oxidation

potentials were cathodically shifted when compared to CoTPP due to the electron withdrawing nature of the bromo-substituents.

Zinc porphyrins show no metal based redox processes. The addition of zinc to the centre of a porphyrin ring has been shown to not affect the HOMO- LUMO band gap, with reported values between 2.15 V and 2.25 V being reported.<sup>33,34</sup> This shows that there are no metal characteristics involved in these processes. The addition of electron withdrawing substituents on the porphyrin ring not only causes the two oxidation processes to occur at more positive potentials but they also affect the difference in the potential at which these processes occur. The more electron withdrawing the substituent, the closer the potentials at which the two oxidations occur. The opposite affect is observed for electron donating substituents. The two oxidation processes occur at more negative potentials and also there is a larger gap in potential between the processes.

Nickel porphyrins have been shown to possess two closely spaced ring based oxidation waves in non-aqueous media. As with Zn-porphyrins, it was found that varying the substituent at the meso position did not have the same effect on each of the two oxidation processes observed.<sup>35</sup> Complexes which had been substituted with electron-withdrawing substituents in the phenyl ring (such as COOCH or NO<sub>2</sub>) showed a single two-electron-transfer process at more positive potentials in the oxidation window however when an electron-donating group was used (such as CH<sub>3</sub> or OCH<sub>3</sub>) two resolved single electron oxidation processes were observed at more negative potentials when compared with simple NiTPP. This substituent effect was further reported by Chang *et al.*<sup>36</sup> By varying the substituents on the porphyrin ring (Fig. 4.13) the potentials between the first oxidation and the second oxidation process varied between 0.24 V to 0.51 V as the basicity of the substituents increases (Table 4.2).

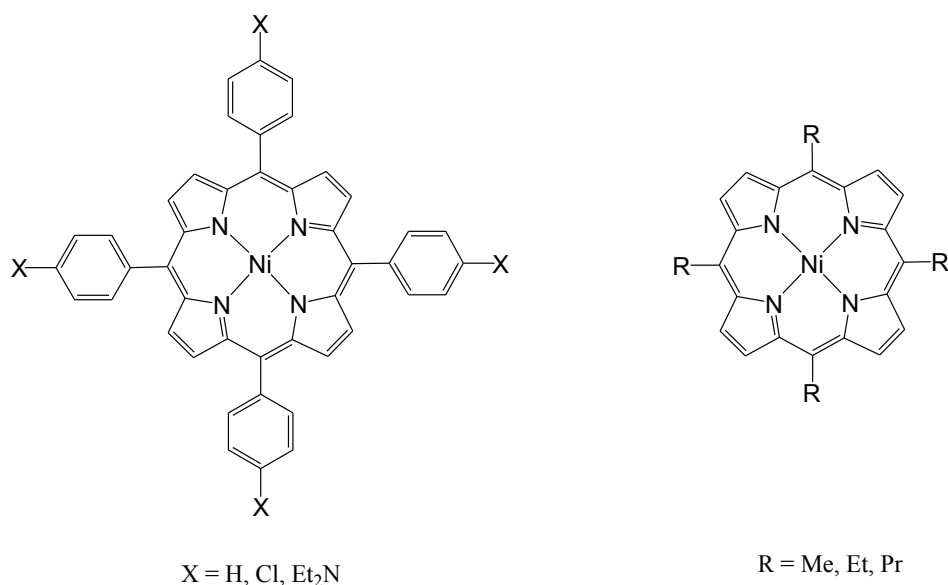


**Figure 4.13-** Structural formulas of various PNi<sup>II</sup> complexes studied by Chang *et al.*<sup>33</sup> where P is para-substituted tetraphenylporphyrin or a tetraalkylporphyrin.

Also notable is the energy gap between the first oxidation and the first reduction which is directly related to the HOMO- LUMO energy gap. As basicity increases this energy gap increases from 1.92 V to 2.36 V showing that there is some metal character involved.

Complex	E <sub>1/2</sub> (vs. SCE)			Potential difference between Ox 1 and Ox 2 (V)
	Red (V)	Ox 1 (V)	Ox 2 (V)	
Ni( <i>p</i> -Cl)TPP	-1.26	1.1	1.34	0.24
NiTPP	-1.31	1.01	1.31	0.3
NiTMeP	-1.36	0.8	1.26	0.46
NiTETP	-1.39	0.81	1.26	0.45
NiTPrP	-1.41	0.81	1.26	0.45
Ni( <i>p</i> -Et <sub>2</sub> N)TPP	-1.36	0.56	1.07	0.51

**Table 4.2-** Half-Wave Potentials for Various Ni<sup>II</sup> Porphyrins in CH<sub>2</sub>Cl<sub>2</sub> with 0.1 M TBAPF<sub>6</sub> supporting electrolyte, quoted vs. SCE (Scan Rate 0.1 V/s), reported by Chang *et al.*<sup>33</sup> (*p*-Cl)TPP = tetra(4-chlorophenyl)porphyrin, (*p*-Et<sub>2</sub>N)TPP = tetra(4-aminophenyl)porphyrin, TMeP = tetramethylporphyrin, TETP = tetraethylporphyrin, TPrP = tetrapropylporphyrin.

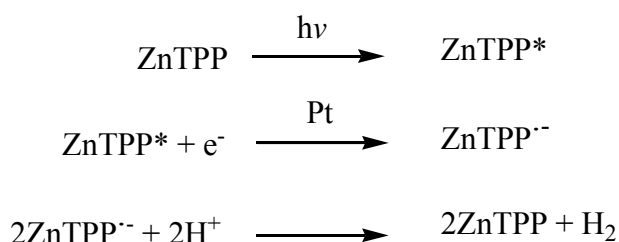


Cheng *et al.*<sup>37</sup> have measured the redox potentials of Co-mono-hydroxyphenyl-triphenylporphyrin (CoHPTPP). Along with two ring based oxidations and two ring based reductions, a  $\text{Co}^{\text{III/II}}$  and  $\text{Co}^{\text{II/I}}$  reductions were observed at 0.03 V and -1.23 V vs. Ag/AgCl respectively. The addition of the Co metal did not have a huge effect on the potentials at which the ring based processes occurred; shifting them  $\sim 0.1$  V to  $-1.64$  V for the first ring based reduction when compared  $-1.50$  V for their freebase counterparts. A similar result was observed for the addition of Ni to the porphyrin ring. No metal based Ni redox processes were observed in the electrochemical window however the potential at which the ring based processes occurred shifted to a slightly more negative potential of  $-1.56$  V.

#### 4.1.1.5. Porphyrins used in the Electrocatalytic Generation of Hydrogen

Electrode surfaces modified with porphyrins have been frequently used in the generation of hydrogen using electrochemical cells. The nature of the substituents and the metal centres which have been incorporated have been shown to greatly influence the electrocatalytic activity of the porphyrin complexes. Kaneko *et al.* are at the forefront of this research and have reported a great deal of studies using metalloporphyrins as catalysts for proton reduction yielding  $\text{H}_2$ .<sup>32,38,40</sup> ZnTPP has been incorporated into a poly(4-vinylpyridine) membrane coated on a platinum electrode in an aqueous solution of pH 4.4.<sup>38</sup> An enhanced photocurrent was observed at potentials below  $-0.40$  V (vs. Ag/AgCl) when irradiated with visible light,  $\lambda < 350$  nm. A series of light on/ light off experiments confirmed that the photocurrent is induced at both the Soret band and the Q-bands of the porphyrins absorbance spectrum. It has been proposed that  $\text{H}_2$  generation using ZnTPP is induced by reductive quenching of  $\text{ZnTPP}^*$  to  $\text{ZnTPP}^-$  through reduction at the platinum electrode.  $\text{ZnTPP}^-$  then facilitates the proton reduction reaction to yield  $\text{H}_2$ . ZnTPP has also been incorporated into a Nafion membrane and coated on a platinum electrode.<sup>39</sup> A photocurrent was also observed for this system when irradiated with visible light,  $\lambda > 390$  nm. This photocurrent was induced under applied potentials of only  $-0.10$  V (vs. Ag/AgCl) in an aqueous solution with pH  $\sim 1.01$ . The magnitude of this photocurrent increases with the application of more negative potentials. As with Abe's previous study<sup>38</sup> almost no current is induced when in the dark. When

the ZnTPP was coated directly onto the electrode surface almost no photocurrent was produced indicating that the Nafion membrane facilitates efficient electron transfer from the surface to the ZnTPP moiety. The lifetime of ZnTPP\* was measured to be ~ twice as long when incorporated into the Nafion membrane also. From the two experiments with both PVP and Nafion membranes a mechanism of photoinduced H<sub>2</sub> production was elucidated (Scheme. 4.2).



**Scheme 4.2-** The mechanism of photoinduced H<sub>2</sub> production at a platinum electrode using ZnTPP incorporated into a Nafion membrane.<sup>39</sup>

The incorporation CoTPP into a Nafion membrane coated on a Pt-working electrode was reported by Abe *et al* also.<sup>40</sup> This system was shown to effectively reduce protons around the theoretical H<sup>+</sup>/H<sub>2</sub> redox potential (-0.25 V vs. Ag/AgCl in a pH 1.01 aqueous solution). The group reported that incorporation of the complex into a Nafion film greatly enhanced the catalytic activity of the system as the electronic communication between the Nafion film and the electrode surface is highly efficient. Hydrogen evolution also occurred at more positive potentials than the bare Pt electrode. After 1 h bulk electrolysis at -0.3 V in a pH 1.0 solution a TON of 2.3 × 10<sup>2</sup> was reported.

Manganese and Iron metalloporphyrins have been reported as highly active electrocatalysts in proton reduction by Taguchi *et al*.<sup>41</sup> The metalloporphyrins were incorporated into a Nafion membrane on a Pt base electrode and dipped into a pH 1.0 aqueous phosphate buffer solution. 4.12 μL and 2.68 μL of hydrogen were produced by the Mn-porphyrin and Fe-porphyrin respectively after 1 hour potentiostatic electrolysis at the theoretical H<sup>+</sup>/H<sub>2</sub> redox potential of -0.25 V.

Knoll *et al*.<sup>42</sup> report the use of a cobalt<sup>II</sup>/ platinum<sup>II</sup> porphyrin in the electrocatalytic reduction of protons to H<sub>2</sub> in a 1.0 M perchloric acid (Fig. 4.14).

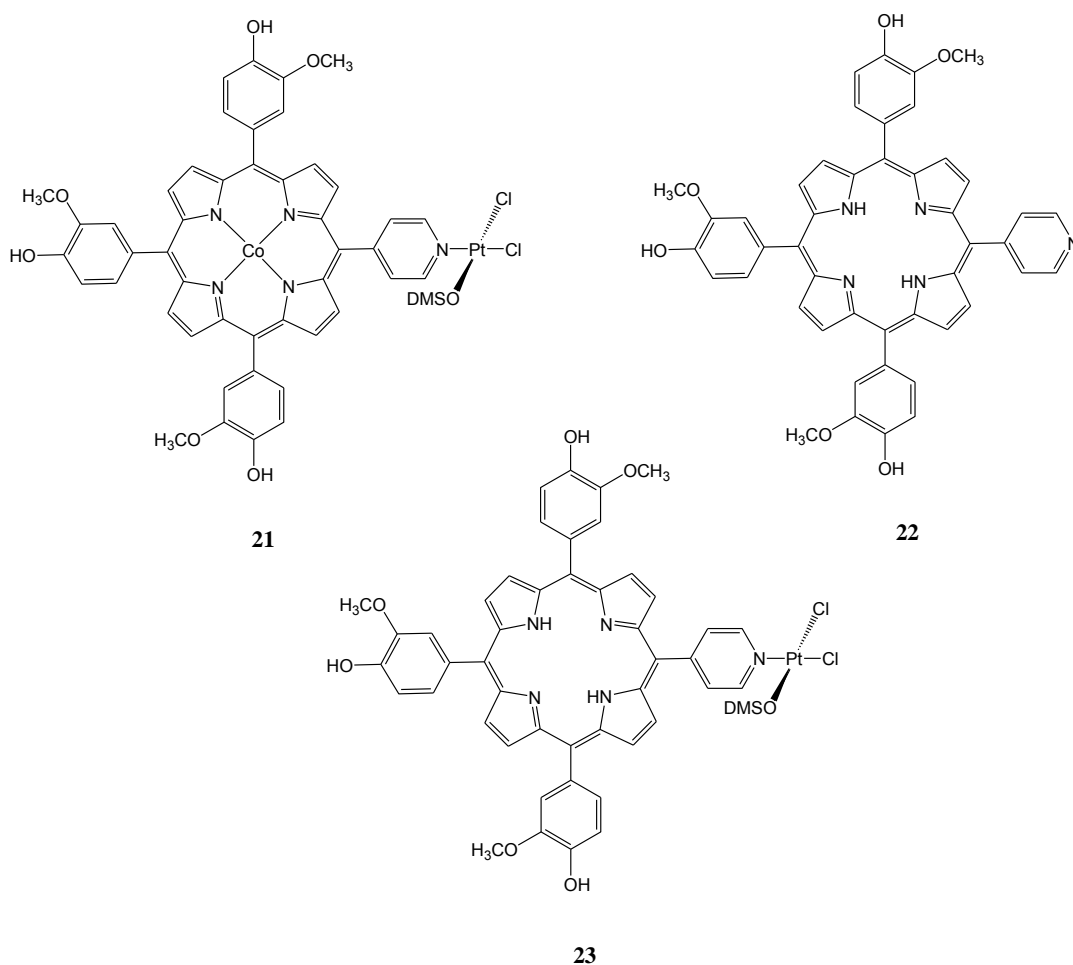


**Figure 4.14- Porphyrins and Co/Pt porphyrins used in the electrocatalytic generation of  $H_2$  by Knoll *et al.*<sup>42</sup>**

They have reported a shift of 0.40 V vs. Ag/ AgCl in onset of the catalytic current when the electrodes have been anodically cycled (scanned at 0.5 Vs<sup>-1</sup> from 0 V to 1.0 V) when compared to the same modified electrodes which have not been anodically cycled. This anodic cycling produced stable electroactive films of the porphyrins and has been shown to efficiently reduce protons to yield  $H_2$ . This was not true for the freebase porphyrin (**23**). When scanning to a positive potential a broad irreversible oxidation peak was observed  $\sim 0.76$  V vs. Ag/ AgCl for **21**. When the scan was reversed in the cathodic direction a reduction wave appears with an  $E_{1/2}$  0.56 V. Scanning again in the anodic direction shows that the initial broad oxidation is no longer present. It is proposed that the anodic cycling of the electrode induces an ECE mechanism (electrochemical-chemical-electrochemical) and produces a stable “quinone” like film on the electrode surface. This ECE mechanism is observable for

**21**, **22** and **23** and is therefore most likely to occur at the peripheral 3-methoxy-4-hydroxyphenyl substituents common to each complex. Knoll proposed that the first broad oxidation can be attributed to the oxidation of these substituents to give a reactive cationic species. These species undergo a demethylation reaction to yield a quinone species. As the CV scan cycles towards the cathodic direction this quinone is reduced to form hydroquinone in an aqueous solution, which then undergoes a reversible oxidation back to quinone.

Fe-porphyrins in the 0 oxidation state have been shown to be very efficient in the catalytic formation of hydrogen.<sup>43</sup> The Fe<sup>0</sup>-porphyrin was generated from Fe<sup>III</sup>-porphyrin, Fe<sup>II</sup>-porphyrin, Fe<sup>I</sup>-porphyrin and Fe<sup>0,2-</sup>-porphyrin successively in DMF. Upon addition of an acid a catalytic current is induced at the Fe<sup>0,2-</sup>-porphyrin formation wave. This catalytic formation of hydrogen is proposed to occur through the formation of an iron-hydride which reacts with a second acid molecule yielding dihydrogen. This catalytic wave appears at -1.46 V vs. NHE.

In a further publication the same research group reported that when using Rh-porphyrins, Rh<sup>II</sup>-hydrides are a key intermediate in the H<sub>2</sub> generation mechanism.<sup>44</sup> These Rh<sup>II</sup>-hydrides are formed from the reduction of Rh<sup>III</sup>-hydrides at negative potentials ~ -1.6 V vs. SCE in the presence of acid in DMSO. Hydrogen is evolved when potentiostatic electrolysis is performed at -1.6 V, however, at more cathodic potentials no hydrogen is formed. It is proposed that the transfer of the hydride to the acid results in the liberation of H<sub>2</sub> using these complexes. It was also reported that changing the solvent from DMSO to butyronitrile, which is a poorer ligand of rhodium, can result in variations in reactivity which can be explained by changes in electron density at the rhodium metal and the hydrogen atoms in the hydride. Less electron density on the hydrogen in the butyronitrile may induce more charge density on the rhodium and the porphyrin ring when bound.<sup>44</sup> This leads to a faster decay of the catalyst in butyronitrile when compared to DMSO.

Collman *et al.*<sup>45</sup> have reported synthesising a series of metalloporphyrin hydrides using Os and Ru as the metal centres. Synthesising the metal-hydride cores allowed for a facile hydrogen production through two proposed parallel pathways; a bimolecular mechanism in which two metal hydrides undergo reductive elimination to form H<sub>2</sub> and another in which the metal-hydride is protonated, in excess acid, resulting in H<sub>2</sub> formation in non-aqueous media. Incorporating D<sub>2</sub>O as a solvent did

not yield HD or D<sub>2</sub> as the product indicating that water is not necessary for the production of H<sub>2</sub> utilising these complexes.

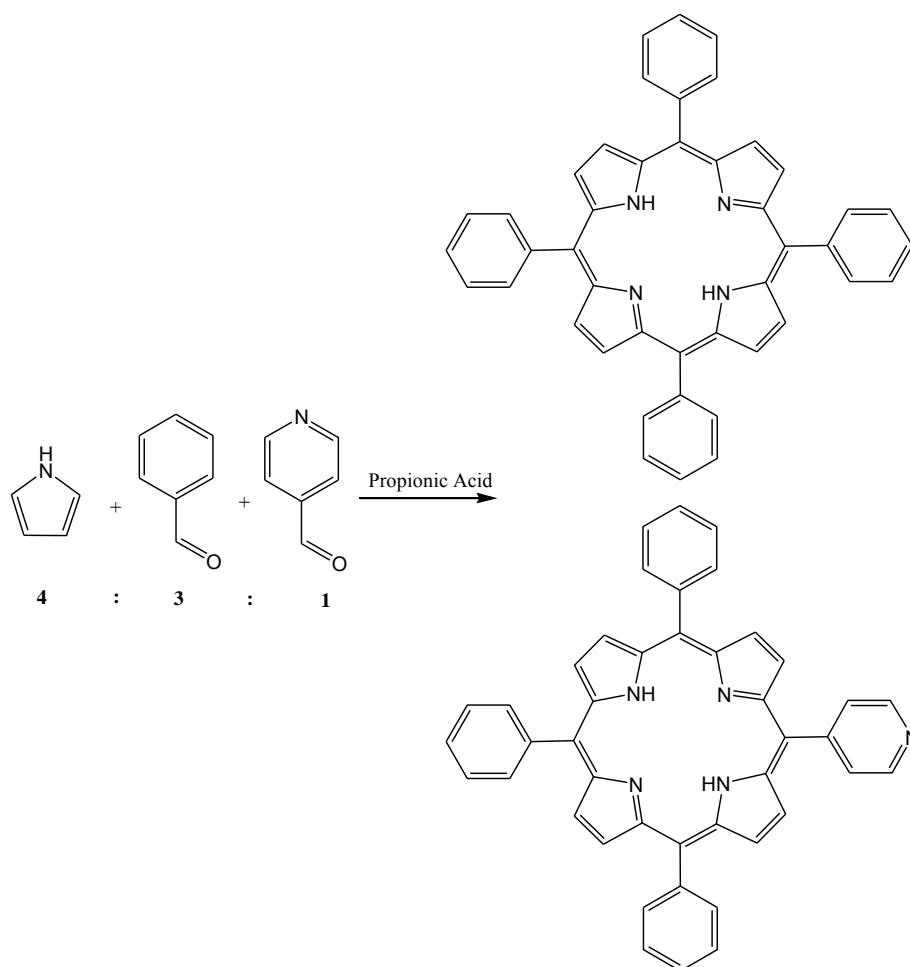
## 4.2. Experimental

All materials and equipment used in this studied are detailed in Chapter 2 sections 2.21 and 2.22. Details of cyclic voltammetry, electrocatalytic studies and photocatalytic studies are also available in Chapter 2 sections 2.23, 2.24 and 2.25.

### 4.2.1. Synthesis

Cobaloxime was prepared according to the method reported in Chapter 3. All porphyrins were synthesised using a method modified from Alder *et al.*<sup>46</sup>

#### 4.2.1.1. Synthesis of Tetraphenyl Porphyrin (H<sub>2</sub>TPP) and Monopyridyltriphenyl Porphyrin (MPyTPP)



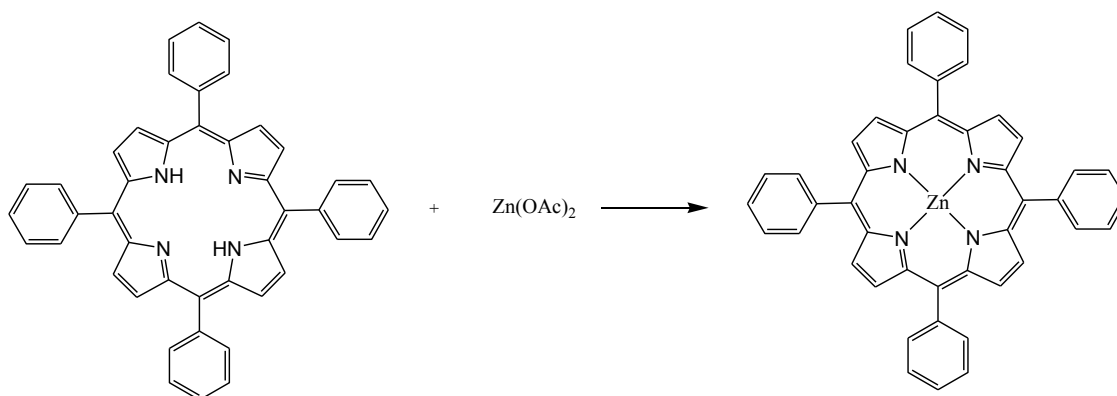
3.5 ml of freshly distilled pyrrole (50 mmol), 4 ml of benzaldehyde (37.5 mmol) and 1.17 ml of 4-pyridine carboxaldehyde (12.5 mmol) were added to 99% propionic acid (175 ml), and brought to reflux temperature. The acidic solution was allowed to reflux for 2 hours. A black solution results. The mixture was allowed to cool to room temperature and was stored in the fridge (2 - 8°C) overnight. The black solution was filtered under vacuum. The purple crystals formed were collected and washed several times with cold methanol to give a bright purple crystalline solid. Purification was carried out using column chromatography on a silica gel. The initial mobile phase used was chloroform : ethanol (98 : 2), moving to 97 : 3 after the first fraction eluted. The first fraction was 5,10,15,20-tetraphenylporphyrin (H<sub>2</sub>TPP). The second fraction eluted was MPyTPP.<sup>46</sup>

% Yield: TPP: 1.23g, 2.0 mmol, 16%

MPyTPP: 0.851 g, 1.38 mmol, 11 %.

<sup>1</sup>H NMR: (400 MHz, CDCl<sub>3</sub>), TPP: 8.83 ppm (s, 8H), 8.2 ppm (dd, J<sub>a</sub>= 7.6 Hz, J<sub>b</sub>= 1.6 Hz, 8H), 7.6 ppm (m, 12H), -2.8 ppm (s, 2 -NH)  
MPyTPP: 9.04 ppm (d, J= 8.0 Hz, 2H), 9.1 ppm (d, J= 5.2 Hz, 2H), 8.88 ppm (s, 4H), 8.81 ppm (d, J= 4.8 Hz, 2H), 8.23 ppm (d, J= 6.4 Hz, 6H), 8.18 ppm (dd, J<sub>a</sub>= 4.4 Hz, J<sub>b</sub>= 1.2 Hz, 2H), 7.78 ppm (m, 9H), -2.85 ppm (s, 2H).

#### 4.2.1.2. Synthesis of Zinc-tetraphenyl Porphyrin (ZnTPP)



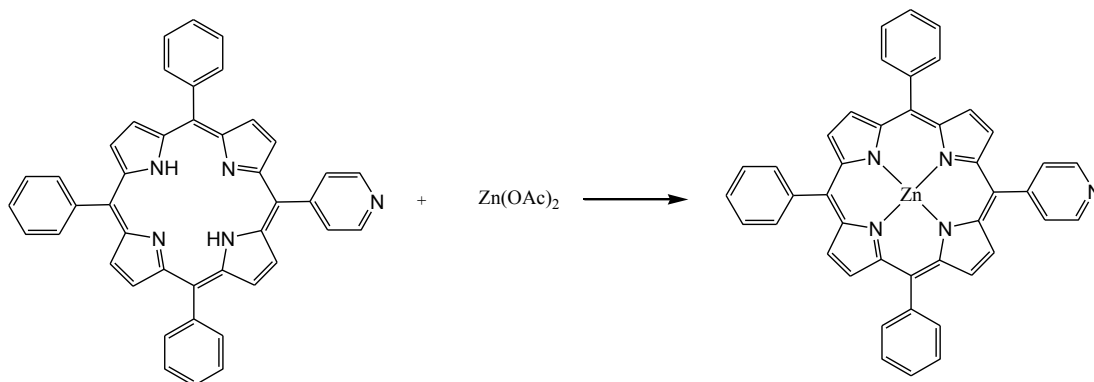
0.1g of TPP (0.162 mmol) was dissolved in 25 ml of chloroform in a clean, dry, round bottomed flask. The solution was purged with nitrogen for 10 min. 0.073g zinc acetate (0.33 mmol) was dissolved in ~ 5 ml methanol and then added to the porphyrin solution. The mixture was stirred under nitrogen overnight at room temperature. All solvents were removed under reduced pressure leaving a purple solid. The solid was dissolved in DCM and washed with 3 x 20 ml portions of 5 % w/v aqueous sodium bicarbonate, followed by 3 x 20 ml portions of water. The organic layer dried over  $\text{MgSO}_4$  and the solvent was removed under reduced pressure. The zinc porphyrin was purified using column chromatography on a silica gel using 100% chloroform as the mobile phase.

% Yield: 0.085 g, 0.126 mmol, 77%.

$^1\text{H}$  NMR: (400 MHz,  $\text{CDCl}_3$ ), 8.88 ppm (s, 8H), 8.15 ppm (dd,  $J_a = 7.4$  Hz,  $J_b = 1.6$  Hz, 8H), 7.69 ppm (m, 12H).



#### 4.2.1.3. Synthesis of Zinc-monopyridyltriphenyl Porphyrin (ZnMPyTPP):

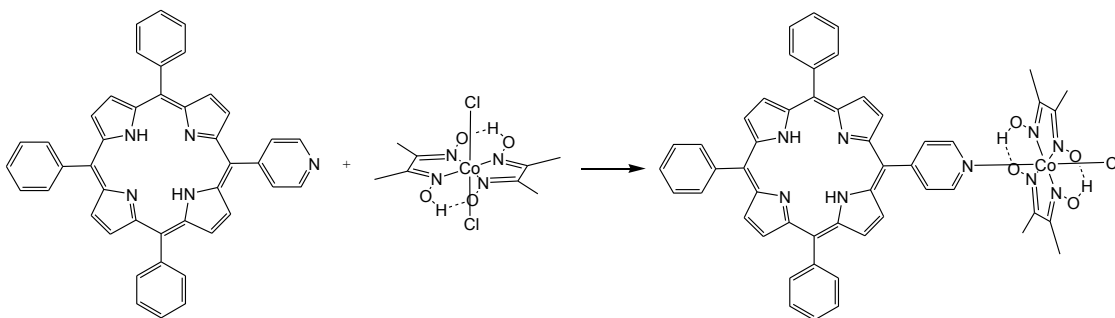


0.1g of MPyTPP (0.163 mmol) was dissolved in 25 ml of chloroform in a clean, dry, round bottomed flask. The solution was purged with nitrogen for 10 min. 0.073g zinc acetate (0.33 mmol) was dissolved in ~ 5 ml methanol and then added to the porphyrin solution. The mixture was stirred under nitrogen overnight at room temperature. All solvents were removed under reduced pressure leaving a purple solid. The solid was dissolved in DCM and washed with 3 x 20 ml portions of 5 % w/v aqueous sodium bicarbonate, followed by 3 x 20 ml portions of water. The organic layer dried over  $\text{MgSO}_4$  and the solvent was removed under reduced pressure. The zinc porphyrin was purified using column chromatography on a silica gel using 100% chloroform as the mobile phase.

% Yield: 0.08 g, 0.118 mmol, 72%.

$^1\text{H}$  NMR: (400 MHz,  $\text{CDCl}_3$ ), 8.873 ppm (d,  $J = 4.8$  Hz, 2H), 8.84 ppm (d,  $J = 4.4$  Hz), 8.52 ppm (d,  $J = 4.4$  Hz, 2H), 8.19 ppm (d,  $J = 7.2$  Hz, 2H), 8.09 ppm (d,  $J = 6.4$  Hz, 2H), 7.7 ppm (m, 9H), 7.42 ppm (d,  $J = 4.4$  Hz, 2H), 6.22 ppm (s, 2H), 1.25 ppm (d,  $J = 4.4$  Hz, 2H)

#### 4.2.1.4. Synthesis of MPyTPP-Cobaloxime



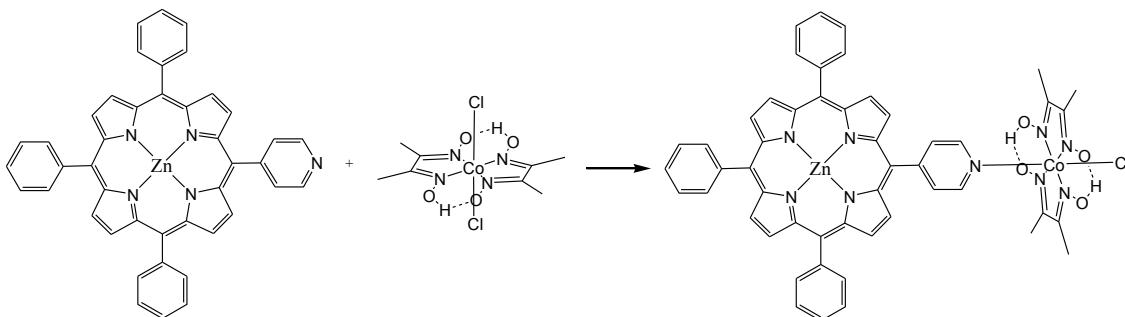
0.06 g of MPyTPP (0.0975 mmol) was added to a clean dry round bottomed flask and dissolved in 5 ml of DCM. 0.035 g of cobaloxime was dissolved in 25 ml of methanol. This solution was added to the round bottomed flask and the mixed solution was degassed with N<sub>2</sub> for 10 min. 20 uL of TEA was added to the reaction vessel and the vessel was sealed. The reaction mixture was allowed to stir for 1 hour in darkness. All solvents were removed under reduced pressure. Purification was carried out using column chromatography using silica and ethanol : chloroform 97 : 3 as the mobile phase. A bright purple-red product results.

% Yield: 0.0724g , 0.0771 mmol, 79%.

<sup>1</sup>H NMR: (400 MHz, CDCl<sub>3</sub>), 12.03 ppm (s, 2 -OH), 8.90 ppm (d, J= 4.8 Hz, 2H), 8.85 ppm (dd, J<sub>a</sub>= 7.6 Hz, J<sub>b</sub>= 4.8 Hz, 4H), 8.65 ppm (d, J= 6.8 Hz, 2H), 8.573 ppm (d, J= 4.4 Hz), 8.18 ppm (m, 6H), 8.09 ppm (dd, J<sub>a</sub>= 5.2 Hz, J<sub>b</sub>= 1.2 Hz, 2H), (7.78 ppm (m, 9H), 2.594 ppm (s, 12H), -2.858 ppm (s, 2H).

Mass Spec: pending results

#### 4.2.1.5. Synthesis of ZnMPyTPP-Cobaloxime



0.066 g of ZnMPyTPP (0.0975 mmol) was added to a clean dry round bottomed flask and dissolved in 5 ml of DCM. 0.035 g of cobaloxime was dissolved in 25 ml of methanol. This solution was added to the round bottomed flask and the mixed solution was degassed with  $N_2$  for 10 min. 20  $\mu$ L of TEA was added to the reaction vessel and the vessel was sealed. The reaction mixture was allowed to stir for 1 hour in darkness. All solvents were removed under reduced pressure. Purification was carried out using column chromatography using silica and ethanol : chloroform 97 : 3 as the mobile phase. A bright purple-red product results.

% Yield: 0.085g, 0.085 mmol, 87%.

$^1H$  NMR: (400 MHz,  $CDCl_3$ ), 12.24 ppm (s, 2  $-OH$ ), 8.96 ppm (d,  $J = 4.8$  Hz, 2H), 8.93 ppm (dd,  $J_a = 6.8$  Hz,  $J_b = 4.8$  Hz, 4H), 8.638 ppm (d,  $J = 4.4$  Hz, 2H), 8.60 ppm (d,  $J = 6.4$  Hz, 2H), 8.17 ppm (m, 6H), 8.07 ppm (d,  $J = 6.4$  Hz, 2H), 7.74 ppm (m, 9H), 2.58 ppm (s, 12H).

Mass Spec: pending results

## 4.3. Results

### 4.3.1. UV-Vis Spectroscopy

Room temperature absorption spectra were obtained for all compounds. Table 4.3 illustrates the absorption maxima ( $\lambda_{\max}$ ) for all compounds in this study. All UV-Vis spectra were carried out using spectrophotometric grade dichloromethane (DCM).

Compound	Soret band $\lambda_{\max}$ (nm), $\epsilon$ ( $\times 10^4 \text{ M}^{-1} \text{ cm}^{-1}$ )	FWHM ( $\times 10^5 \text{ cm}^{-1}$ )	Q- bands $\lambda_{\max}$ (nm), $\epsilon$ ( $\times 10^4 \text{ M}^{-1} \text{ cm}^{-1}$ )
MPyTPP	416 (24.2)	8.33	507 (1.85), 542 (0.70), 583 (0.55), 641 (0.36)
ZnMPyTPP	418 (37.0)	9.09	540 (1.3), 604 (0.60)
TPP	420 (23.5)	6.13	515 (0.94), 550 (0.42), 590 (0.17), 645 (0.15)
ZnTPP	415 (25.3)	6.59	550 (0.99), 620 (0.21)
MPyTPP-Cobaloxime	418 (34.0)	6.45	510 (1.43), 546 (0.77), 584 (0.47), 645 (0.34)
ZnMPyTPP-Cobaloxime	419 (23.7)	7.41	541 (1.19), 645 (0.33)

**Table 4.3-** UV-Vis absorption data and extinction coefficient data for all compounds in this study. All spectra were recorded in spectrophotometric grade DCM. UV-vis spectra are presented in the discussion section.

All of the compounds in this study exhibit strong absorptions in the UV-vis region of the spectrum. The Soret band absorbs strongly at  $\sim 416$  nm, this is due to ligand localised excitation into the second excited state, an  $S_0 - S_2$  transition ( $\pi-\pi^*$ ).<sup>15</sup> The absorbance between 510- 645 nm in each porphyrin complexes listed are generally attributed to  $S_0 - S_1$  ( $\pi-\pi^*$ ) transition to the first, lowest energy excited state and are known as quasi-allowed (Q) bands. Due to the more symmetrical nature of metallated porphyrins the number of these Q-bands is reduced from 4 to 2 following addition of a metal to the centre of the porphyrin ring.

#### 4.3.2. Fluorescence Studies

Room temperature emission spectra were obtained for all compounds. Table 4.4 illustrates the excitation wavelength and emission maxima for all compounds in this study. All emission spectra were obtained using spectrophotometric grade dichloromethane (DCM).

Compound	Excitation (nm)	Emission (nm)	Stokes Shift (cm <sup>-1</sup> )
MPyTPP	416	650, 709	8653, 9934
ZnMPyTPP	418	609, 638	7503, 8249
TPP	420	639, 701	8160, 9544
ZnTPP	415	595, 643	7290, 8544
MPyTPP-Cobaloxime	418	652, 712	8586, 9879
ZnMPyTPP-Cobaloxime	419	615, 634	7606, 8093

**Figure 4.4 - Fluorescence data for all porphyrin compounds in this study. All spectra were recorded in spectrophotometric grade DCM.**

Excitation into the Soret band of each of the porphyrin complexes gave rise to two emission bands with stokes shifts in the range 7290 - 9879 cm<sup>-1</sup>. All of the Zn-metallated porphyrins gave rise to a smaller stokes shift compared to their freebase counterparts. The addition of a cobaloxime moiety had little, to no influence the stokes shift observed for the porphyrin complexes, however, did result in quenching of fluorescence.

#### 4.3.3. Photocatalytic Hydrogen Generation Studies

All experiments to test for the photocatalytic generation of H<sub>2</sub> from water were carried out in triplicate according to the method described in Chapter 2 section 2.3.5.

Full details of experimental conditions are found in appendix B1 and B2.  
All complexes were tested under the conditions listed in Table 4.5.

Exp . No.	Conc. Complex (M)	TEA (%)	Water (%)	Irradiation $\lambda$ (nm)	Irradiation length (hr)
1	$5 \times 10^{-5}$	16.6	10	350	20
2	$5 \times 10^{-5}$	16.6	0	350	20
3	$5 \times 10^{-5}$	16.6	10	470	20
4	$5 \times 10^{-5}$	16.6	0	470	20

**Table 4.5- Experimental conditions for photocatalytic studies.**

No H<sub>2</sub> was detected in the headspace of the sample vial, however it cannot be ruled out that the amount formed was very small and below the limit of detection of the GC.

#### ***4.3.4. Cyclic Voltammetry***

##### **4.3.4.1. Reductive Electrochemistry**

Reductive electrochemistry was carried out on the all porphyrin and porphyrin-cobaloxime complexes in the range 0 V to -2.0 V. The potential window of DCM is between 0 and -2.0 V for reduction processes so experiments were not carried out at lower potential limits. Within this range several reduction process were observed and have been summarised in Table 4.6.

Cyclic Voltammetry Reduction Processes			
Complexes	E <sub>pa</sub> (V)	E <sub>pc</sub> (V)	E <sub>1/2</sub> (V)
Cobaloxime		-1.38 <sup>b</sup>	
MPyTPP	-1.45 <sup>a</sup>	-1.64 <sup>a</sup>	-1.545
	-1.78 <sup>a</sup>	-1.97 <sup>a</sup>	-1.875
ZnMPyTPP		-1.22 <sup>b</sup>	
	-1.62 <sup>a</sup>	-1.73 <sup>a</sup>	-1.675
MPyTPP-Cobaloxime		-1.4 <sup>b</sup>	
	-1.6 <sup>a</sup>	-1.75 <sup>a</sup>	-1.675
ZnMPyTPP-Cobaloxime		-1.51 <sup>b</sup>	
	-1.72 <sup>a</sup>	-1.84 <sup>a</sup>	-1.78
TPP	-1.37 <sup>a</sup>	-1.47 <sup>a</sup>	-1.42
	-1.79 <sup>a</sup>	-1.69 <sup>a</sup>	-1.75
ZnTPP		-1.39 <sup>b</sup>	
	-1.63 <sup>a</sup>	-1.74 <sup>a</sup>	-1.63

**Table 4.6-** The cyclic voltammetry results for the reduction processes of all porphyrins and porphyrin-cobaloxime complexes vs. Ag/AgCl in 0.1MTBAPF<sub>6</sub>/ DCM. a indicates an reversible reduction wave, b indicates an irreversible reduction wave.

All porphyrin complexes exhibited two mono-electronic reductions within the potential window of the solvent. Generally these two reduction processes observed at negative potentials are ascribed to the formation of the porphyrin radical anion, [porph]<sup>•-</sup> and dianion species, [porph]<sup>2-</sup>.<sup>15</sup> The coordination of the cobaloxime to the pridyl sub-unit of the porphyrin ring induces a cathodic shift in the reduction potentials observed.

#### 4.3.4.2. Oxidative Electrochemistry

Oxidative electrochemistry was carried out on the all porphyrin and porphyrin-cobaloxime complexes in the range 0V to 2.0 V. The potential window of DCM is between 0 and 2.0 V for oxidation processes so experiments were not carried out at higher potential limits. Within this range several oxidation processes were observed and have been summarised in Table 4.7.

Cyclic Voltammetry Oxidation Processes			
	E <sub>pa</sub> (V)	E <sub>pc</sub> (V)	E <sub>1/2</sub> (V)
Cobaloxime	1.00 <sup>c</sup>	0.81 <sup>c</sup>	0.90
	1.39		
MPyTPP	0.99 <sup>b</sup>		
	1.74 <sup>b</sup>		
ZnMPyTPP	0.97 <sup>a</sup>	0.89 <sup>a</sup>	0.93
	1.24 <sup>a</sup>	1.13 <sup>a</sup>	1.185
MPyTPP-Cobaloxime	0.89 <sup>c</sup>	0.82 <sup>c</sup>	0.85
	1.30 <sup>b</sup>		
	1.57 <sup>b</sup>		
ZnMPyTPP-Cobaloxime	0.75 <sup>a</sup>	0.57 <sup>a</sup>	0.66
	1.1 <sup>a</sup>	0.87 <sup>a</sup>	0.985
TPP	1.07 <sup>a</sup>	0.98 <sup>a</sup>	1.03
	1.40 <sup>a</sup>	1.30 <sup>a</sup>	1.35
ZnTPP	0.95 <sup>a</sup>	0.86 <sup>a</sup>	0.90
	1.26 <sup>a</sup>	1.16 <sup>a</sup>	1.22

**Table 4.7-** The cyclic voltammetry results for the oxidation processes of all porphyrins and porphyrin-cobaloxime complexes vs. Ag/AgCl in 0.1M TBAPF<sub>6</sub>/ DCM. a indicates an reversible oxidation wave, b indicates an irreversible oxidation wave and c indicates a quasi-reversible oxidation wave.

All porphyrin complexes exhibited two mono-electronic oxidations within the potential window of the solvent. Generally these two reduction processes observed at positive potentials are ascribed to the formation of the porphyrin radical cation, [porph]<sup>•+</sup> and dication species, [porph]<sup>2+</sup>.<sup>15</sup> The coordination of the cobaloxime to the pyridyl sub-unit of the porphyrin ring induces a cathodic shift in the oxidation potentials observed.

#### 4.3.5. Electrocatalytic Hydrogen Generation Studies

All compounds were assessed for their ability to produce hydrogen (Fig 4.21 and Fig 4.22). All experiments were carried out using pH 2.0, 0.1 M NaH<sub>2</sub>PO<sub>4</sub> buffer, a glassy carbon working electrode, an Ag/ AgCl reference electrode filled with 3 M KCl and a platinum wire counter electrode in an airtight v-shaped electrolysis cell. Full details of the experimental set-up are available in Appendix C1.



#### 4.3.5.1 Onset of Catalytic Current

A series of cyclic voltammogram experiments were carried out using both the bare glassy carbon electrode and glassy carbon electrodes with modified surfaces. The scans were performed at  $0.1 \text{ Vs}^{-1}$  from 0V to -1.2 V in pH 2.0, 0.1 M  $\text{NaH}_2\text{PO}_4$  buffer. A substantial new process is visible in these CVs when the cyclic voltammograms produced were compared to similar CVs run in ACN. This process is assigned to the catalytic production of  $\text{H}_2$  in aqueous media and was confirmed through GC analysis of the headspace after the experiment. Table 4.8 details the onset of this process according to the complex used to modify the surface.

Complex	Onset of Catalytic Current (V)
Bare Electrode	-1.15
Cobaloxime	-0.98
MPyTPP	-1.0
MPyTPP-Cobaloxime	-1.1
ZnMPyTPP	-0.87
ZnMPyTPP-Cobaloxime	-0.95
TPP	-0.87
ZnTPP	-1.04

**Table 4.8-** The potential at which the catalytic current onsets through modification of the glassy carbon electrode surface with the complexes utilised in this study. All potentials are quoted vs. Ag/AgCl.

The onset of the catalytic current is altered through coordination of the porphyrin rings to the electron donating cobaloxime unit which is consistent with the CV measurements made in ACN previously (Section 4.3.4.1). The currents produced by the bare electrode were greatly enhanced through modification with the complexes. ZnMPyTPP presented the strongest catalytic current with the onset of this current occurring at 0.87 V.

#### 4.3.5.2. Varying Bulk Electrolysis Potential

MPyTPP/ MPyTPP-Cobaloxime and cobaloxime were chosen as a model series and were tested at various applied electrolysis potentials, the results are shown in Table 4.9.  $1.5 \times 10^{-10}$  moles of each compound was coated on the surface of a glassy carbon electrode and varying potentiostatic electrolysis potentials were applied for one hour in pH 2.0, 0.1 M  $\text{NaH}_2\text{PO}_4$  buffer solution. During these tests a constant potential is applied to the system over the course of a 1 hour experiment. The current passed through the system as a function of  $\text{H}_2$  generation is measured and using Faraday's law of electrolysis is related to the number of moles of  $\text{H}_2$  generated during the experiment. After 1 hour a 1 ml sample of the headspace in the reaction vessel is injected in to the GC where it's actual  $\text{H}_2$  content is measured. The charge passed after one hour at the applied potential was measured and compared to the charge passed by a bare electrode under the same experimental conditions. Each experiment was repeated 3 times and the results are presented below. Full calculation details are available in Appendix C2.

Modification of the electrode surface resulted in the production of  $\text{H}_2$  during bulk electrolysis experiments at less negative potentials. Reasonable TONs were measured for MPyTPP-oxime at an applied potential of -1.2 V while the MPyTPP ligand was capable of generating larger TONs at the same potential, which is consistent with the observed onset of the catalytic current being induced at slightly more positive potentials when the surface is modified with this MPyTPP. Cobaloxime itself is capable of generating reasonably high TONs upon application of a potential of -1.0 V however TONs generated are not as high as those observed when -1.2 V is applied.

Compound	Bulk Electrolysis Applied Potential (V)	Charge Passed After 1 Hour (C)	Echem TON ( $\times 10^3$ )	GC TON ( $\times 10^3$ )
<u>Bare Electrode</u>	-0.7	$3.37 \times 10^{-4}$	-	-
	-0.8	$9.03 \times 10^{-4}$	-	-
	-1	$1.90 \times 10^{-2}$	-	-
	-1.1	$1.99 \times 10^{-2}$	-	-
	-1.2	$2.63 \times 10^{-2}$	-	-
	-1.3	$8.97 \times 10^{-1}$	-	-
<u>MPyTPP</u>	-0.8	$6.27 \times 10^{-2}$	0.2	0*
	-1	$3.07 \times 10^{-2}$	1.1	0*
	-1.1	$6.97 \times 10^{-2}$	2.4	0*
	-1.2	$3.01 \times 10^{-1}$	10.4	6.5
	-1.3	$8.42 \times 10^{-1}$	29.1	10.5
<u>MPyTPP-Oxime</u>	-0.8	$8.17 \times 10^{-4}$	0.3	0*
	-1	$3.62 \times 10^{-2}$	1.3	0*
	-1.1	$8.11 \times 10^{-2}$	2.8	0*
	-1.2	$1.07 \times 10^{-1}$	3.7	1.8
	-1.3	$5.35 \times 10^{-1}$	18.5	2.7
<u>Cobaloxime</u>	-0.7	$4.74 \times 10^{-4}$	0.02	0*
	-0.8	$1.25 \times 10^{-3}$	0.04	0*
	-1	$2.115 \times 10^{-1}$	7.3	6.5
	-1.1	$3.80 \times 10^{-1}$	13.1	8.0
	-1.2	$4.54 \times 10^{-1}$	15.7	10.2
	-1.3	$9.37 \times 10^{-1}$	32.4	21.1

Table 4.9- Results of experiments varying the applied potential during potentiostatic electrolysis of the porphyrin complexes. BE = bulk electrolysis. \* Amount of H<sub>2</sub> generated was below the limit of detection of the GC. All TON are quoted  $\pm$  30%.

#### 4.3.5.3. H<sub>2</sub> Generation TONs

Each compound was tested using an applied potential of -1.2 V for 1 hour and the resulting hydrogen TONs generated were determined. A 1ml sample of the headspace was injected into a GC and the GC calculated TONs were also compared to measure the overall efficiency of the electrochemical reaction (Table 4.10).

Compound	Charge Passed After 1 Hr (C)	Electrochemical TON ( $\times 10^3$ )	GC TON ( $\times 10^3$ )	Efficiency %	Avg current during BE (A)	Current Density (mA/cm <sup>2</sup> )
Cobaloxime	0.454	15.7	8.0	51	$1.52 \times 10^{-4}$	2.18
MPyTPP	0.301	10.4	6.5	62	$1.93 \times 10^{-4}$	2.76
ZnMPyTPP	0.3722	12.9	7.6	59	$9.66 \times 10^{-5}$	1.38
MPyTPP-Oxime	0.107	3.7	1.8	49	$7.52 \times 10^{-5}$	1.07
ZnMPyTPP-Oxime	0.227	7.8	5.1	65	$8.05 \times 10^{-5}$	1.15
TPP	0.395	13.6	8.7	64	$1.08 \times 10^{-4}$	1.55
ZnTPP	0.386	13.5	10.5	78	$1.31 \times 10^{-4}$	1.87

**Table 4.10- Results of electrocatalytic studies for all porphyrin and porphyrin-cobaloxime complexes. BE = bulk electrolysis experiment. All TON are quoted  $\pm 30\%$ .**

## 4.4. Discussion

**Synthesis.** TPP and MPyTPP were synthesised following the Alder method and were isolated in yields of 16 and 11 % respectively.<sup>46</sup> These low yields were expected due to the many mixed porphyrin side products which are formed during the reaction and the difficulty of isolation during column chromatography. Their Zn metallated complexes were produced through an overnight reaction using zinc acetate and have been previously synthesised by other research groups. All spectral data are in agreement with reported data.<sup>46</sup>

The cobaloxime derivatives synthesised are novel to the best of our knowledge, and all spectral data are in agreement with their formulation and compare well to similar compounds which have been previously reported in literature.<sup>28</sup> Coordination of the cobaloxime moiety was achieved through the nitrogen group in the pyridyl substituent on the porphyrin ring following loss of a chloride group from the Co metal centre. Yields of up to 87% were achieved during these synthetic experiments.

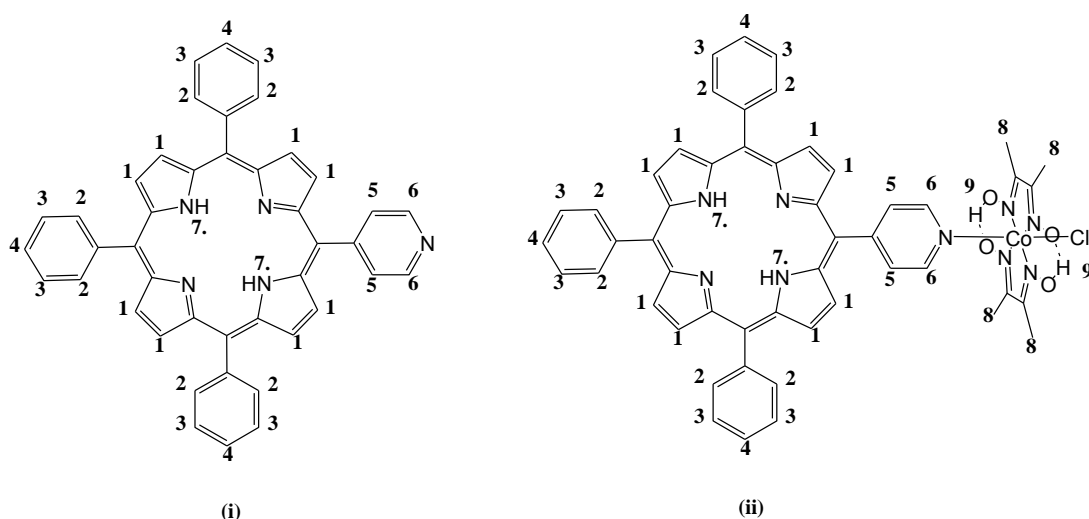
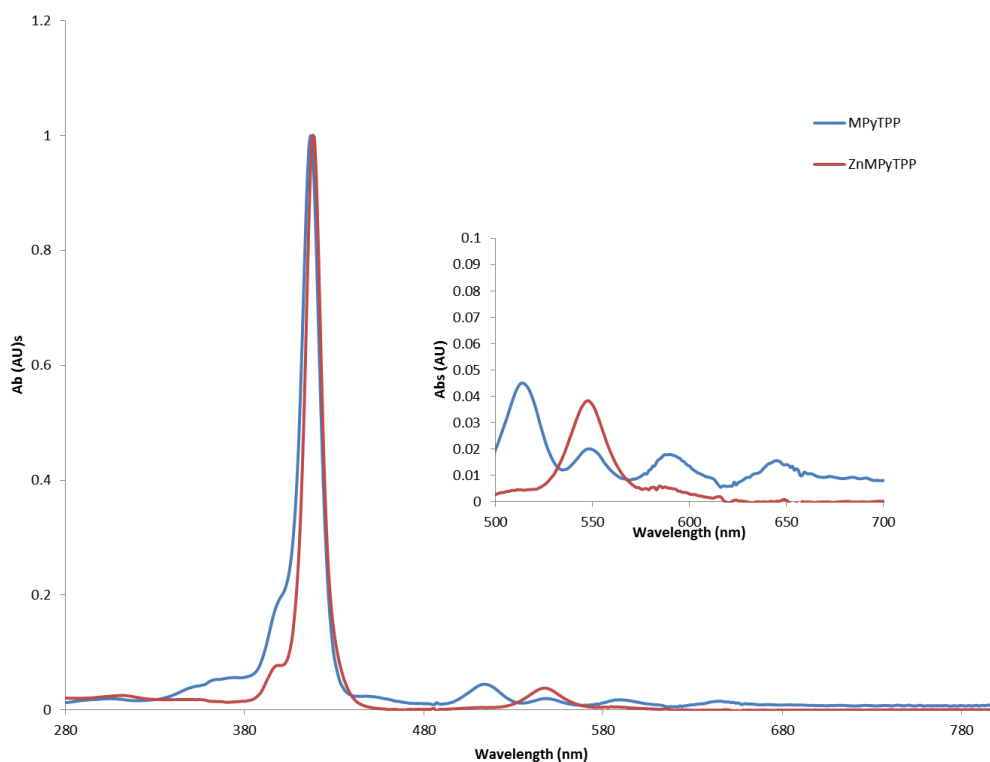


Figure 4.14- Numbering of protons in monopyrrolic-porphyrins and their cobaloxime complexes.

**NMR Spectroscopy.** The  $^1\text{H}$ NMR spectral signals of both MPyTPP and MPyTPP-cobaloxime due to the  $\beta$ -aromatic protons (**1**) on the porphyrin ring system are visible from 9.04 ppm to 8.65 ppm, with the protons closest to the pyridyl group being split into two sets of doublets at 9.04 ppm and 9.1 ppm. The addition of the cobaloxime moiety shifts all of the signals slightly upfield due to the shielding effect of the cobaloxime. The phenyl protons (**2-4**) appear in the aromatic region also. The signal from protons (**2**) appear more downfield than protons (**3**) and (**4**) which are on the outermost periphery of the porphyrin structure. Due to the presence of a lone pair on the nitrogen of the pyridyl group protons (**5**) and (**6**) are observed at quite different ppm values, with (**6**) appearing further upfield than protons (**5**). The two internal NH protons (**7**) are observed at negative ppm values as there is a great amount of shielding due to the ring structure enclosing these protons. Protons (**7**) generally appear at -2 ppm. The disappearance of these protons is used as an indication of successful metallation of the porphyrin ring. The coordination of the to the cobaloxime moiety leads to the appearance of a strong singlet signal at 2.6 ppm (**8**). The OH protons (**9**) on glyoxime subunit gives rise to a broad signal  $\sim$  12.2 ppm.

Examples of the  $^1\text{H}$  NMR of the compounds synthesised in this study are available in appendix D1.

**Electronic Absorbance Spectroscopy.** The absorbance spectra of MPyTPP and ZnMPyTPP are very similar and in agreement with previous studies.<sup>47</sup> After the addition of the Zn metal centre two of the Q-bands are no longer visible. This occurs as the metallated porphyrin possesses  $D_{4h}$  symmetry, which is more symmetrical than its freebase counterpart,  $D_{2h}$ .<sup>15</sup> This loss of two of the Q-bands is also evident when comparing the absorbance spectra of ZnTPP and TPP and ZnMPyTPP-cobaloxime and MPyTPP-cobaloxime.



**Figure 4.16-** UV-Vis spectra of MPyTPP (blue line) and ZnMPyTPP (red line). Q-band region has been expanded in the inset. All spectra were recorded in spectroscopic grade DCM. Conc.  $1.5 \times 10^{-1}$  M.

The Soret band of MPyTPP and ZnMPyTPP were observed at 416 nm and 418 nm respectively (Fig. 4.16). After the addition of a cobaloxime unit to produce MPyTPP-cobaloxime and ZnMPyTPP-cobaloxime the absorbances are red shifted and display their Soret band at 418 nm and 419 nm respectively (Fig. 4.15). This represented a small bathochromic shift of 2 nm and 1 nm when compared to MPyTPP and ZnMPyTPP. This small red-shift was observed by Zhang *et al.*<sup>28</sup> when they studied the absorbance spectra of similar porphyrin-cobaloxime complexes and attribute the difference in spectra to the interaction between the pyridyl-porphyrin and the cobalt centre.

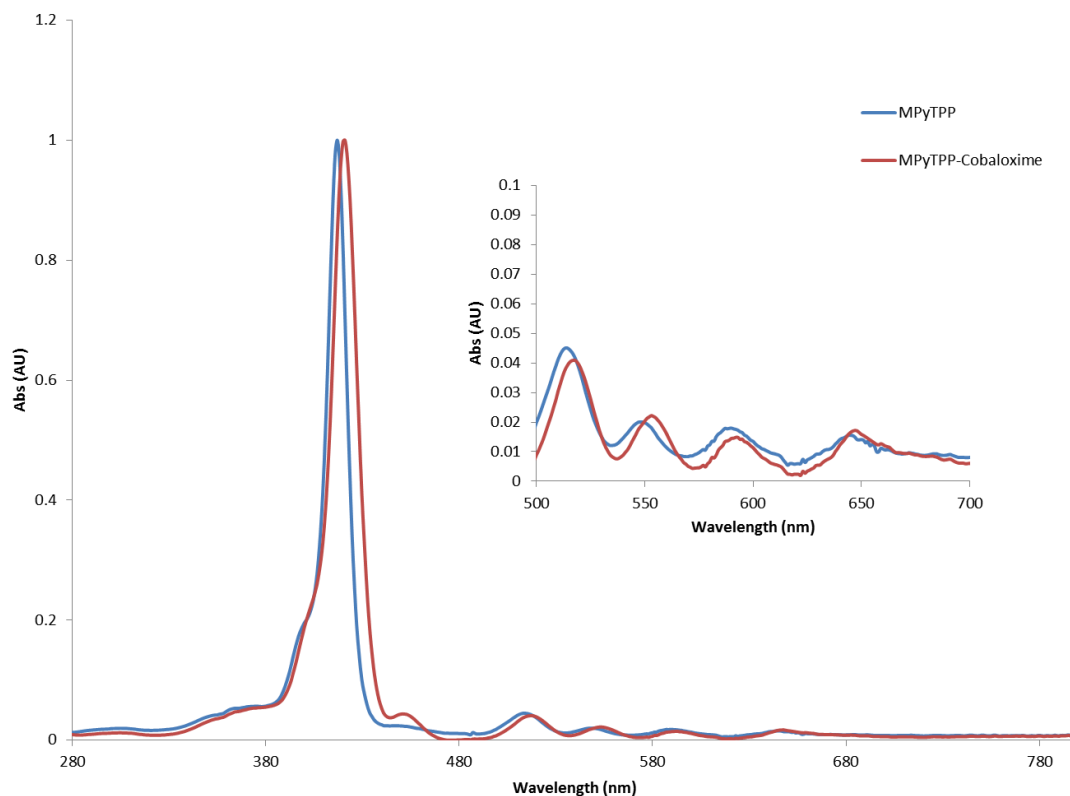


**Figure 4.15 - UV-Vis spectra of MPyTPP (blue line) and MPyTPP-Cobaloxime (red line). Q-band region has been expanded in the inset. All spectra were recorded in spectroscopic grade DCM. Conc.  $1.2 \times 10^{-1}$  M.**

The Soret and Q-bands of the freebase mono-pyridylporphyrins (MPyTPP and MPyTPP-cobaloxime) appear at a shorter wavelength than those of TPP. This represents a hypsochromic shift of 2- 4 nm for the Soret bands and between 4 and 8 nm for the Q-bands. However the Soret of the Zn-metallated mono-pyridylporphyrins (ZnMPyTPP and ZnMPyTPP-cobaloxime) appear at slightly longer wavelengths than the ZnTPP absorbances. These bands are red shifted 3- 4 nm for the Soret bands. The Q-bands of ZnMPyTPP and ZnMPyTPP-cobaloxime are observed at higher energy wavelengths than TPP representing a blue shift of between 9 nm and 16 nm indicating a possible shift in the energy of the first singlet excited state.

It can be observed from the FWHM values given in Table 4.3, the values for the pyridylporphyrins, MPyTPP =  $8.33 \times 10^5 \text{ cm}^{-1}$  and ZnMPyTPP =  $9.09 \times 10^6 \text{ cm}^{-1}$ , are significantly larger than those of TPP at  $6.13 \times 10^5 \text{ cm}^{-1}$  and ZnTPP at  $6.59 \times 10^5 \text{ cm}^{-1}$ , which could suggest higher electronic and vibronic coupling between the  $\pi$ -



ring system and the meso substituted pyridyl groups.<sup>48</sup> The relative intensities of the Q-bands remained unaltered after coordination of the cobaloxime centre indicating that the relative energies of the ground state and the first excited triplet state remain unchanged by substitution

**Fluorescence Spectroscopy.** The absorption and fluorescence spectra of MPyTPP are shown below in Fig. 4.15. As is evident from the graph excitation at 416 nm into the Soret band of the porphyrin gives rise to two unresolved emission bands which is expected for porphyrin complexes.<sup>48</sup>

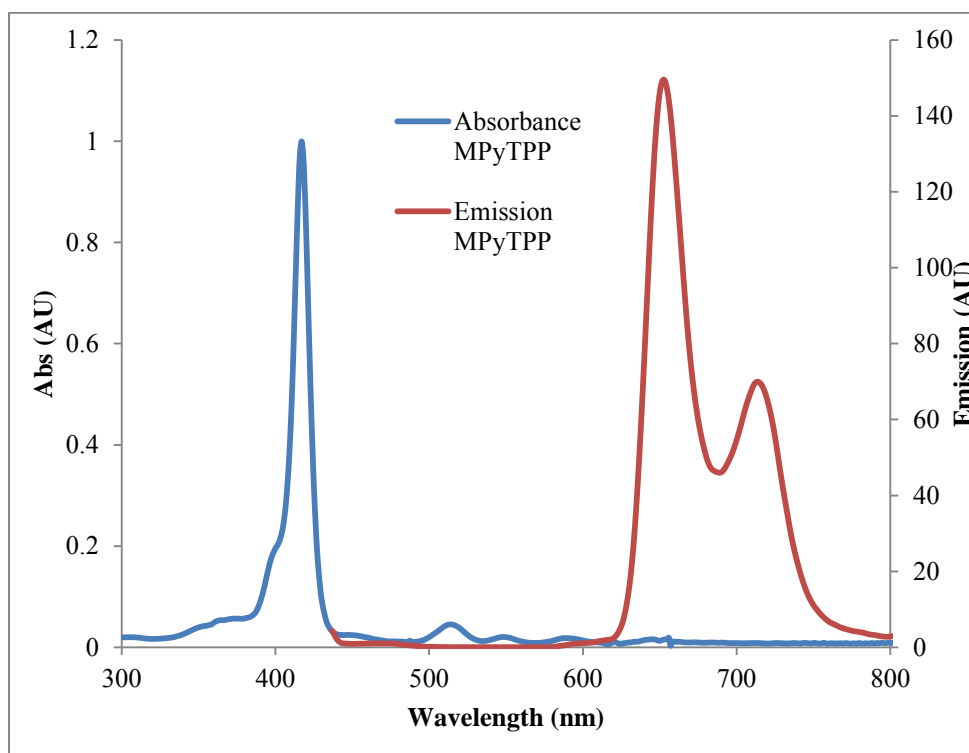
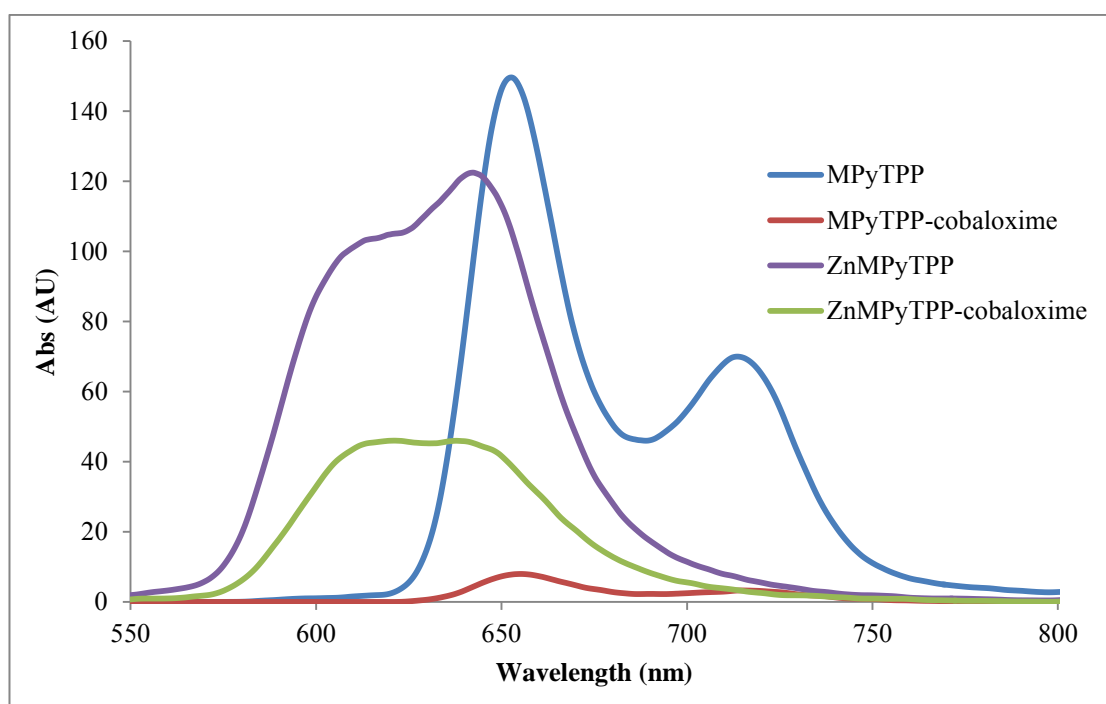


Figure 4.15 – UV-Vis spectrum (blue line) and emission spectrum after excitation at 419nm (red line) of MPyTPP. All spectra were recorded in spectrophotometric grade DCM.  $\lambda_{\text{Ex}} = 416 \text{ nm}$ .

The fluorescence spectra of MPyTPP, ZnMPyTPP and the novel cobaloxime porphyrins studied in this chapter are shown below (Fig. 4.16). The most obvious difference in the fluorescence spectra of the porphyrins and the cobaloxime coordinated porphyrins is that the emission intensity of the cobaloxime derivatives are greatly decreased with respect to their equivalent uncoordinated porphyrins. This quenching indicates electronic communication between the porphyrin ring and the cobalt metal centre. This is most evident when studying the emission spectra of

MPyTPP and MPyTPP-cobaloxime. The quenching of the emission of MPyTPP-cobaloxime is  $\sim 96\%$  when compared to MPyTPP.

The emission profile of the Zn-porphyrins is less defined than the freebased porphyrins. The emission of ZnMPyTPP is somewhat quenched in comparison to MPyTPP suggesting some electronic communication occurs between the ring and the Zn metal centre. The intensity of the emission of ZnMPyTPP-cobaloxime was  $\sim 66\%$  less than that of ZnMPyTPP. This complexation of cobaloxime to the Zn-porphyrins lead to less quenching of the emission band than was evident in the freebase porphyrins, in fact the intensity was decreased by 63% (as opposed to 96%) leading to the conclusion that addition of the Zn metal centre hinders the efficiency of the electron/energy transfer from the porphyrin ring to the cobalt centre in the cobaloxime moiety.



**Figure 4.16-** Emission spectrum of MPyTPP (blue line), MPyTPP-cobaloxime (red line), ZnMPyTPP (purple line) and ZnMPyTPP-cobaloxime (green line). All spectra were recorded in spectrophotometric grade DCM and all complexes are isoabsorptive.  $\lambda_{\text{Ex}}$  MPyTPP = 416 nm, MPyTPP-cobaloxime = 418 nm, ZnMPyTPP = 418 nm and ZnMPyTPP-cobaloxime = 419 nm.

Large Stokes shifts ( $7290\text{ cm}^{-1}$  to  $9879\text{ cm}^{-1}$ ) indicate that the pyridyl-porphyrins undergo considerable excited state structural distributions. The Zn-metallated porphyrins possess the smallest stokes shift owing to their more stable nature and the

less symmetrical structure of the freebased porphyrins. The addition of the cobaloxime moiety does not greatly affect the stokes shifts of the porphyrins.

**Photocatalytic H<sub>2</sub> generation Experiments.** Photoinduced hydrogen evolution catalysed by TPP, ZnTPP, MPyTPP, ZnMPyTPP, MPyTPP-cobaloxime and ZnMPyTPP-cobaloxime were studied. In efforts to develop novel, non-noble metal photocatalytic systems the utilisation of the cobalt glyoxime metal centre is an ideal alternative to expensive and rare metals such as Ru, Ir, Pt and Pd which have been used previously. Using the porphyrin ring as a light harvesting complex, efficient electron transfer through the meso-pyridyl ring to the cobalt catalytic centre was anticipated. At the cobalt centre water would be split through the formation of a metal hydride followed by a bimolecular reductive elimination or the reaction of the metal hydride with another H<sup>+</sup> in solution to yield molecular hydrogen. During the photocatalytic experiments no H<sub>2</sub> was detected using GC analysis; either because the amount formed was lower than the LOD, or no H<sub>2</sub> was produced. Low TONs of H<sub>2</sub> production have been reported for porphyrin and cobaloxime which are similar to those reported in this study. The reasons for the lack of hydrogen produced by these intermolecular systems are at present not clear. The absorption features of the porphyrin unit are closely tuned to the light source, which have wavelengths of 350 and 470 nm, so absorption of light should not be a problem. The regeneration of the porphyrin photosensitiser by the sacrificial agents may be problematic, both from the energetics point of view and the aggressive nature of the radicals formed from TEA during the regenerating process. Importantly it is also worth stating that the limit of detection of the GC used is <100 ppm. Porphyrin rings are known to be efficient light absorbing complexes<sup>15,16</sup> and have been used in a variety of systems as effective electron transfer devices.<sup>17-20</sup> TONs of up to 63 have been reported using porphyrin systems.<sup>24</sup> Cobaloxime complexes have demonstrated efficiencies in the photocatalysed production of hydrogen<sup>49</sup> and achieved TON of up to ~300 have been achieved. However hydrogen production has been reported using a porphyrin photosensitiser and a cobaloxime catalytic centre similar to the complexes reported in this study. Zhang et. al.<sup>50</sup> have shown photoinduced H<sub>2</sub> evolution using complex **12**, **13** and **14** with TEA as a sacrificial donor following irradiation  $\lambda_{\text{exc}} > 400\text{nm}$ . A TON of 22 was reported for **12**. Both **13** showed a far poorer TON of 3 and **14** only produced a trace amount.

**Electrochemistry.** Due to solubility issues accurate concentrations of samples was not possible, however, samples prepared were  $\sim 1$  mmol concentration. The electrochemistry of pyridyl appended porphyrins and their cobaloxime coordinated counterparts have been investigated. For comparison TPP and ZnTPP have been examined under the same conditions and the data have been summarised in Tables 4.6 and 4.7.

Porphyrins are electroactive systems are known to undergo multiple redox processes. Porphyrins generally display one to two ring centred reductions and one to two ring centred oxidations. All of the porphyrins in this study undergo two reduction processes. Generally these two reduction processes observed at negative potentials are ascribed to the formation of the porphyrin radical anion,  $[\text{porph}]^{\cdot-}$  and dianion species,  $[\text{porph}]^{2-}$ .<sup>15</sup>

The redox potentials of TPP and ZnTPP compared well with the literature.<sup>2,51</sup> TPP possesses two reversible mono-electronic reductions at -1.42 V and -1.75 V. MPyTPP possesses two, mono-electronic reversible reductions at  $E_{1/2} = -1.545$  V and -1.875 V respectively presenting a cathodic shift of  $\sim 0.15$  V when compared with the reductions observed for TPP, this is due to electron donation from the pyridyl group. Addition of a Zn metal to the centre of the MPyTPP ring shifts these reductions to the more anodic potentials of -1.22 V and -1.68 V (Fig. 4.17). The same anodic shift was observed when comparing the reduction potentials of TPP and ZnTPP; a shift of  $\sim 0.11$  V was identified upon Zn coordination. The first ring based reduction which occurs on ZnTPP and ZnMPyTPP, however is irreversible but the second reduction is completely reversible,  $I_a/I_c = 1.03$ .

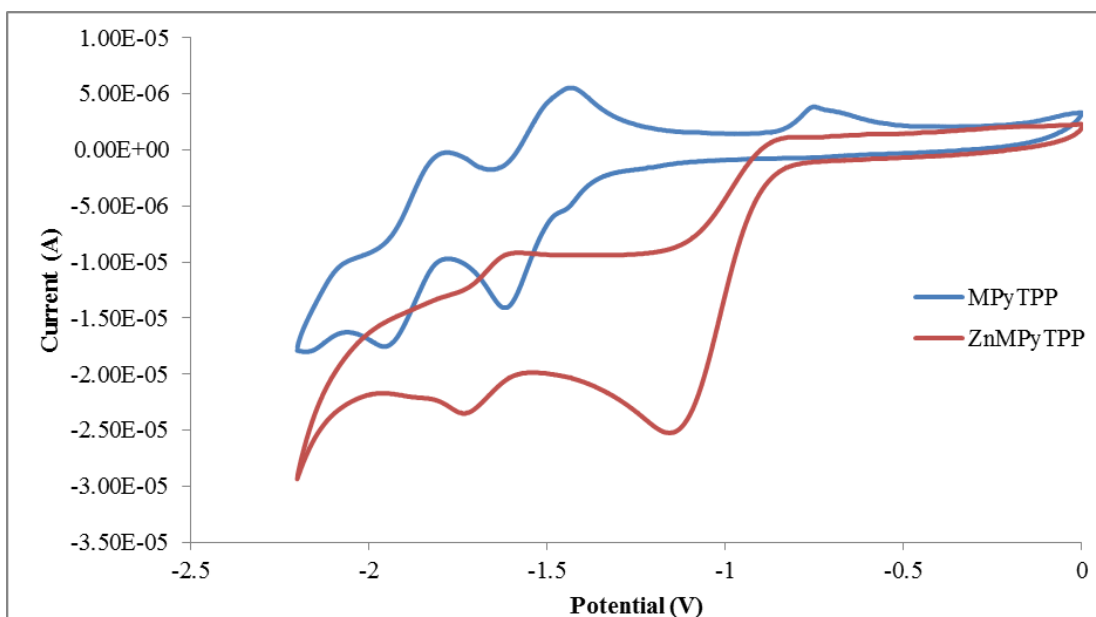


**Figure 4.17**-Cyclic voltammogram of MPyTPP and ZnMPyTPP in 0.1 M TBAPF<sub>6</sub>/ DCM illustrating the reduction processes and the shift to more anodic potentials due to coordination of a Zn metal centre. Scan rate 0.1 Vsec<sup>-1</sup>.

Two reductions were also visible upon complexation of MPyTPP with a cobaloxime group (Fig. 4.18). The ring based reductions occurred at even more negative potentials than ZnMPyTPP yielding a reversible wave at  $E_{1/2} = -1.675$  V. The second ring based reduction was not visible due to the electron donating nature of the cobaloxime moiety inducing more difficult reductions. A second irreversible redox process is visible in the electrochemical window of MPyTPP-cobaloxime at -1.4 V and is attributed to the reduction of the cobalt metal centre,  $\text{Co}^{3+}/\text{Co}^{2+}$  due to its similarity to this reduction in cobaloxime itself (Fig. 4.18).<sup>52</sup>

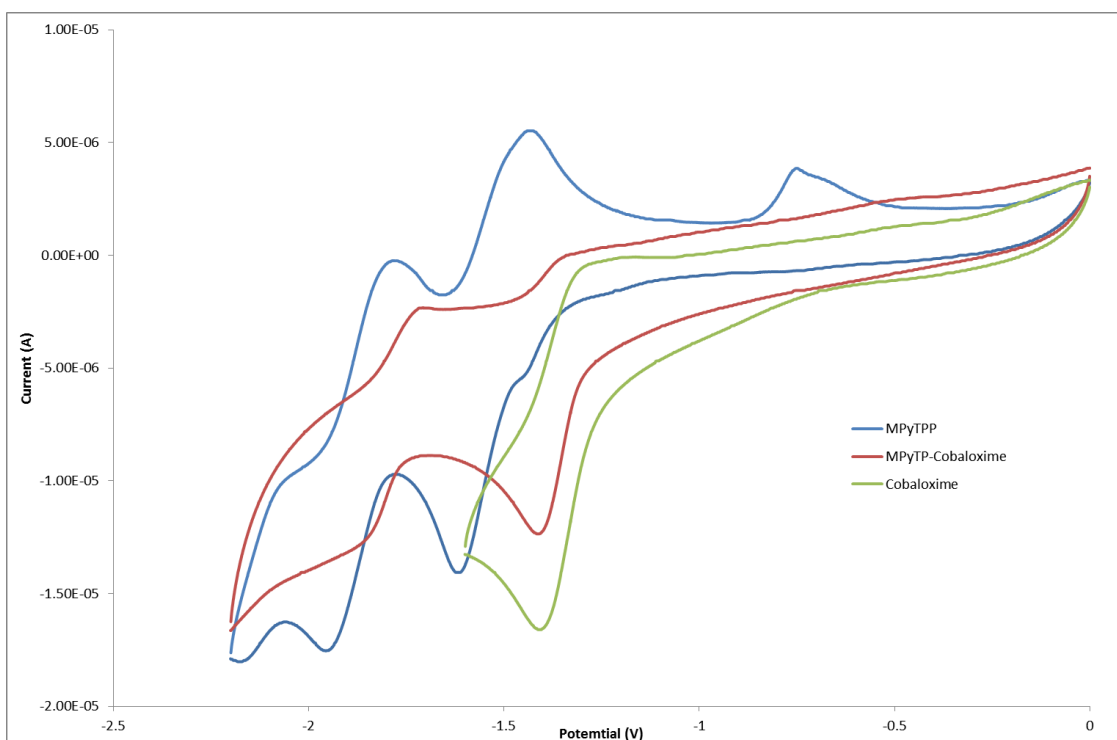


**Figure 4.17-** Cyclic voltammogram of MPyTPP (blue line), MPyTPP-cobaloxime (red line) and cobaloxime (green line) in 0.1M TBAPF<sub>6</sub>/ DCM illustrating their reduction processes. Scan rate 0.1 Vsec<sup>-1</sup>.

The addition of a cobaloxime group to ZnMPyTPP had a similar effect on the redox processes in the porphyrin. The first ring based reduction was shifted cathodically from -1.22 V to -1.78 V. This irreversible process represented a significant shift of 0.53 V due to electron donation from the cobaloxime group. The second ring based reduction was not visible within the potential window of DCM. An irreversible reduction, due to the Co<sup>2+</sup>/ Co<sup>3+</sup> redox couple was observed at -1.51 V.

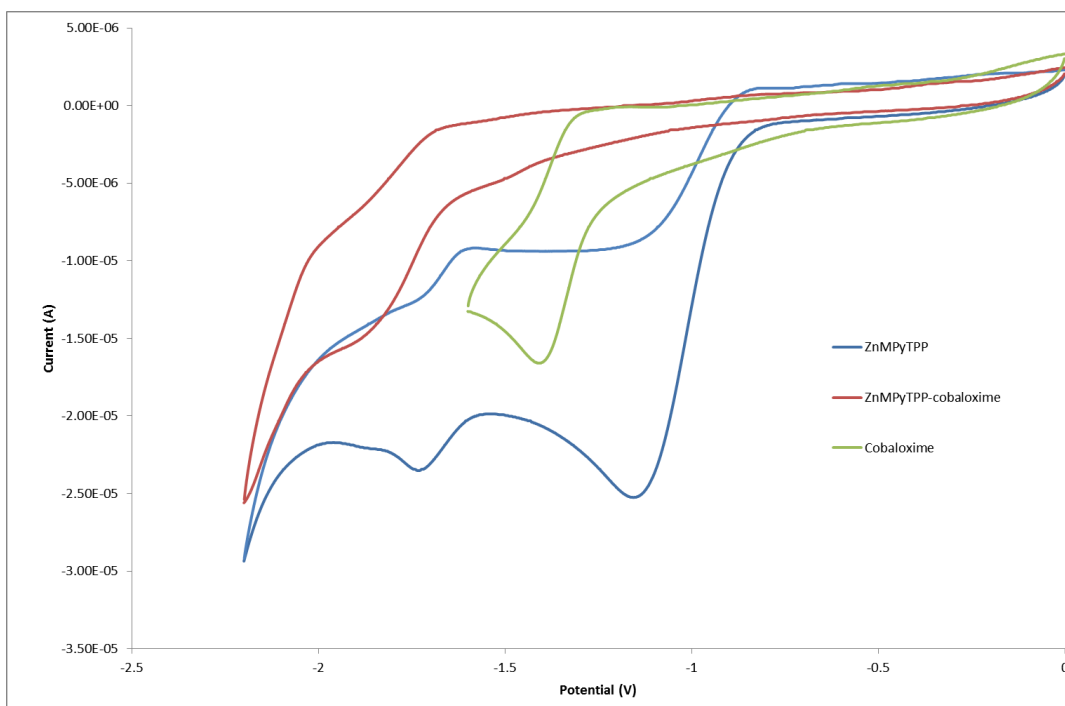


**Figure 4.18-** Cyclic voltammogram of ZnMPyTPP (blue line), ZnMPyTPP-cobaloxime (red line) and cobaloxime (green line) in 0.1 M TBAPF<sub>6</sub>/DCM illustrating their reduction processes. Scan rate 0.1 Vsec<sup>-1</sup>.

Oxidation of a porphyrin species generally consists of two mono-electronic oxidations of the porphyrin ring itself yielding the radical cation, [porph]<sup>•+</sup> and the dication, [porph]<sup>2+</sup>.<sup>15</sup> The oxidation potentials of these processes in TPP and ZnTPP compared well with literature values.<sup>2,51</sup> Introduction of a Zn metal centre induced an cathodic shift of 0.13 V. MPyTPP possesses two, mono-electronic oxidations at 0.99 V and 1.74 V respectively presenting a cathodic shift when compared with the oxidations observed for TPP. The oxidation potentials of the TPP ring shift to more anodic potentials of between 0.12 V and 0.14 V upon Zn coordination. The same trend was observed following addition of a Zn metal to the centre of the MPyTPP ring. This coordination shifts the oxidations to the more anodic potentials of 0.89 V and 0.97 V yielding reversible processes.

One ring based oxidation is visible upon complexation of MPyTPP with a cobaloxime group (Fig. 4.19). This is the second ring based oxidation and it occurred at even more positive potentials than MPyTPP irreversible wave at 1.57 V. The first ring based oxidation process is presumably obscured by an oxidation process at the Co metal centre. This third redox process is quasi-reversible at this scan rate and is

visible in the electrochemical window of MPyTPP-cobaloxime at 0.85 V and is attributed to the oxidation of the cobalt metal centre,  $\text{Co}^{3+}/\text{Co}^{4+}$  due to its similarity to this oxidation in cobaloxime itself (Fig. 4.19).<sup>52</sup> The fourth and irreversible oxidation wave at 1.30 V is another cobaloxime based oxidation and induced the formation of a reduction band at 0.27 V due to decomposition products formed (this reduction is visible at 0.43 V in the cobaloxime CV).

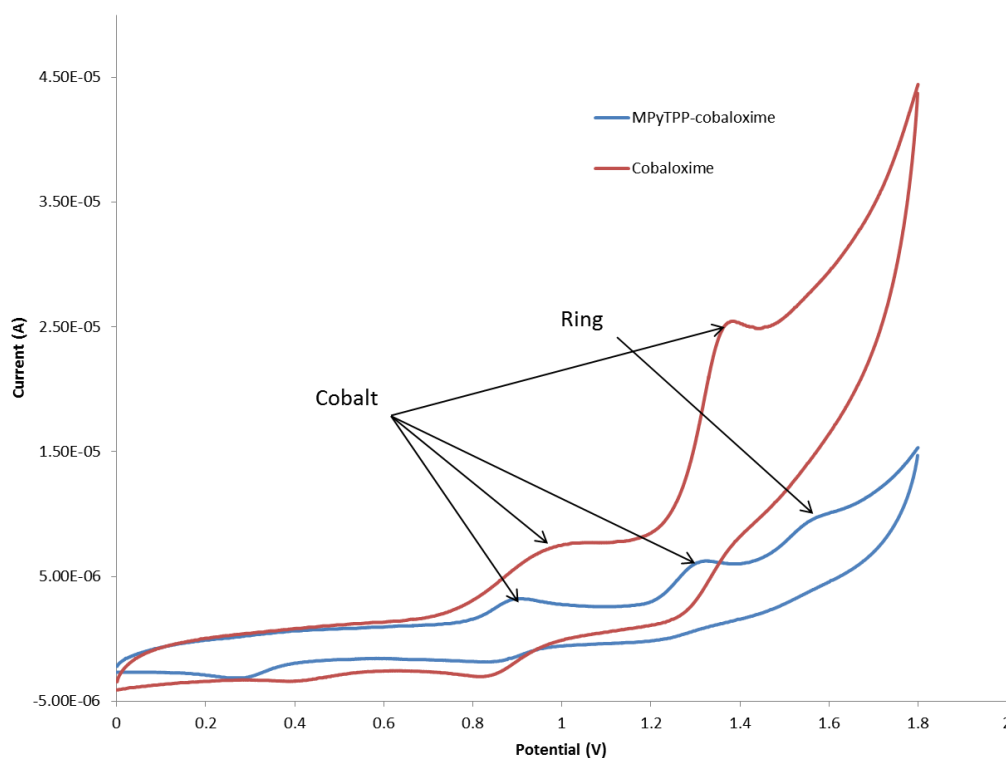


**Figure 4.19-**Cyclic voltammogram of MPyTPP-cobaloxime (blue line) and Cobaloxime (red line) in 0.1 M TBAPF<sub>6</sub>/ DCM illustrating the reduction processes of MPyTPP-cobaloxime and their origin compared to cobaloxime. Scan rate 0.1 Vsec<sup>-1</sup>.

The addition of a cobaloxime group to ZnMPyTPP had a similar effect on the redox processes in the porphyrin. The first ring based oxidation was shifted cathodically from 0.93 V to 0.75 V. This represented a shift of 0.18 V due to electron donation from the cobaloxime group. The second ring based reduction was reversible and shifted from 1.19 V to 0.99 V, a cathodic shift of 0.2 V. No Co based oxidations



were visible within the potential window. These processes were possible obscured by the strong oxidations observed on the porphyrin ring (Fig. 4.20).

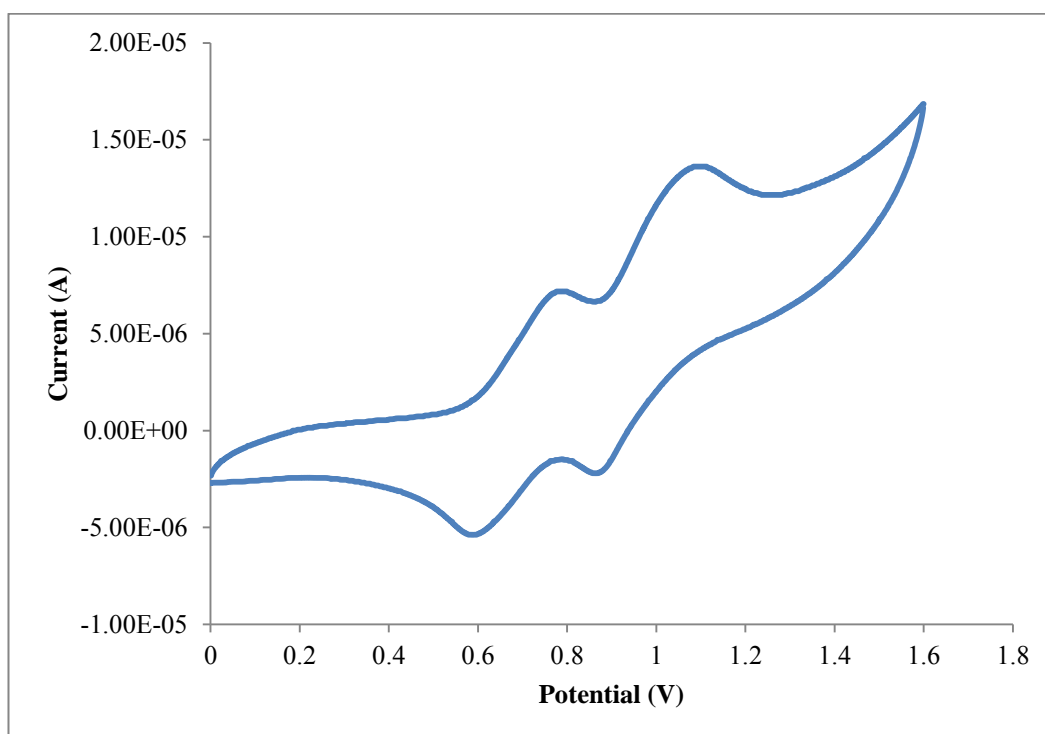


**Figure 4.20-** Cyclic voltammogram of ZnMPyTPP-cobaloxime in 0.1M TBAPF<sub>6</sub>/ DCM illustrating the oxidation processes. Scan rate 0.1 Vsec<sup>-1</sup>.

It has been shown that Zn coordination does not affect the HOMO-LUMO band gap of TPP when complexed however Zn does interact with varying the meso substituted groups.<sup>33,34</sup> This HOMO-LUMO energy gap of TPP and ZnTPP have been measured as  $2.25 \pm 0.15$  V (Table 4.9).<sup>29</sup> This is also similar for MPyTPP and ZnMPyTPP as is evident from Table 4.9. Coordination of the cobaloxime unit leads to a change in HOMO-LUMO energy gap in MPyTPP-cobaloxime (2.93 eV) but not for ZnMPyTPP-cobaloxime (2.13 eV). This suggests that the addition of cobaloxime to MPyTPP destabilises the energy levels within the porphyrin.

Complex	HOMO-LUMO Energy Gap (eV)
MPyTPP	2.23
ZnMPyTPP	2.13
MPyTPP-cobaloxime	<b>2.93</b>
ZnMPyTPP-cobaloxime	2.13
TPP	2.43
ZnTPP	2.23

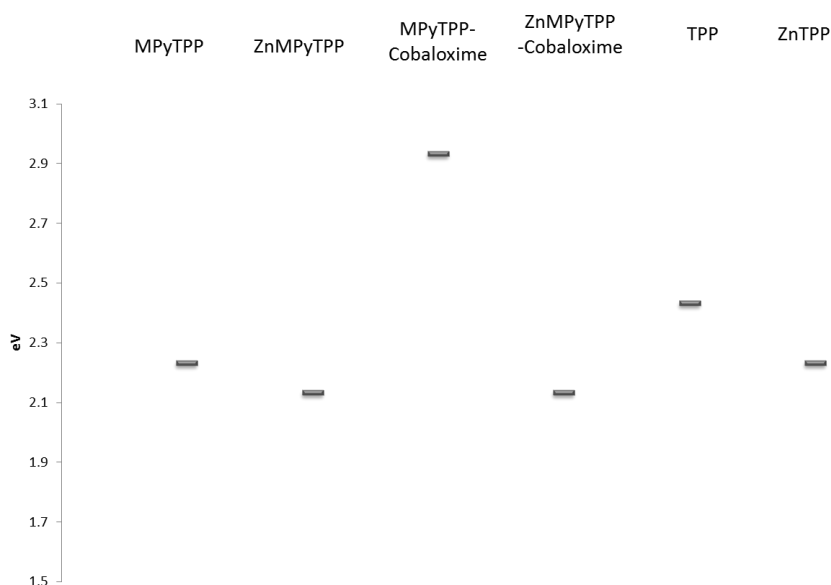


**Table 4.9- HOMO-LUMO energy gaps of complexes studied in this chapter.**

**Electrocatalytic H<sub>2</sub> Generation Experiments.** Electrocatalytic H<sub>2</sub> production was observed at pH 2.0, in 0.1 M NaH<sub>2</sub>PO<sub>4</sub> buffer solution. In Fig. 4.21 the cyclic voltammogram of the bare electrode is compared with electrodes modified with TPP, MPyTPP and MPyTPP-cobaloxime. As is visible from the Fig. 4.21 the catalytic current producing H<sub>2</sub> is generated at 1.15 V vs. Ag/AgCl using a bare electrode. Modification of the surface with TPP induces a strong anodic shift to -0.89 V which also enhances the catalytic current considerably when compared with the bare electrode alone. Modification of the electrode surface with MPyTPP induces a greatly enhanced catalytic current also with the onset of this current occurring at -1.0 V representing an anodic shift of 0.15 V when compared with a bare electrode.

Modification of the same surface with the MPyTPP-cobaloxime complex shows a slightly less enhanced current and the onset occurs at a more negative potential, -1.1 V. The addition of the cobaloxime group to the MPyTPP ligand introduces a Co centred reduction  $\sim -1.0$  V vs. Ag/AgCl, and the ring based reductions are shifted to more negative potentials due to the electron donating nature of the cobaloxime ring. The Co based process on MPyTPP-cobaloxime occurs at a similar potential as the potential at which the catalytic current is induced (Section 4.3.5.1). The 1<sup>st</sup> ring based reduction on TPP and MPyTPP also occur at a similar potential to the generation of the catalytic. Therefore it is proposed that the ring in TPP an MPyTPP is capable of efficiently catalysing the production of H<sub>2</sub> in aqueous media without the aid of a metal. In the cobaloxime derivative it is possibly a Co metal catalysed reaction.

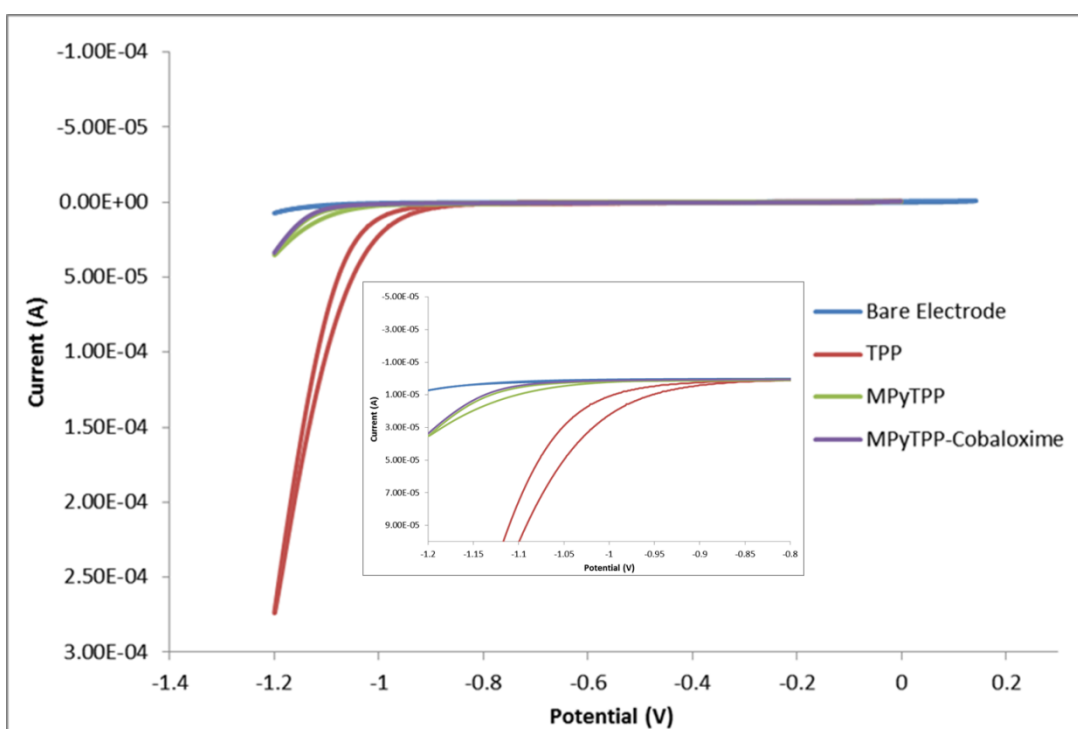


**Figure 4.21-** Typical cyclic voltammogram of a electrode modified with TPP (red line), MPyTPP (green line), MPyTPP-cobaloxime (purple line) and a bare electrode (blue line), in pH 2.0, 0.1 M NaH<sub>2</sub>PO<sub>4</sub> buffer. (Scan rate = 0.1 Vs<sup>-1</sup>). Inset is a closer view at the onset of the catalytic current.

It is evident from the results presented in Table 4.10 that the TONs generated upon modification of the glassy carbon electrode with these three complexes were consistent with observed intensity of the catalytic current induced. The current

density measured over the course of the hour long bulk electrolysis experiment at -1.2 V was measured to be 2.76 mA/cm<sup>2</sup>, producing an electrochemically determined TON of 10.4 x 10<sup>3</sup> when using MPyTPP, while the current density measured when using MPyTPP-cobaloxime was significantly less at 1.07 mA/cm<sup>2</sup> yielding a TON of 3.7 x 10<sup>3</sup>, implying a higher catalytic activity utilising the porphyrin alone. TPP produced the most enhanced catalytic current and also the largest electrocatalytically determined TON of 13.6 x 10<sup>3</sup> after 1 hour. From the graph in Fig. 4.21 it is evident that the catalytic current is enhanced significantly through modification of the surface with TPP when compared with the current produced by MPyTPP. The similarity of the TONs produced using these two systems may be explained by the current density produced at each modified electrode during bulk electrolysis. The current density produced by the TPP system was 1.55 mA/cm<sup>2</sup>; significantly less than the MPyTPP systems at 2.76 mA/cm<sup>2</sup>. The efficiencies of the systems were calculated by injecting a portion of the headspace in the reaction vessel on to a GC and analysing it for its H<sub>2</sub> content. The TPP and MPyTPP systems presented the greatest efficiency at ~ 63% efficiency and MPyTPP-cobaloxime produced a 49% efficiency indicating that the TPP and MPyTPP systems are more reliable electrocatalytic systems as well as yielding higher TONs.

In Fig. 4.22 the cyclic voltammograms of the bare electrode is compared with the electrodes modified with ZnTPP, ZnMPyTPP and ZnMPyTPP-cobaloxime. The bare electrode produced a small catalytic current itself and the onset of this process was visible at -1.15 V. ZnTPP produced a catalytic current at -1.04 V, representing a anodic shift of 0.11 V when compared with the bare electrode. An anodic shift in the onset of the catalytic current was observed for ZnMPyTPP and ZnMPyTPP-cobaloxime at -0.87 V and -0.95 V vs. Ag/AgCl respectively. Owing to the electron donating nature of the cobaloxime moiety, reduction is more difficult on ZnMPyTPP-cobaloxime and therefore the onset of the catalytic current is at more negative potentials. From the results presented in Table 4.6, ZnMPyTPP is the easiest complex to reduce in this study and therefore produces the strongest current.

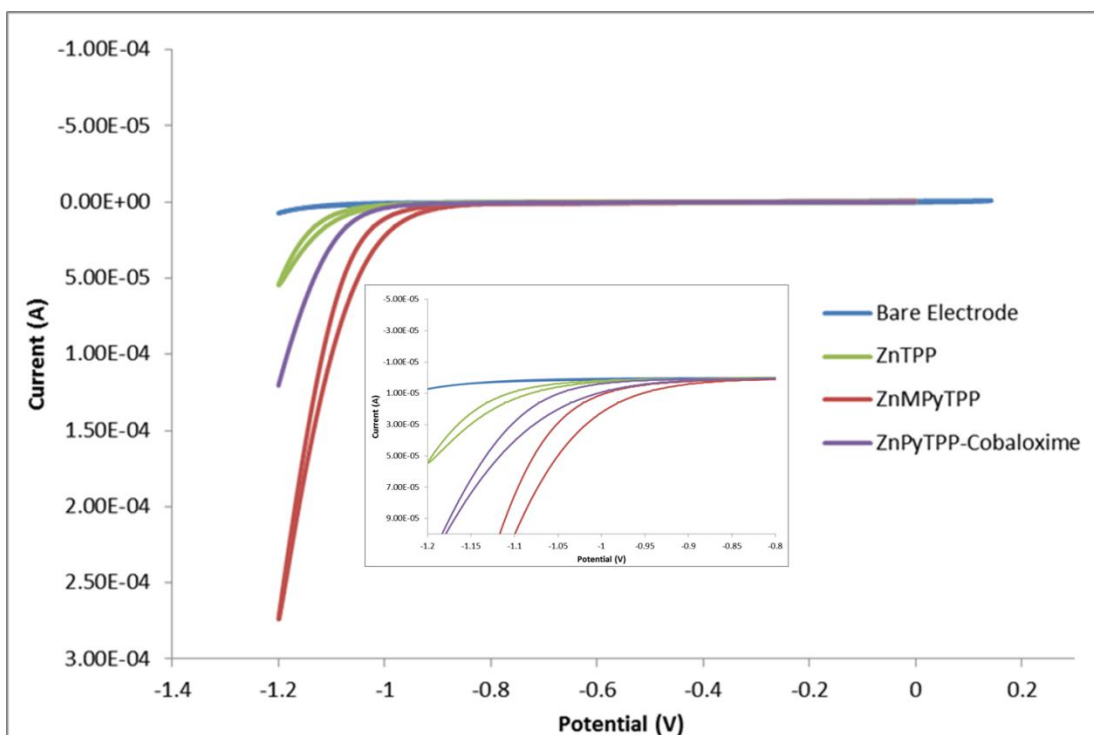


**Figure 4.22-** Typical cyclic voltammogram of a electrode modified with ZnTPP (green line), ZnMPyTPP (red line), ZnMPyTPP-cobaloxime (purple line) and a bare electrode (blue line), in pH 2.0, 0.1 M  $\text{NaH}_2\text{PO}_4$  buffer. (Scan rate =  $0.1 \text{ Vs}^{-1}$ ). Inset is a closer view at the onset of the catalytic current.

ZnMPyTPP produced a current density of  $1.38 \text{ mA/cm}^2$  over the course of the hour long bulk electrolysis experiment at  $-1.2 \text{ V}$ , producing an electrochemically determined TON of  $12.9 \times 10^3$ , while the current density measured when using ZnMPyTPP-oxime was  $1.15 \text{ mA/cm}^2$  and a TON of  $7.8 \times 10^3$  was calculated, implying a higher catalytic activity utilising the metallated porphyrin alone. ZnTPP yielded the highest current density at  $1.87 \text{ mA/cm}^2$  which produced a TON of  $13.5 \times 10^3$ . The ZnTPP system also presented the greatest efficiency at 78% while ZnMPyTPP yielded 59% efficiency and ZnMPyTPP-cobaloxime achieved efficiency of only 49%.

Presented in Table 4.9 are the TONs generated when applying various potentials during bulk electrolysis. As is evident from these results the bare glassy carbon electrode is capable of generating small amounts of  $\text{H}_2$ , unmodified, at potentials above  $-1.2 \text{ V}$  vs.  $\text{Ag/AgCl}$ . The currents generated by the bare electrode are quite weak; however upon bulk electrolysis at  $-1.3 \text{ V}$  the electrode is capable of yielding a strong current ( $9 \times 10^{-1} \text{ A}$ ) after 1 hour potentiostatic electrolysis. MPyTPP/

MPyTPP-Cobaloxime and cobaloxime were chosen as a model series and were tested at various applied electrolysis potentials. When the electrode surface is modified with MPyTPP, strong catalysis begins at -1.1 V yielding an electrochemically determined TON of  $2.4 \times 10^3$  however it is not possible to detect this amount of  $H_2$  on our GC. Upon increasing the potential applied to -1.2 V the electrochemically generated TON is  $10.4 \times 10^3$ , which is confirmed by GC yielding a TON of  $6.5 \times 10^3$ . When the potential applied is lowered to -1.3 V the current passed after one hour is less than that passed by the bare electrode, implying that the modification of the surface is hindering the electrodes capabilities to catalyse the reaction at this potential. When the potential applied is more positive, at -1.0 V, small amounts of  $H_2$  are being generated however the volumes being produced cannot be detected by the GC upon injection of the headspace.

By comparison, when the surface is modified with MPyTPP-cobaloxime reasonable TONs for  $H_2$  generation are detectable when potentials as low as -1.0 V are applied. Electrochemically calculated TONs of  $1.3 \times 10^3$  and  $2.8 \times 10^3$  are observed following bulk electrolysis at -1.0 V and -1.1 V respectively. This shows that MPyTPP-cobaloxime is capable of producing larger TONs for  $H_2$  generation a -1.1 V potentiostatic electrolysis potential than the uncoordinated MPyTPP ligand after bulk electrolysis at the same potential. Similarly to the BODIPY complexes in Chapter 3, MPyTPP, following bulk electrolysis at -1.3 V the current passed was less than that passed by the bare electrode, implying that the modification of the surface is hindering the electrodes capabilities to catalyse the reaction at this potential itself. Cobaloxime itself is capable of generating TONs upon application of a potential of -1.0 V however TONs generated at this potential are not as high as those produced using either MPyTPP or MPyTPP-cobaloxime modified electrodes.

Porphyrin complexes have been commonly used when incorporated into polymer membranes which promote electron movement and supply different mechanisms for this electron flow within an electrocatalytic system. These systems have produced an onset of catalytic current at as low potential as -0.3 V<sup>39</sup> and -0.25 V<sup>41</sup> vs. Ag/AgCl. However systems which have not been incorporated into a polymer have been reported to induce a catalytic current at -1.46 V vs. SCE (Fe-porphyrin)<sup>43</sup> and  $\sim$  -1.6 V vs. SCE (Rh-porphyrin) which indicated the potential of the complexes investigated in this study for use as electrocatalysts in the generation of  $H_2$ . Future

incorporation of these complexes into a polymer membrane could yield even lower reduction potentials and thus provide a more efficient system overall.

## 4.5. Conclusion

The synthesis, characterisation, electrochemistry and photochemistry of mono-pyridylporphyrin compounds and their corresponding cobaloxime derivatives was presented in this chapter. All synthesised complexes were characterised using  $^1\text{H}$  NMR, mass spectrometry and UV-Vis and fluorescence spectroscopy.

Synthesis of TPP and MPyTPP was achieved during one synthetic procedure yielding 16 and 11% respectively. Coordination of the cobaloxime moiety through the nitrogen on the pyridyl substituent on the porphyrin ring was achieved in yields of up to 80%.

All of the compounds in this study exhibit strong absorptions in the UV-vis region of the spectrum. The Soret band was observed  $\sim 416$  nm, and these transitions are assigned to ligand localised  $S_0 - S_2$  ( $\pi-\pi^*$ ) transitions. Also present were Q-band absorbances between 510- 645nm in each porphyrin complexes listed are generally attributed to  $S_0 - S_1$  ( $\pi-\pi^*$ ) transition to the first, lowest energy excited state. Due to the more symmetrical nature of metallated porphyrins the number of these Q-bands reduced from 4 to 2 following addition of a metal to the centre of the porphyrin ring. Complexation of the cobaloxime unit resulted in a small 1 – 2 nm bathochromic shift in all absorbances.

Excitation into the Soret band of each of the porphyrin complexes gave rise to two emission bands with stokes shifts in the range  $7290 - 9879\text{ cm}^{-1}$ . All of the Zn-metallated porphyrins possessed a smaller stokes shift than their freebase counterparts. The addition of a cobaloxime moiety had little to no influence on the stokes shift for the porphyrin complexes as presented here, however the coordination did quench the emission of the porphyrin complex indicating some electronic communication between the ring and the cobaloxime catalytic centre.

Cyclic voltammetry experiments showed all porphyrin complexes exhibit two mono-electronic reductions within the potential window of the DCM solvent. Generally these two reduction processes observed at negative potentials are ascribed to the formation of the porphyrin radical anion,  $[\text{porph}]^-$  and dianion species,  $[\text{porph}]^{2-}$ .<sup>15</sup> The coordination of the cobaloxime to the pyridyl sub-unit of the porphyrin ring induces a cathodic shift in the reduction potentials observed. All porphyrin complexes exhibited two mono-electronic oxidations also. These two processes



observed are ascribed to the formation of the porphyrin radical cation, [porph]<sup>•+</sup> and dication species, [porph]<sup>2+</sup>.<sup>15</sup> The coordination of the cobaloxime to the pyridyl subunit of the porphyrin ring induces a cathodic shift in the reduction potentials observed.

During electrocatalytic H<sub>2</sub> generation experiments TPP exhibited the earliest onset of catalytic current at -0.87 V and TPP and ZnTPP produced the largest GC determined TON over the course of the bulk electrolysis experiment at  $13.6 \times 10^3$  and  $13.5 \times 10^3$  respectively. The efficiency of these systems were also the highest measured at 64 and 78%.

Any H<sub>2</sub> that may have been produced photocatalytically was not detected on the GC during the studies; this is either because it was not produced or the amount produced was lower than the LOD of the GC.

## Bibliography

---

- <sup>1</sup> W.Z. Kuster, *Physiol. Chem.*, **1912**, 82, 463.
- <sup>2</sup> P. Bhyrappa, V. Krishnan, *Inorg. Chem.* **1991**, 30, 239.
- <sup>3</sup> M. J. Crossley, P. L. Burn, *Chem. Comm*, **1991**, 21, 1569.
- <sup>4</sup> Y. Liu, N. Xiang, X. Feng, P. Shen, W. Zhou, C. Weng, B. Zhao, S. Tan, *Chem. Comm.*, **2009**, 2499.
- <sup>5</sup> W. M. Sharman, J. E. van Lier, *Drug Discovery Today*, **1999**, 4, 507.
- <sup>6</sup> E. Brulé, Y. R. de Miguel, *Org. Biomol. Chem.*, **2006**, 4, 599.
- <sup>7</sup> F. li, S. i. Yang, Y. Cicingh, J. Seth, C. H. Martin, D. I. Singh, D. Kim, R. R. Birge, D. F. Bocian, D. Holton, J. S. Lindsey, *J. Am. Chem. Soc.*, **1998**, 120, 10001.
- <sup>8</sup> P. Rothmund, *J. Am. Chem. Soc.*, **1936**, 58, 625.
- <sup>9</sup> A. D. Alder, F. R. Longo, J. D. Finarelli, J. Goldmacher, J. Assour, L. Korsakoff, *J. Org. Chem.*, **1967**, 32, 476.
- <sup>10</sup> A. D. Alder, F. R. Longo, W. Shergalis, *J. Am. Chem. Soc.*, **1964**, 86, 3145.
- <sup>11</sup> J. S. Lindsey, I. C. Schreiman, H. C. Hsu, P. C. Kearney, A. M. Marguerettaz, *J. Org. Chem.*, **1987**, 52, 827.
- <sup>12</sup> G. P. Arsenault, E. Bullock, S. F. MacDonald, *J. Am. Chem. Soc.*, **1960**, 82, 4384.
- <sup>13</sup> C. M. Drain, X. Gong, *Chem. Commun.*, **1997**, 2117.
- <sup>14</sup> D. Shi, R. T. Wheelhouse, *Tet. Lett.*, **2002**, 43, 9341.
- <sup>15</sup> *The Colours of Life: An Iintroduction to the Chemistry of Porphyrins*, L.R. Milgrom, **1997**.

- 
- <sup>16</sup> Metal Ion Solvation and Metal-Ligand Interactions, Volume 5, M. A. Duncan, *Elsevier Science*, **2001**.
- <sup>17</sup> O. Ohno, Y. Ogasawara, M. Asano, Y. Kajii, Y. Kaizu, K. Obi, H. Kobayashi, *J. Phys. Chem.*, **1987**, *91*, 4269.
- <sup>18</sup> O. Gonen, H. Levanon, *J. Chem. Phys.*, **1986**, *84*, 8, 4132.
- <sup>19</sup> A. Berg, M. Rachamim, T. Galili, H. Levanon, *J. Phys. Chem.*, **1996**, *100*, 8791.
- <sup>20</sup> S. I. Yang, S. Prathapan, M. A. Miller, J. Seth, D. F. Bocian, J. S. Lindsey, D. Holten, *J. Phys. Chem. B*, **2001**, *105*, 8249.
- <sup>21</sup> A. J. Mozer, M. J. Griffith, G. Tsekouras, P. Wagner, G. G. Wallace, S. Mori, K. Sunahara, M. Miyashita, J. C. Earles, K. C. Gordon, L. Du, R. Katoh, A. Furube, D. L. Officer, *J. Am. Chem. Soc.*, **2009**, *131*, 15621.
- <sup>22</sup> A. Allegrucci, N. A. Lewcenko, A. J. Mozer, L. Dennany, P. Wagner, D. L. Officer, K. Sunahara, S. Mori, L. Spiccia, *Energy Environ. Sci.*, **2009**, *2*, 1069.
- <sup>23</sup> W. M. Campbell, K. W. Jolley, P. Wagner, K. Wagner, P. J. Walsh, K. C. Gordon, L. Schmidt-Mende, M. K. Nazeeruddin, Q. Wang, M. Grätzel, D. L. Officer, *J. Phys. Chem. C*, **2007**, *111*, 11760.
- <sup>24</sup> M. Zhu, Y. Lu, Y. Du, J. Li, X. Wang, P. Yang, *International Journal of Hydrogen Energy*, **2011**, *36*, 4298.
- <sup>25</sup> H. Hosono, M. Kaneko, *J. Chem. Soc. Faraday Trans.*, **1997**, *93*, 7, 1313.
- <sup>26</sup> T. Dhanasekaran, J. Grodkowski, P. Neta, P. Hambright, E. Fujita, *J. Phys. Chem. A*, **1999**, *103*, 7742.
- <sup>27</sup> J. Grodkowski, P. Neta, *J. Phys. Chem. A*, **2000**, *104*, 1848.

- 
- <sup>28</sup> P. Zhang, M. Wang, C. Li, X. Li, J. Dong, L. Sun, *Chem. Commun.* **2010**, 46, 8806.
- <sup>29</sup> K. M. Kadish, E. Van Caemelbecke, G. Royal, *The Porphyrin Handbook*, vol 8. Academic Press, Burlington, **2000**.
- <sup>30</sup> K. M. Kadish, E. Van Caemelbecke, *J. Solid State Electrochem.*, **2003**, 7, 254.
- <sup>31</sup> G. Hariprasad, S. Dahal, B. G. Maiya, *J. Chem. Soc. Dalton Trans.*, **1996**, 3429.
- <sup>32</sup> F. D'Souza, A. Villard, E. Van Caemelbecke, M. Franzen, T. Boschi, P. Tagliatesta, K. M. Kadish, *Inorg. Chem.*, **1993**, 32, 4042.
- <sup>33</sup> C. Lin, M. Fang, S. Cheng, *Journal of Electroanalytical Chemistry*, **2002**, 531, 155.
- <sup>34</sup> J. A. Hodge, M. G. Hill, H. B. Gray, *Inorg. Chem.*, **1995**, 34, 809.
- <sup>35</sup> A. Wolberg, J. Manassen, *J. Am. Chem. Soc.*, **1970**, 92, 2982.
- <sup>36</sup> D. Chang, T. Malinski, A. Ulman, K. M. Kadish, *Inorg. Chem.*, **1984**, 23, 817.
- <sup>37</sup> X. Cheng, Y. Li, Y. Shi, T. Shi, *Synthesis and Reactivity in Inorganic, Metal-Organic and Nano-Metal Chemistry*, **2006**, 36, 673.
- <sup>38</sup> T. Abe, H. Imai, S. Tokita, D. Wöhrle, M. Kaneko, *J. Porphyr. Phthalocya.*, **1997**, 1, 215.
- <sup>39</sup> T. Abe, H. Imai, M. Endo, M. Kaneko, *Polym. Adv. Technol.*, **2000**, 11, 167.
- <sup>40</sup> T. Abe, F. Taguchi, H. Imai, F. Zhao, J. Zhang, M. Kaneko, *Polym. Adv. Tech.*, **1998**, 9, 559.
- <sup>41</sup> F. Taguchi, T. Abe, M. Kaneko, *J. Mol. Catal. A.*, **1999**, 140, 41.

- 
- <sup>42</sup> J. Knoll, S. Swavey, *Inorganica Chim. Acta.*, **2009**, 362, 2989.
- <sup>43</sup> I. Bhugun, D. Lexa, J. Savéant, *J. Am. Chem. Soc.*, **1996**, 118, 3982.
- <sup>44</sup> V. Grass, D. Lexa, J. Savéant, *J. Am. Chem. Soc.*, **1997**, 119, 7526.
- <sup>45</sup> J. P. Collman, P. S. Wagenhnecht, N. S. Lewis, *J. Am. Chem. Soc.*, **1992**, 114, 5665.
- <sup>46</sup> A.D. Adler, F.R. Longo, J.D. Finarelli, J. Goldmacher, J. Assour, L. Korsalioff, *J. Org. Chem.*, **1967**, 32, 476.
- <sup>47</sup> K. Kalyanasundaram, *Photochemistry of Polypyridyl and Porphyrin Complexes*, Academic Press, London, **1992**, Chapter 12.
- <sup>48</sup> (i) A. Harriman, J. Davila, *Tetrahedron*, **1989**, 45, 4737. (ii) N. M. Boyle, *Ph.D. Thesis*, **2010**, Dublin City University.
- <sup>49</sup> (i) G. N. Schrauzer, L. P. Lee, and J. W. Sibert, *J. Am. Chem. Soc.*, **1970**, 92, 2997. (ii) P. Connolly, J. H. Espenson, *Inorg. Chem.*, **1986**, 25, 2684. (iii) P. Du, J. Schneider, G. Lo, W. (iv) W. Brennessel, R. Eisenberg, *Inorg. Chem.*, **2009**, 48, 1, 4952. (v) A.Fihri, V.t Artero, A. Pereira, M. Fontecave, *Dalton Trans.*, **2008**, 5567.
- <sup>50</sup> P. Zhang, M. Wang, C. Li, X. Li, J. Dong, L. Sun, *Chem. Commun.* **2010**, 46, 8806.
- <sup>51</sup> P. Byrappa, P. Bhavana, *Chem. Phys. Lett.*, **2001**, 349, 399.
- <sup>52</sup> C. Engtrakul, W. J. Shoemaker, J. J. Grzybowski, *Inorg. Chem.*, **2000**, 39, 5161.

## **Chapter 5**

# **Platinum and Palladium Complexes**

Chapter 5 begins with a short introduction to ethynyl-pyrene complexes, including some applications. The literature survey concludes with the use of platinum and palladium catalysts in both intramolecular and intermolecular photocatalytic hydrogen generation. The chapter shows synthetic methods employed and some photophysical measurements of the complexes studied, along with the results of experiments performed to measure the efficacy of the photosensitiser and catalytic centers in intermolecular hydrogen generation.

## Aim

Pyrene is a highly conjugated chromophore which absorbs from the UV into the visible region of the spectrum. Further  $\pi$ -conjugation of the pyrene moiety has been achieved through the addition of ethynyl or thiophene units to further push the absorbance profile of the compounds towards the red in an attempt to utilise these groups as a photosensitiser in the photocatalytic generation of  $H_2$ . Synthesis of a highly conjugated compound in which the photosensitiser and the catalytic centre were covalently linked was attempted, however this proved unsuccessful. Intermolecular  $H_2$  generation have been carried out in solution, where the pyrene moiety acts as the photosensitiser, the Pd/Pt compound acts as the catalytic centre and TEA as the sacrificial agent.

## 5.1. Introduction

### 5.1.1. Pyrene and Ethynylpyrene systems

Pyrene is a colourless, polycyclic aromatic hydrocarbon (PAH). It consists of four fused benzene rings, making it a perifused macrocycle. PAHs are generally produced when products such as coal, oil, and gas are burned but the burning process is not completed. The use of this by-product in an environmentally friendly process would eliminate pyrene from waste.

This chromophore, and more often, its derivatives are used as organic dyes due to their ability to absorb a wide range of wavelengths of light. It is also known to have a very high quantum yield and lifetime, of the nanosecond order, which makes it ideal for use in applications which utilise its triplet state for interactions. Pyrene based molecules readily undergo photoexcitation and have the ability to transfer this energy to bound molecules.<sup>1</sup> This characteristic makes them ideal for use as photosensitisers in the generation of hydrogen. Pyrene compounds have been used for linear molecular wires<sup>2</sup>, luminescent probes<sup>3</sup> and have uses in artificial photosynthesis<sup>4</sup>.

The introduction of pyrene into molecular structures can greatly lengthen the excited state lifetimes of the molecules. Complexation of these conjugated chromophores with a transition metal such as Ru or Pt renders the molecule produced highly

luminescent<sup>3</sup>. Extension of the  $\pi$ -conjugation of the chromophore can lead to changes in the photophysical properties of the pyrene complex. Fine tuning of the optical properties of this type of system has been mainly achieved through routes involving changing the length, substitution, and degree of conjugation within the complexes. These oligomers have gained much interest in recent years and many studies have been published regarding the synthesis of these complexes and their photophysical properties. A review has been published by Leroy-Lhez et al.<sup>5</sup> detailing the optical and electronic properties of polypyridine ligands with extended  $\pi$ -conjugation. Pyrene-containing molecules are known to exhibit unique singlet state properties such as the ability to form intramolecular charge-transfer states that are sensitive to environmental factors.<sup>5</sup> **1** (Fig. 5.1) has been shown to display intense fluorescence emission in the visible region of the spectrum and this emission was not dependent on the nature of the solvent employed, which was proposed to be indicative of the weak electron-accepting property of the bipyridine (bpy) ring.<sup>6</sup> The fluorescence observed in ligand **2** was detected to exhibit strong solvatochromic behaviour which was proposed to be due to the formation of a polar excited-state due to the additional electron-withdrawing effect of the ethynyl group. The introduction of a thiophene ring, which introduced a bent conformation in the molecule, in **3** induced fluorescence emission centred around 488 nm in acetonitrile, which was concluded to arise from a charge transfer state between the pyrene and the thiophene groups.

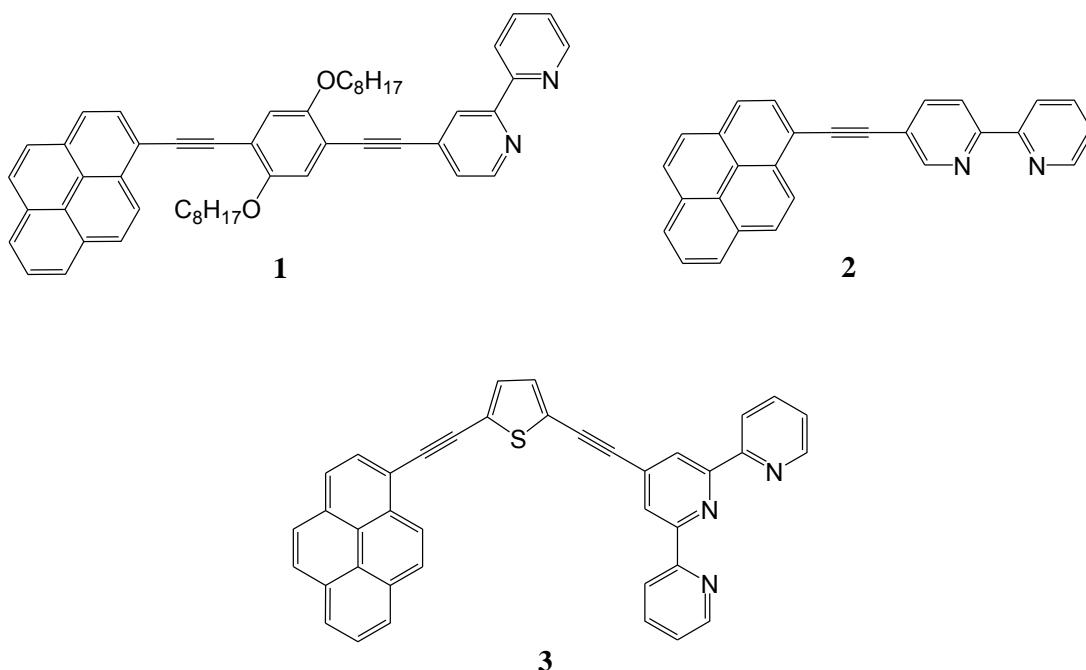
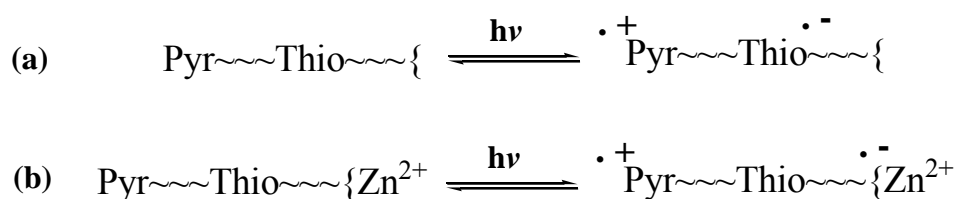


Figure 5.1- Pyrene-polypyridine oligomers studied by Leroy-Lhez et al.<sup>6</sup>



Thiophene is a good electronic conductor through enhancing the  $\pi$ -conjugation and therefore  $\pi$ - delocalisation along the length of a molecule. The addition of a thiophene unit therefore promotes electronic coupling between the terminal groups in a molecule which improves the excited state charge transfer. A pyrene moiety has been tethered to a [2,2':6',2'']-terpyridyl ligand via a diethynylated thiophene linker group for use as a  $\text{Zn}^{2+}$  cation binding receptor (Fig. 5.3).<sup>1</sup> Through cyclic voltammogram experiments it was determined that the pyrene unit was the electron donor and the thiophene unit was the electron acceptor moiety during redox reactions. A low energy band in the absorption spectrum centred at 426 nm, the lowest-energy transition in the ligands spectrum, is attributed to intramolecular charge-transfer (ICT), from the pyrene unit to the thiophene unit (Fig 5.2 (a)). This is further confirmed by the observation of a large stokes shift when the absorption and emission spectra were compared. In acetonitrile solution at room temperature, the ligand displays an emission band at 488 nm. The fluorescence quantum yield was measured to be 0.32 while the fluorescence lifetime is 1.2 ns. Addition of  $\text{Zn}(\text{ClO}_4)_2$  to a solution of the ligand resulted in complexation of the  $\text{Zn}^{2+}$  cation (Fig 5.3) resulting in a shift of the ICT spectral band bathochromically towards the visible region of the spectrum. The intensity of the emission band is also significantly reduced. It is also proposed that upon the addition of the  $\text{Zn}^{2+}$  cation the thiophene unit acts as an electron relay and the charge separated state lies between the pyrene unit and the Zn cation (Fig. 5.2 (b)).



**Figure 5.2-** Pictorial representation of the proposed intramolecular charge transfer state in the ligand (a), and within the  $\text{Zn}^{2+}$  complex (b).<sup>1</sup>

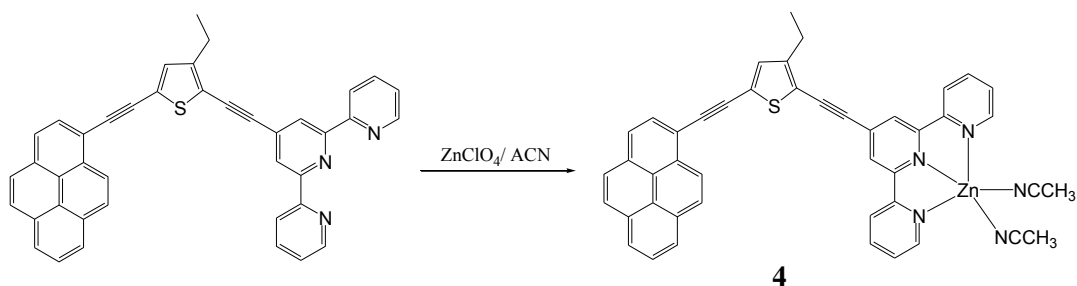


**Figure 5.3 - Pyrene-thiophene-terpyridine complex synthesised by Benniston *et al.*<sup>1</sup> for use in the coordination of the  $\text{Zn}^{2+}$  cation.**

The following year the same research group published a paper which incorporated an bis-anthracene bridge between the thiophene and the terpyridine units in an attempt to finely tune the extent of electron delocalisation which occurs along the molecule (Fig. 5.4).<sup>18</sup> The absorption spectrum of this complex displays a strong absorbance at 490 nm, representing a 74 nm red shift when compared to the previously synthesised non-anthracene containing compound. The complex is also highly fluorescent at room temperature with an emission band centred at 540 nm, observed in ACN. The fluorescence quantum yield measured was 0.35 in acetonitrile while the emission lifetime was 1.9 ns. Again a large Stokes shift was observed suggesting population of an ICT excited state following excitation. The triplet excited state was detected using laser flash photolysis following excitation at 355 nm. The triplet state decays via first-order kinetics with a lifetime of 18  $\mu\text{s}$  in deoxygenated DMSO. Complexation of the  $\text{Zn}^{2+}$  cation again causes a red shift in the absorbance bands and greatly diminishes the emission band strength, with a measured fluorescence quantum yield of 0.16 ns. The Zn complex gave a triplet excited state lifetime of 95  $\mu\text{s}$  following laser flash photolysis in deoxygenated DMSO.  $\text{Zn}^{2+}$  binding to the anthracene containing ligand does not lead to complete delocalisation of electron density onto the terpyridine unit which is what was observed with the non-anthracene containing ligand. As an alternative the  $\text{Zn}^{2+}$  cation enhances the triplet state formation through heavy atom perturbation of the anthracenyl unit.

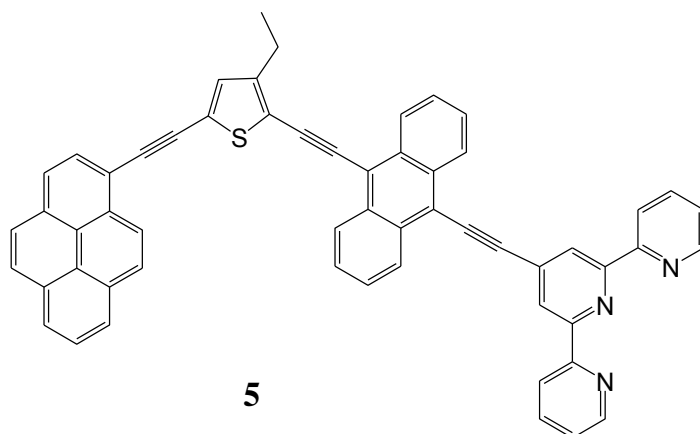


**Figure 5.4 - Incorporation of a bis-anthracene linker into the pyrene-thiophene-terpyridine complex synthesised by Benniston *et al.*<sup>18</sup>**

Li *et al.*<sup>7</sup> have synthesised a series of asymmetrical pyrene derivatives with the aim of extending their absorption bands into the visible region of the spectrum. Through incorporating ethynyl linkers and extended phenyl chains they have successfully extended the absorption from the purple-blue region into the green region (Fig. 5.5).

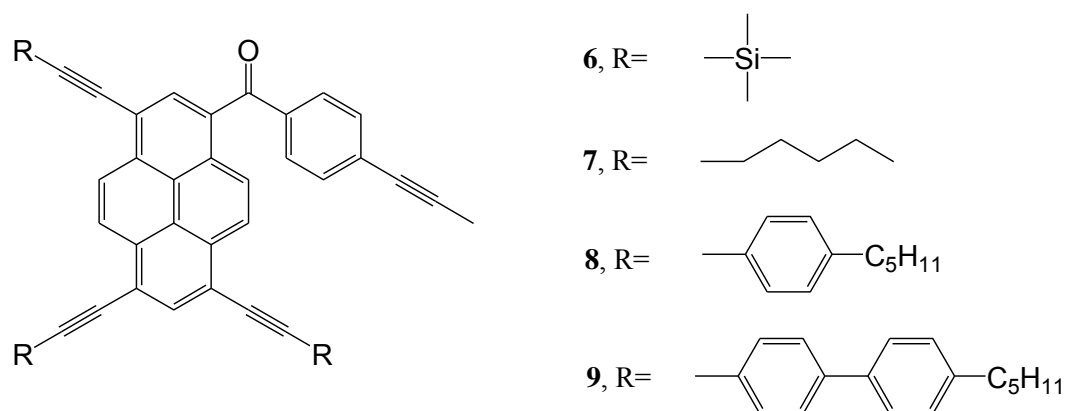


**Figure 5.5 - Extended pyrene complexes capable of absorbing in the blue-green region of the spectrum, developed by Li *et al.*<sup>7</sup>**

Bathochromic shifts in absorbance bands and emission bands were observed from **6** to **9** due to increased conjugation lengths of the substituents with compounds **8** and **9** absorbing out to 458 and 465 nm and emitting at 510 and 518 nm respectively.

Ziessel and coworkers have described the synthesis of pyrene-bipyridine dyads and described their photophysical properties.<sup>8</sup> The absorption spectra of these complexes are comparable to a composite of the two subunits individual spectra. The spectra exhibit a strong  $S_0 - S_1$  ( $\pi - \pi^*$ ) transitions in the blue green region which can be

assigned to the BODIPY chromophore. The presence of much weaker and relatively broad absorption bands located in the UV region are assigned to the  $S_0 - S_2$  ( $\pi - \pi^*$ ) transition on the BODIPY unit also. Stronger transitions within the UV region are attributed to the ( $\pi - \pi^*$ ) transitions localised on the phenyl-ethynyl subunit. Also visible are three strong absorbances assigned to  $\pi - \pi^*$  transitions within the pyrene subunit. Ethynylpyrene bound BODIPY dyes have been developed by Harriman *et al.*<sup>9</sup> which consist of two pyrene units tethered to the boron unit of a BODIPY dye (Fig. 5.6).

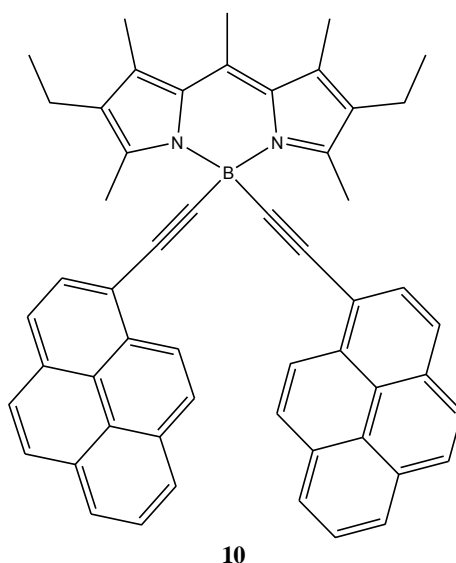


**Figure 5.6 - Bis-ethynylpyrene-BODIPY dye synthesised by Harriman *et al.*<sup>9</sup>**

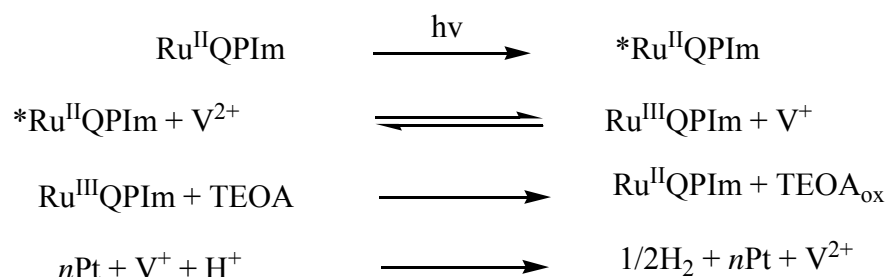
Similarly to Ziessel's observations, the absorption spectra of this type of complex exhibits strong absorbances in the visible region due to the BODIPY unit and higher energy absorbances attributed to the pyrene unit. Fluorescence detected in MeTHF was attributed to fluorescence from the BODIPY unit. This fluorescence signal was found to decay via first-order kinetics with a lifetime of  $6.5 \pm 0.1$  ns and the fluorescence quantum yield was found to be  $0.90 \pm 0.05$  under in solution at room temperature. This suggests that the appended pyrene unit does not perturb the photophysical properties of the BODIPY dye following excitation. No fluorescence was detected from the pyrene unit and time-resolved fluorescence studies made with near-UV excitation confirmed that the pyrene based fluorescence excited states have short lifetimes of less than 50 ps. The researchers proposed that photons collected by the appended pyrene are quantitatively transferred to the BODIPY unit.

### 5.1.2. Platinum and Palladium Photocatalysts in Hydrogen Production

Platinum and palladium are heavy transition metals from group 10 of the periodic table. There has been a great deal of research in the area of thermochemical hydrogen generation using platinum, however for the purpose of this study the focus systems which generate hydrogen photochemically. Though these metals are quite rare and expensive they have been shown to yield high TONs for the production of hydrogen.

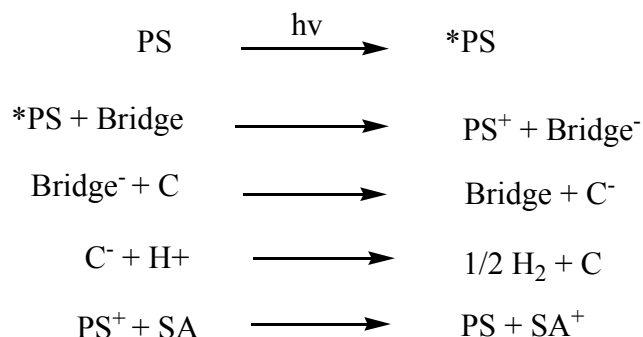
#### 5.1.2.1. Pt/Pd systems Used in Intramolecular H<sub>2</sub> Production

Much of the research using platinum and palladium to generate hydrogen has involved to synthesis of a bimetallic system, utilising Pt/ Pd as a catalytic centre and using another metal in the light harvesting chromophore. In 1998 Suzuki *et al.*<sup>10</sup> reported the synthesis of ruthenium-platinum (Ru- Pt) complexes for the purpose of generating hydrogen. The ruthenium was polymer bound with a linking bridge which was an alkyl viologen, such as 1,1'-dimethyl-4,4'-bipyridinium, and a [Pt(bpy)<sub>2</sub>]<sup>2+</sup> catalytic centre. Yields of H<sub>2</sub> (up to a maximum 0.633 cm<sup>3</sup> after 120 min irradiation with  $\lambda = 400\text{nm}$ ) were reported, however it was noted that the maximum volume of hydrogen generated decreased with increasing degree of quaternisation. This was attributed to a decrease in the efficiency of photosensitised charge separation induced by increasing electrostatic repulsion. An experiment was carried out using repeated light on/ light off runs, and no hydrogen was observed during the dark periods. The volume of hydrogen generated during the light periods of these experiments decreased gradually, and then hydrogen generation completely ceased in the 25<sup>th</sup> repeat run. This was attributed to inactivation of the platinum catalyst. However, hydrogen generation was observed again by irradiating the solution after an addition of more platinum catalyst after the 25th run. UV-vis absorption and emission studies showed that the photosensitiser had not decomposed during the experiment and the following mechanism was proposed (Scheme 5.1).



**Scheme 5.1 - Proposed mechanism for the photocatalytic generation of hydrogen where  $\text{Ru}^{\text{II}}\text{QPIIm}$  = photosensitiser,  $\text{V}^{2+}$  = alkyl-viologen bridging molecule, TEOA = sacrificial donor,  $n\text{Pt}$  = platinum catalytic centre<sup>10</sup>.**

In this mechanism the photosensitiser is excited by light and donates an electron to the alkyl-viologen bridging molecule. The photosensitiser is then reduced by the TEOA sacrificial agent. The alkyl-viologen then passes the electron on to the platinum catalytic centre where it is used to reduce  $\text{H}^+$  to for the desired hydrogen. This is the generally accepted mechanism for all  $\text{H}_2$  generation experiments and is simplified below (Scheme. 5.2)



**Scheme 5.2 - General mechanism for  $\text{H}_2$  production using a Pt/Pd catalytic centre. PS = Photosensitiser, C = catalytic centre, SA = sacrificial agent.**

Toshima *et al.*<sup>11</sup> have used a chromophore based on ruthenium coupled with a platinum catalytic centre to generate hydrogen from water in visible light. The electron transfer system consisted of a ruthenium tris –bipyridine dichloride light harvesting centre with a methyl viologen dichloride bridging molecule and a metal cluster of platinum as the catalytic centre. They showed that the electron transfer rate

directly influenced the rate of hydrogen formation. Furthermore the higher the electron transfer rate constant  $k_e$ , the higher the hydrogen formation constant  $k_{H_2}$ . Sakai *et al.*<sup>12</sup> reported using a Ru-Pt bimetallic system which can photocatalytically generate  $H_2$  from water in the presence of an ethylenediaminetetraacetic acid (EDTA) sacrificial donor. Similar to Toshima, they have used a ruthenium tris-bipyridine moiety as the chromophore and they have used a  $PtCl_2$  catalytic centre (Fig. 5.7). However they only reported a low TON of 5 after 10 hours of irradiation at  $\lambda \geq 390$  nm which they attribute to the formation of platinum colloids which interfere with the catalytic process.

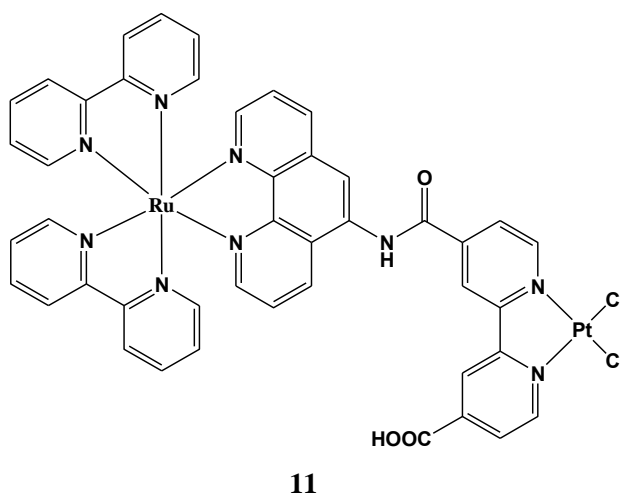


**Figure 5.7 - Ru-Pt Complex utilised by Sakai *et al.*<sup>6</sup>**

Rau *et al.*<sup>13</sup> have reported the use of palladium and ruthenium mixed photocatalytic systems in intermolecular hydrogen generation, they have reported a TON of 56 in 30 hours of irradiation at  $\lambda = 470$  nm in the presence of TEA, as a sacrificial donor. The molecules consisted of a ruthenium (II) 4,4'-di-tert-butyl-2,2'-bipyridine chromophore with a highly conjugated bridging unit (tpphz-tetrapyridophenazine) and a  $PdCl_2$  catalytic centre coordinated to the two nitrogens of the bridging group (Fig. 5.8).

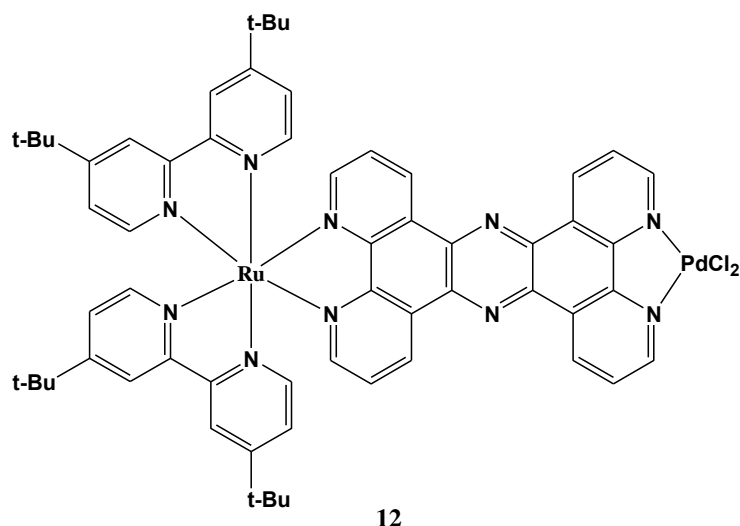


Figure 5.8 - Ru-Pd complex utilised by Rau *et al.*<sup>13</sup>

A large number of organometallic systems have also been investigated for use in H<sub>2</sub> production. The use of an organic photosensitiser is hoped to mimic more closely the model of photosynthesis for energy production and also drive down the price of production. The use of metals can be very expensive and by eliminating the need for a bimetallic system the cost of the system should be greatly reduced. A few examples are discussed below.

Porphyrins have been investigated by many groups for use as photosensitiser molecules along with platinum and palladium catalytic centres. Hosono *et al.*<sup>14</sup> have reported thin films of two viologen linked porphyrins which are in the presence of a H<sub>2</sub>PtCl<sub>2</sub> catalyst and EDTA as a sacrificial agent. These compounds have produced hydrogen intermolecularly from water achieving TON of 5.2 and 16.8 each after 280 hours of irradiation with visible light (720 nm <  $\lambda$  > 390 nm).



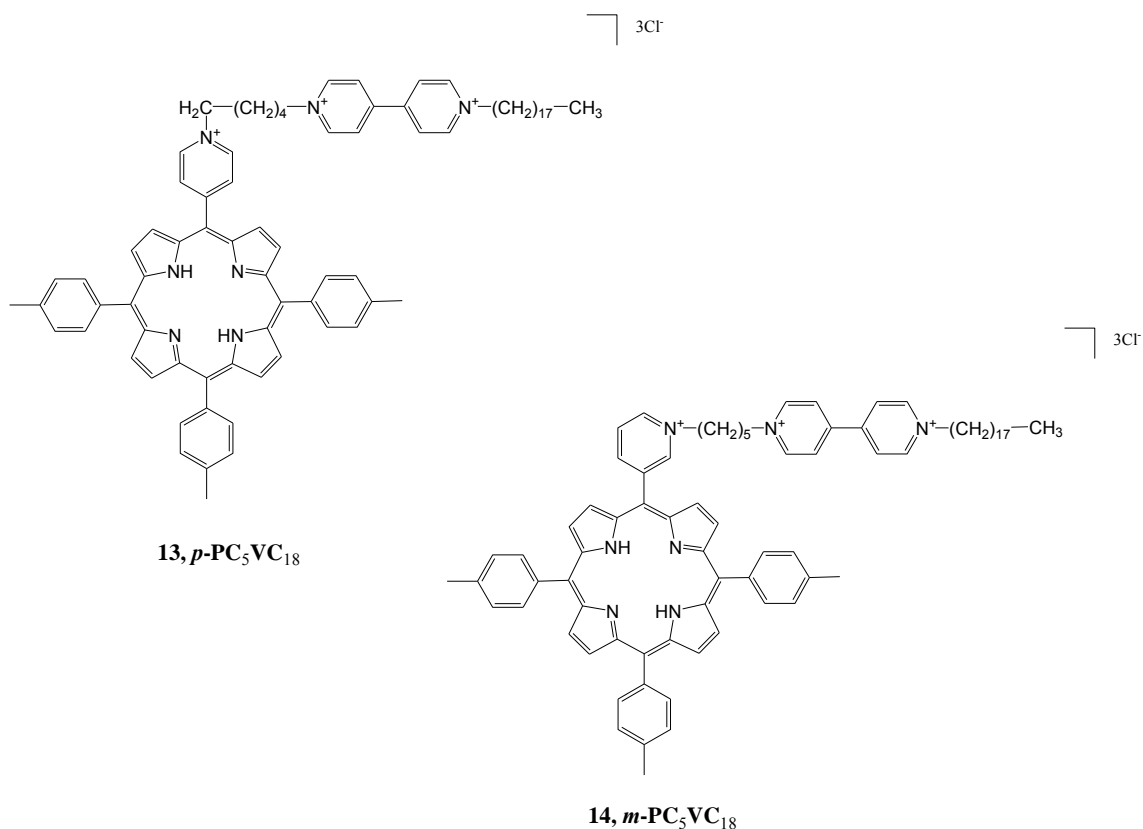


Figure 5.9- Viologen-linked porphyrins photosensitisers used by Hosono *et al.*<sup>14</sup>

Eosin dyes have also been shown to effectively photosensitise the generation of hydrogen<sup>15</sup>. Upon visible light irradiation ( $\lambda \geq 420\text{nm}$ ) a quantum yield of H<sub>2</sub> production of 12.14% was achieved when splitting water using an eosin dye sensitised multi-walled carbon nanotube doped with platinum using a TEOA sacrificial agent.

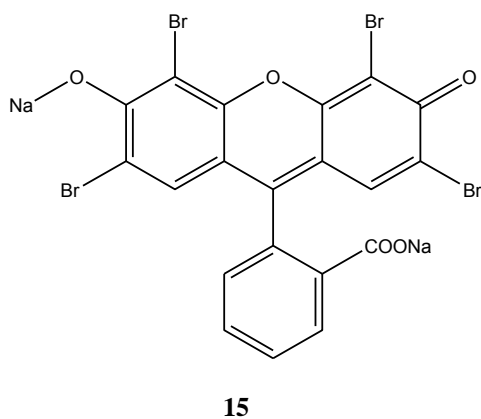
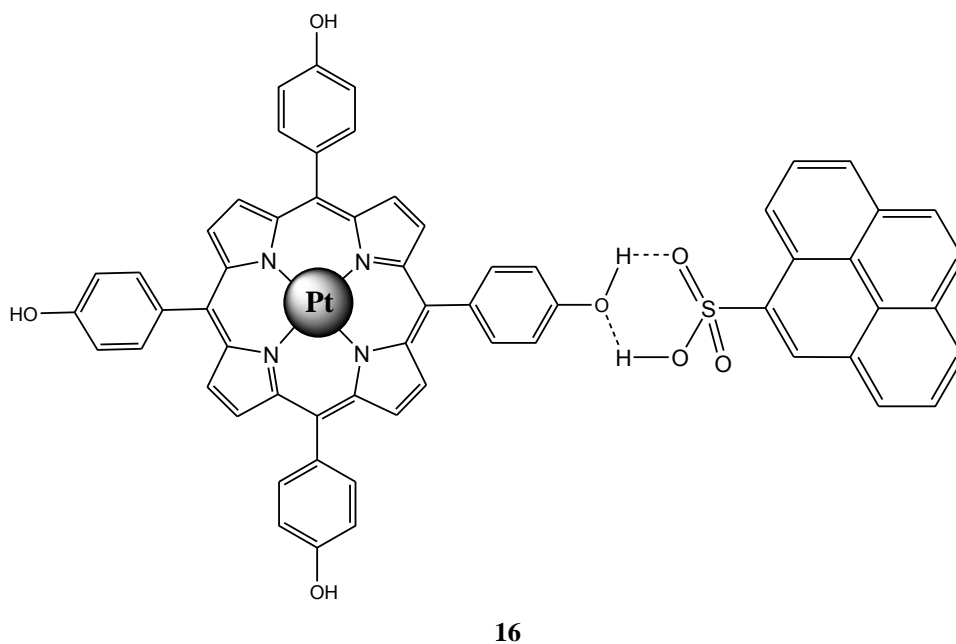


Figure 5.10 - Structure of Eosin dye molecule used by Li *et al.*<sup>15</sup>

H<sub>2</sub> generation has been reported using a porphyrin-pyrene conjugate functionalised Pt nano composite (Fig. 5.11).<sup>16</sup> The authors propose that the light is absorbed by the pyrene unit triggering electron transfer to the porphyrin ring followed by transfer to the Pt nano-particle inducing H<sub>2</sub> formation at the Pt centre. TONs of 63 were reported following 12 hours broad band UV-Vis irradiation in the presence of EDTA as sacrificial agent.



**Figure 5.11-** Porphyrin-pyrene conjugate functionalised Pt nano composite utilised by Zhu *et al.*<sup>16</sup> in the photogeneration of H<sub>2</sub>.

#### 5.1.2.2. Pt/Pd systems Used in Intermolecular H<sub>2</sub> Production

Intermolecular H<sub>2</sub> generation systems which have been developed have mainly consisted of a photosensitiser (PS) and an unbound platinum or palladium colloid for use as a catalytic centre.

Tinker *et al.*<sup>17</sup> reported using an Ir photosensitiser together with a platinum colloid to generate H<sub>2</sub> from water without the use of an electron relay. A system composing of 6.25 μmol of a heteroleptic iridium (III) photosensitizer [Ir(ppy)<sub>2</sub>(bpy)]<sup>+</sup> (ppy = 2-phenylpyridine, bpy = bipyridine), **17**, 0.3 μmol platinum colloid (K<sub>2</sub>PtCl<sub>2</sub>) catalytic

centre, and TEOA sacrificial reductant was utilised yielding a hydrogen TON of 63, based on Pt, after 20 hours irradiation at (Fig. 5.12).

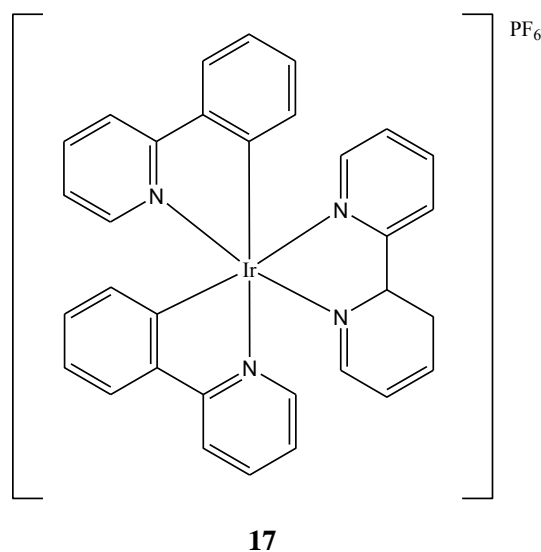


**Figure 5.12- [Ir(ppy)<sub>2</sub>(bpy)]PF<sub>6</sub> photosensitiser utilised by Tinker *et al.* in conjunction with platinum colloid for the generation of H<sub>2</sub>.<sup>17</sup>**

It was observed that upon increasing the concentration of K<sub>2</sub>PtCl<sub>2</sub> in the reaction solution the H<sub>2</sub> generating reaction was actually hindered, and this effect could not be resolved through addition of higher concentrations of PS. This was attributed to a faster aggregation of the platinum colloid which is generated in situ from the K<sub>2</sub>PtCl<sub>2</sub>. It has been previously been shown that colloidal particle size can greatly affect the H<sub>2</sub> evolution during an experiment with larger particles producing less H<sub>2</sub>.<sup>18</sup>

More recent work from the same group utilised an Ir photosensitiser of the type [Ir(C<sup>^</sup>N)<sub>2</sub>(N<sup>^</sup>N)](PF<sub>6</sub>), with various ring substituents (Fig. 5.13), in the presence of K<sub>2</sub>PdCl<sub>2</sub> and TEA as sacrificial agent.<sup>19</sup> It was found that the highest TON of 312 was achieved when the C<sup>^</sup>N substituent = 5-methyl-2-(4-fluorophenyl)pyridine (F-mppy) and the N<sup>^</sup>N substituent = 5,5'-ditrifluoromethyl-2,2'-bipyridine (dFbpy) following irradiation at 465 nm for 1 hour.

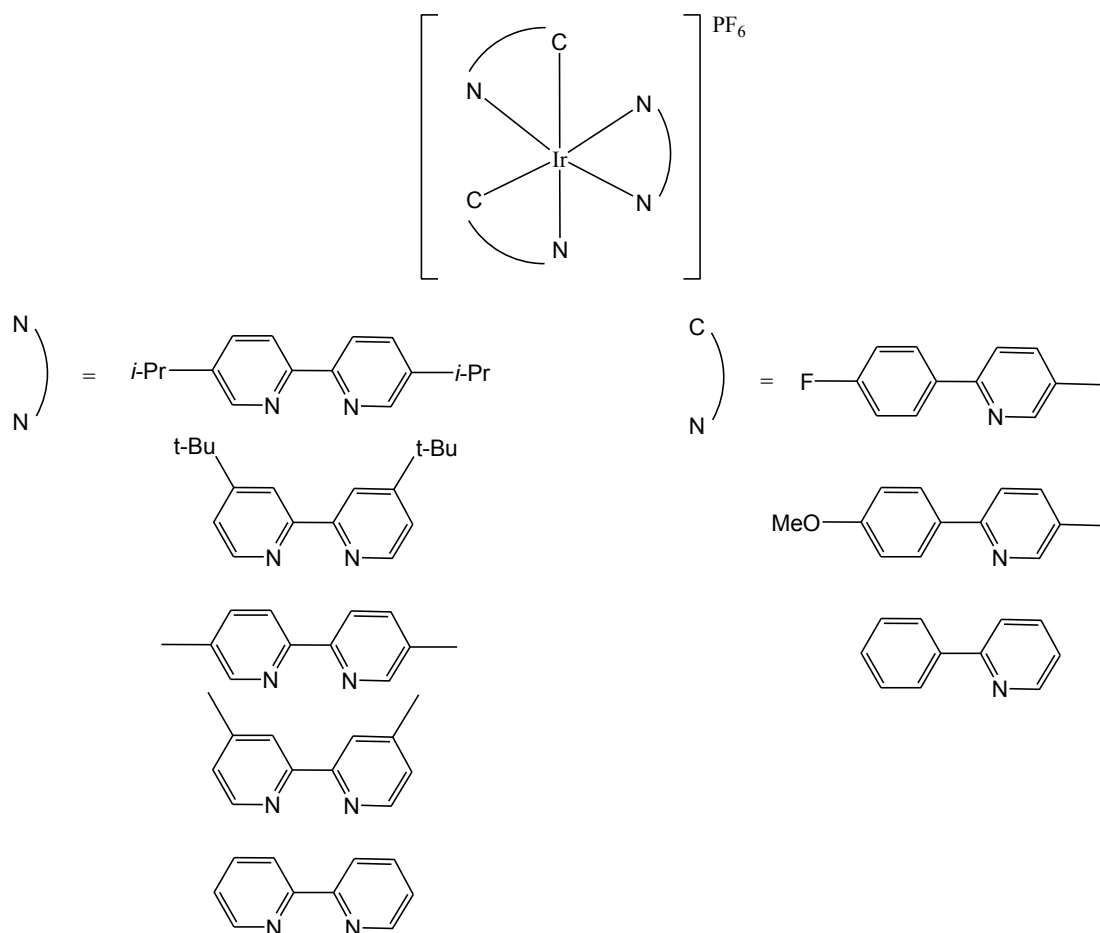


**Figure 5.13-  $[\text{Ir}(\text{C}^{\wedge}\text{N})_2(\text{N}^{\wedge}\text{N})](\text{PF}_6)$  photosensitisers utilised by Curtin *et al.* in conjunction with palladium colloid for the generation of  $\text{H}_2$ .<sup>19</sup>**

The TON generated during the experiments suggested that steric bulk greatly enhanced the longevity of the photosensitiser before decomposition occurred. TEM and mercury poisoning tests were carried out which determined that the  $\text{K}_2\text{PdCl}_2$  metal catalyst forms an active colloidal species in situ which in turn catalyses the  $\text{H}_2$  generation reaction.

Soman *et al.*<sup>20</sup> reported the synthesis of cyclometallated iridium–Pt/Pd dinuclear complexes containing the bridging ligand 2,2':5',2''-terpyridine (BPP) and a peripheral phenylpyridine (ppy) ligand which produce  $\text{H}_2$  photochemically following irradiation with both visible (470nm) and UV (350nm light). Both complexes in which the Pt/Pd catalytic centre was covalently bound (Fig. 5.14) and complexes with unbound Pt/Pd (in the form of  $[\text{Pd}(\text{CH}_3\text{CN})_2\text{Cl}_2]$  or  $[\text{Pt}(\text{CH}_3\text{CN})_2\text{Cl}_2]$ ) were tested.

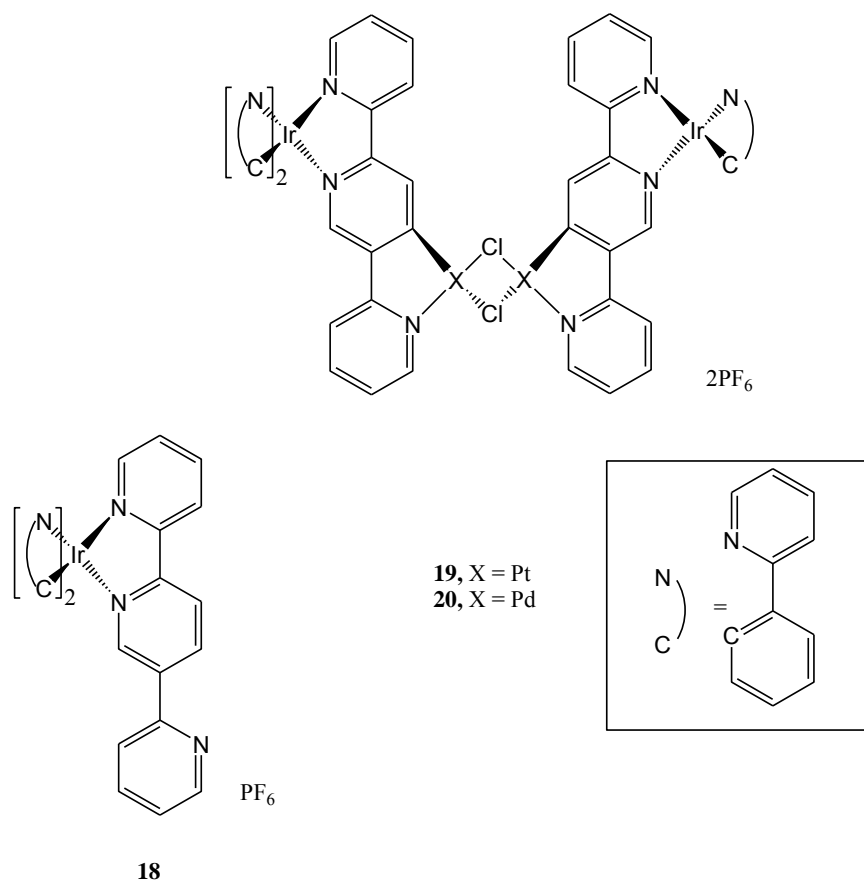


**Figure 5.14- Cyclometallated iridium–Pt/Pd dinuclear complexes synthesised by Soman *et al.*<sup>20</sup>**

Visible light (470 nm) irradiation of the heteronuclear  $[\text{Ir}(\text{ppy})_2(\text{BPP})\text{PtCl}]_2(\text{PF}_6)_2$  (**19**) or  $[\text{Ir}(\text{ppy})_2(\text{BPP})\text{PdCl}]_2(\text{PF}_6)_2$  (**20**) complexes yielded TONs of 308 and 254 respectively after 18 hours in an acetonitrile solution containing 10% water and 2.15 M TEA as sacrificial agent. Upon irradiation with UV light (350 nm) the TONs yielded were 65 for **19** and 16 for **20** respectively. Inter molecular  $\text{H}_2$  generation studies followed the same trend with TONs of 245 and 166 measured following 470 nm irradiation and TONs of 117 and 124 following 350 nm irradiation of 1 : 1 molar ratio solutions of  $[\text{Ir}(\text{ppy})_2(\text{BPP})]\text{PF}_6$  (**18**) and  $[\text{Pd}(\text{CH}_3\text{CN})_2\text{Cl}_2]$  or  $[\text{Pt}(\text{CH}_3\text{CN})_2\text{Cl}_2]$  respectively. The authors attributed this wavelength dependence to the tendency of 470 nm irradiation to populate the lowest energy singlet and/or singlet excited states ( $\text{S}_1$  and  $\text{T}_1$ ) causing a flow of electrons away from the Ir metal centre towards the bridging ligand and on towards the Pt/ Pd metal centre, while irradiation at 350nm induces a flow of electrons from the Pt/Pd metal centre towards the Ir centre as 350 nm light tends to populate the  $\text{S}_3$  state and its associated triplet state  $\text{T}_6$ . Also

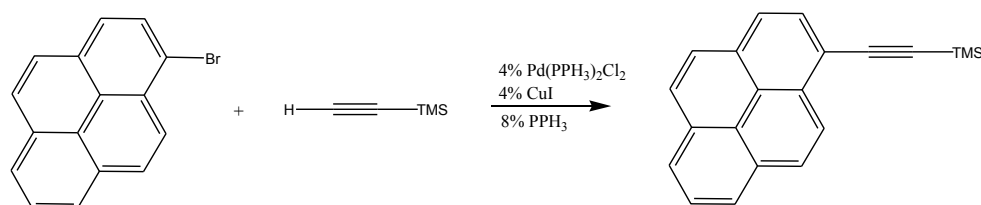
observed was the lower TONs yielded during the intermolecular H<sub>2</sub> generation experiments as this process depend on both photosensitiser and catalytic being in close proximity in solution for the H<sub>2</sub> producing reaction to occur.

## 5.2. Experimental

All materials and equipment used in this studied are detailed in Chapter 2 sections 2.21 and 2.22. Details of photocatalytic studies are also available in Chapter 2 section 2.25.

### 5.2.1. Synthesis

#### 5.2.1.1. Synthesis of 1-trimethylsilylethynylpyrene (Pyrene-TMS)



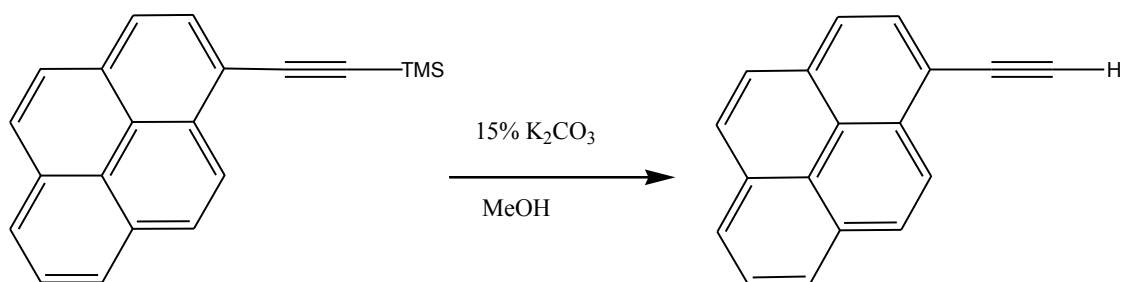
To a clean, dry round bottomed flask 25 ml of diisopropylamine was added and purged with nitrogen for 10 min. 0.5g (1.77 mmol) of 1-bromopyrene (Pyrene-Br) was added and the mixture was purged with nitrogen for a further 10 min. 0.05g (0.071 mmol) of Pd(PPh<sub>3</sub>)<sub>2</sub>Cl<sub>2</sub>, 0.035g (0.071 mmol) CuI and 0.037g (0.142 mmol) PPh<sub>3</sub> were added to the reaction vessel. 0.37 ml (2.66 mmol) of ethynyltrimethylsilane was added and the reaction vessel was sealed and allowed to reflux (88°C) overnight under nitrogen.

The solvent was removed under reduced pressure. The crude product and was extracted from the resulting solid by adding portions of a mixture of dichloromethane and hexane (4 ml and 20 ml respectively). After each addition the liquid layer was decanted off until it ran clear. The organic phase was dried over MgSO<sub>4</sub>. The solvent was removed. The product was purified using column chromatography on silica, Hexane: DCM, 25:75 to yield a yellow solid.<sup>21</sup>

% Yield: 0.509 g, 1.7054 mmol, 96%

<sup>1</sup>H NMR: (400 MHz, CDCl<sub>3</sub>), 8.53 ppm (d, J = 9.06 Hz, 1H), 8.1 ppm (m, 8H), 0.36 ppm (s, 9H)

### 5.2.1.2. Synthesis of 1-ethynylpyrene (Pyrene-H)



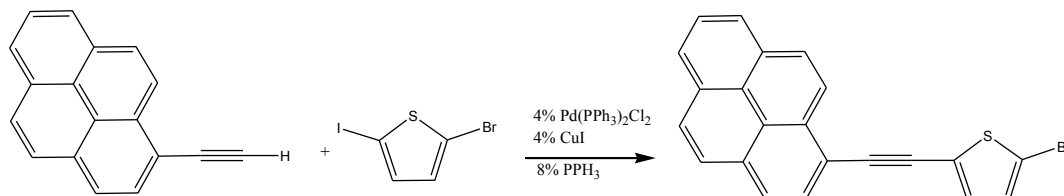
20 ml of freshly distilled methanol was added to a clean, dry round bottomed flask and purged with nitrogen for 10 min. 0.4g (1.3 mmol) of 1-trimethylsilylethynylpyrene was added and allowed to dissolve. 0.024g (0.17 mmol) of  $\text{K}_2\text{CO}_3$  was added and the solution was allowed to stir under nitrogen for 4 hours. The solvent was removed under reduced pressure. The residue was dissolved in ~100 ml of dichloromethane and washed with 4 x 25 ml of 5% (w/v) aqueous  $\text{NaHCO}_3$ . The organic phase was dried over  $\text{MgSO}_4$ . The solvent was removed. The product was purified using silica, Hexane: DCM, 25:75 to yield a light brown solid.

% Yield: 0.2068 g, 0.9139 mmol, 70%

$^1\text{H}$  NMR: (400 MHz,  $\text{CDCl}_3$ ), 8.5 ppm (d,  $J = 8.8$  Hz, 1H), 8.15 ppm (m, 8H), 3.6 ppm (s, 1H)



### 5.2.1.3. Synthesis of 2-bromo-5-pyren-1-ylethynyl-thiophene (Pyrene-Thio-Br)



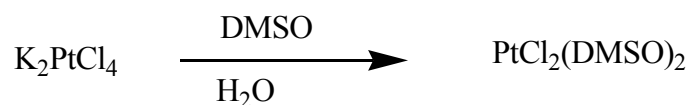
20 ml of dry, distilled diisopropylamine was added to a clean, dry round bottomed flask and purged with N<sub>2</sub> for 10 min. 0.2g (0.88 mmol) of 1-ethynylpyrene was added and the mixture was purged with nitrogen for a further 10 min. 0.024g (0.0348 mmol) of Pd(PPh<sub>3</sub>)<sub>2</sub>Cl<sub>2</sub>, 0.006g (0.0348 mmol) CuI and 0.020g (0.0696 mmol) PPh<sub>3</sub> were added to the reaction vessel. 0.098g (0.6 mmol) of 5-bromo-2-iodothiophene was added and the reaction vessel was sealed and allowed to reflux (88 °C) overnight under nitrogen. A mustard-brown solution results.

The solvent was removed under reduced pressure. The crude product and was extracted from the resulting solid by adding portions of a mixture of dichloromethane and hexane (4 ml and 20 ml respectively). After each addition the liquid layer was decanted off until it ran clear. The organic phase was dried over MgSO<sub>4</sub>. The solvent was removed. The product was purified using column chromatography on silica, Hexane: DCM, 80:20 to yield a bright yellow solid.<sup>21</sup>

% Yield: 0.178 g, 0.46 mmol, 52%

<sup>1</sup>H NMR: (400 MHz, CDCl<sub>3</sub>), 8.54 ppm (d, J = 9.2 Hz, 1H), 8.12 ppm (m, 8H), 7.18 ppm (d, J = 4.0 Hz, 1H), 7.035 ppm (d, J = 4.0 Hz, 1H)

#### 5.2.1.4. *Synthesis of PtCl<sub>2</sub>(DMSO)<sub>2</sub>*

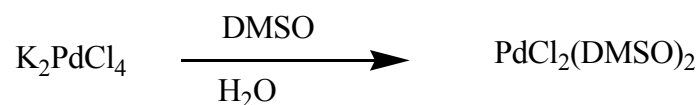


0.23g (0.554 mmol) of potassium tetrachloroplatinate and 0.118 ml (1.66 mmol) of dimethylsulphoxide were added to a clean, dry beaker. 5 ml of purified water was added and the reaction mixture was stirred with a glass rod until all solids had dissolved. The beaker was covered with tin foil and allowed to sit in the back of the fumehood overnight. The yellow crystalline solid resulting was collected through vacuum filtration.

% Yield: 0.319 g, 0.49 mmol, 88%

Elemental Analysis: Results Pending

#### 5.2.1.5. Synthesis of $\text{PdCl}_2(\text{DMSO})_2$



0.312g (0.554 mmol) of potassium tetrachloropalladate and 0.118 ml (1.66 mmol) of dimethylsulphoxide were added to a clean, dry beaker. 5 ml of purified water was added and the reaction mixture was stirred with a glass rod until all solids had dissolved. The beaker was covered with tin foil and allowed to sit in the back of the fumehood overnight. The brown crystalline solid resulting was collected through vacuum filtration.

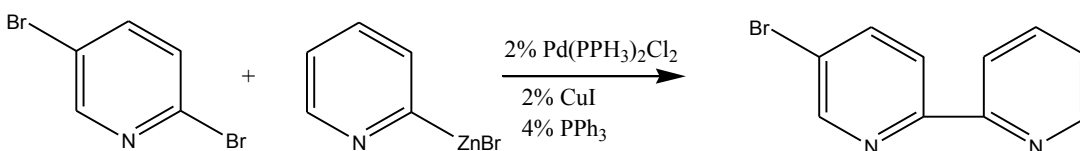
% Yield: 0.285 g, 0.507 mmol, 91%

Elemental Analysis: Results Pending

### 5.2.2. Attempted Synthesis of Covalently Bound Photosensitisers and Catalytic Centres

Synthesis was attempted to covalently link pyrene based photosensitisers and bpy based catalytic centres. Synthesis of 5.2.2.1 – 5.2.2.8, 5.2.2.10 and 5.2.2.13 were previously reported however this synthesis has been reported as the complexes have been used in further attempted synthesis (5.2.2.9, 5.2.2.12, 5.2.2.14)

#### 5.2.2.1. Synthesis of 5-bromo-[2,2']-bipyridine



A flow of nitrogen was allowed to flow through an extremely dry and clean round bottomed flask. 1.18g (5 mmol) of 2,5-dibromopyridine, 0.14g (0.2 mmol) of  $\text{Pd(PPh}_3)_2\text{Cl}_2$ , 0.038g (0.2 mmol) of CuI and 0.105g (0.4 mmol) were added to the flask. 10 ml (5 mmol) of 2-pyridylzinc was added and the reaction was allowed to stir overnight under nitrogen.

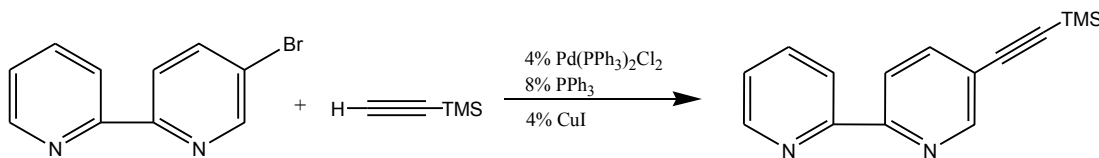
A small amount of the reaction mixture was added to 500 ml of a saturated solution of EDTA/ $\text{Na}_2\text{CO}_3$  and this was washed with 3 x 100 ml of dichloromethane. This was repeated until all of the reaction mixture had been added. The organic phase was dried over  $\text{MgSO}_4$ . The solvent was allowed to evaporate in the fumehood overnight. Purification was carried out using a silica solid phase and a hexane: ethyl acetate 9:1 mobile phase to yield a white iridescent solid.

% Yield: 1.058 g, 4.5 mmol, 90%

$^1\text{H NMR}$ : (400 MHz,  $\text{CDCl}_3$ ), 8.7 ppm (d, 1H), 8.6 ppm (d, 1H), 8.38 ppm (d, 1H), 8.34 ppm (d, 1H), 7.95 ppm (dd, 1H), 7.82 ppm (td, 1H), 7.34 ppm (td, 1H)

### 5.2.2.2. Synthesis of 5-trimethylsilylethynyl-[2,2']-bipyridine

#### (Method 1)



To a clean, dry round bottomed flask 20 ml of triethylamine was added and purged with nitrogen for 10 minutes. 0.2g (0.85 mmol) of 5-bromo-[2,2']-bipyridine was added and the mixture was purged with nitrogen for a further 10 min. 0.036g (0.051 mmol) of Pd(PPh<sub>3</sub>)<sub>2</sub>Cl<sub>2</sub>, 0.01g (0.051 mmol) CuI and 0.027g (0.102 mmol) PPh<sub>3</sub> were added to the reaction vessel. 0.177 ml (1.275 mmol) of ethynyltrimethylsilane was added and the reaction vessel was sealed and allowed to stir overnight under nitrogen.

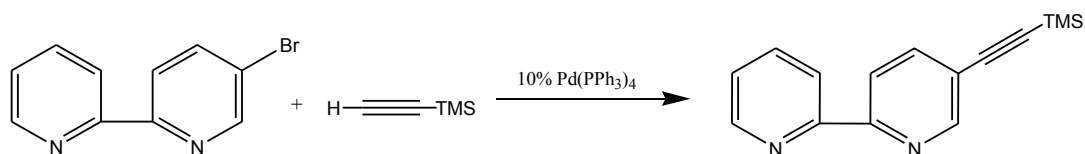
The reaction was allowed to stir under inert conditions overnight and then refluxed (88 °C) for ~24 hr to allow the reaction to run to completion. The amine was allowed to evaporate in the back of the fumehood. The residue was dissolved in ~100 ml of dichloromethane and washed with 4 x 25 ml of 5% (w/v) aqueous NaHCO<sub>3</sub>. The organic phase was dried over MgSO<sub>4</sub>. The solvent was allowed to evaporate in the back of the fumehood. The product was purified using column chromatography on silica, Hexane:DCM:Et<sub>3</sub>N, 75:25:1 to yield an orange solid.<sup>21</sup>

% Yield: 0.067g, 0.265 mmol, 31%

<sup>1</sup>H NMR: (400 MHz, CDCl<sub>3</sub>), 8.72 ppm (d, 1H), 8.67 ppm (d, 1H), 8.4 ppm (d, 1H), 8.37 ppm (d, 1H), 7.85 ppm (dd, 1H), 7.81 ppm (td, 1H), 7.37 ppm (td, 1H), 0.27 ppm (s, 9H)

### 5.2.2.3. Synthesis of 5-trimethylsilylethynyl-[2,2']-bipyridine

#### (Method 2)

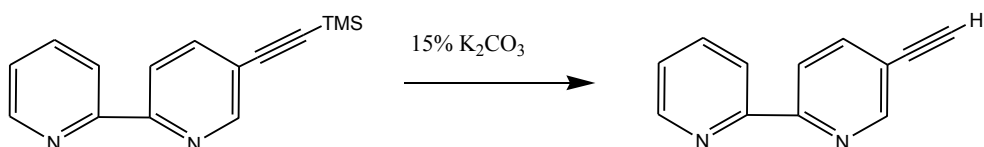


0.01 ml (0.7 mmol) of ethynyltrimethylsilane was dissolved in 12 ml of acetonitrile and added to a clean dry round bottomed flask. 0.235 g (1 mmol) of 5-bromo-[2,2']-bipyridine was dissolved in a mixture of 40 ml of benzene and 12 ml of triethylamine. This mixture was added drop wise to the stirring reaction vessel. The resulting mixture was vigorously degassed with N<sub>2</sub> for 10 min. 0.081g (0.07 mmol) of Pd(PPh<sub>3</sub>)<sub>4</sub> was added to the flask and the reaction vessel was sealed. The reaction was allowed to stir overnight at 60°C under inert conditions.. The solvent was allowed to evaporate overnight in the back of the fumehood. The resulting solid was washed with cold hexane followed by cold methanol resulting in a dark brown solid.

% Yield: 0.08g, 0.317 mmol, 32%

<sup>1</sup>H NMR: (400 MHz, CDCl<sub>3</sub>), 8.72 ppm (d, 1H), 8.67 ppm (d, 1H), 8.4 ppm (d, 1H), 8.37 ppm (d, 1H), 7.85 ppm (dd, 1H), 7.81 ppm (td, 1H), 7.37 ppm (td, 1H), 0.27 ppm (s, 9H)

#### 5.2.2.4. Synthesis of 5-ethynyl-[2,2']-bipyridine

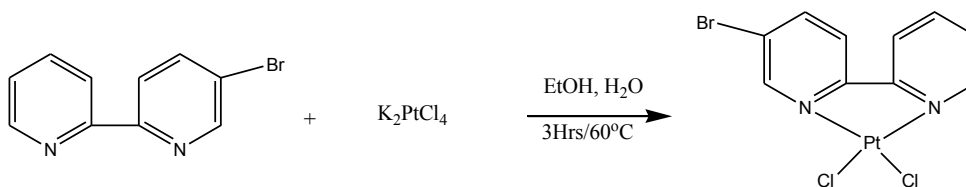


20 ml of freshly distilled methanol was added to a clean, dry round bottomed flask and purged with nitrogen for 10 minutes. 0.05g (0.2 mmol) of 5-trimethylsilylethyln-[2,2']-bipyridine was added and allowed to dissolve. 0.0052 g (0.03 mmol) of K<sub>2</sub>CO<sub>3</sub> was added and the solution was allowed to stir under nitrogen for 4 hours. The solvent was removed under reduced pressure. The residue was dissolved in ~100 ml of dichloromethane and washed with 4 x 25 ml of 5% (w/v) aqueous NaHCO<sub>3</sub>. The organic phase was dried over MgSO<sub>4</sub>. The solvent was allowed to evaporate in the back of the fumehood to yield a brown solid. The product was purified using silica, Hexane:DCM:Et<sub>3</sub>N, 75:25:1 to yield an orange solid.

% Yield: 0.026g, 0.144 mmol, 72%

<sup>1</sup>H NMR: (400 MHz, CDCl<sub>3</sub>), 8.76 ppm (d, 1H), 8.69 ppm (d, 1H), 8.43 ppm (d, 1H), 8.42 ppm (d, 1H), 7.9 ppm (dd, 1H), 7.88 ppm (td, 1H), 7.34 ppm (td, 1H), 3.29 ppm (s, 1H)

**5.2.2.5. Synthesis of Platinum(5-bromo-[2,2']-bipyridine)dichloride (Method 1):**



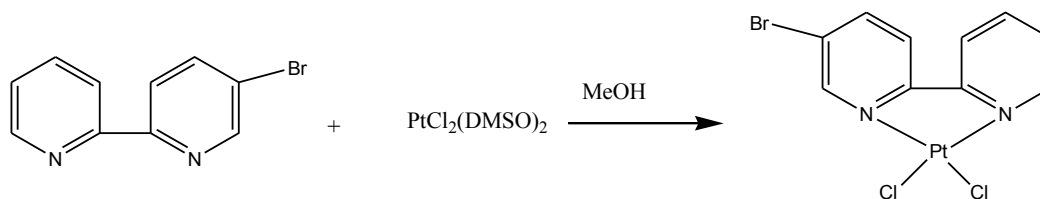
0.154g (0.37 mmol) of potassium tetrachloroplatinate was dissolved in 100 ml of boiling purified water. This mixture was added to a clean and dry 250ml round bottomed flask and allowed to cool. 0.087g (0.37 mmol) of 5-bromo-[2,2']-bipyridine was dissolved in 25 ml of warm ethanol. Once the reaction mixture in the round bottomed flask had cooled to  $\sim 60^\circ C$  the ethanol and 5-bromo-[2,2']-bipyridine mixture was added to the flask. The reaction vessel was sealed and allowed to stir at  $60^\circ C$  overnight. The reaction mixture was cooled and the mixture was placed in the refrigerator overnight. The orange precipitate was collected the following day through vacuum filtration.

% Yield: 0.128g, 0.26 mmol, 70%

$^1H$  NMR: (400 MHz, DMSO- $d_6$ ), 8.69 ppm (d, 1H), 8.62 ppm (d, 1H), 7.93 ppm (dd, 1H), 7.91 ppm (dd, 1H), 7.76 ppm (d, 1H), 7.71 ppm (d, 1H), 7.57 ppm (td, 1H), 7.01 ppm (td, 1H)



**5.2.2.6. Synthesis of Platinum(5-bromo-[2,2']-bipyridine)dichloride (Method 2):**

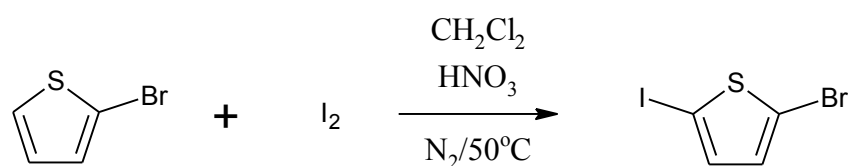


0.326g (0.5 mmol) of  $\text{PtCl}_2(\text{DMSO})_2$  and 0.116g (0.5 mmol) of 5-bromo-[2,2']-bipyridine were added to a clean, dry round bottomed flask. 15 ml of methanol was added and the reaction mixture was purged with  $\text{N}_2$  for 5 min until the solids dissolved. The reaction mixture was allowed to reflux under inert conditions for 4 hours. The reaction mixture was then allowed to cool to room temperature and then placed in the fridge (2 - 5 °C) overnight. The solvent was removed under reduced pressure. An orange solid results.

% Yield: 0.251g, 0.49 mmol, 98%

$^1\text{H}$  NMR: (400 MHz,  $\text{DMSO-d}_6$ ), 8.7 ppm (d, 1H), 8.63 ppm (d, 1H), 7.93 ppm (dd, 1H), 7.91 ppm (dd, 1H), 7.77 ppm (d, 1H), 7.71 ppm (d, 1H), 7.58 ppm (td, 1H), 7.02 ppm (td, 1H)

#### 5.2.2.7. Synthesis of 2-bromo-5-iodothiophene

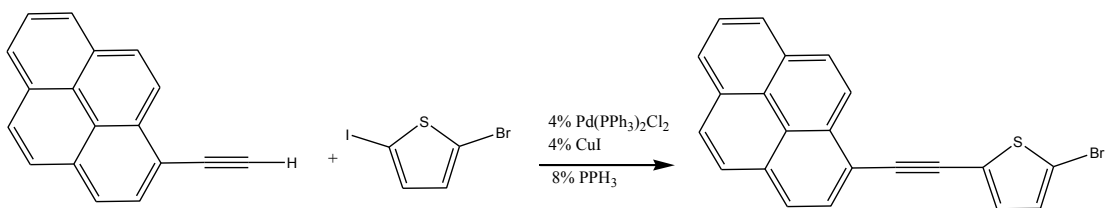


8 ml of dichloromethane, 0.38 ml (3.9 mmol) of 2-bromothiophene and 6.0 ml of 8.5 M nitric acid were added to a clean dry round bottomed flask containing 0.50g (2.0 mmol) of iodine. The mixture was allowed to stir under nitrogen at 50°C for 5 hours. The reaction was quenched with ~50 ml of water. The organic phase was extracted with 3 x 20 ml of dichloromethane and this was then washed with 3 x 20 ml of 50% (w/v) aqueous sodium thiosulphate. The organic phase was dried over MgSO<sub>4</sub>. Purification was carried out using Kuglerohr distillation (95 °C) to yield a clear oil.<sup>22</sup>

% Yield: 1.59 g, 3.82 mmol, 98%

<sup>1</sup>H NMR: (400 MHz, CDCl<sub>3</sub>), 7.02 ppm (d, 1H), 6.73 ppm (d, 1H)

#### 5.2.2.8. Synthesis of 2-bromo-5-pyren-1-ylethynyl-thiophene:

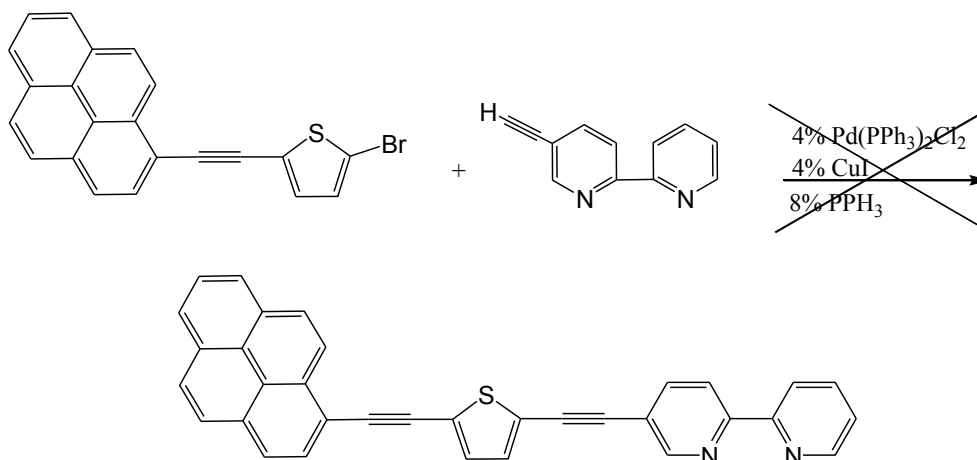


20 ml of dry, distilled diisopropylamine was added to a clean, dry round bottomed flask and purged with N<sub>2</sub> for 10 min. 0.2g (0.88 mmol) of 1-ethynylpyrene was added and the mixture was purged with nitrogen for a further 10 min. 0.024g (0.0348 mmol) of Pd(PPh<sub>3</sub>)<sub>2</sub>Cl<sub>2</sub>, 0.006g (0.0348 mmol) CuI and 0.020g (0.0696 mmol) PPh<sub>3</sub> were added to the reaction vessel. 0.098g (0.6 mmol) of 5-bromo-2-iodothiophene was added and the reaction vessel was sealed and allowed to reflux (88°C) overnight under nitrogen. A mustard-brown solution results. The solvent was removed under reduced pressure. The crude product and was extracted from the resulting solid by adding portions of a mixture of dichloromethane and hexane (4 ml and 20 ml respectively). After each addition the liquid layer was decanted off until it ran clear. The organic phase was dried over MgSO<sub>4</sub>. The solvent was removed. The product was purified using column chromatography on silica, Hexane: DCM, 80:20 to yield a bright yellow solid.<sup>21</sup>

% Yield: 0.178g, 0.46mmol, 52%

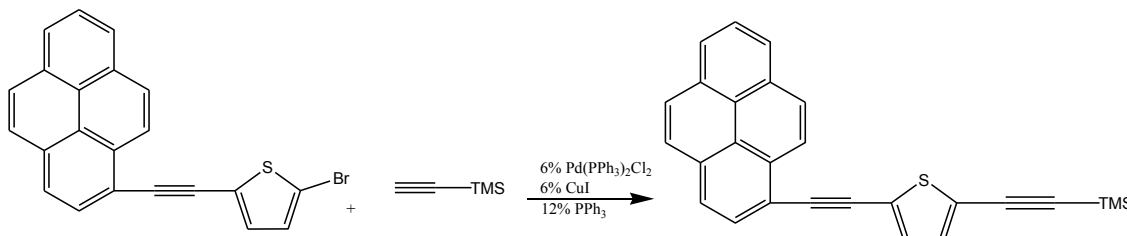
<sup>1</sup>H NMR: (400 MHz, CDCl<sub>3</sub>), 8.54 ppm (d, 1H), 8.12 ppm (m, 8H), 7.18 ppm (d, 1H), 7.035 ppm (d, 1H)

#### 5.2.2.9. Synthesis of 5-(5-Pyren-1-ylethynyl-thiophen-2-ylethynyl)-[2,2']bipyridine



20 ml of dry, distilled diisopropylamine was added to a clean, dry round bottomed flask and purged with N<sub>2</sub> for 10 min. 0.08g (0.21 mmol) of 2-bromo-5-pyren-1-ylethynyl-thiophene was added and the mixture was purged with nitrogen for a further 10 minutes. 0.001g (0.008 mmol) of Pd(PPh<sub>3</sub>)<sub>2</sub>Cl<sub>2</sub>, 0.002g (0.008 mmol) CuI and 0.004g (0.016 mmol) PPh<sub>3</sub> were added to the reaction vessel. 0.038g (0.21 mmol) of 5-ethynyl-[2,2']-bipyridine was added and the reaction vessel was sealed and allowed to reflux (88°C) overnight under nitrogen. A mustard-brown solution results. The solvent was removed under reduced pressure. The crude product was extracted from the resulting solid by adding portions of a mixture of dichloromethane and hexane (4 ml and 20 ml respectively). After each addition the liquid layer was decanted off until it ran clear. The organic phase was dried over MgSO<sub>4</sub>. The solvent was removed.<sup>21</sup> No Product was successfully isolated.

**5.2.2.10. Synthesis of 2-ethynyl-trimethylsilyl-5-pyren-1-yl-ethynyl-thiophene:**

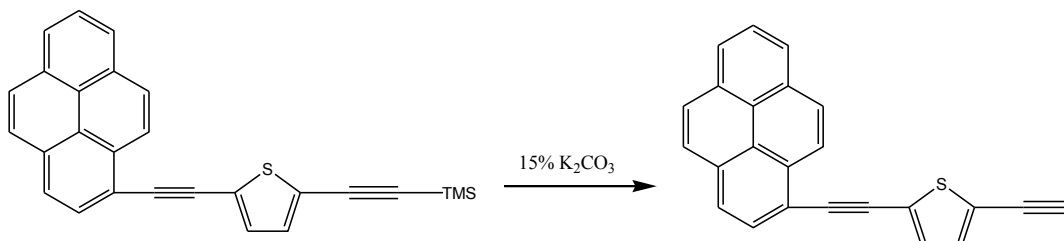


0.1g (0.26 mmol) of 2-bromo-5-pyren-1-yl-ethynyl-thiophene and 15 ml of dry distilled diisopropylamine was added to a clean, dry round bottomed flask. The mixture was purged with N<sub>2</sub> for 10 min. 0.0112g (0.016 mmol) of Pd(PPh<sub>3</sub>)<sub>2</sub>Cl<sub>2</sub>, 0.008g (0.032 mmol) of PPh<sub>3</sub> and 0.003g (0.016 mmol) of CuI were added the mixture was purged with N<sub>2</sub> for a further 5 min. 0.054 ml (0.39 mmol) of ethynyltrimethylsilane was added and the reaction vessel was sealed. The reaction was allowed to reflux (84°C) overnight under inert conditions. The amine was removed under reduced pressure. The crude product was extracted from the resulting solid by adding portions of a mixture of dichloromethane and hexane (4 ml and 20 ml respectively). After each addition the liquid layer was decanted off until it ran clear. The organic phase was dried over MgSO<sub>4</sub>. The solvent was removed. The product was purified using column chromatography on silica, using 100% hexane as the mobile phase yielding an orange-yellow solid.<sup>21</sup>

% Yield: 0.081g, 0.2 mmol, 77%

<sup>1</sup>H NMR: (400 MHz, CDCl<sub>3</sub>), 8.58 ppm (d, 1H), 8.14 ppm (m, 8H), 7.265 ppm (d, 1H), 7.18 ppm (d, 1H), 0.275 ppm (s, 9H)

#### 5.2.2.11. Synthesis of 2-ethynyl-5-pyren-1-ylethynyl-thiophene:

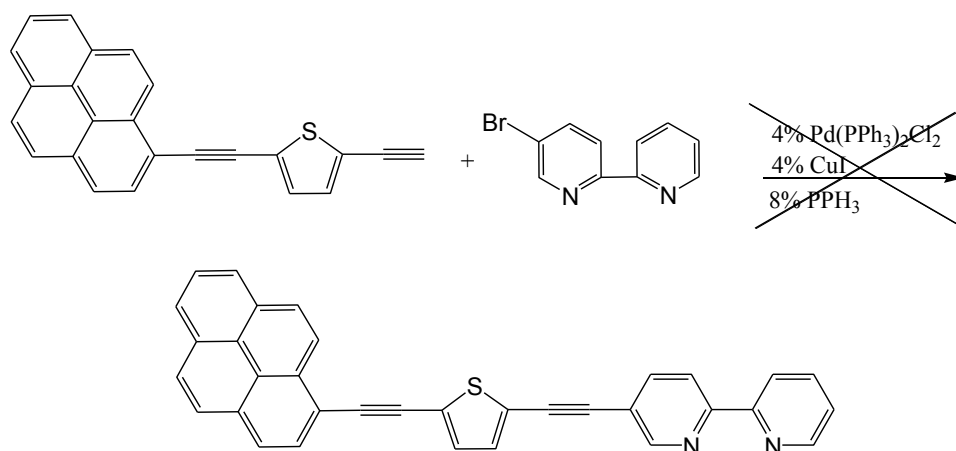


20 ml of dry, distilled methanol was added to a clean, dry round bottomed flask and purged with N<sub>2</sub> for 10 min. 0.2g (5 mmol) of 2-ethynyl-trimethylsilyl-5-pyrenyl-ethynyl-thiophene was added and the mixture was purged for a further 5 min or until the solid dissolved (~2 ml of triethylamine was added to aid dissolution). 0.010g (0.075 mmol) K<sub>2</sub>CO<sub>3</sub> was added and the reaction vessel was sealed. The reaction mixture was allowed to stir under inert conditions for 4-5 hours. The solvent was removed under reduced pressure yielding a brown-orange solid.

% Yield: 0.125g, 3.8 mmol, 76%

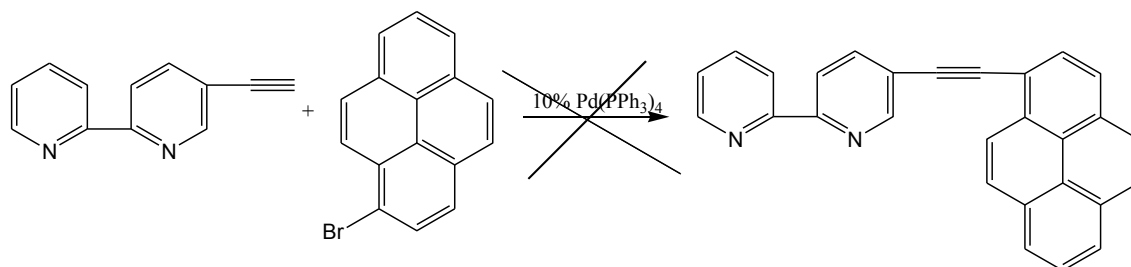
<sup>1</sup>H NMR: (400 MHz, CDCl<sub>3</sub>), 8.56 ppm (d, 1H), 8.1 ppm (m, 8H), 7.27 ppm (d, 1H), 7.23 ppm (d, 1H), 3.46 ppm (s, 1H)

#### 5.2.2.12. Synthesis of 5-(5-Pyren-1-ylethynyl-thiophen-2-ylethynyl)-[2,2']bipyridine



20 ml of dry, distilled diisopropylamine was added to a clean, dry round bottomed flask and purged with N<sub>2</sub> for 10 min. 0.06g (0.18 mmol) of 2-ethynyl-5-pyren-1-ylethynyl-thiophene was added and the mixture was purged with nitrogen for a further 10 min. 0.001g (0.008 mmol) of Pd(PPh<sub>3</sub>)<sub>2</sub>Cl<sub>2</sub>, 0.002g (0.008 mmol) CuI and 0.004g (0.016 mmol) PPh<sub>3</sub> were added to the reaction vessel. 0.042g (0.18 mmol) of 5-bromo-[2,2']-bipyridine was added and the reaction vessel was sealed and allowed to reflux (88°C) overnight under nitrogen. A mustard-brown solution results. The solvent was removed under reduced pressure. The crude product and was extracted from the resulting solid by adding portions of a mixture of dichloromethane and hexane (4 ml and 20 ml respectively). After each addition the liquid layer was decanted off until it ran clear. The organic phase was dried over MgSO<sub>4</sub>. The solvent was removed.<sup>21</sup> No product was successfully isolated.

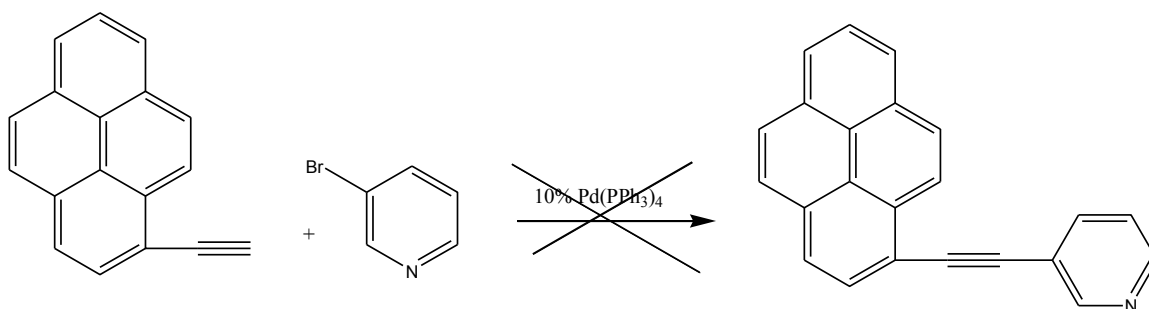
### 5.2.2.13. Synthesis of 5-pyren-1-ethynyl-[2,2']-bipyridine:



0.03g (0.166 mmol) of 5-ethynyl-[2,2']-bipyridine was dissolved in 6 ml of acetonitrile and added to a clean dry round bottomed flask. 0.051g (0.1826 mmol) of 1-bromopyrene was dissolved in a mixture of 20 ml of benzene and 6 ml of triethylamine. The 1-bromopyrene mixture was added drop wise to the stirring of 5-ethynyl-[2,2']-bipyridine mixture in the round bottomed flask. The resulting mixture was vigorously degassed with  $\text{N}_2$  for 5 min. 0.019g (0.166 mmol) of  $\text{Pd(PPh}_3)_4$  was added to the reaction vessel and it was sealed. The mixture was allowed to stir at  $60^\circ\text{C}$  overnight under inert conditions. The solvent was removed and the resulting solid was washed with cold hexane followed by cold methanol.<sup>21</sup> No product was successfully isolated.



#### 5.2.2.14. Synthesis of 3-(1-ethynylpyrene)-pyridine:



To a clean, dry, round bottomed flask 20 ml of diisopropylamine was added and purged with N<sub>2</sub> for 5 minutes. 0.127ml (1.32 mmol) of 3-bromopyridine was added and the mixture was purged with N<sub>2</sub> for a further 5 minutes. 0.2g (0.88 mmol) of 1-ethynylpyrene and 0.092g (0.08 mmol) of Pd(PPh<sub>3</sub>)<sub>4</sub> were added and the reaction vessel was sealed. The reaction mixture was allowed to stir overnight under inert conditions. The solvent was removed under reduced pressure. Purification was carried out using column chromatography on silica with Pentane: DCM, 9: 1 as mobile phase yielding a bright yellow powdery solid.<sup>21</sup> Product was not successfully isolated.

## 5.3 Results

### 5.3.1. Synthesis

As outlined earlier the aim of the work carried out in this thesis is the synthesis and investigation the photocatalytic properties for hydrogen generation of intramolecular assemblies based on an organic photosensitiser, example shown in Figure 1.4. This involves a considerable amount of synthetic work, since the photosensitiser needs to be connected to the photocatalytic centre via a suitable bridge. In this manner an intramolecular reaction sequence is envisaged that allows for a photoinduced electron transfer from the light absorbing part of the assembly to the catalytic centre. However, in this chapter, problems were encountered in the synthetic process. While the photosynthetic centre could successfully be connected to the thiophene based bridge, the connection of the catalytic centre to this moiety was not achieved. So while a range of pyrene compounds were prepared such as 1-ethynylpyrene and 2-bromo-5-pyren-1-ylethynyl-thiophene the intramolecular pyrene/(Pt/Pd) assembly was not obtained. The synthetic aspects of this work are further considered in the discussion part of this chapter. While the intramolecular pyrene/(Pt/Pd) assembly could not be prepared the individual photosensitiser and catalytic components could be synthesised in dependently. It was therefore decided to carry out intermolecular rather than intramolecular photocatalytic studies which are discussed below.

### 5.3.2. UV-Vis Spectroscopy

Room temperature absorption spectra were obtained for all compounds. Table 5.1 illustrates the absorption maxima ( $\lambda_{\text{max}}$ ) for all compounds in this study. All UV-Vis spectra were carried out using spectrophotometric grade dichloromethane (DCM).

Compound	$\lambda_{\text{max}}$ (nm), $\epsilon$ ( $\times 10^6 \text{ M}^{-1} \text{ cm}^{-1}$ )
Pyrene-Br	317 (1.09*), 330 (2.62*), 346 (3.76*)
Pyrene-TMS	336 (1.27), 347 (2.82), 367(4.19)
Pyrene-H	325 (1.25), 341 (3.07), 359 (4.35)
Pyrene-Thio-Br	309 (2.75), 370 (4.43), 375 (4.73), 397 (4.74)

**Table 5.1-** UV-Vis absorption data for all compounds in this study. All spectra were recorded in spectrophotometric grade DCM. \*  $\epsilon = 10^{-5} \text{ M}$

All of the compounds in this study exhibit strong absorptions in the UV-vis region of the spectrum which are associated with ligand localised  $\pi - \pi^*$  transitions.<sup>23</sup> The addition of a thiophene substituent increases the conjugation of the system leading to a red shift of  $\sim 20 \text{ nm}$  in the  $\lambda_{\text{max}}$ .

### 5.3.3. Fluorescence Spectroscopy

Room temperature emission spectra were obtained for all pyrene compounds in this study. Table 5.2 illustrates the excitation wavelength and emission maxima for all compounds in this study. All emission spectra were obtained using spectrophotometric grade dichloromethane (DCM).

Compound	Excitation (nm)	Emission (nm)	Stokes Shift ( $\text{cm}^{-1}$ )
Pyrene-TMS	336	384, 404, 424	1274
Pyrene-H	325	385, 406, 426	1813
Pyrene-Thio-Br	309	404, 425	436

**Table 5.2-** Fluorescence properties of all pyrene compounds in this study. Stokes shift calculated between most intense absorbance band and most intense emission band. All spectra were recorded in spectrophotometric grade DCM.

### 5.3.4. Photocatalytic H<sub>2</sub> generation

All experiments to test for the intermolecular photocatalytic generation of H<sub>2</sub> from water were carried out in triplicate. All solvents used were completely dried and deaerated before use. THF was distilled over sodium and benzophenone before use. Water used was deionised. Triethylamine was distilled over NaOH before use. All experiments were carried out under an argon atmosphere. Each photosensitiser (**1** – **4**, Fig. 5.14) was tested in the presence of both catalytic centres (**A** and **B**, Fig. 5.14) for their H<sub>2</sub> generating efficiencies. The photolysis experiment a (1:1) 5 x 10<sup>-5</sup> M solution of the photosensitiser and catalyst to be tested was dissolved in THF. 1.2 ml of this solution was added to a 5 ml septa capped gas tight vial. 0.6 ml of the sacrificial donor triethylamine (16.6 % (v/v)) was added along with 0.2 ml of deionised water (10 % (v/v)) as proton source or 0.2 ml THF to make a 0% water mixture. The solutions were photolysed for 20 hours using a UV light (350 nm) LED light array. After 20 hours a 0.5 ml sample of the headspace in the reaction vial was collected using a gas-tight syringe. These samples were injected into a series CP-3800 gas chromatograph with both TCD and FID detectors in use in conjunction with one another. The peak area response was measured and compared to a series of standards to elucidate the number of moles of H<sub>2</sub> produced during the experiment. The GC was calibrated for H<sub>2</sub> using standard gas mixtures obtained from 0.01% (100 ppm), 0.1% (1000 ppm), 1% (10000 ppm) and 5% (50000ppm).

Full details of experimental conditions are found in appendix B1 and B2.

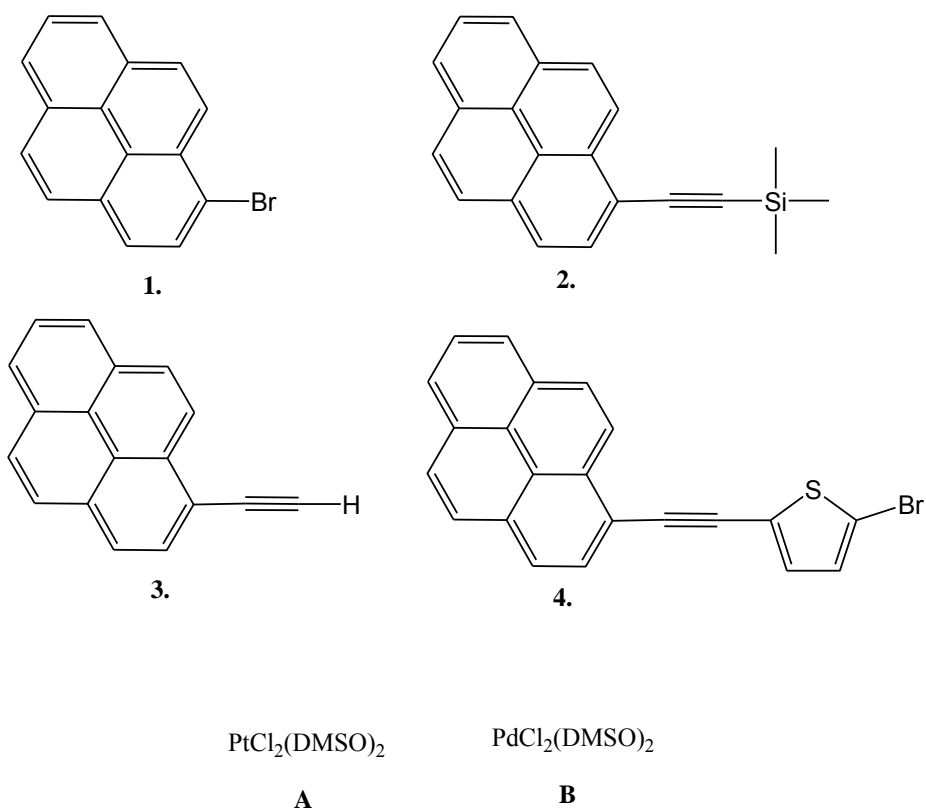


Figure 5.15- Labelling of photosensitisers and catalytic centres for intermolecular photocatalytic  $\text{H}_2$  generation experiments.

All complex mixtures were tested under the conditions listed in Table 5.3.

Exp . No.	Complexes	Conc. Photosensitiser and Catalyst 1:1 (M)	TEA (%)	Water (%)	Irradiation $\lambda$ (nm)	Irradiation length (hr)
1	X + A	$5 \times 10^{-5}$	16.6	10	350	20
2	X + A	$5 \times 10^{-5}$	16.6	0	350	20
3	X + B	$5 \times 10^{-5}$	16.6	10	350	20
4	X + B	$5 \times 10^{-5}$	16.6	0	350	20

Table 5.3- Experimental conditions for photocatalytic studies, X = photosensitisers 1 - 4.

No H<sub>2</sub> was measured in the headspace of the sample vial, however as the limit of detection of the GC is quite high, the intermolecular generation of H<sub>2</sub> cannot be definitively eliminated.

## 5.4. Discussion

**Synthesis.** Conjugation of starting materials with acetylene bridges was carried out using traditional Sonogashira Coupling methods. The Pd<sup>0</sup> catalyst needed for this type of reaction was produced *in-situ* using Pd(PPh<sub>3</sub>)<sub>2</sub>Cl<sub>2</sub> and PPh<sub>3</sub>. All spectral data are in agreement with reported data.<sup>3,8,24</sup> All compounds were obtained in good yields.

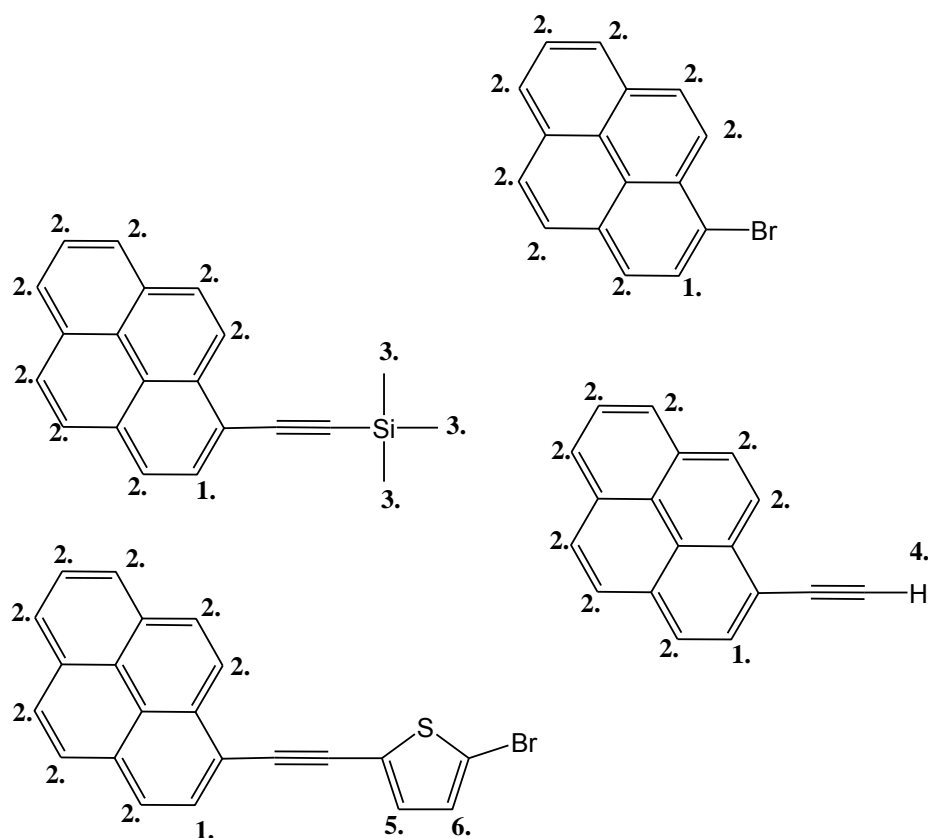
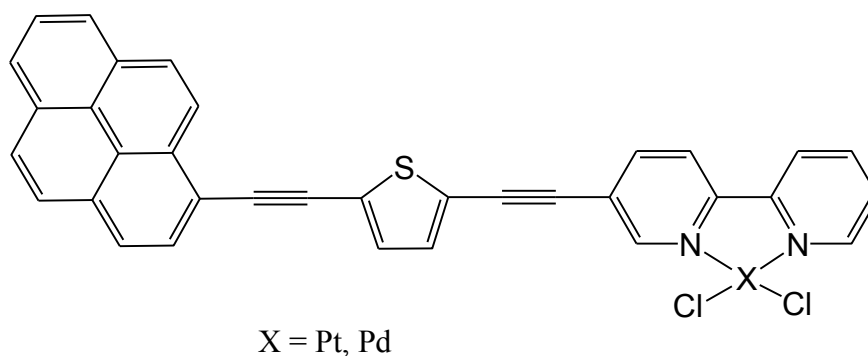


Figure 5.16- Numbering of protons in extended pyrene complexes.

**NMR Spectroscopy.** Proton signals due to the aromatic protons on the pyrene (1 and 2) unit can be observed between 8.54 and 8.1 ppm in the <sup>1</sup>H NMR spectra. Due to substitution on the pyrene macrocycle the doublet produced from proton 1 is

found further downfield on the NMR spectrum due to the shielding effect of the substituent group. Due to the similar environment experienced by protons **2**, a large multiplet is produced due to the signals of all 8 of these protons. Addition of an alkynyl TMS group gave rise to a strong sharp multiplet at 0.36 ppm (**3**) due to the 9 protons on the CH<sub>3</sub> groups within the unit. When the TMS substituent is removed yielding a single proton (**4**), the strong singlet is no longer visible and a sharp singlet at 3.6 ppm is observed due to the deprotected group. Further extending the conjugation and aromaticity through addition of a thiophene group leads to the observation of two doublet signals (**5** and **6**) at 7.18 and 7.035 ppm in the aromatic region. Examples of <sup>1</sup>H NMR are available in appendix D1.

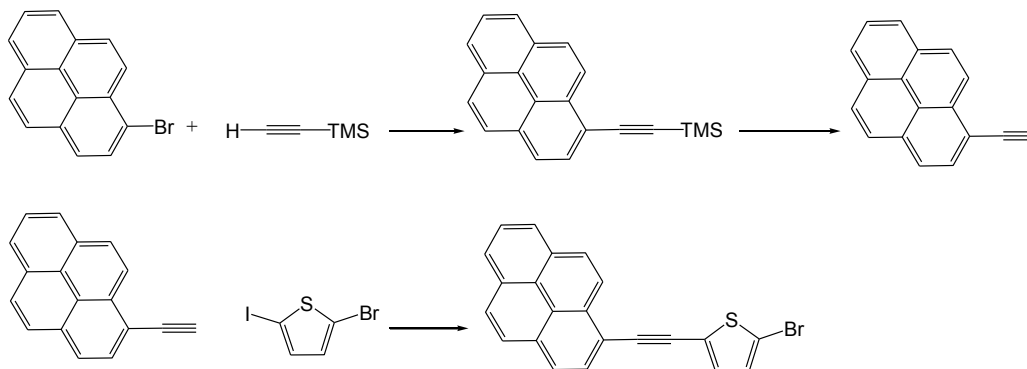
**Attempted Synthesis.** Synthesis of a covalently linked PS and catalytic centre was attempted; however this synthesis proved difficult and unfortunately isolation of the final product was not successful. The main aim of the attempted synthesis was to yield the highly conjugated molecule exhibited in Fig. 5.17. The extended conjugation would further shift the absorbance of the complexes into the visible region of the spectrum, thus producing a system which could generate H<sub>2</sub> following irradiation with visible light.



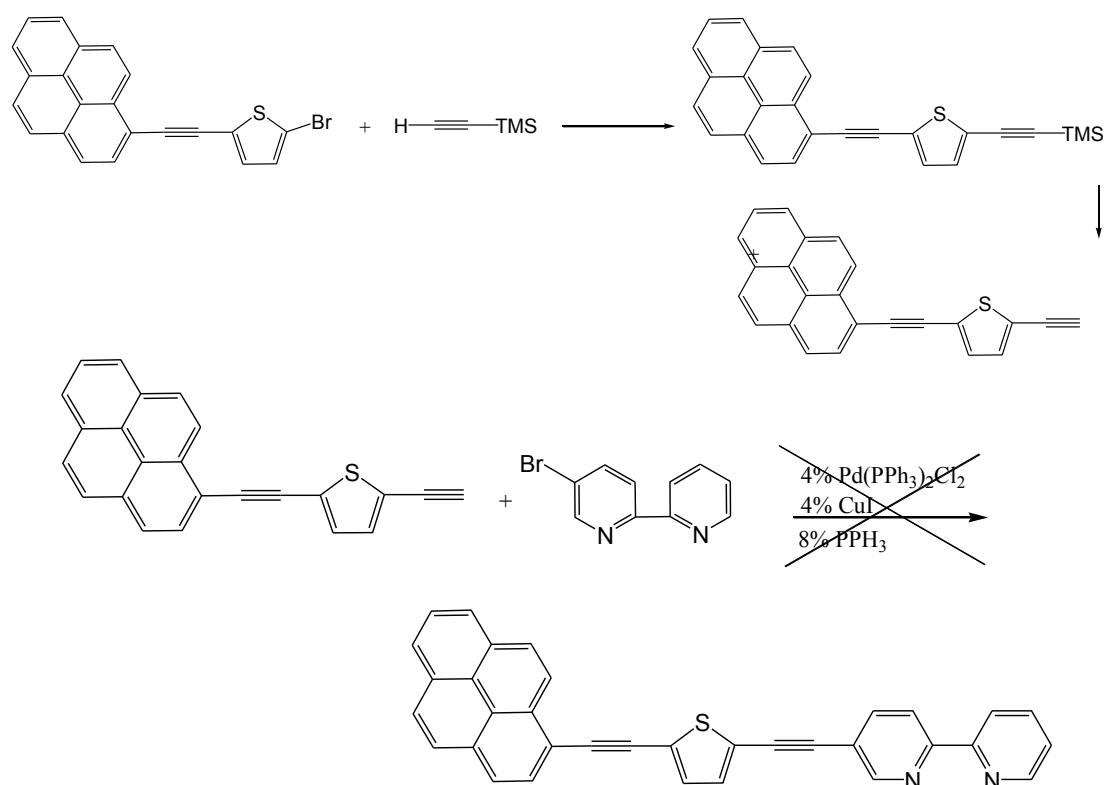
**Figure 5.17- Target molecule 1 for attempted synthesis in this study.**

Two synthetic routes were employed while attempting the synthesis of this molecule (illustrated below). Route 1 employed extending the conjugation of the pyrene chromophore followed by coordination of the bipyridine (bpy) unit using Sonogashira coupling between a bromo group in the bpy molecule with a deprotected ethynyl group on the pyrene molecule, however the final reaction proved unsuccessful.

Route 2 employed extending the conjugation of the bpy moiety followed by coordination of the pyrene chromophore unit using Sonogashira coupling between a bromo group in the pyrene molecule with a deprotected ethynyl group bpy molecule, however the final reaction, again, proved unsuccessful.

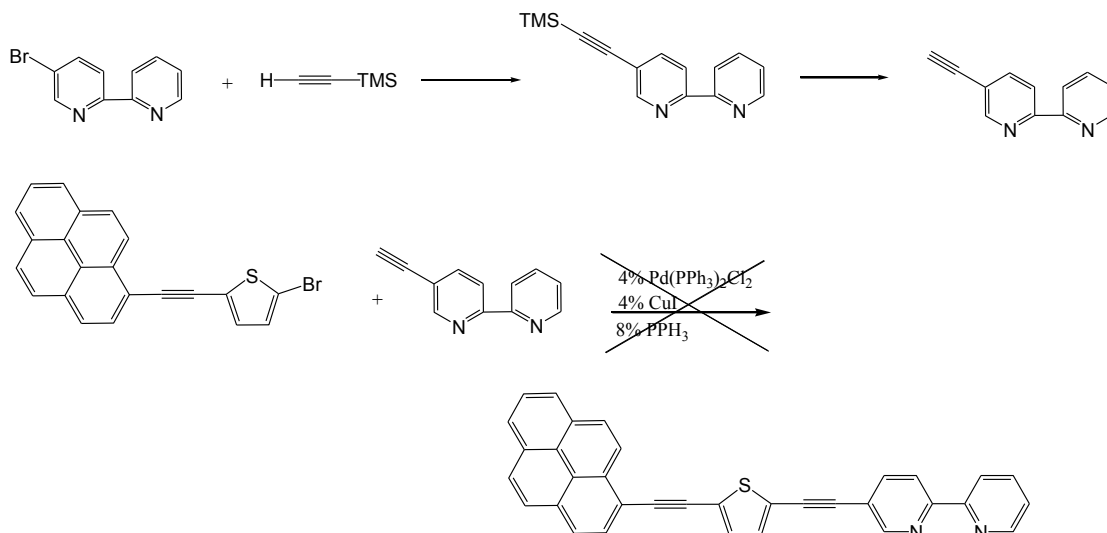


**Route 1:**





**Route 2:**



A second target molecule was proposed (Fig. 5.18) as a possible resolution to the problems experienced during synthesis. Synthesis of the conjugated organic ligand again proved unsuccessful.

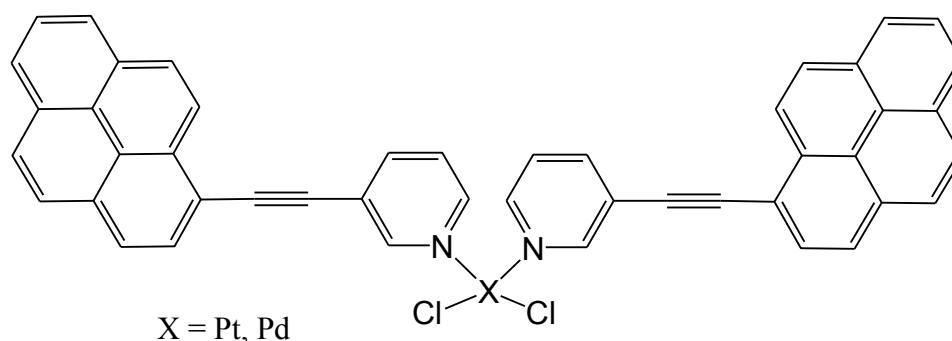


**Figure 5.18-** Target molecule 2 for attempted synthesis in this study.

It was decided that intermolecular  $\text{H}_2$  generation between the unbound photosensitiser and the Pt/Pd catalyst would be investigated.

**Electronic Absorbance Spectroscopy.** Room temperature UV-Vis absorbance spectra were obtained for all pyrene ligands in this study. All spectra were recorded in spectrophotometric grade DCM. All compounds exhibit strong absorbances in the UV region of the spectrum which are attributed to  $\pi - \pi^*$  transitions.<sup>23</sup> The extension of the conjugation due to addition of an alkynyl bridging group lead to a red shift in the  $\lambda_{\text{max}}$  absorbances in the complexes. (Fig. 5.19).

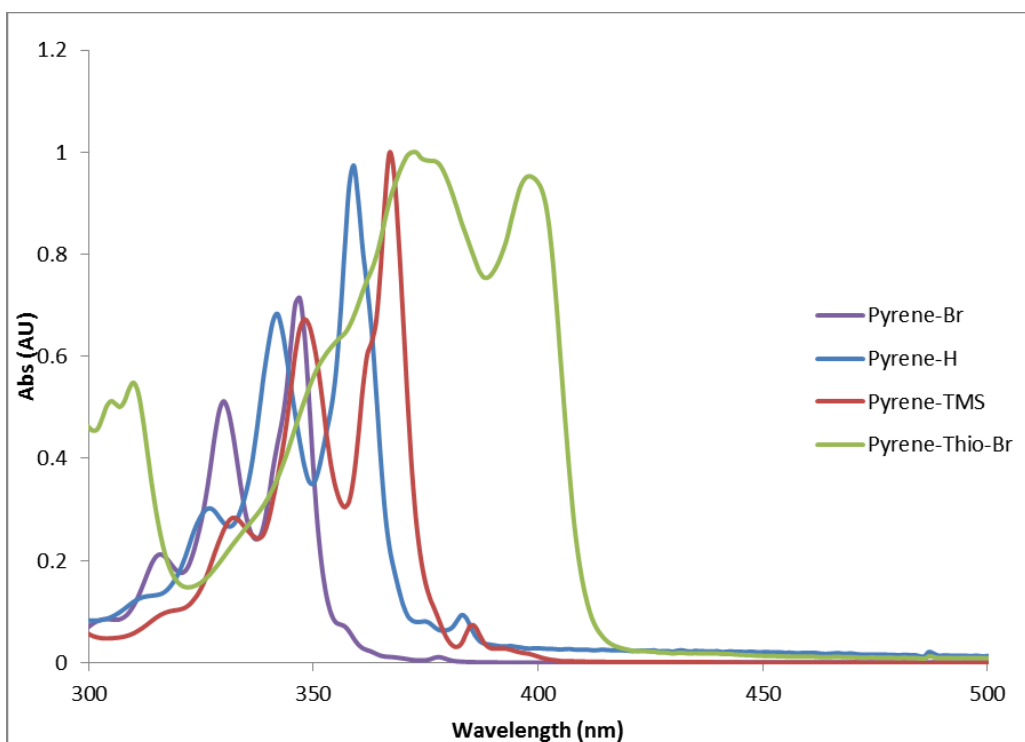
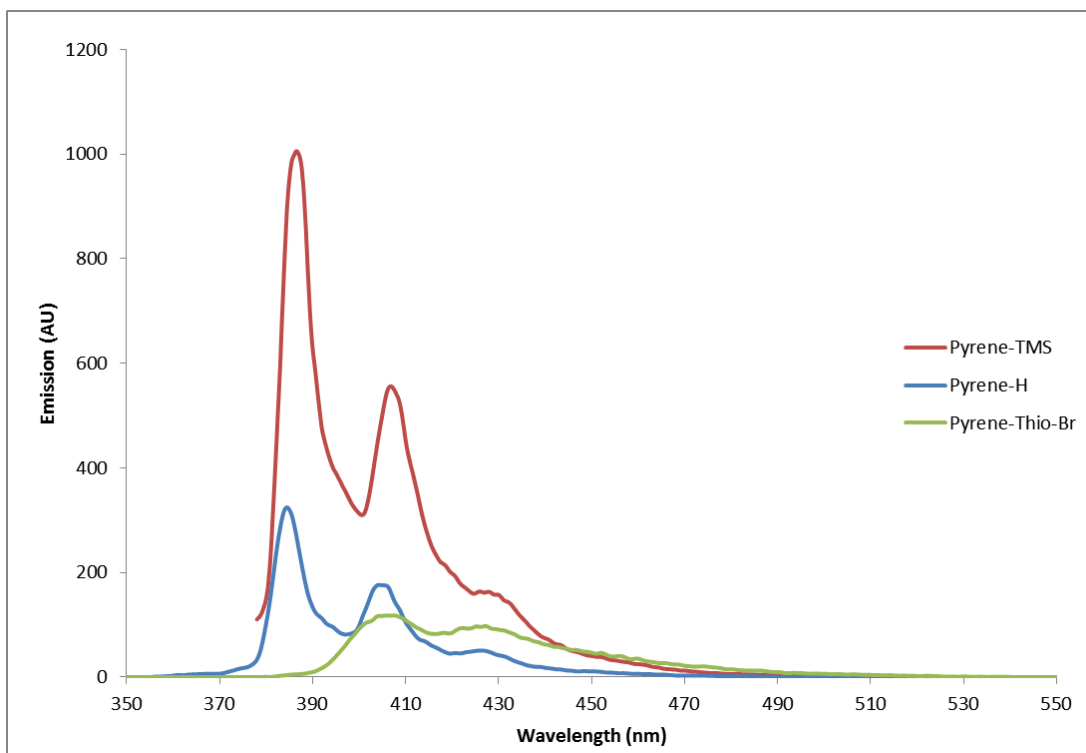


**Figure 5.19-** UV-Vis spectra of Pyrene-Br (purple line), Pyrene-H (blue line), Pyrene-TMS (red line) and Pyrene-Thio-Br (green line). All spectra were recorded in spectroscopic grade DCM.

Incorporation of a thiophene group further extends the  $\pi$ -conjugation inducing a  $\sim 20$  nm bathochromic shift in absorbances pushing them out towards the visible region. In addition to pyrene based transitions the Pyrene-Thio-Br exhibits thiophene based transitions in the region between 290 and 320 nm.

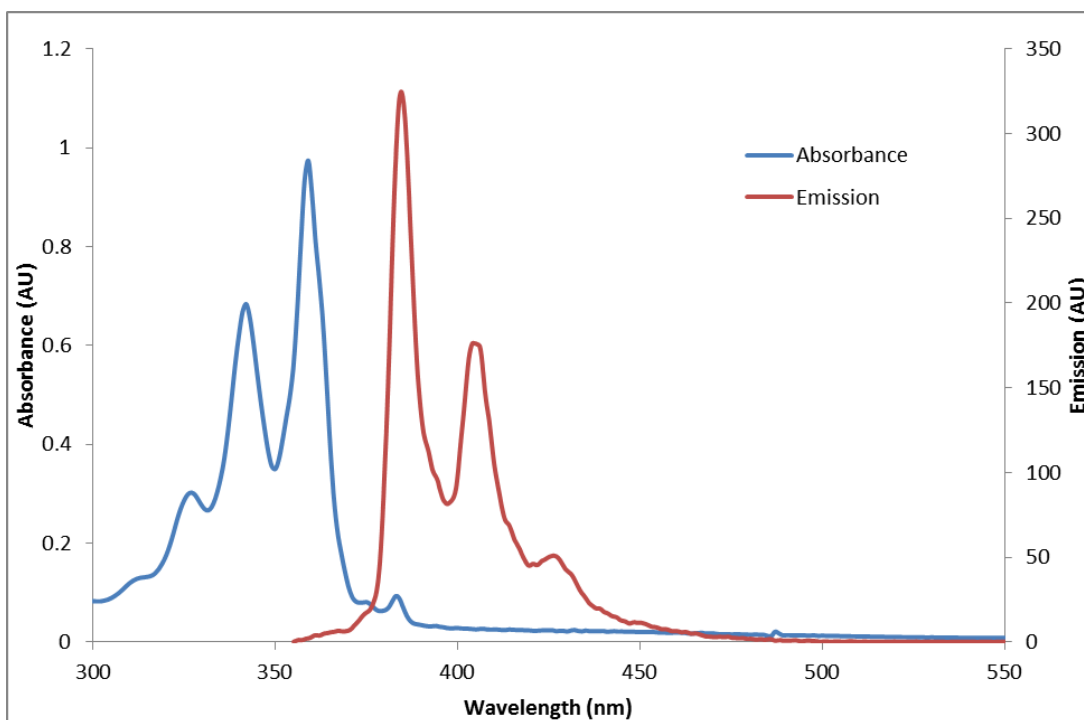
**Fluorescence Spectroscopy.** As shown in Fig 5.20 both Pyrene-TMS and Pyrene-H exhibit sharp but unresolved emission bands at  $\sim 384$  nm and 405 nm. A weaker shoulder is also observed at  $\sim 425$  nm following excitation into each of the absorbance bands in the UV-Vis spectrum. Only a slight shift of  $\sim 2$  nm is observed in the wavelength of these emission bands indicating that the same excited state is responsible for the observed emission in each case. Also evident from Fig. 5.16 excitation of Pyrene-Thio-Br results in the appearance of two broad emission bands at 404 nm and 425 nm. This represents a bathochromic shift of  $\sim 20$  nm to lower energy wavelengths. This may be explained due to the increased conjugation due to

the thiophene unit altering the HOMO-LUMO energy gap. Also evident is the significant reduction in emission intensity upon coordination of a thiophene unit which is attributed to electronic communication between the pyrene chromophore and the thiophene bridge.



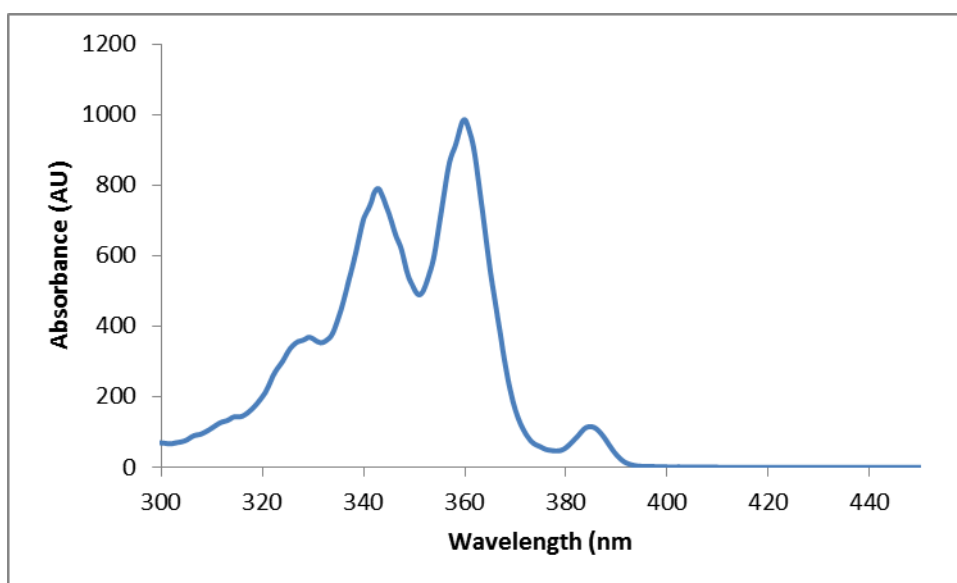
**Figure 5.20- Emission spectrum of Pyrene-TMS (red line), Pyrene-H (blue line) and Pyrene-Thio-Br (green line). All spectra were recorded in spectrophotometric grade DCM.  $\lambda_{\text{Ex}}$  Pyrene-TMS = 336, Pyrene-H = 325 nm and Pyrene-Thio-Br = 436 nm.**

Fig. 5.21 illustrates the UV-Vis absorbance spectrum and the emission spectrum of Pyrene-H in spectrophotometric grade DCM. A small Stokes shift is observed between the most intense band of the absorbance spectrum at 359 nm and the most intense emission band at 384 nm (Stokes shift of  $1813 \text{ cm}^{-1}$ ).



**Figure 5.21- UV-Vis spectrum (blue line) and emission spectrum after excitation at 336nm (red line) of Pyrene-H. All spectra were recorded in spectrophotometric grade DCM.**

Excitation of Pyrene-H (and all pyrene complexes) at the emission band wavelength, 384 nm, results in the generation of an excitation spectrum, almost identical to the UV-Vis spectrum.



**Figure 5.22- Excitation spectrum of Pyrene-H upon excitation into the emission band at 384 nm. Spectrum was recorded in spectrophotometric grade DCM.**

**Photocatalytic Hydrogen Generation Experiments.** Unfortunately no H<sub>2</sub> was detected in the headspace of any of the vials during the photocatalytic experiments. Low TONs of H<sub>2</sub> production have been reported for Pt and Pd catalytic systems which are similar to those reported in this study. The reasons for the lack of hydrogen produced by these intermolecular systems are at present not clear, however, it is proposed that either no H<sub>2</sub> has been produced photochemically or the amount produced was below the limit of detection for our instrument. The lifetime (of the ns order) of the pyrene ligands is however rather short and without a covalent pathway present electron transfer from the photosensitiser to the catalytic centre may be inefficient. In addition the regeneration of the pyrene by the sacrificial agents may be problematic, both from the energetics point of view and the aggressive nature of the radicals formed from TEA during the regenerating process. Importantly it is also worth stating that the limit of detection of the GC used is <100 ppm. Sakai *et al.*<sup>12</sup> have utilised an intramolecular Ru-Pt bimetallic system (Fig. 5.7) which can photocatalytically generate H<sub>2</sub> TONs of 5 after 10 hours of irradiation. The catalytic centre is a platinum dichloride group, similar to the PtCl<sub>2</sub>(DMSO)<sub>2</sub> complex utilised in the experiments in section 5.3.4. The authors have attributed the low TON numbers to the formation of platinum colloids which interfere with the catalytic process. During this study, observation of the sample vials after irradiation for 20 hours revealed a small amount of dark solid was present in the sample vials which could be indicative of the formation of platinum and palladium colloids during these experiments also. It has been generally noted that intermolecular H<sub>2</sub> generation is less efficient than intramolecular H<sub>2</sub> production as the efficiency depends upon interactions between molecules which are free in solution rather than a direct bond between the photosensitiser and catalytic centre, ensuring that electron transfer can occur at a higher rate. Hosono *et al.*<sup>14</sup> have reported the use of a platinum catalyst for the intermolecular generation of H<sub>2</sub>. Thin films of two viologen linked porphyrins (Fig. 5.9), in the presence of a H<sub>2</sub>PtCl<sub>2</sub> catalyst and EDTA as a sacrificial agent have produced hydrogen intermolecularly from water achieving TON of 5.2 and 16.8 each after 280 hours of irradiation with visible light (720 nm < λ > 390 nm). A porphyrin-pyrene conjugate functionalised Pt nano composite (Fig. 5.11) has been reported to generate TONs up to 63 following 12 hours irradiation using broad band UV-Vis

light in the presence of EDTA.<sup>16</sup> The H<sub>2</sub> gas produced was measured using a GC coupled with a TCD detector, similar to the instrument used in this proposal. The pyrene utilised as a photosensitiser in these experiments is similar to the chromophores used in this study however direct conjugation of the porphyrin-Pt catalytic centre is reported in these complexes through a hydrogen bonding interface allowing electron transfer to occur more readily.

## 5.5. Conclusion

This chapter discussed the synthesis, characterisation and photochemistry extended pyrene complexes and platinum and palladium dichloride catalytic centres. All synthesised complexes were characterised using  $^1\text{H}$  NMR, UV-Vis spectroscopy and fluorescence spectroscopy and compared well to literature.<sup>23,24</sup>

The UV-vis spectra of the ligands show strong absorbances in the UV-Vis region of the spectrum. This indicates ligand localised  $\pi$ -  $\pi^*$  transitions.<sup>23</sup> The extension of the conjugation, due to addition of an alkynyl bridging group, lead to a red shift in the  $\lambda_{\text{max}}$  absorbances in the complexes. Incorporation of a thiophene group further extends the  $\pi$ -conjugation inducing a  $\sim 20$  nm bathochromic shift in absorbances pushing them out towards the visible region.

Pyrene-TMS and Pyrene-H exhibit sharp but unresolved emission bands at  $\sim 384$  nm and  $405$  nm. A weaker shoulder is also observed at  $\sim 425$  nm. Only a slight shift of  $\sim 2$  nm is observed in the wavelength of these emission bands indicating that the same excited state is responsible for the observed emission in each case. Excitation of Pyrene-Thio-Br results in the appearance of two broad emission bands at  $404$  nm and  $425$  nm. This represents a bathochromic shift of  $\sim 20$  nm to lower energy wavelengths. This may be explained due to the increased conjugation due to the thiophene unit altering the HOMO-LUMO energy gap. Excitation of all pyrene complexes at the strongest emission band wavelength resulted in the generation of an excitation spectrum, almost identical to the UV-Vis spectrum.

Although no  $\text{H}_2$  was detected during the photocatalytic  $\text{H}_2$  generation experiments, the production of  $\text{H}_2$  cannot be definitively eliminated as the LOD of the detector in the GC is high. Low TONs of  $\text{H}_2$  production have been measured and reported in the literature.<sup>12,14,16</sup> As the photosensitiser is not directly bound to the catalytic centre, the reliance on interactions of the components in solution and/or the formation of platinum/palladium colloids may explain the low efficiency of the pyrene-Pt/Pd systems studied.

## Bibliography

---

- <sup>1</sup> A. C. Benniston, A. Harriman, D. J. Lawrie, A. Mayeux, K. Rafferty, *Dalton Trans.*, **2003**, 4762.7.
- <sup>2</sup> Paul, F.; Lapinte, C. *Coord. Chem. Rev.*, **1998**, 178.
- <sup>3</sup> E. O. Danilov, I. E. Pomestchenko, S. Kinayyigit, P. L. Gentili, M. Hissler, R. Ziessel, F. N. Castellano, *J. Phys. Chem. A*, **2005**, 109, 2465.
- <sup>4</sup> S. Chakraborty, T. J. Wadas, H. Hester, R. Schmehl, R. Eisenberg, *Inorg. Chem.*, **2005**, 44, 6865.
- <sup>5</sup> S. Leroy-Lhez, F. Fages, *C. R. Chimie*, **2005**, 8, 1204.
- <sup>6</sup> S. Leroy-Lhez, A. Parker, P. Lapouyade, C. Belin, L. Ducasse, J. Oberlè , F. Fages, *Photochem. Photobiol. Sci.*, **2004**, 3, 949.
- <sup>7</sup> Y. Li, D. Wanga, L. Wanga, Z. Li a, Q. Cui, H. Zhang, H. Yang, *J. Lumin.*, **2012**, 132, 1010.
- <sup>8</sup> A. Harriman, M. Hissler, R. Ziessel, *Phys. Chem. Chem. Phys.*, **1999**, 1, 4203.
- <sup>9</sup> A. Harriman, G. Izzet, R. Ziessel, *J. Am. Chem. Soc.*, **2006**, 128, 10868.
- <sup>10</sup> M. Sukuki, S. Kobayashi, S. Uchida, M. Kimura, K. Hanabusa, H. Shirai, *Polymer*, **1998**, 39, 1539.
- <sup>11</sup> N. Toshima, K. Harakawa, *Appl. Surf. Sci.*, **1997**, 121, 534.
- <sup>12</sup> H. Ozawa, M. Haga, K. Sakai, *J. Am. Chem. Soc.*, **2006**, 128, 4926.
- <sup>13</sup> S. Rau, B. Schafer, D. Gliet, E. anders, M. Rudolf, M. Friedrich, H. Gorts, W. Henry, J. G. Vos, *Angew. Chem. Int. Ed.*, **2006**, 45, 6215.



- 
- <sup>14</sup> H. Hosono, M. Kaneko, *J. Chem. Soc. Faraday Trans.*, **1997**, 97, 7, 1313- 1319.
- <sup>15</sup> Q. Li, L. Chen, G. Lu, *J. Phys. Chem. C*, **2007**, 111, 11494.
- <sup>16</sup> M. Zhu, Y. Lu, Y. Du, J. Li, X. Wang, P. Yang, *Int. J. Hydrogen Energ.*, **2011**, 36, 4298.
- <sup>17</sup> L. L. Tinker, N. D. McDaniel, P. N. Curtin, C. K. Smith, M. J. Ireland, S. Bernhard, *Chem.–Eur. J.*, **2007**, 13, 8726.
- <sup>18</sup> J.M. Lehn, J. P. Sauvage, *Nouv. J. Chim.*, **1977**, 1, 449.
- <sup>19</sup> P.N. Curtin, L. L. Tinker, C. M. Burgess, E. D. Cline, S. Bernhard, *Inorg. Chem.*, **2009**, 48, 10498.
- <sup>20</sup> S. Soman, G. Singh Bindra, A. Paul, R. Groarke, J. C. Manton, F. M. Connaughton, M. Schulz, D. Dini, C. Long, M. T. Pryce, J. G. Vos, *Dalton Trans.*, **2012**, 41, 12678.
- <sup>21</sup> K. Sonogashira, Y. Tohda, N. Hagihara. *Tetrahedron Lett.*, **1975**, 16, 50, 4467.
- <sup>22</sup> B.T. Holmes, W.T. Pennington, T. W. Hawkes, *Molecules* **2002**, 7, 447.
- <sup>23</sup> A. C. Benniston, A. Harriman, D. J. Lawrie, S. A. Rostron, *Tetrahedron Lett.*, **2004**, 45, 2503.
- <sup>24</sup> A. Coleman, *Ph. D. Thesis*, **2008**, Dublin City University.

## **Chapter 6**

### **Concluding Remarks and Future Work**

This chapter presents the overall conclusions of this thesis and also suggests future work which could advance the understanding of the photochemical and electrochemical process occurring throughout the various chapters.

In this thesis a range of compounds, some novel, were synthesised and assessed for their ability to produce hydrogen both photocatalytically and electrocatalytically.

Chapters 2, 3 and 4 were concerned with measuring the electrocatalytic efficacy of cobalt based systems with regards to the H<sub>2</sub> generating process. Key performance indicators in this process were discussed including the onset of catalytic current, TON of H<sub>2</sub> generation, current density and the Faradaic efficiency at the applied potentiostatic potential (-1.2 V). While all complexes studied displayed catalytic activity for proton reduction in acidic media the largest TON was produced by 3-pyridine-BODIPY-cobaloxime, at  $16.5 \times 10^3$ , at an applied potential of -1.2 V for 1 hour. The earliest onset of catalytic current was measured at -0.8 V, produced using electrodes modified with 4-pyridine-BODIPY-cobaloxime. As the number of moles of “active” catalyst on the surface could not be accurately measured, the TONs quoted are expected to be an order of magnitude lower than the actual figures which make the results comparable with most of the systems which have been published to date, however improvements on calculating the active catalyst for future studies is paramount. Different approaches to thin film of catalyst formation on the electrode surface have been suggested and including electrodeposition and spin coating rather than the dropcast method used in this study. The utilisation of these methods may further improve the amount of active catalyst on the electrode surface due to more homogeneous deposition of catalyst.

The results from chapter 2 suggested that all four Co<sub>2</sub>(CO)<sub>6</sub> derivatives are less efficient in proton reduction, possibly due to decomposition of the complex during the bulk electrolysis experiment. This decomposition was also noted during the solution cyclic voltammogram experiments. Addition of DPPM to the cobalt carbonyl complex, producing Co<sub>2</sub>(CO)<sub>4</sub>DPPM derivatives, increased the stability of the complexes, improving their electrocatalytic properties. Upon utilisation of a cobaloxime catalytic centre in chapter 3 and 4 an earlier onset in the catalytic current was observed for all complexes when compared with the cobalt carbonyl complexes and thus the cobaloxime derivatives produce higher TONs of H<sub>2</sub> production at an applied potential of -1.2 V. Electrocatalytic studies in chapter 4 also indicated the ability of metal free complexes to catalyse the proton reduction process; in fact the metal free complexes produced higher TONs than their cobaloxime counterparts.

With a view to generate higher TONs of hydrogen (both photocatalytically and electrocatalytically), the synthesis of the BODIPY and porphyrin ligands which are

fully substituted on the periphery through the introduction of electron withdrawing groups, such as F or CN groups, similar to the work of Nepomnyashchii et al,<sup>1</sup> proves a promising prospect. It is proposed that these additions would shift the onset of the catalytic current during electrocatalytic H<sub>2</sub> generation studies to more anodic potentials, thus using less energy to reduce the complexes and produce H<sub>2</sub> more efficiently. Work by Hariprasad et al.<sup>2</sup> exhibited that through incorporating Br groups at both the *meso* and  $\beta$  positions of the porphyrin ring the reduction processes are shifted to significantly less negative potentials. This would further decrease the overpotential required for electrocatalytic H<sub>2</sub> production. The introduction of alkynyl groups at the boron centre in BODIPY complexes has also been shown to have a similar effect on the redox potentials of BODIPY complexes.<sup>3</sup> Further synthesis extending the conjugation of the systems at the boron group, for instance with alkynylpyrene groups, would not only shift potential for electrocatalytic H<sub>2</sub> production anodically but would also further red-shift the absorbance profile of the complexes facilitating photocatalytic H<sub>2</sub> generation using visible light.

Future work would include optimisation of the electrocatalytic study's experimental setup. To eliminate any interference of products formed at the counter electrode usage of a H shaped cell is proposed. This set-up would include a salt bridge between the working and counter electrodes which would not allow passage of products from one side of the cell to the other; however it would allow the efficient passage of charge. During experimentation it was noted that a build-up of hydrogen bubbles on the electrode hinders the catalytic efficiency of the cell as the film on the electrode surface is no longer in contact with the buffer solution. Agitation of the bulk solution through stirring could stop the build-up of these bubbles allowing the constant flow of current from the working electrode. The pH of the buffer solution employed plays a large role in the overall efficacy of the systems. Employing lower pH buffers may induce larger quantities of hydrogen to be produced during experiments. Light may also have an effect on the overall number of moles of hydrogen produced during an experiment. Future work would include performing the experiments in complete darkness or under a visible light lamp which would allow for uniform irradiation. When calculating the number of moles of hydrogen produced, standard atmospheric pressure is assumed in the headspace of the cell. This pressure is not necessarily accurate, due to the collection of H<sub>2</sub> in this

headspace, therefore precise measurement of this pressure would need to be quantified.

Stability studies of the complexes synthesised should be performed to determine the optimum length of catalytic cycle ble in the generation of hydrogen both photocatalytically and electrocatalytically. Varying the length of each experiment and measuring H<sub>2</sub> generated at a variety of time points would lead to the evolution of a stability profile detailing any induction period or plateau at which hydrogen is no longer generated.

For any of the complexes studied no hydrogen was observed in the gas chromatography measurements as produced photocatalytically, although optimisation of the experimental parameters may improve the number of moles of hydrogen produced. Varying the concentration of catalyst and sacrificial agent (TEA) may lead to a more efficient system. Increasing the amount of water in the reaction vial may also lead to a higher yield of hydrogen also. The wavelength of light used during the irradiation could be varied and the light used could be tailored to promote the transfer of electrons from the photosensitiser to the catalytic centre.

## Bibliography

---

<sup>1</sup> A. B. Nepomnyashchii, S. Cho, P. J. Rossky, A. J. Bard, *J. Am. Chem. Soc.*, **2010**, 132, 17550.

<sup>2</sup> G. Hariprasad, S. Dahal, B. G. Maiya, *J. Chem. Soc. Dalton Trans.*, **1996**, 3429.

<sup>3</sup> J. Suk, K. M. Omer, T. Bura, R. Ziessel, A. J. Bard, *J. Phys. Chem. C*, **2011**, 115, 15361.

## Appendix:

### A1: Quantum Yield Method

All quantum yields were carried out using a liquid-phase potassium ferrioxalate actinometer. The actinometer was prepared by mixing three volumes of 1.5 M  $\text{K}_2\text{C}_2\text{O}_4$  solution with one volume of 1.5 M  $\text{FeCl}_3$  solution in water, and stirring in complete darkness. The precipitated  $\text{K}_3\text{Fe}(\text{C}_2\text{O}_4)_3 \cdot 3\text{H}_2\text{O}$  was then recrystallised three times from hot water and dried in a current of warm air. To prepare 1 L of 0.006M  $\text{K}_3\text{Fe}(\text{C}_2\text{O}_4)_3 \cdot 3\text{H}_2\text{O}$  solution, 2.947 g of the precipitate was dissolved in 800 ml water, 100 ml 1.0 N sulphuric acid was added and filled to the mark with water, again in complete darkness. While the 0.15 M actinometric solution required 73.68 g of precipitate to be added to the same volumes of liquid. For all quantitative work the preparation and manipulation of the ferrioxalate solutions must be carried out in a darkroom, using a red photographic safelight. The light intensity in a photochemical reaction is determined by irradiating ferrioxalate solution and monitoring the subsequent change in absorbance at 510 nm. A carousel was used to house both the actinometer and sample cells so that they were equally exposed to a uniform amount of irradiation throughout the duration of each experiment. The carousel operated inside a black box to prevent any stray light reaching the sample or actinometer solutions. An autopipette was to ensure all volumes were accurately measured.

For each actinometric measurement a quartz cuvette was charged with 3 ml ( $V_1$ ) of ferrioxalate solution. The cell was placed in the carousel and irradiated for the time shown in the results section (A2). After the allocated irradiation time ( $t$ ), the solution was well mixed and an aliquot volume (0.5 ml,  $V_2$ ) was pipette into a volumetric flask (10 ml,  $V_3$ ). Buffer solution of volume equal to half the volume of photolyte placed in the flask was added (0.25 ml), so too was 2 ml phenanthroline solution (0.1 % by weight solution in water). The solution was diluted with distilled water to the volume mark ( $V_3$ ) and mixed well. The flask was wrapped in tinfoil and the solution was allowed

develop. After one hour, the absorbance of the solution was measured in a 1cm cell at 510 nm using a spectrophotometer using a blank iron free solution as a reference.

The number of  $\text{Fe}^{2+}$  ions ( $n_{\text{Fe}^{2+}}$ ) formed during photolysis can be calculated from:

$$n_{\text{Fe}^{2+}} = \frac{6.023 \times 10^{20} V_1 V_3 \log_{10} (I_0/I)}{V_2 l \epsilon}$$

where

$V_1$  = Volume of actinometer solution irradiated (ml)

$V_2$  = Volume of aliquot taken for analysis (ml)

$V_3$  = Final volume to which the aliquot  $V_2$  is diluted (ml)

$\log_{10} (I_0/I)$  = measured optical density of the solution

$l$  = path length of the spectrophotometer cell used (cm)

$\epsilon$  = experimental value of the molar extinction coefficient of  $\text{Fe}^{2+}$

complex, determined from the slope of the calibration plot (approx. equal to  $1.11 \times 10^4 \text{ l mol}^{-1} \text{ cm}^{-1}$ ).

The number of quanta absorbed by the actinometer ( $n_a$ ) per second is obtained from

$$n_a = n_{\text{Fe}^{2+}} / \Phi_\lambda t$$

where  $t$  is the time in seconds

$\Phi_\lambda$  is the quantum yield of  $\text{Fe}^{2+}$  formation.

For each sample under investigation, a solution of known concentration was prepared so that the optical density of each was  $0.3 \pm 0.1$  AU at 430 nm. A 10 % excess of triphenyl phosphine was used as a trapping ligand throughout the measurements and added to each solution immediately prior to irradiation. Each sample cuvette was accurately charged with 3 ml of the alkynyl dicobalthexacarbonyl / triphenylphosphine solution. The sample cell was placed in the carousel, along with the 3ml actinometric solutions in cells, and all were irradiated in parallel. The change in absorbance of the sample solution was measured at 430 nm to calculate the yield of CO loss that occurred.



Hexacarbonyl Complex	$\epsilon$ ( $M^{-1} \text{ cm}^{-1}$ ) at 430 nm
<b>1-ethynylpyrene <math>\text{Co}_2(\text{CO})_6</math></b>	2975
<b>Pyrene-ethynylferrocene <math>\text{Co}_2(\text{CO})_6</math></b>	3476
Photolytic substitution products	$\epsilon$ ( $M^{-1} \text{ cm}^{-1}$ ) at 430 nm
<b>1-ethynylpyrene <math>\text{Co}_2(\text{CO})_5\text{PPh}_3</math></b>	4491
<b>Pyrene-ethynylferrocene <math>\text{Co}_2(\text{CO})_5\text{PPh}_3</math></b>	6607

**Extinction coefficients of dicobalt hexacarbonyl complexes and corresponding pentacarbonyl complexes at 430 nm. All measurements were recorded in spectrophotometric grade heptane.**

## A2: Quantum Yield Calculations

### (a) Quantum yield determinations of CO loss for $[(\mu_2\text{-1-ethynylpyrene})\text{-Co}_2(\text{CO})_6]$ (**1**)

All values were measured at 430nm

Molar excitation coefficients at 430 nm

$(\mu_2\text{-1-ethynylpyrene})\text{-Co}_2(\text{CO})_6$  (**1**)       $2975 \text{ M}^{-1} \text{ cm}^{-1}$

$(\mu_2\text{-1-ethynylpyrene})\text{-Co}_2(\text{CO})_5(\text{PPh}_3)$        $4491 \text{ M}^{-1} \text{ cm}^{-1}$

#### *Irradiation of 1 at 313 nm (2 min)*

Absorbance of sample at 313nm = 0.2707

Increase in intensity of band at 430 nm = 0.028

Molar increase =  $4.78 \times 10^{-6}$  molar

Moles converted per second =  $3.98 \times 10^{-8}$  moles/s

For a  $3 \text{ cm}^3$  sample, number of molecules photolysed per second =  $7.2 \times 10^{13}$  molecules/s

#### *Change in absorbance of actinometer solution at 510 nm*

Absorbance at 510 nm = 0.281

Number of  $\text{Fe}^{2+}$  ions =  $9.23 \times 10^{16}$  ions

Using a quantum yield for  $\text{Fe}^{2+}$  production of 1.24 at 313 nm

Number of photons emitted by the source at 313 nm =  $7.4 \times 10^{16}$

Number of photons emitted per second by the source at 313 nm =  $6.2 \times 10^{14}$  photons/s

Absorbance of sample at 313nm = 0.2707

Therefore number of photons absorbed by the sample =  $2.85 \times 10^{14}$  photons/s

Quantum yield of photochemical reaction is  $(7.2 \times 10^{13}) / (2.85 \times 10^{14}) = 0.252$

#### *Irradiation of 1 at 365 nm (3 min)*

Absorbance of sample at 365nm = 0.320

Increase in intensity of band at 430 nm = 0.0538

Molar increase =  $1.3 \times 10^{-6}$  molar

Moles converted per second =  $7.2 \times 10^{-9}$  moles/s

For a  $3 \text{ cm}^3$  sample, number of molecules photolysed per second =  $1.3 \times 10^{13}$  molecules/s

*Change in absorbance of actinometer solution at 510 nm*

Absorbance at 510 nm = 0.0334

Number of  $\text{Fe}^{2+}$  ions =  $1.097 \times 10^{17}$  ions

Using a quantum yield for  $\text{Fe}^{2+}$  production of 1.21 at 365 nm

Number of photons emitted by the source at 365 nm =  $9.066 \times 10^{16}$

Number of photons emitted per second by the source at 365 nm =  $5.04 \times 10^{14}$  photons/s

Absorbance of sample at 365nm = 0.281

Therefore number of photons absorbed by the sample =  $2.62 \times 10^{14}$  photons/s

Quantum yield of photochemical reaction is  $(1.3 \times 10^{13}) / (2.62 \times 10^{14}) = 0.104$

***Irradiation of 1 at 405 nm (20 sec)***

Absorbance of sample at 405nm = 0.311

Increase in intensity of band at 430 nm = 0.0101

Molar increase =  $8.5 \times 10^{-7}$  molar

Moles converted per second =  $4.29 \times 10^{-8}$  moles/s

For a  $3 \text{ cm}^3$  sample, number of molecules photolysed per second =  $7.76 \times 10^{13}$  molecules/s

*Change in absorbance of actinometer solution at 510 nm*

Absorbance at 510 nm = 0.101

Number of  $\text{Fe}^{2+}$  ions =  $3.9 \times 10^{16}$  ions

Using a quantum yield for  $\text{Fe}^{2+}$  production of 1.14 at 405 nm

Number of photons emitted by the source at 405 nm =  $3.42 \times 10^{16}$

Number of photons emitted per second by the source at 405 nm =  $1.71 \times 10^{15}$  photons/s

Absorbance of sample at 405nm = 0.311

Therefore number of photons absorbed by the sample =  $8.72 \times 10^{14}$  photons/s  
 Quantum yield of photochemical reaction is  $(7.76 \times 10^{13}) / (8.72 \times 10^{14}) = 0.089$

***Irradiation of 1 at 546 nm (20 sec)***

Absorbance of sample at 546nm = 0.2715

Increase in intensity of band at 430 nm = 0.57226

Molar increase =  $3.44 \times 10^{-6}$  molar

Moles converted per second =  $1.72 \times 10^{-7}$  moles/s

For a  $3 \text{ cm}^3$  sample, number of molecules photolysed per second =  $3.1 \times 10^{14}$  molecules/s

***Change in absorbance of actinometer solution at 510 nm***

Absorbance at 510 nm = 0.0249

Number of  $\text{Fe}^{2+}$  ions =  $4.9 \times 10^{16}$  ions

Using a quantum yield for  $\text{Fe}^{2+}$  production of 0.15 at 546 nm

Number of photons emitted by the source at 546 nm =  $3.3 \times 10^{17}$

Number of photons emitted per second by the source at 546 nm =  $1.63 \times 10^{16}$  photons/s

Absorbance of sample at 546nm = 0.2707

Therefore number of photons absorbed by the sample =  $7.58 \times 10^{15}$  photons/s

Quantum yield of photochemical reaction is  $(3.1 \times 10^{14}) / (7.58 \times 10^{15}) = 0.041$

**(b) Quantum yield determinations of CO loss for  $[(\mu_2\text{-pyrene-ethynylferrocene})\text{-Co}_2(\text{CO})_6]$  (2)**

Molar excitation coefficients at 430 nm

$(\mu_2\text{-pyrene-ethynylferrocene})\text{-Co}_2(\text{CO})_6$  (2)  $3476 \text{ M}^{-1} \text{ cm}^{-1}$

$(\mu_2\text{-pyrene-ethynylferrocene})\text{-Co}_2(\text{CO})_5(\text{PPh}_3)$   $6607 \text{ M}^{-1} \text{ cm}^{-1}$

***Irradiation of 2 at 313 nm (3 min)***

Absorbance of sample at 313nm = 0.315

Increase in intensity of band at 430 nm = 0.0384

Molar increase =  $1.5 \times 10^{-6}$  molar

Moles converted per second =  $6.39 \times 10^{-9}$  moles/s

For a  $3 \text{ cm}^3$  sample, number of molecules photolysed per second =  $1.15 \times 10^{13}$  molecules/s

*Change in absorbance of actinometer solution at 510 nm*

Absorbance at 510 nm = 0.1758

Number of  $\text{Fe}^{2+}$  ions =  $5.46 \times 10^{17}$  ions

Using a quantum yield for  $\text{Fe}^{2+}$  production of 1.24 at 313 nm

Number of photons emitted by the source at 313 nm =  $4.41 \times 10^{17}$

Number of photons emitted per second by the source at 313 nm =  $2.45 \times 10^{15}$  photons/s

Absorbance of sample at 313nm = 0.315

Therefore number of photons absorbed by the sample =  $1.48 \times 10^{14}$  photons/s

Quantum yield of photochemical reaction is  $(1.15 \times 10^{13}) / (1.48 \times 10^{14}) = 0.078$

***Irradiation of 2 at 365 nm (2 min)***

Absorbance of sample at 365nm = 0.357

Increase in intensity of band at 430 nm = 0.137

Molar increase =  $1.597 \times 10^{-6}$  molar

Moles converted per second =  $1.33 \times 10^{-8}$  moles/s

For a  $3 \text{ cm}^3$  sample, number of molecules photolysed per second =  $2.4 \times 10^{13}$  molecules/s

*Change in absorbance of actinometer solution at 510 nm*

Absorbance at 510 nm = 0.00972

Number of  $\text{Fe}^{2+}$  ions =  $3.19 \times 10^{16}$  ions

Using a quantum yield for  $\text{Fe}^{2+}$  production of 1.21 at 365 nm

Number of photons emitted by the source at 365 nm =  $2.636 \times 10^{16}$

Number of photons emitted per second by the source at 365 nm =  $2.2 \times 10^{14}$  photons/s

Absorbance of sample at 365nm = 0.357

Therefore number of photons absorbed by the sample =  $1.23 \times 10^{14}$  photons/s  
Quantum yield of photochemical reaction is  $(2.4 \times 10^{13}) / (1.23 \times 10^{14}) = 0.195$

*Irradiation of 2 at 405 nm (20 sec)*

Absorbance of sample at 405nm = 0.323

Increase in intensity of band at 430 nm = 0.1256

Molar increase =  $1.56 \times 10^{-6}$  molar

Moles converted per second =  $7.8 \times 10^{-8}$  moles/s

For a 3 cm<sup>3</sup> sample, number of molecules photolysed per second =  $1.408 \times 10^{14}$  molecules/s

*Change in absorbance of actinometer solution at 510 nm*

Absorbance at 510 nm = 0.0611

Number of Fe<sup>2+</sup> ions =  $4.8 \times 10^{16}$  ions

Using a quantum yield for Fe<sup>2+</sup> production of 1.14 at 405 nm

Number of photons emitted by the source at 405 nm =  $4.21 \times 10^{16}$

Number of photons emitted per second by the source at 405 nm =  $2.1 \times 10^{15}$  photons/s

Absorbance of sample at 405nm = 0.311

Therefore number of photons absorbed by the sample =  $1.12 \times 10^{15}$  photons/s

Quantum yield of photochemical reaction is  $(1.408 \times 10^{14}) / (1.12 \times 10^{15}) = 0.126$

*Irradiation of 2 at 546 nm (1 min)*

Absorbance of sample at 546nm = 0.

Increase in intensity of band at 430 nm = 0.609

Molar increase =  $2.5 \times 10^{-5}$  molar

Moles converted per second =  $3.5 \times 10^{-7}$  moles/s

For a 3 cm<sup>3</sup> sample, number of molecules photolysed per second =  $6.3 \times 10^{14}$  molecules/s

*Change in absorbance of actinometer solution at 510 nm*

Absorbance at 510 nm = 0.0478

Number of  $\text{Fe}^{2+}$  ions =  $1.57 \times 10^{17}$  ions

Using a quantum yield for  $\text{Fe}^{2+}$  production of 0.15 at 546 nm

Number of photons emitted by the source at 546 nm =  $1.047 \times 10^{18}$

Number of photons emitted per second by the source at 546 nm =  $1.74 \times 10^{16}$  photons/s

Absorbance of sample at 546nm = 0.2707

Therefore number of photons absorbed by the sample =  $6.35 \times 10^{15}$  photons/s

Quantum yield of photochemical reaction is  $(6.3 \times 10^{14}) / (6.35 \times 10^{15}) = 0.099$

## **B1: Photocatalytic Hydrogen Turnover Number Experiment**

All hydrogen turnover number measurements were carried out using a Varian cp-3800 gas chromatography utilising a thermal conductivity detector coupled with a flame ionisation detector. All solvents used were dried and deaerated before use and all solutions prepared were prepared under Schlenk methods. ACN was distilled over  $\text{CaH}_2$  before use. Water used was deionised. Triethylamine was distilled over NaOH before use.

$5 \times 10^{-5}$  M solutions of the catalysts/ photosensitisers were prepared in completely dry and deaerated ACN. 1.2 ml of the catalyst/ photosensitiser solution, 0.2 ml (10%)  $\text{H}_2\text{O}$  and 0.6 ml (30%) TEA were added to a suitable gas tight vial and irradiated at various (350 nm or 470 nm) wavelengths for an average of 20 hours. Alternatively for the 0% water experiments 0.2 ml of ACN was added to replace the water. After the allocated time passed 250  $\mu\text{L}$  of the headspace in the vial was injected onto the GC and the area of the peak which corresponds to  $\text{H}_2$  was recorded.

For the photolysis reaction in acetonitrile, the septa capped deoxygenated photolysis reaction vial (5 ml full volume) containing 3 ml of the reaction solution was used. The solutions were photolysed using a blue light (470 nm) or UV light (350 nm) LED light arrays shown in Fig A1. After 20 h photolysis time, the amount of hydrogen produced was measured by gas chromatography using gas tight syringe. Samples of the syringe (250  $\mu\text{L}$ ) were injected into a series CP-3800 Gas Chromatograph equipped with a 5 Å molecular sieves column and polymer supported silica column purchased from Varian Inc (UK) using ultra-high purity nitrogen as the carrier gas. The signals were amplified with a Varian Star Workstation Chromatography Data system. The system was calibrated for hydrogen signal sensitivity by hydrogen standard measurements. The total amount of hydrogen produced in a photolysis experiment was obtained by the sum of hydrogen found in the gas phase (hydrogen found in the solution phase was assumed to be negligible).



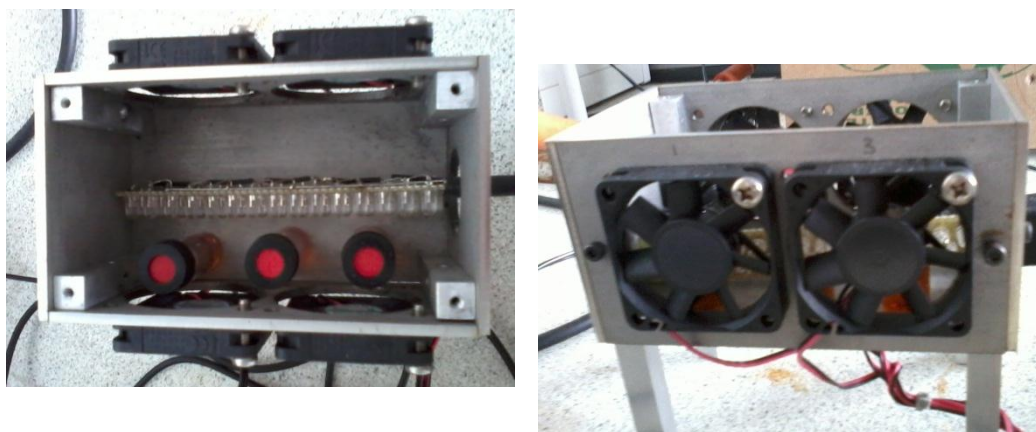


**Figure A1 - Irradiation chamber used for photocatalytic experiments. LED strip of lights is place in the chamber equidistant from the sample vials and the four fans keep the chamber cool to insure that the reaction occuring is not thermocatalytic.**

A range of catalysts and photosensitisers have been tested for H<sub>2</sub> production both intermolecularly and intramolecularly. By varying the combination of photosensitiser and catalyst it was hoped to illucidate the optimum combination which would yield the highest TONs.

## B2: Photocatalytic Hydrogen Turnover Number Calculations

### (a): TON of Experiment 1

- To calculate the concentration (in ppm) of hydrogen generated:

$$\frac{\text{Average Area of H}_2 \text{ Peak}}{x} = \frac{\text{Area of standard H}_2}{\text{Conc. in ppm of H}_2}$$

Therefore

$$\frac{5.09}{x} = \frac{1.66}{1000 \text{ ppm}}$$
$$x = 3066.27 \text{ ppm}$$

- To calculate the number of moles of H<sub>2</sub> produced the ideal gas law is applied (PV= nRT):

P = (x (calculated above) / 1 x 10<sup>6</sup>) x 1 atm pressure in Pa.

V = Area of the headspace in the vial in m<sup>3</sup>.

n = Number of moles of H<sub>2</sub> produced.

R = 8.314 J/K<sup>-1</sup>mol<sup>-1</sup>

T = Room temperature ie. 298 K

Therefore:

$$n = \frac{((3066.27 \text{ ppm}/1 \times 10^6) \times 101325 \text{ Pa})(2.9 \times 10^{-6} \text{ m}^3)}{(8.314 \text{ m}^3 \text{ Pa K}^{-1}\text{mol}^{-1})(298\text{K})}$$

$$n = 3.637 \times 10^{-8} \text{ mol}$$

- TON:

$$\frac{\text{No. moles of H}_2 \text{ produced}}{\text{No. moles catalyst used}}$$

$$\text{Number of moles of catalyst used} = (5 \times 10^{-5})(1.2 \times 10^{-3}) = \mathbf{6.0 \times 10^{-8} \text{ mol}}$$

Therefore TON =

$$\frac{3.637 \times 10^{-8} \text{ moles}}{6.0 \times 10^{-8} \text{ moles}} = \mathbf{1}$$

## C1: Electrocatalytic Hydrogen Turnover Number (TON) Experiment

All electrocatalytic experiments were carried out in a 2 necked V-shaped electrochemical cell, using a glassy carbon working electrode with an area of  $0.07\text{cm}^2$ , a platinum wire counter electrode and a Ag/AgCl reference electrode filled with 3 M KCl (Fig. A2 ).

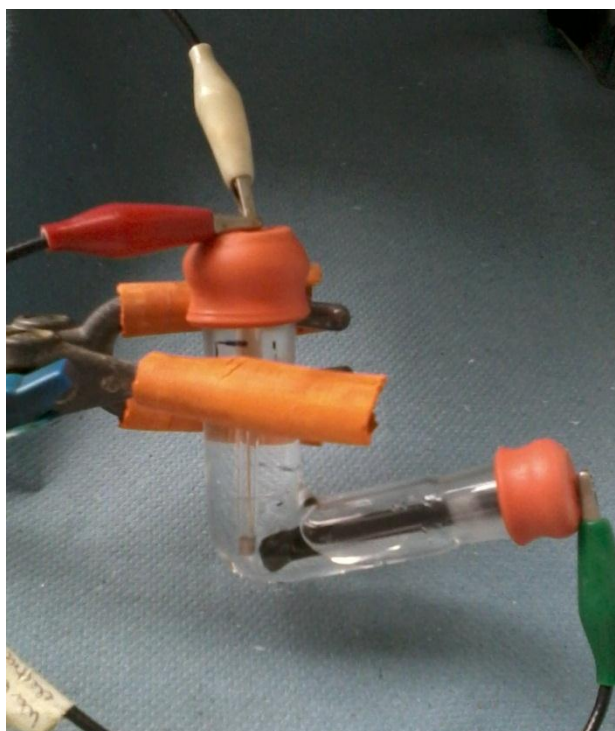


**Figure A2 - Electrocatalytic studies setup, green wire- glassy carbon working electrode, red wire- platinum counter electrode, white wire- Ag/AgCl reference electrode.**

A  $1 \times 10^{-4}$  M solution of each sample was prepared in dimethylformamide (DMF).  $1.5\ \mu\text{L}$  of this sample was then drop cast on the surface of the glassy carbon electrode and allowed to dry overnight in complete darkness. The V-shaped cell was filled with 15ml of 0.1 M  $\text{NaH}_2\text{PO}_4$  buffer at pH 2.0. The sample coated glassy carbon electrode, along with the platinum wire counter and Ag/AgCl reference electrodes, were placed into the cell and the cell was sealed with a suba-seal in each neck. The buffer was degassed with

BIP grade argon for 20 min. prior to each experiment. Bulk electrolysis experiments were carried out on each sample at varying potentials from -0.7 to -1.3 V.

## C2: Electrocatalytic Hydrogen Turnover Number Calculations

(a.) Calculation of number of moles of catalyst cast onto the gc electrode surface:

A  $1 \times 10^{-4}$  M solution of each sample was prepared and 1.5  $\mu$ L of these solutions was drop cast onto the gc surface. Therefore  $1.5 \times 10^{-10}$  moles sample was cast onto the electrode surface.

(b.) Electrochemical calculation of number of moles of H<sub>2</sub> produced:

After bulk electrolysis the current change ( $I_t$ ) over the duration of the experiment can be measured. According to Faraday's laws of electrolysis:

$$n = \left( \frac{I_t}{F} \right) \left( \frac{1}{z} \right)$$

$n$  = number of moles of H<sub>2</sub> produced.

$F$  = Faraday's constant (96485 C mol<sup>-1</sup>).

$z$  = the valency number of ions of the substance (electrons transferred per ion).

Therefore the number of moles of hydrogen produced for

(c.) Electrochemically determined H<sub>2</sub> generation TON:

$$\text{TON} = \frac{\text{No. moles of H}_2 \text{ produced}}{\text{No. moles catalyst used}}$$

(d.) GC determined H<sub>2</sub> generation TON:

As with the photocatalytic studies the GC was used to determine the electrocatalytic TON of H<sub>2</sub>.

**Example: TON of Experiment 1:**

3-pyridine-BODIPY modified electrode following bulk electrolysis at -1.2 V for 1 hour.

- Electrochemically determined H<sub>2</sub> TON:

Charge passed over 1 hour experiment = 0.1604 C

Faradays constant = 96485 C mol<sup>-1</sup>

z = 2e<sup>-</sup> needed to produce H<sub>2</sub>

Therefore:

$$\left( \frac{0.1604 \text{ C}}{96485 \text{ C mol}^{-1}} \right) \left( \frac{1}{2} \right) = 8.312 \times 10^{-7} \text{ moles}$$

TON =

$$\frac{8.312 \times 10^{-7} \text{ moles}}{1.5 \times 10^{-10} \text{ moles}} = 5541 = 5.5 \times 10^3$$

- GC determined H<sub>2</sub> TON:

$$\frac{\text{Average Area of H}_2 \text{ Peak}}{x} = \frac{\text{Area of standard H}_2 \text{ peak}}{\text{Conc. in ppm of H}_2 \text{ standard}}$$

Therefore

$$\frac{936.4}{x} = \frac{140}{1000 \text{ ppm}}$$

$$x = \mathbf{6648.81 \text{ ppm}}$$

- To calculate the number of moles of H<sub>2</sub> produced the ideal gas law is applied (PV= nRT):

P = partial pressure due to H<sub>2</sub> produced (x (calculated above) / 1x 10<sup>6</sup>) x 1 atm pressure in Pa.

V = Area of the headspace in the vial in m<sup>3</sup>.

n = Number of moles of H<sub>2</sub> produced.

R = Plank's constant = 8.314 J/K<sup>-1</sup>mol<sup>-1</sup>

T = Room temperature in K

Therefore:

$$n = \frac{((6648.81 \text{ ppm} / 1 \times 10^6) \times 101325 \text{ Pa})(2.9 \times 10^{-6} \text{ m}^3)}{(8.314 \text{ m}^3 \text{ Pa K}^{-1} \text{ mol}^{-1})(298 \text{ K})}$$

$$n = \mathbf{7.882 \times 10^{-7} \text{ mol}}$$

$$\text{TON: } \frac{\text{No. moles of H}_2 \text{ produced}}{\text{No. moles catalyst used}}$$

$$\frac{7.882 \times 10^{-7} \text{ moles}}{1.5 \times 10^{-10} \text{ moles}} = 5201 = 5.2 \times 10^3$$

- **Determining the Efficiency of the System:**

The efficiency of the system refers to the efficacy of the system to produce H<sub>2</sub> relative to the current passed during the experiment. This is measured by calculating the TON which has been determined using Faradays law of electrolysis, and comparing this result with the TON which has been calculated through injection of the headspace into the GC, measuring the actual number of moles of H<sub>2</sub> gas produced.

The efficiency =

$$\frac{\text{Electrochemically Determined TON}}{\text{GC Determined TON}} \times 100$$

e.g. 3-pyridine-BODIPY after bulk electrolysis at -1.2 V for 1 hour:

Electrochemically determined TON = 5541

GC determined TON = 5201

Therefore the efficiency of the system =

$$\frac{5541}{5201} \times 100 = 94\%$$

- **Determining Current Density:**

Current density is a measurement of the flow of current per unit area. During a bulk electrolysis experiment the average current throughout the experiment is measured. The area of the electrode surface has been measured to be 0.07 cm<sup>2</sup>.



Therefore the current density =

$$\frac{\text{Average Current During Bulk Electrolysis (mA)}}{\text{Area of Electrode Surface (cm}^2\text{)}}$$

e.g. 3-pyridine-BODIPY, bulk electrolysis at -1.2 V for 1 hour:

Average current during bulk electrolysis =  $3.429 \times 10^{-2}$  mA

Area of electrode =  $7 \times 10^{-2}$  cm<sup>2</sup>

Therefore current density =

$$\frac{3.429 \times 10^{-2} \text{ mA}}{7 \times 10^{-2} \text{ cm}^2} = 0.49 \text{ mA/cm}^2$$

## D1: $^1\text{H}$ NMR Spectra

### Chapter 2- $\mu_2$ -(alkyne)Cobalt Carbonyl Complexes

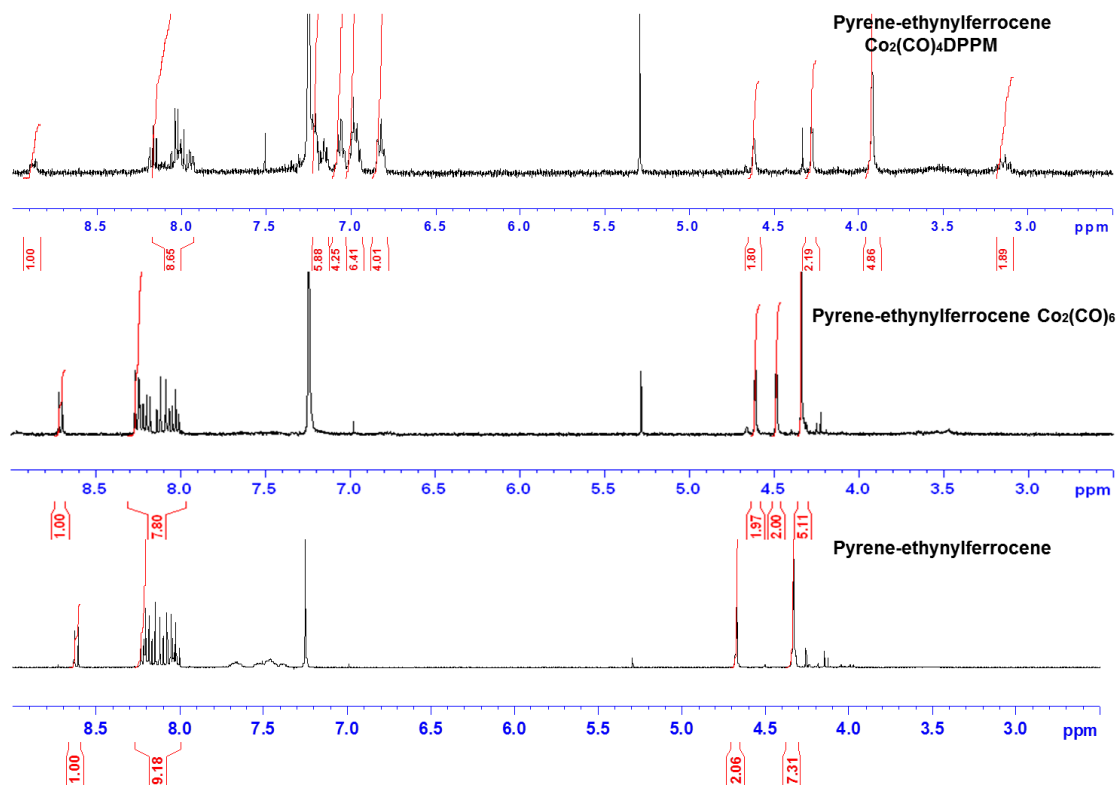


Figure A3:  $^1\text{H}$ NMR spectra of pyrene-ethynylferrocene,  $\mu^2$ - pyrene-ethynylferrocene  $\text{Co}_2(\text{CO})_6$  and  $\mu^2$ - pyrene-ethynylferrocene  $\text{Co}_2(\text{CO})_4\text{DPPM}$ . All spectra were recorded in deuterated chloroform ( $\text{CDCl}_3$ ).

### Chapter 3- BODIPY-Cobaloxime Complexes

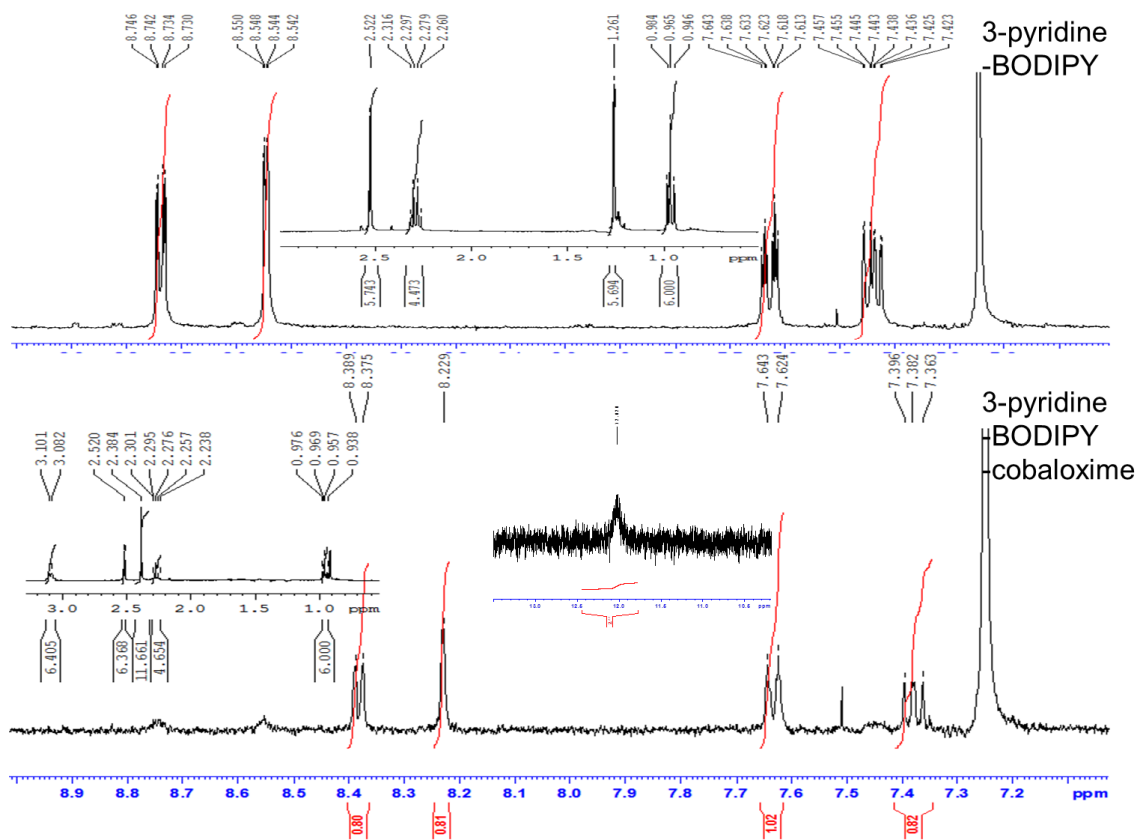
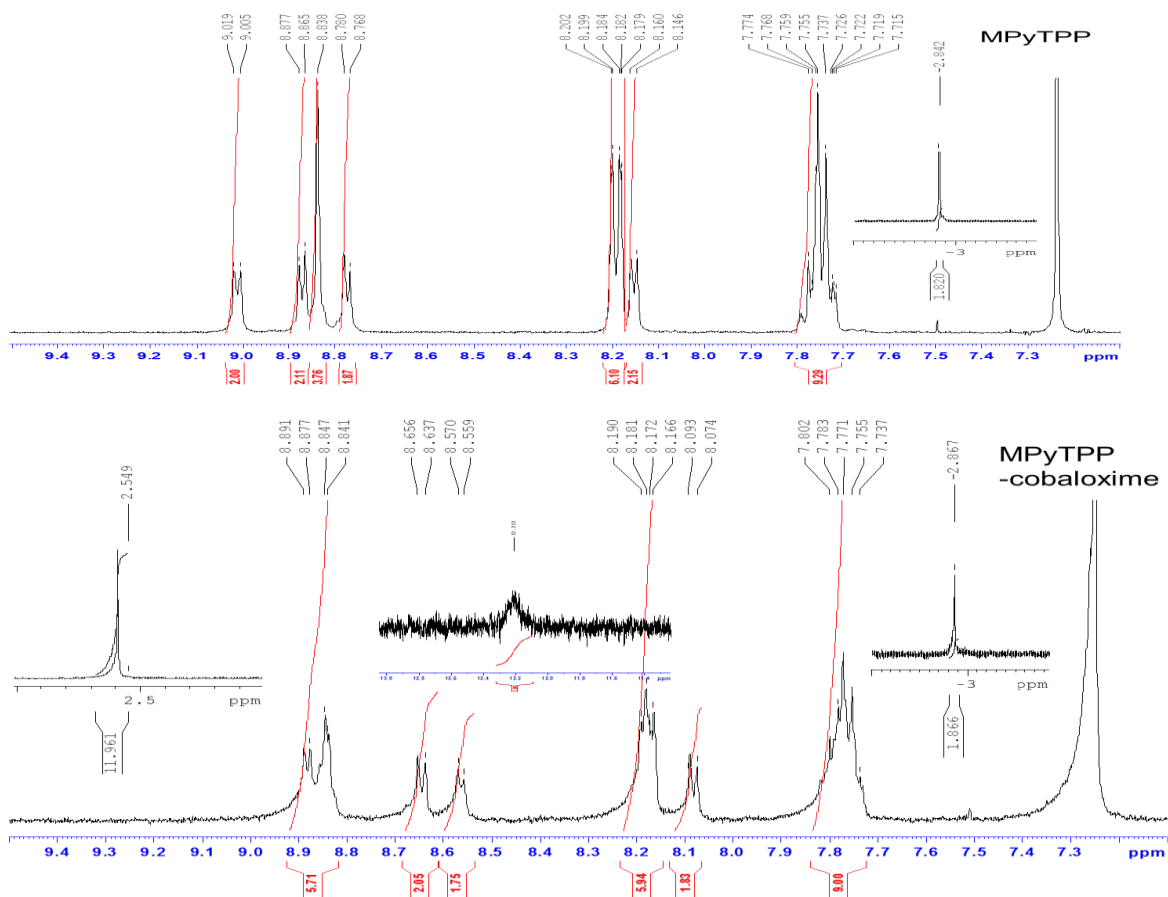


Figure A4- Comparison of <sup>1</sup>H NMR spectra of 3-pyridine-BODIPY and 3-pyridine-BODIPY-cobaloxime. Spectra were recorded in deuterated chloroform (CDCl<sub>3</sub>).

## Chapter 4- Porphyrin Complexes



**Figure A5- Comparison of  $^1\text{H}$ NMR spectra of MPyTPP and MPyTPP-cobaloxime. Spectra have been recorded in deuterated chloroform ( $\text{CDCl}_3$ ).**

## Chapter 5- Pt/Pd Systems

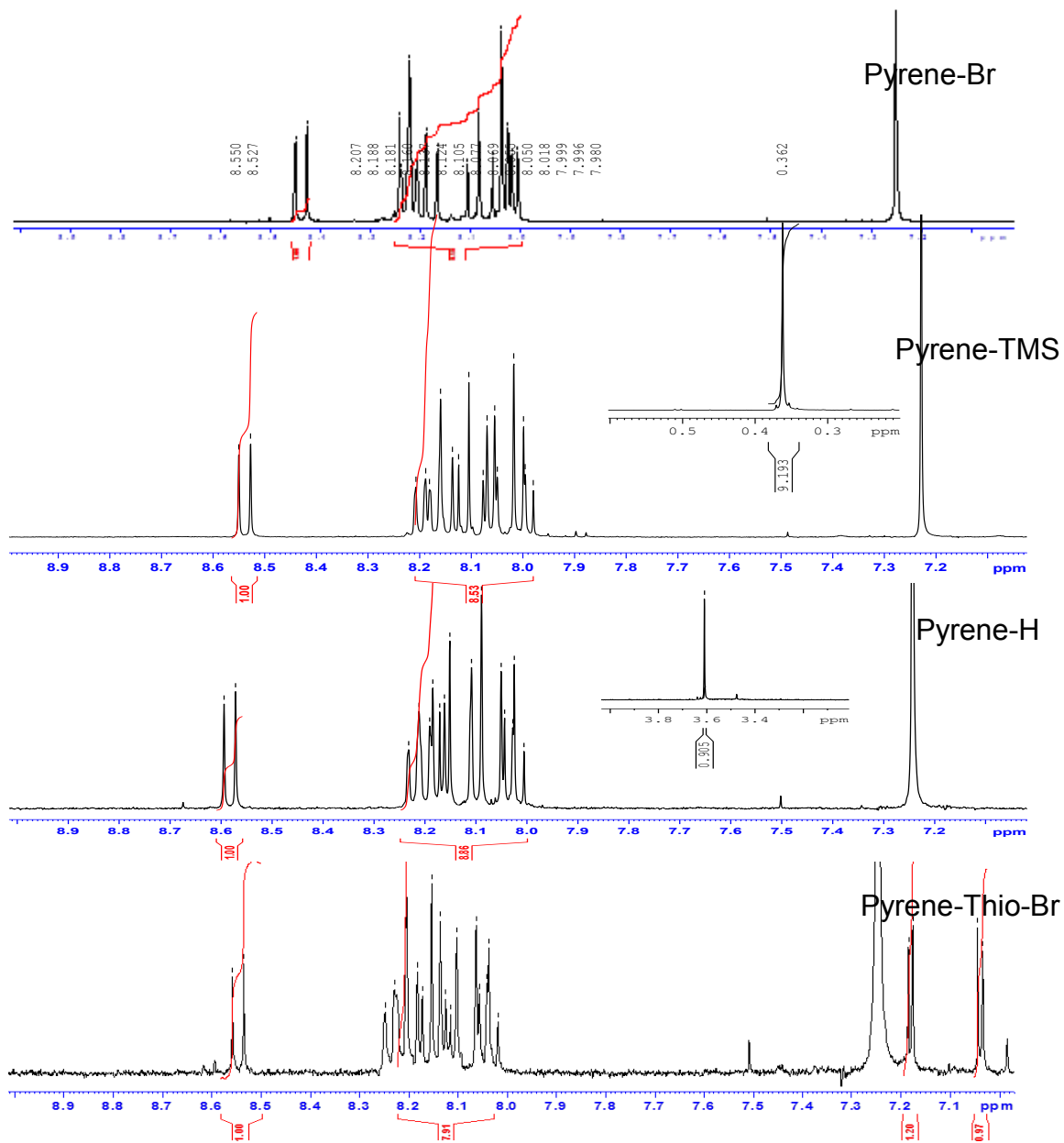


Figure A6- Comparison of  $^1\text{H}$ NMR spectra of extended pyrene complexes. Spectra have been recorded in deuterated chloroform ( $\text{CDCl}_3$ ).

# Excited State Dynamics and Activation Parameters of Remarkably Slow Photoinduced CO Loss from ( $\eta^6$ -Benzene)Cr(CO)<sub>3</sub> in *n*-Heptane Solution: A DFT and Picosecond-Time-Resolved Infrared Study

Ian P. Clark,<sup>†</sup> Michael W. George,<sup>‡</sup> Gregory M. Greetham,<sup>†</sup> Emma C. Harvey,<sup>§</sup> Conor Long,<sup>\*,§</sup> Jennifer C. Manton,<sup>§</sup> and Mary T. Pryce<sup>§</sup>

*School of Chemical Sciences, Dublin City University, Dublin 9, Ireland, Central Laser Facility, Science and Technology Facilities Council, Rutherford Appleton Laboratory, Harwell Science and Innovation Campus, Didcot, OX11 0QX, United Kingdom, and School of Chemistry, University of Nottingham, Nottingham, NG7 2RD, United Kingdom*

*Received: July 7, 2010; Revised Manuscript Received: August 27, 2010*

This text redacted due to 3rd party copyright  
This text redacted due to 3rd party copyright  
This text redacted due to 3rd party copyright  
This text redacted due to 3rd party copyright  
This text redacted due to 3rd party copyright  
This text redacted due to 3rd party copyright  
This text redacted due to 3rd party copyright  
This text redacted due to 3rd party copyright  
This text redacted due to 3rd party copyright  
This text redacted due to 3rd party copyright  
This text redacted due to 3rd party copyright  
This text redacted due to 3rd party copyright  
This text redacted due to 3rd party copyright  
This text redacted due to 3rd party copyright  
This text redacted due to 3rd party copyright  
This text redacted due to 3rd party copyright  
This text redacted due to 3rd party copyright  
This text redacted due to 3rd party copyright  
This text redacted due to 3rd party copyright  
This text redacted due to 3rd party copyright  
This text redacted due to 3rd party copyright

[illegible]

[illegible]



[illegible]

[illegible]

[illegible]

[illegible]

[illegible]

[illegible]

[illegible]

[illegible]



[illegible]

[illegible]

[illegible]

[illegible]

[illegible]


# Photochemistry of ( $\eta^6$ -Anisole)Cr(CO)<sub>3</sub> and ( $\eta^6$ -Thioanisole)Cr(CO)<sub>3</sub>: Evidence for a Photoinduced Haptotropic Shift of the Thioanisole Ligand, a Picosecond Time-Resolved Infrared Spectroscopy and Density Functional Theory Investigation

Ian P. Clark,<sup>†</sup> Michael W. George,<sup>§</sup> Gregory M. Greetham,<sup>‡</sup> Emma C. Harvey,<sup>†</sup> Conor Long,<sup>†,\*</sup> Jennifer C. Manton,<sup>†</sup> Hazel McArdle,<sup>†</sup> and Mary T. Pryce<sup>†</sup>

<sup>†</sup>School of Chemical Sciences, Dublin City University, Dublin 9, Ireland

<sup>‡</sup>Central Laser Facility, Science & Technology Facilities Council, Research Complex at Harwell, Rutherford Appleton Laboratory, Didcot, OX11 0QX, United Kingdom

<sup>§</sup>School of Chemistry, University of Nottingham, Nottingham, NG7 2RD, United Kingdom

 Supporting Information

This text redacted due to 3rd party copyright  
This text redacted due to 3rd party copyright  
This text redacted due to 3rd party copyright  
This text redacted due to 3rd party copyright  
This text redacted due to 3rd party copyright  
This text redacted due to 3rd party copyright  
This text redacted due to 3rd party copyright  
This text redacted due to 3rd party copyright  
This text redacted due to 3rd party copyright  
This text redacted due to 3rd party copyright  
This text redacted due to 3rd party copyright  
This text redacted due to 3rd party copyright  
This text redacted due to 3rd party copyright  
This text redacted due to 3rd party copyright  
This text redacted due to 3rd party copyright

[illegible]

[illegible]



[illegible]

[illegible]

[illegible]

[illegible]

[illegible]

[illegible]

[illegible]

[illegible]



Contents lists available at [SciVerse ScienceDirect](http://www.sciencedirect.com)

## Journal of Organometallic Chemistry

journal homepage: [www.elsevier.com/locate/jorganchem](http://www.elsevier.com/locate/jorganchem)

The synthesis, structural characterization and *in vitro* anti-cancer activity of novel N-{6-(ferrocenyl) ethynyl-2-naphthoyl} amino acid and dipeptide ethyl esters

Andy G. Harry<sup>a</sup>, James Murphy<sup>b</sup>, William E. Butler<sup>a,b</sup>, Rachel Tiedt<sup>b</sup>, Áine Mooney<sup>a,b</sup>, Jennifer C. Manton<sup>a</sup>, Mary T. Pryce<sup>a</sup>, Norma O'Donovan<sup>b</sup>, Naomi Walsh<sup>b</sup>, John Crown<sup>c</sup>, Dilip K. Rai<sup>d</sup>, Peter T.M. Kenny<sup>a,b,\*</sup>

<sup>a</sup> School of Chemical Sciences, Dublin City University, Dublin 9, Ireland

<sup>b</sup> National Institute for Cellular Biotechnology, Dublin City University, Dublin 9, Ireland

<sup>c</sup> Dept. of Medical Oncology, St. Vincent's University Hospital, Dublin 4, Ireland

<sup>d</sup> Dept. of Food Biosciences, Teagasc Food Research Centre, Ashtown, Dublin 15, Ireland

This text redacted due to 3rd party copyright  
This text redacted due to 3rd party copyright  
This text redacted due to 3rd party copyright  
This text redacted due to 3rd party copyright  
This text redacted due to 3rd party copyright  
This text redacted due to 3rd party copyright  
This text redacted due to 3rd party copyright  
This text redacted due to 3rd party copyright  
This text redacted due to 3rd party copyright  
This text redacted due to 3rd party copyright  
This text redacted due to 3rd party copyright  
This text redacted due to 3rd party copyright  
This text redacted due to 3rd party copyright  
This text redacted due to 3rd party copyright

0022-328X/\$ – see front matter © 2012 Elsevier B.V. All rights reserved.

<http://dx.doi.org/10.1016/j.jorganchem.2012.11.041>

Please cite this article in press as: A.G. Harry, et al., Journal of Organometallic Chemistry (2012), <http://dx.doi.org/10.1016/j.jorganchem.2012.11.041>

[illegible]

[illegible]

[illegible]

[illegible]

[illegible]

[illegible]